UNIVERSITY OF KENT

SCHOOL OF PHYSICAL SCIENCES

Symbiotic Supramolecular Chemistry – The Development of Smart Soaps

By

Lisa-Jane White

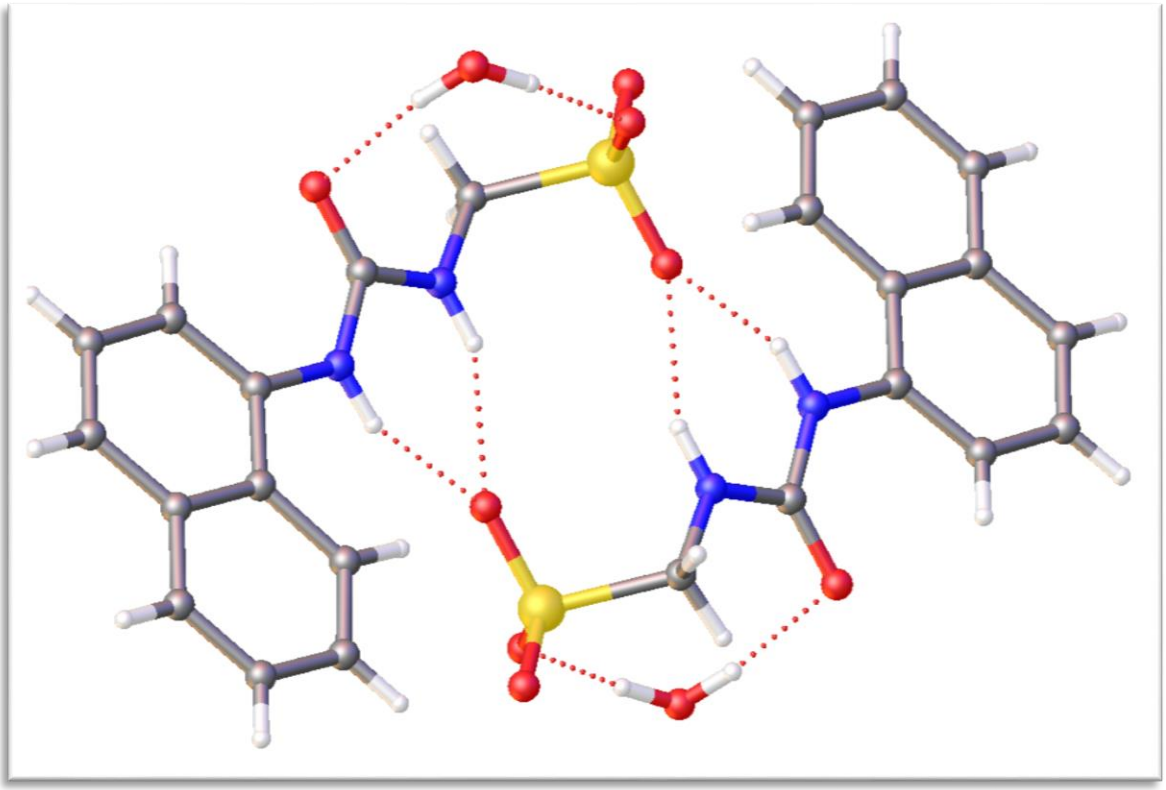

Thesis for the Masters of Science by Research

September 2017

UNIVERSITY OF KENT

ABSTRACT

SCHOOL OF PHYSICAL SCIENCES

Masters of Science by Research

SYMBIOTIC SUPRAMOLECULAR CHEMISTRY – THE DEVELOPMENT OF SMART SOAPS

By Lisa-Jane White

Supramolecular chemistry is continually being explored, applied and expanded in many countries all over the world. The complexity of this area of science means that it is continually researched.

This study has demonstrated the importance of the self-assembly between surfactants structures and supramolecular aggregation. Within this thesis the design, synthesis, characterization and binding properties of five amphiphilic molecules are discussed. These molecules were investigated in the gaseous phase, solid and solution states by a variety of complementary analytical techniques with the results demonstrating that the anionic monomers have a propensity to self-associate into a variety of aggregated species.

A selection of ^{1}H and DOSY NMR experiments were conducted in DMSO-d_6, providing evidence that these molecules tend to form dimeric rather than larger aggregated species. The presence of hydrogen bonding was further confirmed by ^{1}H NMR self-association studies, showing a down field change in chemical shift due to both the urea NH. The data when fitted to dimerization/Equal K (EK) binding model showed that the dimerization constant increases in line with the increase of aromatic substituents. By direct observation it was established that the sulfonate-anion molecules self-associated through intermolecular hydrogen bonds to form aggregated species of either irregular or spherical shape in solution. The size and type of these species was both concentration, and solute dependent. CMC values and dimerization constants correlated well with the computationally derived E_{max} and E_{min} values, giving preliminary evidence that self-association properties may be predicted by low level computational modelling methods. This innovative, cohesive branch of supramolecular chemistry will revolutionise the study and scope of non-covalent interactions beyond the molecule.

Table of Contents

Parts of this work has been published as:

"Towards quantifying the role of hydrogen bonding within amphiphile self-association and resultant aggregate formation" L.J. White, N.J. Wells, L.R. Blackholly, H.J. Shepherd, B. Wilson, G.P. Bustone, T.J. Runacres and J.R Hiscock, Chemical Science, 2017

Additional publication:

'Frustrated' hydrogen-bonded self-associated systems as templates towards DNA incorporated nanostructure formation. T.L. Gumbs, L.J. White, N.J. Wells, H.J. Shepherd and J.R. Hiscock, Supramolecular Chemistry, 2017

Acknowledgements

I would like to express my upmost thanks to my supervisor Dr Jennifer Hiscock for all of her help, support and endless guidance throughout the year. And I look forward to continuing my academic journey with you. I would also like to thank my second supervisor Dr Ewan Clark, for giving me the opportunity to study for my MSc Chem-R.

I would like to thank all the members of the Hiscock group for your advice, your friendship and for being there when 'science is being science'.

I would also like to thank the Army Research Office (US) for their funding.

I would like to express a huge thankyou to Helena Shephard, Neil Wells and Kevin Howland for your help with interpreting the single crystal-XRD, DOSY NMR and ESI-MS data.

And finally, my wonderful husband Paul who is not only supportive of my work, but is an amazing dad to our gorgeous boys and has been my rock throughout my academic journey.

Abbreviations

Å	Ángström
CDI	1,1'-Carbonyldiimidazole
CMC	Critical Micelle Concentration
d	Doublet (NMR)
DCM	Dichloromethane
DLS	Dynamic Light Scattering
DMSO	Dimethylsulfoxide
DNA	Deoxyribonucleic acid
FTIR	Fourier transform infra-red spectroscopy
HBA	Hydrogen bond acceptor
HBD	Hydrogen bond donator
hr	Hour
ESI-MS	Electron spray ionization- Mass Spectrometry
J	Coupling constant (NMR)
K_a	Association constant
LMWM	Low molecular weight monomers
m	Multiplet (NMR)
m.p	Melting point
m/z	Mass to charge ratio (Mass Spectroscopy)
NMR	Nuclear magnetic resonance spectroscopy
pka	Acid dissociation constant
ppm	Parts per Million
q	Quartet (NMR)
t	Triplet (NMR)
TBA	Tetrabutylammonium
TEA	Tetraethylammonium
TMA	Tetramethylammonium
UV-vis	Ultraviolet – visible spectroscopy
XRD	X-Ray diffraction
µL	Micro-litres

1. Introduction

First introduced by Jean-Marie Lehn in 1969 is the term supramolecular chemistry. Supramolecular chemistry is defined as chemistry 'beyond the molecule', and is the study of highly complex chemical systems that result from the association of two or more chemical entities that are held together by non-covalent intermolecular forces.[1] This field of chemistry has accomplished a fully identifiable place in the way todays scientists think about material chemistry where intermolecular bonding is extremely important yet astonishing subtle, but influential.

Supramolecular chemistry is still in its infancy, therefore is significantly under developed compared to that of the covalent bond,[2] which was discovered by American chemist Gilbert Lewis in 1913. Where he proposed a theory of 'valence' in the form of a dot structured diagram that identified the existence of two different types of bond. The polar (formed by the transfer of electrons) and the non-polar which did not involve electron transfer.[3] This field of molecular chemistry has developed substantially since its birth in 1828. The defining point being when, whilst conducting an experiment with ammonium cyanate Friedrich Wöhler contributed to the foundation of modern chemistry by unexpectedly accomplishing the first synthesis of urea crystals (Figure 1).[4]

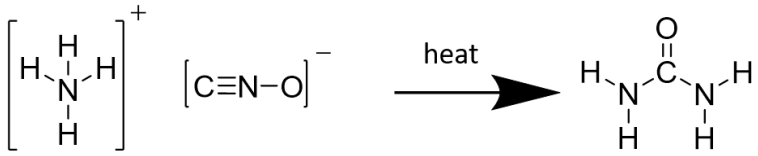

Figure 1 - Friedrich Wöhler's breakthrough synthesis of ammonium cyanate (inorganic compound) into urea crystals (organic compound).[4]

This discovery planted seeds of doubt with regard to Vitalism's scientific utility, "it was not possible to produce organic molecules from inorganic molecules".[5] Subsequently, from this point onwards a vast display of complex molecular structures, by a meticulous method of the assembly and breaking of covalent bonds between a series of atoms were established.

Supramolecular Chemistry was borne almost five decades later, when initially postulated by Johannes Diderik van der Waals, were the existence of 'intermolecular forces'.[6] Following this Emil Fisher coined the lock and key concept between enzymes and substrates,[7] which led to the notion for the recognition of the intermolecular interactions with proteins. This hypothesis subsequently led to a greater understanding for the essential design of drugs,[8] resulting in this field of chemistry being categorised as host-guest chemistry.

Following this, in the early twentieth century Latimer and Rodebush began to explore and progressively understand in more detail the non-covalent bond, in the form of the 'hydrogen bond'.[9] Consequently, due to their highly selective structure specific interaction's this led to these concepts becoming applicable to synthetic systems. This notion led to the development of crown ethers in 1960 by Charles J. Pederson.[10] The year of 1969 saw Jean-Marie Lehn[11] and Donald J. Cram[12] build upon Pederson's fundamental discovery, developing an increasing sophisticated series of compounds which exhibit a more advanced selectivity when forming complexes (Figure 2).[13] This revolutionary work ensured recognition by the awarding of the Nobel Prize in chemistry in 1987. Ultimately, laying the foundations for which can only be described as one of the most dynamic and increasingly growing areas of chemical research.[14]

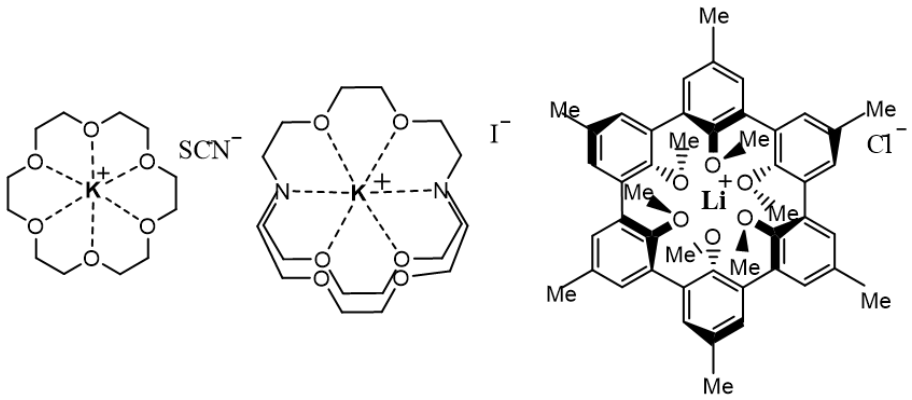

Figure 2 - The series of complexes developed by Pederson (crown ether), Lehn (cryptate) and Cram (spherand) respectively. Left to right.[13]

Molecular species can either assemble through preorganised synthesis, usually resulting in the binding of covalent bonds[15] or self-assemble to form ordered aggregates through intermolecular bonds (usually non-covalent) by the method of self-sorting, Figure 3.[16]

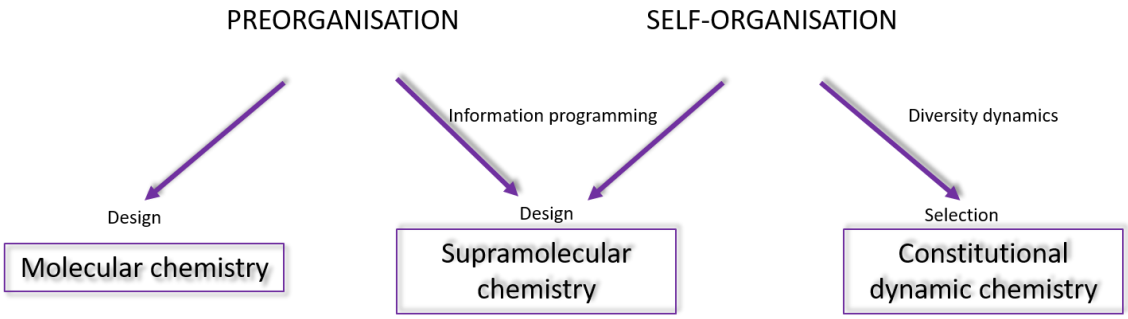

Figure 3 - Preorganisation and self-organisation principles for molecular, supramolecular chemistry and constitutional dynamic chemistry.[16]

This process of self-assembly by non-covalent intermolecular bonding comprises of diverse levels of complexity: It can be as complex as the extraordinary structure of the cell membrane,[17] fashioned by a bilayer of phospholipids[18] embedded with functional proteins.[19] Or, as simple as the dimerization of two small building blocks determined by the formation of hydrogen bonds.

Today the modern scientist is continually utilizing the supramolecular principle in the exploration for novel amphiphiles.[20]

An example of this is observed in a study by Wang and co-workers, who by synthesising amide and urea derivatives have discovered efficient organo-gelators which encompass a built-in functionality that could potentially be useful in sensing local environment changes[21] and also in a study by Hiscock and co-workers where a simple anthracene-based binary organogel exhibited capabilities of behaving as a responsive material towards the chemical warfare agent Soman.[22]

The field of supramolecular chemistry is a highly notable and broad multidisciplinary and interdisciplinary field of science providing a vastly abundant ground for the originality of scientists from all origins. Those of which include biological specificity where intermolecular forces are an understandably ubiquitous feature in the structure of both proteins[23] and thus more significantly 'nucleic acids'.[24] In molecular biology hydrogen bonds determine and stabilize the shapes of biological molecules, as seen in Watson-Crick base pairing (1953) where the intermolecular hydrogen bonds of two complementary nucleotides, such as adenine bound by two hydrogen bonds with thymine, and guanine with cytosine bound through three hydrogen bonds (Figure 4) this binding method keeps the strands of a DNA helix together.[25]

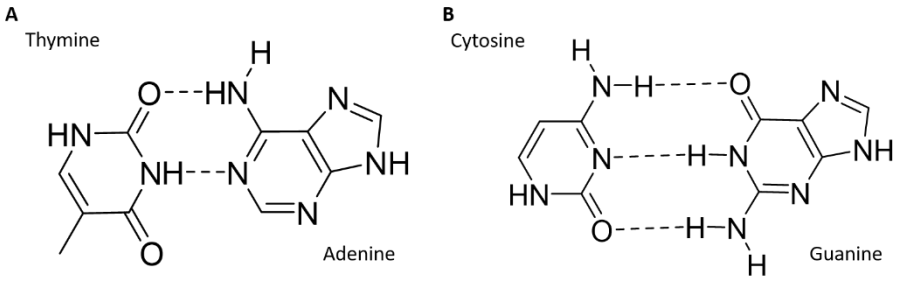

Figure 4 -Watson-Crick base pairing, A) thymine and adenine bonded by two hydrogen bonds, B) cytosine and guanine bonded three hydrogen bonds.

Hydrogen-bonded self-associated systems have also been developed as templates towards DNA incorporated nanostructure formation, where the hydrogen bond donating and accepting thymine substituents co-ordinate with guest species such as a complimentary DNA base adenine.[26]

Additional areas where intermolecular forces are researched are: Physical chemistry which explores the theoretical and experimental studies of interactions.[27] Organic Chemistry where synthetic procedures are studied[28] and co-ordination chemistry, which investigates metal-ion ligand complexes[29], this is just to name a few.

1.1 Non-covalent interactions

As previously mentioned a non-covalent interaction differs from that of a covalent bond as it does not comprise of the sharing of electrons. Non-covalent interactions arise due to electrostatic interactions between the electron distribution of monomer X and monomer Y which ultimately enable the self-association process to occur. This balance of attractive and repulsive interactions (Figure 5) essentially contribute to the formation of extended structures, such as a dimer, trimer…. Etc, by the means of intermolecular interactions of all permanent charges and multipoles.

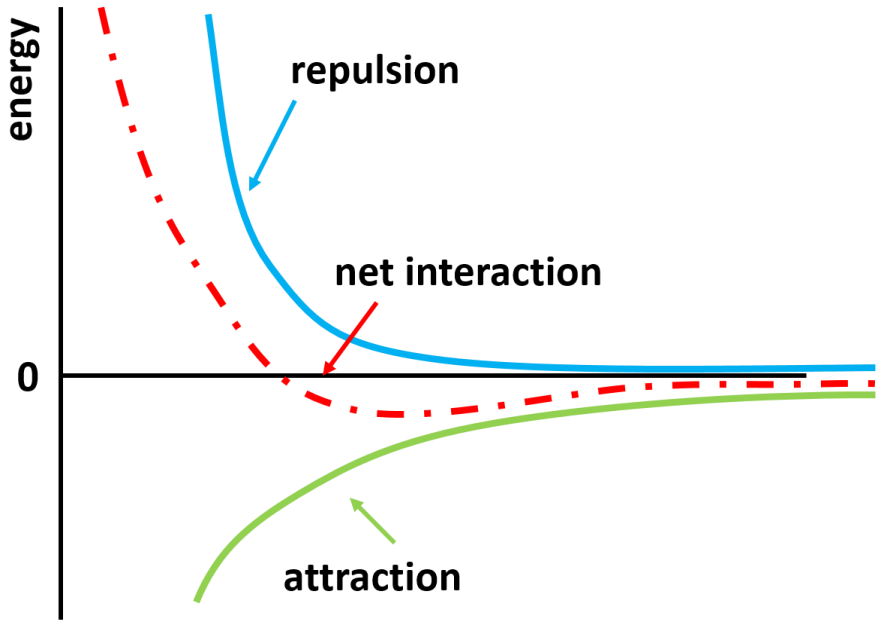

Figure 5 - Schematic representing the interaction between two atoms, demonstrating the repulsion and attraction interactions.

These interactions can be as weak as van der Waals interactions, which are generally less than 4 KJ mol^{-1} or the strength of a strong chemical bond with a stabilization of 200 KJ mol^{-1}.[30]

There are several different intermolecular non-covalent interactions, all of which have intermediate bond strengths (between 4 and 200 KJ $mol^{-1)}$ that contribute to the stabilisation of a self-assembled complex. These include Ion-dipole interactions, where an ion such as Na^{+} bonds with polar molecules such as water, the strength of these type of interaction ranges from 50-200 KJ mol^{-1} (Figure 6A). [31] Dipole-Dipole interactions, which exhibit energies ranging from 5-50 KJ mol^{-1} and are formed when there is an alignment of one dipole with another (Figure 6B).[32] The hydrogen bond (Figure 6C), which has a interaction strength range of 4 - 165 KJ mol^{-1},[33] with < 12 KJ mol^{-1} being weak electrostatic, 16 - 20 KJ mol^{-1} mainly electrostatic and < 60 KJ mol^{-1} strong mainly covalent interactions.[25] The average bond lengths of these hydrogen bonds range from 1.2 Å to 4.0 Å. Both strength and length of the hydrogen bond are heavily reliant on the functional groups involved in the bonding mode.

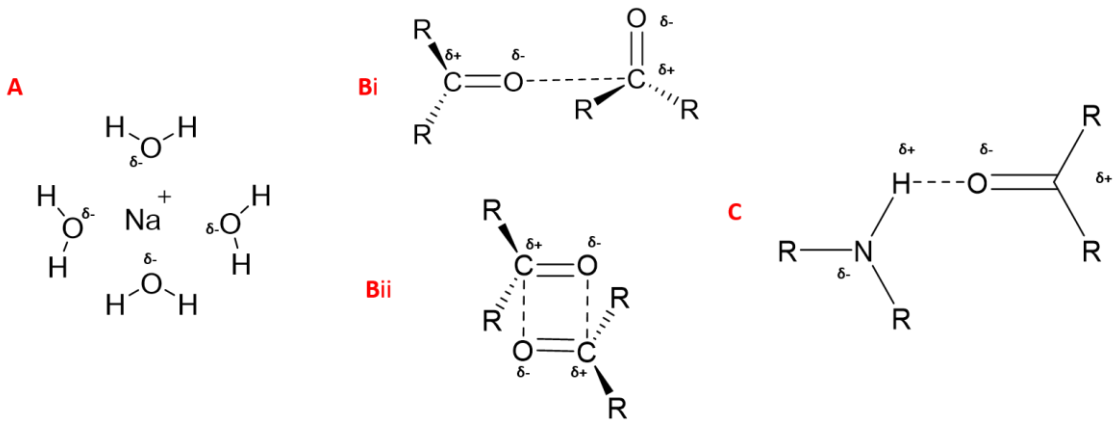

Figure 6 - Intermolecular bond type examples A) ion-dipole, Bi) dipole-dipole, single poles on adjacent molecules ii) dipole-dipole-opposing alignment of one dipole to the other, C) hydrogen bond.

There are a variety of geometries that the hydrogen bond can adopt these are: linear, bent, bifurcated (donating and accepting), trifurcated, and three-centre bifurcated, Figure 7.[34]

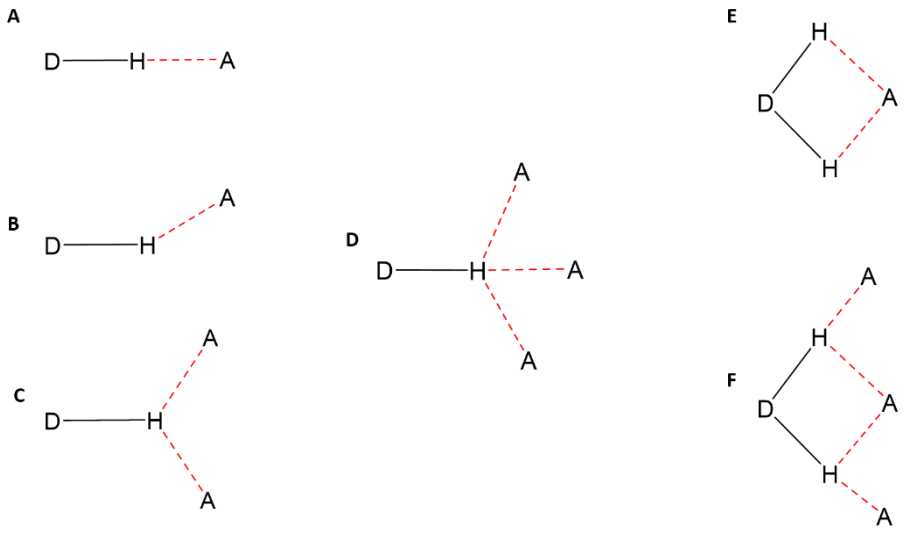

Figure 7 - Example of different types of hydrogen bridges; linear (A), bent (B), donating bifurcated (C), trifurcated (D), accepting bifurcated (E) and three-centred bifurcated (F). [34]

The main structural feature that differentiates between the hydrogen bond and other intermolecular interactions such as the van der Waals forces is its preference for linearity. Hydrogen bond directionality is quite flexible at both the donor and acceptor sites with the angular characteristics being dependent on donor polarity of a simple complex. However, the more molecular species involved in the self-assembly process the more variables there are to consider, such as the preference for a hydrogen bond to from a six membered ring.[34] Dr Thomas Steiner when studying the degree of directionality of the hydrogen bond in the solid state observed the following trend where directionality increases with the decrease in polarity; $-CH_3 < C{=}CH_2 < C{\equiv}C\text{-}H < O\text{-}H$.[35]

Hydrogen bonding modes are stereotypically based on the geometric properties that we have previously discussed. One particular area where the hydrogen bond has been extensively investigated are the binding modes between anionic molecules. These molecules have been constructed with subunits of either urea[36] linked with an anionic sulfonate/phosphonate hydrophilic substituent[37] or thiourea.[38, 39]

Both of these moieties are frequently used in the synthesis of receptors due to their hydrogen bond donating and accepting abilities,[40] and as a result generate supramolecular structures through self-assembly of their own components when there is both an attraction and an equilibrium with each other.

A large quantity of hydrogen bonding data has been gathered over the years from both theoretical and experimental perspectives. This data has included the analysis of the geometry of the atoms involved,[41] along with the type of atom itself.[42] Nitrogen and oxygen atoms are the most commonly investigated hydrogen bond acceptors. A study by Gregoret and co-workers surveyed a set of protein structures for the purpose of evaluating the prevalence and geometry of sulfur-containing hydrogen bonds, they concluded that due to the sulfur atoms electronic structure this atom was also compatible with hydrogen bond formation in proteins. However, the strength of these bonds is weaker (12.97 KJ mol^{-1}) than the oxygen-hydrogen bond formation (13.38 KJ mol^{-1}). This is due to the increased length of the hydrogen bond involved with the sulfur atom, with R(oxygen---H) having a bond length of 2.18 Å and the R(sulphur---H) exhibiting a bond length of 1.653 Å.[43] This length increase is attributed to the size difference between the sulfur atom and the oxygen atom, the larger size results in a more diffuse electron cloud.[44]

Building upon Gregorets research, a study by Zhou et al. determined the importance of the role that sulfur containing hydrogen bonds (SCHB) play in certain biological processes, such as the stabilization of protein structure and in the regulation of protein functions. Detailed characteristics of the geometric formation were analysed, it was concluded that the sulfur atom is a poor H-bond acceptor however, a sulphydryl group is a good H-bond donator, and statistical analysis showed the ratio probability of donor to acceptor is 5:1.[45] A theoretical comparison study of hydrogen bond formation between the oxygen atom and the sulfur atom was compiled by Wierzejewska and co-workers.

Their research focussed on areas concerning the geometry, binding energies and the natural bond orbitals of complexes dimethylsulfide with nitric acid $(CH_3)_2S\text{-}HNO_3$ and dimethylether with nitric acid $(CH_3)_2O\text{-}HNO_3$. The results confirmed that the sulfur is close in hydrogen bond acceptor strength to the oxygen, revealing a differing in binding energies of 5.93 kJ mol^{-1} between the two atoms. The study concluded that both complexes $(CH_3)_2O\text{-}HNO_3$ and $(CH_3)_2S\text{-}HNO_3$ are stable hydrogen bonding structures of perpendicular orientation.[46]

An amphiphilic molecule contains both hydrophobic and hydrophilic components and can be neutral, anionic, cationic or a zwitterionic (Figure 8). An anionic surfactant consists generally of negatively charged headgroups and positively charged counter cations (such as sodium, potassium, or ammonium ions). Carboxylate, sulphonate, and phosphate are the frequently used polar groups.[47]

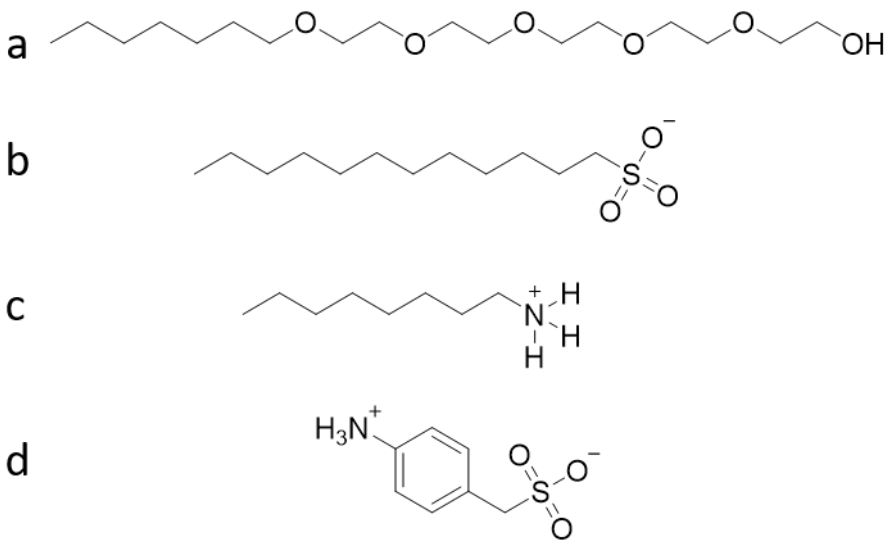

Figure 8 - Examples of non-ionic, anionic, cationic and zwitterionic (a –d respectively).

There are two forms of amphiphile, the conventional and the supra-amphiphile as seen in Figure 9. The latter refers to the conventional amphiphile that is constructed on the basis of non-covalent interactions, for instance hydrogen bonding, $\boldsymbol{\pi - \pi}$ stacking and host-guest interactions amongst others. The supra-amphiphile can be fabricated in two different ways.

The first would be to create amphiphilicity through dynamic covalent bonding or through non-covalent interactions.[48] The second is to modulate amphiphilicity by the modification of conventional covalent amphiphiles using the methods of non-covalent synthesis. Aside from the conventional single-chain head-to-tail supra-amphiphile there are three additional variations. 1) The bola-form supra-amphiphile, this variation possesses two hydrophilic head groups linked through a hydrophobic skeleton, the self-assembly behaviour of bola-form is moderately unalike that of the conventional aggregate.[49] 2) Polymeric supra-amphiphile, prepared through the connection of two or more polymeric sections by non-covalent interactions.[50] 3) Multichain head-to-tail supra-amphiphiles, there are numerous forms of this type of aggregate, which are where either just the hydrophobic or just the hydrophilic part has multiple tails, or when both the hydrophobic and hydrophilic components have multiple tails.[51]

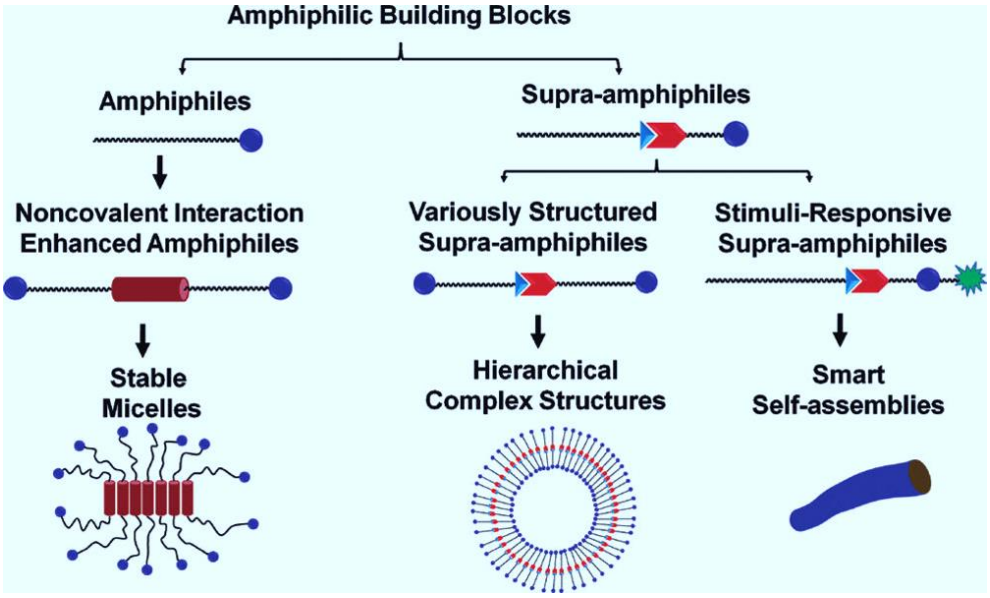

Figure 9 - Amphiphilic building blocks for self-assembly.[51]

Anion recognition is an ever-expanding area of interest within the field of supramolecular chemistry. This is attributed to the application ability of these systems in the biological, environmental and clinical areas.[52]

An amphiphilic molecule is one of the most powerful building block components for self-assembly. The self-assembly processes of these anionic species are continually explored, the structure and properties are essential in enabling these self-assembled systems to form. Recognised components of anionic surfactants incorporate a combination of hydrogen bond donor and accepting groups, a positively charged component for effective electrostatic interactions such as the before mentioned counter cation and a suitable framework onto what these structural components can be assembled (Figure 10).[53]

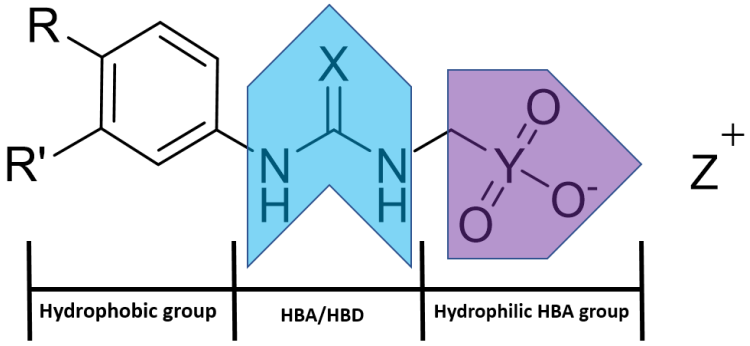

Figure 10 - General anionic structure outlining the essential components required to form a dimeric species.[53]

The amphiphile outlined in Figure 10 has only one HBD group (X = S or O) yet two HBA groups (Y = S) the competitiveness of these two substituents gives rise to these systems being 'frustrated' resulting in the possibility of a variety of intermolecular binding modes. Urea (thiourea)-anion binding modes include dimer and tape formations, whereas urea-urea (thiourea-thiourea) binding modes are *anti*-stacking and *syn*-stacking (Figure 11).[54] These binding modes are dependent on the chemical composition of the molecule and the solvent in which the molecules are dissolved. The solvent system plays an integral part in the self-association process of these 'frustrated' systems, affecting the strength, the stability and the type of hydrogen bond formed. The solvent system can cause the amphiphilic molecules to self-associate into an assortment of structures such as micelles, vesicles or planar bilayers. Changes in solvent conditions can potentially cause the aggregates to transform from one structure to another.[55]

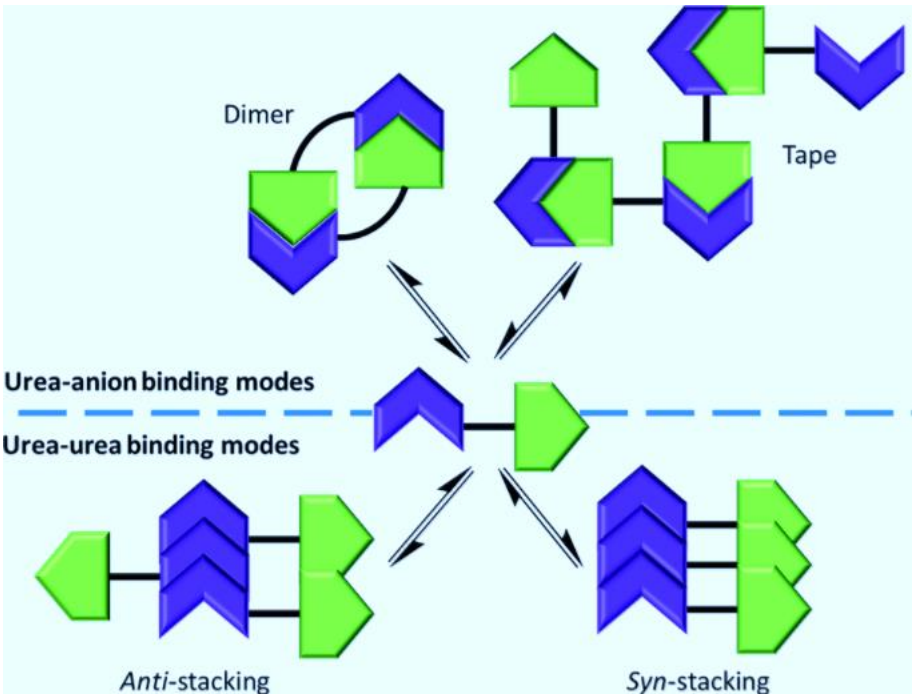

Figure 11 - Possible self-associated hydrogen bonded modes of anionic molecule.[54]

Due to the amphiphilic nature of these molecular species they are able to form micellar structures, operational by dispersing the molecule in aqueous environments, with the resulting hydrophilic head favourably interacting with the aqueous phase and the hydrophobic tail residing in the non-polar solvent (or air). This then causes the amphiphiles to aggregate forming differing molecular assemblies. This is dependent on the co-ordinating and repelling forces between the hydrophobic tails and the hydrophilic head groups of the component molecule and that of the surrounding medium.

In a study by Wang et al., entitled amphiphilic building blocks for self-assembly from amphiphiles to supra-amphiphiles, strategies were introduced for the fabrication of robust assemblies through the self-assembly of amphiphiles. It was proposed that nature can be mimicked, by the linking of functional moieties, via the mechanism of non-covalent bonding, for instance, stimuli-responsive groups. This innovation means that a guest molecule can be encapsulated within the aggregate and when activated by a specific external stimulus becomes weakened causing the nano-structure to disassemble releasing the guest molecule.

This study concluded that supra-amphiphiles were the perfect building blocks for responsive nanoscale carriers and the structure of soft materials.[56] It is predicted that these branches of supra-amphiphile will ultimately bridge the divide between supramolecular chemistry and colloidal science. The ability to control the self-assembly and disassembly of these building blocks through control of not only the properties, but of also the ordered arrangements leads to the enablement of tailor made structure and functions.[57]

The formation of anion-receptor complexes[58] as well as the self-association of low molecular weight monomers,[59] through the formation of hydrogen bonds (in particular those with urea functionalities)[60] is well established as is the self-assembly of amphiphilic compounds.[61] Recent studies by Hiscock and co-workers have investigated the self-association properties of a series of ten novel 'frustrated' amphiphilic salts. By the introduction of anionic guest species,[62] or altering the substituents on the general structure or the counter cation they were able to gain an understanding of how the chemical composition alters the hydrogen bonding modes adopted by this class of amphiphile. It was discovered that the hydrogen bond length and angle altered according to the modulation of the HBD acidity through the substitution of substituents on the aromatic ring, or exchanging between the urea oxygen/ thiourea sulphur. This directly affected the interior angle of the dimeric species formed.[49]

Molecular self-assembly in surfactant solution[63] is ubiquitous in biological systems, underlying the formation of a wide variety of complex biological structures. This is due to amphiphiles being able to self-assemble to form spherical aggregated structures which can be manipulated to specific sizes and shapes. These can then be applicable as templates for the assembly of nanostructured aggregates which can then mimic biomineralization processes. This mimicry is possible as these self-assembled systems exhibit bioinspired properties which display those similar of an array of materials found naturally. This is in addition to their self-healing behaviour and ability to be activated by a specific stimulus.

This has led to an increased interest into the application of amphiphiles either cationic[64] or anionic, as antimicrobial agents. Due to despite continuing efforts there remains a cumulative occurrence of resistance amongst pathogenic bacteria to common antibiotics. Laverty discusses the importance of anionic antimicrobial peptides and how these are becoming just as significant as those that are cationic in nature.[65] A disadvantage of many anionic antimicrobial peptides was the necessity to possess a cation that will behave as cofactor for biocidal activity. However, surfactant associated amphiphiles have a counter cation present which can be in the form of tetrabutylammonium or similar, this then acts as a linkage between the anionic antimicrobial and the cell membrane of the anionic microbial. This enables the transport of the anionic antimicrobial to intracellular targets whilst causing no damage to the membrane structure.[66]

1.2 Project aims

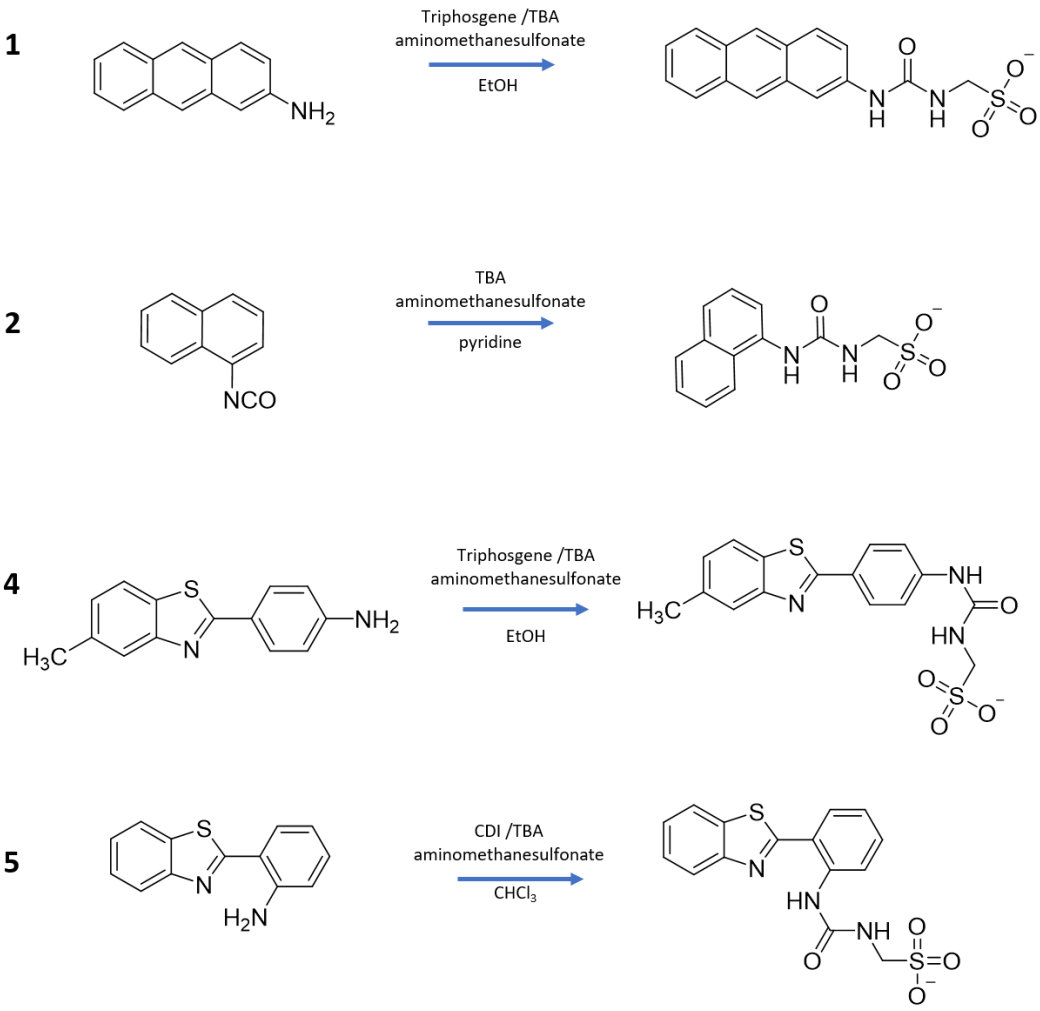

Figure 12 - Synthesis scheme of compounds **1**, **2**, **4** and **5**.

As we have discussed in detail intermolecular interactions such as the hydrogen bond are a key driving force towards molecular self-assembly. Low molecular weight amphiphilic molecules that are formed containing functional groups such as urea or thiourea, covalently linked by a spacer and an anionic substituent are of specific interest due to their hydrogen bond donating and accepting abilities.[67]

- A collection of compounds synthesised by Hiscock and co-workers that have similarities to the general structure (Figure 10), have been proven to exhibit positive antimicrobial activity against *S. aureus* and measurable activity against *E.coli*.

Therefore, it is of utmost importance that we can directly observe the compounds within this study to gain a greater understanding as to their self-association properties.

- The aim of this project is to develop a series of intrinsically fluorescent amphiphilic salts (Figure 12) and to observe their molecular self-association properties by a combination of complimentary techniques in the solution, solid and gaseous states. The techniques used to explore the larger aggregate structures include: Single crystal XRD, DLS, ^{1}H NMR and DOSY NMR. The global properties of these molecules will be explored using microscopy observations and attained CMC data.
- It is hypothesised that these low molecular weight monomers (LMWM) self-associate through intermolecular interactions into larger aggregates.

2. Investigation into the self-association properties of the amphiphile

2.1 Introduction

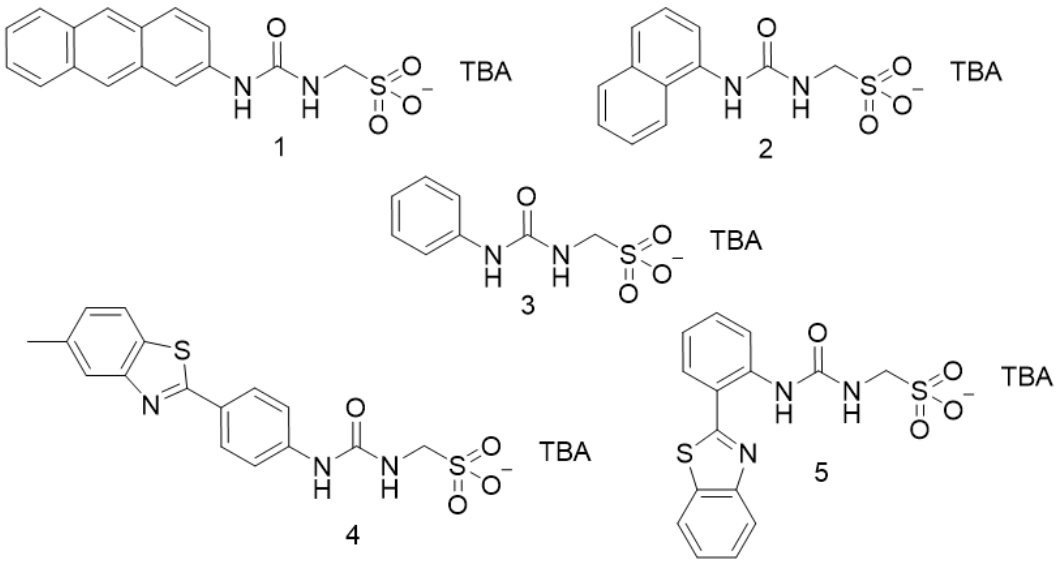

Figure 13 - Compounds **1** - **5**, a series of sulfonate-urea based amphiphilic salts.

A series of analytical techniques will be used to explore the structure-activity relationship properties of five amphiphilic salts that all contain the urea functionality, and a sulfonate group (Figure 13). The techniques used to study this group of molecules are as follows: single crystal X-ray diffraction, tensiometry, DLS, computational modelling and electron spray ionization mass spectrometry (ESI-MS). Compounds **1, 2, 4** and **5** are intrinsically fluorescent sulfonate-urea based amphiphilic salts therefore using the following methods: fluorometry, ultra-violet visible spectroscopy (UV-vis), and transmission and fluorescence microscopy (enabling visualisation, which regards to how these aggregates self-assemble in specific solvent conditions). Therefore, allowing comparison as to the effects of the addition of benzothiazole and increasing of the quantity of aromatic substituents.

Due to the hydrophobic nature of the aromatic substituent and the hydrophilic nature of the anionic group, it is hypothesised that they will self-associate through the formation of intermolecular bonds to form spherical aggregated structures. These for the first time can be directly observed due to the intrinsically fluorescent properties of four of these compounds. The data gathered from all experimental methods will be analysed and comparisons made where suitable to determine if it is possible to predict the self-association behaviour in this class of amphiphiles.

2.2 Solid state – Single crystal X-ray diffraction

Single crystal X-ray diffraction, first developed in 1912 by Laue, Friedrich and Knipping [68] is a routinely used non-destructive analytical technique in the field of supramolecular chemistry. Where the covalent or non-covalent bonding modes present within the solid state can be identified. Through slow evaporation of a DMSO: H_2O solution containing **1**, **2**, **4**, and **5** single crystals were obtained. The single crystal X-ray structure of **3** has previously been reported by Hiscock et al. in their study entitled 'Frustrated' hydrogen bond mediated amphiphile self-assembly - a solid state study, where it was determined that the bond lengths and angles were influenced by the acidity of the hydrogen bond donating groups present within the monomeric structure. In this study the crystal structure obtained for **3** exhibits a tape formation through a urea-anion binding mode (Figure 14). Also observed was the additional coordination of a water molecule to the anionic sulfonate substituent, through additional hydrogen bonds.[49]

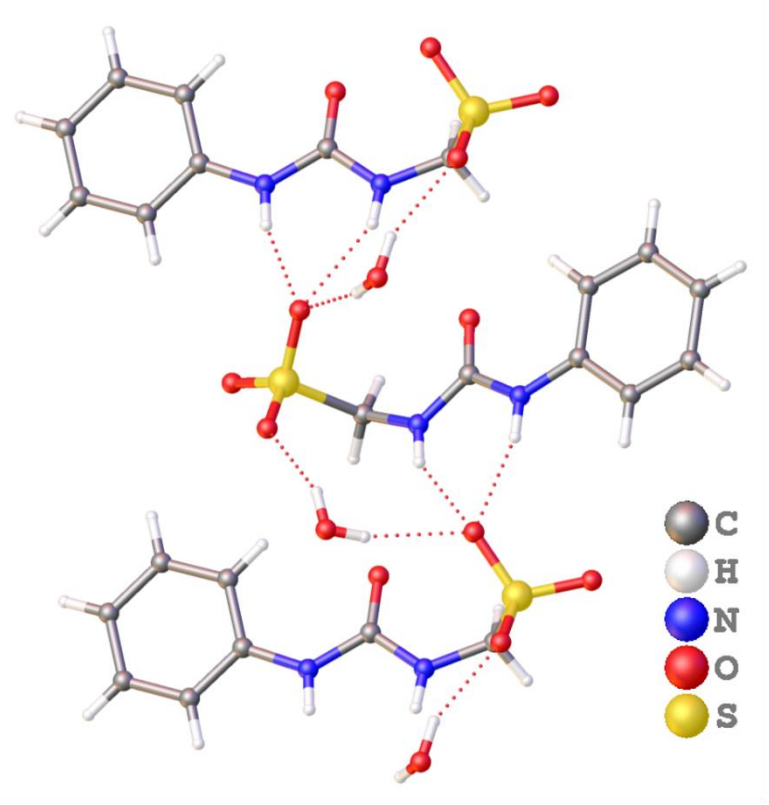

Figure 14 - Single crystal X-ray structure of compound **3**, exhibiting hydrogen bonded tape formation through a urea-anion binding mode.[49] TBA counter cation has been omitted for clarity.

Crystallography data obtained and refined by Dr Jennifer Hiscock.

2.2.1 Results and discussion

It is commonly known that anthracene oxidizes[69] to hydroxyanthracenes[70] or anthraquinone (Figure 15).[71]

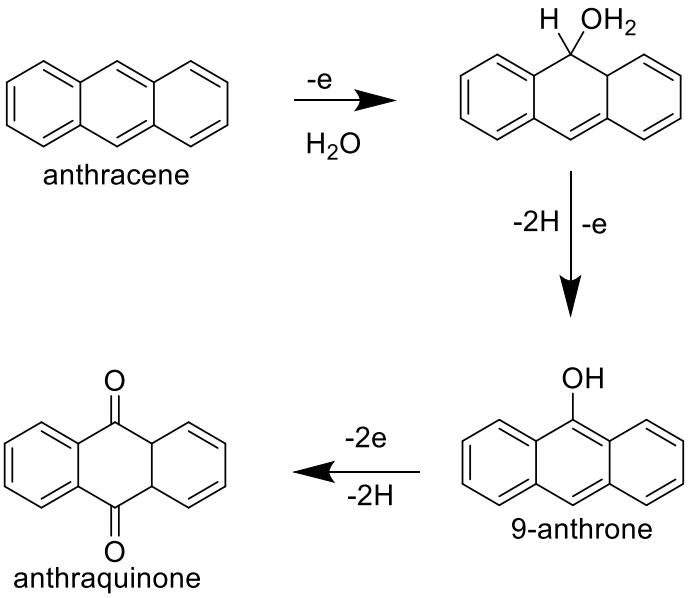

Figure 15 - Reaction mechanism for the oxidation of anthracene to hydroxyanthracene to anthraquinone.[72]

From crystals obtained after the two-week crystallization process it was observed that the anthracene substituent of compound **1** is susceptible to this process (Figure 16). The single crystal X-ray structure illustrated in Figure 16 also shows the non-planar dimerization of the molecules via four intermolecular bonds between the sulfonate-urea substituents which has an interior hydrogen bond angle of 15 ^{o}, this was calculated from the intersecting planes of the urea substituents (Figure 17). To ensure the purity of **1** ^{1}H NMR studies were performed periodically whist studying the self-association properties in both the solution and gas phase.

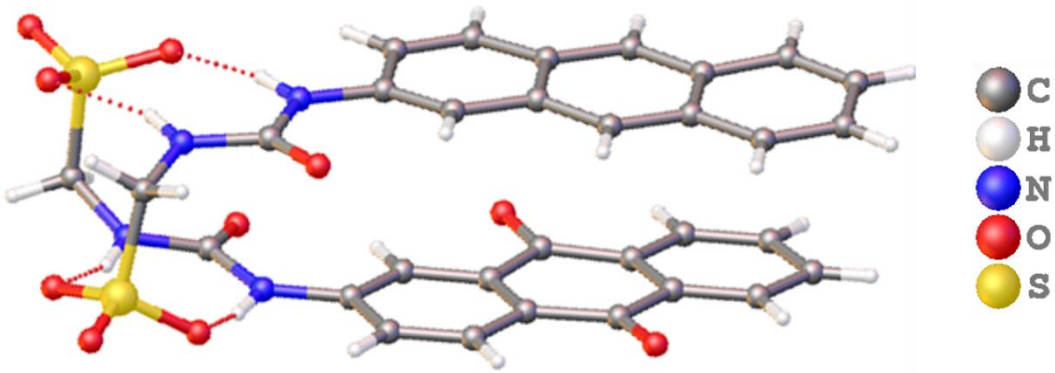

Figure 16 - Single crystal X-ray structure of compound **1**, demonstrating dimerization through the urea-anion complexation. TBA counter cation has been omitted for clarity.

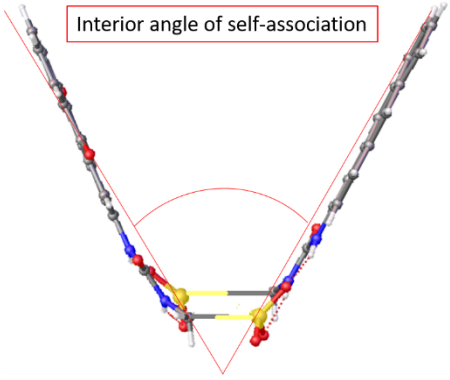

Figure 14 - Ball and stick representation of interior angle of self-association calculated from the intersecting planes of the urea substituents.

The crystal structure for compound **2** (Figure 18), also demonstrates the formation of a dimer species through the sulfonate-urea substituent, as we observed for **1.** However, for **2** the NH HBD groups are shown to bond with one HBA sulfonate oxygen. The geometry of this complex is planar with an interior hydrogen bond angle of 180 ^{o} dissimilar to that of **1**.

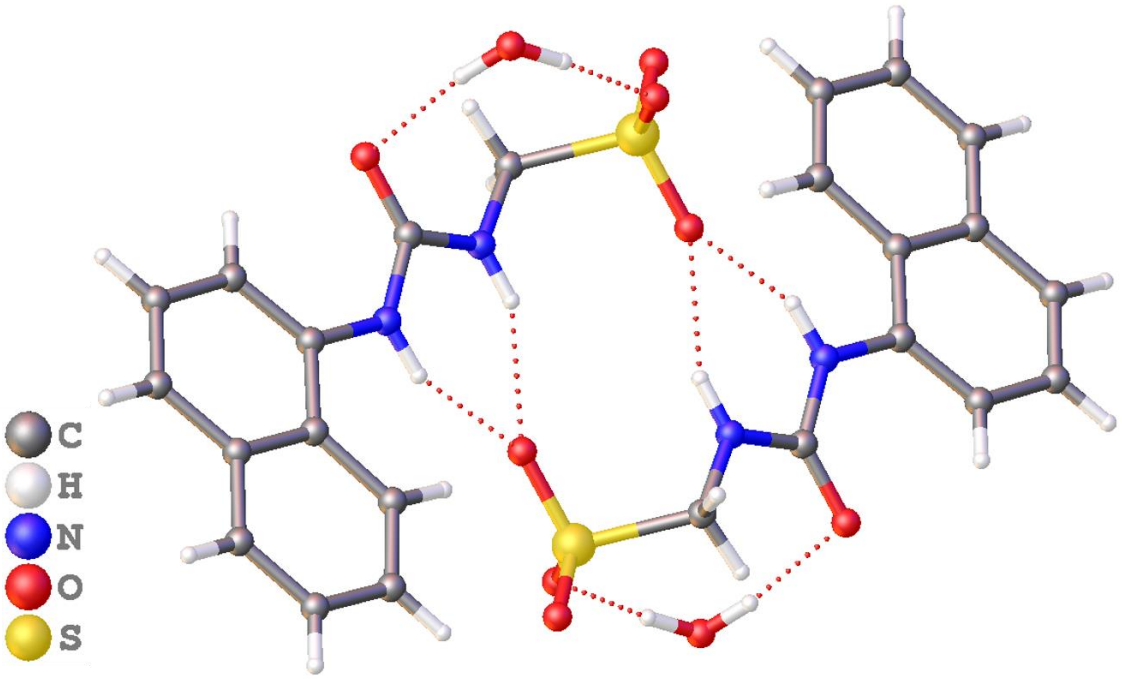

Figure 15 - Single Crystal X-ray structure of compound **2**, demonstrating dimerization through the urea-anion complexation. TBA counter cation has been omitted for clarity.

Compound **4** binds through intermolecular interactions of the urea NH to the sulfonate anionic moiety (Figure 19). In this case though, the hydrogen bond donating groups are self-associating with a different hydrogen bond accepting sulfonate oxygen, unlike those formed in compounds **1** and **2**. This bonding mechanism causes the molecular structure to twist, forming a non-planar dimer with a hydrogen bond interior angle of 56 ^{o}.

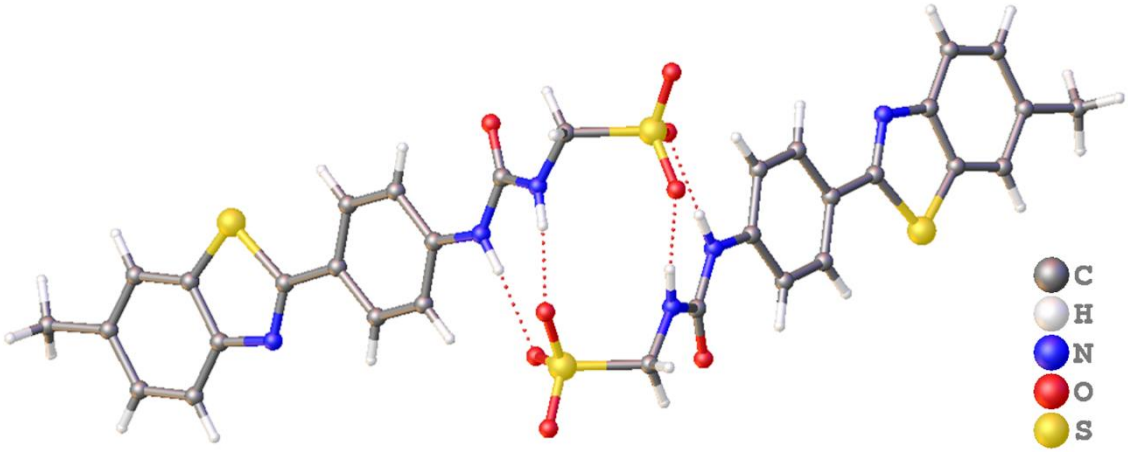

Figure 19 - Single Crystal X-ray structure of compound **4**, demonstrating dimerization through the urea-anion complexation. TBA counter cation has been omitted for clarity.

The structure for compound **5** demonstrates formation of a planar dimer species with a self-associating interior angle of 180 °. The dimer formed is stabilised through intermolecular interactions of one hydrogen bond donating urea NH and the hydrogen bond accepting sulfonate moiety of each molecule. As observed in Figure 20, the second urea NH has formed an intramolecular hydrogen bond with the benzothiazole nitrogen.

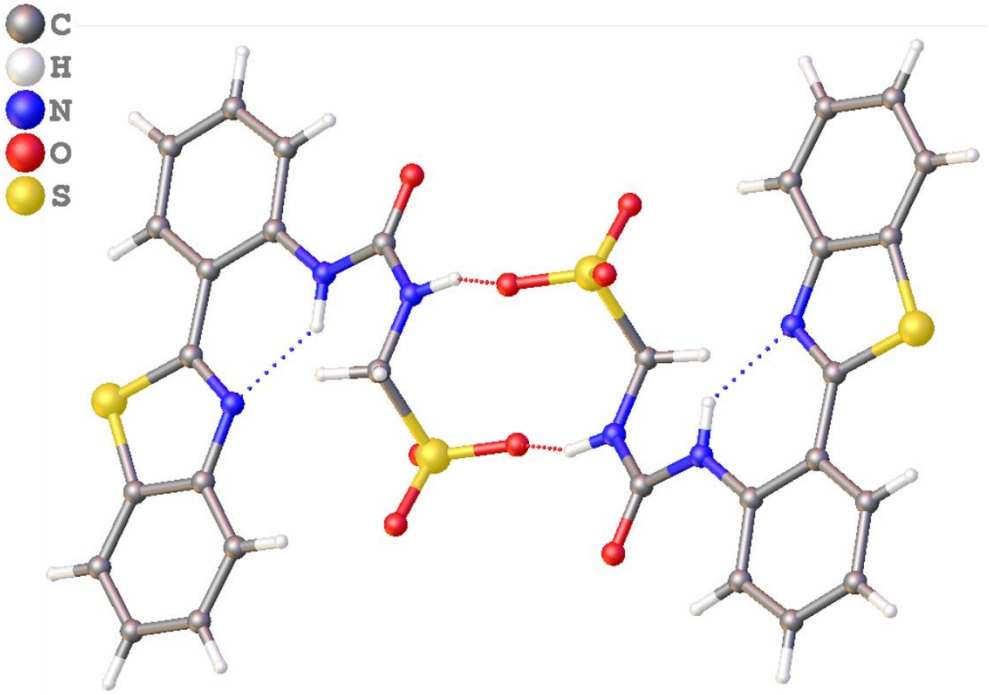

Figure 20 - Single Crystal X-ray structure of compound **5**, demonstrating dimerization through the urea-anion complexation and intramolecular bond formation. TBA counter cation has been omitted for clarity.

The hydrogen bond distances and angles for **1**, **2**, **4** and **5**, calculated from single crystal X-ray structures can be seen in Table 1. As we can see the hydrogen bond length from donor to acceptor (D—A) range from 2.6 - 3.4 Å with hydrogen bond angles between D-H—A ranging from 123 - 178 °.

Table 1 - Hydrogen bond distances and angles calculated from single crystal X-ray structures.

Compound	Hydrogen bond donor	Hydrogen atom	Hydrogen bond acceptor	Hydrogen bond length (D•••A) (Å)	Hydrogen bond angle (D-H•••A) (°)
1	N1	H1	O8	2.855 (14)	156.8 (8)
1	N2	H2	O10	2.976 (17)	155.3 (9)
1	N3	H3	O6	2.956 (13)	167.0 (7)
1	N4	H4	O5	2.967 (14)	163.0 (7)
2	N2	H2	O3	2.864 (3)	151.88 (13)
2	N1	H1a	O3	2.858 (3)	155.21 (13)
2	O5	H5b	O1	2.821 (3)	170.08 (17)
2	O5	H5c	O2	2.813 (3)	160.56 (16)
4	N2	H2	O2	2.865 (5)	170.9 (3)
4	N3	H3	O4	2.896 (5)	127.8 (2)
4	O5	-	O4	2.826 (7)	-
4	C6	H6	O3	3.371 (6)	159.3 (3)
4	C16b	H16b	S1	3.794 (5)	157.7 (2)
4	C14	H14	O1	3.375 (5)	162.2 (3)
5	N3	H3	O4	2.853 (2)	140.47 (13)
5	N2	H2	N1	2.697 (3)	137.56 (12)
5	N2	H2	O2	3.410 (2)	133.09 (12)
5	C12	H12	O1	2.836 (3)	123.43 (14)
5	C2	H2a	O3	3.383 (3)	178.10 (16)

The anionic substituents and the hydrogen bond donating urea groups are key substituents in self-association, aiding in the formation of stable intermolecular bonded dimer species.

Compounds **1**, **2**, and **4** are all stabilised through the formation of four intermolecular hydrogen bonds, with each of the NH groups acting as a hydrogen bond donator. **1**, **2**, **4** and **5** are shown to adopt the dimer formation, with interior angles of 15 º, 180 º, 56 º, and 180 º respectively. Further stabilisation through interactions of the electron rich and electron poor aromatic ring systems causes the aromatic moieties to form a stacked non-planar arrangement. Therefore **1** has an interior angle that is approximately four times smaller than that of **4**. The analogous structure obtained for **4** illustrates the formation of a dimerised species. Although this compound demonstrates the same binding mechanism as **1**. The NH urea forms a hydrogen bond with the opposite hydrogen bond accepting sulfonate oxygen atom resulting in the geometry of this complex to be non-planar.

The planar structure of **2** demonstrates hydrogen bond formation of both HBD NH with a single sulfonate oxygen and an additional hydrogen bond co-ordinating to a water molecule with both the urea and sulfonate oxygen atoms.

We have demonstrated that a key factor in forming stable hydrogen bonded dimerized species for the discussed compounds is the presence of four hydrogen bonds, four hydrogen bond donating NH urea's and two hydrogen bond accepting sulfonate groups. The planar structure of compound **5** however, forms an intramolecular bond between the nitrogen of the benzothiazole and the NH of one of the urea's. This steric hindrance limits the number of HBD donating groups available for intermolecular hydrogen bond formation. As a result this dimeric complex is only stabilised through the formation of two intermolecular bonds. It is hypothesised that this may be a limiting factor in the formation of larger self-assembled aggregate structures.

2.2 Gas Phase: Mass spectrometry

Over the last decade ESI-MS has emerged as a significant bio-analytical tool, due to its ability to provide qualitative information towards the detection of analyte molecules. These molecules must first be converted to ions.[73] In negative ionisation mode a trace of ammonia solution is added to aid deprotonation of the sample molecule.[74] Non-covalent interactions, such as the hydrogen bond are routinely studied in the solid[75] and solution states.[76] However, it has also been identified that these non-covalent associations continue to persist in the gas phase. ESI-MS provides an innovative approach to studying these intermolecular interactions.[77] This technique was utilised with compounds **1** - **5** to determine if dimerization or self-association is limited to the solid and solution states for this class of amphiphile or whether these compounds exhibit dimeric species in the gaseous phase.

2.2.1 Results and discussion

As expected the data obtained from the ESI-MS study reveal that in the gas phase compounds **1** - **5** exist in the monomeric state $[M]^-$ or the dimeric state $[M+M]^{2-}$ with correspondence between the theoretical and actual m/z peaks seen in Table 2.

Table 2 - High resolution mass spectrometry theoretical and experimentally derived values for **1** – **5**.

Compound	m/z $[M]^-$		m/z $[M+M+1]^-$	
	theoretical	actual	theoretical	actual
1	329.0602	329.0567	659.1204	659.1210
2	279.0445	278.9615	559.089	558.9373
3	229.0289	229.0292	459.0578	459.0649
4	376.0431	376.0390	753.0862	753.0864
5	362.0275	362.0261	Not observed	

In addition to this we have also identified the presence of the mono-protonated sulfonate-urea dimeric species $([M+M+H])^-$ for **1** - **4**. Using **1** as an example (Figure 21) we observe the m/z peak corresponding to the anionic monomer $([M])^-$ or dimer $([M+M])^{2-}$ at 339.0567 and the protonated dimeric species $([M+M+H])^-$ which is 2(339.0567) + 1.007 at 659.1210, this is a good indication that the dimerized species is present (for this molecule) in the gaseous phase. This trend is also apparent for compounds **2** - **4**. These protonated dimeric species $([M+M+H])^-$ are not determined to be due to the concentration of the analyte present. Sample preparation was completed to ensure optimization, resulting in a very low concentration of the analysed sample (1 mg in 1 mL, diluted further by a factor of one hundred giving the concentrations at $\approx 1.6 \times 10^{-6}$ mol).

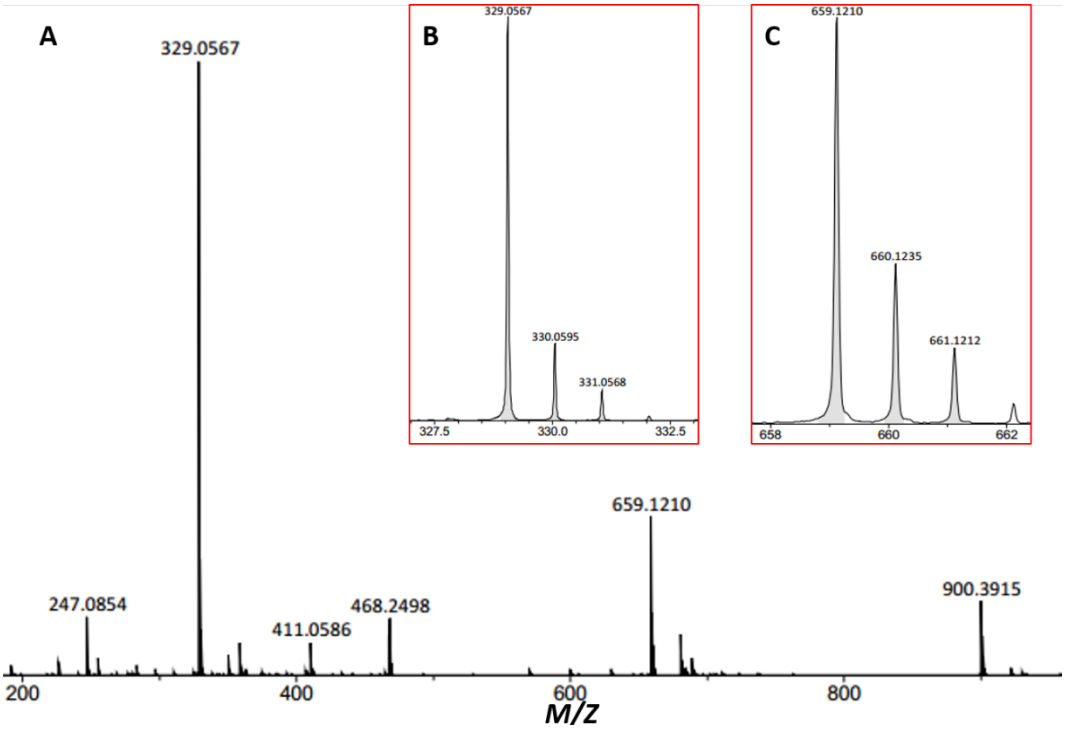

Figure 21 - Electrospray mass spectrometry spectrum of compound **1**, showing both the monomeric and protonated dimeric species (A), monomeric species (B) and protonated dimeric species (C).

The protonated dimerized species is not present in the spectra for **5**, this is attributed to the intramolecular bond formed within this compound as previously identified in the solid-state studies. If we compare the proposed self-association process between **1** and **5** (Figure 22), the combination of the protonation of the sulfonate group and intramolecular bond inhibits the ability for **5** to self-associate. The protonated sulfonate renders this site unavailable for hydrogen bonding, and the intramolecular bond between the nitrogen of the benzothiazole and the urea NH limits the availability of hydrogen bond formation with another monomer due to steric hindrance.

The ESI-MS data demonstrates that the non-covalent bonds of **1** - **4** do not dissociate under this soft ionization technique, so therefore their dimeric complexes exist in the gas phase. However, although present, the stability of these dimeric compounds is unknown compared to those in the solvent state. Additionally, the presence of these dimer species in the gas phase means that in this study, coulombic repulsion does not prevent the anionic compounds coming together.

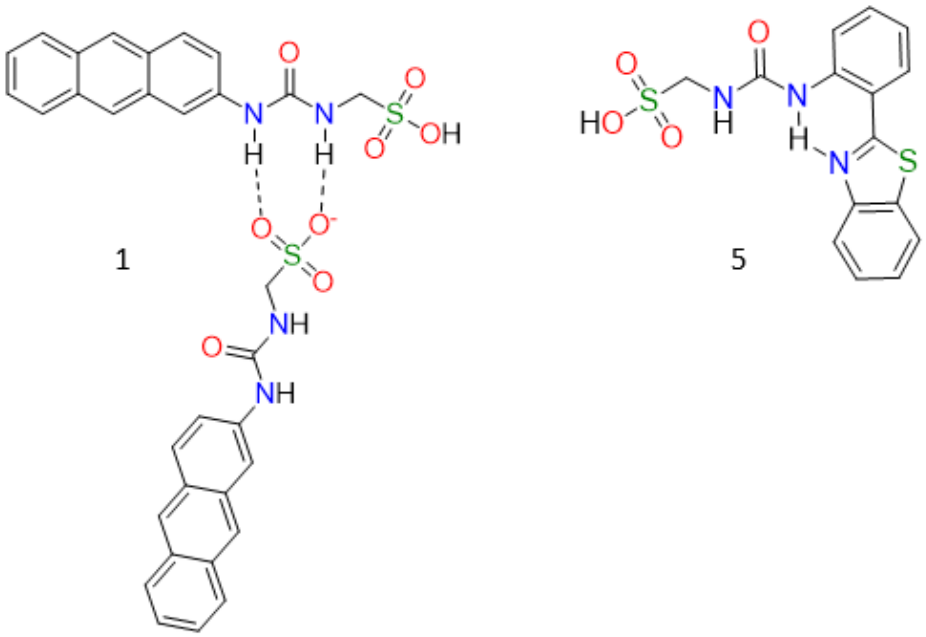

Figure 22 - Proposed protonated dimeric species of **1** and protonated monomer of **5**, as observed in the gas phase.

All ESI-MS spectra that display the abundance percentage of different isotopes for **1** - **5** are presented in appendix Figure S250 - 254.

2.3 Solution state studies

The solid and gas states involve exploration into self-assembled intermolecular binding methods of the anionic component of the amphiphile.

The solution state introduces solvent-solute interactions, these interactions can exert influence on the molecular binding modes that aid in the formation of larger self-assembled systems such as inverse micelles where surfactant monomers in a non-polar solvent invert[78] or micelles (Figure 23).

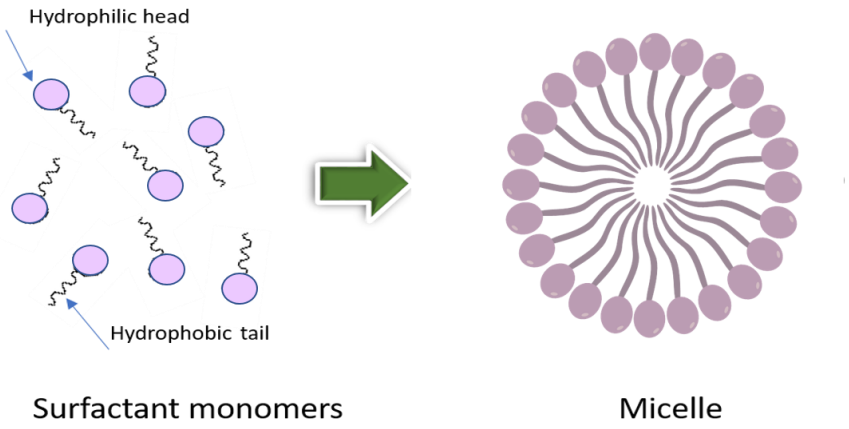

Figure 23 - Schematic of micelle formation from surfactant monomers.

It is known that solvents such as dimethylsulfoxide and water interact with other solutes as well as with each other through hydrogen bond formations between the oxygen atom of the DMSO, and the protons of the water molecule. The hydrogen bond donating or accepting moieties of the solvent consequently compete with the HBA/HBD sites of the solute and as a result instruct the type of self-associated aggregates formed.

Compounds **1** - **5** all contain hydrophilic sulfonate groups and HBD/HBA moieties so therefore the self-assembly of these molecules may be heavily influenced by the solvent systems which they are in. To test this hypothesis and the self-association of these amphiphilic salts a variety of solvent systems (chosen due to comparative solubility) are used within the range of methods applied in this study. These are: DMSO, DMSO:H_2O 1:1, 1:4, 3:7 and H_2O:EtOH 1:19.

2.3.1 Dynamic light scattering (DLS)

DLS is a frequently used method to determine the sphere size distribution and the state of motion of a particle, emulsion or molecule which have been dissolved or dispersed in a solvent system. The Brownian motion of small matter in solution causes light to be scattered at different intensities. Changes in these intensities enable the particle size of the analysed substance to be determined using the Stokes-Einstein translational diffusion constant, Equation 1.[79]

Equation 1 - The Stokes-Einstein relation that links diffusion coefficient measured by DLS.

$$D_h = \frac{k_B T}{3\pi\eta D_t}$$

D_h = *H*ydrodynamic diameter
D_t = translational diffusion constant
k_B = Boltzmann's constant
T = thermodynamic temperature
η = dynamic viscosity

It is commonly assumed that these small molecules or particles scatter light weakly. However, there are circumstances when this scattered light is much stronger, such as in gel formations or other fluid like systems.[80] Dynamic light scattering along with other methods is commonly used to assist in the exploration of molecular self-assembly providing quantitative data.[62]

Limitations of this method include the measurement of the hydrodynamic radius of a particle as opposed to the projected area diameter. This hydrodynamic sphere is formed of a thin dipole layer of the solvent adhering to the particle surface. With DLS it is this sphere and the core inorganic particle that are analysed for the determination of particle size distribution. This measurement is calculated based on the assumption that the particle is spherical (Figure 24). However, in practice the particles in solution are non-spherical, dynamic and solvated and because of this the calculated measurements from the diffusional properties of the particle will be indicative of the hydrodynamic sphere. Furthermore, large particles present within the solution will still be accounted during data analysis even if they are in small quantities.[81] For volume or number distributions particle refractive index calculation is required.

However, as the compounds being analysed are novel and a refractive index is not available at present the average intensity size distribution data will be used within this study.

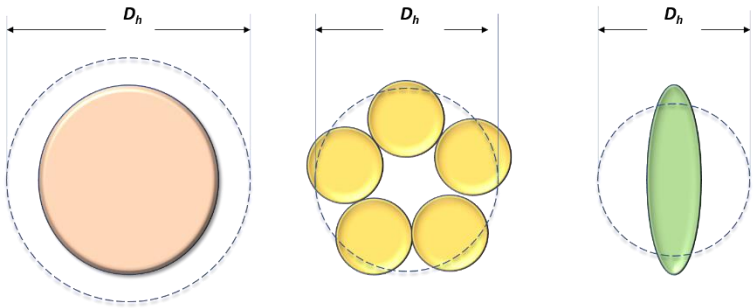

Figure 24 - Schematic demonstrating the hydrodynamic radius (D_h) measured using DLS gives the diameter of a sphere that diffuses the same way as the particle.

The self-association properties of compounds **1**, **3** - **4** and **5** in the previously mentioned solvent systems were investigated using DLS size distribution studies. To ensure the molecules in solution were in an equilibrium state having reached a thermodynamic minimum the samples were subjected to an annealing process. This process involved heating the samples from 25 ^{o} to 40 ^{o} then cooling back to 25 ^{o}.

2.3.2 Results and discussion

The measured DLS data is presented as a correlation curve that contains all the information with regards to the diffusion of particles within the sample being measured. The correlation curve should be smooth with concurrence of size distribution for all runs (nine in this instance) for all samples measured. Correlograms were obtained for samples **1** - **5** at each point during the annealing process, the results confirm that achieving thermodynamic minimum results in greater correlation of particle diffusion. Figures 25 - 28 illustrates example DLS correlation graphs of compound **1** at a concentration of 55.6 mM. These obtained graphs allow us to observe the transition through the three-stage annealing process.

Comparisons of these graphs demonstrate that the initial 25 ^{o} and at 40 ^{o}C series of runs do not correlate as well as the correlation curve of compound **1** after the annealing process. This confirms the need for these compounds to reach a thermodynamic minimum to ensure the aggregate size is optimized. All additional correlograms are available in appendix Figures S31 - 118.

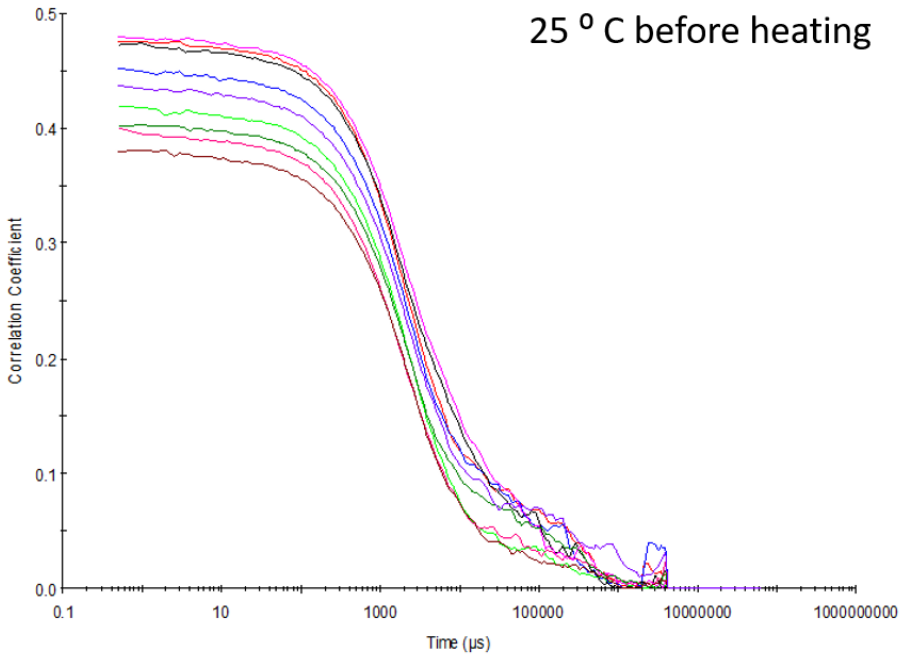

Figure 25 - Raw correlation data for 9 DLS runs at 25 °C before heating to 40 °C with compound **1** at a concentration of 55.6 mM in DMSO.

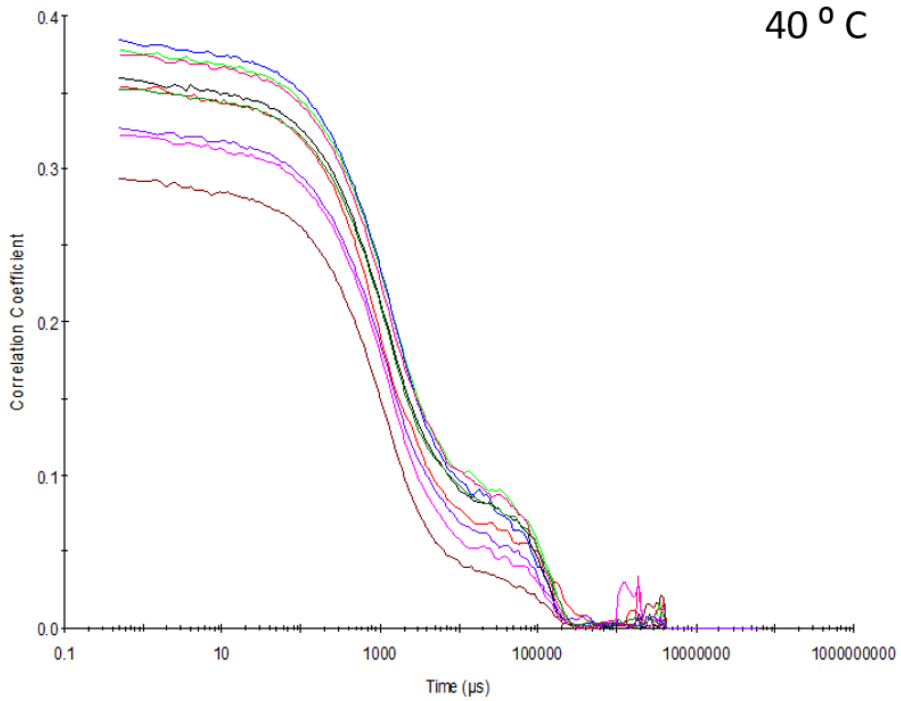

Figure 26 - Raw correlation data for 9 DLS runs at 40 °C with compound **1** at a concentration of 55.6 mM in DMSO.

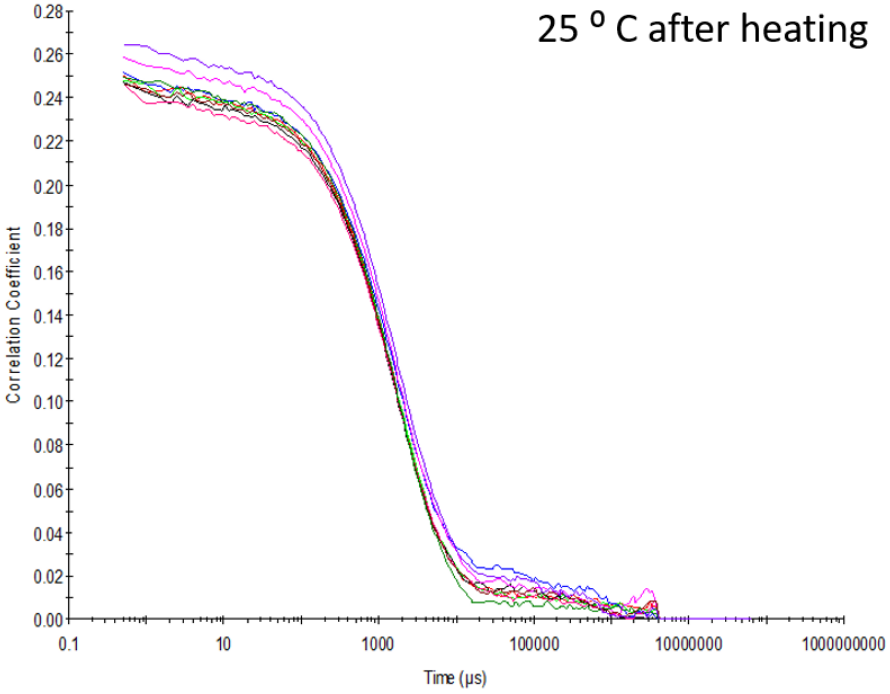

Figure 27 - Raw correlation data for 9 DLS runs at 25 °C after heating to 40 °C with compound **1** at a concentration of 55.6 mM in DMSO.

DLS studies of **1** and **3** - **5** in a DMSO solution demonstrate the presence of three different sized structures (Table 3). Structure one with an approximate diameter of 1 - 58 nm, structure two 100 - 600 nm and structure three > 600 nm.

Table 3 - Average intensity particle size distributions (to 3 sig.fig.) for compounds **1, 3, 4** and **5**, calculated from 9 DLS runs. Samples were prepared in series, with an aliquot of the most concentrated solution undergoing serial dilution and measured at 25 ^{o}C after heating to 40 ^{o}C and cooling to 25 ^{o}C.

Solvent	Conc. (mM)	**1** peak maxima		**2** peak maxima	**3** peak maxima		**4** peak maxima		**5** peak maxima	
DMSO	111	459	1718	*a**	955	3091	615	1.11	712	3580
	55.6	825	58.8	*a**	825		615	1.11	825	220
	5. 56	531	106	*a**	615**		396	1.11	1106	
	0.56	531		*a**	531		396		531	0.72

a* - DLS Size distribution in a solution of DMSO for compound **2** could not be gathered due to the inherent absorbance and fluorescent characteristics of this compound.

From these results, it can be observed that unlike **1**, **3** and **5,** compound **4** does not aggregate into the largest of the species. However, it does show that the smaller aggregates of an estimated 1 nm are more persistent within this complex, these smaller aggregates could be artefacts attributed to small single molecules, observed in Figure 28.

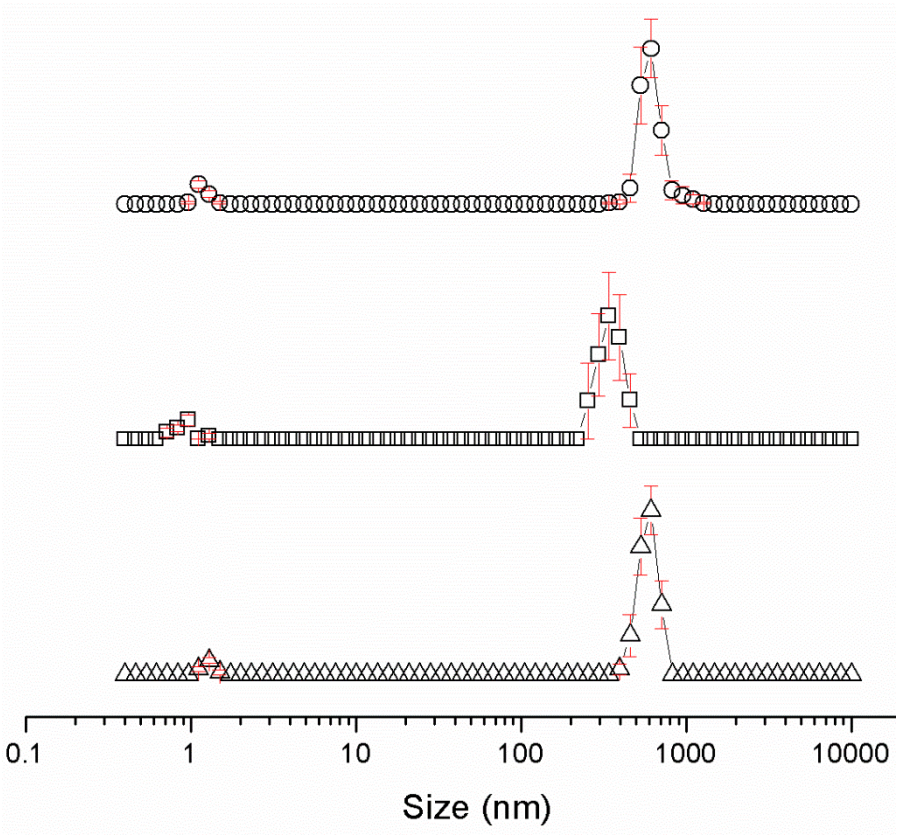

Figure 28 - Average intensity particle size distribution, calculated from 9 DLS runs, of aggregates formed by dissolving compound **4** at a concentration of 111 mM in DMSO (1 mL) at Δ) 25 °C, □) heating to 40 °C and ○) cooling to 25 °C. Smaller and mid-sized aggregates present at ≈ 1 nm and 600 nm respectively.

Compound **5** demonstrates that these larger aggregate structures are primarily present at higher concentrations (Figure 29) and are hypothesised to be attributed to the aggregation of smaller complexes. It is visible that upon further dilution the occurrence of these larger structures decreases. It is observed that as expected that there is a general pattern occurring which demonstrates a decrease in aggregate size corresponding with a decrease in concentration. An overview of these results giving a full range of aggregate sizes from comparison of peak widths can be seen in graphical format in Figure 30. The full data sets are available in the appendix Figures S118 - 174.

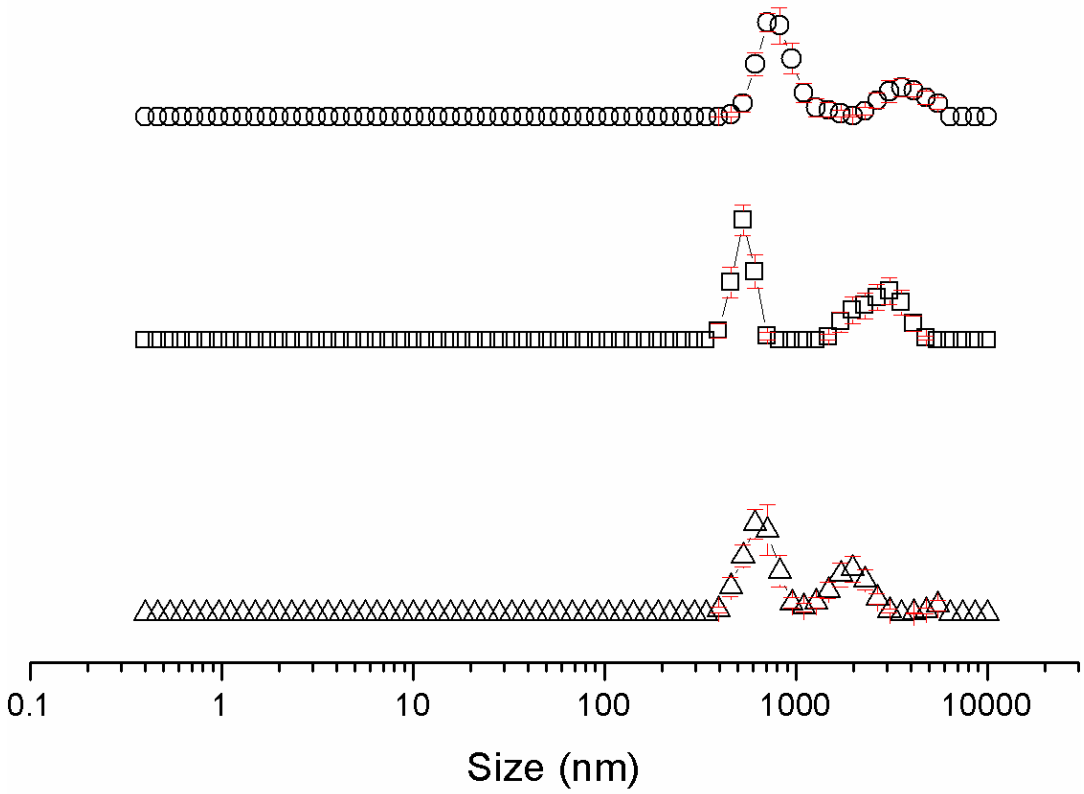

Figure 29 - Average intensity particle size distribution, calculated from 9 DLS runs, of aggregates formed by dissolving compound **5** at a concentration of 111 mM in DMSO at Δ) 25 ^{o}C, □) heating to 40 ^{o}C and ○) cooling to 25 ^{o}C. Mid-sized and large aggregates present at ≈ 600 nm and > 600 nm respectively.

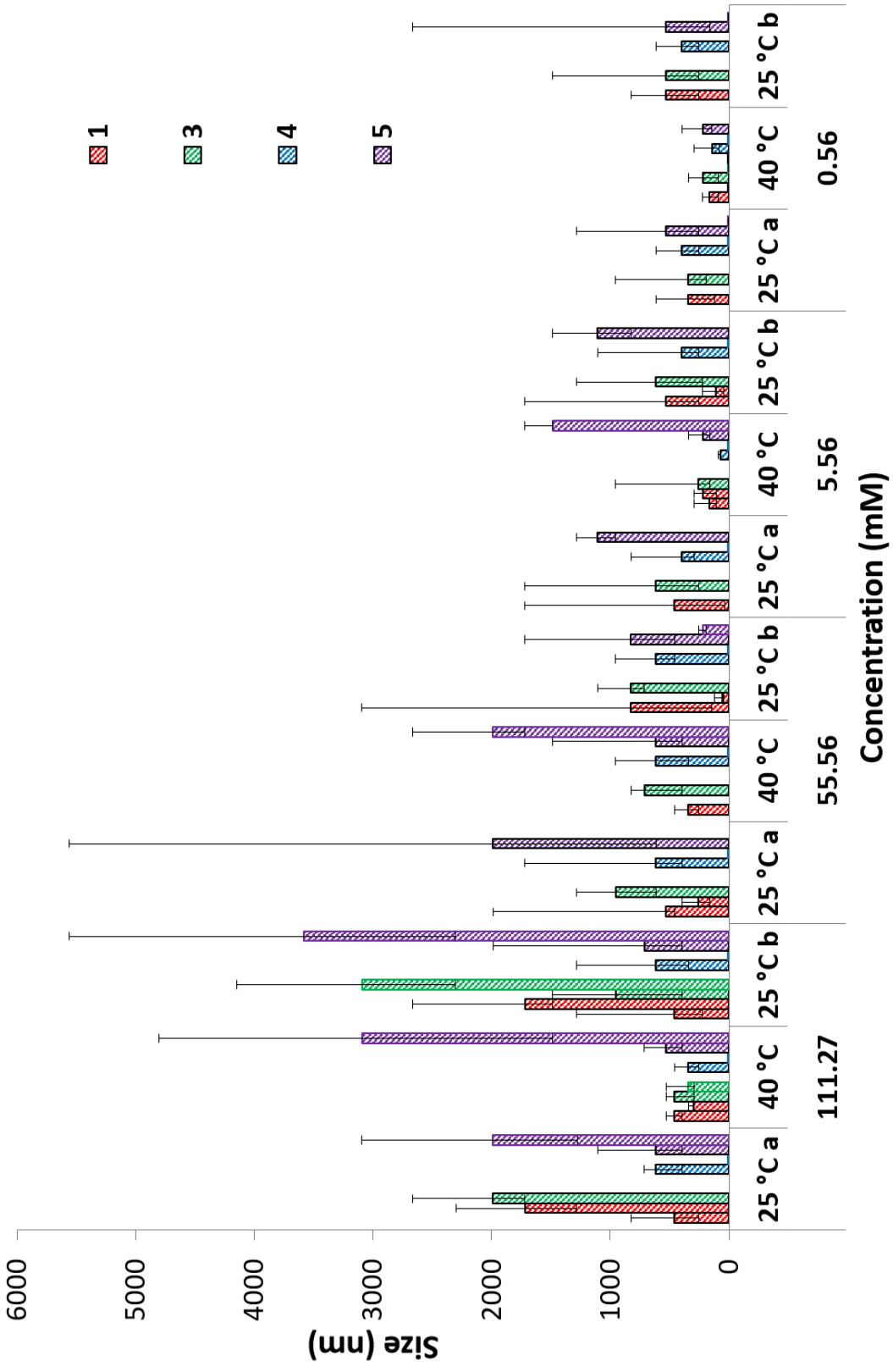

Figure 30 - Comparison of DLS peak maxima of compounds **1**, and **3** - **5**, showing the full range of aggregate size distribution in DMSO, values taken throughout the annealing process.

In altering the solvent system of compounds **1** - **5** it was possible to see to what effect the solvents had on the formation of the self-associated species. However, increasing polarity by the addition of water decreased solubility, as a consequence this factor determined the concentrations of the amphiphilic salts studied. A comparison of those structures formed can be seen in Table 4. It is evident from these results that the addition of water in the first instance to form a DMSO:H_2O 1:1 mixture increases the aggregate size. At a concentration of 5.56 mM the aggregate sizes change from ≈ 400 - 600 nm to 600 - 2300 nm upon first addition. Further increasing the percentage of H_2O in these solvent systems results in a general decrease in aggregate structure size to ≈ 300 - 1200 nm (DMSO: H_2O 3:7). To further explore this study, and increase molarity the DMSO solvent was replaced with ethanol across the series of amphiphilic salts. The observed aggregate sizes were; at 5.56 mM for **1** - **5** ≈. 200 - 300 nm (EtOH:H_2O 1:19). Figure 31 illustrates that the size of the aggregates continues to decrease to an ≈ 200 nm, this is evident for all compounds **1** - **5** (giving a full range of aggregate sizes from comparison of peak widths).

Table 4 - Average intensity particle size distribution of compounds **1** - **5**, calculated from 9 DLS runs in different solvent conditions at concentrations of 5.56 mM and 0.56 mM. Samples were prepared in series, with an aliquot of the most concentrated solution undergoing serial dilution and measured after heating to 40 ^{o}C and cooling to 25 ^{o}C.

Solvent conditions		Conc. (mM)	**1** peak maxima		**2** peak maxima		**3** peak maxima		**4** peak maxima		**5** peak maxima	
DMSO		5. 56	531	106	*a*		615		396	1.11	1106	
		0.56	531		*a*		531		396		531	0.72
DMSO : H_2O	1 : 1	5. 56	1990		615		1990	459	220	1281	2305	255
		0.56	1106		955		531		955		712	2669
	3 : 7	5. 56	342		825		1106		459	78.8	1281	
		0.56	396		396		615		615		342	
	1 : 4	0.56	58.8	342	342	68	712		91.3	615	825	
EtOH : H_2O	1 : 19	5. 56	220		164		220		58.8	295	295	
		0.56	164		255		396	0.83	122		220	

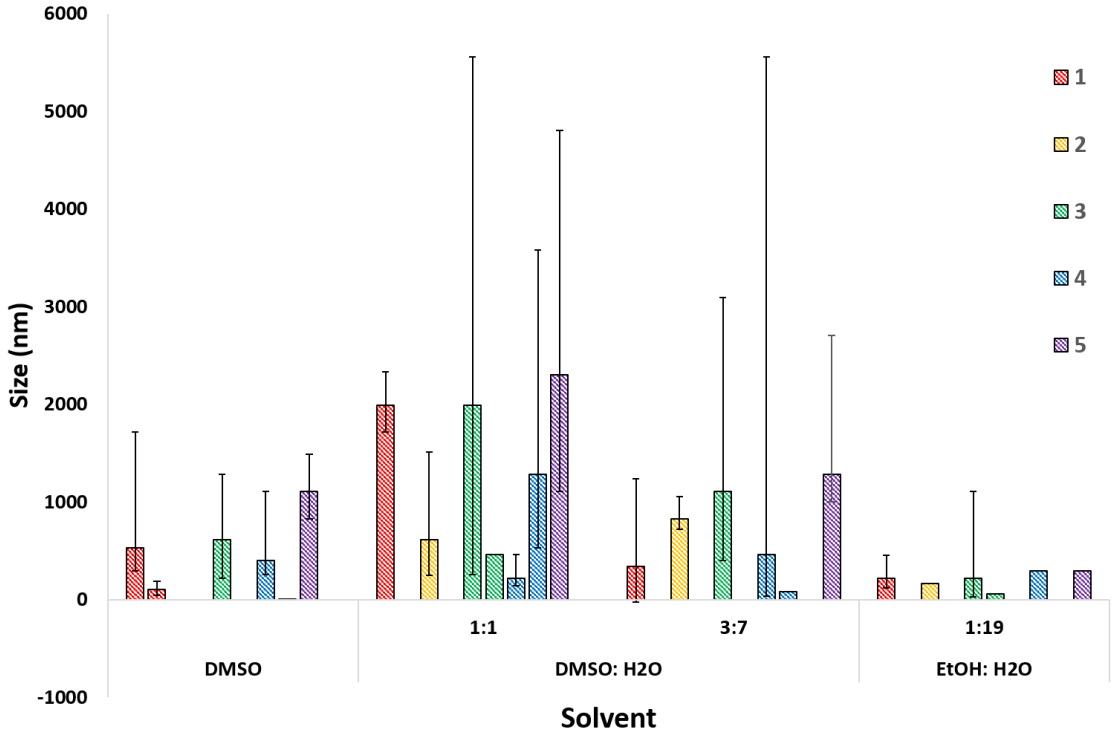

Figure 31 - Full range of intensity particle size distribution of compounds **1** - **5**, calculated from 9 DLS runs in different solvent conditions at a concentration of 5.56 mM.

The self-association of compounds **1** and **3** - **5** in a solution of DMSO demonstrated the existence of three different sized structures. The smallest structure ≈ 1- 58 nm in diameter is expected to be that of the sulfonate-urea monomeric or dimeric species. These structures are predominantly present in all concentrations of compound **4** and remain stable throughout the annealing process. The mid-size structures ≈ 100 - 600 nm formed in **1** and **3** - **5** are attributed to a larger self-associated species and although there appears to be some structure disruption when heated, it is apparent that these aggregated systems re-generate to form stable self-associated structures. Mostly observed in compound **5** are the occurrence of the largest of aggregates, identified at a size > 600 nm, these are shown to decrease when heated or diluted. This supports the theory that they are formed from the coalescence of smaller structures. The concentration dependence of these structures correlate with the understanding that the hydrogen bonded network will be destabilised by decreasing concentration this is attributed to competitive association with solvent molecules.

Upon heating of the compounds, the applied energy in the systems causes disruption of the weak non-covalent binding mechanisms that hold these super-structures together. As we have discussed, a limitation of size distribution data obtained from DLS is biased towards larger structures, this is due to the dependence of the intensity to the sixth power of the diameter.[82] The presence of the smaller structures at an ≈ 1 nm in **4** and the non-existence of the largest of aggregates leads us to believe that in **1**, **3** and **5** few, yet large aggregates observed in solution are masking the presence of the smaller assemblies like those we see in **4.** This is proposed to be specifically the case when the difference in size of these aggregates can be greater than 900 nm.

Excluding evidence of the monomeric or dimeric species in the EtOH: H_2O mixture, compounds **1** - **5** demonstrate the formation of only a single type of aggregated structure, exhibiting the following trend; **3** (400 nm) > **2** (260 nm) > **5** (220 nm) > **1** (160 nm). Dividing this amphiphilic family up into two sub groups and by discussing them independently it is observed that the extent of self-association is related to molecular structure. Sub group one contains compounds **1**, **2** and **3** which have decreasing aromatic ring system substituents of anthracene, naphthalene and phenyl respectively. It is observed that the decrease in aggregate size **3** < **2** < **1** is in correlation with the increase of aromaticity **1** > **2** > **3.** Sub group two contains compounds **4** and **5** both of which have benzothiazole substituents. Comparisons between these two compounds show that the intramolecular hydrogen bonded compound **5** forms larger structures in all solvent systems than compound **4**.

As we have identified in Figure 31, the initial increase in polarity from DMSO, to a 1:1 DMSO:H_2O solution appears to stabilise the formation of larger aggregates. Where further increase of water decreases the size of the aggregates observed. The substitution of DMSO to ethanol enabled the solute-solvent and solute-solute structure activity of these compounds to be studied further.

The results demonstrate self-association between the molecules in solution decreases with increased quantities of H_2O. This can be attributed to solute-solvent interactions where the solvent binds with the solute molecule, thus limiting the quantity of available hydrogen bond accepting sites. Full data set of count rates and size distribution graphs available in appendix Figure S191 - S252.

2.4 Ultra-Violet visible spectroscopy and fluorometry studies

Techniques such UV-Vis spectroscopy and fluorometry are routinely used as a preliminary study, with the sole purpose of gaining information as to aid further analytical methods such as fluorescence microscopy. To be able to identify which filters are most appropriate for our microscopy studies, these analytical methods were used. UV-Vis spectroscopy methods were applied to enable the wavelength at which the sample absorbs to be attained. This information was then used as a guide for the fluorometry studies where the excitation and emission properties of the amphiphilic salts were then determined. All samples were prepared in solvent systems analogous to those used throughout the solution state studies.

2.4.1 Results and discussions

The results from the UV-Vis studies determine that **1**, **2**, **4** and **5** all absorb light in the region of 294 nm - 356 nm (Table 5). This information was then used to identify the wavelength ranges that excitation/emission peaks would be present at for the fluorescent spectroscopy studies.

Table 5 - Absorbance properties of compounds **1**, **2**. **4** and **5.**

Abs	Solvent				
λ (nm)	DMSO	DMSO: H_2O			EtOH: H_2O
		1:1	3:7	1:4	1:19
1	339	357	356	356	356
2	308	295	286	289	283
4	338	334	331	331	327
5	295	298	294	294	293

Shown in Figures 32 - 35 are the results obtained from the fluorometry studies of compounds **1**, **2**, **4** and **5** in a DMSO solution, these data are also displayed in tabulated format (Table 6). The table displays the excitation and emission values, along with the calculated stokes shift. These results demonstrate that **1**, **2**, **4** and **5** have an excitation value between 220 and 338 nm and an emission value between 376 and 440 nm. From this table, we can see that **1** has a large stokes shift of > 158 nm (Figure 32), because of this we were unable to directly observe this compound using any of the suitable filters for the microscopy studies. Fluorescent molecular compounds which have a large stokes shift exhibit relatively low brightness. These compounds are also prone to fast photobleaching due to poor photostability.[83] At the other end of the scale, a small stokes shift < 25 nm results in self-quenching and measurement error.[84] Fortunately although **2** and **5** (Figures 33 and 35) have a relatively small stokes shift they do not fall into this category and as a result, using a suitable filter **4** we were able to directly visualise them in most solvent systems. However, it was not possible to directly observe **2** due to incompatibility with the available filters. Full data sets for UV-Vis and fluorometry studies are visible in appendix Figure S186 - 225.

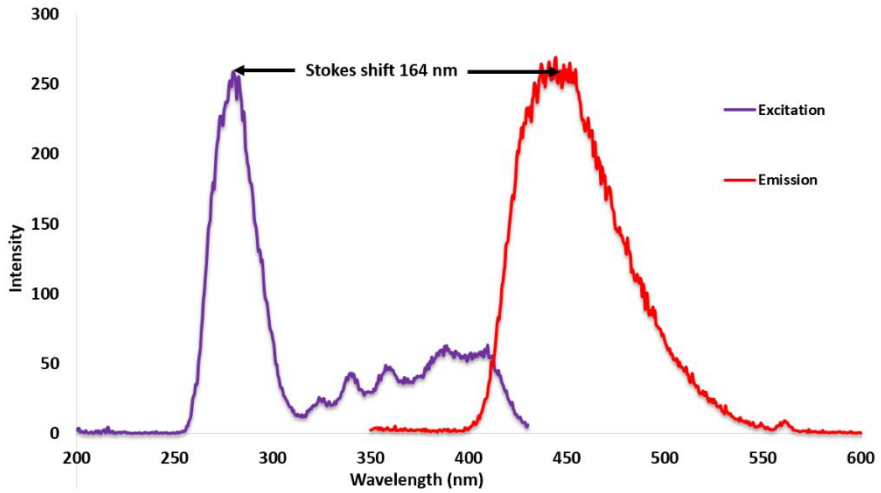

Figure 32 - Fluorescence spectra of compound **1** (0.003 mM) in a solution of DMSO. Displaying a large stokes shift of 164 nm.

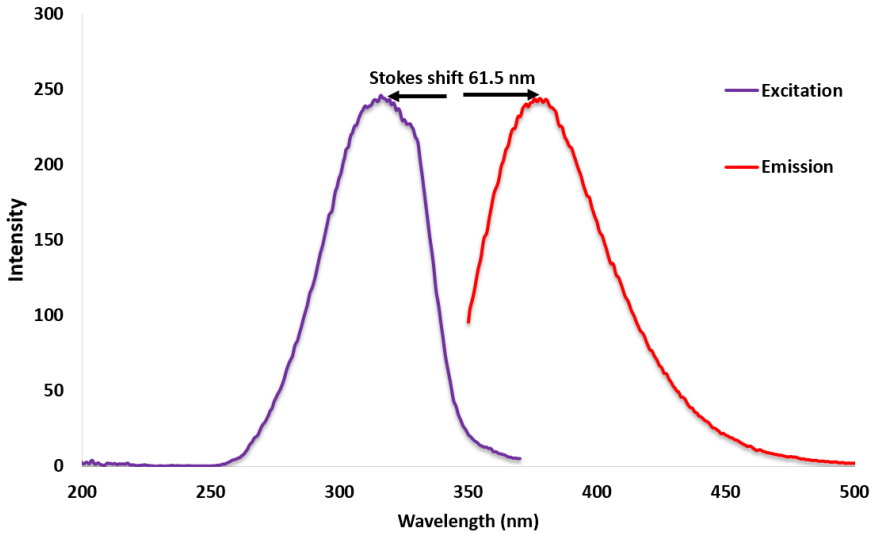

Figure 33 - Fluorescence spectra of compound **2** (0.003 mM) in a solution of DMSO. Displaying a stokes shift of 61.5 nm.

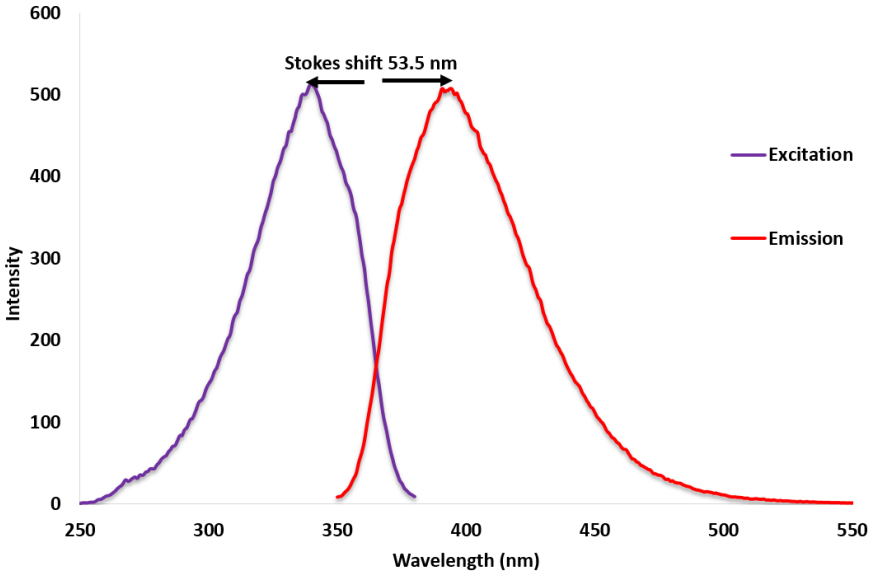

Figure 34 - Fluorescence spectra of compound **4**(0.003 mM) in a solution of DMSO. Displaying a stokes shift of 53.5 nm.

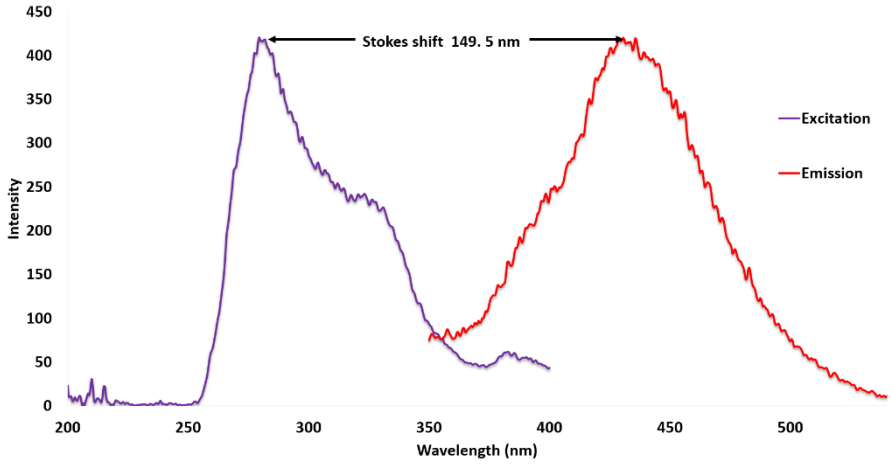

Figure 35 - Fluorescence spectra of compound **5** (0.003 mM) in a solution of DMSO. Displaying a stokes shift of 149.5 nm.

Table 6 - Excitation and emission properties of compounds **1**, **2, 4** and **5.**

λ_{max} (nm)		Solvent				
		DMSO	DMSO: H_2O			EtOH: H_2O
			1:1	**3:7**	**1:4**	**1:19**
1	λ_{ex}	280.5	275.8	272.2	273.6	259.5
	λ_{em}	444.5	440.5	436.5	432.1	437.4
	$\Delta\lambda_{ST}$	164.0	164.7	164.3	158.5	177.9
2	λ_{ex}	315.0	336.5	294.1	295.5	223.5
	λ_{em}	376.5	395.1	376.9	377.2	380.0
	$\Delta\lambda_{ST}$	61.5	58.6	82.8	81.7	156.5
4	λ_{ex}	338.6	334.5	332.5	332.2	331.0
	λ_{em}	392.1	395.2	394	397.4	398.5
	$\Delta\lambda_{ST}$	53.5	60.7	61.5	65.2	67.5
5	λ_{ex}	280.4	280.3	283.3	285.0	228.5
	λ_{em}	429.9	419.4	418.9	417.1	415.2
	$\Delta\lambda_{ST}$	149.5	139.1	135.6	132.1	186.7

The excitation and emission values obtained enabled the most appropriate filters to aid visualization to be identified. These were determined to be: DAPI and GFP which are for molecules that fluoresce within the excitation ≈ 350 nm and 480 nm and emission ≈ 450 nm and 510 nm ranges respectively.

2.5 Microscopy

Fluorescent molecules are readily visualised using fluorescence optical imagery. This technique allows for the details of cellular/molecular organization to be probed with a precision unlike other methods, ultimately enabling confirmation as to whether the molecules are self-assembling to form proposed structures. This method has emerged as an attractive modality to study molecular interactions of fluorescent molecules,[85] cell biology[86,87] and disease processes.[88] Kaeser and Schenning utilised this technique to explore the transformation upon addition of a dye, from cylindrical objects into spherical aggregated units, through π-π interactions within the conjugated system.[89]

Compounds **1**, **2**, **4** and **5** were developed as intrinsically fluorescent amphiphiles to enable the opportunity for direct observation of the aggregate structures in the solution state. Using transmission and fluorescent microscopy allows for direct comparison to other non-direct techniques such as DLS and NMR, thus providing both qualitative and quantitative data. Due to the highly fluorescent nature of these compounds photobleaching during the imaging process occurred, leading to a loss of fluorescent emission intensity. Therefore, in one or both images some amphiphile aggregates could not be captured. Using both microscopy techniques aided in capturing some images that were susceptible to this, as well as enabling the highly concentrated locations of the sulfonate-urea anion to be identified. The ability to directly observe these compounds is a huge breakthrough in gaining a greater understanding into the self-associated aggregated structure formation of this class of amphiphile in the solution state. There are however limitations of observation techniques such as microscopy. Any direct observations may not be representative of the bulk sample and therefore can be susceptible to sample bias. This method also only allows for the retrieval of qualitative rather that quantitative data and should therefore combined with other comparative studies such as NMR and DLS.

In line with techniques previously reported by Levin[90] 10 µl of the appropriate sample was pipetted onto the centre of an agarose pad, covered with a coverslip and secured in place restricting any movement or evaporation of the solvent. The solvent systems used in this study were analogous to those used in the DLS studies, this allows for direct comparisons to be made. As previously discussed any aggregates of compounds **1** and **2** could not be observed using transmission or fluorescence techniques due to the excitation and emission properties of these compounds resulting in inherent background fluorescence.

2.5.2 Results and discussion

From the microscopy images obtained it is apparent that compound **4** in an EtOH:H_2O 1:19 solvent mixture forms irregular shaped conglomerates of smaller species that are ≈ 105 nm (Figure 36). However, substituting the EtOH for DMSO at the equivalent ratio causes the amphiphilic salts to self-associate into a spherical aggregate unit with the same diameter measurement of ≈ 105 nm (Figure 37). In a solution of just DMSO we again see these spherical aggregated structures, the size of these 'superstructures' are now much larger at ≈ 363 nm as seen in Figure 38.

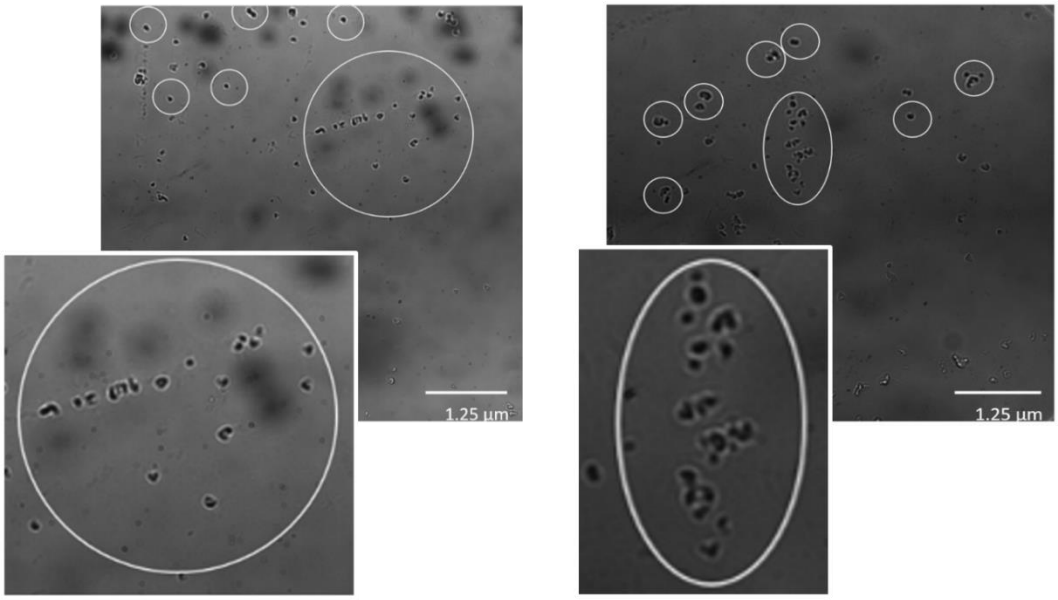

Figure 36 - A selection of transmitted light microscope images of compound **4** (0.50 mM) in an EtOH:H_2O 1:19 solutions. Examples of the aggregate structures have been circled for clarity.

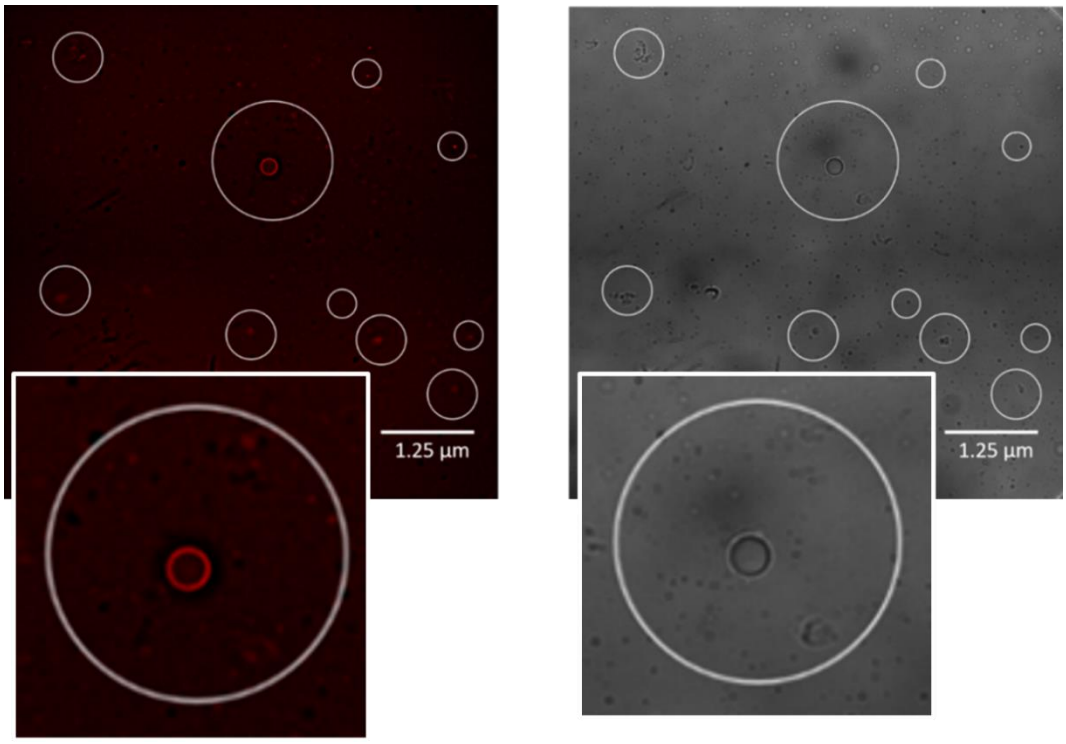

Figure 37 - A selection of DAPI filter composite images (left) and transmitted light images (right) of compound **4** at a concentration of 0.50 mM in a solution of DMSO:H_2O 1:19. Evidence of aggregate structures are circled for clarity.

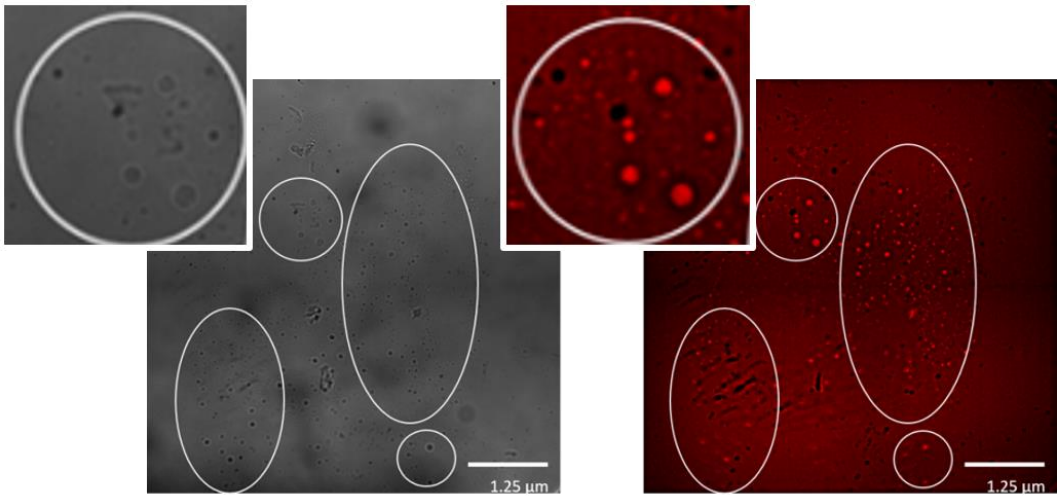

Figure 38 - A selection transmitted light images (left) and DAPI filter composite images (right) of compound **4** at a concentration of 0.50 mM in DMSO. Evidence of aggregate structures are circled for clarity.

From the microscopy methods used we were able to identify that compound **5** forms spherical aggregates in all solvent systems. However, the diameter size of these structures alters depending on the system of which it is dissolved. In an EtOH:H_2O 1:19 solution we see structures that are an ≈ 275 nm (Figure 39). In DMSO: H_2O 1:1 the aggregated structures measure ≈ 650 nm (Figure 40), in DMSO: H_2O 3:7 ≈ 300 nm (Figure 41) and in just DMSO ≈ 255 nm (Figure 42).

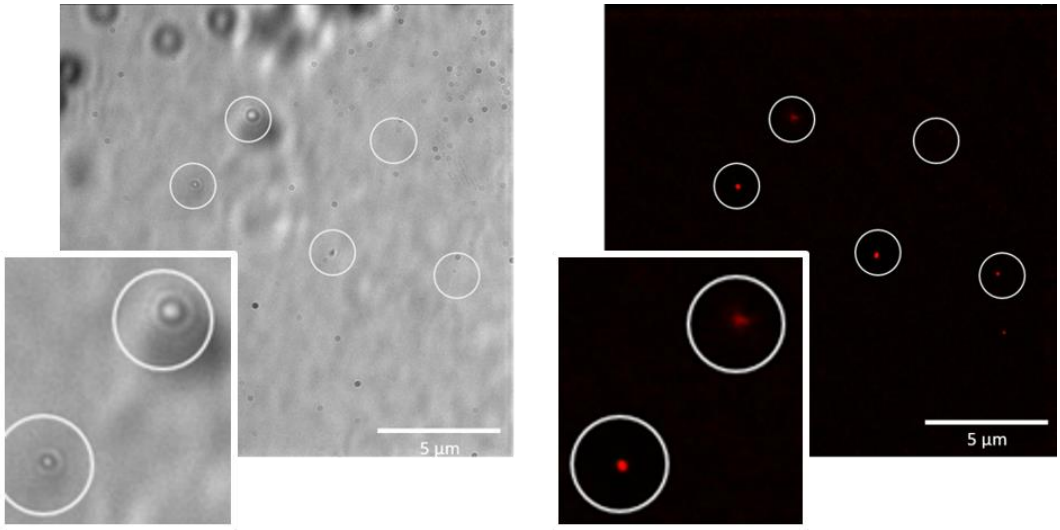

Figure 39 - A selection of transmitted light images (left) and DAPI filter composite images (right) of compound **5** at a concentration of 0.50 mM in a solution of EtOH:H_2O 1: 19. Evidence of aggregate structures are circled for clarity.

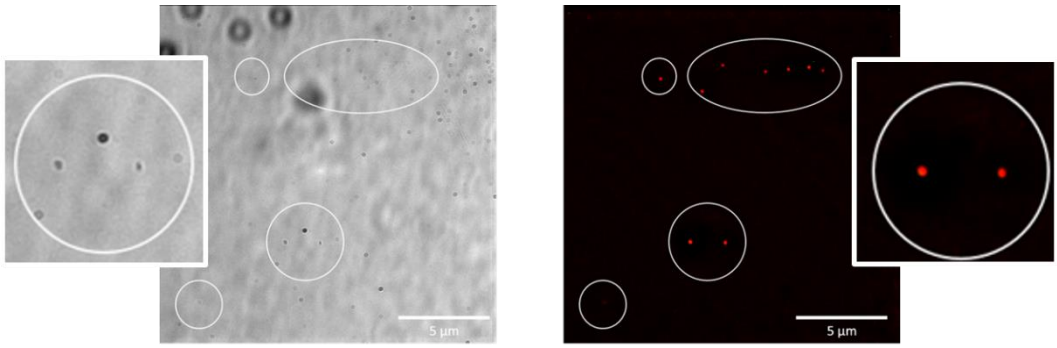

Figure 40 - A selection of transmitted light images (left) and DAPI filter composite images (right) of compound **5** at a concentration of 0.50 mM in a solution of DMSO: H_2O 1: 1. Evidence of aggregate formation are circled for clarity.

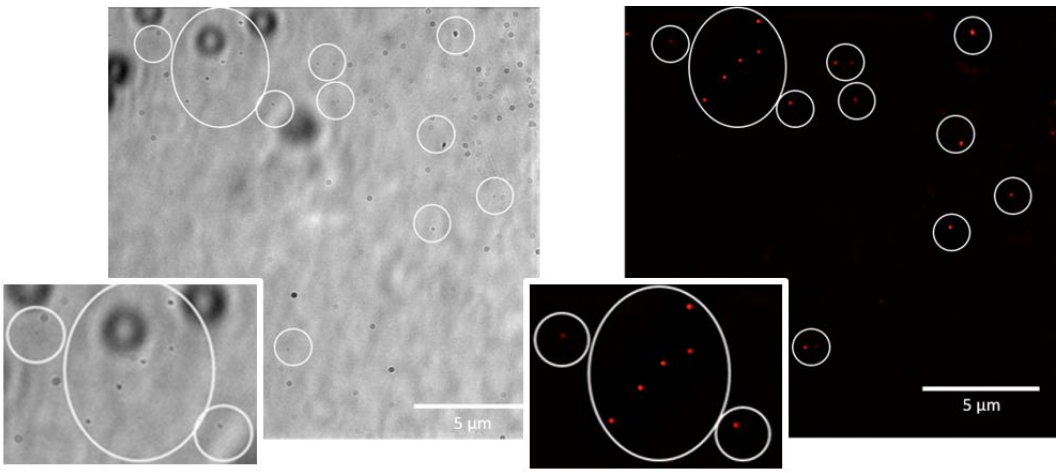

Figure 41 - A selection of transmitted light images (left) and DAPI/ GFP filter overlay images (right) of compound **5** at a concentration of 0.50 mM in a solution of DMSO: H_2O 3: 7. Evidence of aggregate structures are circled for clarity.

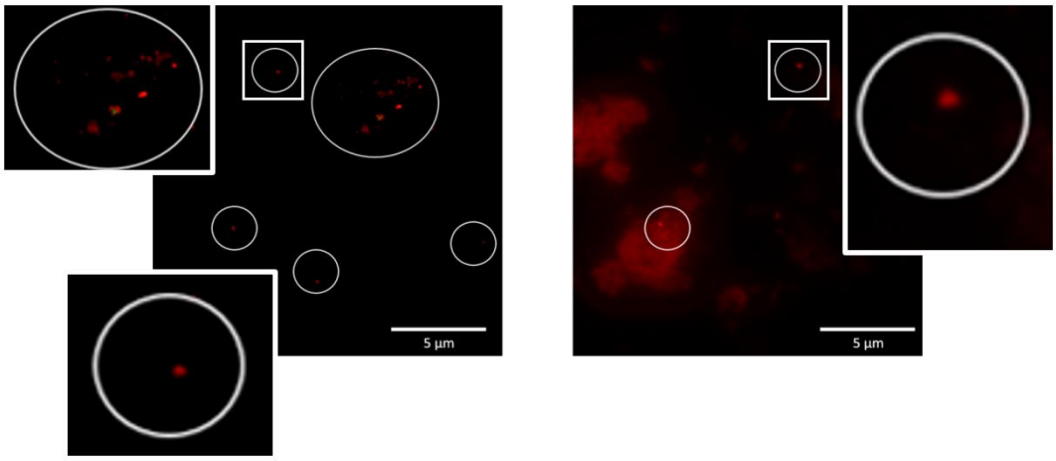

Figure 42 - A selection of DAPI filter images of compound **5** at a concentration of 0.50 mM in DMSO. Evidence of aggregate structures are circled for clarity

As we have identified the solvent system of which the compound is in plays an integral role in the self-association of these amphiphilic salts to form spherical aggregated structures, with the sizes of these dependent on the solution type. Compound **4** in EtOH:H_2O forms aggregates 105 nm in diameter of varying geometries, these are expected to have been generated from conglomerates of smaller aggregated species. Whereas, Compound **5** in the same solvent system forms spherical species which demonstrate little internal structure.

It is hypothesised that in this system and in the DMSO:H_2O 1:19 mixtures for both **4** and **5**, that the molecules self-associate into aggregated structures with the hydrophilic sulfonate-urea substituents forming the outer structure and the hydrophobic moieties positioning themselves within the spherical unit. Full range of images available in appendix Figure S236 - 244.

A comparison of average structural size through microscopy and DLS methods of the aggregated species for compounds **4** and **5** (Figure 43) establish that the average size of the observed aggregate structures is in good agreement. In most instances, it was observed that the average diameter size of the aggregates measured using DLS were slightly larger than those observed via the microscopy methods, this increase is probably due to the DLS measurement incorporating the hydrodynamic solvation sphere of which surrounds the aggregated structure. The size of all observed structures by these microscopy techniques are within the spread of aggregate sizes that were observed via DLS.

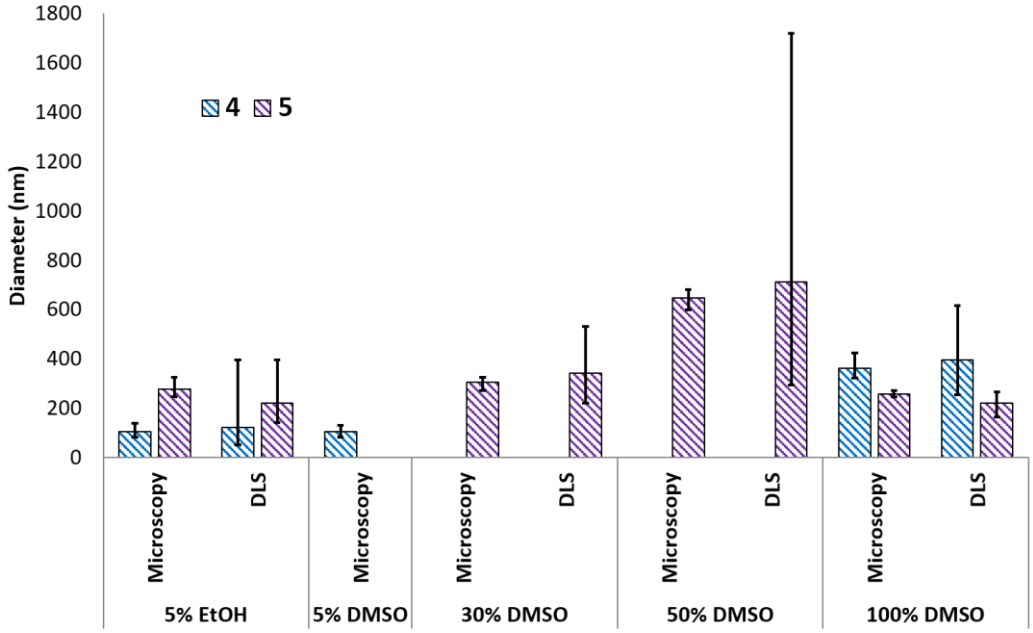

Figure 43 - Bar graph comparing the spread of aggregate sizes obtained from DLS average intensity size distribution studies in a range of solvent systems of compounds **4** and **5** (0.56 mM) with the spread of aggregate sizes of structures observed through microscopy methods in the same solution mixtures (0.5 mM).

2.6 NMR Studies

2.6.1 Quantitative NMR studies

There are several techniques which can be employed to explore the binding characteristics of a molecule those of which include; ^{1}H NMR,[91] ^{15}N NMR,[92] and Diffusion Ordered Spectroscopy (DOSY).[93] We observed in the DLS studies that we had two identifiable species present for compound **4** in DMSO, where the diameter size was measured to be an ≈ 1 nm including the hydrodynamic solvation sphere and the other larger aggregate being ≈ 400 nm. The relatively low count rate for **4** in DMSO (Appendix Figure S175 - 180) implies that the majority of the self-associated amphiphiles existing in this solvent system are either monomeric or dimeric in nature. To establish if this was indeed the case and to gain an understanding as to the size of the self-associated species that are observed by ^{1}H NMR, a proof of principle ^{1}H NMR DOSY experiment was conducted with **4** (55.6 mM). This experiment mirrored the annealing process used in the DLS studies so as to gain a comparative result (*Note, this study was completed and the data analysed by Dr J. Hiscock, and Neil Wells (University of Southampton)).

To further explore this hypothesis and determine if there was loss of compound within the DMSO solution when studied using DLS, an additional experimental study was completed. This was conducted by comparative peak integration using ^{1}H NMR and by doping a 111 mM DMSO-d_6 solution of **4** with 5 µl of dichloromethane. In addition to these studies a further two experiments were conducted with **4** (6 mM) in D_2O spiked with EtOH (25 µl) and DMSO (5 µl) respectively. This study was completed to determine loss of compound in analogous solvents to those used within the microscopy and DLS studies.

2.6.1.1 Results and discussion

According to the results generated and analysed for the ^{1}H NMR DOSY studies by J. Hiscock and N. Wells, it is apparent that the TBA counter cation has a different diffusion constant from that of the sulfonate-urea anion. This demonstrates that these two species are not strongly co-ordinated in the solution state (Figure 44). The ^{1}H NMR DOSY study enabled the translational diffusion constant to be obtained, applying this to the Stokes- Einstein equation[94] it was possible to calculate the hydrodynamic diameter of the sulfonate-urea anion. It must be taken into consideration that these values should be treated with caution, as with DLS, the size of these approximations assume that the structure observed is a sphere and that the size of the complex is large compared to that of the solvent.[95] Due to these systems existing in fast exchange the diffusion constants were obtained from the aromatic CH and CH_2 signals as opposed to the NH signals. The results obtained gave upper and lower limits for the hydrodynamic radius of **4** at 26 °C (1.61 nm ≤ d_H ≥ 1.66 nm), after being heated to 39 °C (1.44 nm ≤ d_H ≥ 1.51 nm) and then cooled back to 26 °C (1.58 nm ≤ d_H ≥ 1.61 nm). The comparative size of these structures calculated by DLS at thermodynamic minimum was 1.12 nm (Figure 28), which correlates well with the ^{1}H DOSY NMR results. However, the larger structures observed in the DLS studies were not visible via this NMR method. It is therefore hypothesised that these larger structures are not able to be observed by this NMR method due to them being either NMR silent, therefore existing in concentrations that are too low or due to the size of the aggregate being too large.

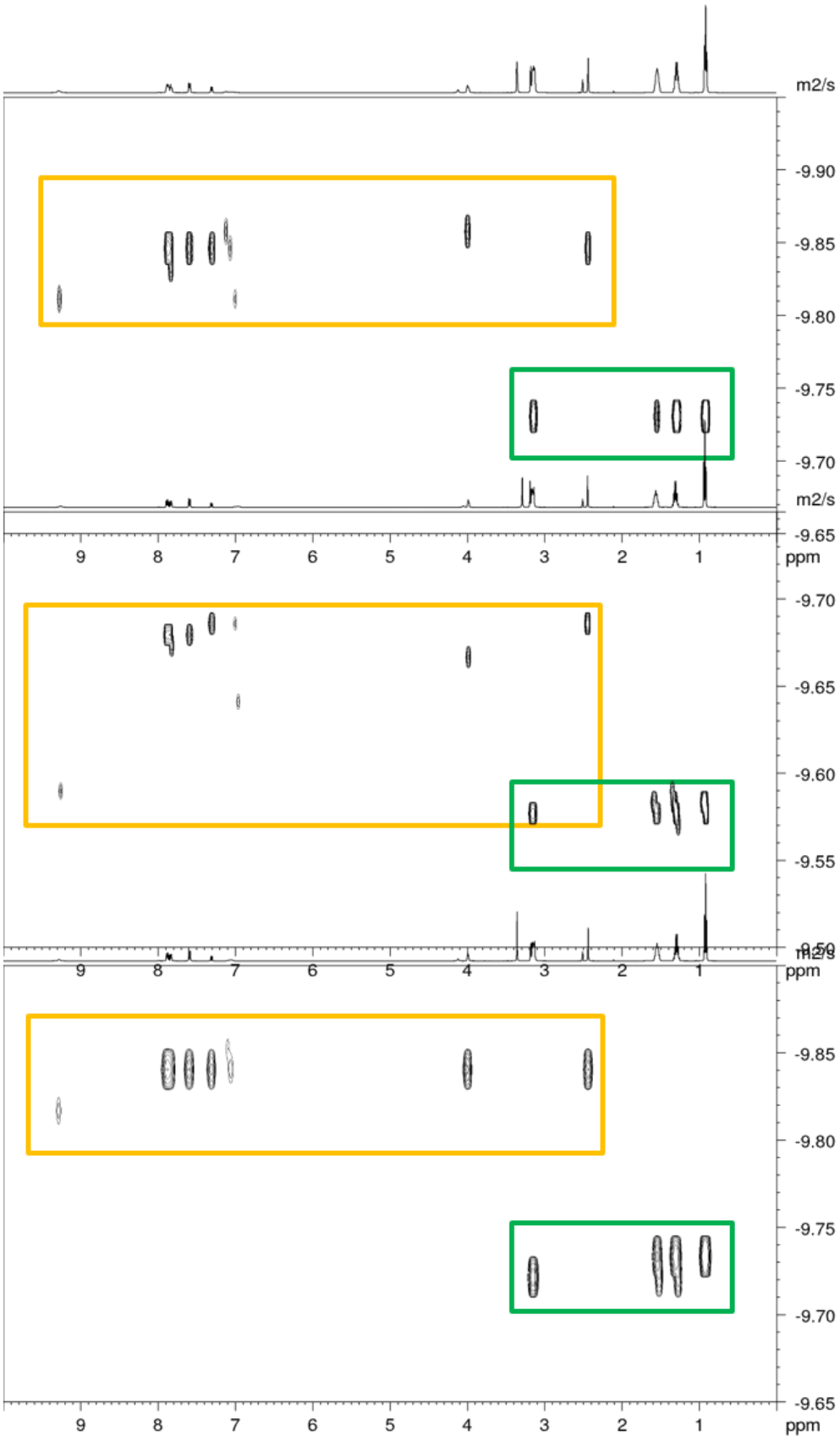

Figure 44 - ^{1}H NMR DOSY of compound **4** (55.6 mM) in DMSO-d_6 conducted at 26.15 ^{o}C (A), 38.65 ^{o}C (B) and 25.96 ^{o}C (C). Anionic compound is highlighted in yellow, TBA counter cation highlighted in green. Image courtesy of J. Hiscock

It was hypothesised previously during the conduction of the DLS experiments that the larger structures do not exist in large quantities within the solution state. To prove this theory a series of further ^{1}H NMR studies were completed. These studies were conducted with additional scans so as to ensure that the information received encompassed the full sample as this experiment was determination of possible loss of product. The results of these show that in a DMSO-d_6 solution the comparative peak integration of the aromatic CH and sulfonate-urea CH_2 with the DCM signal show no apparent loss of the amphiphile from the solution. This confirms our hypothesis that the larger aggregated structures only exist in very small quantities, therefore are not detectable under the NMR conditions exploited within this study (Figure 45).

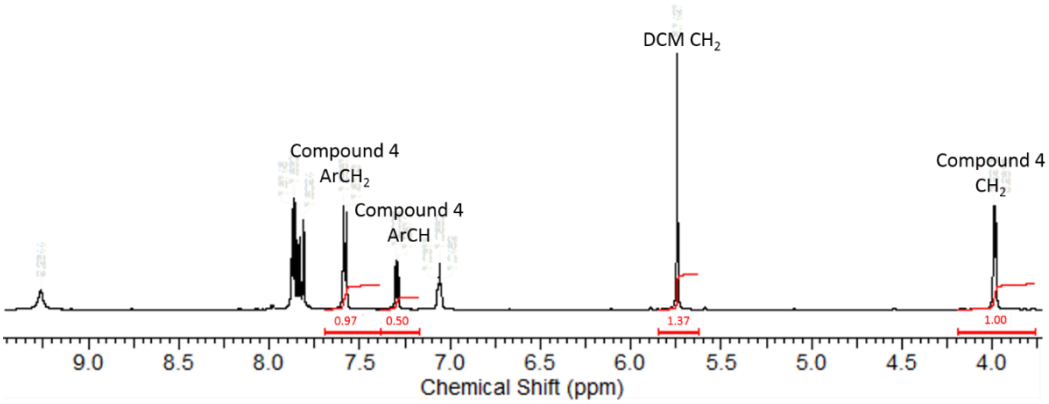

Figure 45 - ^{1}H NMR of compound **4** (0.035 g, 0.05 mM) and dichloromethane (0.007 mg, 0.08 mM) in DMSO-d_6.

The following two ^{1}H NMR experiments were compiled in analogous solvents to those used in the DLS and microscopy studies. The results show that when compound **4** was doped with ethanol there is a 10 % loss of the sulfonate-urea anion, and when doped with DMSO there appears to be an apparent loss of 14 % (Figures 46 - 47). It is hypothesized that this lost material is invisible during the NMR studies due to being removed from the solution state forming solid state aggregates, therefore NMR silent. These NMR studies conclude that only a very small percentage of sulfonate-urea anion is contained within these larger self-associated assemblies and the majority of compound remains in the solution state.

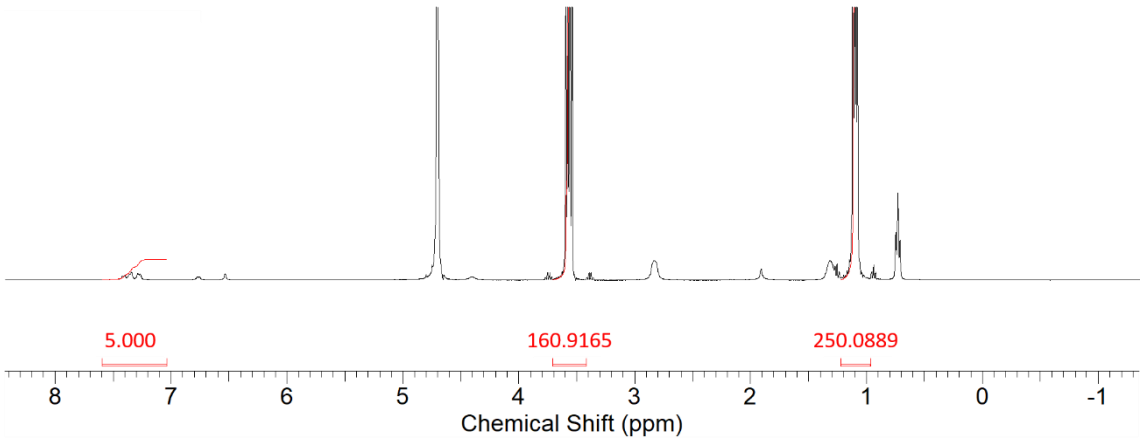

Figure 46 - ^{1}H NMR spectrum with a delay (d_1 = 60 s) of compound **4** (0.037 g, 5.9 mM) and ethanol (25 µl, 0.43 mM) in D_2O. An apparent 9.99% loss of compound was observed upon comparative signal integration.

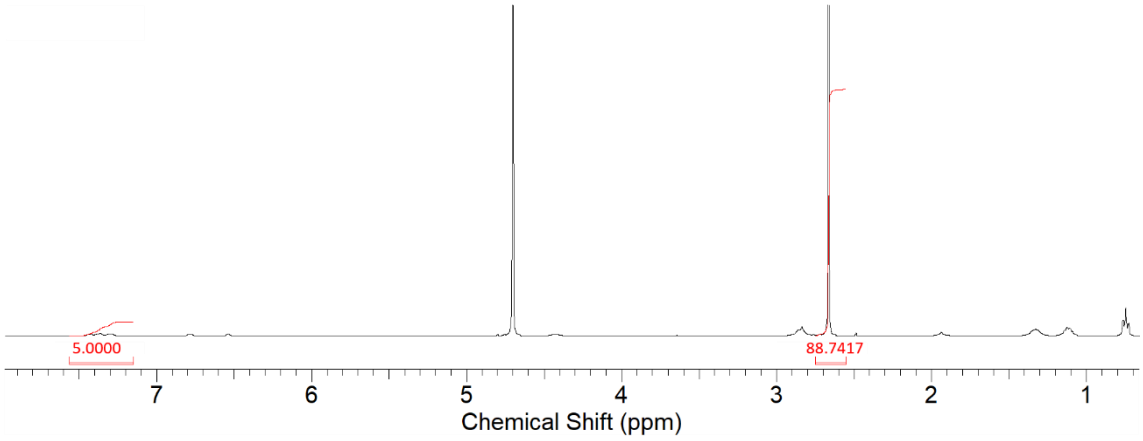

Figure 47 - ^{1}H NMR spectrum with a delay (d_1 = 60 s) of compound **4** (0.035 g, 5.6 mM) and DMSO (5 µl, 0.07 mM) in D_2O. An apparent 13.52 % loss of compound was identified upon comparative signal integration.

2.6.2 ^{1}H NMR self-association studies

In order to gain an understanding of the molecular level self-associated interactions ^{1}H NMR was used to conduct a series of dilution studies. Where samples were prepared in series with an aliquot of the most concentrated solution undergoing serial dilution**.** This method allows for direct observations as to the binding mechanisms of the HBD urea-NH groups at different molarities. A stack plot of compound **1** (Figure 48) is displayed for clarification purposes. Stack plots for compounds **2** - **5** are available for viewing in appendix Figures S16 - 30.

2.6.2.1 Results and discussions

As we can observe in Figures 48 (illustrative representation) and 49 (graphical representation) there is a ^{1}H NMR down-field change in chemical shift with increasing concentration, for both urea NH resonances of compound **1**. With the NH situated closest to the sulfonate-urea exhibiting a greater change. Compounds **2 - 4** (Figures 50 - 52) exhibit this same pattern. It was not possible to get data about the NH group that is situated closest to the aromatic substituent for compound **5** (Figure 53), due to being positioned at a similar ppm to that of one of the aromatic CH peaks. As we identified in the solid-state studies this NH forms an intramolecular bond with the benzothiazole nitrogen. We would therefore not expect to see a large change in chemical shift for this moiety. We do however see an NMR down-field change in chemical shift for the NH resonance closest to the sulfonate-urea. The change of chemical shift is greater for compounds **1**, **3** and **4** between the ranges of 0.3 - 0.7 ppm, with compound **2** being significantly lower at 0.07 ppm.

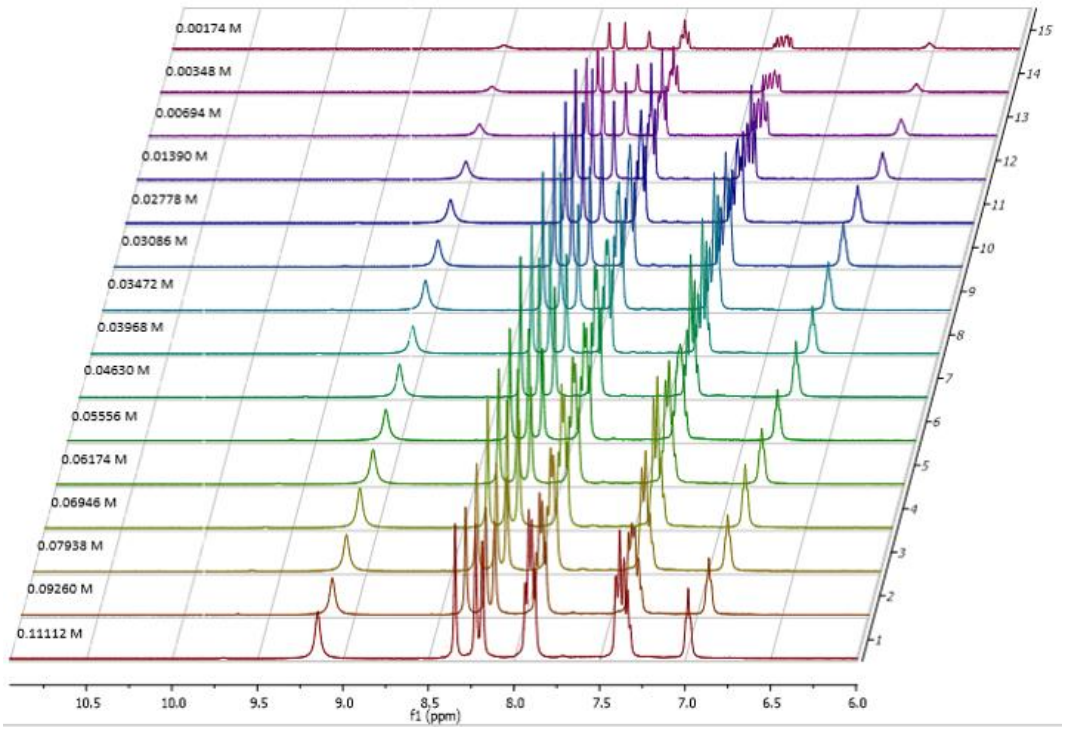

Figure 48 - Enlarged ^{1}H NMR stack plot of compound **1** in DMSO-d_6 0.5% H_2O solution. Samples were prepared in series with an aliquot of the most concentrated solution undergoing serial dilution.

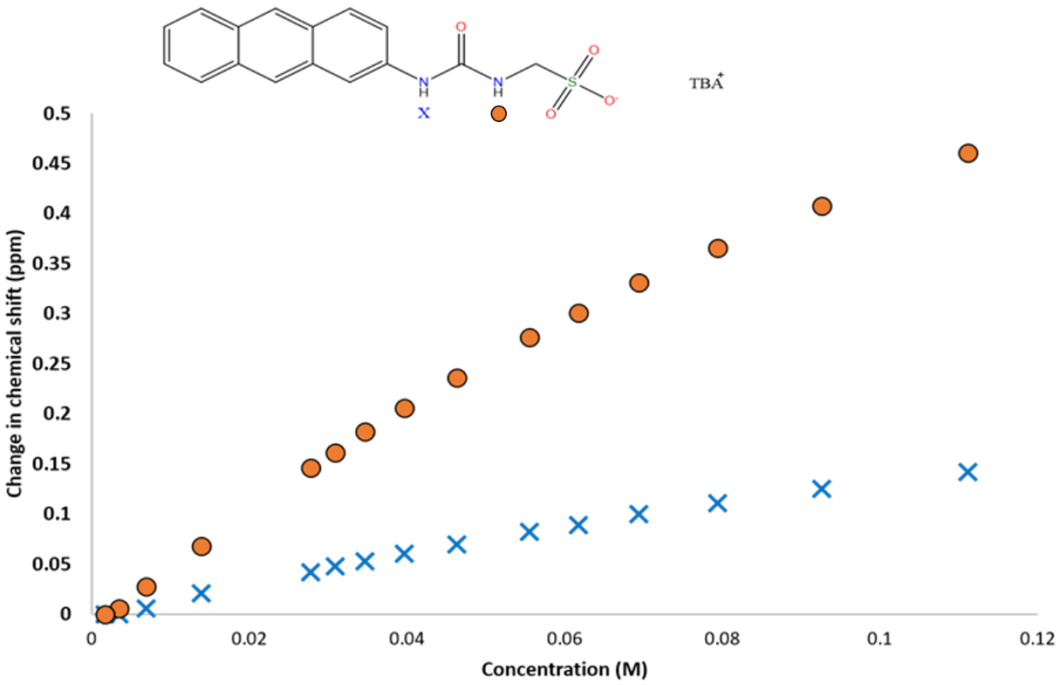

Figure 49 - Graph illustrating the ^{1}H NMR down-field change in chemical shift of urea NH resonances with increasing concentration of compound **1** in DMSO-d_6 0.5% H_2O (298 K).

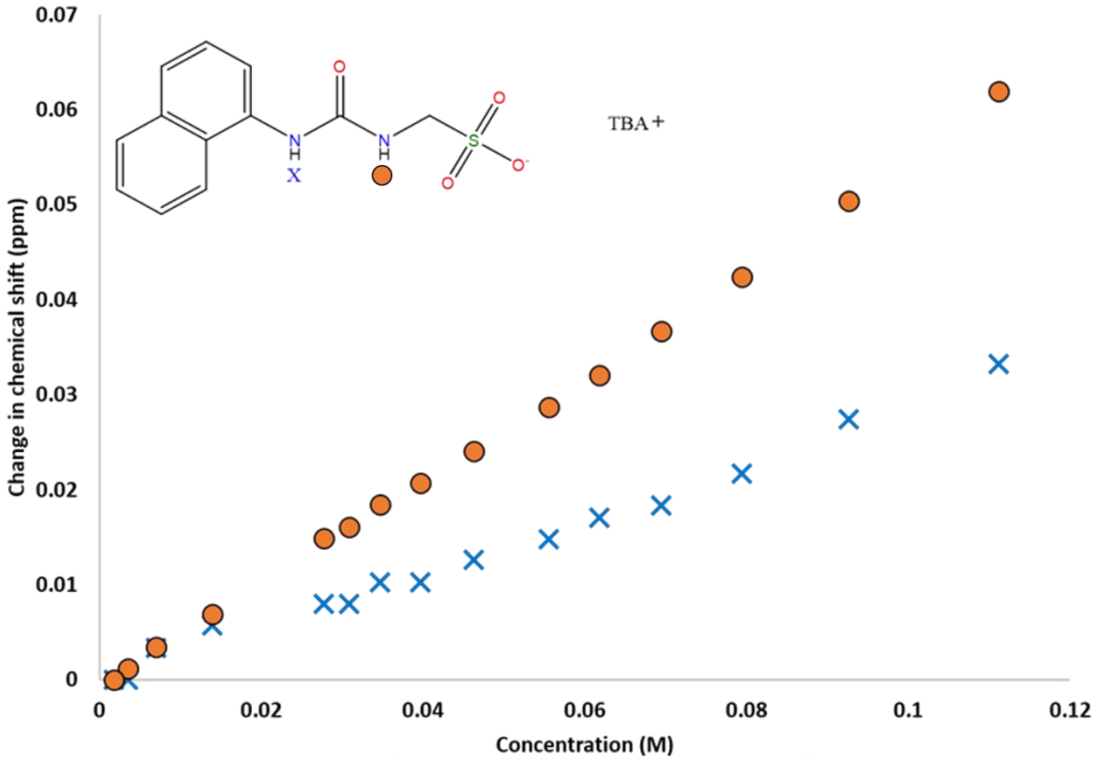

Figure 50 - Graph illustrating the ^{1}H NMR down-field change in chemical shift of urea NH resonances with increasing concentration of compound **2** in DMSO-d_6 0.5% H_2O (298 K).

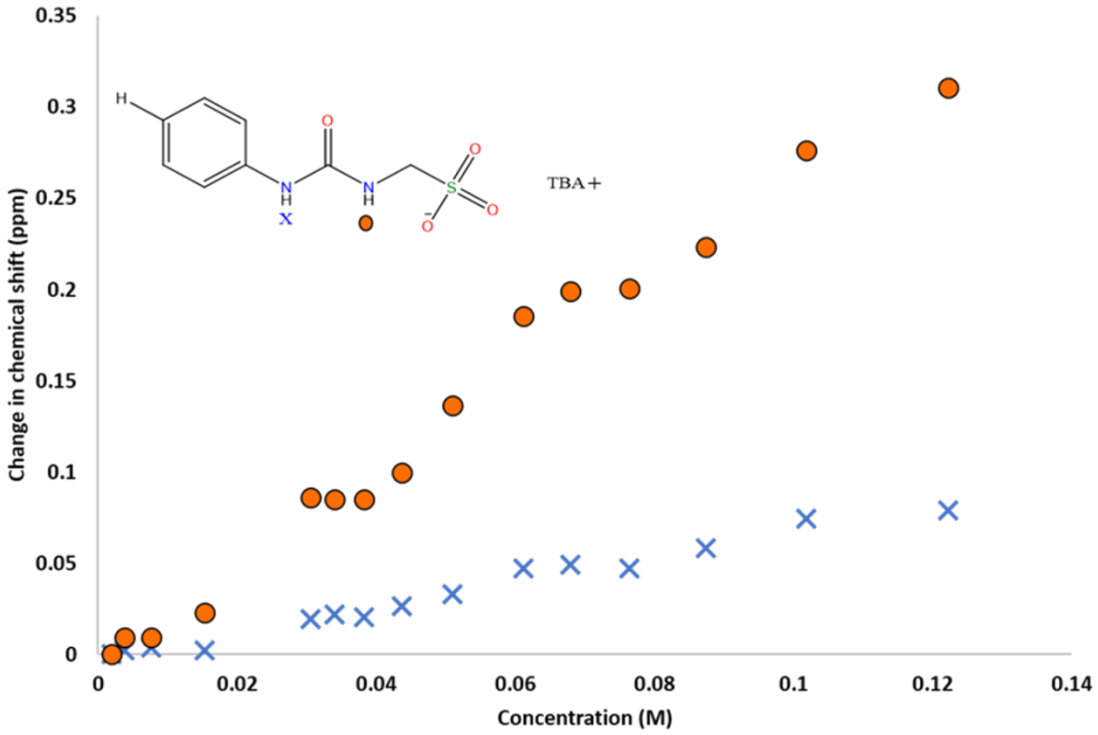

Figure 51 - Graph illustrating the ^{1}H NMR down-field change in chemical shift of urea NH resonances with increasing concentration of compound **3** in DMSO-d_6 0.5% H_2O (298 K).

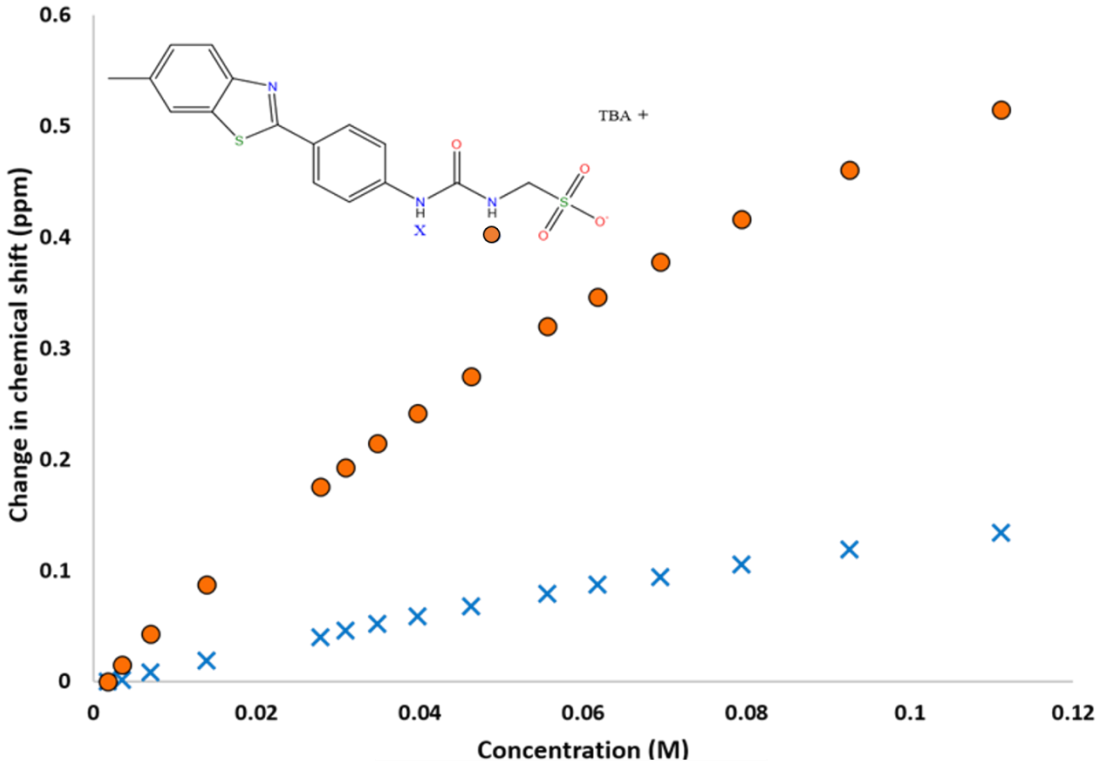

Figure 52 - Graph illustrating the ^{1}H NMR down-field change in chemical shift of urea NH resonances with increasing concentration of compound **4** in DMSO-d_6 0.5% H_2O (298 K).

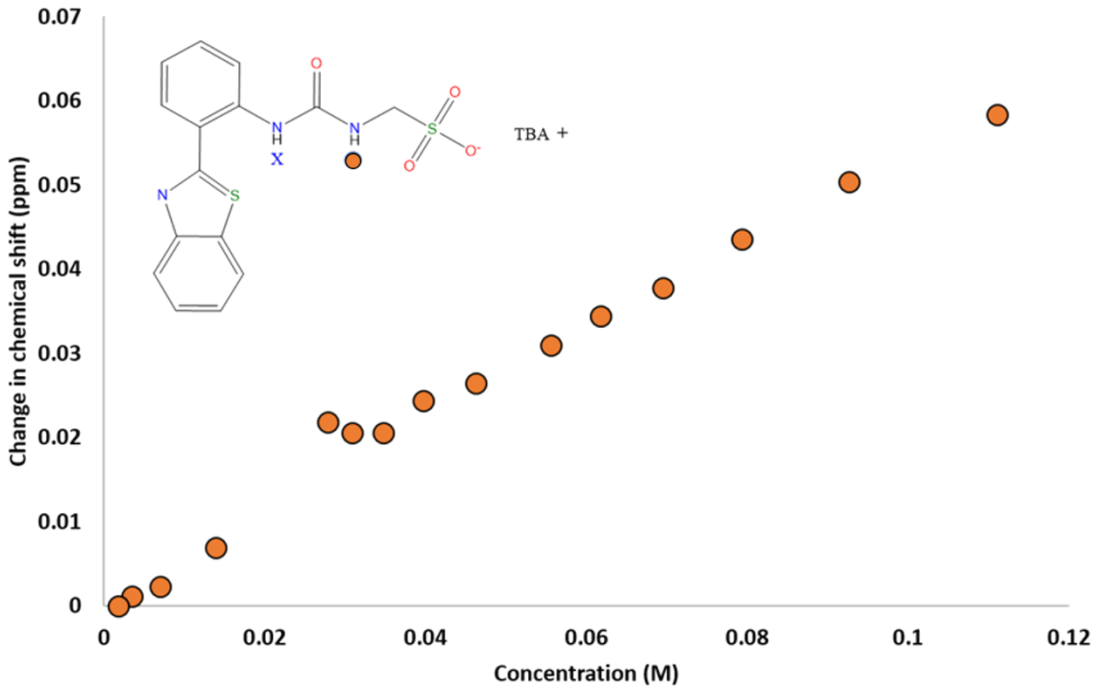

Figure 53 - Graph illustrating the ^{1}H NMR down-field change in chemical shift of urea NH resonances with increasing concentration of compound **5** in DMSO-d_6 0.5% H_2O (298 K).

The presence of hydrogen bonding in the self-association of **1 - 4**, through both of the urea NH groups was confirmed by ^{1}H NMR dilution studies in DMSO-d_6/0.5% H_2O. As shown in Figures 49 - 52, a down-field change in chemical shift for those resonances attributed to the NH groups of the urea functionality was observed with increasing concentration. This correlates with the understanding that the stabilisation of the hydrogen bonded network will be increased with increasing concentration, due to fewer solvent molecules being present, therefore reducing competitive association to the HBD/HBA sites.

The change in chemical shift for **2** was significantly lower than those of **1**, **3** and **4**, this can be attributed to steric hindrance between the aromatic substituents and the urea NH and as a result restrains the formation of hydrogen bonds.

This study confirms the presence of intermolecular hydrogen bond formation which would be expected to lead to the dimeric species observed in previous studies.

To gain a qualitative understanding of the intermolecular bonding mechanisms of a self-assembling system, both concentration and temperature[96] dependent measurements are frequently obtained and analysed. This enables the transition process from the molecular dissolved state to the aggregate state to be probed, essentially allowing for the strength of intermolecular binding mechanisms to be determined. In a study to investigate the effectiveness of such techniques Meijer and co-workers built upon their previous research study of employing concentration-dependent methods[97] to understand the self-assembly mechanism. They evaluated both approaches with the purpose of identifying and providing quantitative data for both isodesmic and cooperative self-assembly systems. Despite having fundamental differences with respect to the aggregation formation mechanisms, distinguishing between the two is a delicate issue. Examples of the key differences by means of the general linear aggregation system, Figure 54 (**A**) are as follows: the co-operative assembly is where the initial association constant (k_2) differs from all subsequent association constants (k_3, k_4, k_5….k_i). The coEK aggregation model for one-component linear aggregation (homogeneous) binding model is described as Figure 54 (**B**).[98]

A

$$M + M \overset{k_2}{\leftrightarrow} M_2 + M \overset{k_3}{\leftrightarrow} M_3 + M \overset{k_4}{\leftrightarrow} M_4 + M \overset{k_5}{\leftrightarrow} \ldots \overset{k_i}{\leftrightarrow} M_i$$

B

$$k_E = k_2/_p = k_3 = k_4 \ldots\ldots\ldots\ldots k_i$$

Where p is the cooperatively induced difference in free energy $\Delta\Delta\Delta G_{coop} = k_2/ k_E$)

$p < 1$: Positive cooperativity

$p = 1$: Non-cooperative

$p > 1$: Negative cooperativity

Figure 54 - One component general linear aggregation system (**A**) and coEK binding model (**B**).[100]

In this system Meijer and co-workers looked at how to distinguish isodesmic from coorperative supramolecular polymerisation. In isodesmic assembly it was identified that there was a gradual increase in the length and quantity of aggregated species (where $k_E = k_2 = k_3 = k_4 \ldots k_i$) and that long nanometre-sized objects are formed at high concentrations or for high association constants. However, in the case of coorperative assembly there was a bimodal of distribution of monomers and elongated structures throughout the self-assembly process.

Concentration-dependent spectroscopy measurements are only one way of obtaining data points which can establish the self-assembly mechanism of a molecule, there are additional techniques that can also be used to establish the self-assembly mechanism. Meijer and co-workers investigated the self-assembly mechanism of a supra-molecular system by using UV/Vis spectroscopy temperature-dependent techniques. In this singular experiment they were able to explore the complete transition from the monomeric state (at high temperatures) to the polymeric state (at low temperatures).[99]

The data obtained from the ^{1}H NMR dilution studies in this study was used to enable the self-association constants to be determined using Bindfit v0.5[100] (software designed by Meijer), enabling us to identify the binding models of compounds **1** - **5** (Table 7)**.**

The data obtained was fitted to both the dimerization/Equal K (EK)[101,102] and cooperative equal K (CoEK) models as can be observed in Table 6. Further supporting the hypothesis that we are predominantly observing dimeric species within the DMSO-d_6 - 0.5% H_2O solution. The dimerization/Equal K model was determined to give the best fit in the case for this class of amphiphile. The following trend was identified: as we increase the aromaticity of the amphiphile from phenyl through to anthracene then through to benzothiazole we increase the dimerization/Equal K (EK) constant; **4** (2.7 M^{-1}) > **1** (1.5 M^{-1}) > **5** (0.6 M^{-1}) > **3** (0.3 M^{-1}) > **2** (0.1 M^{-1}).

This trend inversely correlates with the size of the aggregated structures identified in the DLS studies where the smaller the self-associated aggregate, the stronger the self-association constant. We also see that the intramolecular hydrogen bond again interferes with the self-association of compound **5** resulting in the self-association constant to be lower than that of **4**. For all self-association constant data links see appendix Figure S16 -30.

Table 7 - Self association constants (M^{-1}) calculated for **1** - **5** in a DMSO-d_6 0.5% H_2O solution at 298K.

Compound	EK model (M^{-1})		CoEK model (M^{-1})		
	K_e	K_{dim}	K_e	K_{dim}	p
1	2.9 ± 0.4983 %	1.45 ± 0.25 %	8.62 ± 1.10 %	4.31 ± 0.54 %	0.5 ± 2.52 %
2[a]	<0.1 ± 1.52 %	<0.1 ± 0.76 %	0.53 ± 43.09 %	0.27 ± 21.55 %	0 ± 47.04 %
3	0.61 ± 3.03 %	0.3 ± 1.51 %	12.98 ± 5.75 %	6.49 ± 2.87 %	0.17 ± 23.77 %
4	5.34 ± 0.61 %	2.67 ± 0.31 %	12.95 ± 0.70 %	6.47 ± 0.35 %	0.5 ± 2.04 %
5	1.15 ± 2.05 %	0.57 ± 1.06 %	6.19 ± 8.82 %	3.1 ± 4.41 %	0.43 ± 17.81 %

a -Data fitted using L-BFGS-B (quasi-Newton) as opposed to Nelder-Mead (Simplex) methods.

2.7 Surface tension, critical micelle concentration (CMC) and zeta potential studies

The amphipathic nature of surfactant molecules is responsible for their properties. The hydrophobic effect drives the assemblies of monomeric units in too much larger structures.[103] Williams and co-workers whilst first discussing the importance of determining the CMC value, state that measurements using other techniques such as light scattering and diffusion mobility can only be performed accurately when the sample is at a concentration above the CMC, "where the concentration of micelles is finite"[104] (Figure 55). However, we know that critical micelle concentration is not necessary for detection of the initial formation of micelles as they have proven to be present in dilute solutions (as we have observed during our solution studies). It is only when additional solute molecules are introduced do we begin to recognise the aggregation

of spherical units and it is this concentration that should ultimately be recognized as the critical micelle concentration although due to detection restrictions it is not possible for this figure to be generated.[105] However, it is necessary to understand that micellar structures can be present below the calculated CMC values.

There are varying factors that can affect the stability of colloidal dispersions, these can be aggregation, coagulation or external factors such as the solvent system that the particles are in. The stability of the colloidal dispersions of compounds **1** - **5** was realised by obtaining zeta potential measurements at a concentration of 5.56 mM. To enable comparative measurements, an analogous solution was used to that of the surface tension/CMC measurements.

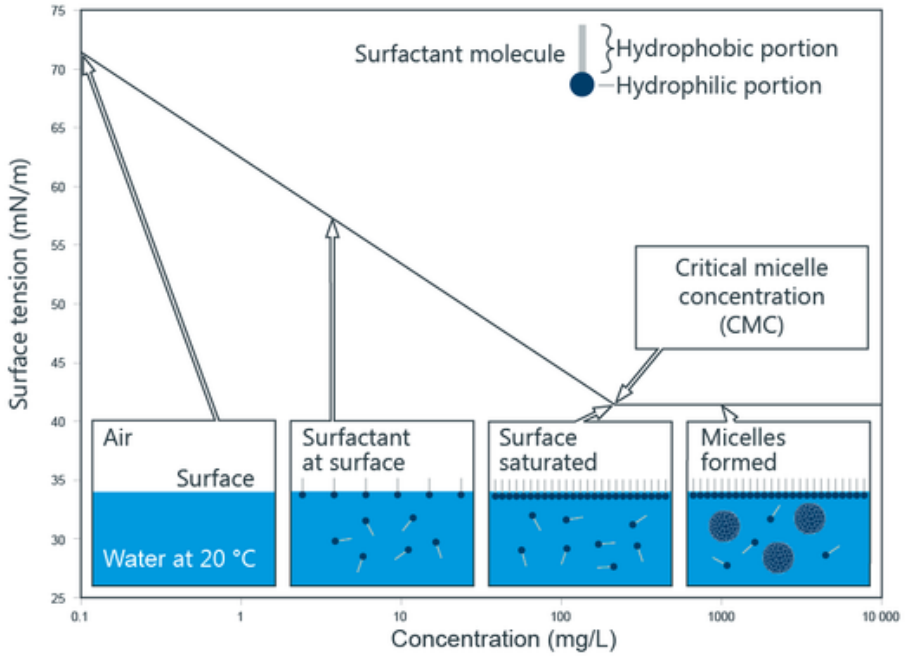

Figure 55 - Schematic illustration of the point Williams initially determined critical micelle concentration (CMC) to be calculated.[104]

The purpose of identifying the CMC within this study is to gain an understanding of the structure-activity relationships of compounds **1** - **5** by observing the transformation of these amphiphiles from monomeric surfactant solution to micellar solution. The properties of compounds **1** - **5** were tested for their surfactant properties using the pendant drop method in an EtOH:H_2O 1:19 solvent system.

The samples were prepared in series with an aliquot of the most concentrated solution undergoing serial dilution. Attempts were made to study these compounds in DMSO. However, due to the hydroscopic nature of this solvent the results were found to be unreproducible. The calculation of the CMC within this study was completed in an analogous fashion to those conducted by Costas and co-workers.[106]

2.7.1 Results and discussion

The CMC values calculated for **1** - **5** (Figures 56 - 60) using a plot of concentration against surface tension are reviewed in Table 8. It can be observed that the critical micelle concentration exhibits the following trend **4** < **1** < **5** < **2** < **3** demonstrating an 80 fold increase in the observed CMC values between **4** and **3**. Surface tension measurements all fall within the range of 43 - 49 mM/m with a trend that is as follows **1** < **4** < **2** < **3** < **5** and zeta potential measurements exhibit the following trend **3** < **5** < **1** < **2** < **4**.

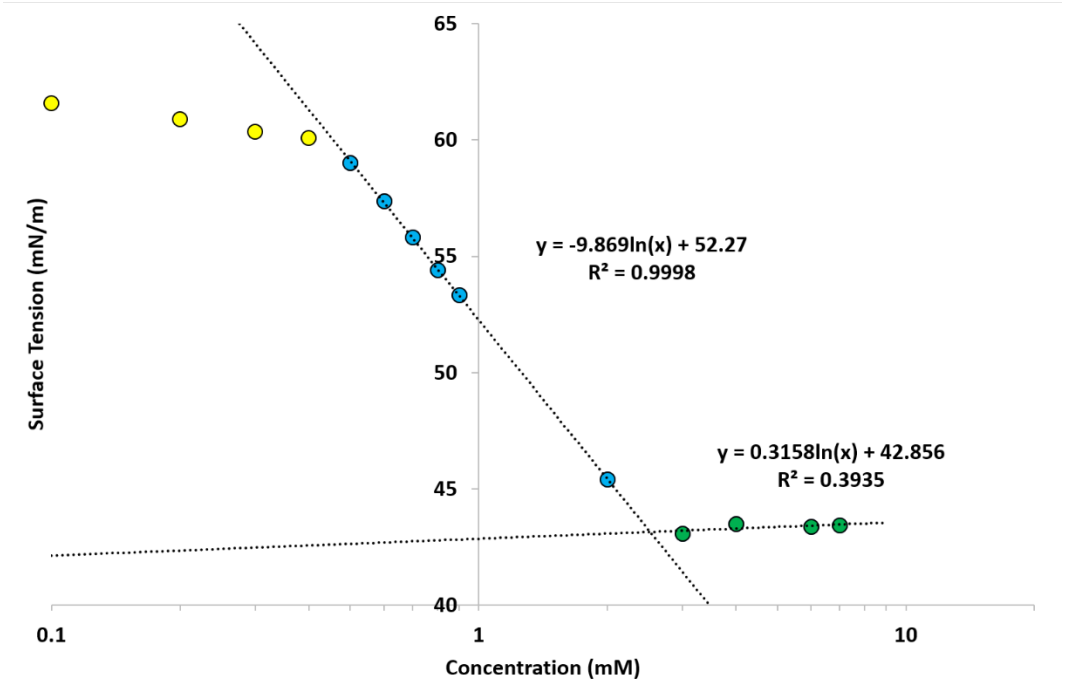

Figure 56 - Calculation of CMC for compound **1** in an EtOH: H_2O 1: 19 mixture using surface tension measurements.

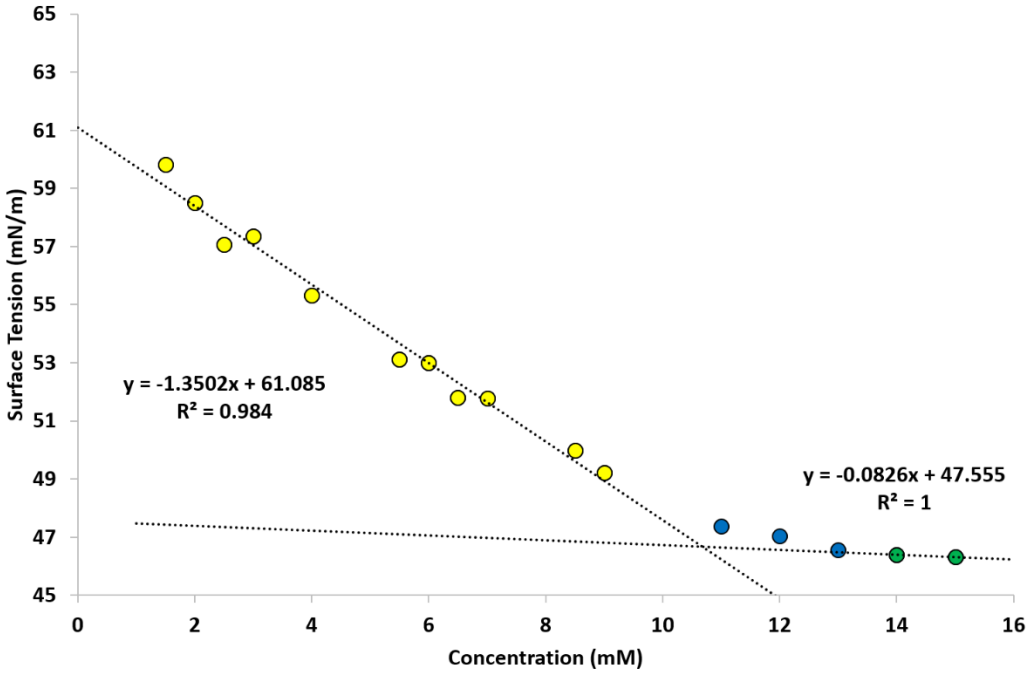

Figure 57 - Calculation of CMC for compound **2** in an EtOH: H_2O 1: 19 mixture using surface tension measurements.

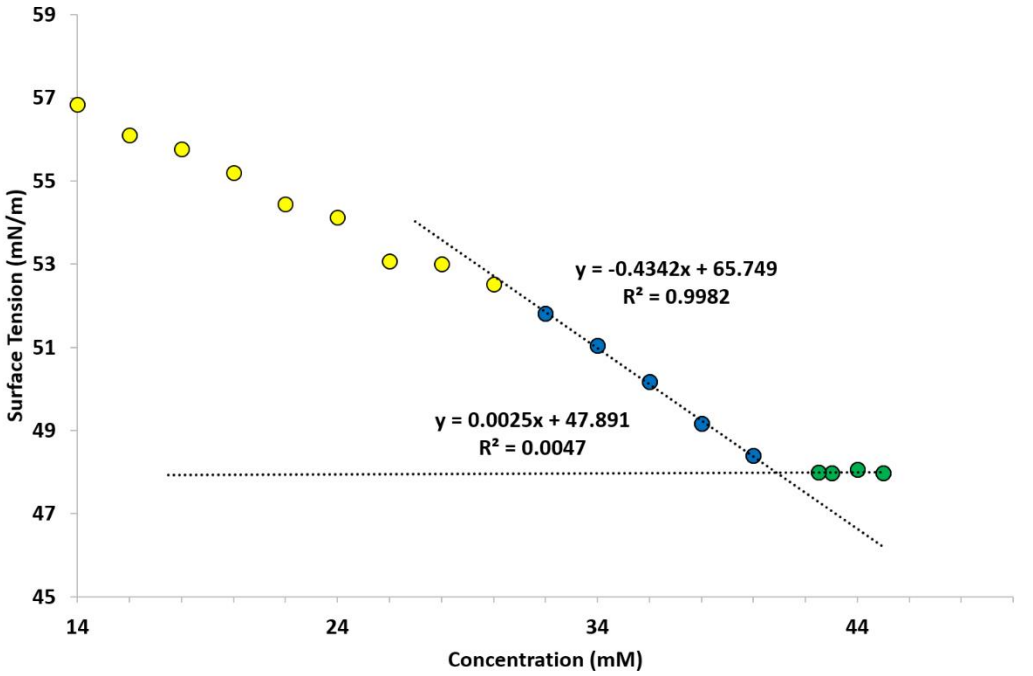

Figure 58 - Calculation of CMC for compound **3** in an EtOH: H_2O 1: 19 mixture using surface tension measurements.

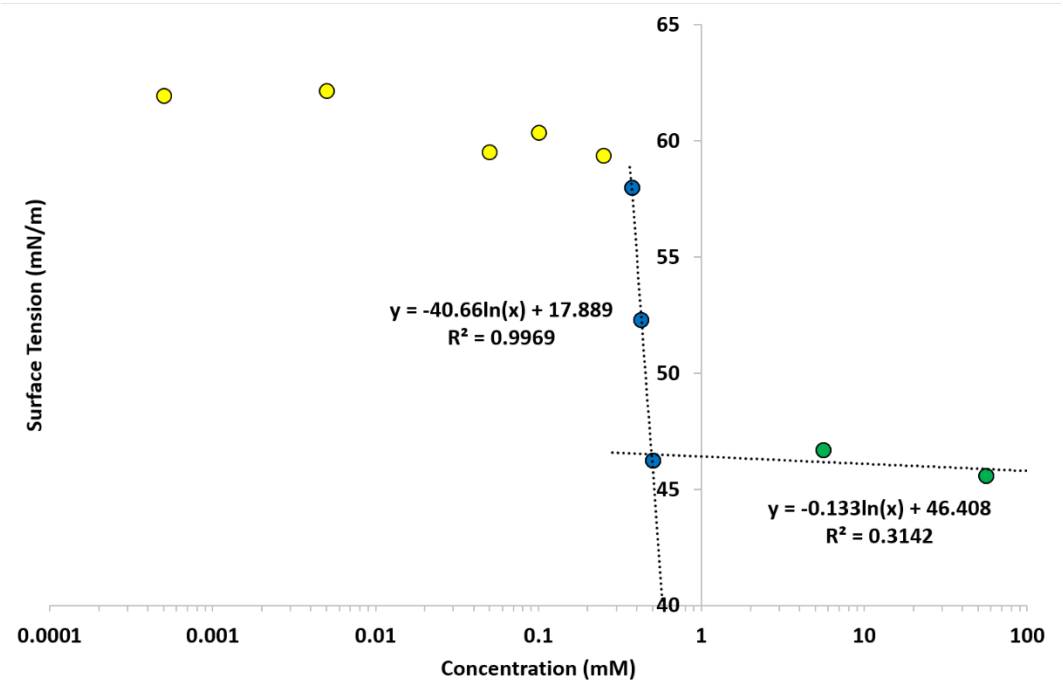

Figure 59 - Calculation of CMC for compound **4** in an EtOH: H_2O 1: 19 mixture using surface tension measurements.

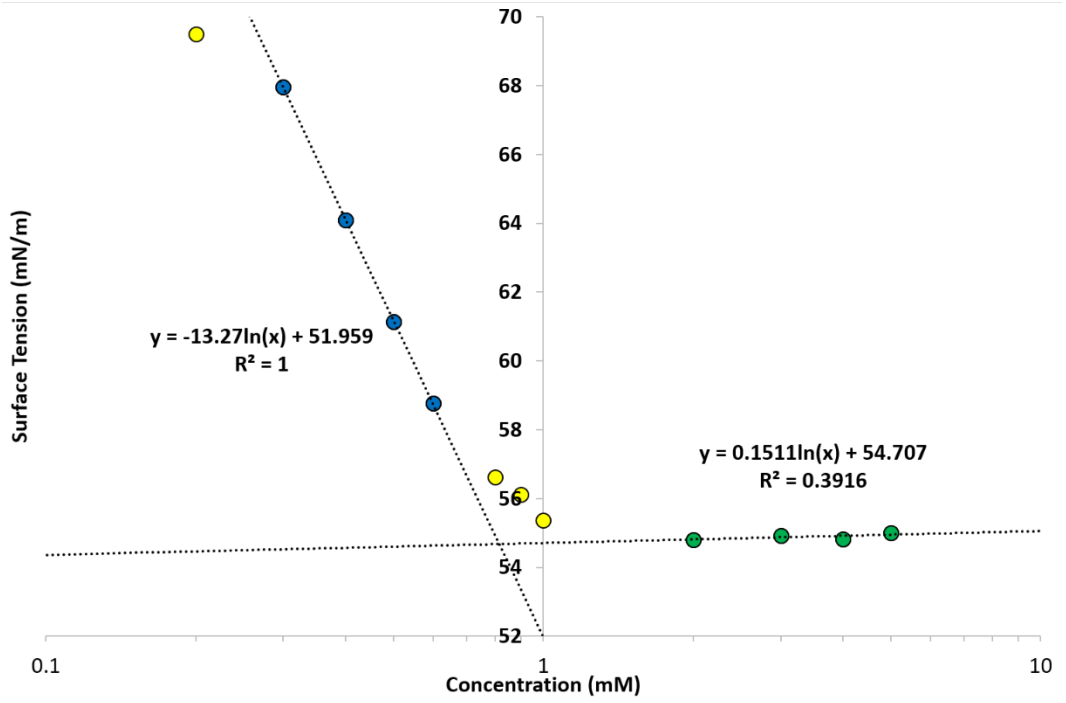

Figure 60 - Calculation of CMC for compound **5** in an EtOH: H_2O 1: 19 mixture using surface tension measurements.

The surface tension of water is very high, reported in literature is 72.75 mM/m[107] with the hydrophobic part of the molecule acting as a dielectric media between the water dipoles at the interface, causing the degree of hydrogen bonds among these molecules to decrease.[108] Surfactant addition to this water solution decreases the surface tension of the solution until the interface becomes saturated with the monomeric surfactant and as a result surface tension measurement will be much lower than those observed for water. The values that we observe for compounds **1** - **5** all fall within the range of 43 - 49 mM/m as can be expected.

Comparative zeta potential measurements (Table 8) demonstrate that in an EtOH:H_2O 1:19 solution the aggregated species of **1**, **2**, **4** and **5** exhibit electrically stabilized colloids. A measurement more positive than +30 mV or more negative than -30 mV is considered stable. When the potential is less than these values the attractive forces exceeds the electrostatic repulsion causing the dispersion to break of flocculate. Compound **3** has a zeta potential value that implies that there is incipient stability (±10 to ±30) of the colloidal species.[109]

Table 8 - Zeta potential and surface tension measurements for **1** - **5** obtained at 5.56 mM. Calculated CMC values for **1** - **5.**

Compound	EtOH: H_2O 1:19		
	zeta potential (mV)	CMC (mM)	surface tension (mN/m)
1	-82	2.52	43.15
2	-96	10.67	46.67
3	-19	40.89	47.90
4	-101	0.50	46.50
5	-79	9.54	48.71

The zeta potential measurements for **2**, **3** and **5** were obtained at a concentration below that of the calculated CMC values.

However, as previously mentioned does not mean that stable aggregated species do not exist in solution it just means that they may be undetectable by this method.[110] Therefore the threshold surfactant concentration at which self-aggregation occurs is not entirely dependent on the critical micelle concentration. The obtained CMC values for **1** - **5** were then compared with the previously discussed dimerization constants (chapter 2.6.2.1) and the results reveal a correlation between these two experimentally derived values (Figure 61). Where it is shown that as the strength of the dimerization constant increases the CMC value decreases.

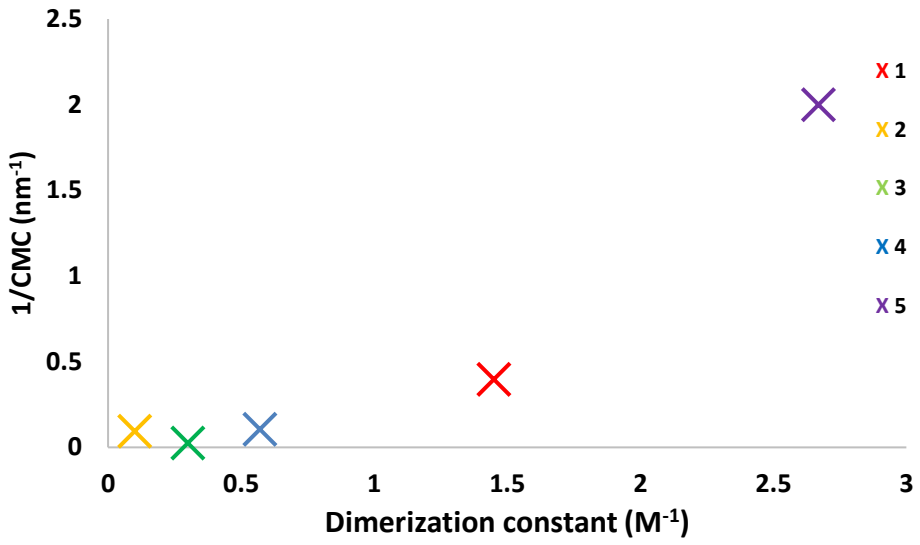

Figure 61 - Relationship between reciprocal CMC values and dimerization constants obtained for compounds **1 - 5.**

2.8 Low level computational chemistry

Computational chemistry is frequently combined with organic chemistry to assist in solving chemical problems. Theoretical chemistry incorporates structure and property prediction using efficient computer programs. The prediction of intermolecular hydrogen-bonding to form molecular tapes from a single molecule requires knowledge of the chemistry involved, the geometry of the single molecule and the identity of the hydrogen bond donators and acceptors. Crystal structure prediction software programmes are frequently designed to enable the determination of the crystal structure of an organic molecule.[111]

These programmes initially analyse the chemical diagram, and essentially the thermodynamic stability of the structure.[112] A further example of computational study is the calculation of electrostatic potential maps. This method is becoming more frequently used due to the qualitative interpretation of nucleophilic and electrophilic reactions.[113] For structure and function of a molecule the electrostatic field both within and surrounding the molecule are of central importance. Using an energy minimised structure and simple high throughput method of semi-empirical modelling, computationally derived electrostatic potential maps are frequently used to calculate E_{max} and E_{min} surface values that correlate with experimentally derived values.[114]

To determine the most favourable protonation site of the sulfonate-urea anion a series of computationally derived electrostatic potential maps were calculated by a method in line with work produced by Stewart[115] using Spartan 16" with semi-empirical PM6 modelling methods to derive comparative E_{max} and E_{min} values. It is hypothesised that the computational data obtained from this study will correlate with the experimentally derived dimerization constants and CMC values for **1** - **5**.

2.8.1 Results and discussion

The E_{max} and E_{min} values of **1** - **5** derived from the computational studies (Figures 62 - 66) show that the charge distribution throughout the series of sulfonate-urea amphiphiles is similar. This distribution is as follows; there are two negative regions observed. The more negative E_{min} value is attributed to the HBA sulfonate anion, and the other negative region is the urea-oxygen. The largest E_{max} value is situated in the urea NH region. The E_{max} and E_{min} values for **1** - **5** exhibit the following trend **4** > **1** > **2** > **5** > **3**, which is as follows when divided into the two subgroups; **1** > **2** > **3** and **4** > **5**.

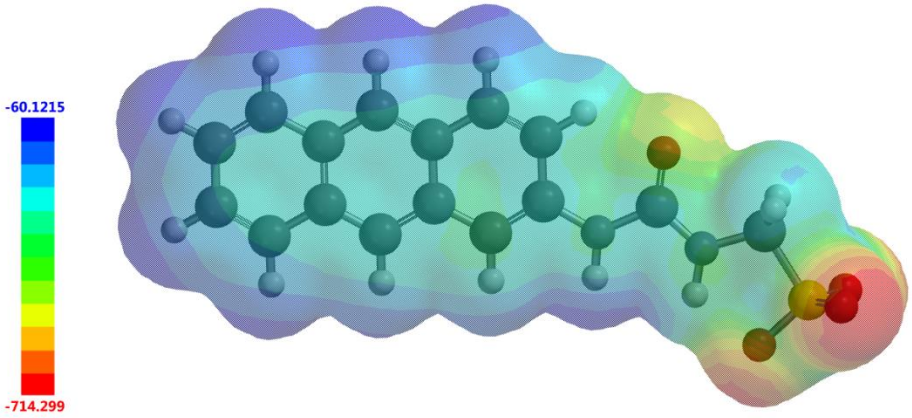

Figure 62 - Electrostatic potential map calculated for **1** using semi-empirical PM6 modelling methods. E_{max} and E_{min} values depicted in the figure legends are given in KJ/mol.

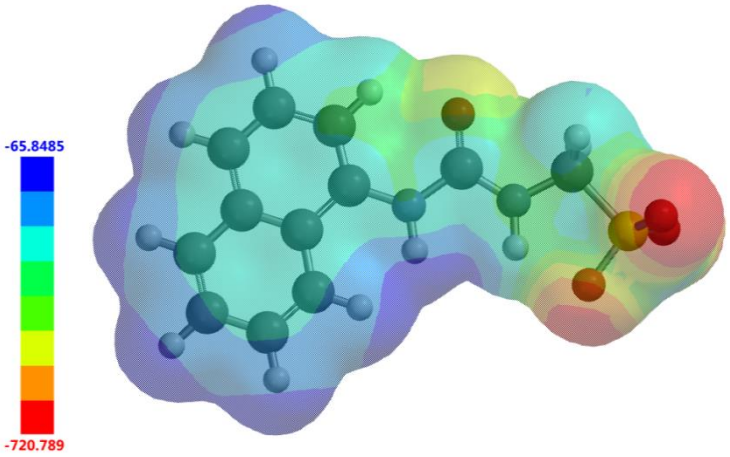

Figure 63 - Electrostatic potential map calculated for **2** using semi-empirical PM6 modelling methods. E_{max} and E_{min} values depicted in the figure legends are given in KJ/mol.

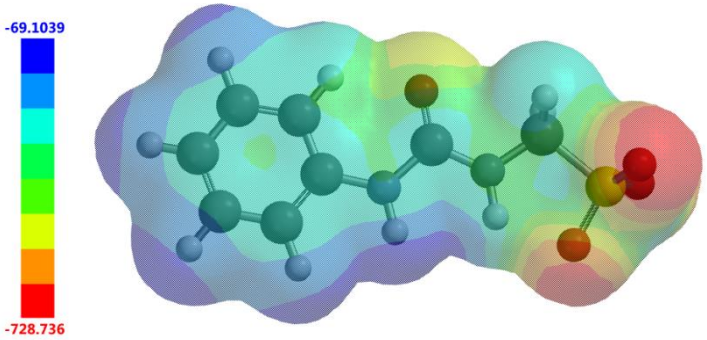

Figure 64 - Electrostatic potential map calculated for **3** using semi-empirical PM6 modelling methods. E_{max} and E_{min} values depicted in the figure legends are given in KJ/mol.

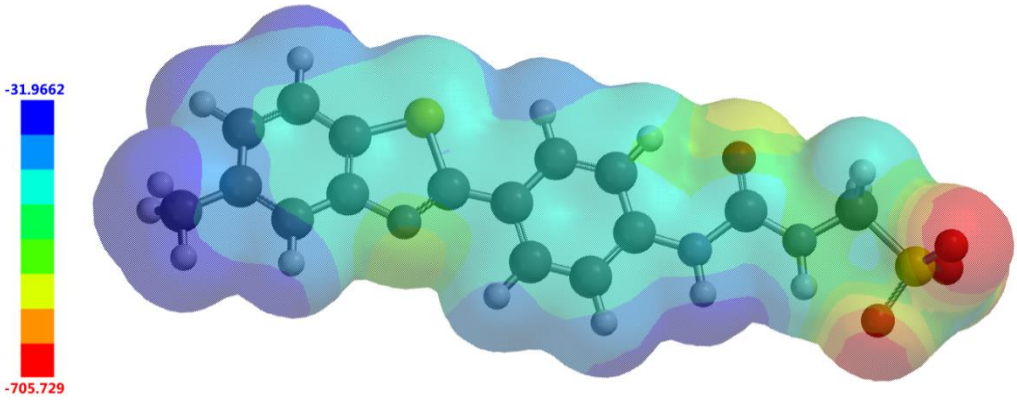

Figure 65 - Electrostatic potential map calculated for **4** using semi-empirical PM6 modelling methods. E_{max} and E_{min} values depicted in the figure legends are given in KJ/mol.

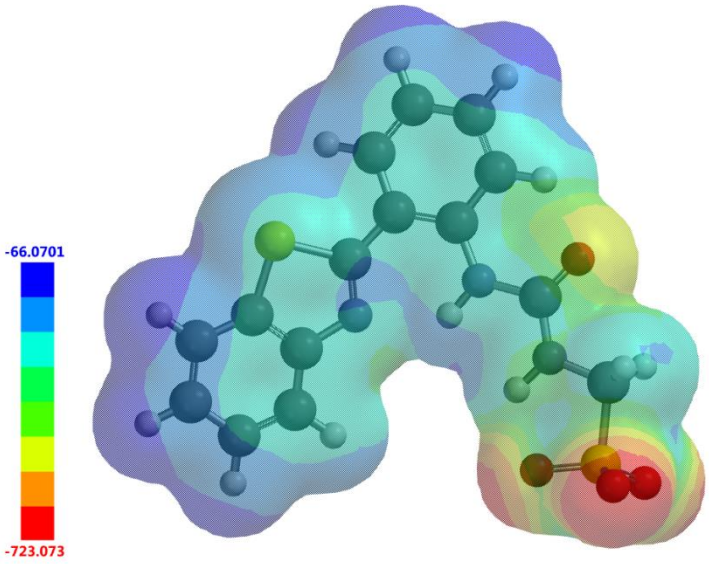

Figure 66 - Electrostatic potential map calculated for **5** using semi-empirical PM6 modelling methods. E_{max} and E_{min} values depicted in the figure legends are given in KJ/mol.

To determine if there was any form of identifiable relationship between the E_{max} and E_{min} values and the critical micelle concentration/dimerization constants a series of comparative graphs were created, the results from these can be seen in Figures 67 - 69.

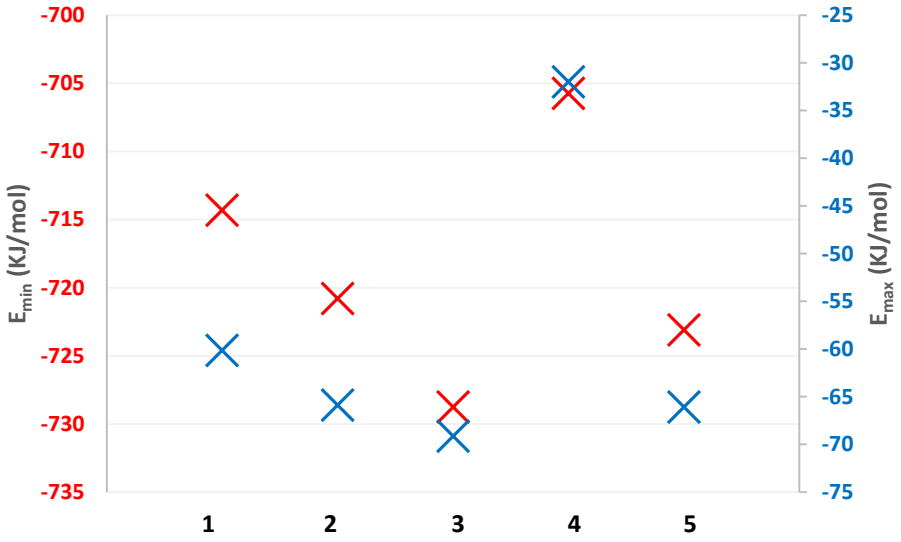

Figure 67 - Comparison of E_{max} and E_{min} values obtained for **1 - 5.**

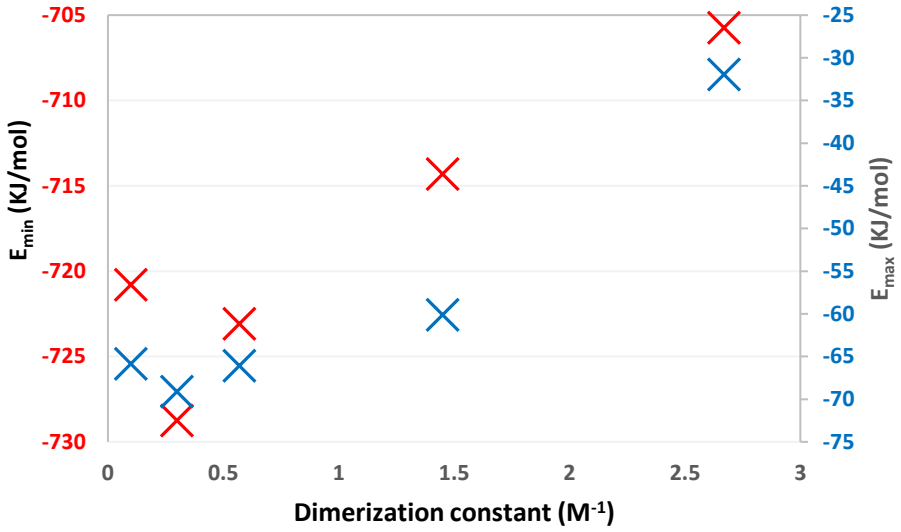

Figure 68 - Comparison of dimerization constant and E_{max} / E_{min} values obtained for **1 - 5.**

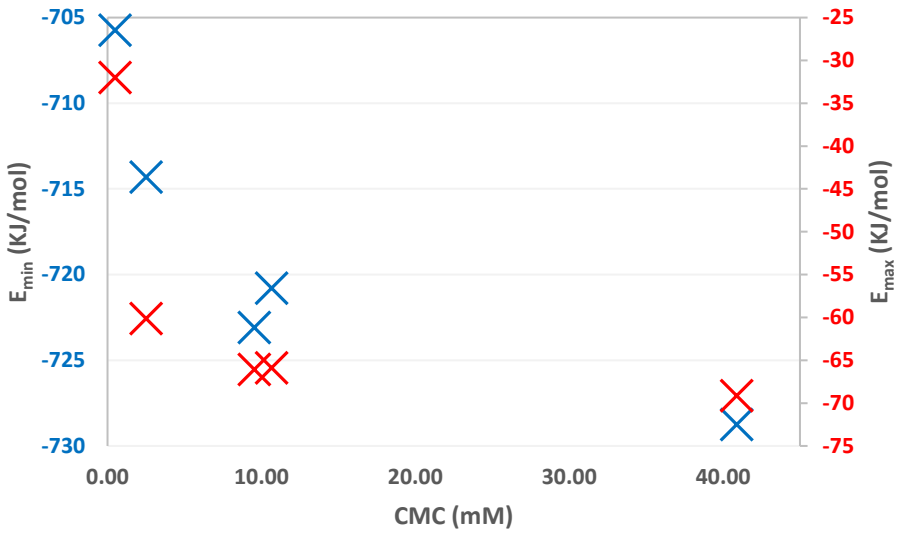

Figure 69 - Comparison of CMC and E_{max} / E_{min} values obtained for **1** - **5.**

Upon comparison of the E_{max} and E_{min} values of **1** - **3** from the computationally derived electrostatic potential maps, we can observe that there is a general increase in E_{max} and E_{min} values with increasing aromaticity from phenyl, naphthalene to anthracene. This trend is similar to what was observed when analysing the dimerization constants (Figure 68), and inverse to that of the CMC observations (Figure 69). These results obtained from the in-silico studies has demonstrated that we have direct correlation with the results obtained from those experimentally derived, proving that the critical micelle concentration of a compound is dependent on the dimerization process. This revelation indicates that these properties for this type of amphiphile may be predicted by this low level computational modelling technique. The trend for **4** and **5** continues throughout these series of studies where **4** > **5**, primarily due to the presence of the intramolecular bond between the urea NH and the benzothiazole nitrogen in **5**. An overall decrease in partial positive surface charge (E_{max}) from - 69 to - 32 KJ/mol suggests deactivation at the hydrogen bond accepting sulfonate-urea anion site.

2.9 Conclusion

In conclusion the synthesis, design and properties of five amphiphilic salts, four of which are novel and intrinsically fluorescent in nature (**1**, **2**, **4** and **5**) have been discussed. It has been demonstrated that the physical state and the competitive solvent system in which these salts are dissolved plays an integral role in their self-association properties. Solid-state single crystal X-ray diffraction studies show that compounds **1**, **2**, **3** and **4** all self-associate through the intermolecular binding of four hydrogen bonds resulting in the formation of a dimeric species. It was also discovered that **5** forms an intramolecular bond between the urea NH and the benzothiazole nitrogen, this limits the amount of HBD sites available to form intermolecular hydrogen bonds. Therefore, the self-associated dimer is stabilised by just two bonds instead of the previously mentioned four. Observed in the gas phase, ESI-MS results showed the presence of protonated sulfonate-urea dimers for compounds **1** - **4.** In this instance proof of dimerization for **5** was not unequivocally obtained. It is hypothesised that this is due to the intramolecular hydrogen bond observed in the solid state destabilising dimer formation, as there are fewer HBD groups free to form intermolecular hydrogen bonds.

The fluorescence properties of **1**, **2**, **4** and **5** were then explored in the solution state, from these results it was determined that it was not possible to directly observe **1** and **2** using microscopy techniques due to **1** exhibiting a large stokes shift and for **2** an appropriate filter was not available. However, the fluoresce properties of **4** and **5** allowed for direct observation using transmitted light or a DAPI filter. These observations established that the sulfonate-anion molecules were self-associating, forming aggregated species of either irregular or spherical shape, dependent on the solution in which the salt were dissolved. There are however limiting factors with this method, those being that only a sample of the bulk of these compounds were observed, therefore it must be considered that other shapes/sizes of species may be present in

the solution, yet not directly observed via this technique. Photobleaching was also apparent, so all structures present were not able to be visualised.

In various solvent systems a complementary combination of DLS, tensiometry, ^{1}H NMR and zeta potential studies allowed for the size distribution and stability of the self-associated structures to be investigated. Due to the inherent absorbance and fluorescence characteristics of **2**, it was not possible to gain information using DLS in a 100% DMSO solution. In DMSO this series of amphiphile were shown to predominantly form dimeric structures. However, as the percentage of water in the solution was increased we saw an increased percentage of larger aggregated species being formed. These aggregated structures exhibited the following trend **3** > **2** > **5** > **1** > **4**, and when separated into two subgroups **3** > **2** > **1.** The decrease in aggregate size correlates with an increase of aromaticity. Sub-group two showed intramolecular bonded **5** to form larger aggregates than more stable **4**, these super structures were then directly observed using microscopy techniques.

The obtained CMC values and dimerization constants when compared with the E_{max} and E_{min} values for **1** - **5** demonstrated that these values correlated well, providing evidence that it may be possible to predict the properties of this class of amphiphile through the dimerization constant and/or simple low level computational modelling techniques. From the results of these studies it is hypothesised that the strength of the experimentally derived dimerization self-association properties of the five amphiphilic salts discussed are dependent on the HBD capabilities of the urea (predicted through computational modelling). And that the aromatic substituents that form the structure have an overall effect on the stability and size of the self-associated aggregated species.

To conclude, we have now, for the **first** time been able to directly observe these compounds. This method combined with other comparative studies such as NMR and DLS, is a huge breakthrough in enabling the gaining of a greater understanding into the self-associated aggregated structure formation of this class of amphiphile in the solution state.

3. Further Work

Preliminary studies of the molecules discussed herein have focused on the exploration of the self-association properties of the sulfonate-urea based amphiphilic salt with step-wise modifications to the aromatic substituent.

Further work will focus on the adaption of this class of compound[49, 61] to allow us to establish quantitative structure-activity relationships. Through the following five steps;

1. Extension of the alkyl chain length between the urea and sulfonate (Figure 70). This addition will alter the acidity/basicity and spatial arrangement of the sulfonate-urea.[116]

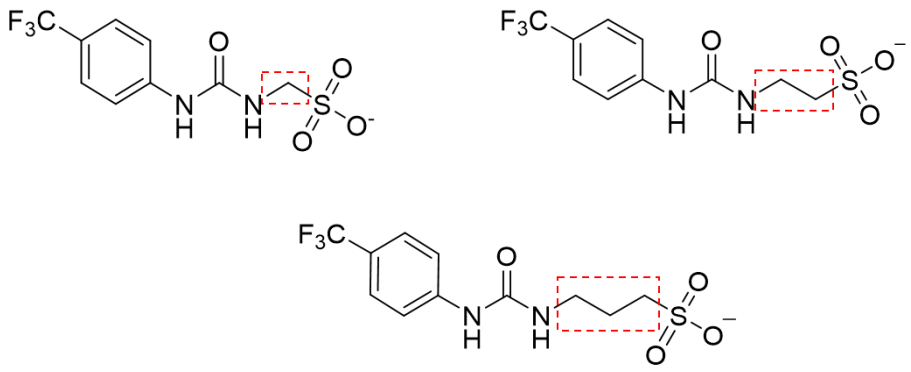

Figure 70 - Molecular structure, indicating the area where the extension to the alkyl chain length occurs. Cation emitted for clarity.

2. Substitution of the urea functionality for a thiourea moiety, this adjustment alters the properties of the hydrogen electron donating and accepting substituents due to increase acidity of the HBD NH groups. It would be explored as to whether this modification has an overall effect on the stability and self-association of the molecule.

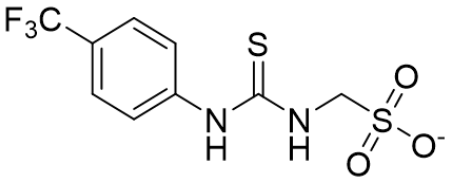

Figure 71 - Proposed molecular structure with the urea oxygen substituted for a sulfur atom.

3. Any potential anion-cation coordination, or strength of ion pair effects, within the system will be investigated by looking at the polarization value of the counter cation. The higher the polarization value, the more diffuse the cationic charge and therefore the weaker any potential ion pair interactions would be expected to be. The weaker the ion pair interactions, the more available the anion will be to form self-associative hydrogen bonds. This investigation will aid us in gaining an understating as to how important the choice of cation is. It is hypothesized that tetramethylammonium (TMA) cation will have a noticeable effect on the HBA sulfonate moiety due to the cation strongly co-ordinating with the anion. However, a tetrahexylammonium (THA) counter cation will have the reverse effect on the anion due to ion distribution throughout the alkyl.
4. Exploring the importance of the negative charge. Previously reported structures[49, 61] have identified that the anion/ HBA substituent plays a fundamental role in the self-assembly process. The strength of the inter-molecular bonds and colloidal dimensions are influenced by a variety of factors which include; electrostatic repulsive interactions between the surface electrons of the polar functional groups, and the hydrophobic effect.[117] Comparing neutral and anionic molecules in the same amphiphilic class will aid in determining how important this anionic head group is towards self-assembly development (Figure 72).

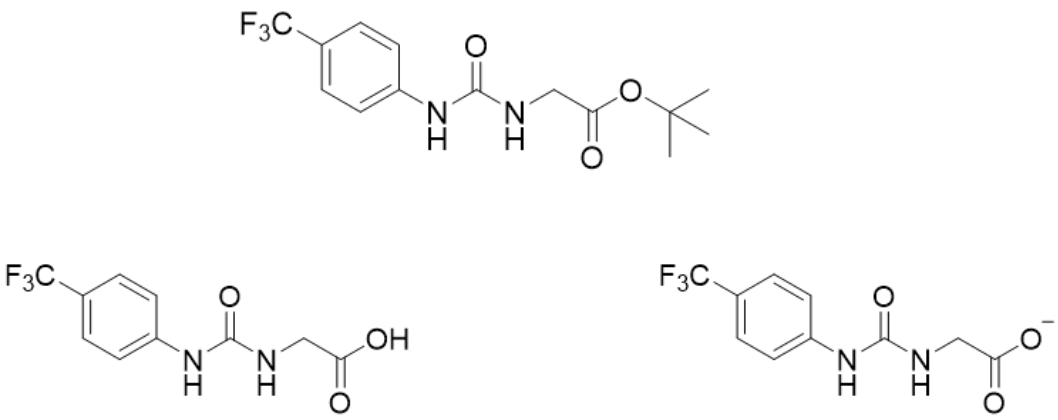

Figure 72 - Proposed molecular structures of both neutral and anionic monomers.

5. Explore the importance of the specific anion. It is well-known that sulfonate and carboxylate groups are frequently involved in intermolecular binding interactions. The relative hydrogen bonding affinities of sulfonate (SO_3-)-urea and carboxylate (COO^-)-urea amphiphilic salts in DMSO-d_6 have been evaluated to be COO^- > SO_3-.[118] Further work would be to explore and compare the surfactant structure-supramolecular aggregate relationships of molecules with these anionic functional groups (Figure 73).

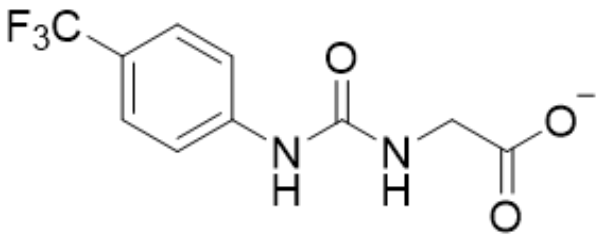

Figure 73 - Proposed molecular structure showing the substituted carboxylate anion group.

4. Experimental techniques

General remarks: All reactions were performed under slight positive pressure of nitrogen using oven dried glassware. NMR spectra were determined using a Jeol ECS-400, Bruker AV2 500, Bruker AV2 400 or Bruker AV3 600 MHz spectrometer with the chemical shifts reported in parts per million (ppm), calibrated to the centre of the solvent peak set. All solvents and starting materials were purchased from commercial sources where available. High resolution mass spectra were collected using a Bruker micrOTOF-Q mass spectrometer or a SYNAPT G2-S Mass Spectrometer. Melting points were recorded in open capillaries using a Stuart SMP10 melting point apparatus. Infrared (IR) spectra were recorded using a Shimadzu IR-Affinity 1, and reported in wavenumbers (cm^{-1}). DLS studies were performed using a Malvern Zetasizer Nano ZS. UV-Vis were recorded using a Shimadzu UV-1800, and reported in nm. Fluorometric measurements were obtained using a Perkin Elmer LS-50 Luminescence Spectrometer. Tensiometry performed using a Biolin Scientific Theta Attension optical tensiometer with data analysis conducted using one attension software.

Transmission and Fluorescence Microscopy: Samples were visualised using an Olympus IX71 microscope with PlanApo 100x OTIRFM-SP 1.49 NA lens mounted on a PIFOC *z*-axis focus drive (Physik Instrumente, Karlsruhe, Germany), fitted onto an ASI motorised stage (ASI, Eugene, OR), with the sample holder, objective lens and environmental chamber held at the required temperature. Samples were illuminated using LED light sources (Cairn Research Ltd, Faversham, UK) with appropriate filters (Chroma, Bellows Falls, VT). Samples were visualised using either a Zyla 5.5 (Andor) CMOS camera, and the system was controlled with Metamorph software (Molecular Devices). 10 µl of the appropriate sample was pipetted onto the centre of an agarose pad, covered with a coverslip and secured in place. Images were analysed using Metamorph software. Filters used to aid visualization within these studies: DAPI excitation 360 nm and emission 460 nm, and GFP excitation 480 nm and emission 510 nm.[1]

DLS studies: Studies conducted with compounds **1 - 5** were prepared in series with an aliquot of the most concentrated solution undergoing serial dilution. Sample sizes were kept to 1 mL. All solvents used for DLS studies were filtered to remove particulates from the solvents. Samples were heated to the appropriate temperature and allowed to equilibrate for 2 minutes and then a series of 10 'runs' were performed with each sample to give enough data to derive an appropriate average. In some instances, the raw correlation data indicated that a greater amount of time may be needed for the samples to reach a stable state. For this reason, only the last 9 'runs' were included in the average size distribution calculations.

Zeta potential studies: All solvents used for Zeta potential studies were filtered to remove particulates from the solvents. Samples were heated to the appropriate temperature and allowed to equilibrate for 2 minutes and then a series of 10 'runs' at 25 ^{o}C were performed with each sample to give enough data to derive an appropriate average. In some instances, the raw correlation data indicated that a greater amount of time may be needed for the samples to reach a stable state. For this reason, only the last 9 'runs' were included in the average size distribution calculations.

HRMS studies: Samples were dissolved in HPLC-grade methanol at a concentration of 1 mg/mL before being diluted 1 in 100 in methanol. 10 µL of sample was injected into a flowing stream of 10 mM ammonium acetate in 95% methanol in water (flow rate: 0.02 mL/min) and the flow directed into the electrospray source of the mass spectrometer. Mass spectra were acquired in the negative ion mode and data processed in Bruker's Compass Data Analysis software or Mass Lynx software utilising a lock mass.

UV-Vis studies: Samples were prepared in series with an aliquot of the most concentrated solution undergoing serial dilution. All solutions underwent an annealing process and were allowed to rest for approximately 2 minutes before undergoing analysis. The absorbance of solutions was noted at equilibrium temperature of 298.15K.

Fluorometry studies: Samples were prepared in series with an aliquot of the most concentrated solution undergoing serial dilution. All solutions underwent an annealing process and were allowed to rest for approximately 2 minutes before undergoing analysis. Compounds **1**, **2** and **4** were analysed at a concentration of 0.003 mM and compound **5** at a concentration of 0.03 mM.

Tensiometry studies: Samples were prepared in series with an aliquot of the most concentrated solution undergoing serial dilution. All solutions underwent an annealing process and were allowed to rest for approximately 2 minutes before undergoing analysis. Surfactant adsorption behaviour and critical micelle concentrations (CMC's) are determined by surface tension measurements using axisymmetric drop shape analysis with a pendant-drop apparatus. A succession of 3 droplets were measured for each sample and an average for these measurements reported.

Self-association constant calculation: All association constants were calculated using the freely available bindfit programme (http://app.supramolecular.org/bindfit/). All the data relating to the calculation of the association constants can be accessed online, through the links given for each complexation event.

5. Synthesis

Compound 1: Triphosgene (0.445 g, 1.50 mM) was added to a stirring solution of 2-aminoanthracene (0.62 g, 3.0 mM) in ethyl acetate (30 mL). The mixture was heated at reflux overnight. Tetrabutylammonium (TBA) hydroxide (1 N) in methanol (1.73 ml) was added to aminomethanesulfonic acid (0.19 g, 1.7 mM) at room temperature and taken to dryness to give the tetrabutylammonium sulfonate salt. This salt was then added to the original reaction mixture, which was then heated for a further 4 hours at reflux. The resultant mixture was then filtered and the filtrate taken to dryness, re-dissolved in chloroform (10 mL) and washed with water (10 mL). The organic fraction was then taken to dryness. The pure product was obtained by flash chromatography (100 % ethyl acetate followed by 100 % methanol).

The methanol fraction was taken to dryness with further addition of TBAOH (0.1 mL) to give the pure product as a dark yellow/brown solid. Yield 43 % (0.74 g, 1.3 mM); MP : 98 °C; ^{1}H NMR (400 MHz, DMSO-d_6): δ: 9.11 (br, s, 1H, NH), 8.41 (s, 1H), 8.30 (s, 1H), 8.21 (s, 1H), 7.97 (dd, *J* = 12.97, 8.00 Hz, 3H), 7.50 – 7.29 (m, 3H), 6.80 (t, *J* = 5.67 Hz, 1H), 3.98 (t, *J* = 8.12 Hz, 2H), 3.23 – 3.00 (m, 8H), 1.64 – 1.43 (m, 8H), 1.38 – 1.20 (m, 8H), 0.91 (t, *J* = 7.32 Hz, 12H); ^{13}C{^{1}H} NMR (100 MHz, DMSO-d_6): δ: 155.2 (CO), 138.1 (ArC), 132.7 (ArC), 132.2 (ArC), 130.3 (ArCH), 129.2 (ArC), 128.6 (ArCH), 128.5 (ArCH), 128.1 (ArCH), 126.3 (ArCH), 125.9 (ArC), 124.9 (ArCH), 124.5 (ArCH), 121.4 (ArCH), 111.1 (ArCH), 58.0 (CH_2), 56.6 (CH_2), 23.6 (CH_2), 19.7 (CH_2) , 14.0 (CH_3); IR (film): ν = 3290 (NH stretch), 1689, 1215, 1176, 887; HRMS for the sulfonate-urea ion ($C_{15}H_{22}N_3O_4S_2$) (ESI^-): m/z: act: 362.0261 $[M]^-$ cal: 362.0275 $[M]^-$.

Compound 2: Aminomethanesulfonic acid (0.33 g, 3.0 mM) was added to a stirring solution of 1-naphthyl isocyanate (0.28 mL**,** 3.0 mM) in pyridine (10 mL). The mixture was heated to 60 ^{o}C overnight and the precipitate removed by filtration and the filtrate taken to dryness. The resulting residue was dissolved in a solution of tetrabutylammonium (TBA) hydroxide (1 N) in methanol (1.2 ml) and taken to dryness, dissolved in dichloromethane (40 mL) and washed with water (40 mL). The organic phase was then taken to dryness. The pure product was obtained through precipitation from ethyl acetate (30 mL) as pale brown solid with a yield of 31% (0.49 g, 0.94 mM); Melting point: 78 ^{o}C; ^{1}H NMR (400 MHz, DMSO-d_6): δ: 8.80 (s, 1H), 8.17 (d, *J* = 7.99 Hz, 1H), 8.09 (d, *J* = 5.44 Hz, 1H), 7.88 (d, *J* = 8.18 Hz, 1H), 7.60 – 7.46 (m, 3H), 7.41 (t, *J* = 7.89 Hz, 1H), 7.11 (t, *J* = 5.68 Hz, 1H), 3.94 (d, *J* = 5.72 Hz, 2H), 3.21 – 3.05 (m, 8H), 1.64 – 1.40 (m, 8H), 1.41 – 1.21 (m, 8H), 0.92 (t, *J* = 7.31 Hz, 12H); ^{13}C{^{1}H} NMR (100 MHz, DMSO-d_6): δ: 155.40 (CO), 135.76 (ArC), 134.17 (ArC), 128.79 (ArCH), 126.37 (ArCH), 126.14(ArCH), 125.82(ArCH), 125.59 (ArCH), 122.21 (ArCH), 121.78 (ArCH), 116.10 (ArC), 57.99 (CH_2), 56.71 (CH_2), 23.53 (CH_2), 19.67 (CH_2), 13.95 (CH_3); IR (film): ν = 3321 (NH stretch), 1700, 1245, 1174, 879; HRMS for the sulfonate-urea ion ($C_{12}H_{11}N_2O_4S$) (ESI^-): m/z: act: 278.9615 $[M]^-$ cal: 279.0445$[M]^-$.

Compound 3: This compound was synthesised in line with previously published methods.[52]

Compound 4: Aminomethanesulfonic acid (0.23 g, 2.1 mM) was added to tetrabutylammonium (TBA) hydroxide (1 N) in methanol (2.1 ml, 2.1 mM) and taken to dryness. Triphosgene (0.31 g, 1.0 mM) was added to a stirring solution of 4-(6-methylbenzothiazol)aniline (0.5 g, 2.0 mM) in ethyl acetate (30 mL) and the mixture heated at reflux for 4 hours. The tetrabutylammonium salt was then dissolved in ethyl acetate (10 mL) and added to the reaction mixture and heated at reflux overnight, filtered and the solid washed with ethyl acetate (10 mL). The impurities were removed through the recrystallization, followed by filtration of the solid from methanol. The filtration was then taken to dryness to give the pure product as a yellow solid with a yield of 65% (0.81 g, 1.3 mM); Melting Point: 98 ^{o}C; ^{1}H NMR (400 MHz, DMSO-d_6): δ: 9.25 (s, 1H), 7.95 – 7.75 (m, 4H), 7.58 (d, *J* = 8.74 Hz, 2H), 7.37 – 7.20 (m, 1H), 6.98 (t, *J* = 5.88 Hz, 1H), 3.96 (d, *J* = 5.88 Hz, 2H), 3.20 – 3.01 (m, 9H), 2.43 (s, 3H), 1.63 – 1.43 (m, 9H), 1.40 – 1.17 (m, 9H), 0.91 (t, *J* = 7.32 Hz, 13H); ^{13}C{^{1}H} NMR (100 MHz, DMSO-d_6): δ: 166.7 (CO), 154.8 (ArC), 152.4 (ArC), 144.1 (ArC), 135.7 (ArC), 134.8 (ArC), 128.4 (ArCH, ArCH), 128.3 (ArCH, ArCH), 126.0 (ArC), 122.4 (ArCH), 122.2 (ArCH), 118.1 (ArCH), 60.0 (CH_2), 56.5 (CH_2), 23.6 (CH_2), 21.6 (CH_3), 19.7 (CH_2), 14.02 (CH_3); IR (film): ν = 2984 (NH stretch), 1697, 1176, 1035, 843; HRMS for the sulfonate-urea ion ($C_{16}H_{14}N_3O_4S_2$) (ESI$^-$): m/z: act: 376.0390 [M]$^-$ cal: 376.0431 [M]$^-$.

Compound 5: A mixture of 2-(2-Aminophenyl)benzothiazole (0.39 g, 1.7 mM) and 1,1′-Carbonyldiimidazole (0.28 g, 1.7 mM) were heated at reflux for 3 hours in chloroform (10mL). A mixture of aminomethanesulfonic acid (0.19 g, 1.7 mM) and tetrabutylammonium (TBA) hydroxide (1 N) in methanol (1.7 ml) were added to anhydrous pyridine (2 mL) at room temperature. This solution was added to the original reaction mixture which was heated at reflux overnight. The resultant solid was removed by filtration and the filtrate taken to dryness, dissolved in methanol (30 mL) and a precipitate removed by filtration. The filtrate was taken to dryness, dissolved in ethyl acetate (20 mL) and washed with water (20 mL). The organic fraction was then taken to dryness then dissolved in ethyl acetate (30 mL) where precipitation occurred.

The precipitate was removed by filtration to give the pure product a pale-yellow solid with a yield of 42% (0.26 g, 0.42 mM); Melting Point: 168 ^{o}C; ^{1}H NMR (400 MHz, DMSO-d_6): δ: 10.67 (s, 1H) 8.45 (d, *J* = 7.77 Hz, 1H), 8.30 (d, *J* = 7.79 Hz, 1H), 8.15 (d, *J* = 7.92 Hz, 1H), 7.85 (br s,d, *J* = 7.72 Hz, 2H), 7.58 (t, *J* = 7.58 Hz, 1H), 7.47 (tt, *J* = 11.69, 7.49 Hz, 2H), 7.10 (t, *J* = 7.52 Hz, 1H), 3.96 (s, 2H), 3.23 – 2.99 (m, 8H), 1.62 – 1.44 (m, 8H), 1.41 – 1.19 (m, 8H), 0.92 (t, *J* = 7.32 Hz, 12H); ^{3}C{^{1}H} NMR (100 MHz, DMSO-d_6): δ: 167.9 (CO), 154.9 (ArC), 153.3 (ArC), 139.8 (ArC), 133.8 (ArC), 132.0 (ArCH), 130.5 (ArCH), 127.0 (ArCH), 126.3 (ArCH), 124.0 (ArCH), 122.4 (ArCH), 122.0 (ArCH), 120.9 (ArCH), 119.3 (ArC), 58.0 (CH_2), 56.8 (CH_2), 23.6 (CH_2), 19.7 (CH_2), 14.0 (CH_3); IR (film): ν = 3275 (NH stretch), 1670, 1186, 1041, 879; HRMS for the sulfonate-urea ion ($C_{15}H_{12}N_3O_4S_2$) (ESI^-): m/z: act: 362.0261 $[M]^-$ cal: 362.0275 $[M]^-$.

5. References

1 . Lehn, J. M, *Angew. Chem. Int. Ed.*, **1988**, 27, 89-112
2 . Olenyuk, B,; Fechtenkötter, A,; Stang, P. J*, J. Chem. Soc*., **1998**, 11, 1707-1728
3 . Lewis, G. N, *J. Am. Chem. Soc.*, **1916**, 38 (4), 762-785
4 . Cohen, P. S.; Cohen, S. M, *J. Chem. Edu*., **1996**, 73 (9), 883-886
5 . Kirschner, M.; Gerhart, J,; Mitchison, T, *Cell*, **2000**, 100 (1), 79-88
6 . Margenau, H, *Rev. Mod. Phys*., **1939,** 1, 11
7 . Nagendrappa, G. *Resonance*, **2011**, 16, 606-618
8 . Schneider, H. *Int. J. Mol. Sci*., **2015**, 16, 6694-6717
9 . Lehn, J. M, *Angew. Chem. Int. Ed.,* **1990**, 29 (11), 1304-1319
10 . Cram, D. J, *Angew. Chem. Int. Ed***., 1988**, 27, 1009
11 . "Press Release: The 1987 Nobel Prize in Chemistry". *Nobelprize.org.* Nobel Media AB 2014. Web. 4 Feb 2017. <http://www.nobelprize.org/nobel_prizes/chemistry/laureates/1987/press.html>
12 . Gale, P. A, *Chem. Soc. Rev*., **2007**, 36, 141-142
13 . Morokuma, K, *Acc. Chem. Res.*, **1977**, 10 (8), 294-300
14 . Aoudia, M,; Al-Maamari, T,; Al-Salami, F, *Colloids and Surfaces A: Physicochemical and Engineering Aspects*, **2009**, 335 (1-3), 55-61
15 . Lehn, J. M, *Chem. Soc. Rev*., **2007**, 36, 151-160
16 . Saha, M. L,; Schmittel, M, *Org. Biomol, Chem.*, **2012**, 10, 4651-4684
17 . Verkleij, A. J,; Zwaal, R. F. A,; Roelofsen, B,; Comfurius, P,; Kastelijn, D,; van Deenen, L. L. M, *Biochim. Biophys. Acta. - Biomembranes*, **1973**, 323 (2), 178-193
18 . Perugini, M. A,; Schuck, P,; Howlett, G. J, *J. Biol. Chem.*, **2000**, 275, 36758-367656
19 . Steck, T. L, *J. Cell. Biol*., **1974**, 62 (1), 1-19

20 . Jing, L,; Dujuan, Z,; Wenxiu, H,; Zhonghao, L,: Yuxia, L, *J. Colloid and Interface Sci.*, **2017**, 487, 239-249
21 . Wang, G,; Goyal, N,; Mangunuru, H. P. R,; Yang, H,; Cheuk, S,; Narasimha Reddy, P. V, *J. Org. Chem.*, **2015**, 80, 733-743
22 . Hiscock, J. R,; Sambrook, M,; Ede, J,; Wells, N. J,; Gale, P, *J. Mater. Chem.,* **2015,** 3, 1230-1234
23 . Steed, J. W, *Supramol. Chem.*, **2015**, 27 (11-12), 731-733
24 . Fersht, A. R,; Shi, J,; Knill-Jones, J,; Lowe, D, M,; Wilkinson, A, J,; Blow, D, M,; Brick, P,; Carter, P,; Waye, M. M. Y,; Winter, G, *Nature*., **1985**, 314, 235-238
25 . Cisse, I. I,; Kim, H,; Ha, Taekjip, *Nature Structural & Molecular Biology*, **2012**, 19, 623-627
26 . Gumbs, T. L,; White, L. J,; Wells, N. J,; Shepherd, H. J,; Hiscock, J. R, *Supramol. Chemistry.*, **2017**, DOI: 10.1080/10610278.2017.1351613
27 . Dingley, A,; Grzesiek. S, *J. Am. Chem. Soc*., **1998**, 129 (33), 8293-8297
28 . Lehn, J. M, *Angew. Chem. Int. Ed*., **1990**, 29 (11), 1304-1319
29 . Godula, K,; Sames, D, *Science*, **2006**, 312, 67-72
30 . Latimer, M. W.; Rodebush W. H, *J. Am. Chem. Soc*., **1920**, 42 (7), 1419-1433
31 . Pedersen, C. P, *Angew. Chem. Int. Ed*., **1988**, 27 (8), 1021-1027
32 . Steed, J. W.; Atwood, J. L, *Supramolecular Chemistry second edition*; John Wiley & Sons: Chichester, 2009
33 . Grabowski, S. J, *J. Phys. Chem.*, **2001**,105, 10739-10746
34 . Bonnet, A,; Chisholm, J,; Sam Motherwell, W. D,; Jones, W, *CrystEngComm*, **2005**, 7(9), 71-75
35 . Steiner, T, *Angew. Chem. Int. Ed*., **2002**, 41 (1), 48-76
36 . Smith, P,; Reddington, M,; Wilcox, C, *Tetrahedron Lett.*, **1992**, 33 (41), 6085-6088
37 . Muller, G,; Culberson, J. C,; Roy, G,; Ziegler, J,; Walters, D. E,; Kellogg, M. S,; Schiffman, S, S,; Warwick, Z. S. J, *J. Med. Chem.*, **1992**, 35, 1747-1751
38 . Pfeffer, F,; Krger, P,; Gunnlaugsson, T, *Org. Biomol. Chem.*, **2007**, 5, 1894-1902
39 . Gale, P,; Garcia-Garrido, S,; Garric, J, *Chem. Soc. Rev*., **2008**, 37, 151-190
40 . Gale, P, *Coord. Chem. Rev*., **2003**, 240, 1-226
41 . Sifaoui, H,; Lugowska, K,; Domanska, U,; Modaressi, A,; Rogalski, *J. Colloid and Interface Sci.*, **2007**, 314 (2), 643-650
42 . Ammal, S,; Venuvanalingam, P*, J. Chem. Soc.*, **1998**, 94, 2669-2674
43 . Wierzejewska, M,; Saldyka, M, *Chem. Phys. Lett.,* **2004**, 391, (1-3), 143-147
44 . Gregoret, L. M,; Rader, S. D,; Fletterick, R. J,; Cohen, F. E, *Proteins*, **1991**, 99-107
45 . Zhou, P,; Tian, F,; Lv, F,; Shang, Z, *Proteins*, **2009**, 76, 151–163
46 . Chin, D. N,; Tahas, G,; Palmore, G,; Whiteside, M, *J. Am. Chem. Soc*., **1999**, 121, 2115-2122
47 . Bondy, C. R,; Gale, P. A,; Loeb, S. J, *J. Am. Chem. Soc.*, **2004**, 126, 5030-5031
48 . Steiner, T, *Angew. Chem. Int. Ed*., **2002**, 41, 48-76
49 . Xing, Y,; Wang, C,; Han, P,; Wang, Z,; Zhang, X, *Langmuir*, **2012**, 28, 6032-6036
50 . Zou, J.; Tao, F.; Jiang, M, *Langmuir,* **2007**, 23, 12791
51 . Wang, C,; Wang, Z,; Zhang, X*, Acc. Chem. Res.*, **2012**, 45 (4), 608-618
52 . Blackholly, L. R,; Shepherd, H. J,; Hisckock, J. R, *CrystEngComm*, **2016**, 18, 7021-7028

53 . Diaz, I,; Mohino, F,; Blasco, T,; Sastre, E,; Perez-Pariente, J, *Micrporus and Mesoporous Materials*, **2005**, 80 (1-3), 33-42
54 . Versluis, F.; Tomatsu, I.; Kehr, S.; Fregonese, C.; Tepper, A. W. J. W.; Stuart, M. C. A.; Ravoo, B. J.; Koning, R. I.; Kros, A, *J. Am. Chem. Soc*., **2009**, 131, 13186–13187
55 . Wang, C,; Wang, Z,; Zhang, X*, Langmuir,* **2014***,* 30, 1531-1535
56 . Kang, Y,; Liu, K,; Zhang, X, *Langmuir*, **2014**, 30, 5989-600
57 . Busschart, N,; Caltagirone, C,; Van Rossom, W,; Gale, P . *A, Chem. Rev.*, **2015,** 115, 8038
58 . De Greef, T,; Smulders, M,; Wolffd, M,; Schenning, A,; Sijbesma, R,; Meijer, E, *Chem. Rev.*, **2009**, 109, 5687
59 . Lortie, F,; Boileau, S,; Bouteiller, L, *Chem. Eur. J.*, **2003**, 9, 3008
60 . Foley, P,; Pour, A,; Beach, E,; Zimmerman, J, *Chem. Soc. Rev.*, **2012**, 41, 1499
61 . Hiscock, J. R,; Bustone, G. P,; Wilson, B,; Belsey, K. E,; Blackholly, L. R, *Soft Matter*, **2016**, 12, 4221-4228
62 . Palmer, B. J,; Liu, J, *Langmuir*, **1996**, 12, 746-753
63 . Peschel, A, *Trends Microbiol.*, **2002**, 10 (4), 179-186
64 . Laverty, G,; Gorman, S. P,; Gilmore, B. F, *Int. J. Mol. Sci.*, **2011**, 12 (10), 6566-6596
65 . Brogden, K. A,; de Lucca, A. J,; Bland, J,; Elliott, S, *Proc. Natl. Acad. Sci. USA*, **1996**, 93 (1), 412-416
66 . Israelachvili, J. N,; Mitchell, J,; Ninham, B, *Biomembranes,* **1977**, 470 (2), 185-201
67 . Kelly, R,; Kim, M. H, *J. Am. Chem. Soc.*, **1994**, 116 (16), 7072-7080
68 . Rangel-Yagui, C. O,; Pessoa-Jr, A,; Blankschtein, D, *Braz. J. Chem. Eng.,* **2004**, 21 (4)
69 . Hildebrandt, G, *Cryst. Res. and Technol.*, **1993**, 28 (6), 747-766
70 . Cordeiro, D. S,; Corio, O, *J. Braz. Chem. Soc.*, **2009**, 20 (1)
71 . Mallakin, A,; Dixon, D. G,; Greenberd, B. M, *Ecotoxicol. Environ. Saf.*, **1999**, 43, 204-212
72 . Tovide, O, *Sens. Actuators B Chem.*, **2014**, 205, 184-192
73 . Phillips, M, *Chem. Rev.*, **1929**, 6 (1), 157-174
74 . Dillard, J. G, *Chem. Rev.*, **1973**, 73 (6), 589-643
75 . Ho, C,; Chan, M,; Cheung, R,; Law, L,; Ng, K,; Suen, M,: Tai, H, *Clin. Biochem. Rev.*, **2003**, 24 (1), 3-12
76 . Steiner, T, *Angew. Chem.,* **2002**, 41 (1), 48-76
77 . Caltagirone, C,; Hiscock, J. R,; Hursthouse, M. B,; Light, M. E,; Gale, P. A, *Chem. Eur. J.,* **2008**, 14 (33), 10236-10243
78 . Karvar, M,; Strubbe, F,; Beunis, F,; Kemp, R,; Smith, N,; Goulding, M,; Neyts, K, *Langmuir*, **2014**, 30 (41), 12138-12143
79 . Smith, R. D,; LightWahl, K. J,; Winger, B. E,; Loo, J. A, *Org. Mass Spectrom.,* **1992**, 27, 811-821
80 . Maret, G,; Wolf, P. E, *Z. Phys. B. Condensed Matter*, **1987**, 65, 409-413
81 . Holthoff, H,; Egelhaaf, S. U,; Borkovec, M,; Schurtenberger, P,; Sticher, H, *Langmuir*, **1996**, 12, 5541-5549
82 . Heisel, K,; Krishnan, *Biopolymers*, **2014**, 102, 69-77,
83 . Sednev, M. V,; Belov, V. N,; Hell, S. W, *Methods Appl. Fluoresc*., 2015, 3
84 . Peng, X,; Song, F,; Lu, E,; Wang, Y,; Zhou, W,; Fan, J,; Gao, Y, *J. Am. Chem. Soc.*, **2005**, 127, 4170-4171

85 . Amin, S,; Barnett, G. V,; Pathak, J. A,; Roberts, C. J,; Sarangapani, P. S, *Curr. Opin. Colloid Interface Sci.*, **2014**, 19 (5), 438-449
86 . Ye, Y,; Zheng, Y,; Ji, C,; Shen, J,; Yin, M, *ACS Appl. Mater. Interfaces*, **2017**, 9 (5), 4534-4539
87 . Kotagirl, N,; Sakon, J,; Han, H,; Zharov, V,; Kim, J, *Nanoscale,* **2016**, 8, 12658-12667
88 . Choy, G,; O'Connor, S,; Diehnn, F, *BioTechniques*, **2003**, 35, 1022-1030
89 . Takashi, F,; Yoshie, H,; Hideo, H,; Makio, T,; Kiwamu, S,; Yoshiharu, H, *Nature*, **1995**, 374, 555-559
90 . Kaeser, A,; Schenning, A, *Adv. Mater.*, **2010**, 22 (28), 2985-2997
91 . Levin, P. A, *Mol. Cell. Microbiol.*, **2002**, 31, 115-132
92 . Minkenberg, C. B,; Florusse, L,; Eelkema, R,. Koper, G. J. M,; van Esch, J. H, *J. Am. Chem. Soc.*, **2009**, 131, 11274-11275
93 . Haushalter, K. A,; Lau, J,; Roberts, J. D, *J. Am Chem. Soc.*, **1996**, 118 (37), 8891-8896
94 . Avram, L,; Chen, Y, *Chem. Soc. Rev.*, **2015**, 44, 586-602
95 . Patterson, J. P,; Robin, M. P,; Chassenieux, C,; Colombani, O, *Chem. Soc. Rev.*, **2014**, 43, 2412-2425
96 . Macchioni, A,; Ciancaleoni, G,; Zuccaccia, C,; Zuccaccia, D, *Chem. Soc. Rev.*, **2008**, 37, 479-489
97 . Irie, M,; Fukaminato, T,; Fukaminato, T,; Sasaki, T,; Tamai, N,; Kawai, T, *Nature*, **2002**, 420, 759-760
98 . Smulders, M,; Nieuwenhuizen, M,; De Greef, T,; van der Schoot, P,; Schenning, A,; Meijer, E, *Chem. Eur. J*., **2010**, 16, 362-367
99 . Von Krbek, L,; Schalley, C,; Thordarson, P, *Chem. Soc. Rev*., 2017, advanced article
100. Cantekin, S,; Balkenende, D,; Smulders, M,; Palmans, A,; Meijer, E, *Nature*, **2011**, 3, 42-46
101. Thordarson, P,; Sewell, K,; Efremova, V, Bindfit v0.5, www.supramolecular.org.
102. Evstigneev, M. P,; Buchelnikov, A. S,; Kostjukov, V. V,; Pashkova, I. S,; Evstigneev, V. P, *Supramol. Chem.*, **2013**, 25, 199-203
103. Stoesser, P. R,; Gill, S. J, *J. Phys. Chem.*, **1967**, 71, 564-567
104. Handler, D, *Nature London,* **2005**, 640-7.
105. Williams, R. J,; Phillips, J. N,; Mysels, K. J, *Trans. Faraday. Soc.*, **1955**, 51, 728-737
106. Wells, J. M, *Chromatography*, **2015**, 2, 580-593
107. Pineiro, A,; Banquy, S,; Perez-Casas, S,; Tovar, E,; Garcia, A,; Villa, A,; Amigo, A,; Mark, A, Costas, M, *J. Phys. Chem.*, **2007**, 111, 4383-4392
108. Kalova, J,; Mares, R, *Int. J. Thermophy.*, **2015**, 36 (7), 1396-1404
109. Chakraborty, T,; Chakraborty, I,; Ghosh, S, *Arab. J. Chem.*, **2011**, 4 (3), 265-270
110. Ruckenstein, E,; Nagarajan, R, *J. Phys. Chem.*, **1975**, 79, 2622-2626
111. Paulin, L,; Wheland, G. W, *J. Chem. Phys.*, **1933**, 1, 362- 376
112. Price, S. L, *Chem. Soc. Rev.*, **2014**, 43, 2098-2111
113. Wierzejewska, M,; Saldyka, M, *Chem. Phys. Lett.*, **2004**, 391 (1-3), 143-147
114. Gilson, M,; Sharp, K,; Honig, B, *J. Comput. Chem.,* **1988**, 9 (4), 327-335
115. Hunter, C. A, *Angew. Chem. Int. Ed.*, **2004**, 43, 5310-5324
116. Stewart, J. J. P, *J. Mol. Model.*, **2007**, 13, 1173-1213
117. Chandler, D, *Nature London*, **2005**, 437, 640-7

Appendix

Table of Contents

Characterisation NMR

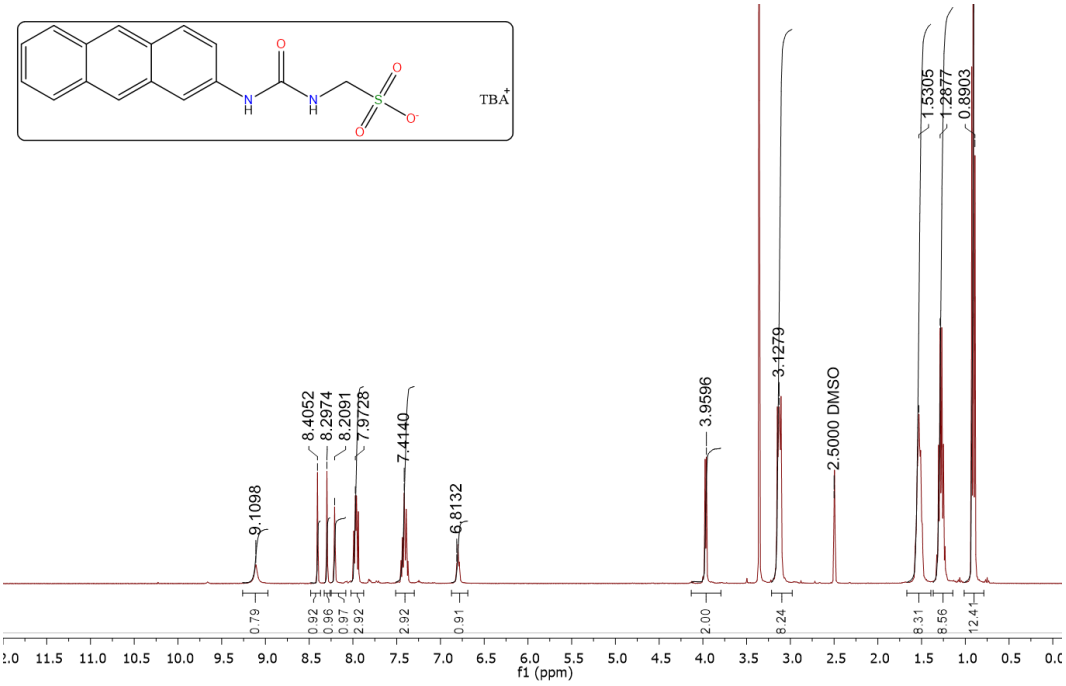

Figure S6 – ^{1}H NMR of compound **1** in DMSO-d_6.

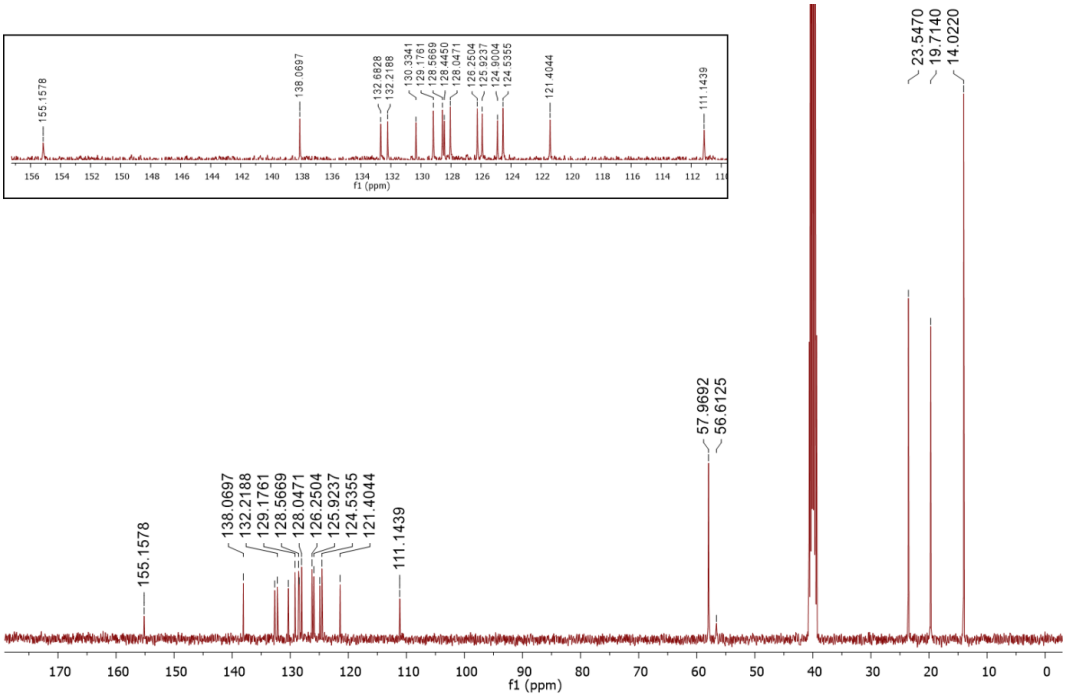

Figure S7 – ^{13}C NMR of compound **1** in DMSO-d_6.

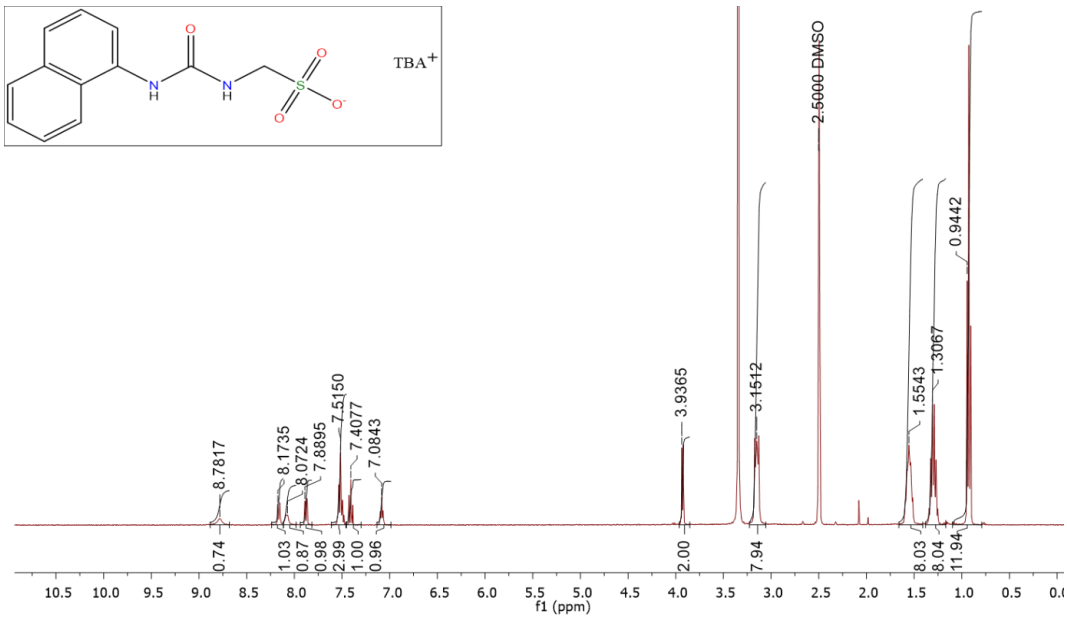

Figure S8 – ^{1}H NMR of compound **2** in DMSO-d_6.

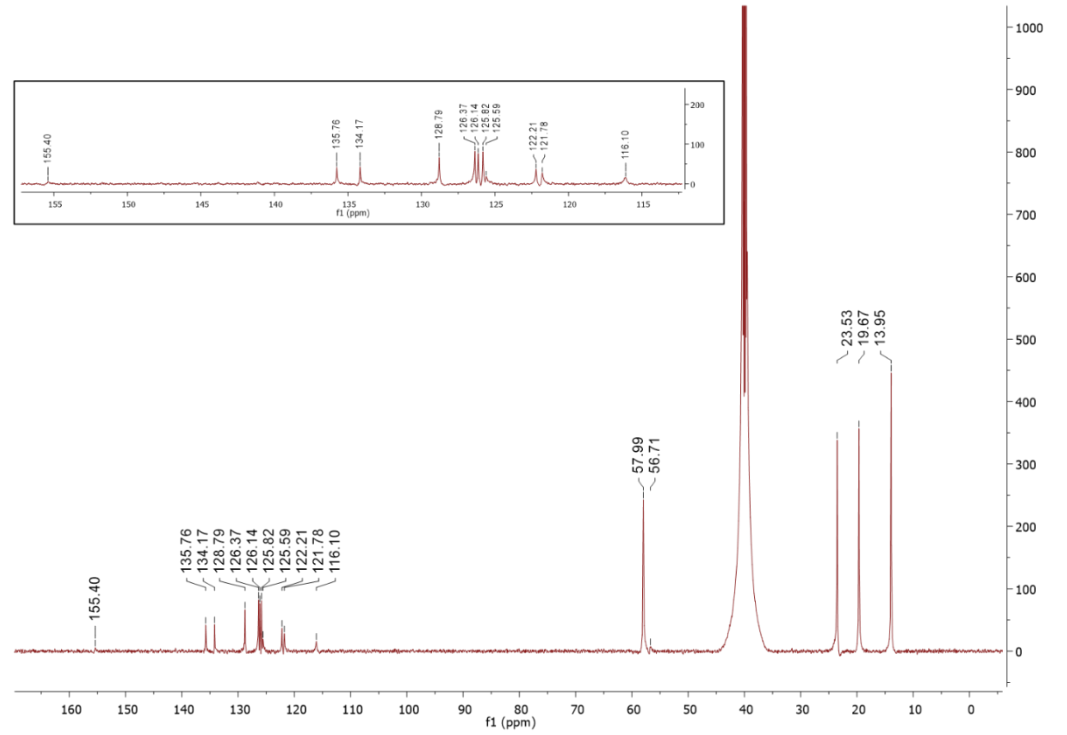

Figure S9 – ^{13}C NMR of compound **2** in DMSO-d_6.

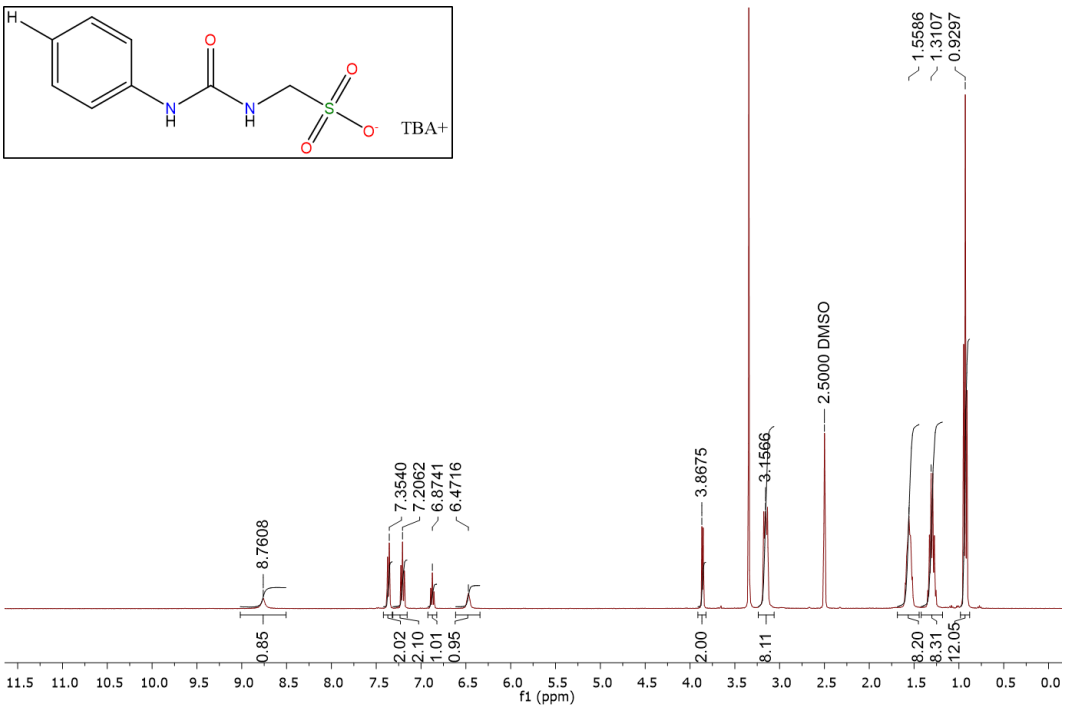

Figure S10 – ^{1}H NMR of compound **3** in DMSO-d_6.

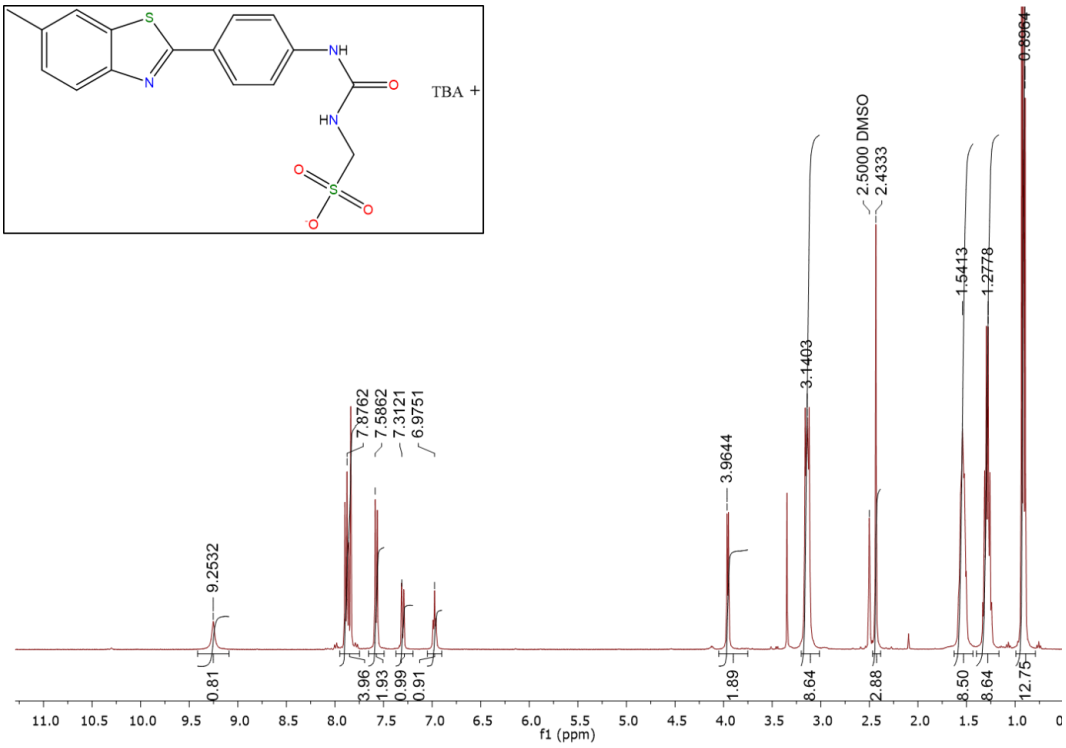

Figure S11 – ^{1}H NMR of compound **4** in DMSO-d_6.

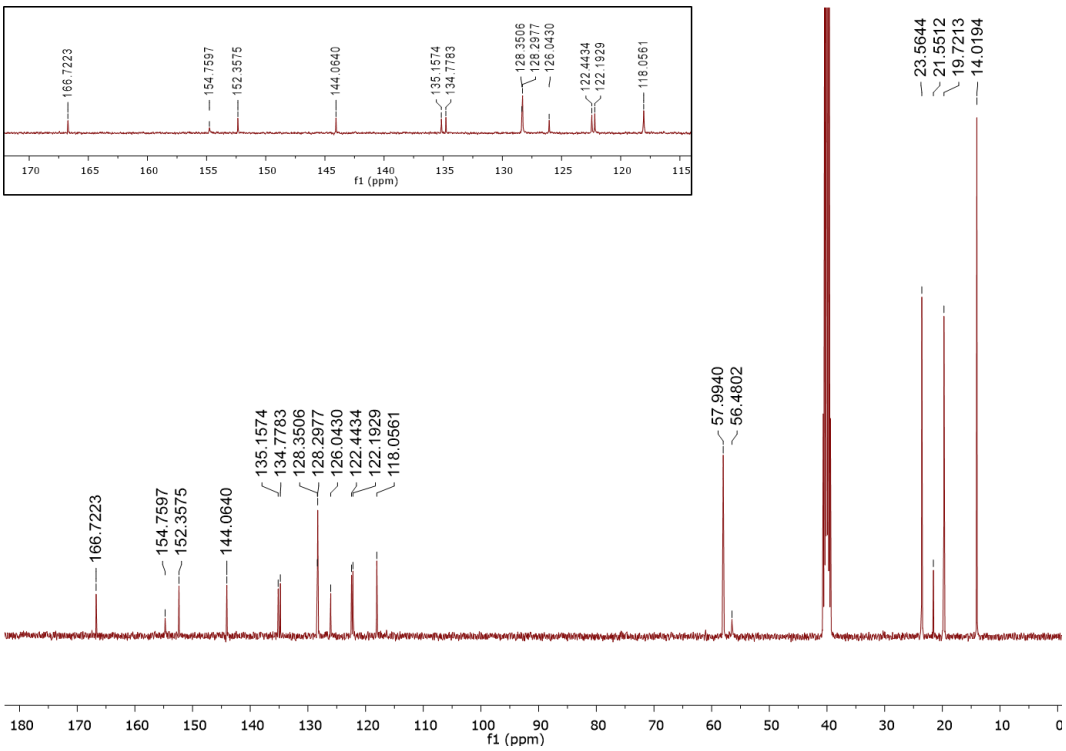

Figure S12 – ^{13}C NMR of compound **4** in DMSO-d_6.

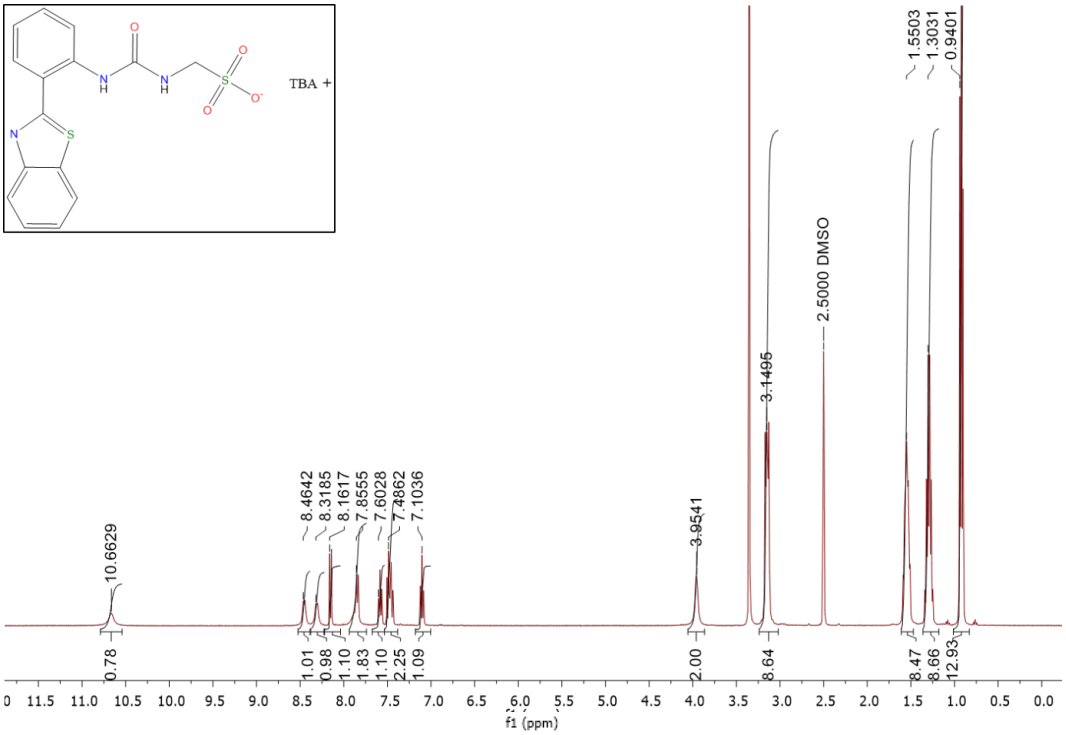

Figure S13 – ^{1}H NMR of compound **5** in DMSO-d_6.

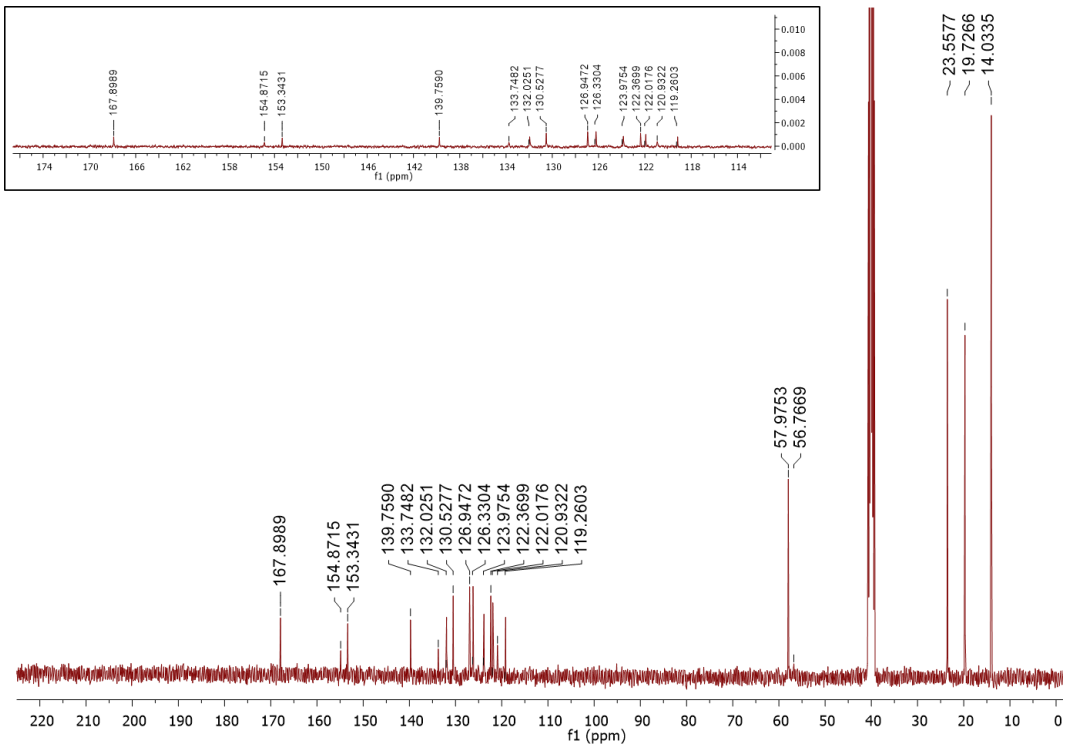

Figure S14 – ^{13}C NMR of compound **5** in DMSO-d_6.

^{1}H DOSY NMR experiments

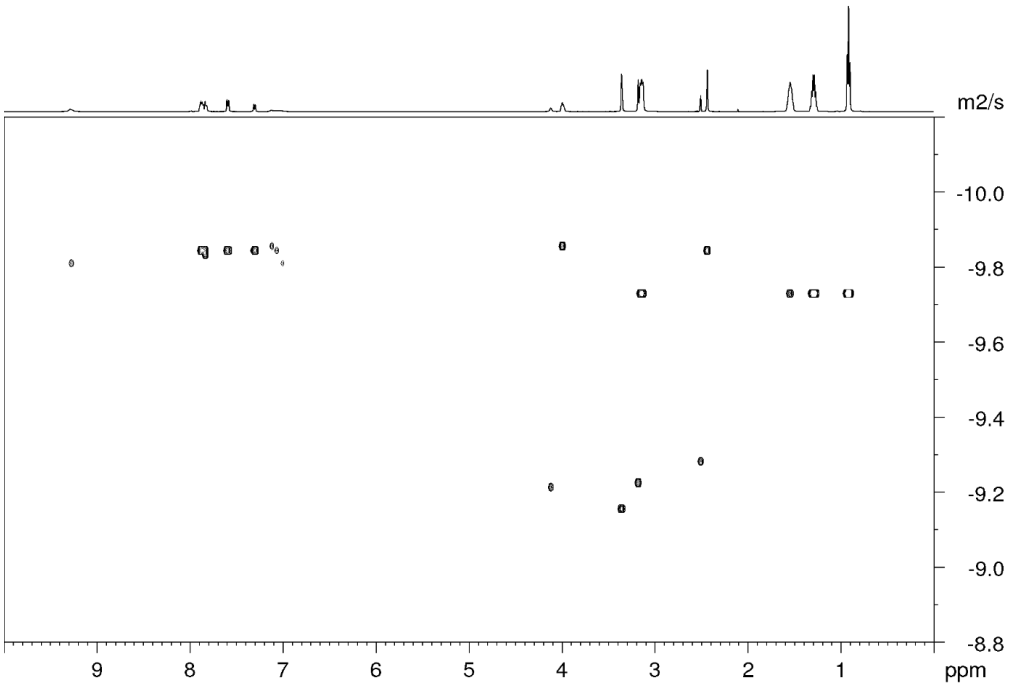

Figure S15 – ^{1}H DOSY of compound **4** (55.56 mM) in DMSO-d_6 conducted at 299.3 K.

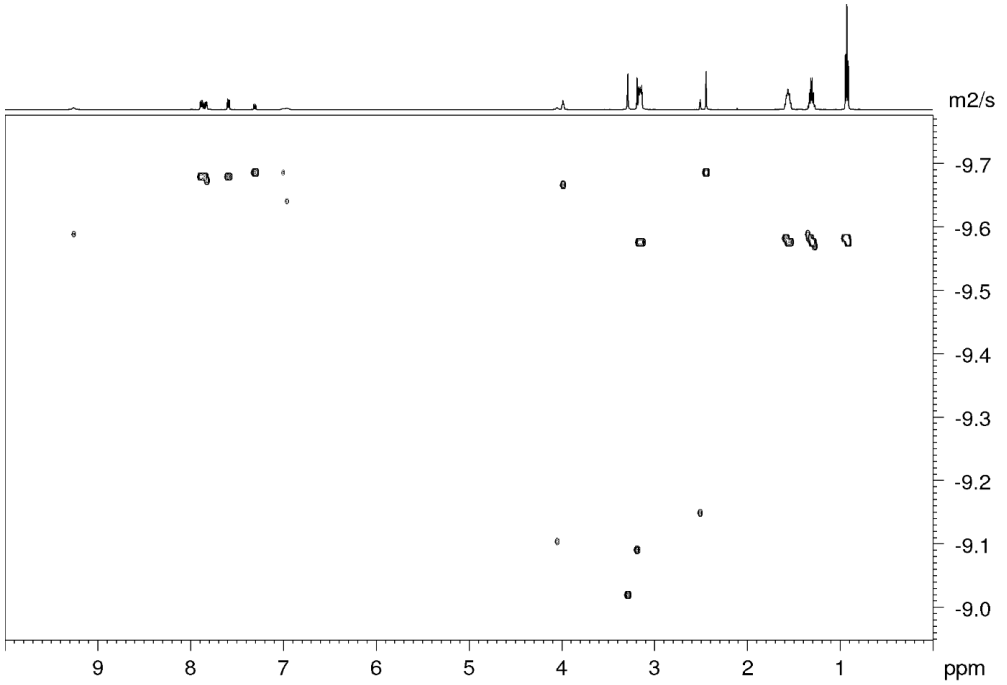

Figure S16 – ^{1}H DOSY of compound **4** (55.56 mM) in DMSO-d_6 conducted at 311.8 K.

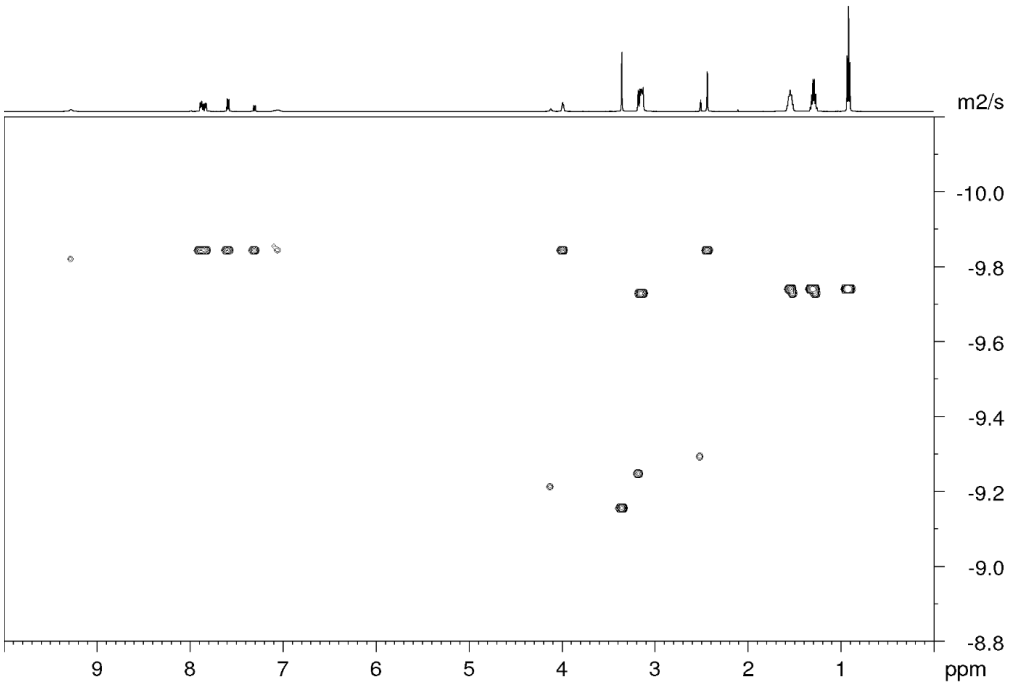

Figure S17 – ^{1}H DOSY of compound **4** (55.56 mM) in DMSO-d_6 conducted at 299.1 K after heating to 311.8 K.

Quantitative ^{1}H NMR experiments

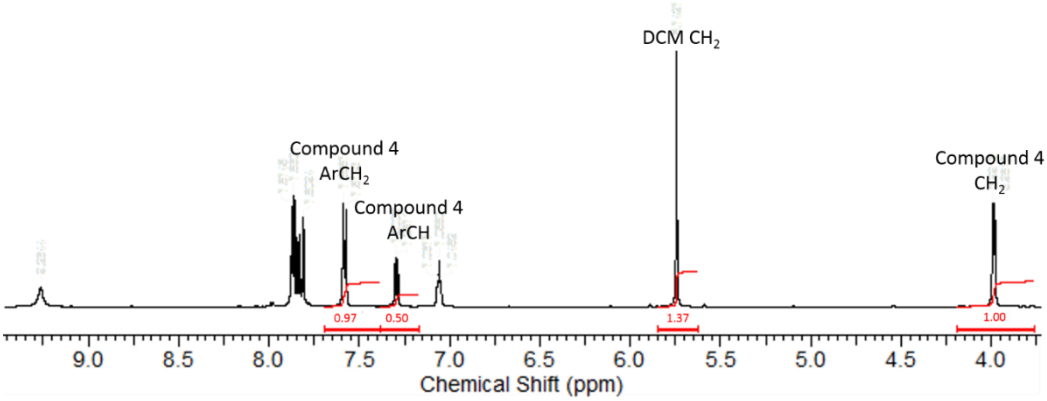

Figure S18 - ^{1}H NMR of compound **4** (0.035 g, 0.05 mM) and dichloromethane (0.007 mg, 0.08 mM) in DMSO-d_6.

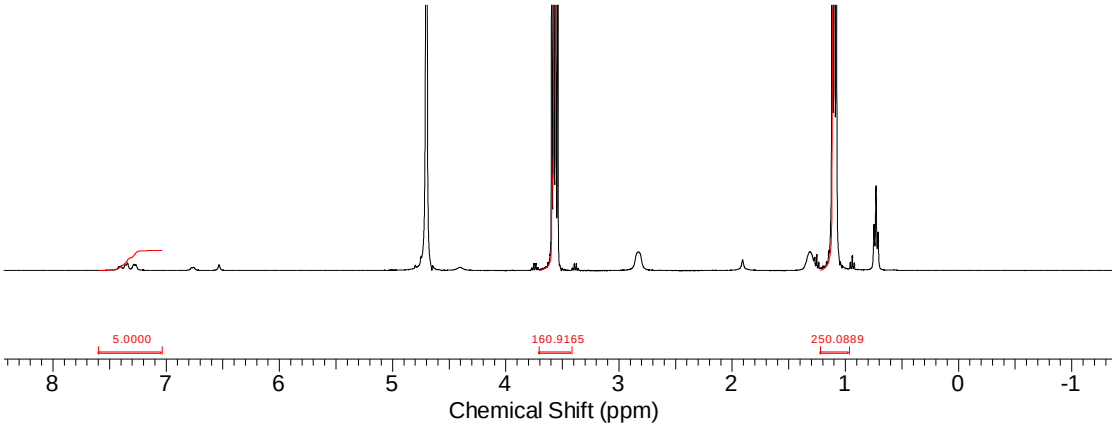

Figure S19 – ^{1}H NMR spectrum with a delay (d_1 = 60 s) of compound **4** (0.037 g, 5.91 mM) and ethanol (25 µl, 0.43 mM) in D_2O. An apparent 9.99% loss of compound was observed upon comparative signal integration.

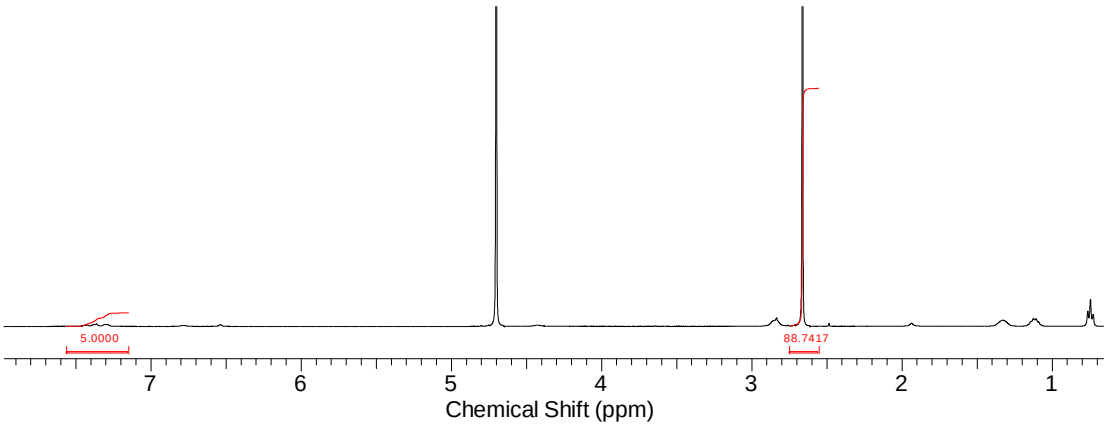

Figure S20 – ^{1}H NMR spectrum with a delay (d_1 = 60 s) of compound **4** (0.035 g, 5.57 mM) and DMSO (5 µl, 0.07 mM) in D_2O. An apparent 13.52 % loss of compound was identified upon comparative signal integration.

^{1}H NMR self-association studies

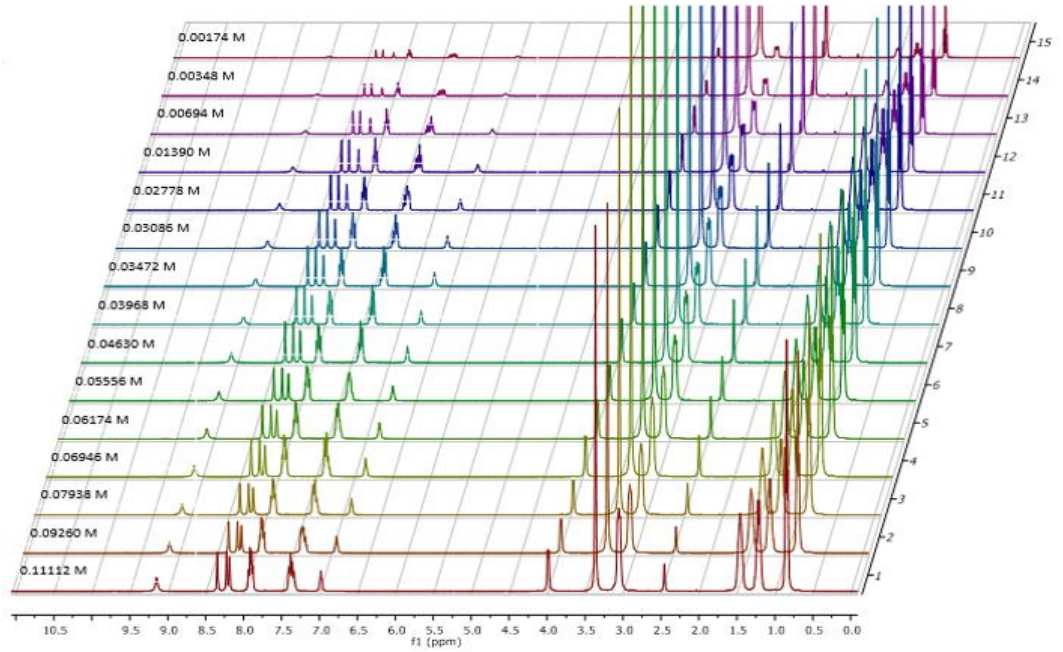

Figure S21 – ^{1}H NMR stack plot of compound **1** in a DMSO-d_6 5% H_2O solution. Samples were prepared in series with an aliquot of the most concentrated solution undergoing serial dilution.

Figure S22 – Enlarged ^{1}H NMR stack plot of compound **1** in a DMSO-d_6 5% H_2O solution.

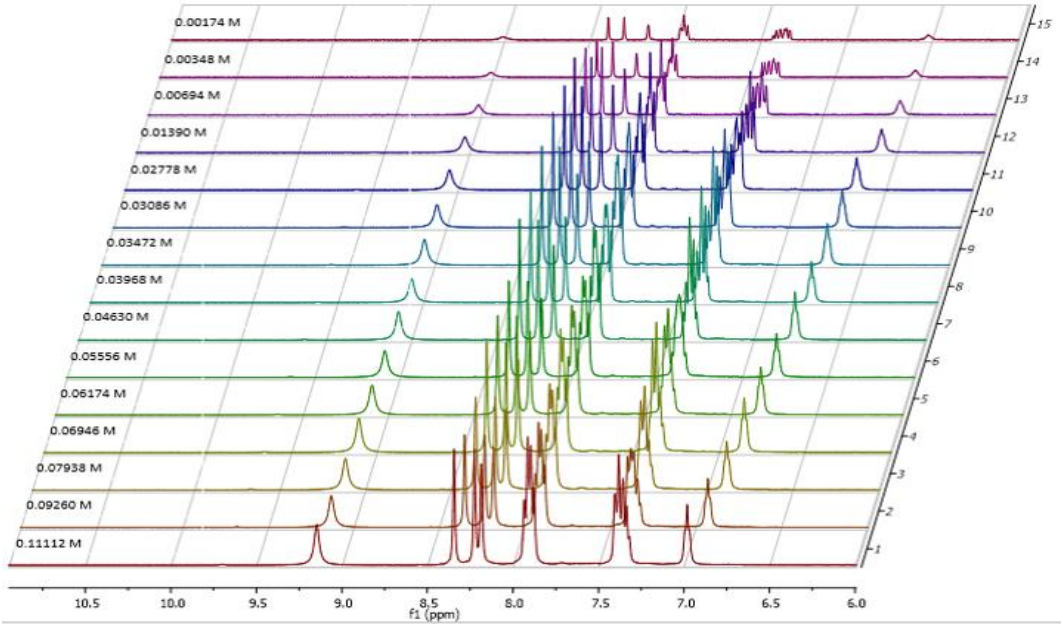

Samples were prepared in series with an aliquot of the most concentrated solution undergoing serial dilution.

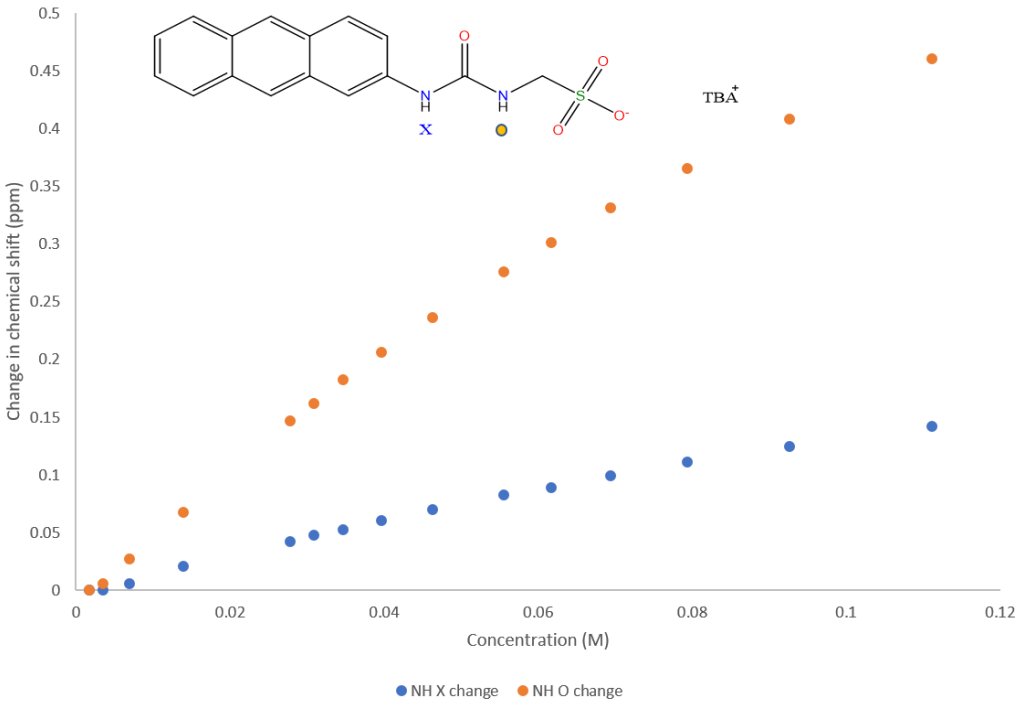

Figure S23 - Graph illustrating the ^{1}H NMR down-field change in chemical shift of urea NH resonances with increasing concentration of compound **1** in DMSO- d_6 5% H_2O (298 K).

Self-association constant calculation

Compound **1** – Dilution study in DMSO-d_6 5% H_2O. Values calculated combining the data gathered from both NH 1 and 2.

Equal K/Dimerization model

K_e = 2.90 M^{-1} ± 0.4983 % K_{dim} = 1.45 M^{-1} ± 0.2492 %

http://app.supramolecular.org/bindfit/view/230dfa2b-daa3-44e5-bdea-65ce98de9d06

CoEK model

K_e = 8.62 M^{-1} ± 1.0817 % K_{dim} = 4.31 M^{-1} ± 0.5409 % ρ = 0.50 ± 2.5165 %

http://app.supramolecular.org/bindfit/view/d404f32d-a98a-4dd2-a513-3611349b02ee

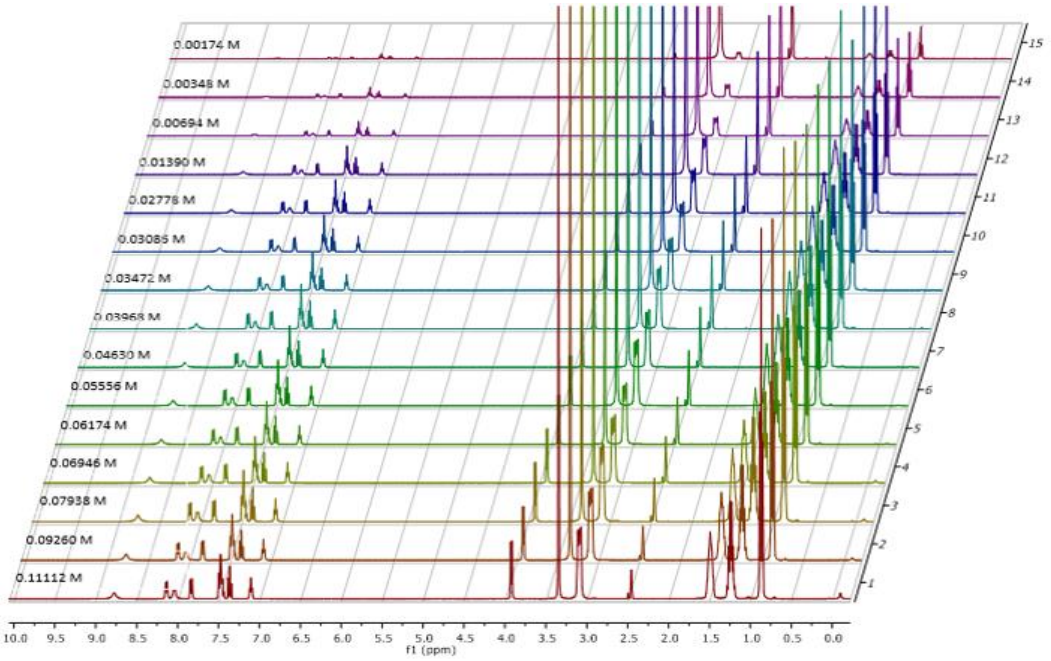

Figure S24 - ^{1}H NMR stack plot of compound **2** in a DMSO-d_6 5% H_2O solution. Samples were prepared in series with an aliquot of the most concentrated solution undergoing serial dilution.

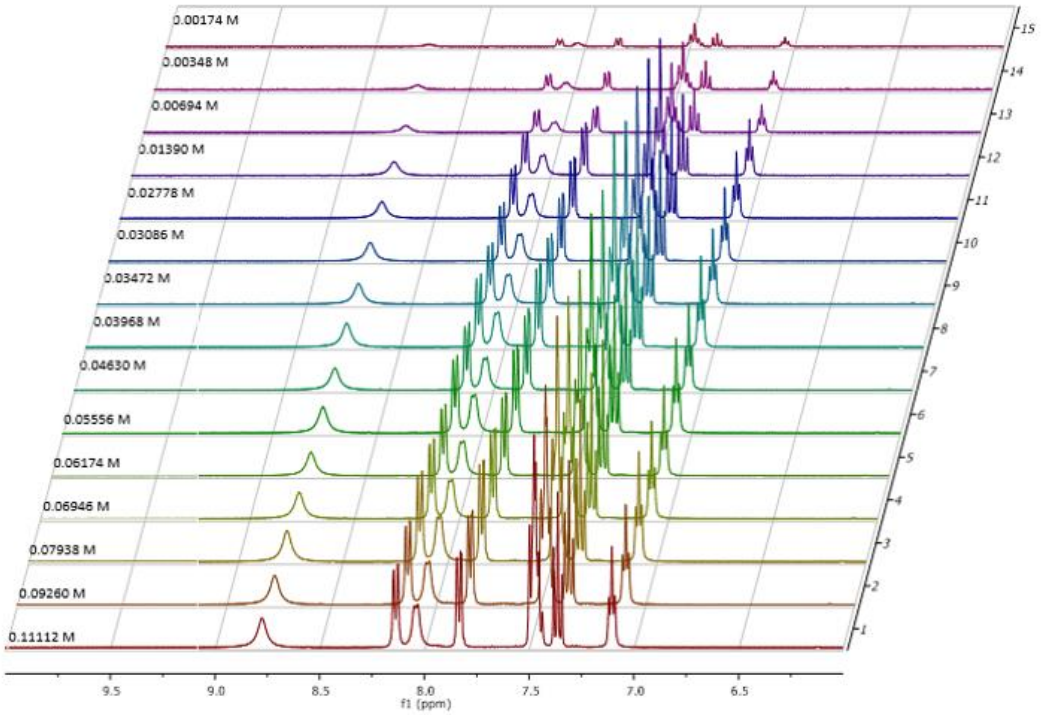

Figure S25 – Enlarged ^{1}H NMR stack plot of compound **2** in a DMSO-d_6 5% H_2O solution. Samples were prepared in series with an aliquot of the most concentrated solution undergoing serial dilution.

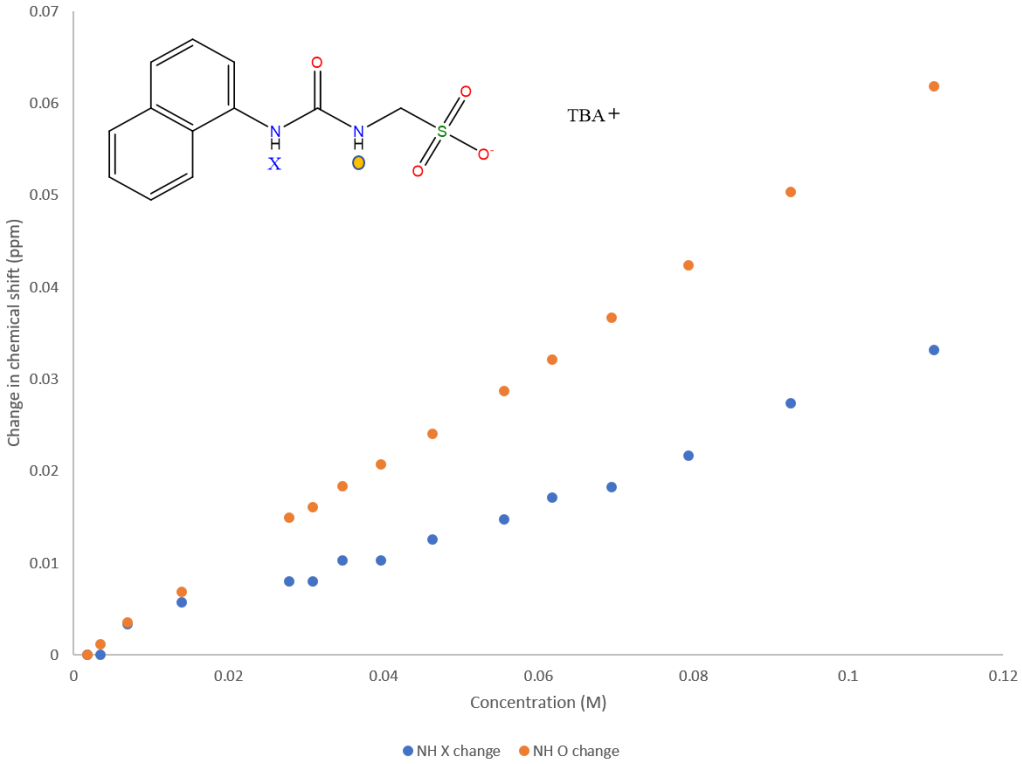

Figure S26 - Graph illustrating the ^{1}H NMR down-field change in chemical shift of urea NH resonances with increasing concentration of compound **2** in DMSO- d_6 5% H_2O (298 K).

Self-association constant calculation

Compound **2** – Dilution study in DMSO-d_6 5% H_2O. Values calculated combining the data gathered from both NH 1 and 2.

Equal K/Dimerization model

K_e = 0.03 M^{-1} ± 1.5195 % K_{dim} = 0.01 M^{-1} ± 0.7597 %

http://app.supramolecular.org/bindfit/view/b1102806-e844-49bc-84b3-bafd8a2dbcbb

CoEK model

K_e = 0.53 M^{-1} ± 43.0910 % K_{dim} = 0.27 M^{-1} ± 21.5455 % ρ = 0.00 ± 47.0444 %

http://app.supramolecular.org/bindfit/view/a4df1a0a-4903-4624-b2f5-d2ecc5edd3ed

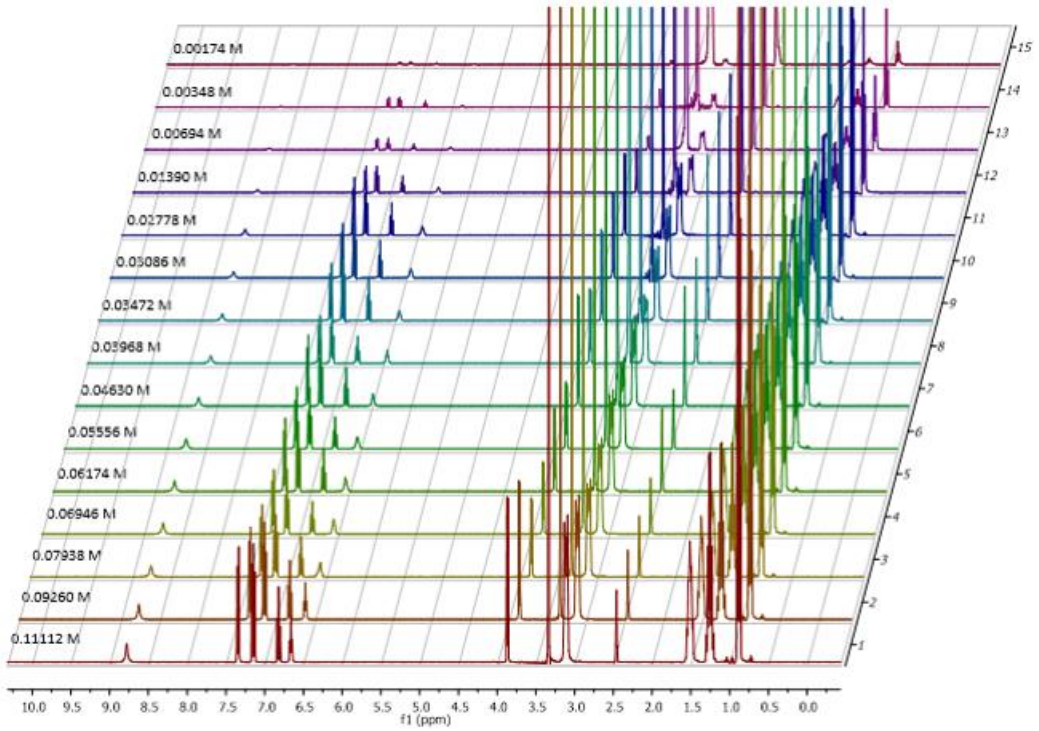

Figure S27 - ^{1}H NMR stack plot of compound **3** in a DMSO-d_6 5% H_2O solution. Samples were prepared in series with an aliquot of the most concentrated solution undergoing serial dilution.

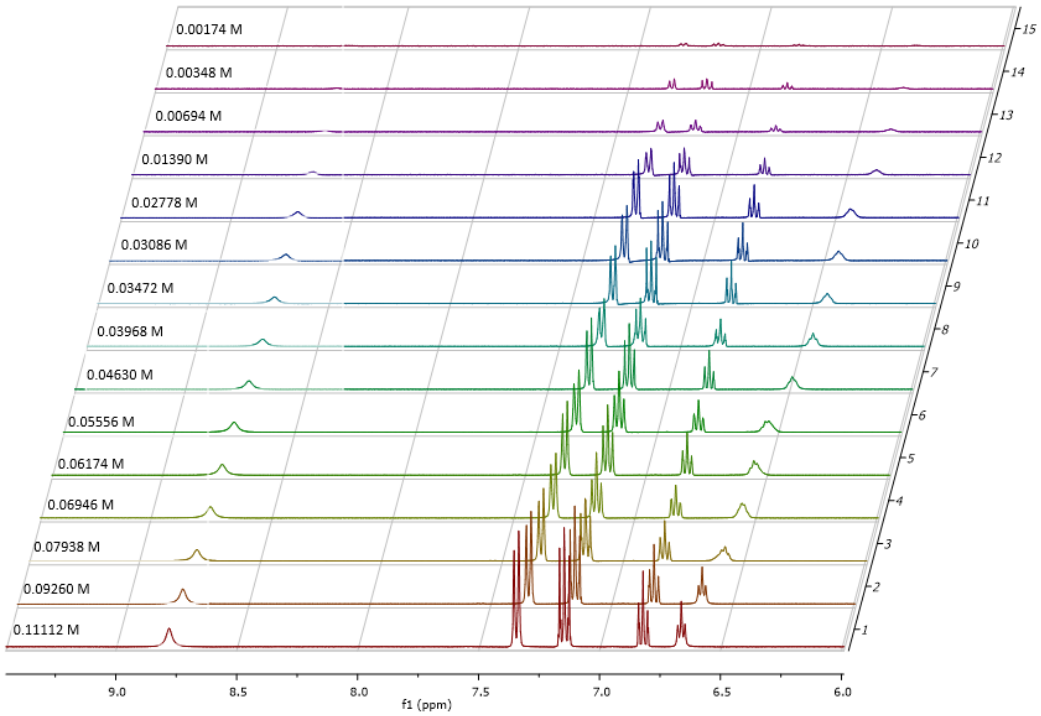

Figure S28 – Enlarged ^{1}H NMR stack plot of compound **3** in a DMSO-d_6 5% H_2O solution. Samples were prepared in series with an aliquot of the most concentrated solution undergoing serial dilution.

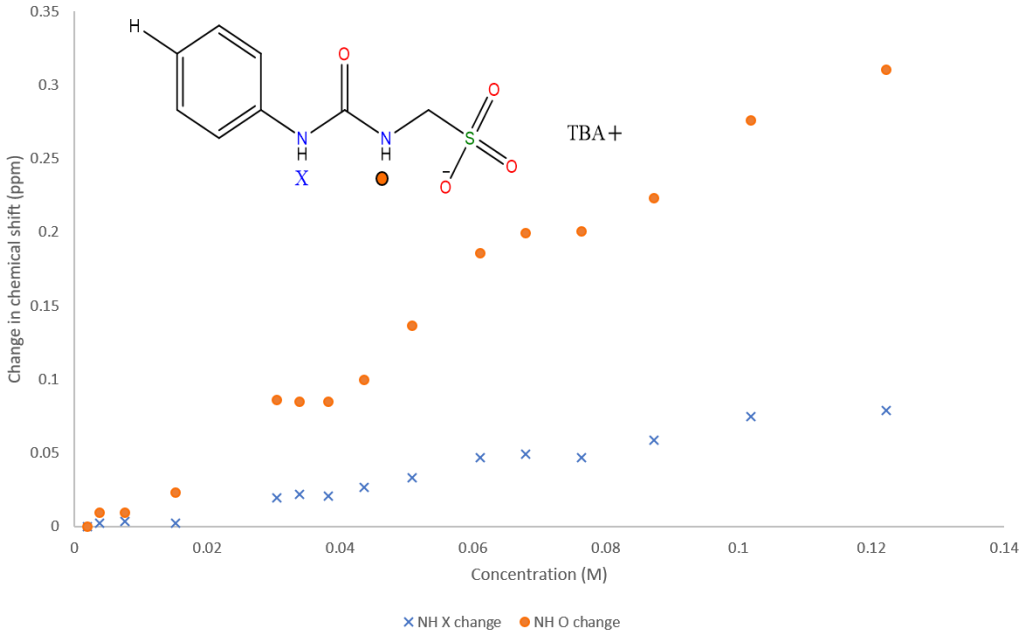

Figure S29 - Graph illustrating the ^{1}H NMR down-field change in chemical shift of urea NH resonances with increasing concentration of compound **3** in DMSO-d_6 5% H_2O (298 K).

Self-association constant calculation

Compound **3** – Dilution study in DMSO-d_6 5% H_2O. Values calculated combining the data gathered from both NH 1 and 2.

Equal K/Dimerization model

K_e = 0.61 M^{-1} ± 3.0255 % K_{dim} = 0.30 M^{-1} ± 1.5128 %

http://app.supramolecular.org/bindfit/view/82f6ee49-a329-40d1-8025-1adb091e0f87

CoEK model

K_e = 12.98 M^{-1} ± 5.7461 % K_{dim} = 6.49 M^{-1} ± 2.8731 % ρ = 0.17 ± 23.7749 %

http://app.supramolecular.org/bindfit/view/6fd2fbc5-dbb0-4e7d-b60d-e6620e47ceff

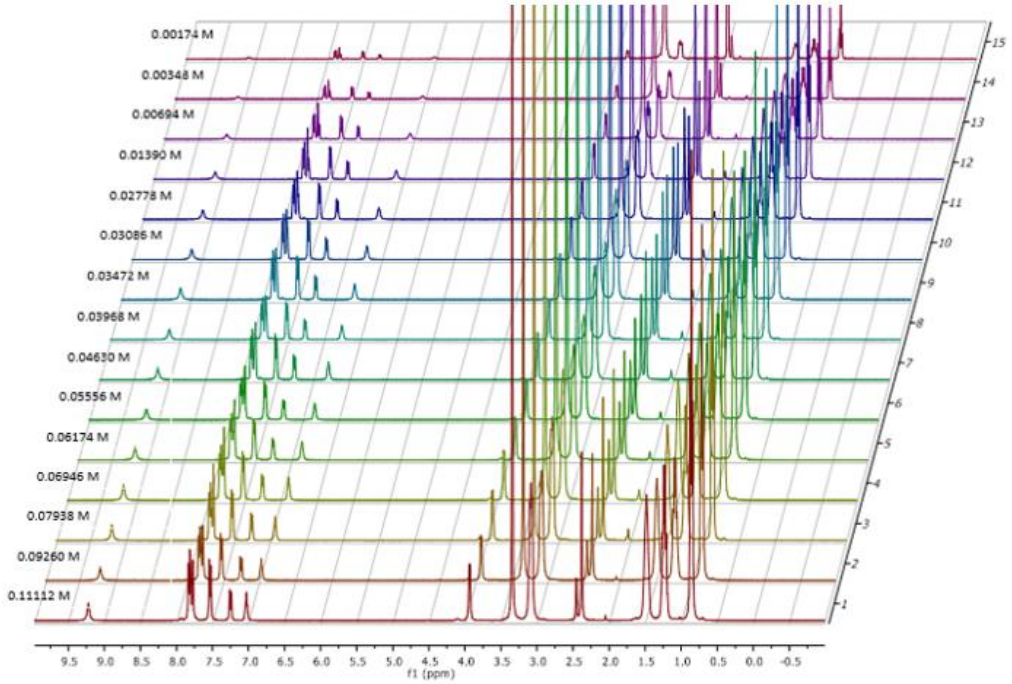

Figure S30 – ^{1}H NMR stack plot of compound **4** in a DMSO-d_6 5% H_2O solution. Samples were prepared in series with an aliquot of the most concentrated solution undergoing serial dilution.

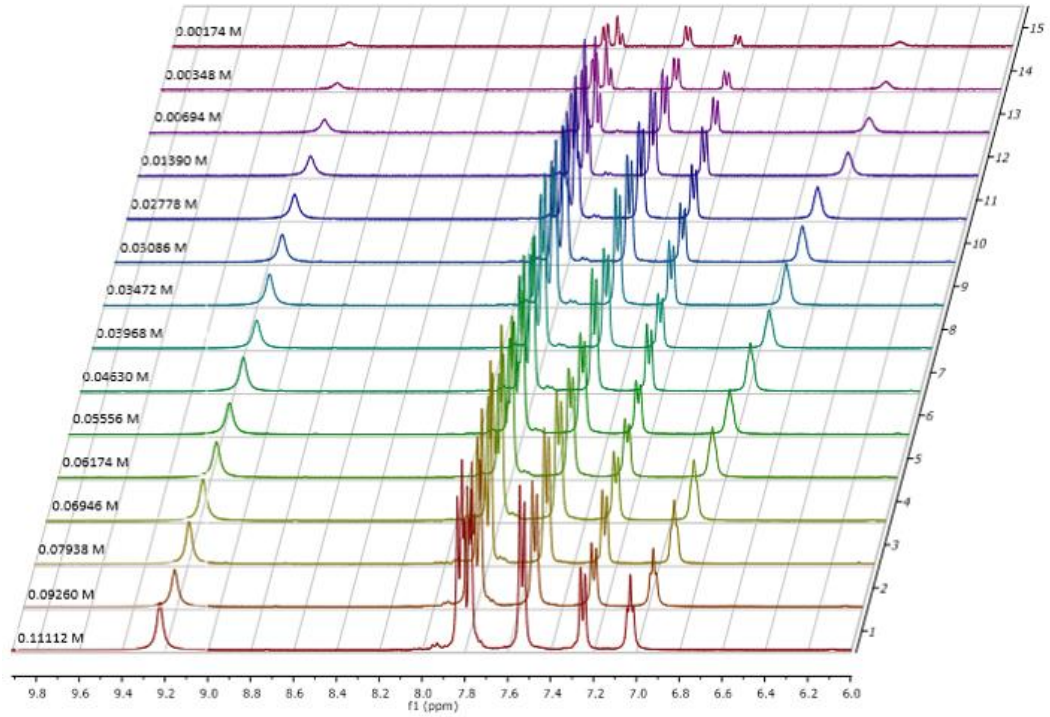

Figure S31 – Enlarged ^{1}H NMR stack plot of compound **4** in a DMSO-d_6 5% H_2O solution. Samples were prepared in series with an aliquot of the most concentrated solution undergoing serial dilution.

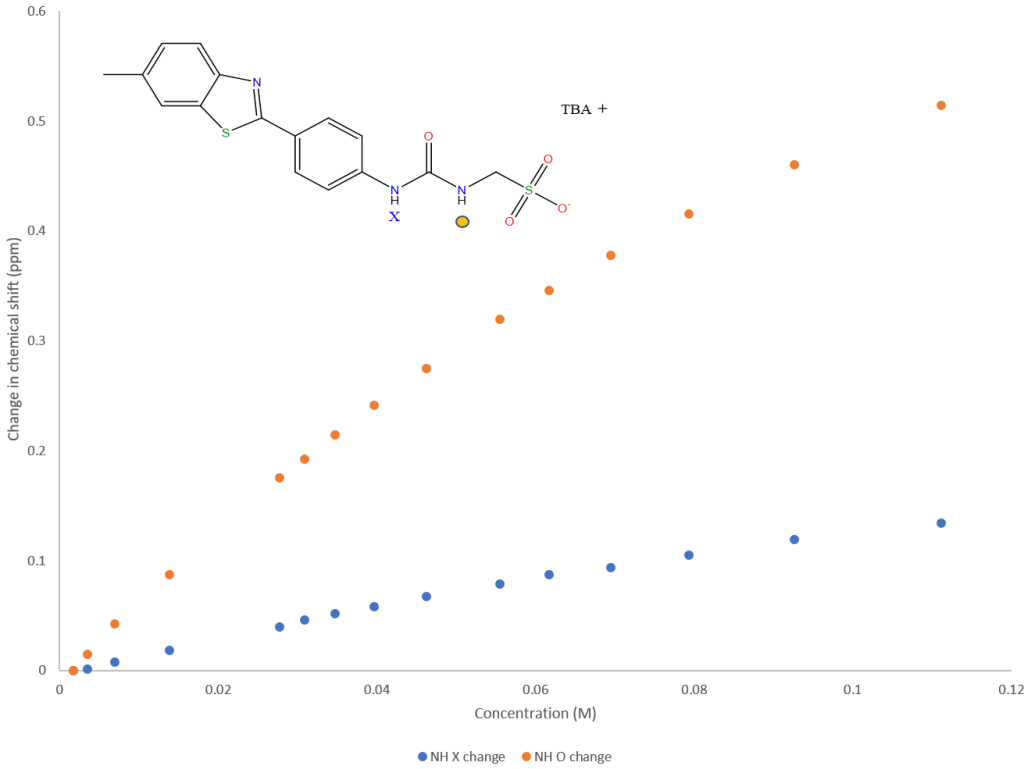

Figure S32 - Graph illustrating the ^{1}H NMR down-field change in chemical shift of urea NH resonances with increasing concentration of compound **4** in DMSO-d_6 5% H_2O (298 K).

Self-association constant calculation

Compound **4** – Dilution study in DMSO-d_6 5% H_2O. Values calculated combining the data gathered from both NH 1 and 2.

Equal K/Dimerization model

K_e = 5.34 M^{-1} ± 0.6112 % K_{dim} = 2.67 M^{-1} ± 0.3056 %

http://app.supramolecular.org/bindfit/view/ef5fa21f-a268-46aa-87ef-ebf751300648

CoEK model

K_e = 12.95 M^{-1} ± 0.6971 % K_{dim} = 6.47 M^{-1} ± 0.3485 % ρ = 0.50 ± 2.0433 %

http://app.supramolecular.org/bindfit/view/de1c6c54-3f86-4e43-8063-4ad17361d6da

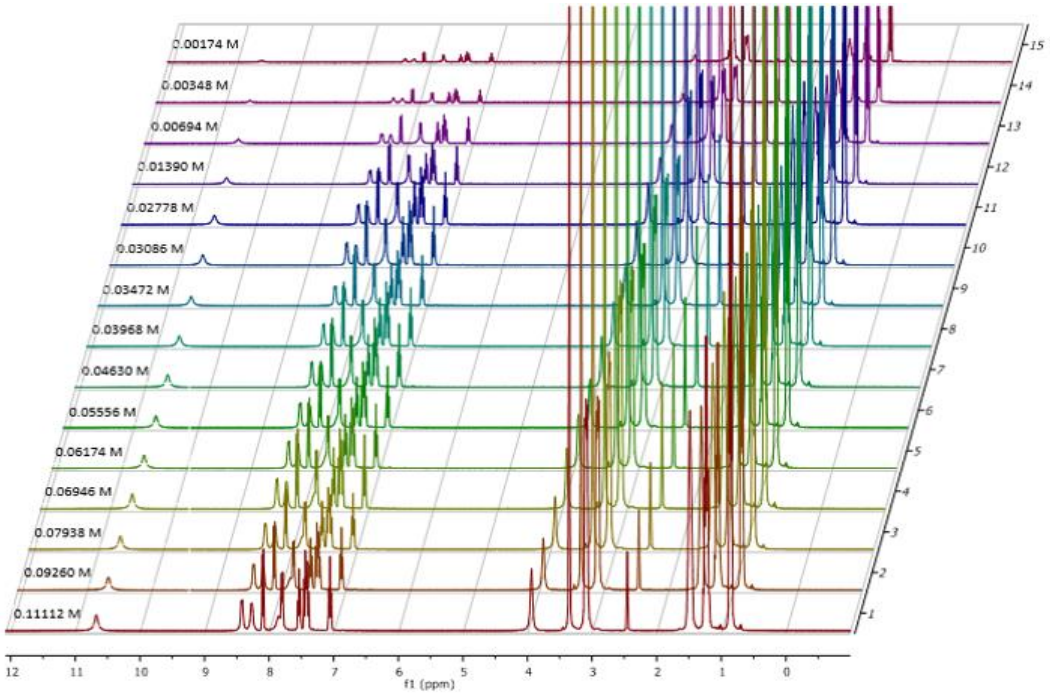

Figure S33 – ^{1}H NMR stack plot of compound **5** in a DMSO-d_6 5% H_2O solution. Samples were prepared in series with an aliquot of the most concentrated solution undergoing serial dilution.

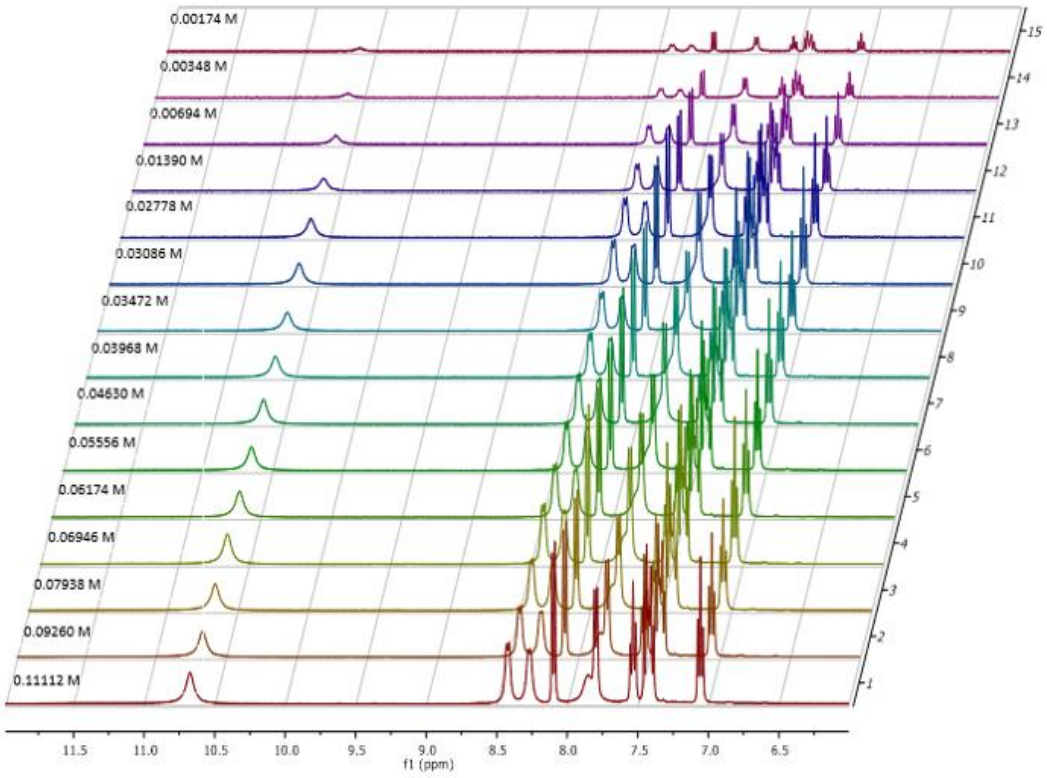

Figure S34 – Enlarged ^{1}H NMR stack plot of compound **5** in a DMSO-d_6 5% H_2O solution. Samples were prepared in series with an aliquot of the most concentrated solution undergoing serial dilution.

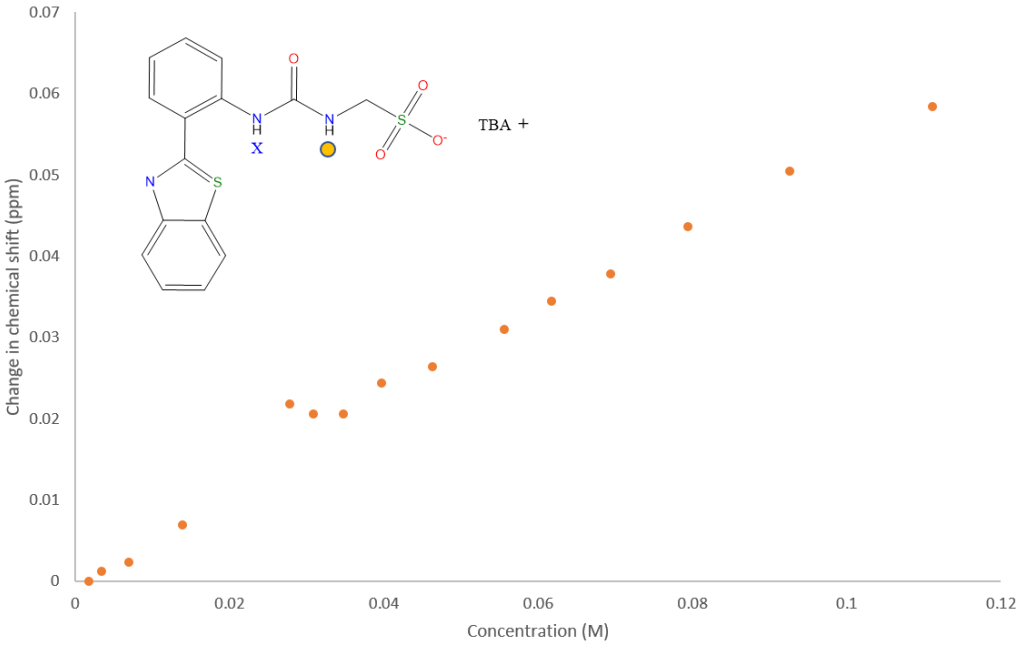

Figure S35 - Graph illustrating the ^{1}H NMR down-field change in chemical shift of urea NH resonances with increasing concentration of compound **5** in DMSO-d_6 5% H_2O (298 K).

Self-association constant calculation

Compound **5** – Dilution study in DMSO-d_6 5% H_2O. Values calculated from data gathered from NH 1

Equal K/Dimerization model

K_e = 1.15 M^{-1} ± 2.0521 % K_{dim} = 0.57 M^{-1} ± 1.0610 %

http://app.supramolecular.org/bindfit/view/0780d95f-ffc6-428d-b327-a9c32dbcce60

CoEK model

K_e = 6.19 M^{-1} ± 8.8173 % K_{dim} = 3.10 M^{-1} ± 4.4087 % ρ = 0.43 ± 17.8122 %

http://app.supramolecular.org/bindfit/view/101ed3ba-862a-4486-b8b7-af27b5cffdf0

DLS data

Correlation data

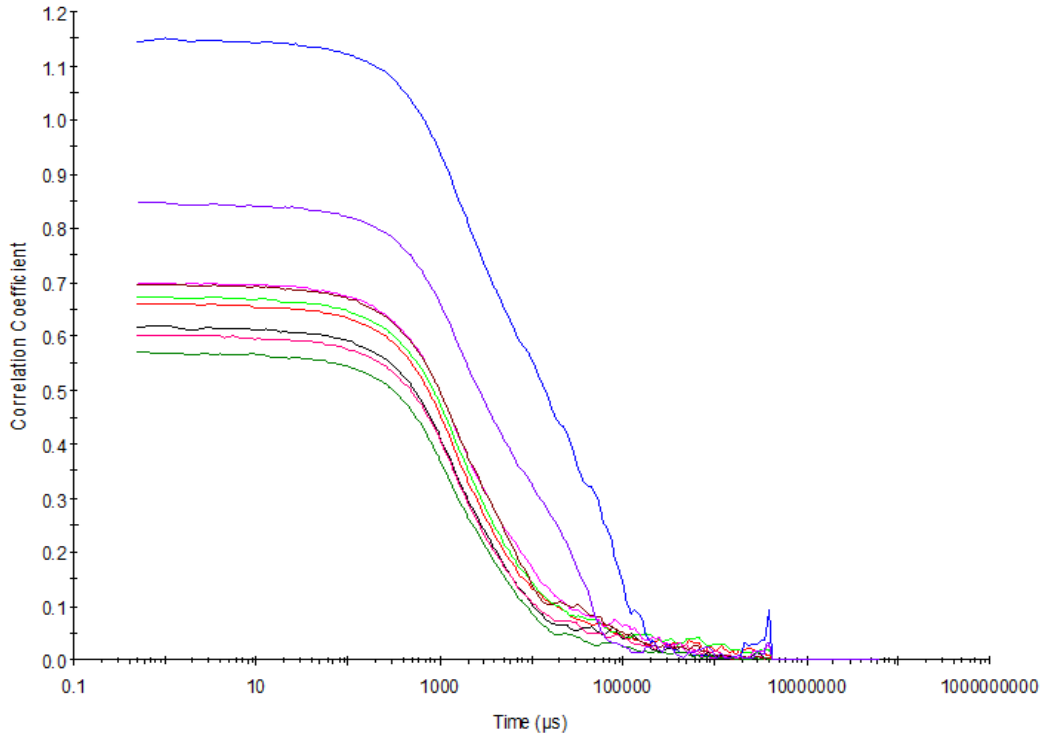

Figure S36 – Raw correlation data for 9 DLS runs at 25 °C before heating to 40 °C with compound **1** at a concentration of 111.12 mM in DMSO.

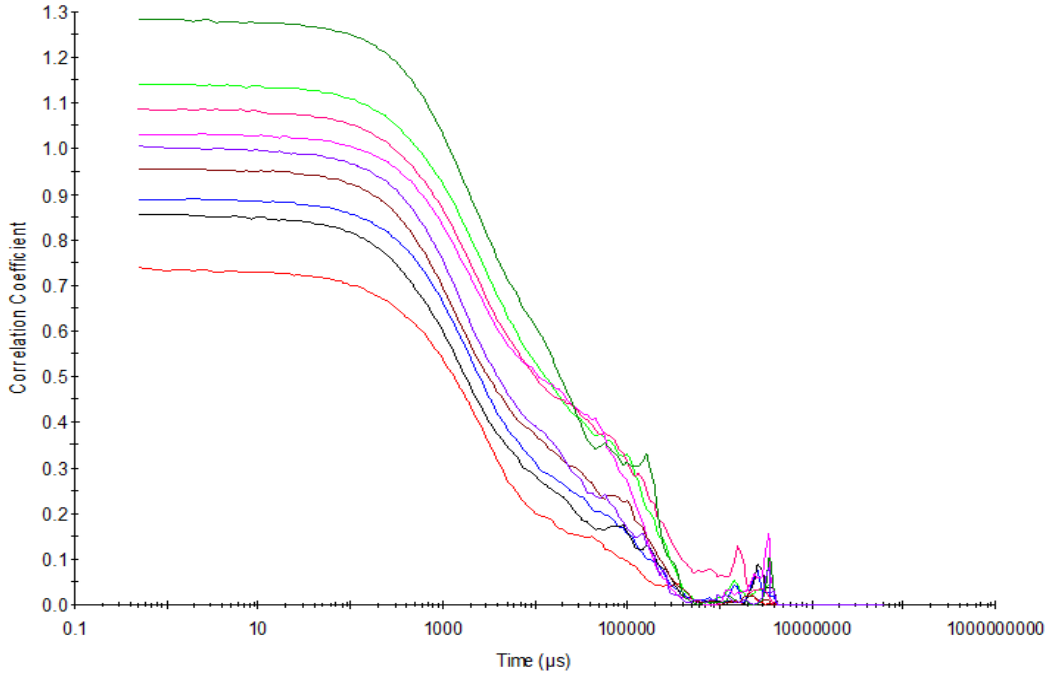

Figure S37 – Raw correlation data for 9 DLS runs at 40 °C with compound **1** at a concentration of 111.12 mM in DMSO.

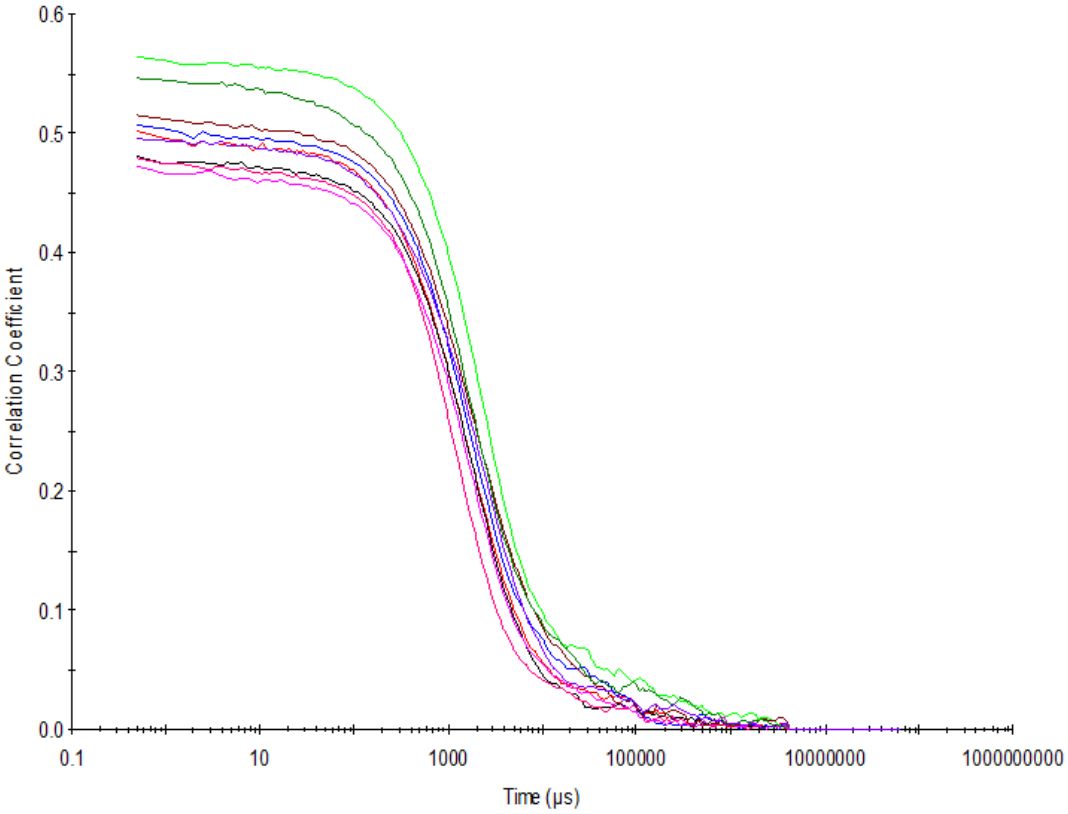

Figure S38 – Raw correlation data for 9 DLS runs at 25 °C after heating to 40 °C with compound **1** at a concentration of 111.12 mM in DMSO.

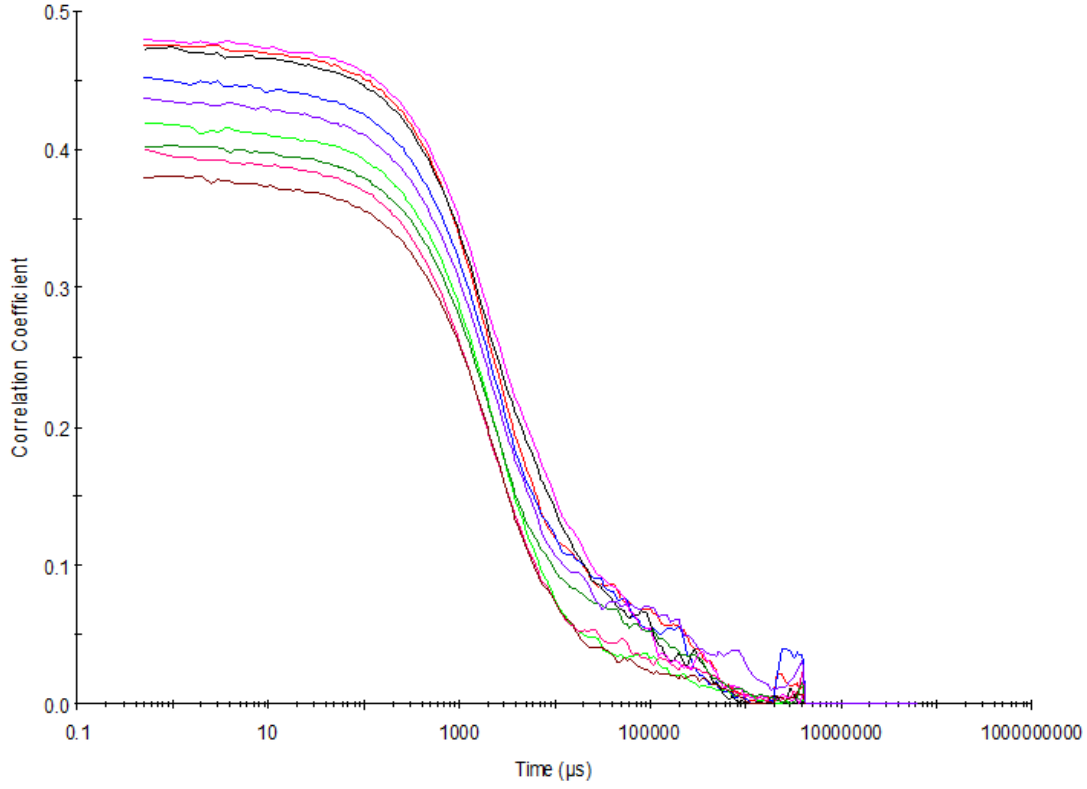

Figure S39 – Raw correlation data for 9 DLS runs at 25 °C before heating to 40 °C with compound **1** at a concentration of 55.56 mM in DMSO.

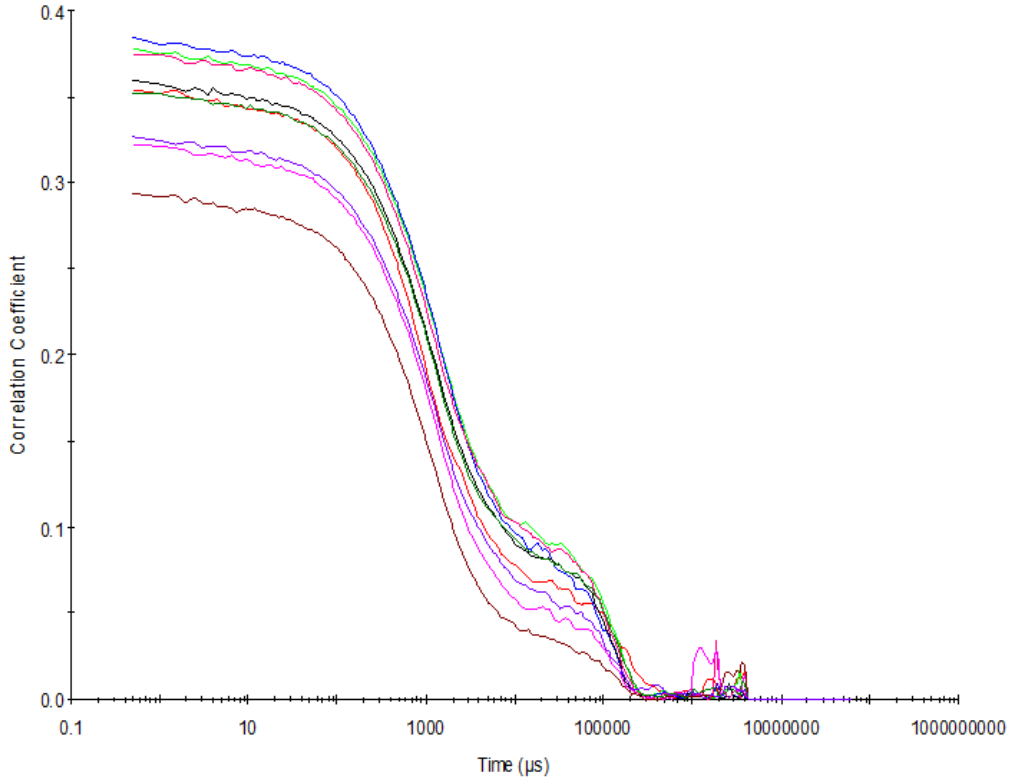

Figure S40 – Raw correlation data for 9 DLS runs at 40 °C with compound **1** at a concentration of 55.56 mM in DMSO.

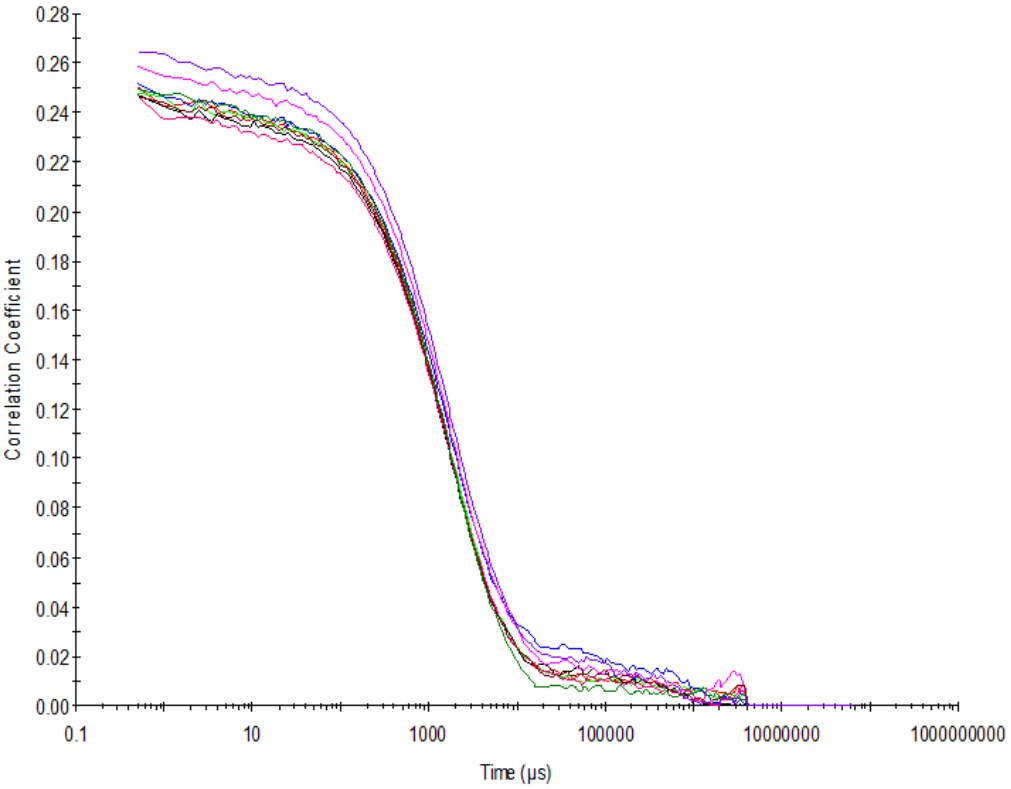

Figure S41 – Raw correlation data for 9 DLS runs at 25 °C after heating to 40 °C with compound **1** at a concentration of 55.56 mM in DMSO.

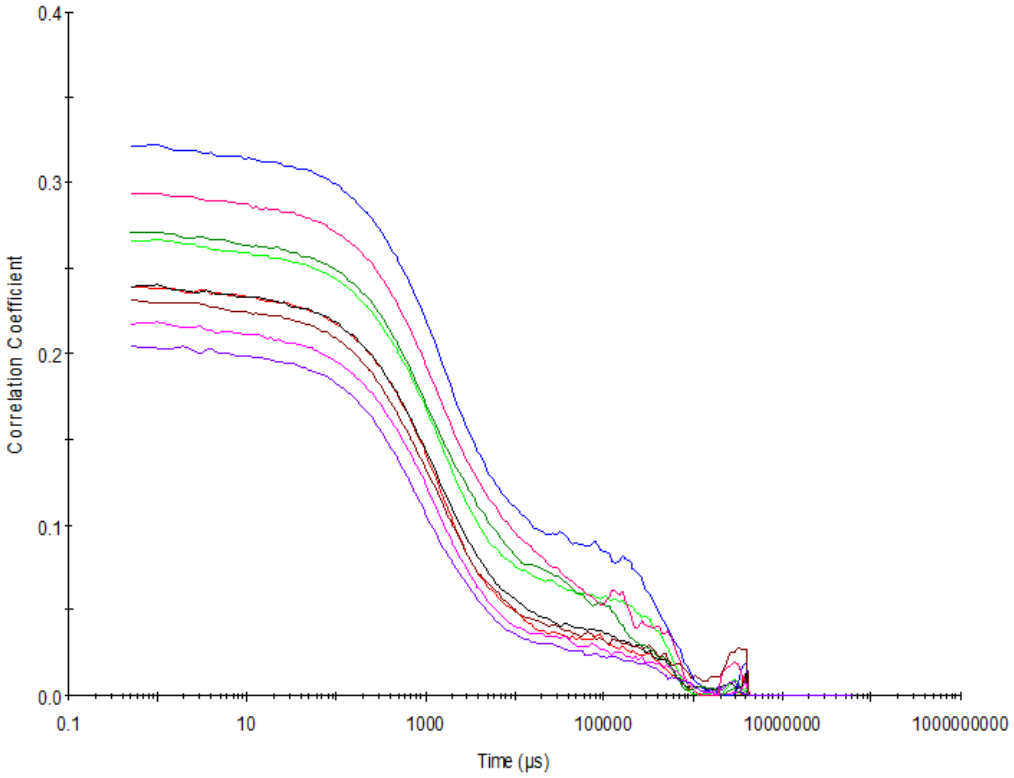

Figure S42 – Raw correlation data for 9 DLS runs at 25 °C before heating to 40 °C with compound **1** at a concentration of 5.56 mM in DMSO.

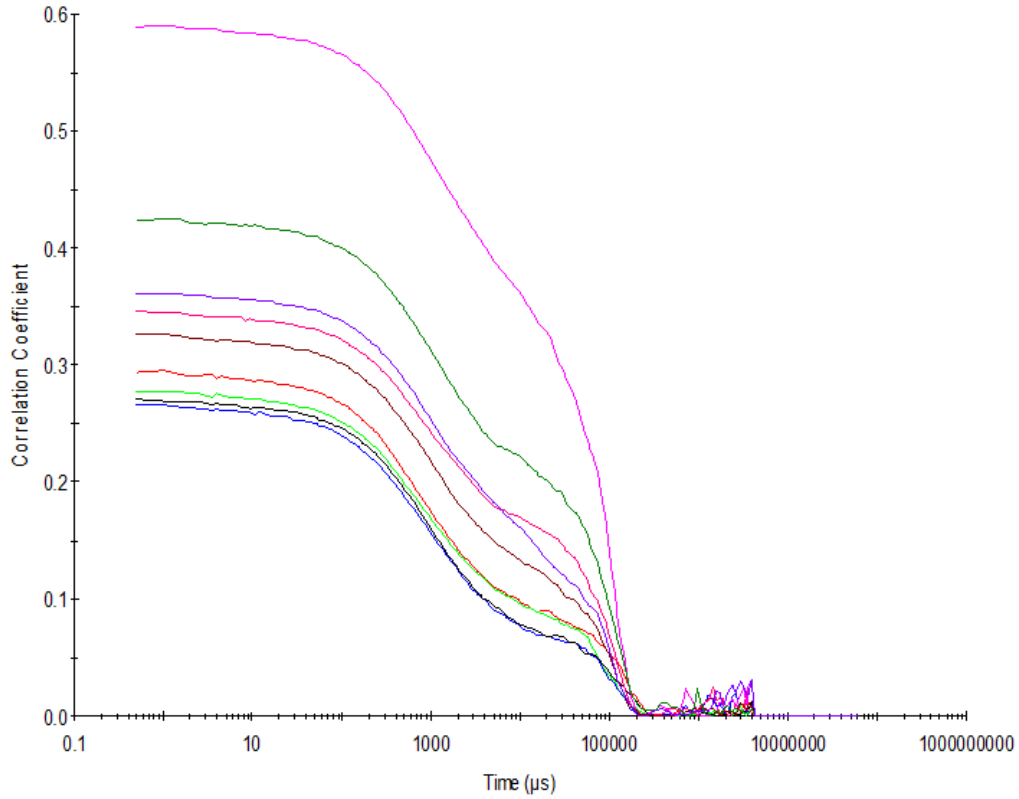

Figure S43 – Raw correlation data for 9 DLS runs at 40 °C with compound **1** at a concentration of 5.56 mM in DMSO.

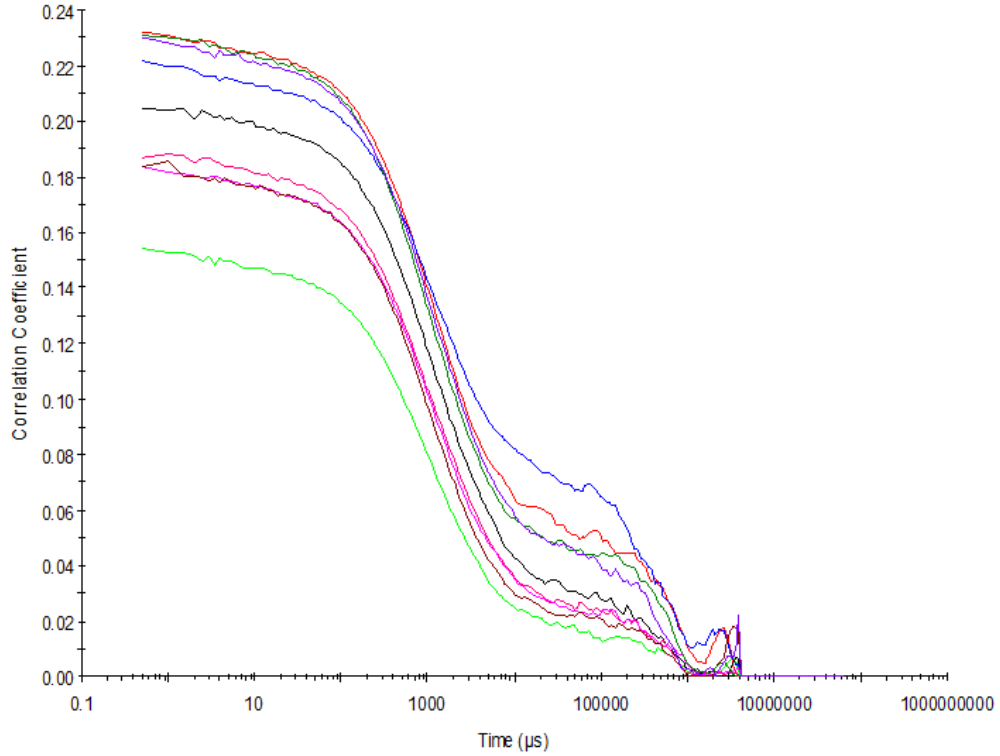

Figure S44 – Raw correlation data for 9 DLS runs at 25 °C after heating to 40 °C with compound **1** at a concentration of 5.56 mM in DMSO.

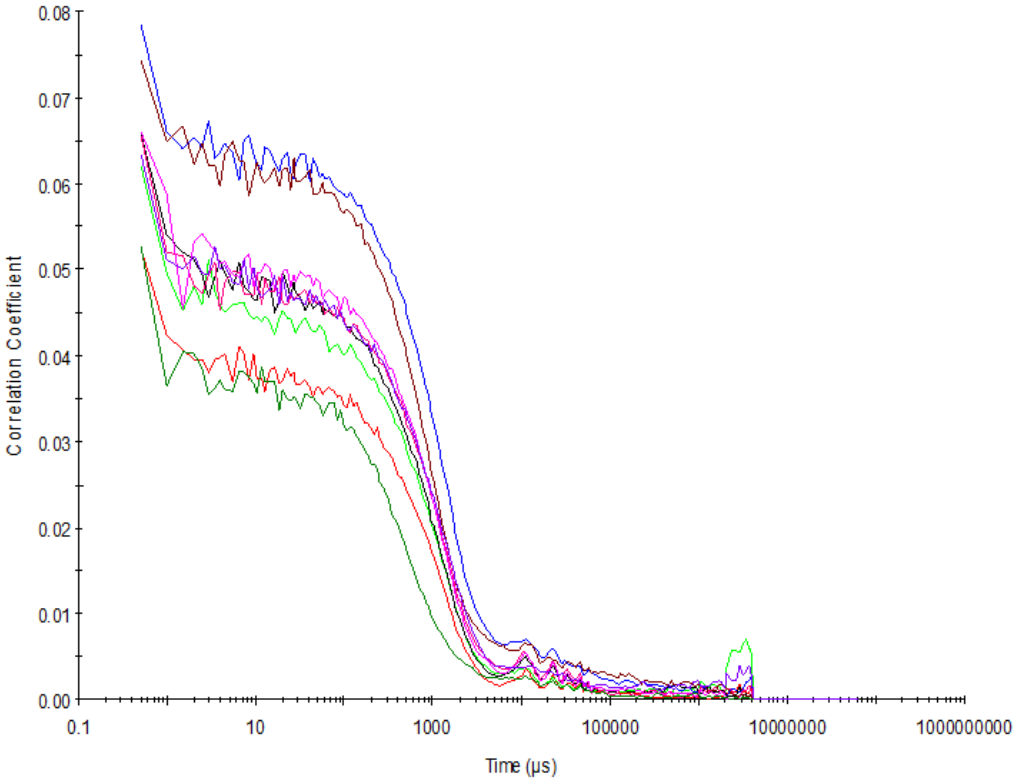

Figure S45 – Raw correlation data for 9 DLS runs at 25 °C before heating to 40 °C with compound **1** at a concentration of 0.56 mM in DMSO.

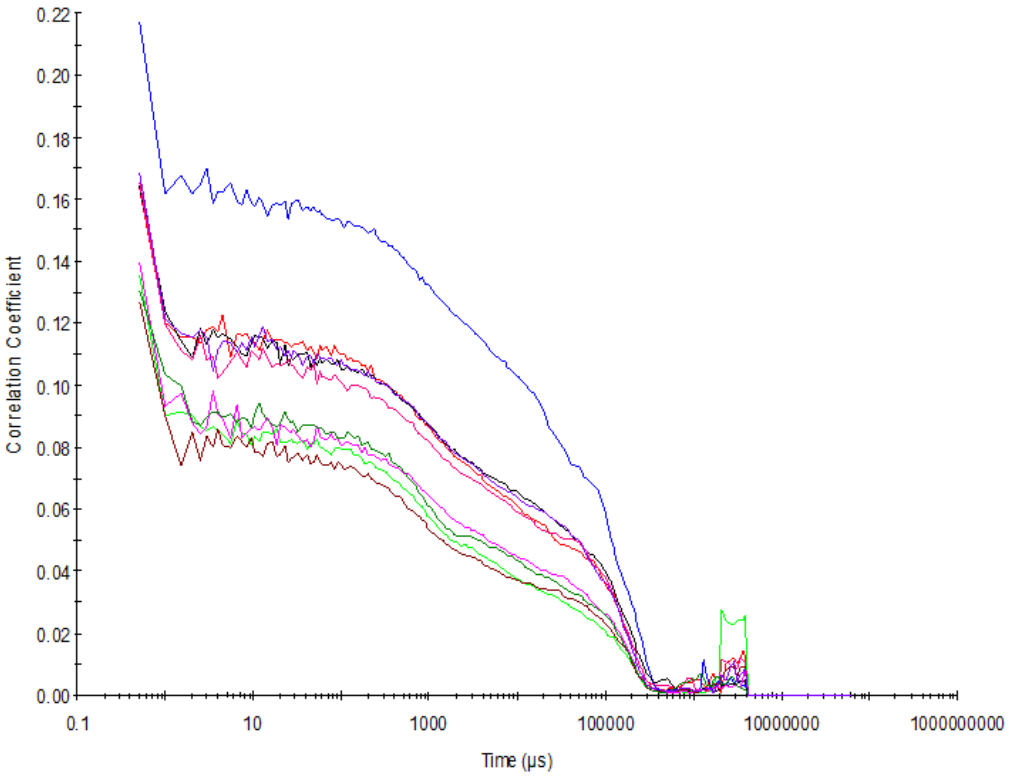

Figure S46 – Raw correlation data for 9 DLS runs at 40 °C with compound **1** at a concentration of 0.56 mM in DMSO.

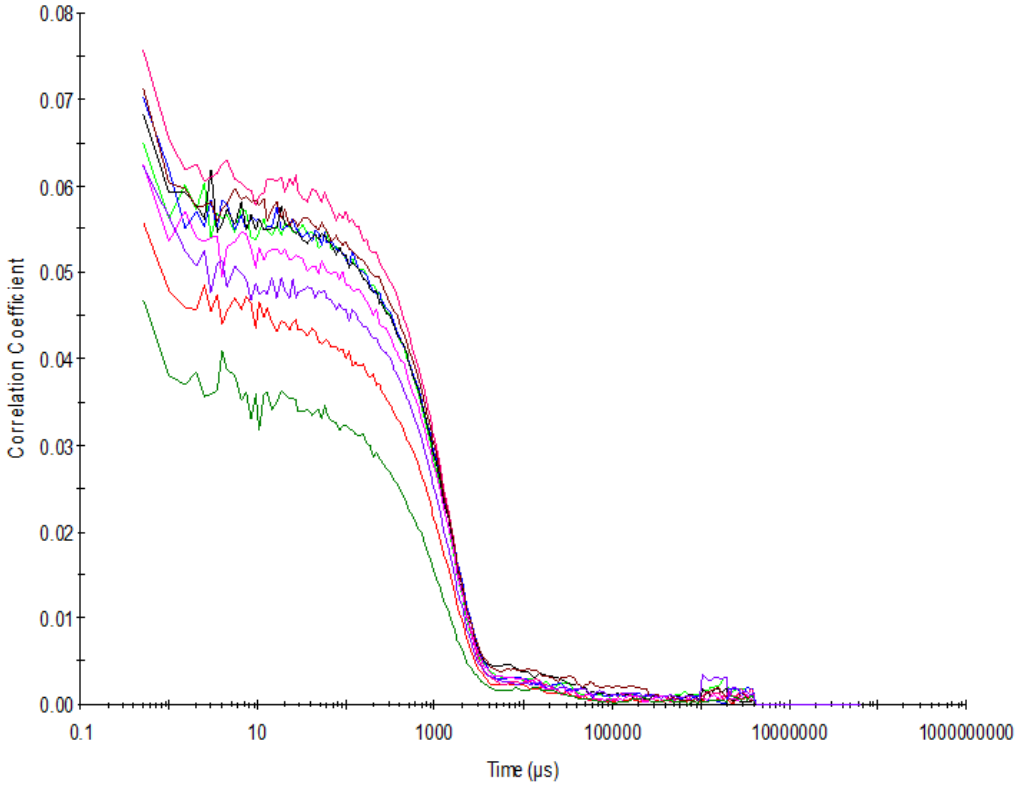

Figure S47 – Raw correlation data for 9 DLS runs at 25 °C after heating to 40 °C with compound **1** at a concentration of 0.56 mM in DMSO.

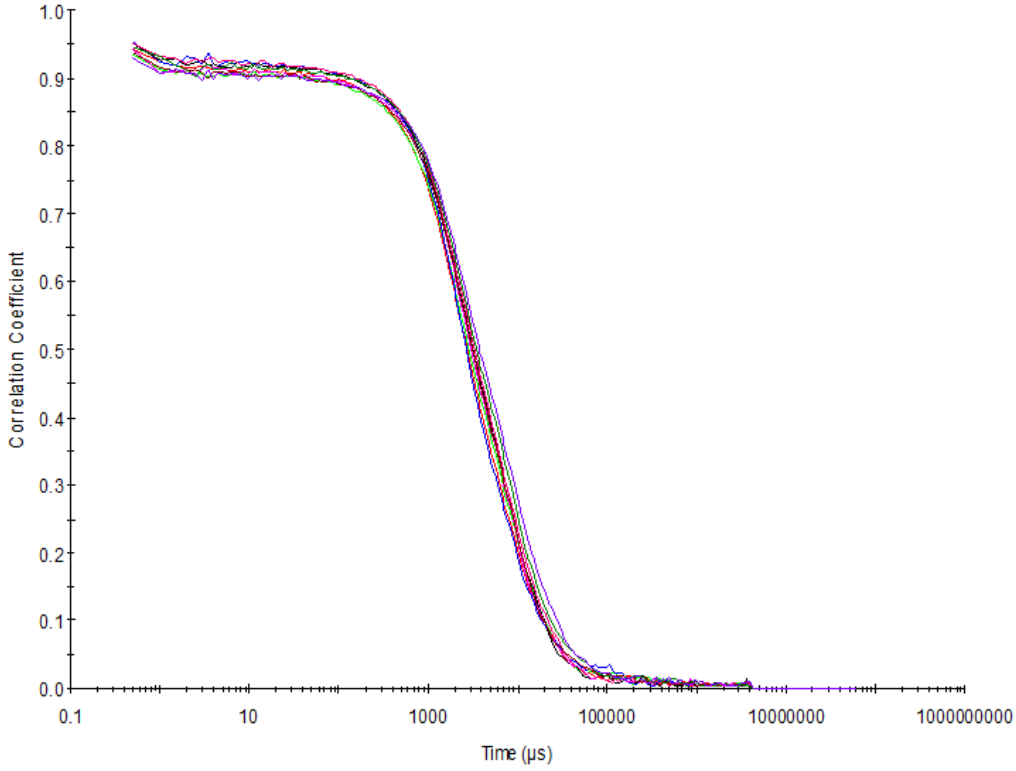

Figure S48 – Raw correlation data for 9 DLS runs at 25 °C after heating to 40 °C with compound **1** at a concentration of 55.56 mM in DMSO: H_2O 1: 1.

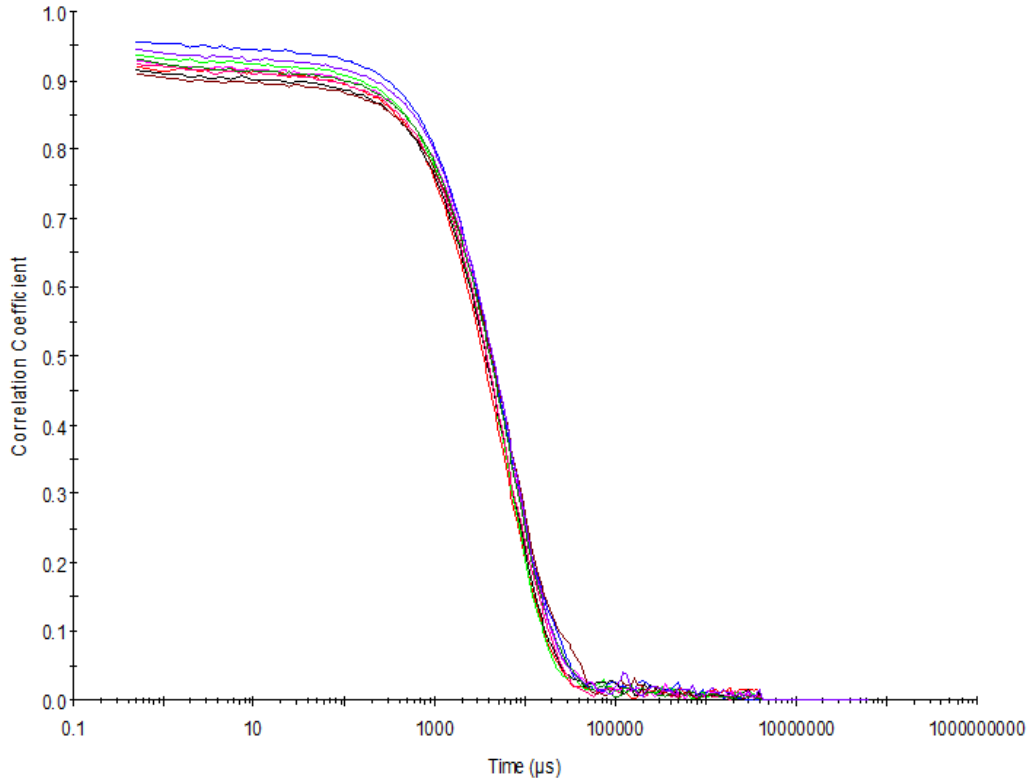

Figure S49 - Raw correlation data for 9 DLS runs at 25 °C after heating to 40 °C with compound **1** at a concentration of 5.56 mM in DMSO: H_2O 1: 1.

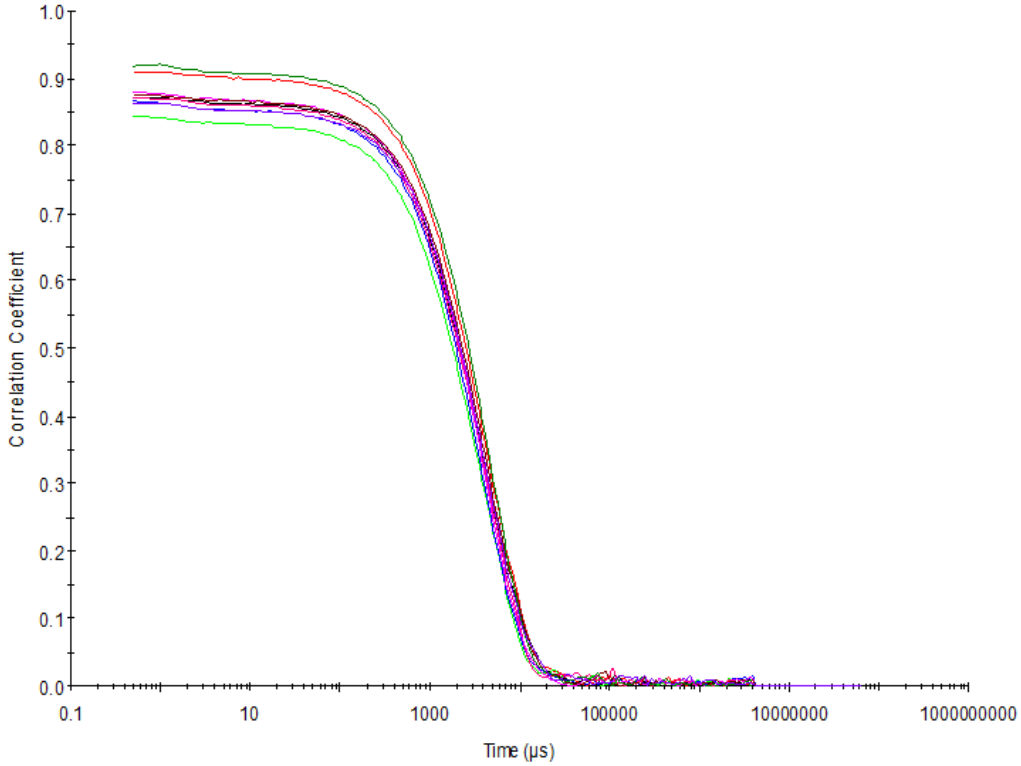

Figure S50 - Raw correlation data for 9 DLS runs at 25 °C after heating to 40 °C with compound **1** at a concentration of 0.56 mM in DMSO: H_2O 1: 1.

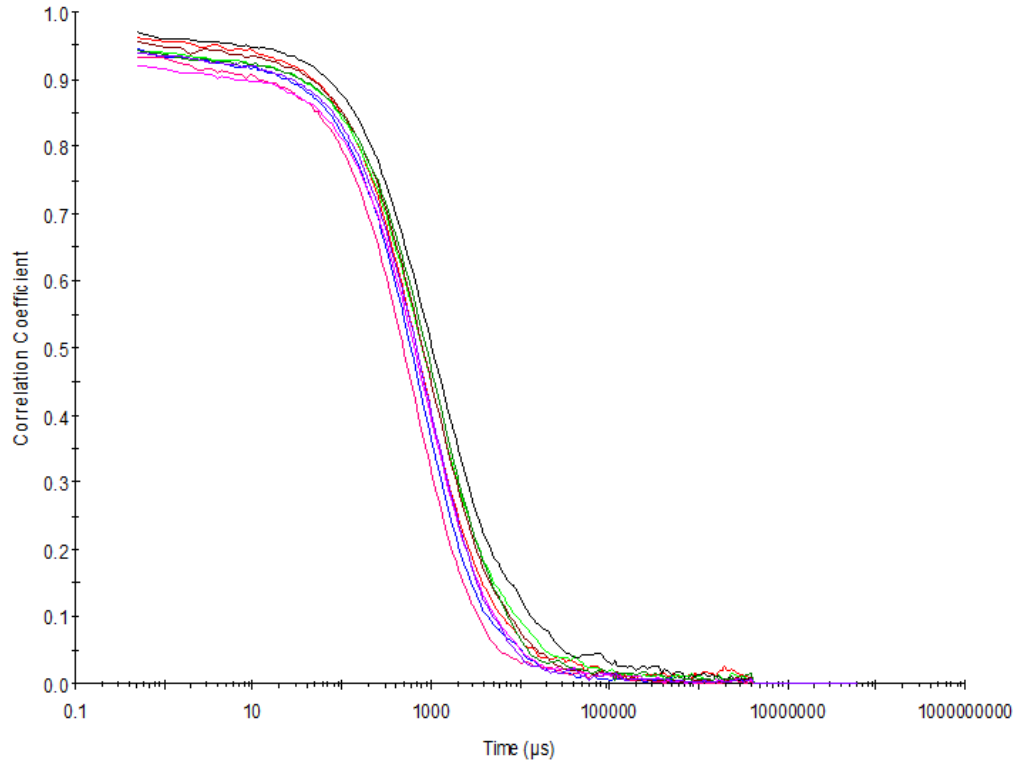

Figure S51 - Raw correlation data for 9 DLS runs at 25 °C after heating to 40 °C with compound **1** at a concentration of 5.56 mM in DMSO: H_2O 3: 7.

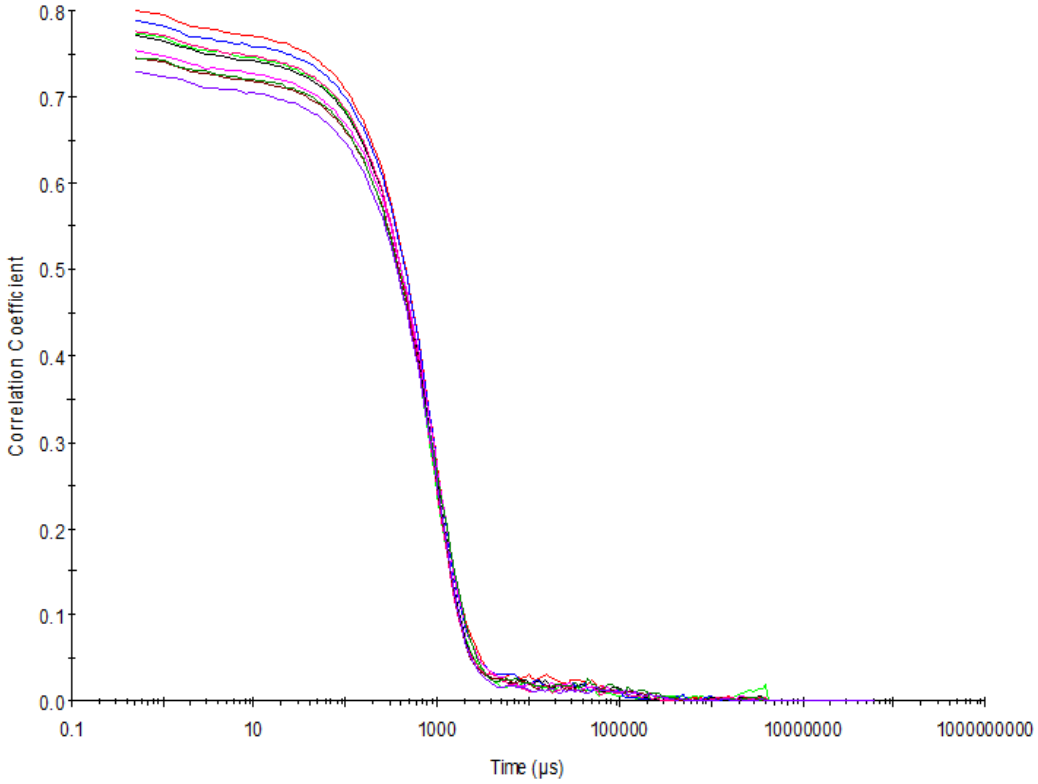

Figure S52 - Raw correlation data for 9 DLS runs at 25 °C after heating to 40 °C with compound **1** at a concentration of 0.56 mM in DMSO: H_2O 3: 7.

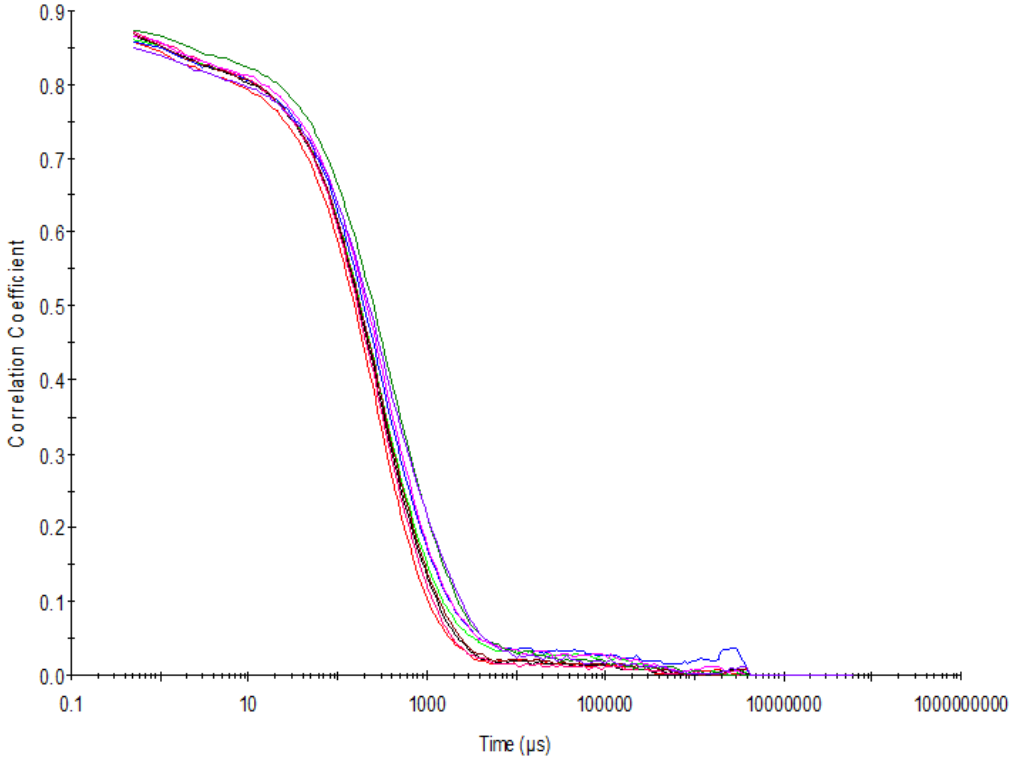

Figure S53 - Raw correlation data for 9 DLS runs at 25 °C after heating to 40 °C with compound **1** at a concentration of 0.56 mM in DMSO: H_2O 1: 4.

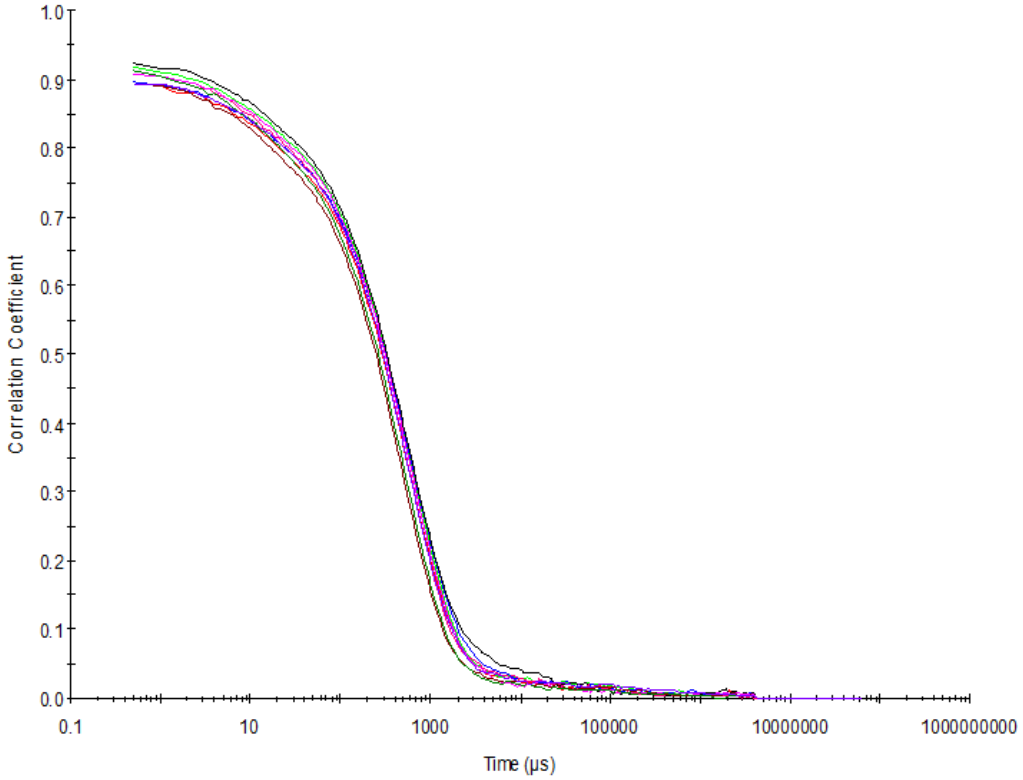

Figure S54 - Raw correlation data for 9 DLS runs at 25 °C after heating to 40 °C with compound **1** at a concentration of 5.56 mM in EtOH: H_2O 1: 19.

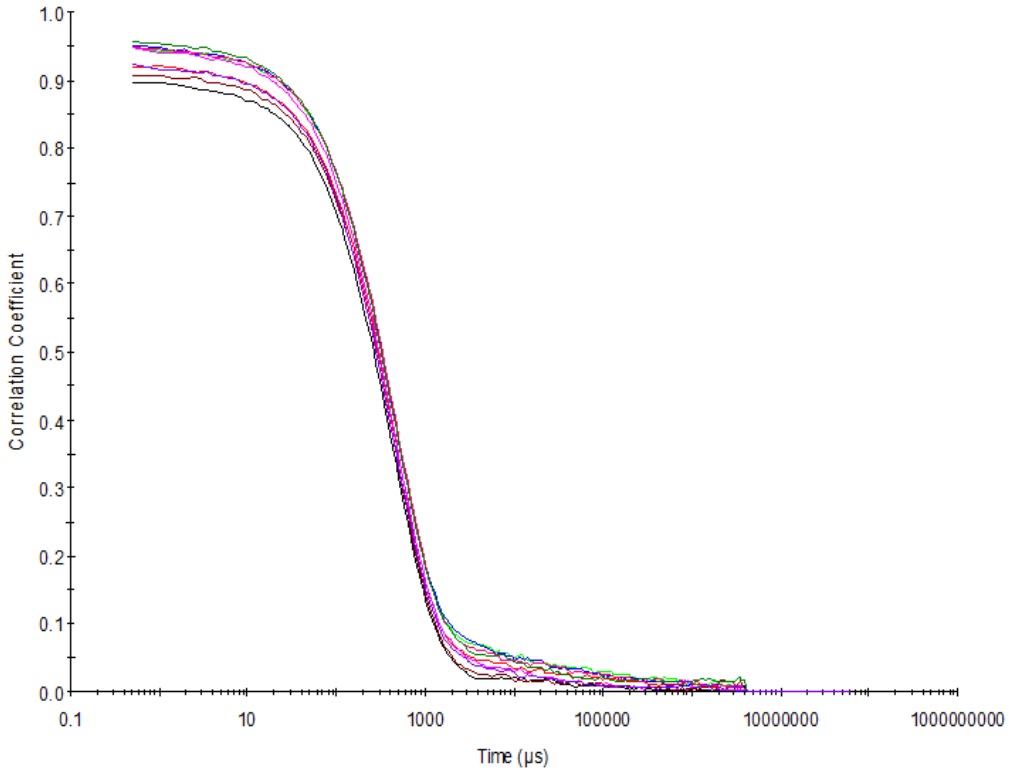

Figure S55 - Raw correlation data for 9 DLS runs at 25 °C after heating to 40 °C with compound **1** at a concentration of 0.56 mM in EtOH: H_2O 1: 19.

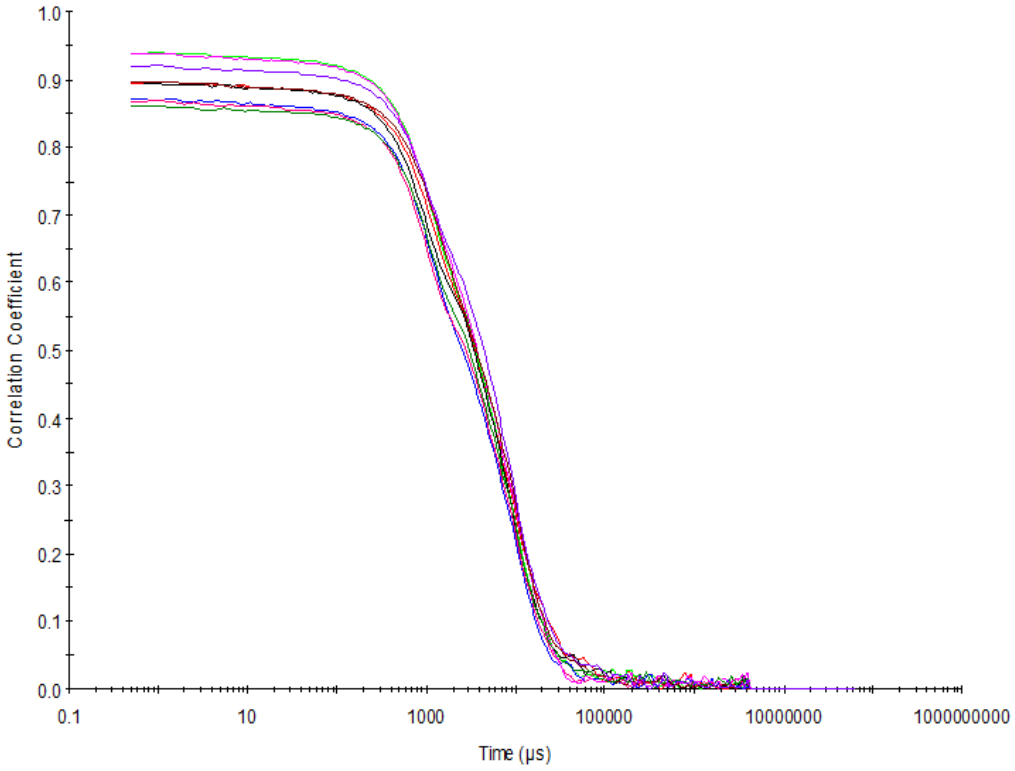

Figure S56 - Raw correlation data for 9 DLS runs at 25 °C after heating to 40 °C with compound **2** at a concentration of 55.56 mM in DMSO: H_2O 1: 1.

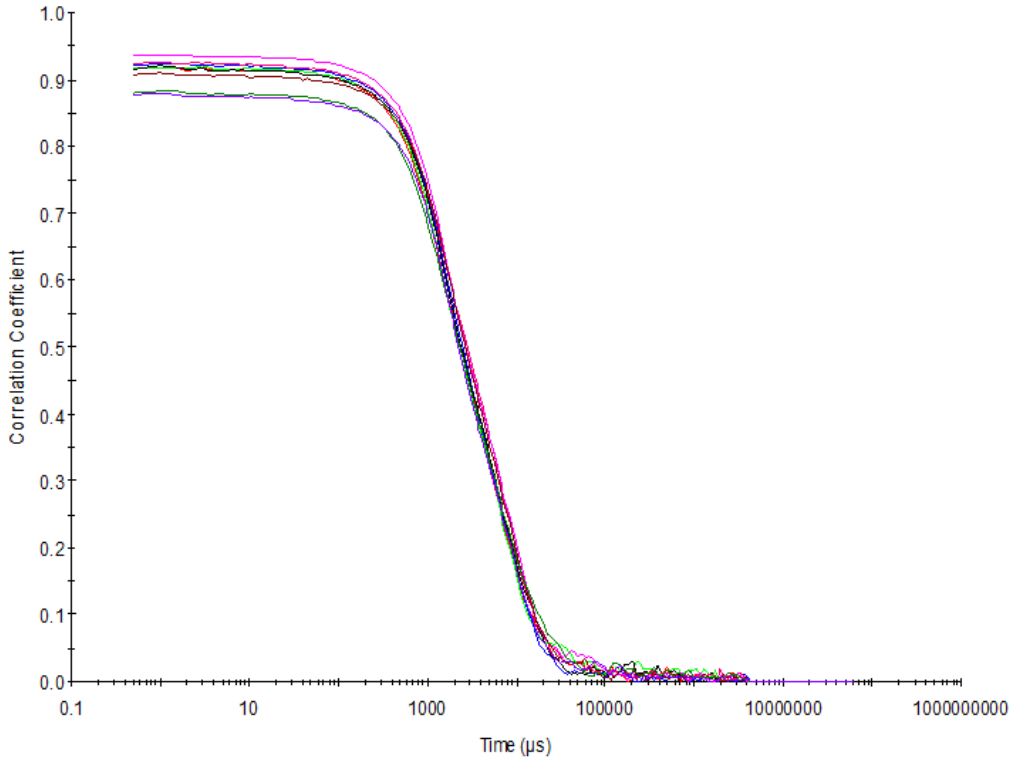

Figure S57 - Raw correlation data for 9 DLS runs at 25 °C after heating to 40 °C with compound **2** at a concentration of 5.56 mM in DMSO: H_2O 1: 1.

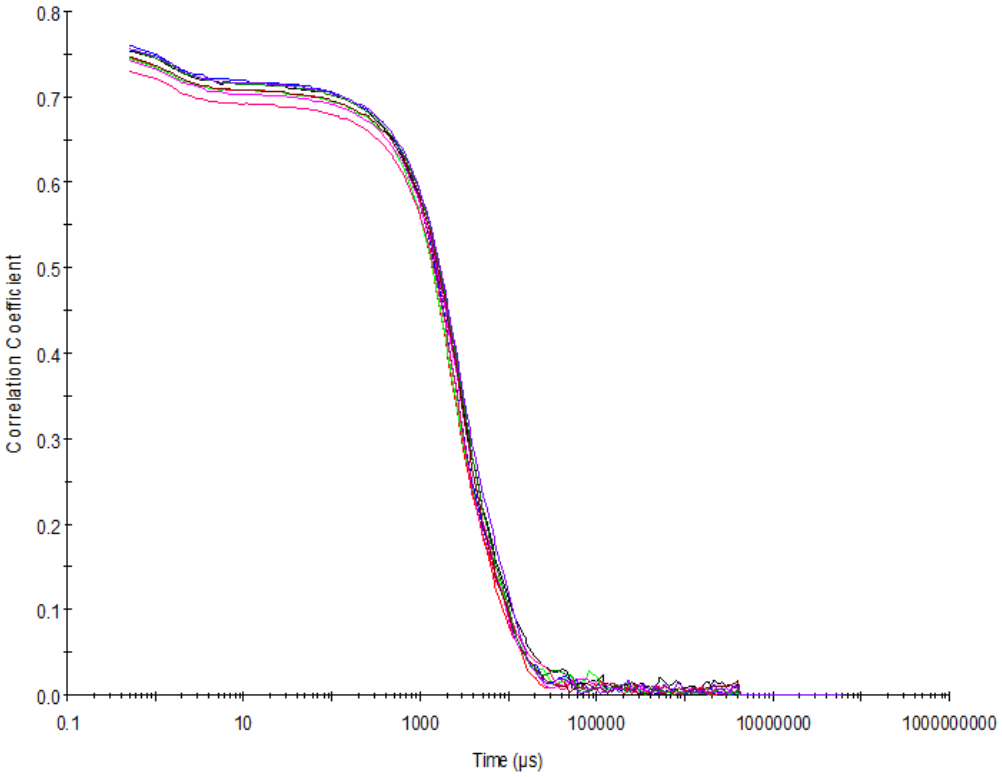

Figure S58 - Raw correlation data for 9 DLS runs at 25 °C after heating to 40 °C with compound **2** at a concentration of 0.56 mM in DMSO: H_2O 1: 1.

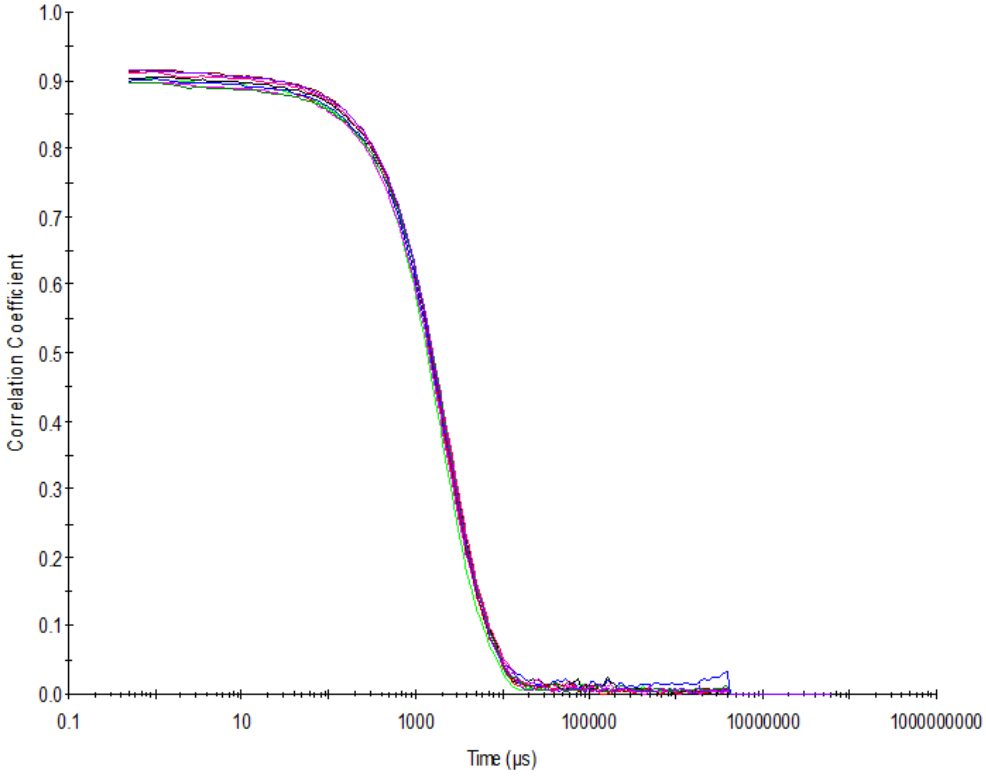

Figure S59 - Raw correlation data for 9 DLS runs at 25 °C after heating to 40 °C with compound **2** at a concentration of 5.56 mM in DMSO: H_2O 3: 7.

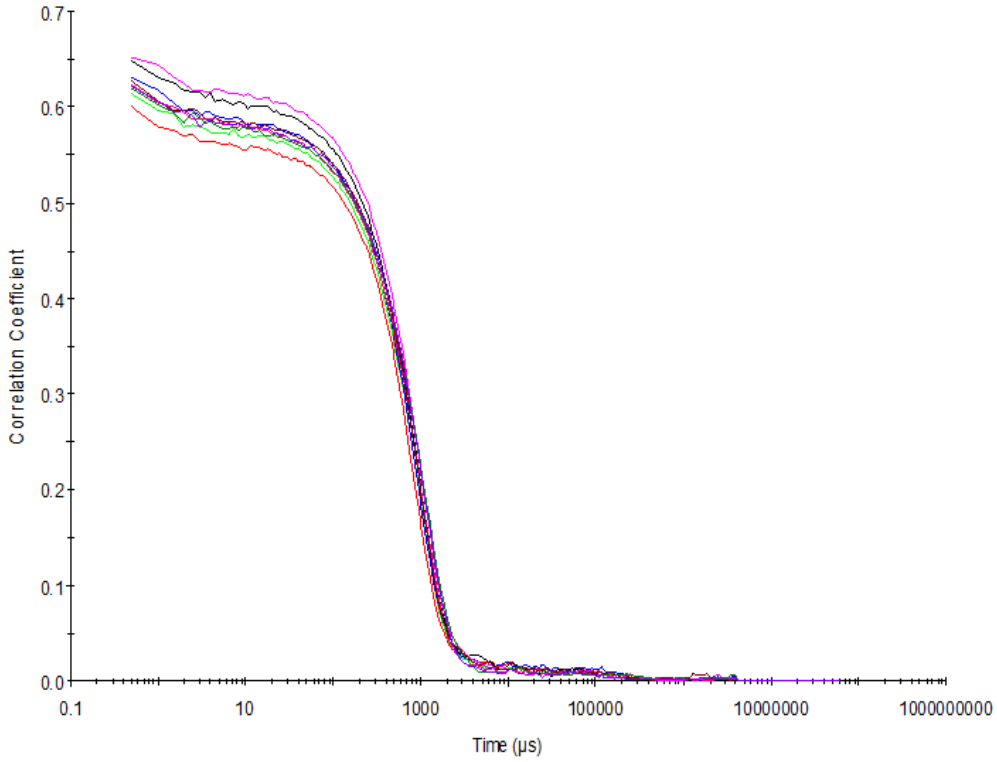

Figure S60- Raw correlation data for 9 DLS runs at 25 °C after heating to 40 °C with compound **2** at a concentration of 0.56 mM in DMSO: H_2O 3: 7.

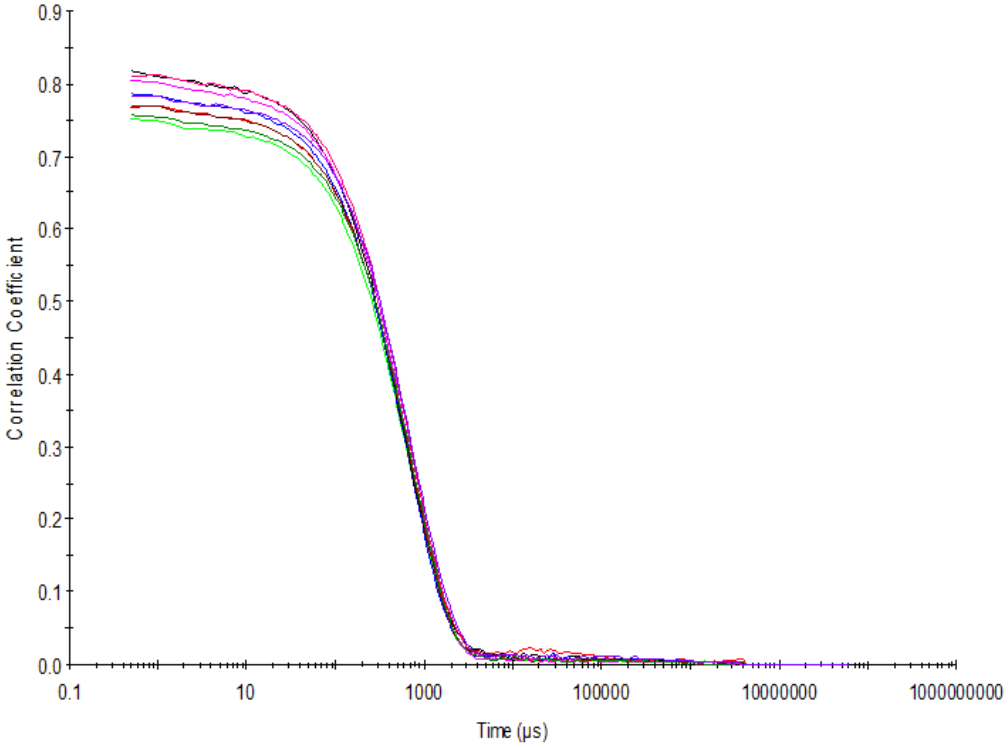

Figure S61 - Raw correlation data for 9 DLS runs at 25 °C after heating to 40 °C with compound **2** at a concentration of 0.56 mM in DMSO: H_2O 1: 4.

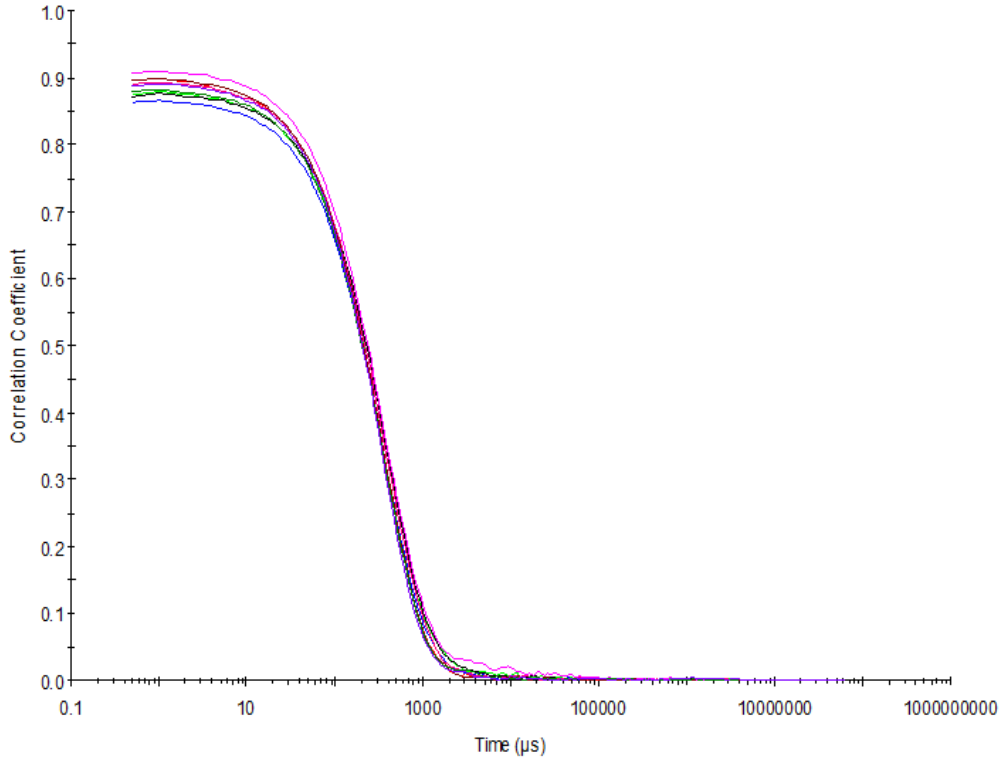

Figure S62 - Raw correlation data for 9 DLS runs at 25 °C after heating to 40 °C with compound **2** at a concentration of 5.56 mM in EtOH: H_2O 1: 19.

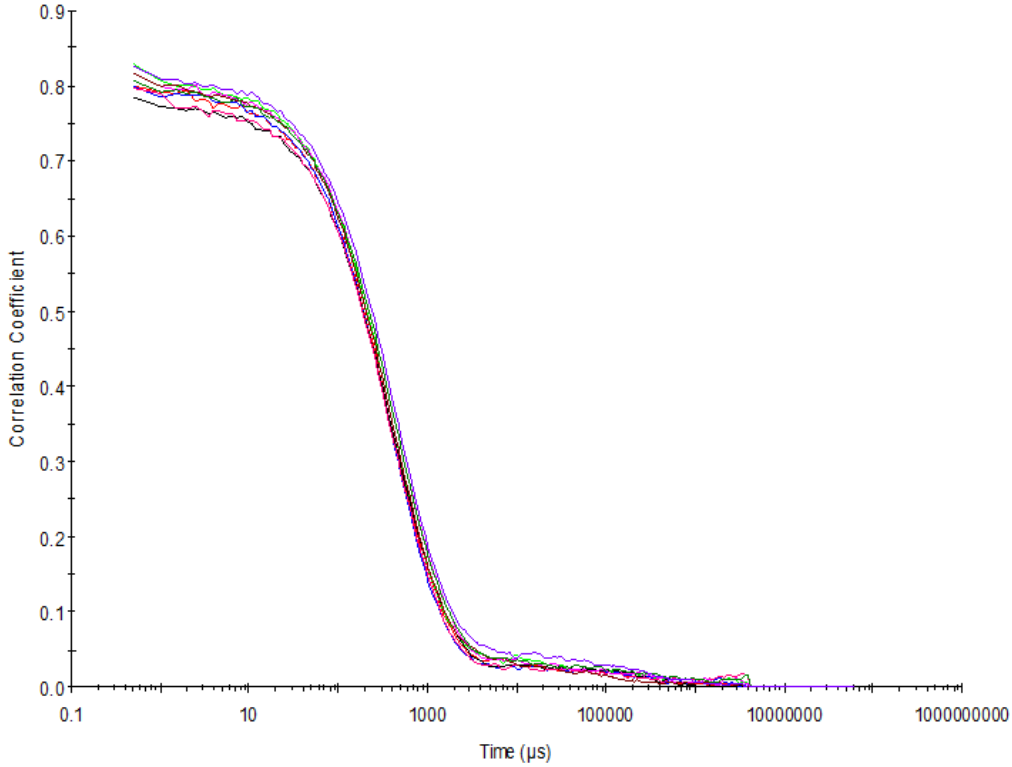

Figure S63 - Raw correlation data for 9 DLS runs at 25 °C after heating to 40 °C with compound **2** at a concentration of 0.56 mM in EtOH: H_2O 1: 19.

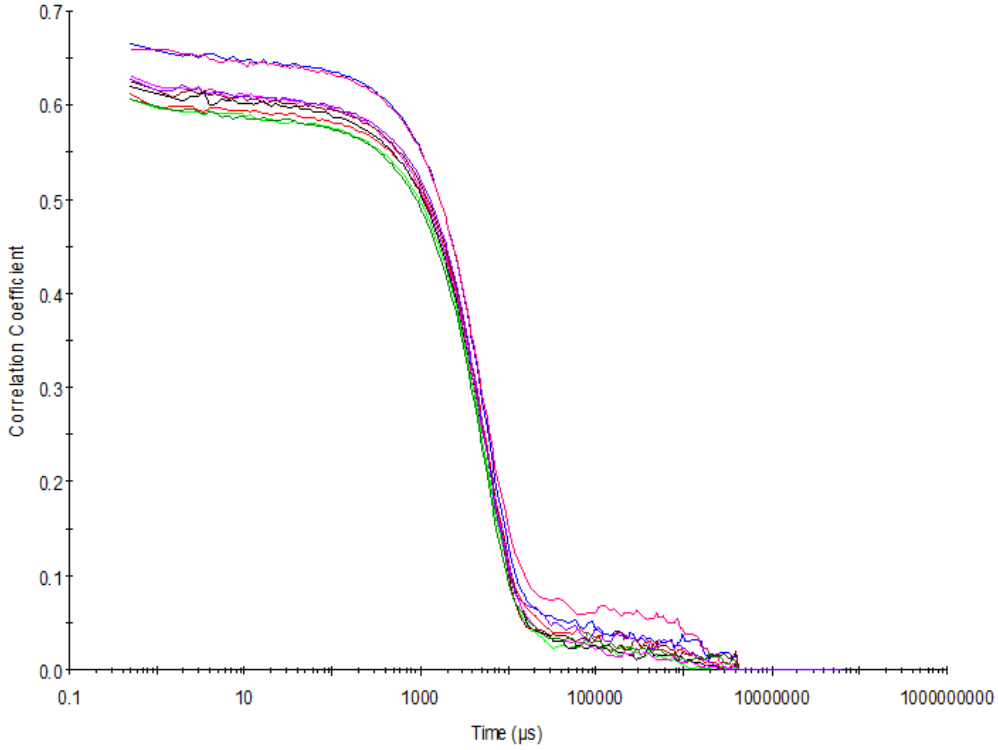

Figure S64 – Raw correlation data for 9 DLS runs at 25 °C before heating to 40 °C with compound **3** at a concentration of 111.12 mM in DMSO.

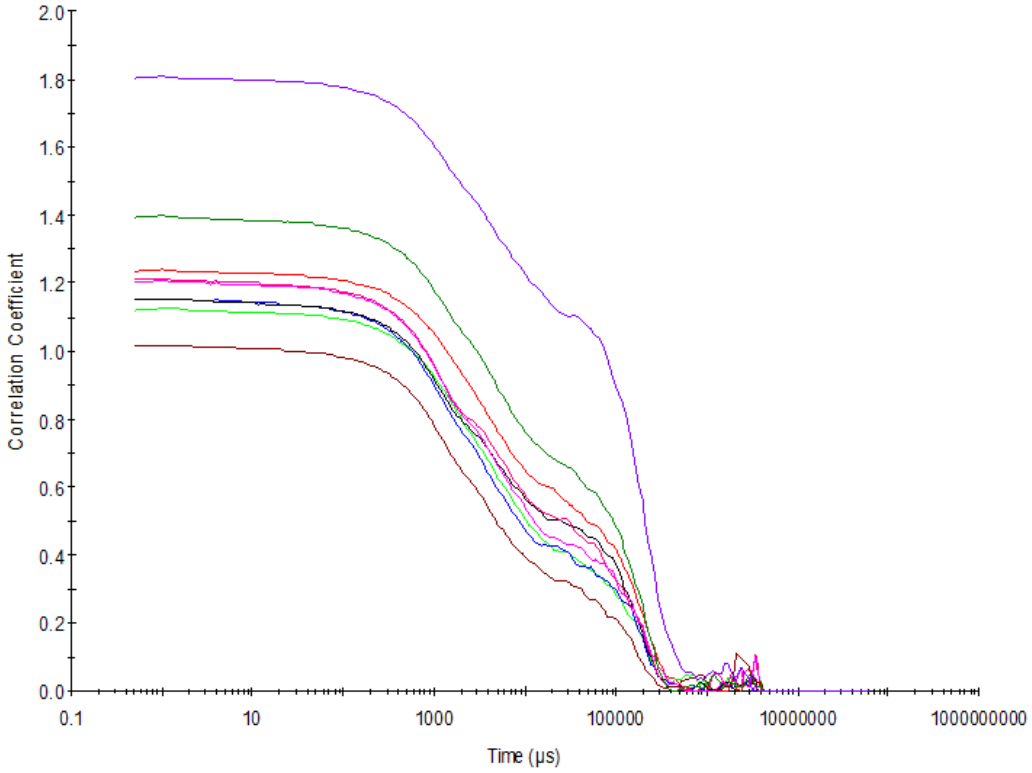

Figure S65– Raw correlation data for 9 DLS runs at 40 °C with compound **3** at a concentration of 111.12 mM in DMSO.

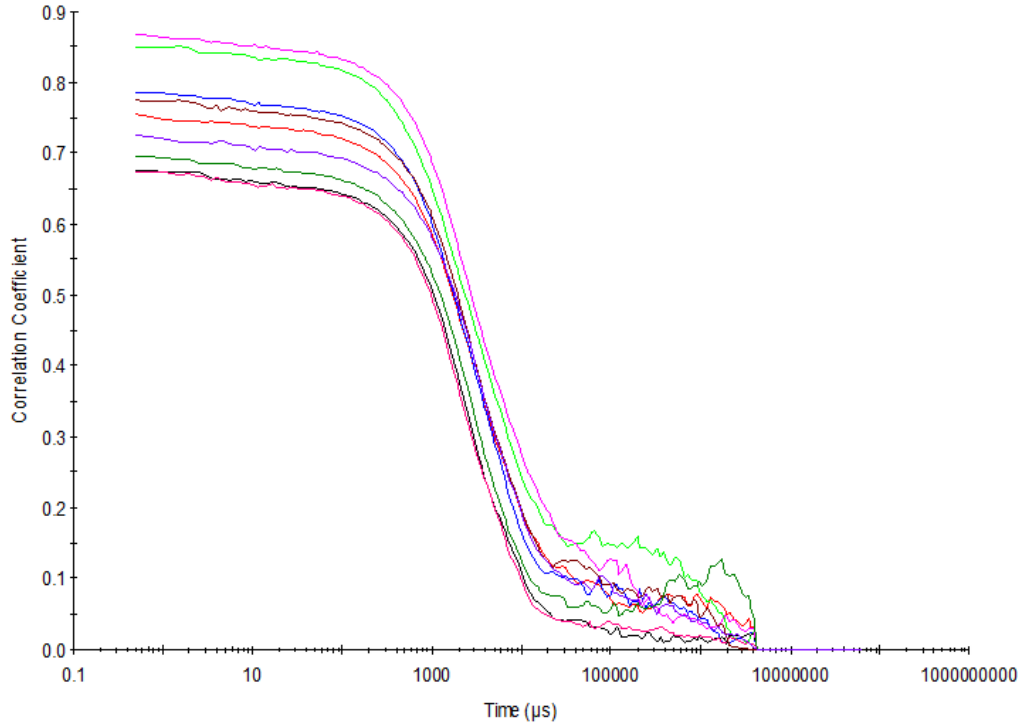

Figure S66 – Raw correlation data for 9 DLS runs at 25 °C after heating to 40 °C with compound **3** at a concentration of 111.12 mM in DMSO.

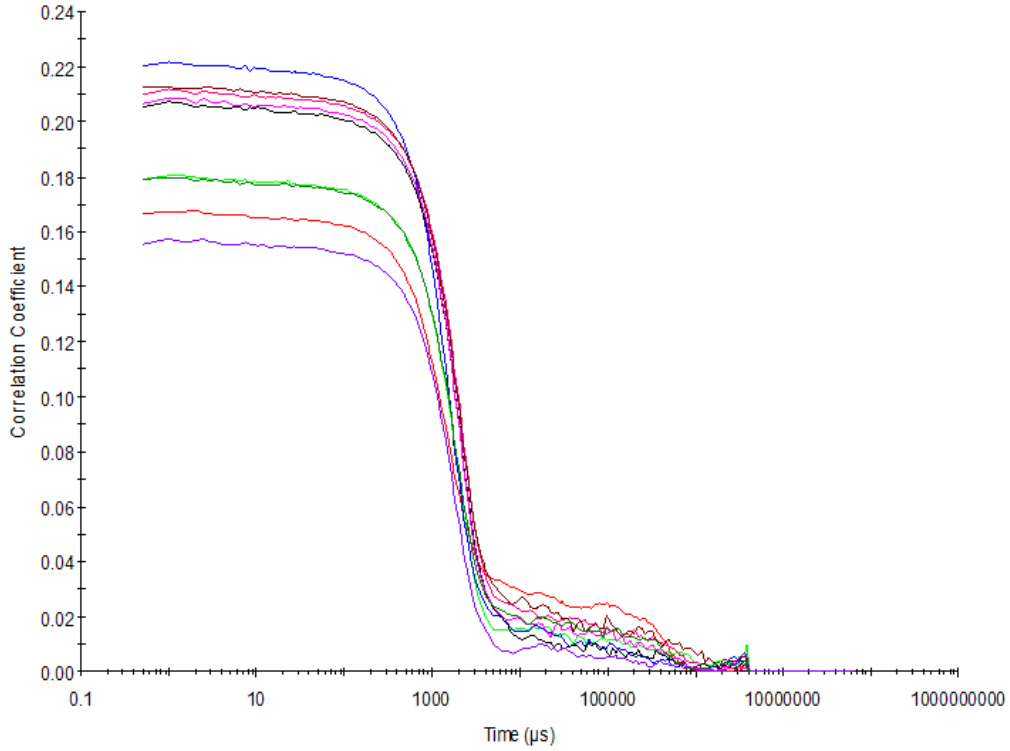

Figure S67– Raw correlation data for 9 DLS runs at 25 °C before heating to 40 °C with compound **3** at a concentration of 55.56 mM in DMSO.

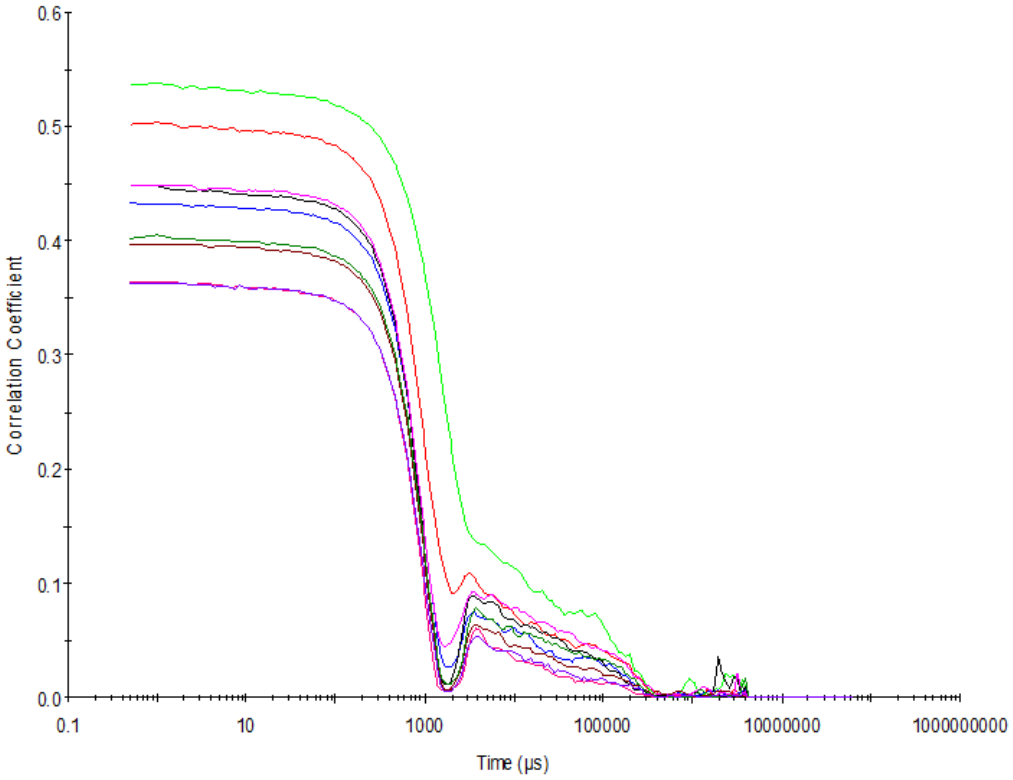

Figure S68 – Raw correlation data for 9 DLS runs at 40 °C with compound **3** at a concentration of 55.56 mM in DMSO.

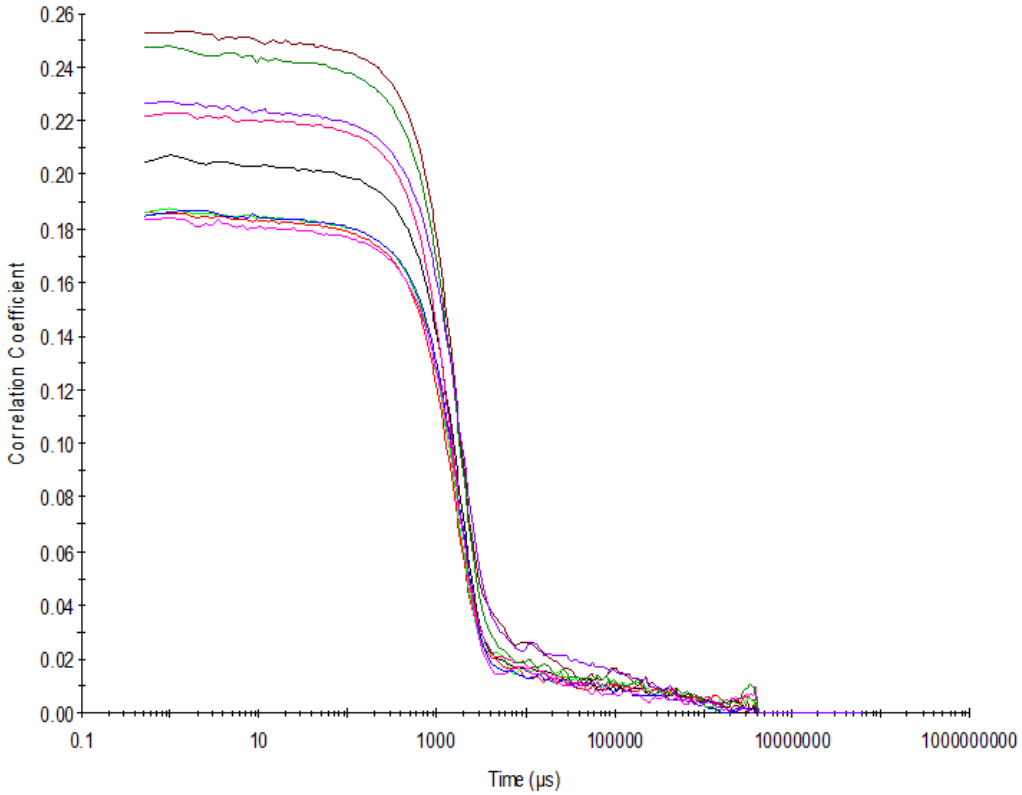

Figure S69 – Raw correlation data for 9 DLS runs at 25 °C after heating to 40 °C with compound **3** at a concentration of 55.56 mM in DMSO.

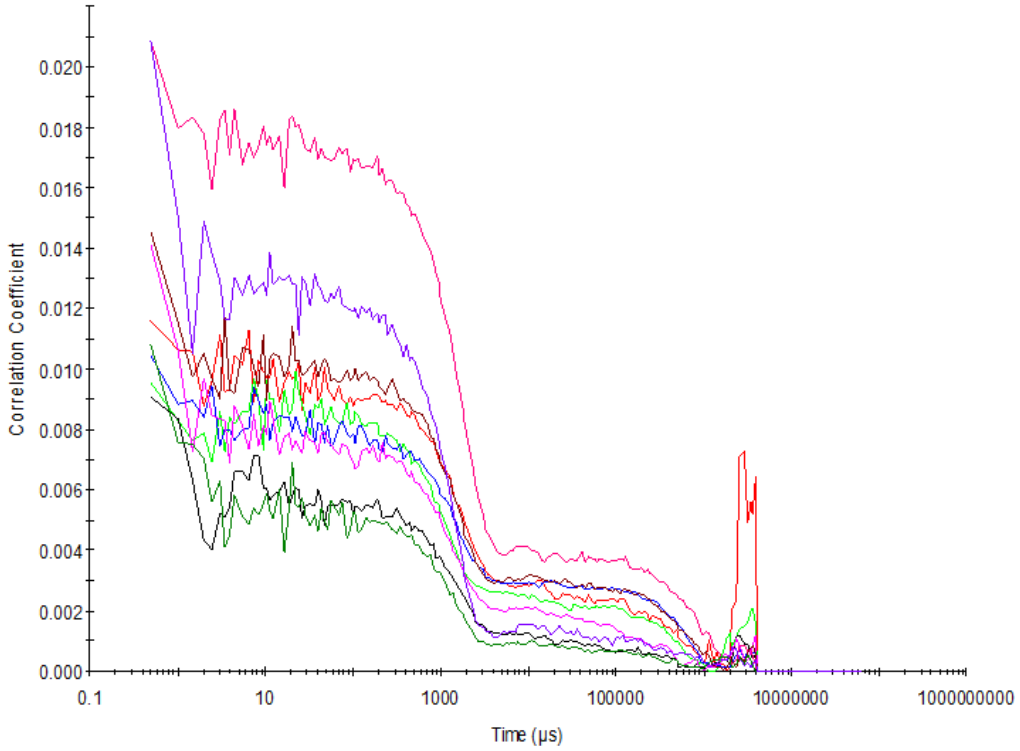

Figure S70 – Raw correlation data for 9 DLS runs at 25 °C before heating to 40 °C with compound **3** at a concentration of 5.56 mM in DMSO.

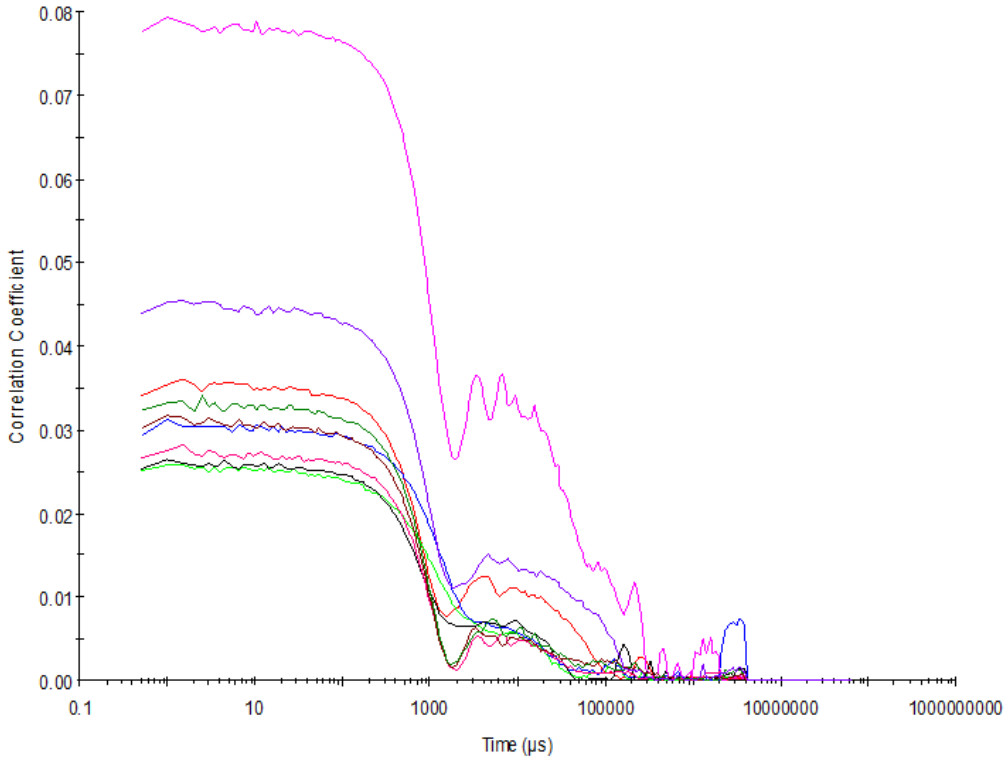

Figure S71 – Raw correlation data for 9 DLS runs at 40 °C with compound **3** at a concentration of 5.56 mM in DMSO.

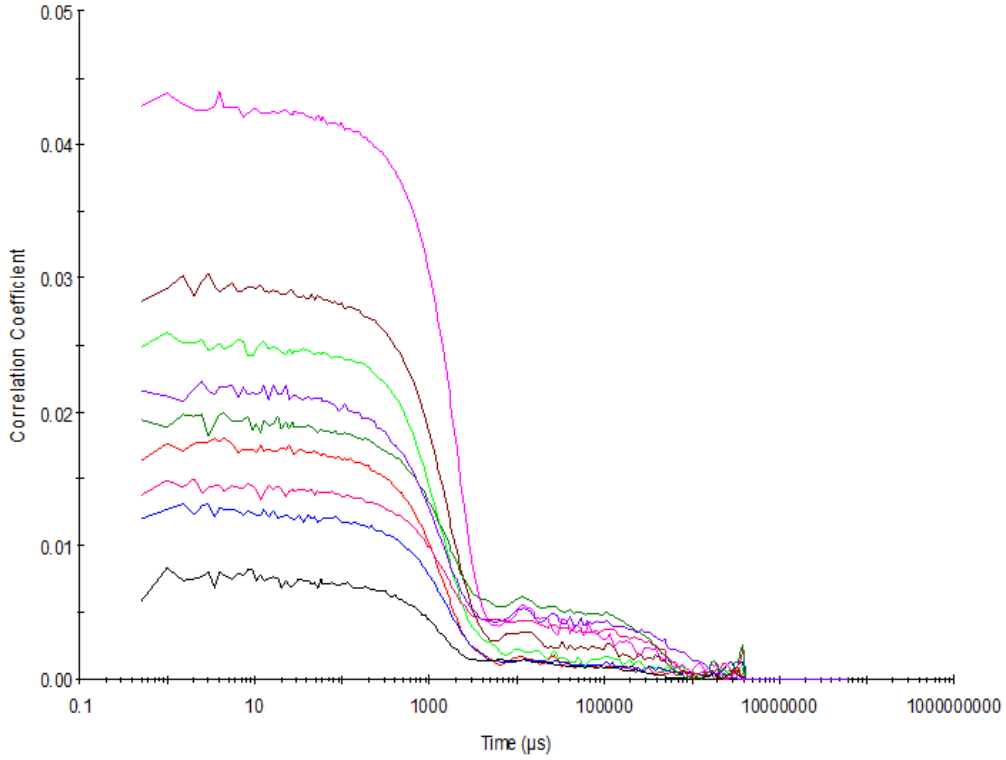

Figure S72 – Raw correlation data for 9 DLS runs at 25 °C after heating to 40 °C with compound **3** at a concentration of 5.56 mM in DMSO.

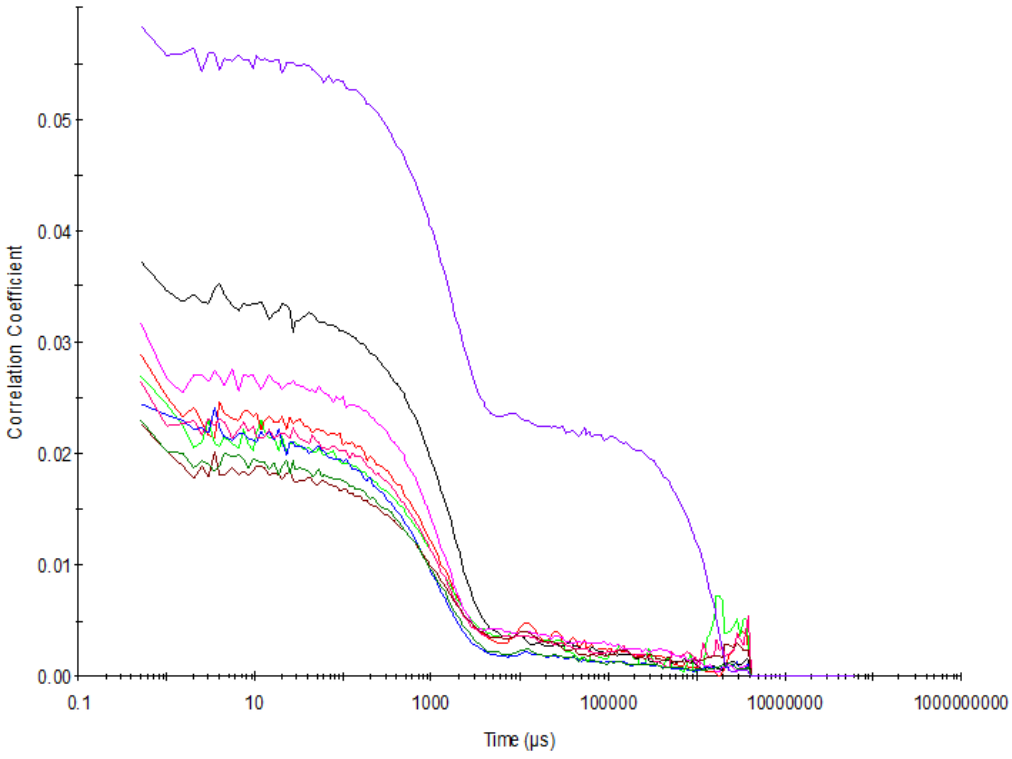

Figure S73 – Raw correlation data for 9 DLS runs at 25 °C before heating to 40 °C with compound **3** at a concentration of 0.56 mM in DMSO.

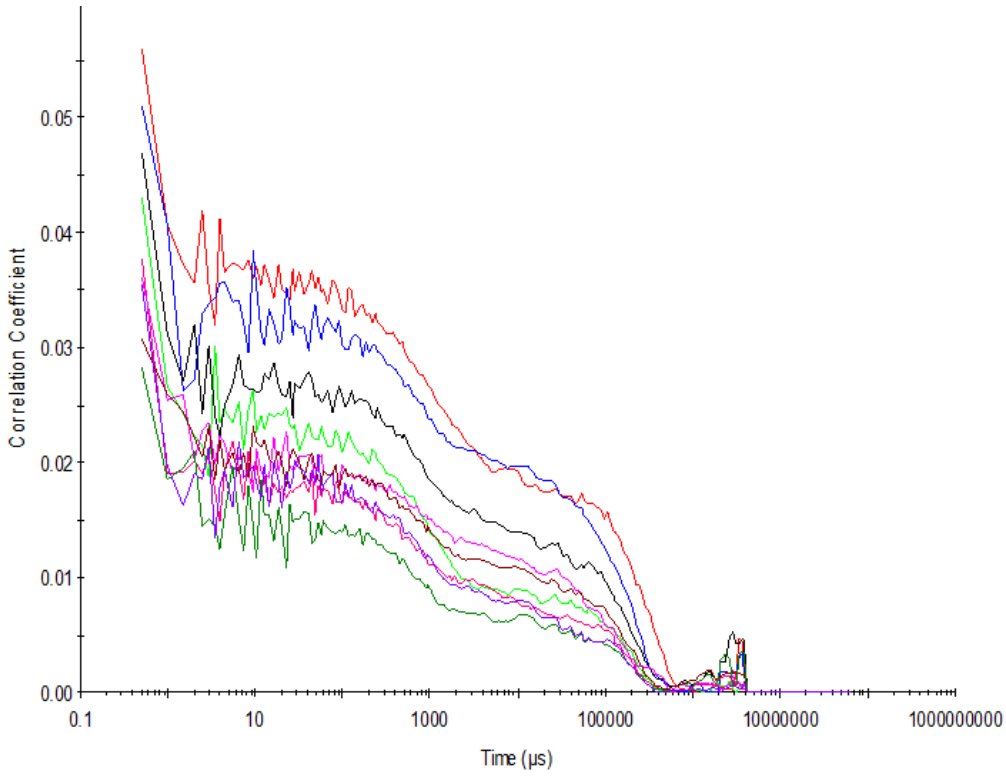

Figure S74 – Raw correlation data for 9 DLS runs at 40 °C with compound **3** at a concentration of 0.56 mM in DMSO.

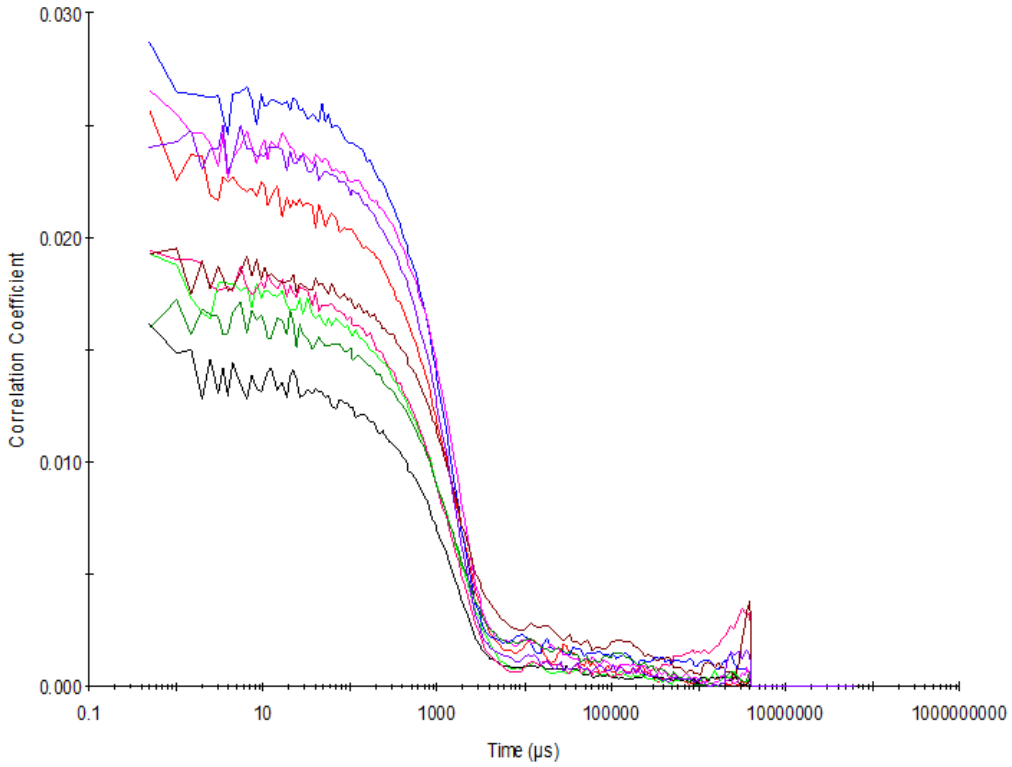

Figure S75 – Raw correlation data for 9 DLS runs at 25 °C after heating to 40 °C with compound **3** at a concentration of 0.56 mM in DMSO.

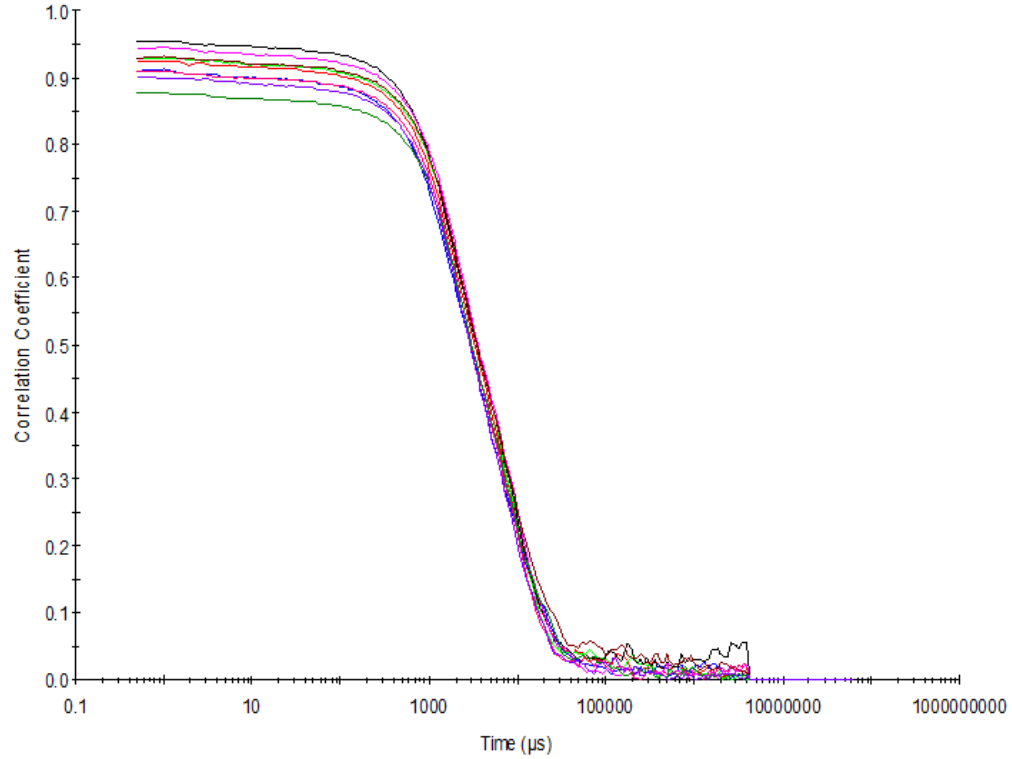

Figure S76 - Raw correlation data for 9 DLS runs at 25 °C after heating to 40 °C with compound **3** at a concentration of 55.56 mM in DMSO: H_2O 1: 1.

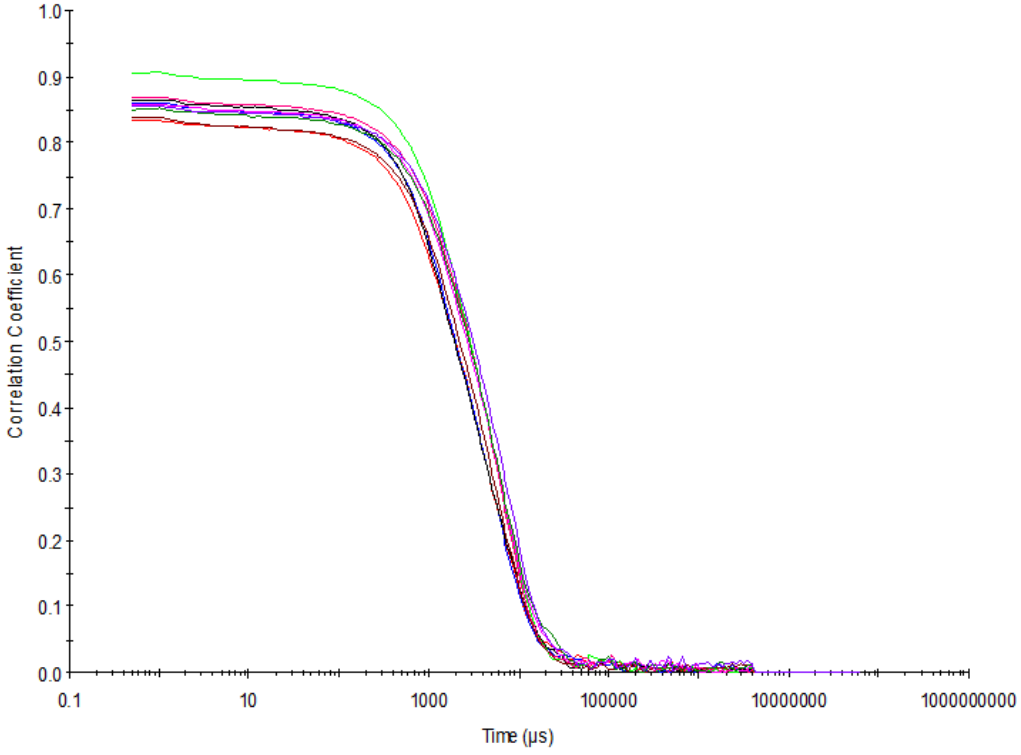

Figure S77 - Raw correlation data for 9 DLS runs at 25 °C after heating to 40 °C with compound **3** at a concentration of 5.56 mM in DMSO: H_2O 1: 1.

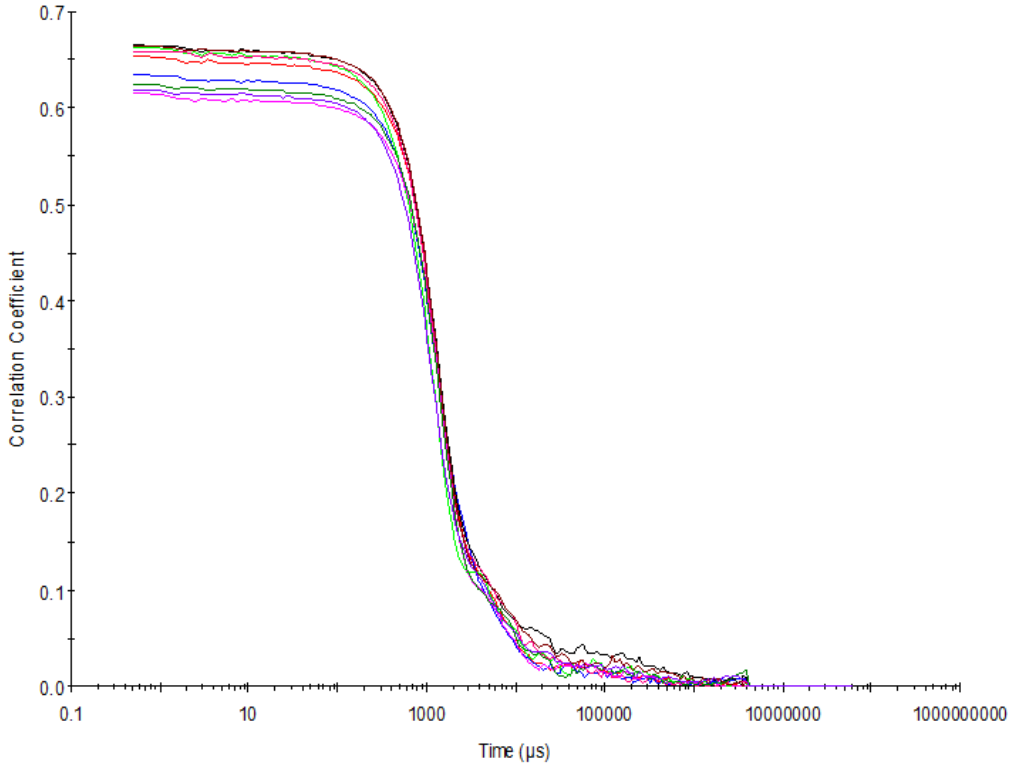

Figure S78 - Raw correlation data for 9 DLS runs at 25 °C after heating to 40 °C with compound **3** at a concentration of 0.56 mM in DMSO: H_2O 1: 1.

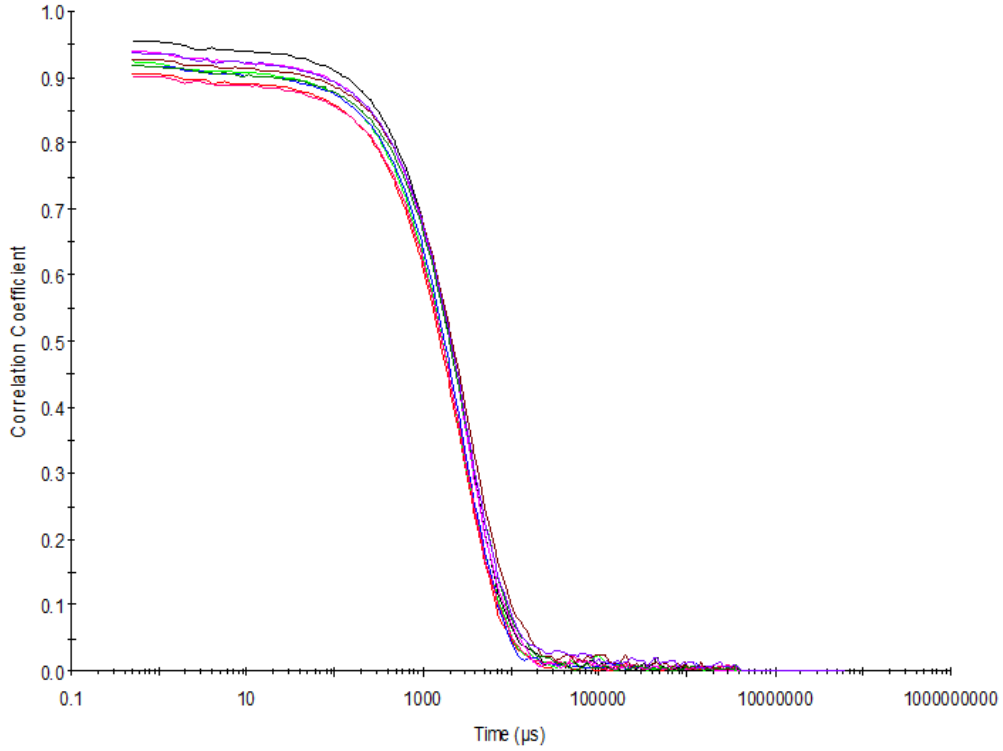

Figure S79 - Raw correlation data for 9 DLS runs at 25 °C after heating to 40 °C with compound **3** at a concentration of 5.56 mM in DMSO: H_2O 3: 7.

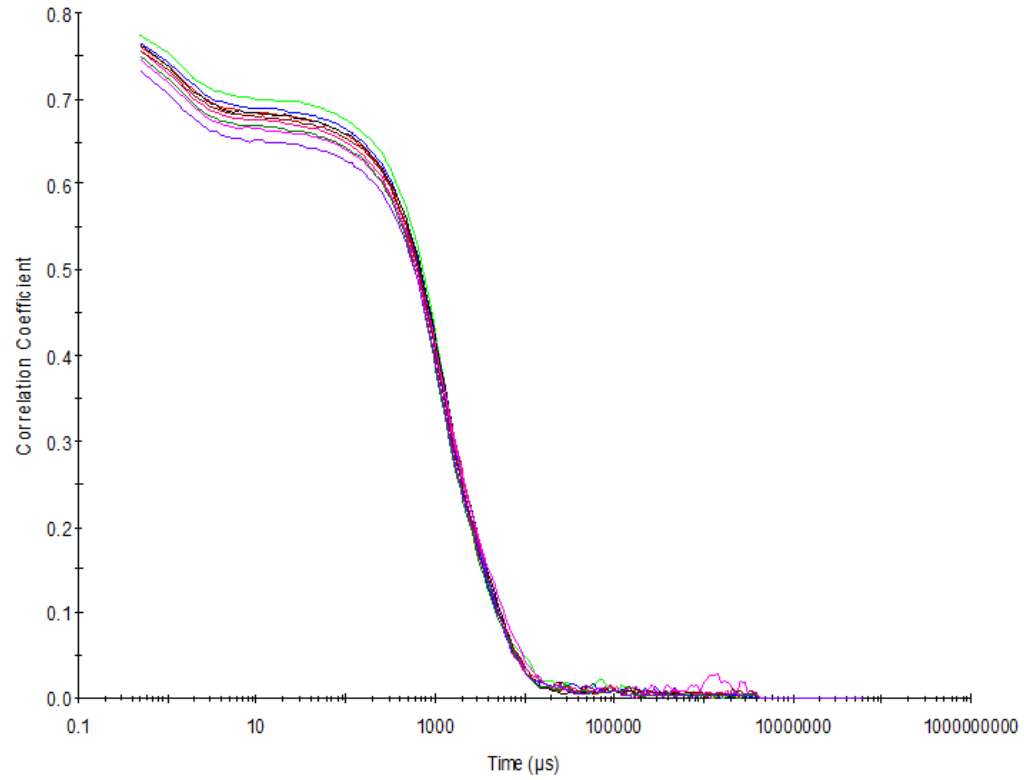

Figure S80 - Raw correlation data for 9 DLS runs at 25 °C after heating to 40 °C with compound **3** at a concentration of 0.56 mM in DMSO: H_2O 3: 7.

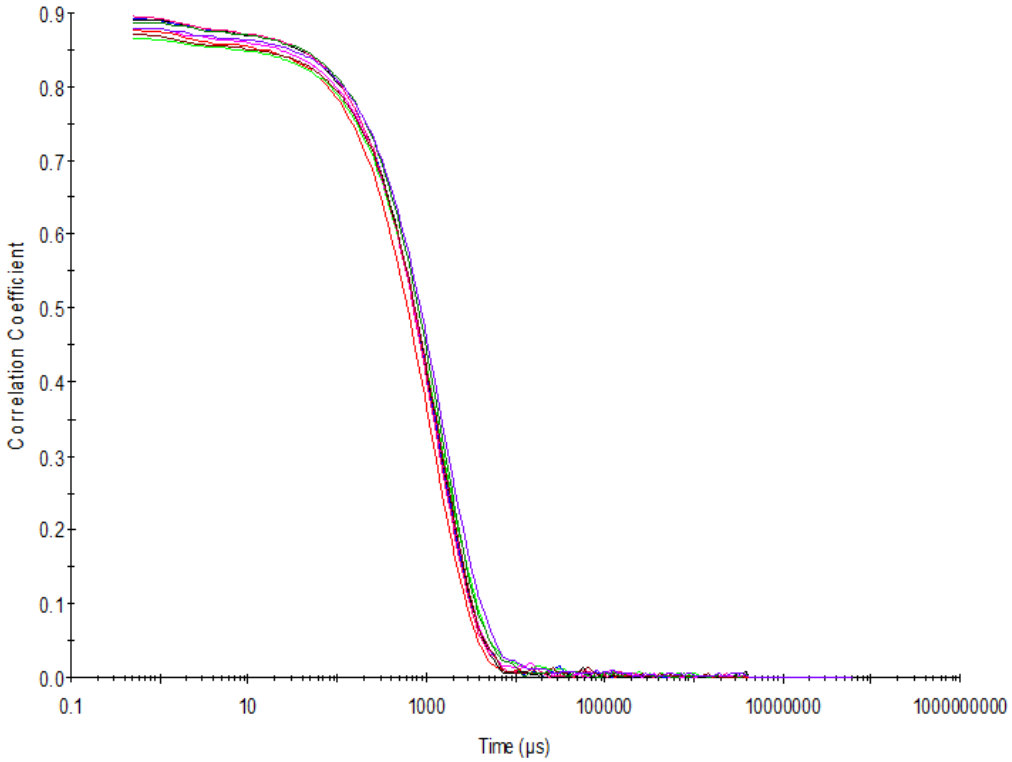

Figure S81 - Raw correlation data for 9 DLS runs at 25 °C after heating to 40 °C with compound **3** at a concentration of 0.56 mM in DMSO: H_2O 1: 4.

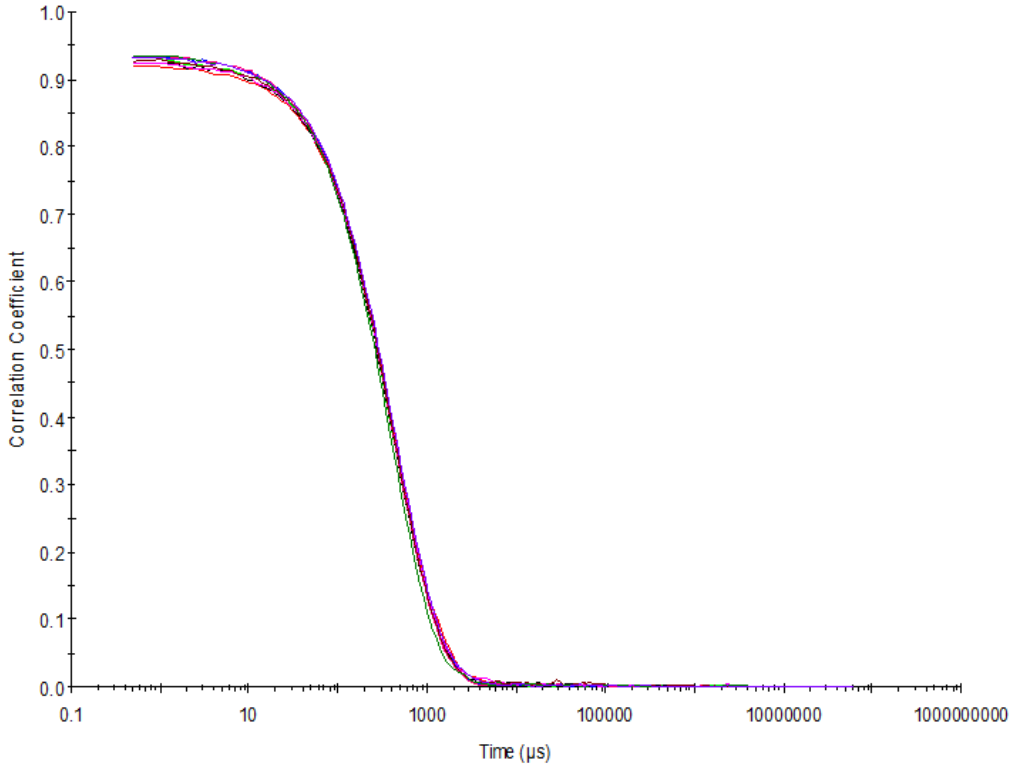

Figure S82 - Raw correlation data for 9 DLS runs at 25 °C after heating to 40 °C with compound 2 at a concentration of 5.56 mM in EtOH: H_2O 1: 19.

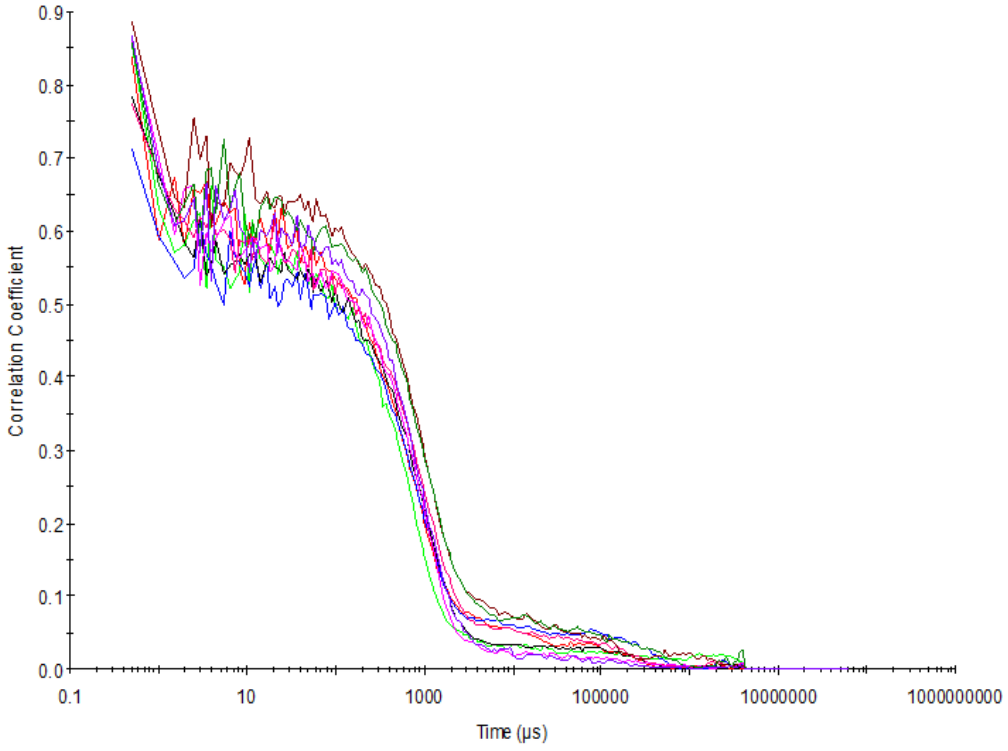

Figure S83 - Raw correlation data for 9 DLS runs at 25 °C after heating to 40 °C with compound **3** at a concentration of 0.56 mM in EtOH: H_2O 1: 19.

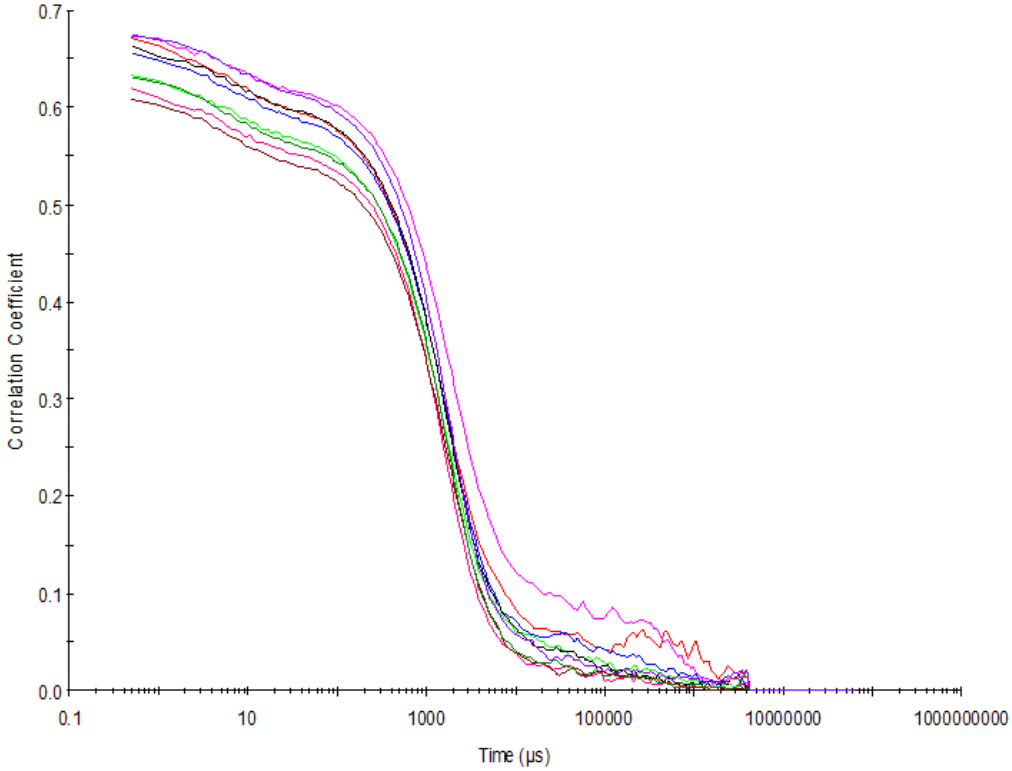

Figure S84 – Raw correlation data for 9 DLS runs at 25 °C before heating to 40 °C with compound **4** at a concentration of 111.12 mM in DMSO.

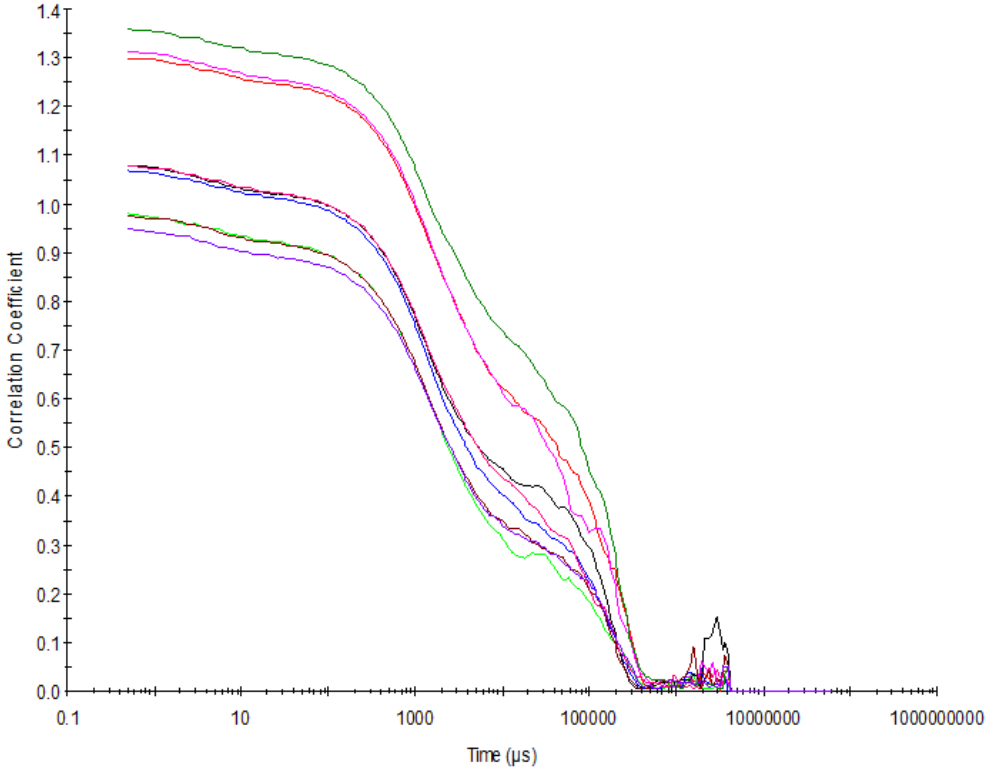

Figure S85 – Raw correlation data for 9 DLS runs at 40 °C with compound **4** at a concentration of 111.12 mM in DMSO.

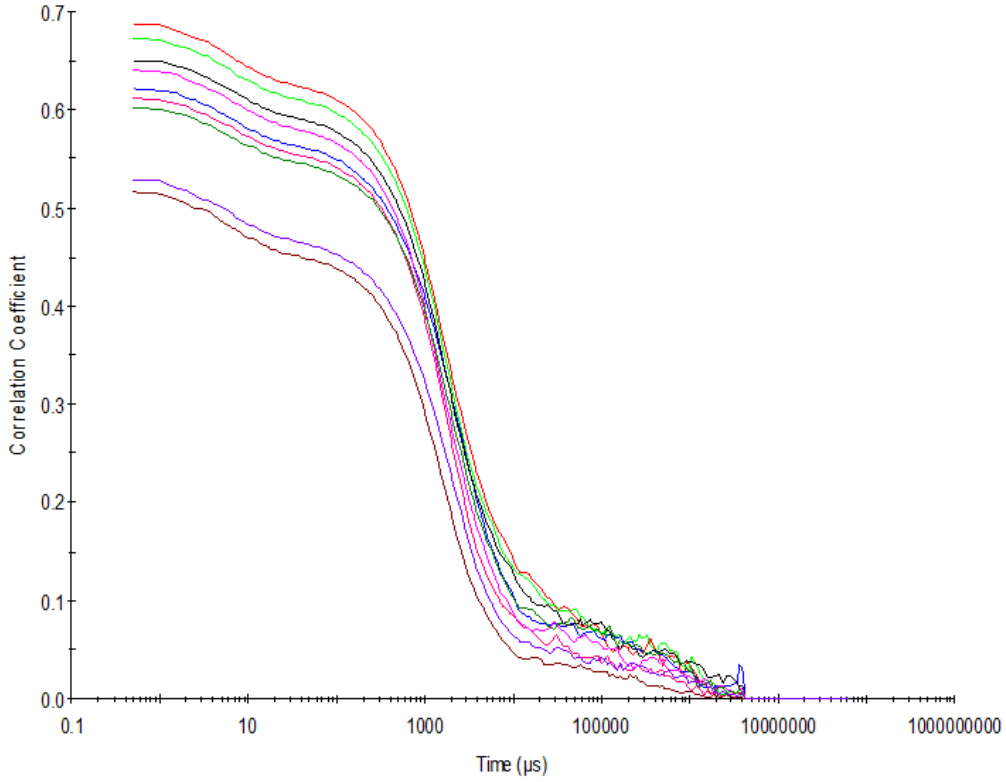

Figure S86 – Raw correlation data for 9 DLS runs at 25 °C after heating to 40 °C with compound **4** at a concentration of 111.12 mM in DMSO.

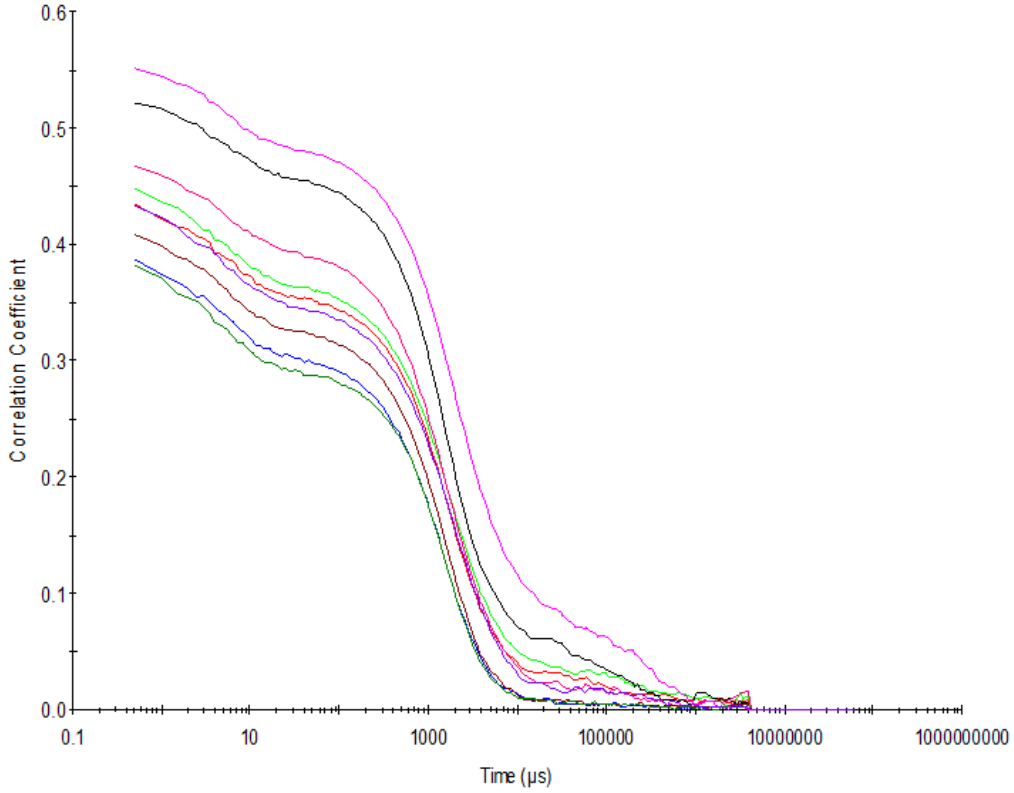

Figure S87 – Raw correlation data for 9 DLS runs at 25 °C before heating to 40 °C with compound **4** at a concentration of 55.56 mM in DMSO.

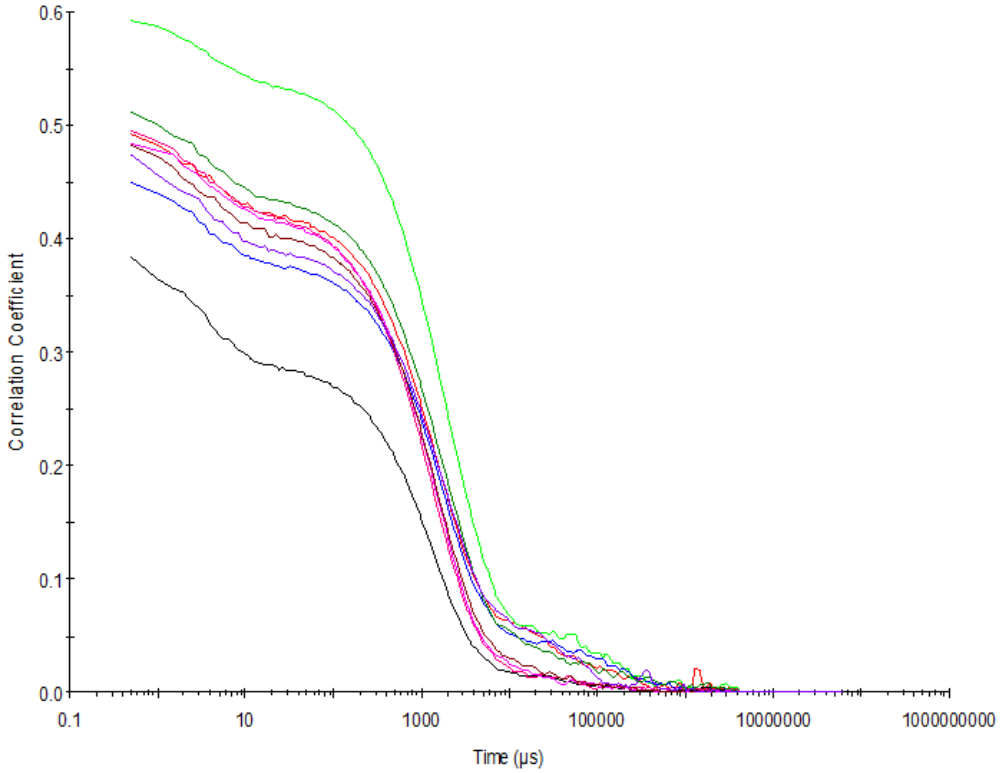

Figure S88– Raw correlation data for 9 DLS runs at 40 °C with compound **4** at a concentration of 55.56 mM in DMSO.

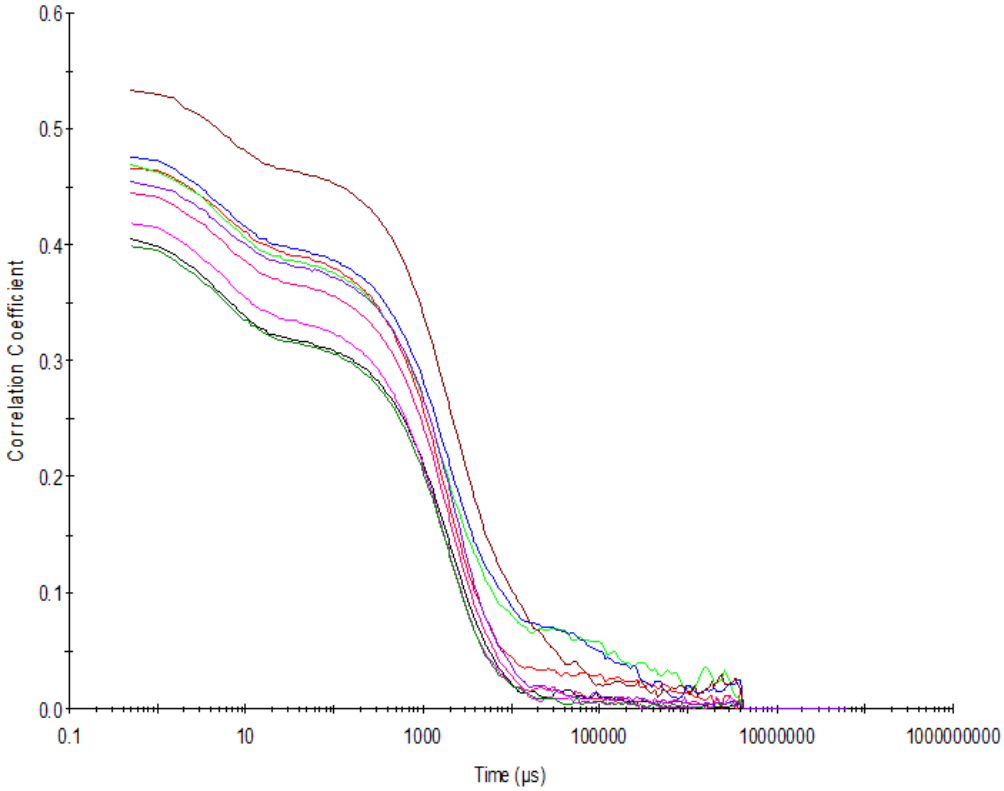

Figure S89 – Raw correlation data for 9 DLS runs at 25 °C after heating to 40 °C with compound **4** at a concentration of 55.56 mM in DMSO.

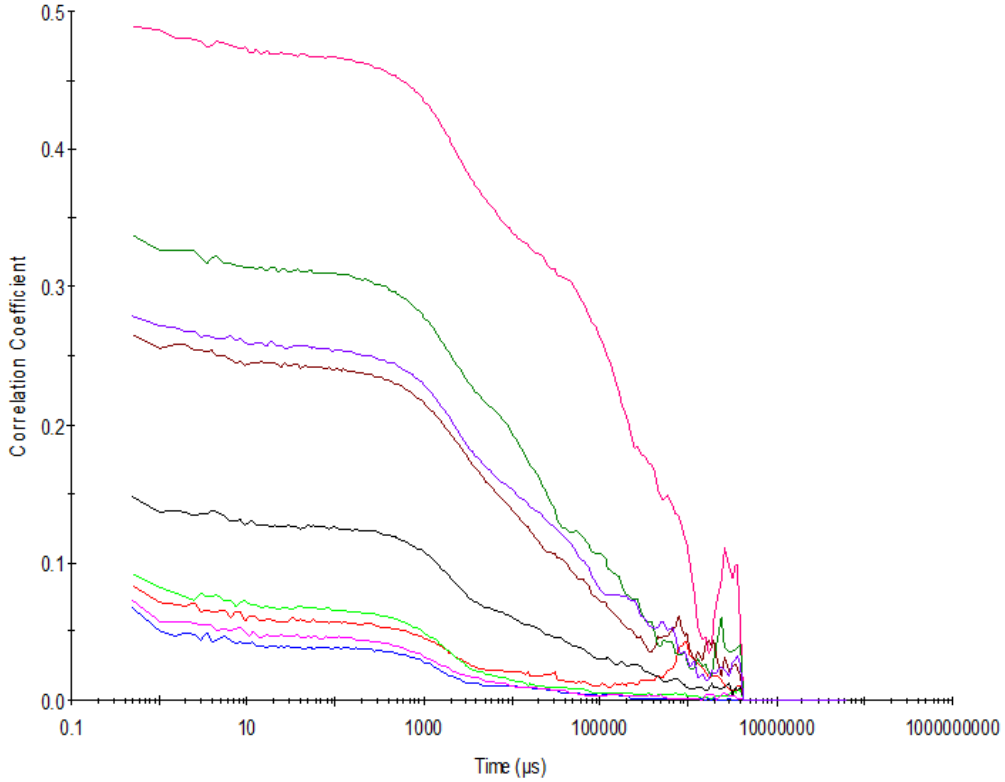

Figure S90 – Raw correlation data for 9 DLS runs at 25 °C before heating to 40 °C with compound **4** at a concentration of 5.56 mM in DMSO.

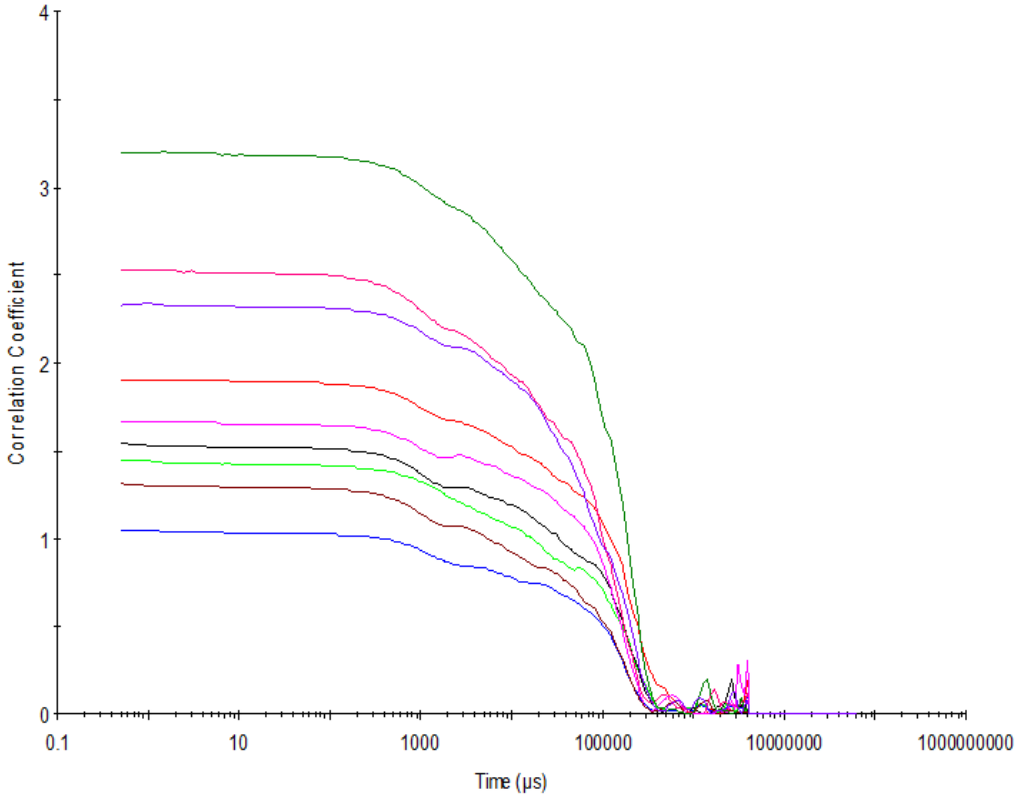

Figure S91 – Raw correlation data for 9 DLS runs at 40 °C with compound **4** at a concentration of 5.56 mM in DMSO.

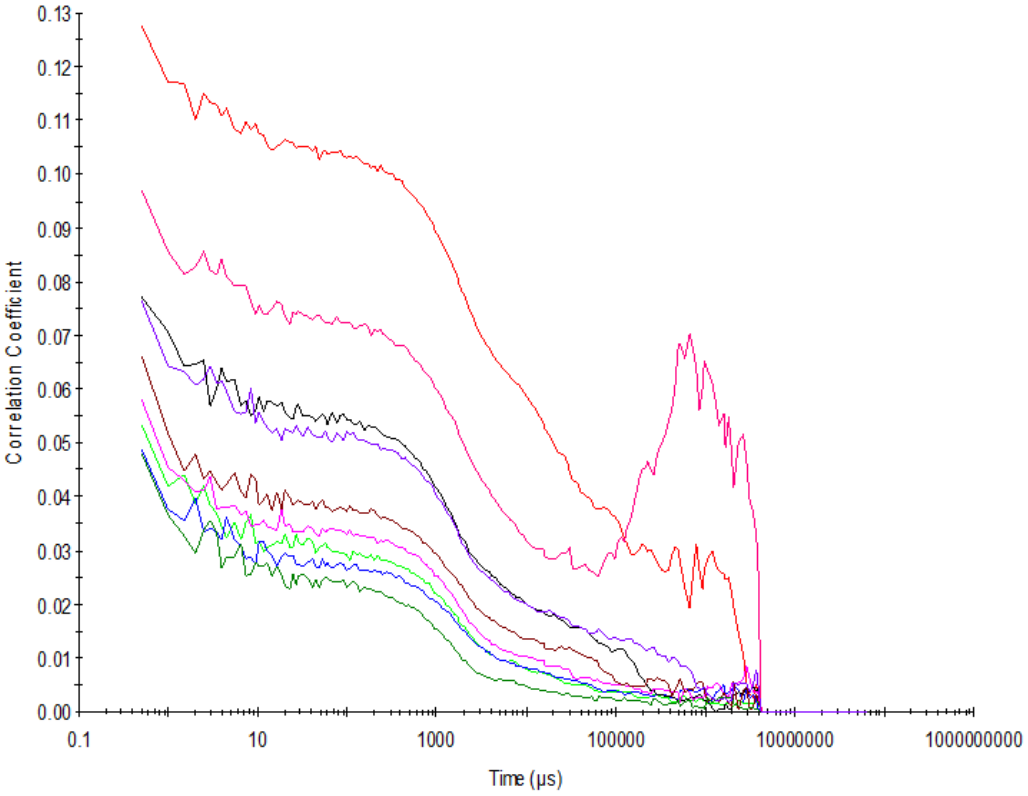

Figure S92 – Raw correlation data for 9 DLS runs at 25 °C after heating to 40 °C with compound **4** at a concentration of 5.56 mM in DMSO.

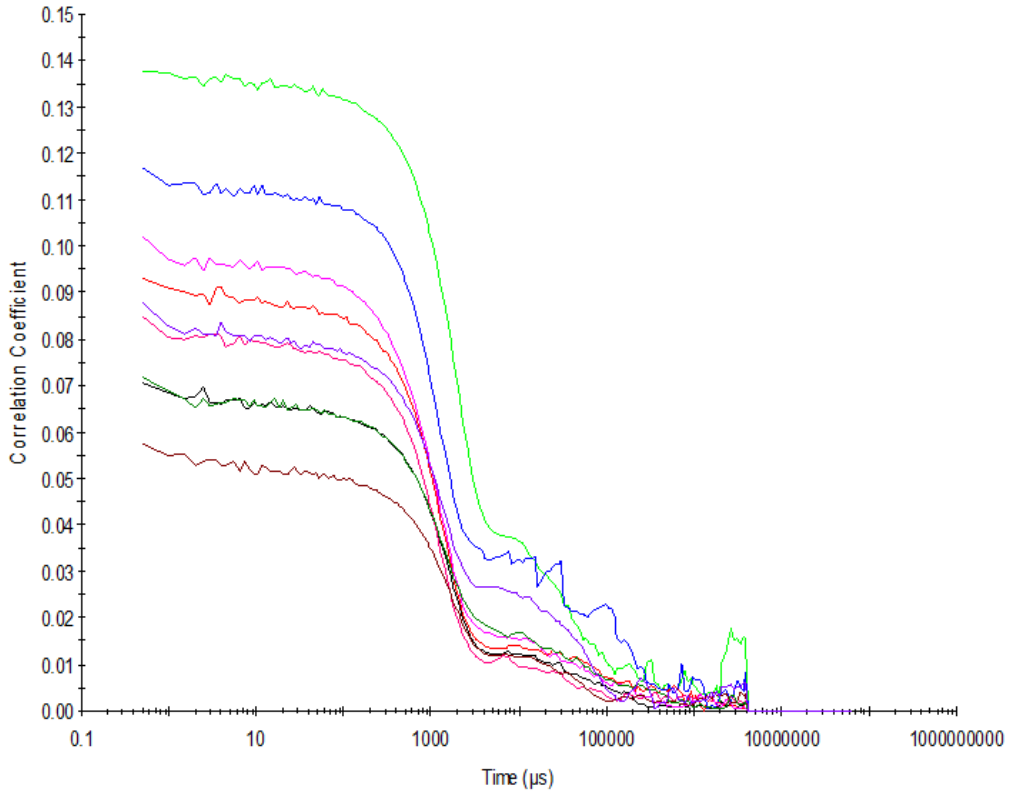

Figure S93 – Raw correlation data for 9 DLS runs at 25 °C before heating to 40 °C with compound **4** at a concentration of 0.56 mM in DMSO.

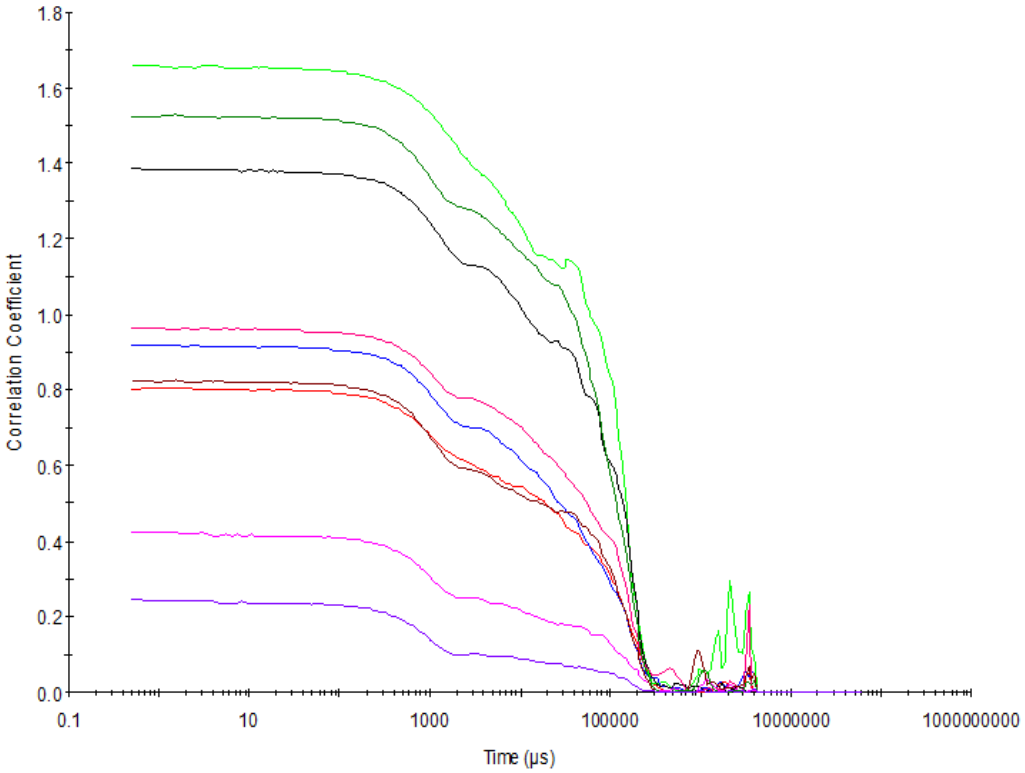

Figure S94 – Raw correlation data for 9 DLS runs at 40 °C with compound **4** at a concentration of 0.56 mM in DMSO.

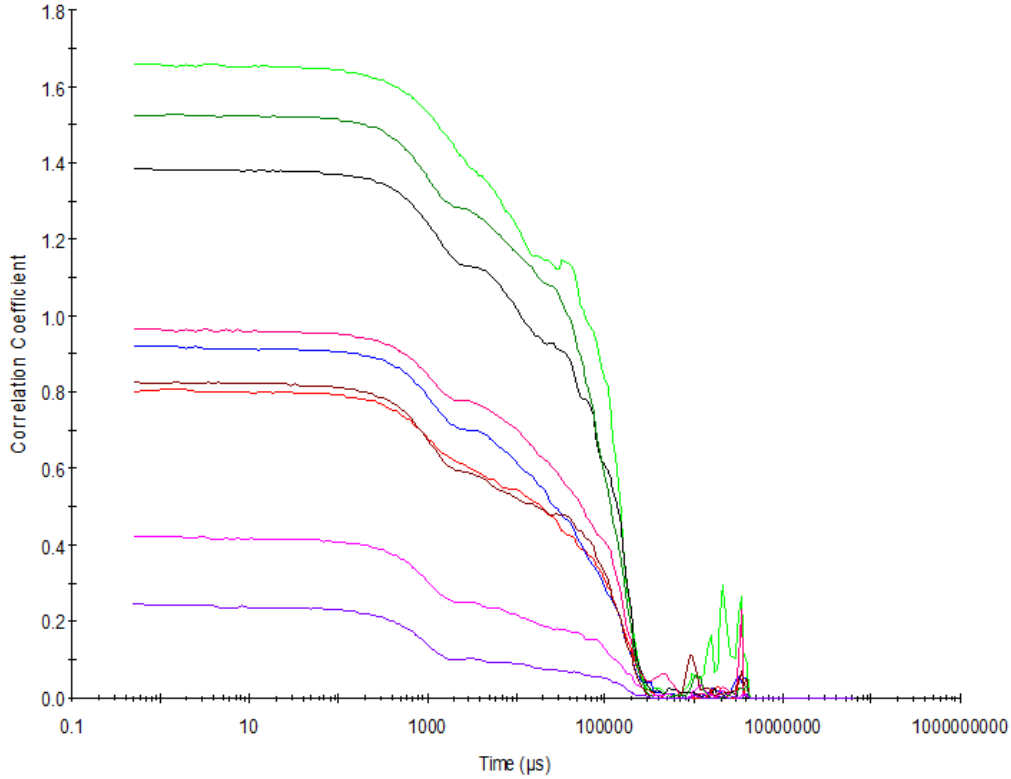

Figure S95 – Raw correlation data for 9 DLS runs at 25 °C after heating to 40 °C with compound **4** at a concentration of 0.56 mM in DMSO.

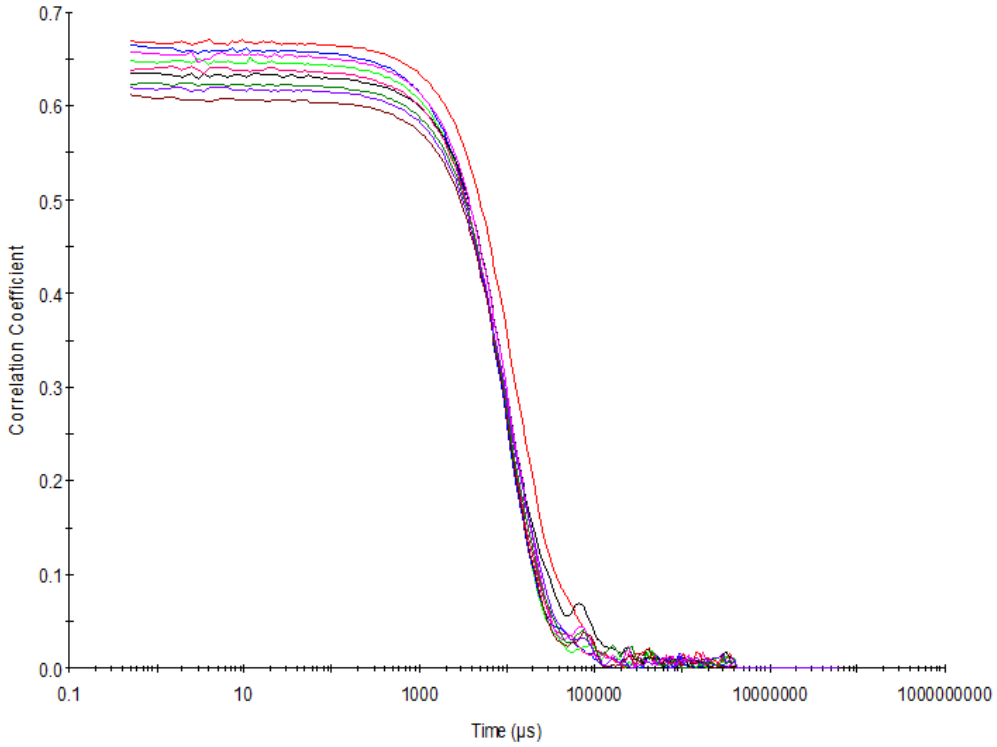

Figure S96 - Raw correlation data for 9 DLS runs at 25 °C after heating to 40 °C with compound **4** at a concentration of 55.56 mM in DMSO: H_2O 1: 1.

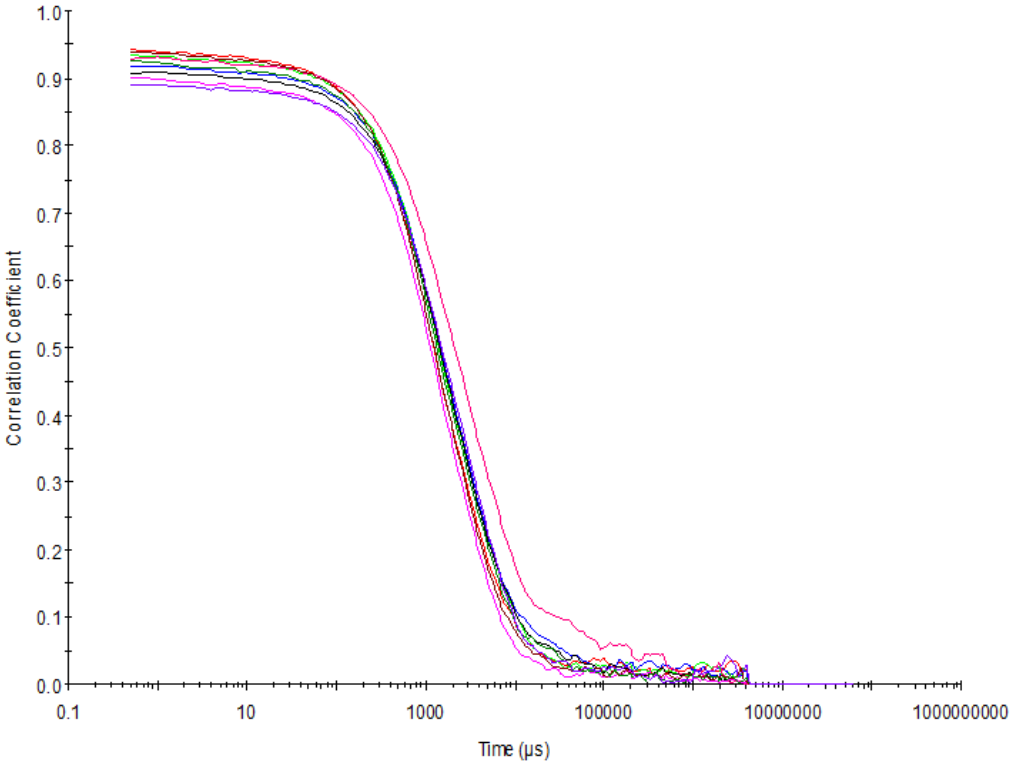

Figure S97 - Raw correlation data for 9 DLS runs at 25 °C after heating to 40 °C with compound **4** at a concentration of 5.56 mM in DMSO: H_2O 1: 1.

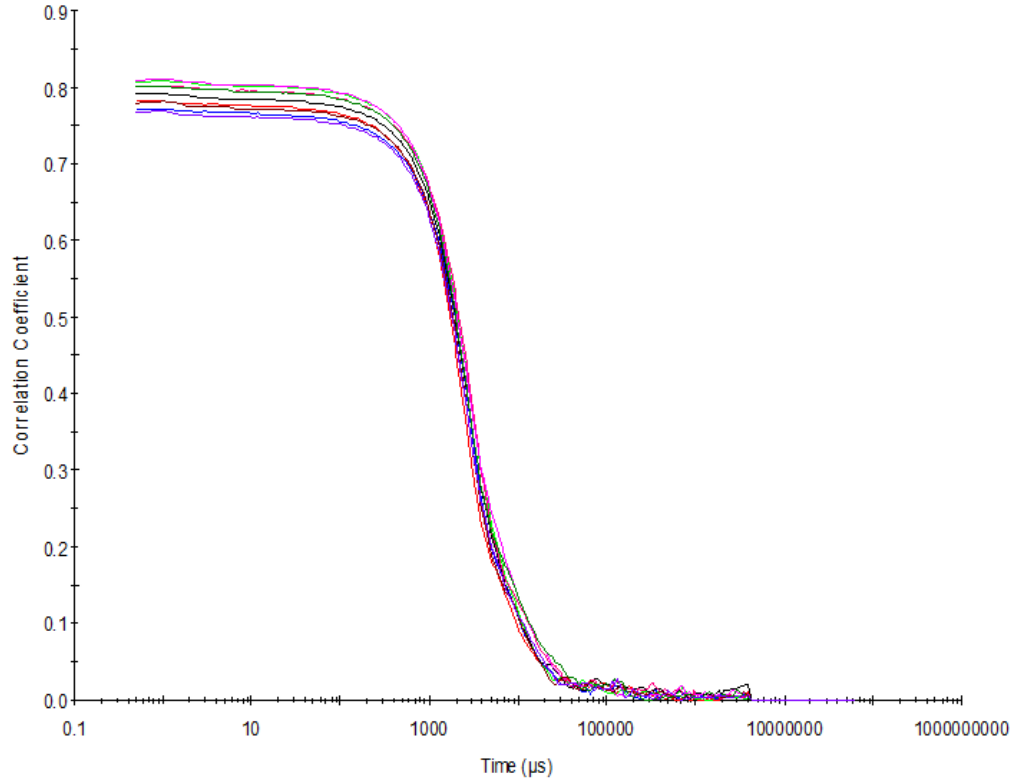

Figure S98 - Raw correlation data for 9 DLS runs at 25 °C after heating to 40 °C with compound **4** at a concentration of 0.56 mM in DMSO: H_2O 1: 1.

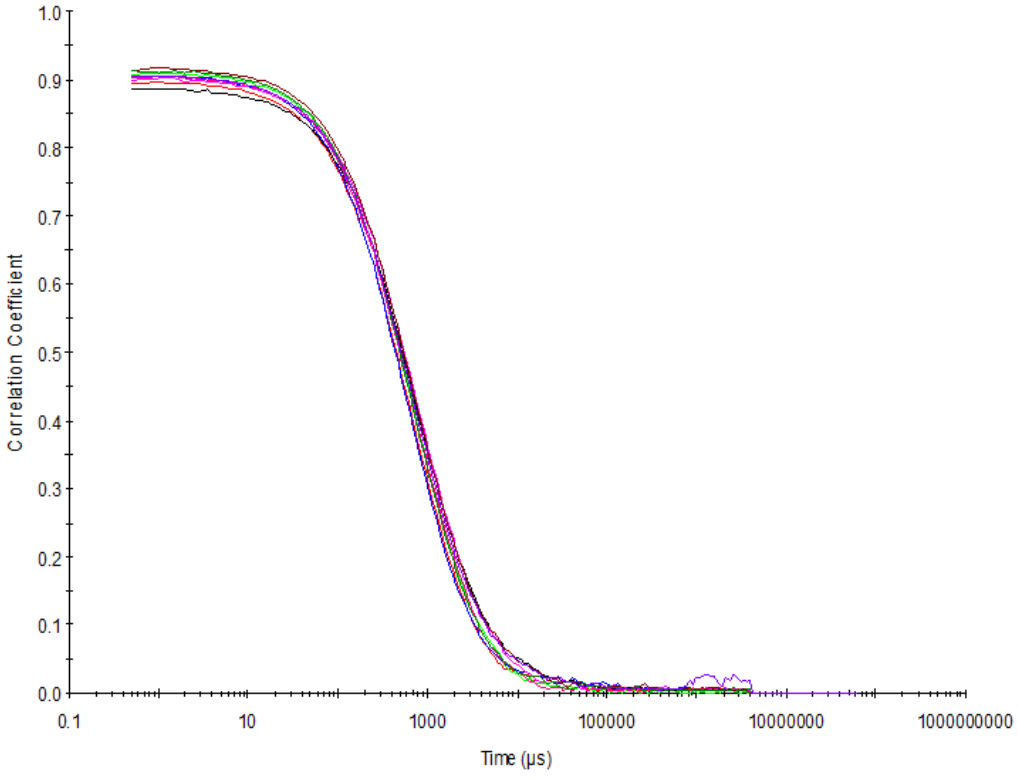

Figure S99 - Raw correlation data for 9 DLS runs at 25 °C after heating to 40 °C with compound **4** at a concentration of 5.56 mM in DMSO: H_2O 3: 7.

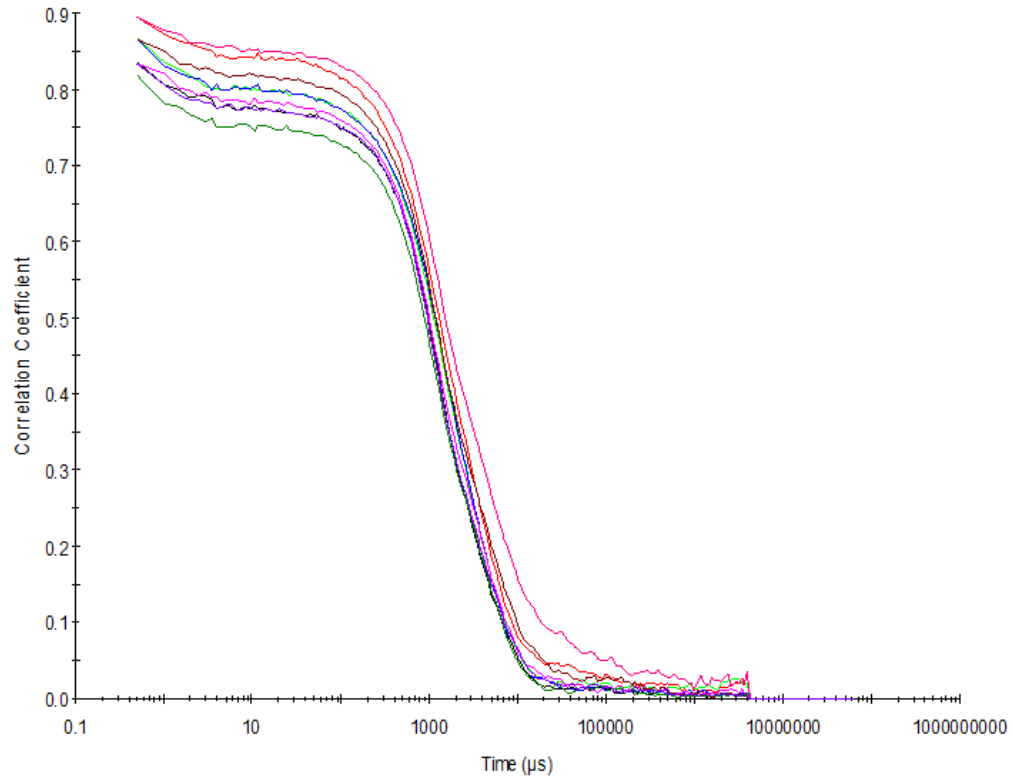

Figure S100 - Raw correlation data for 9 DLS runs at 25 °C after heating to 40 °C with compound **4** at a concentration of 0.56 mM In DMSO: H_2O 3: 7.

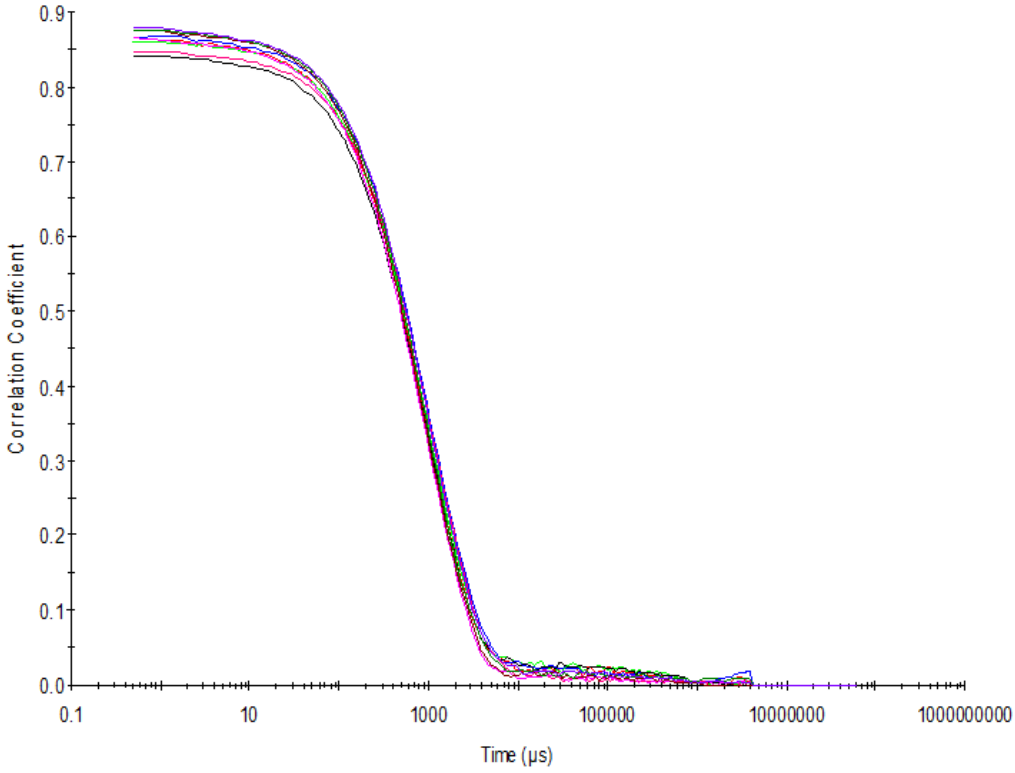

Figure S101 - Raw correlation data for 9 DLS runs at 25 °C after heating to 40 °C with compound **4** at a concentration of 0.56 mM in DMSO: H_2O 1: 4.

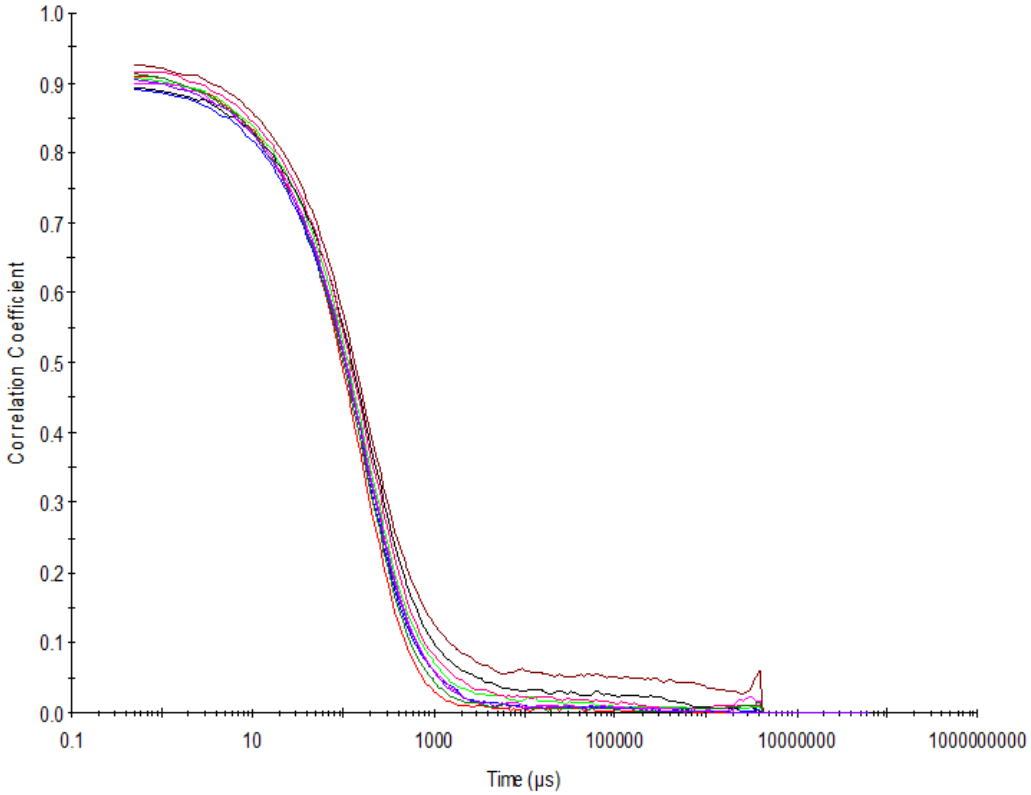

Figure S102 - Raw correlation data for 9 DLS runs at 25 °C after heating to 40 °C with compound **4** at a concentration of 5.56 mM in EtOH: H_2O 1: 19.

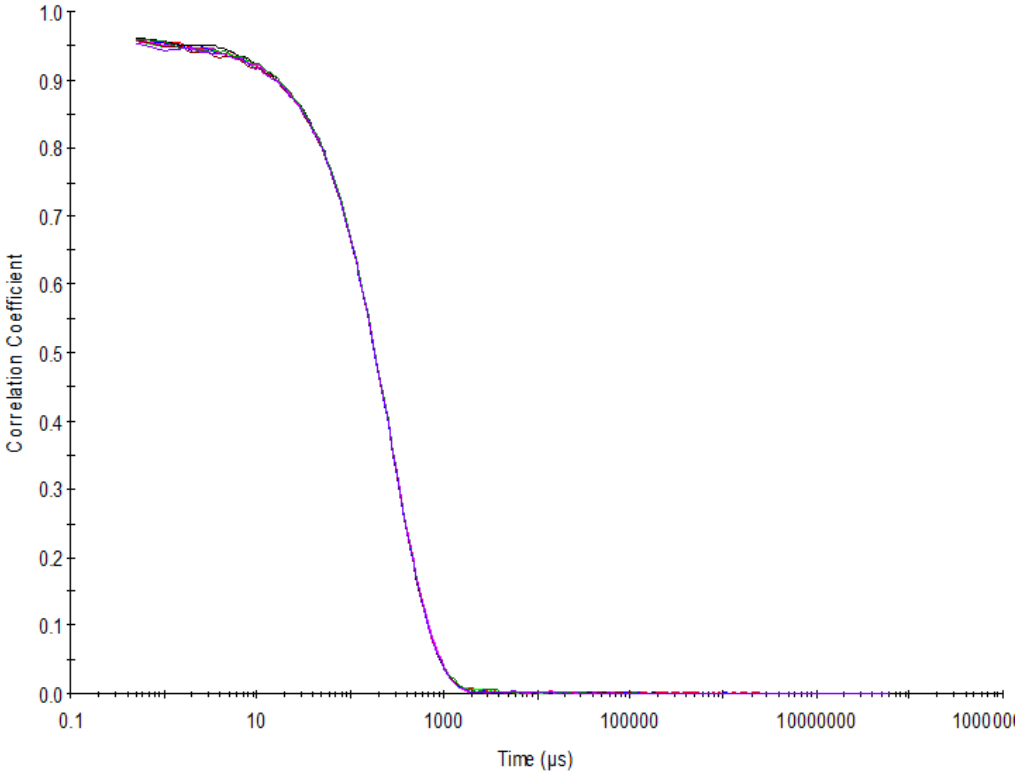

Figure S103 - Raw correlation data for 9 DLS runs at 25 °C after heating to 40 °C with compound **4** at a concentration of 0.56 mM in EtOH: H_2O 1: 19.

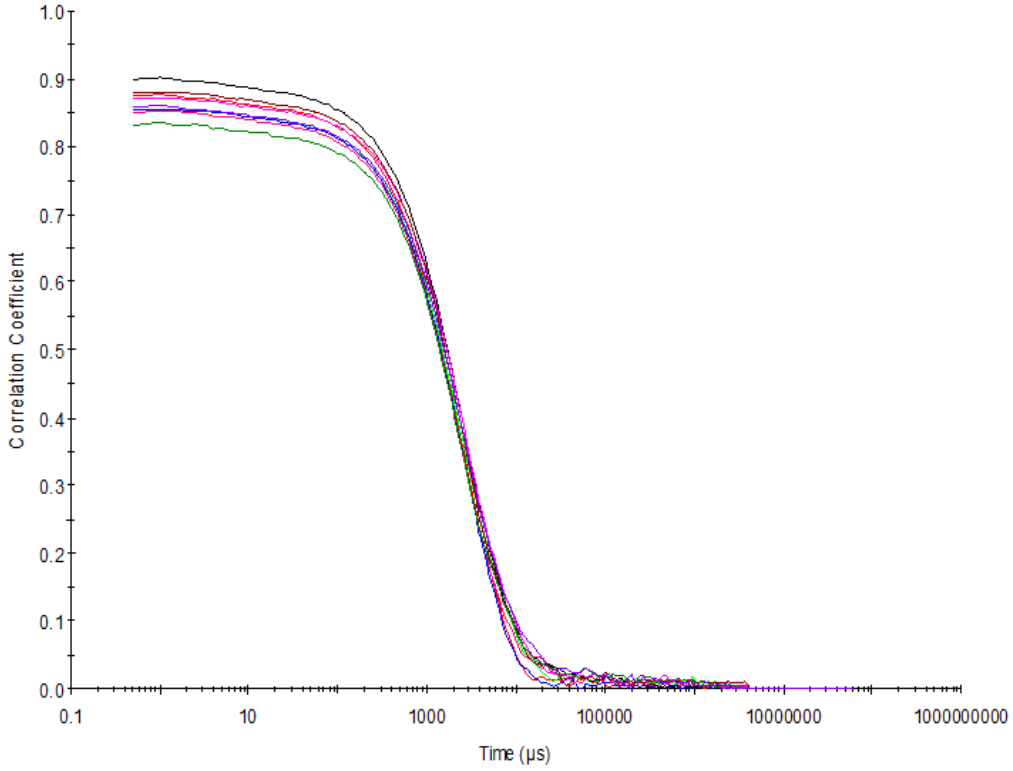

Figure S104 – Raw correlation data for 9 DLS runs at 25 °C before heating to 40 °C with compound **5** at a concentration of 111.12 mM in DMSO.

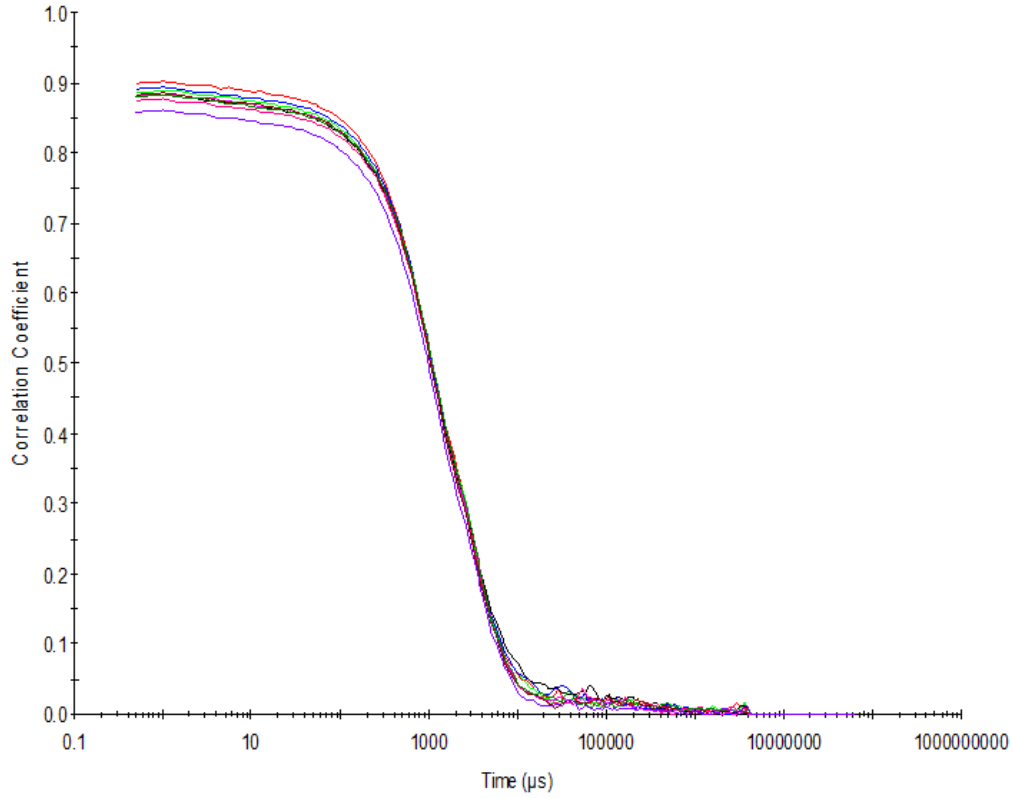

Figure S105 – Raw correlation data for 9 DLS runs at 40 °C with compound **5** at a concentration of 111.12 mM in DMSO.

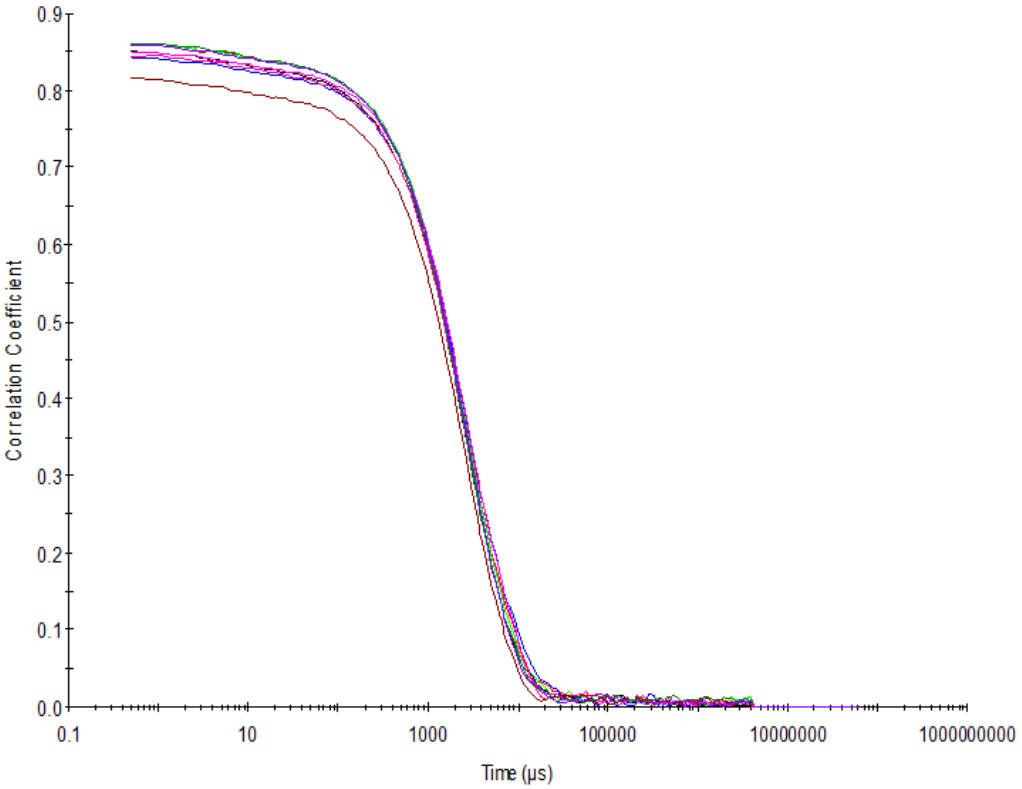

Figure S106 – Raw correlation data for 9 DLS runs at 25 °C after heating to 40 °C with compound **5** at a concentration of 111.12 mM in DMSO.

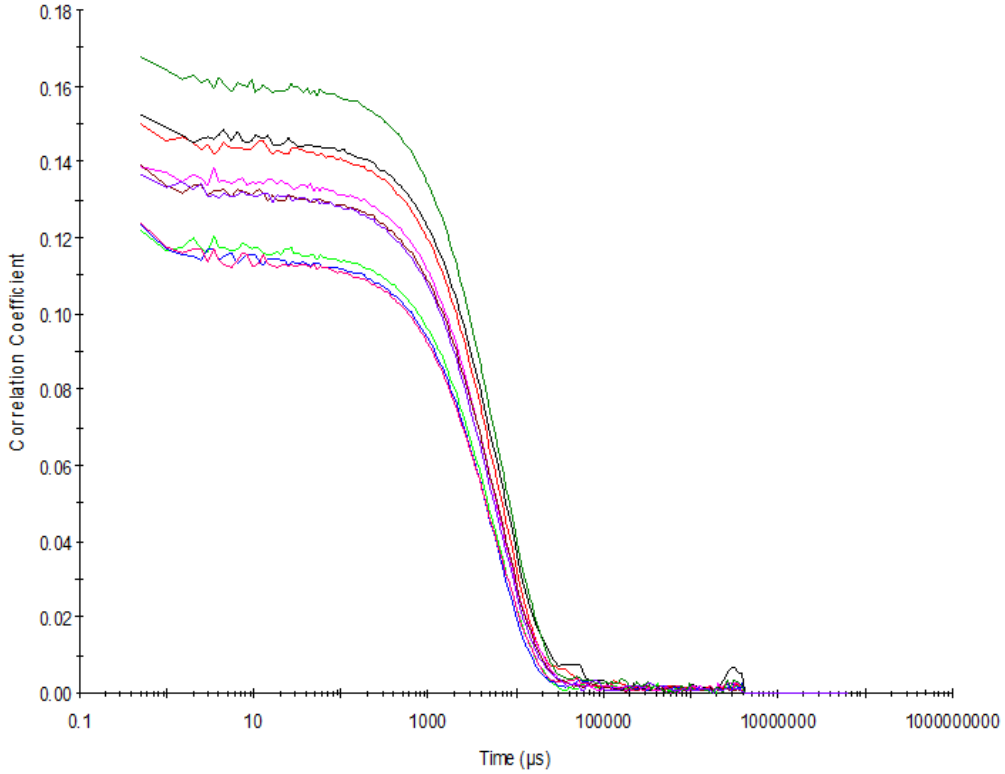

Figure S107 – Raw correlation data for 9 DLS runs at 25 °C before heating to 40 °C with compound **5** at a concentration of 55.56 mM in DMSO.

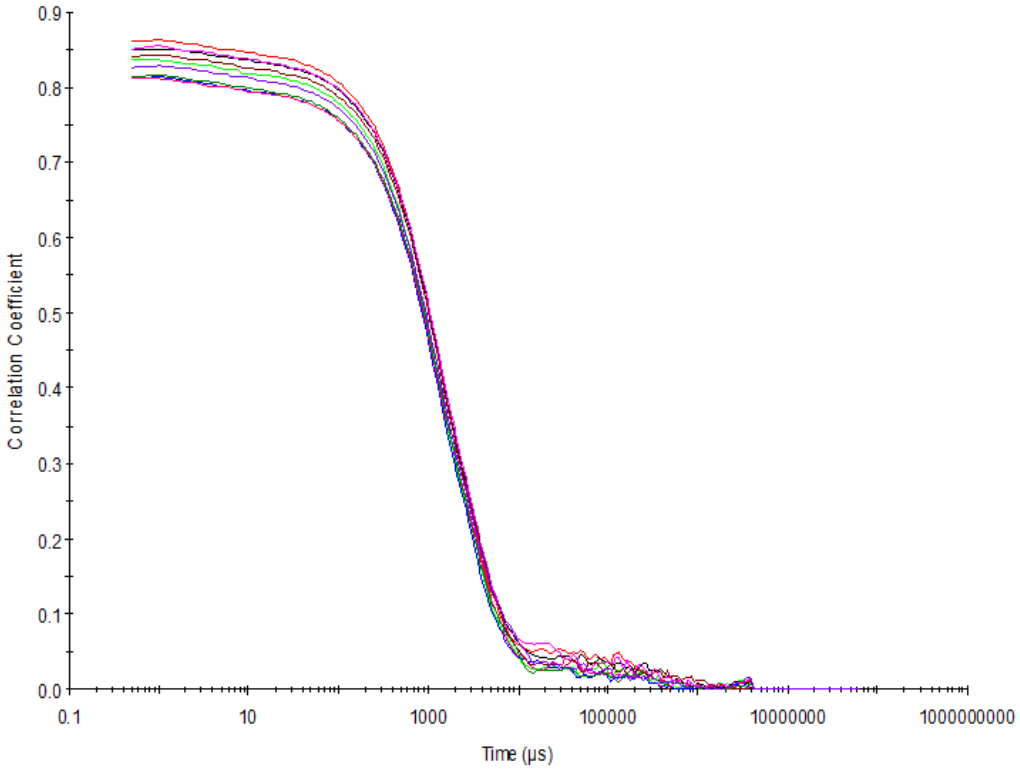

Figure S108 – Raw correlation data for 9 DLS runs at 40 °C with compound **5** at a concentration of 55.56 mM in DMSO.

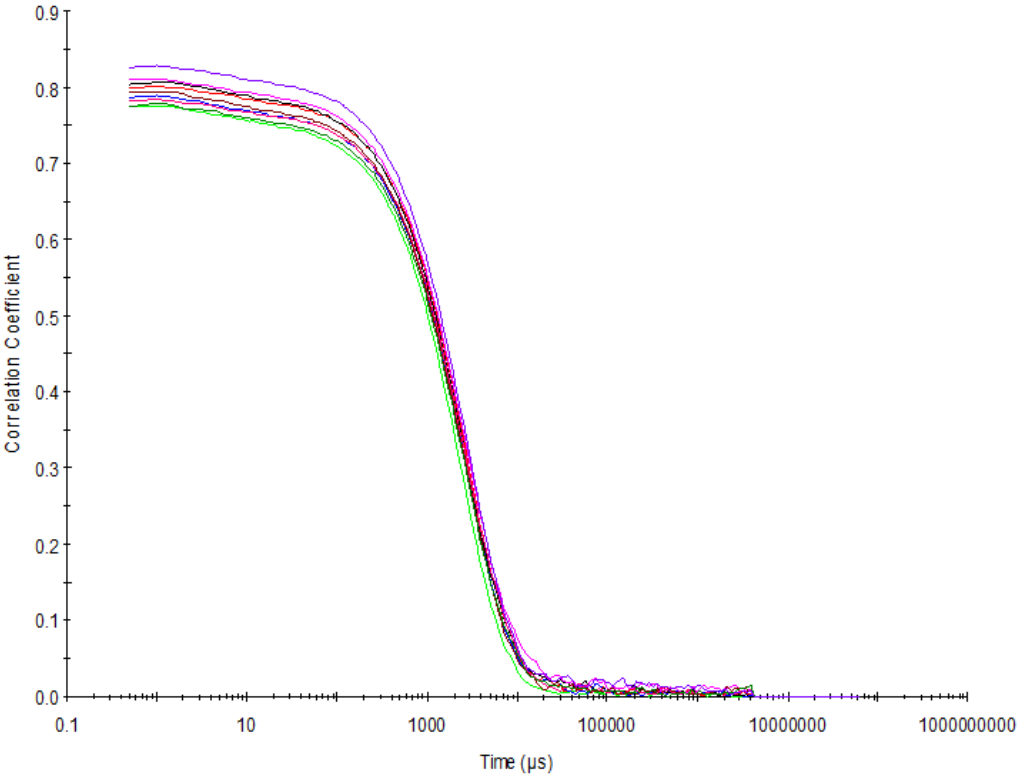

Figure S109 – Raw correlation data for 9 DLS runs at 25 °C after heating to 40 °C with compound **5** at a concentration of 55.56 mM in DMSO.

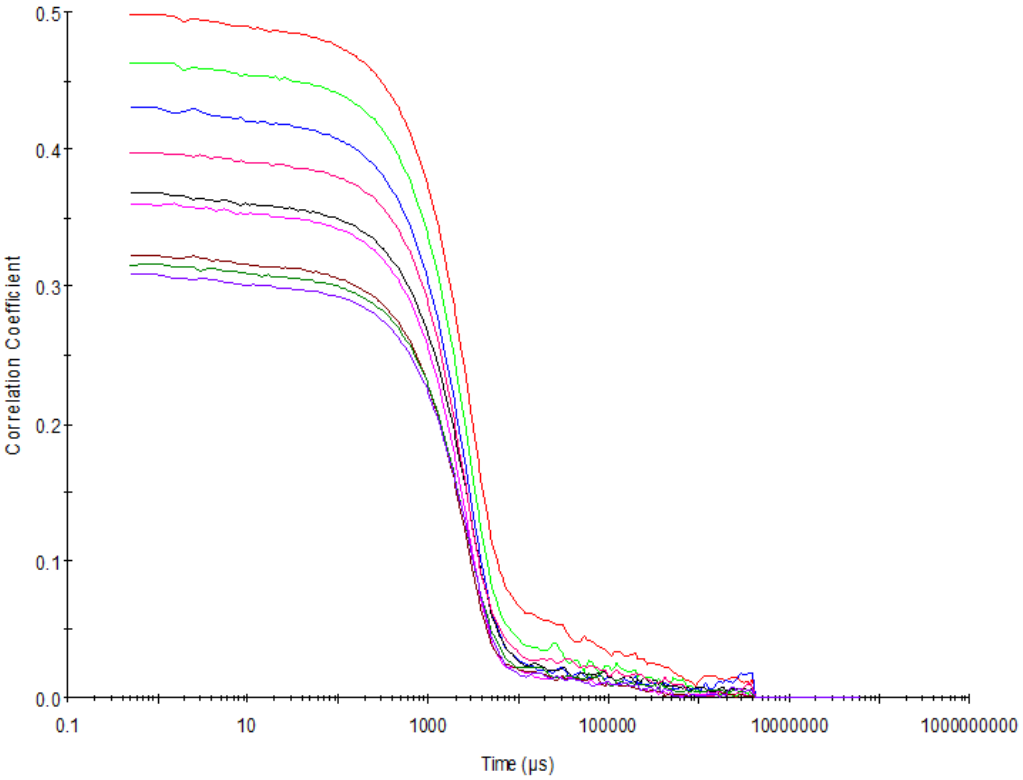

Figure S110 – Raw correlation data for 9 DLS runs at 25 °C before heating to 40 °C with compound **5** at a concentration of 5.56 mM in DMSO.

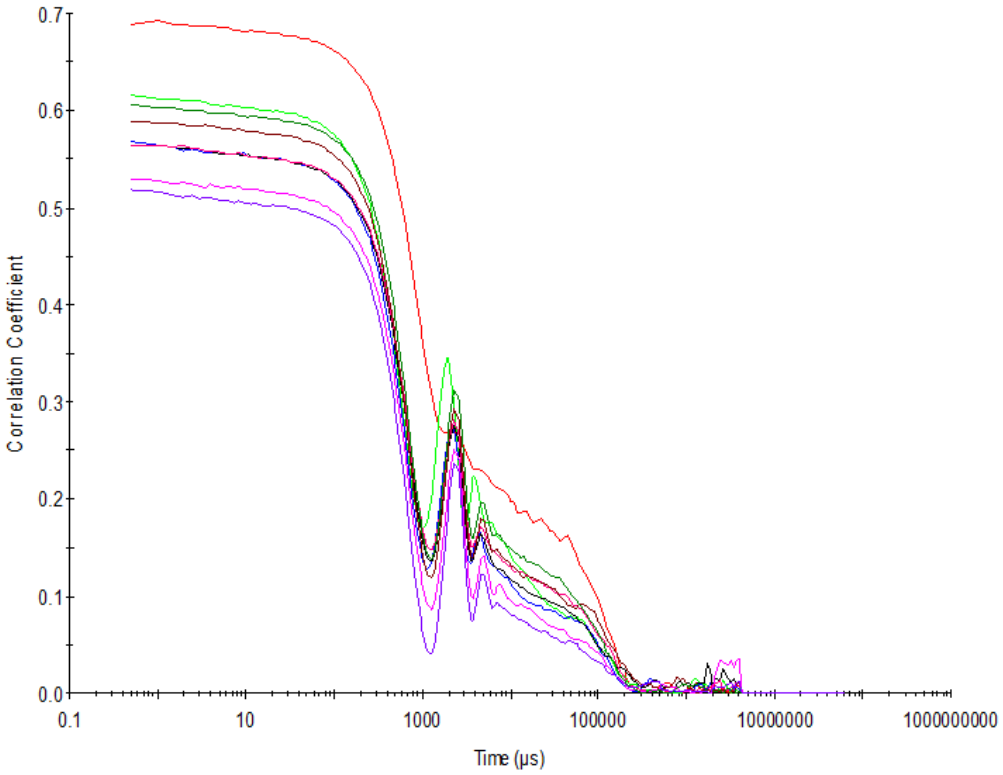

Figure S111 – Raw correlation data for 9 DLS runs at 40 °C with compound **5** at a concentration of 5.56 mM in DMSO.

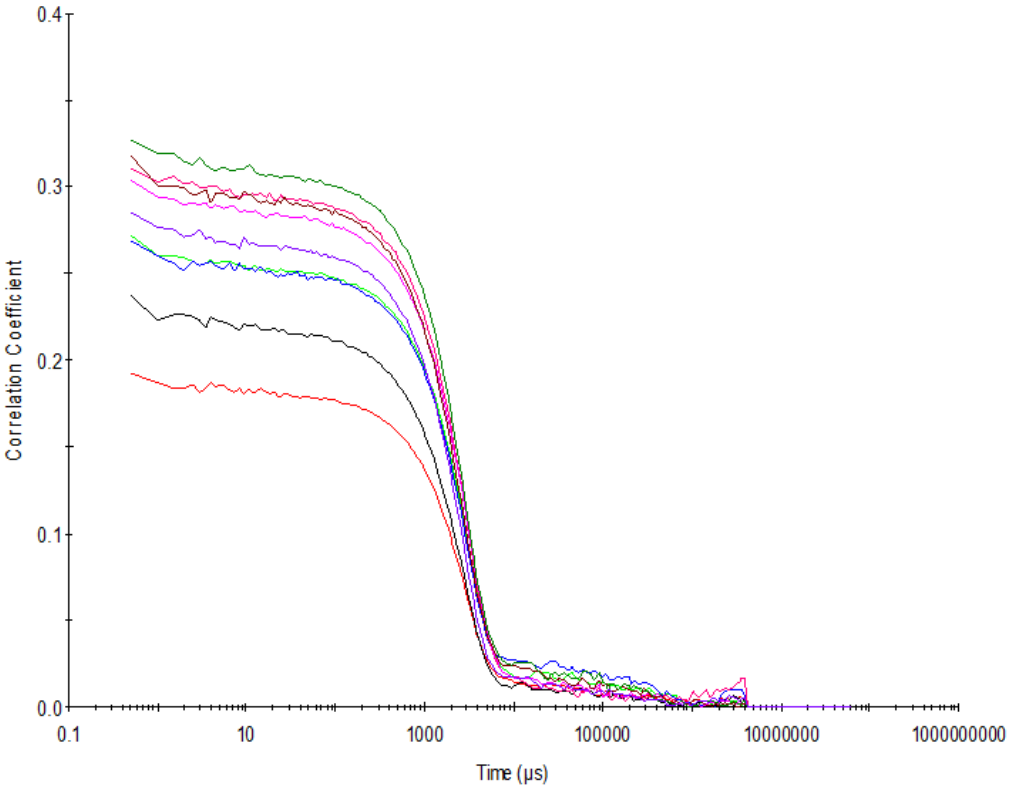

Figure S112 – Raw correlation data for 9 DLS runs at 25 °C after heating to 40 °C with compound **5** at a concentration of 5.56 mM in DMSO.

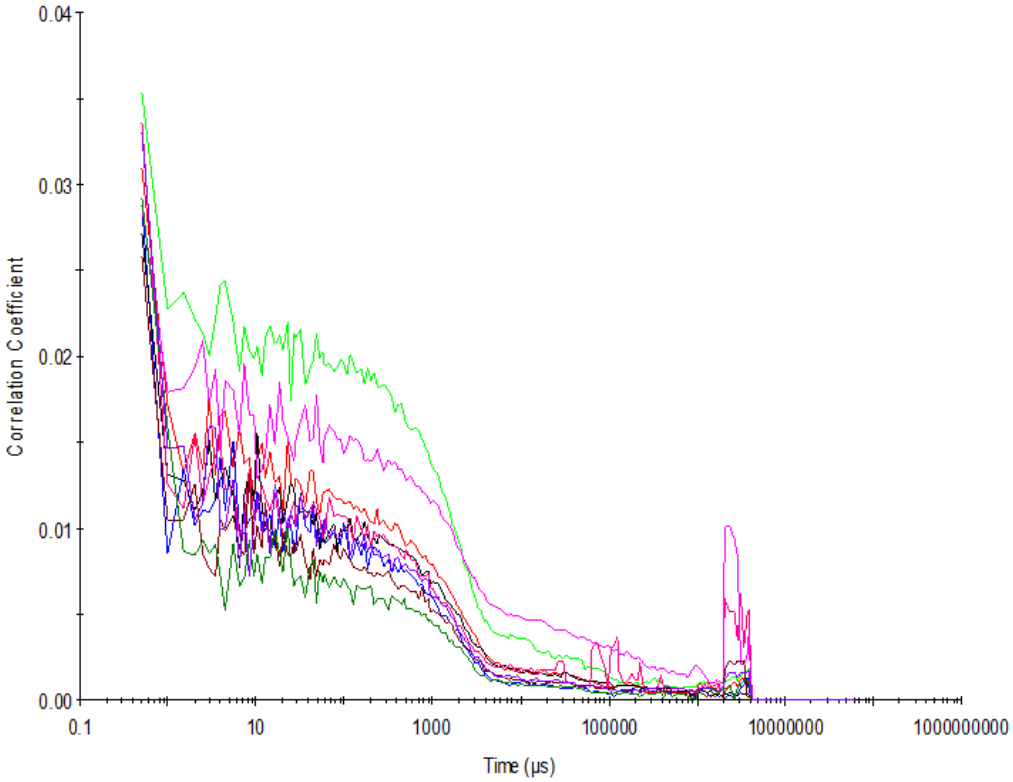

Figure S113 – Raw correlation data for 9 DLS runs at 25 °C before heating to 40 °C with compound **5** at a concentration of 0.56 mM in DMSO.

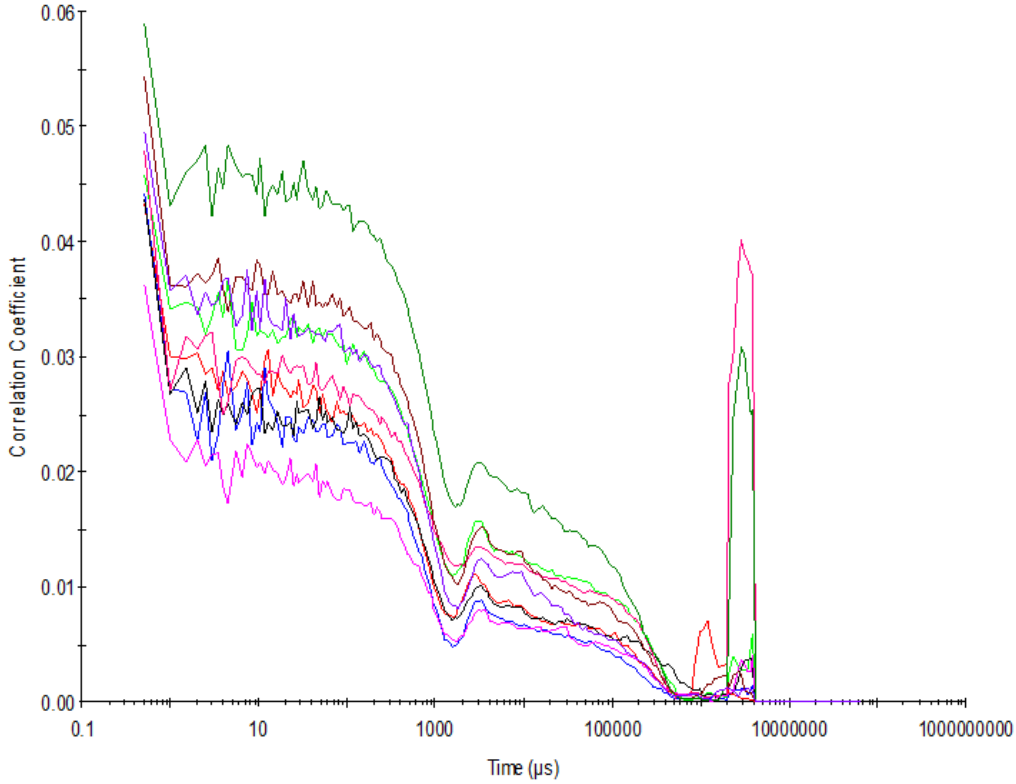

Figure S114 – Raw correlation data for 9 DLS runs at 40 °C with compound **5** at a concentration of 0.56 mM in DMSO.

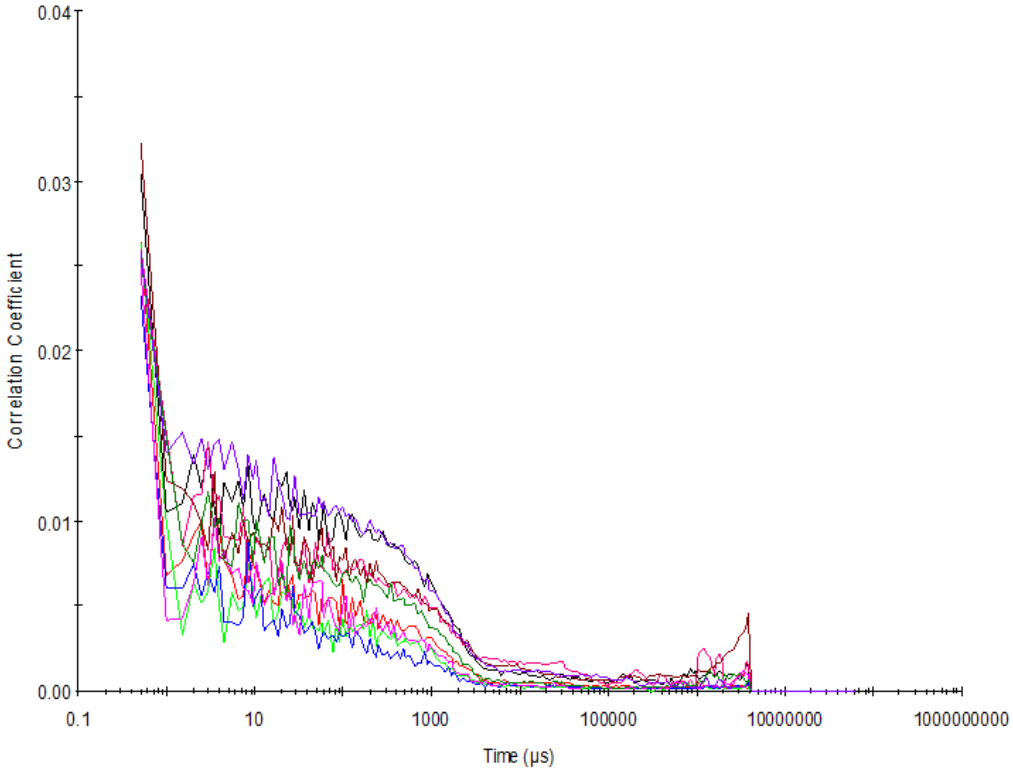

Figure S115 – Raw correlation data for 9 DLS runs at 25 °C after heating to 40 °C with compound **5** at a concentration of 0.56 mM in DMSO.

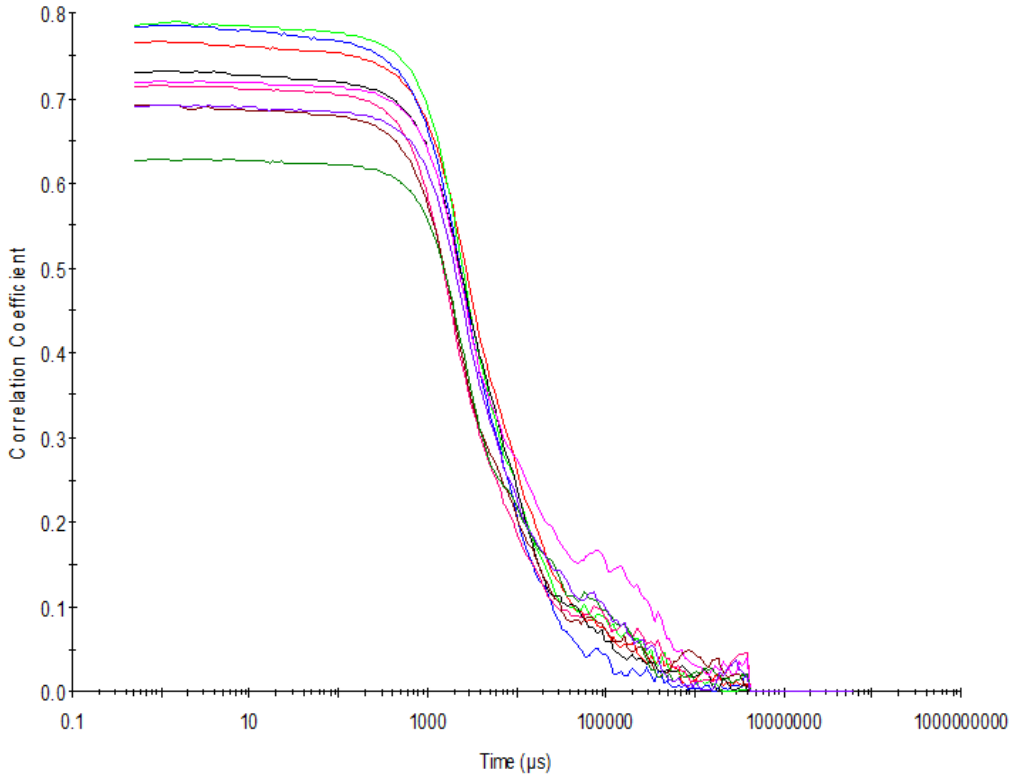

Figure S116 - Raw correlation data for 9 DLS runs at 25 °C after heating to 40 °C with compound **5** at a concentration of 55.56 mM in DMSO: H_2O 1: 1.

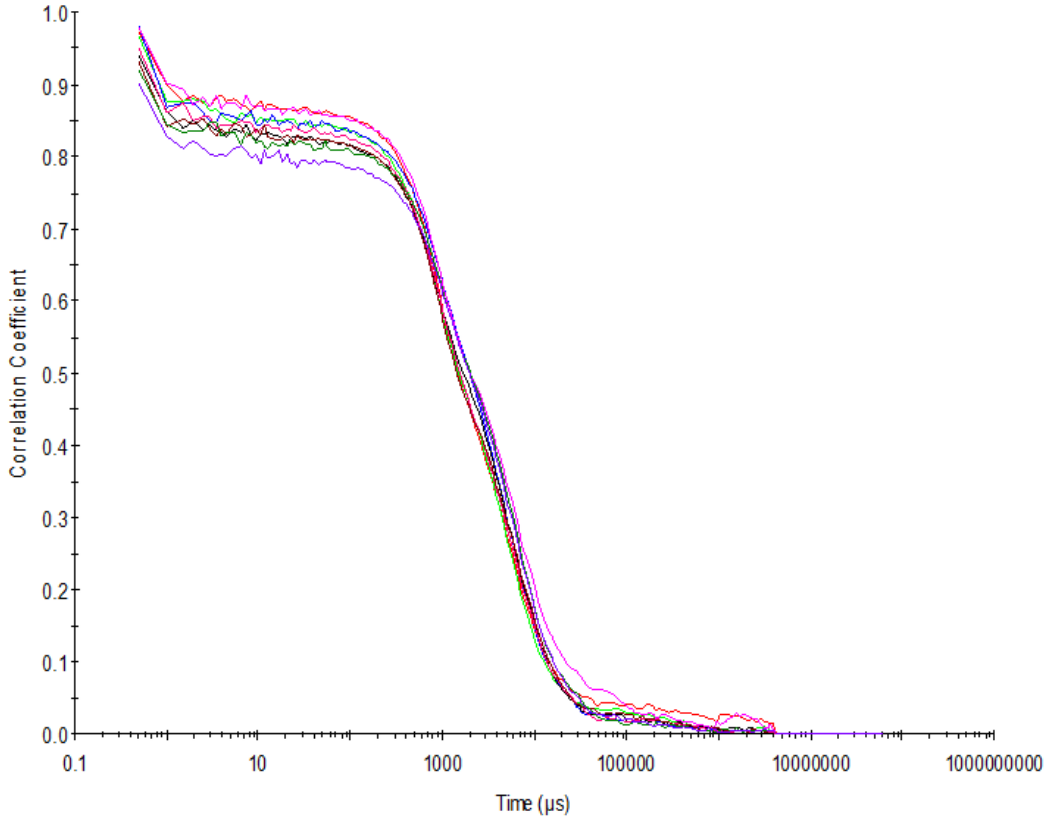

Figure S117 - Raw correlation data for 9 DLS runs at 25 °C after heating to 40 °C with compound **5** at a concentration of 5.56 mM in DMSO: H_2O 1: 1.

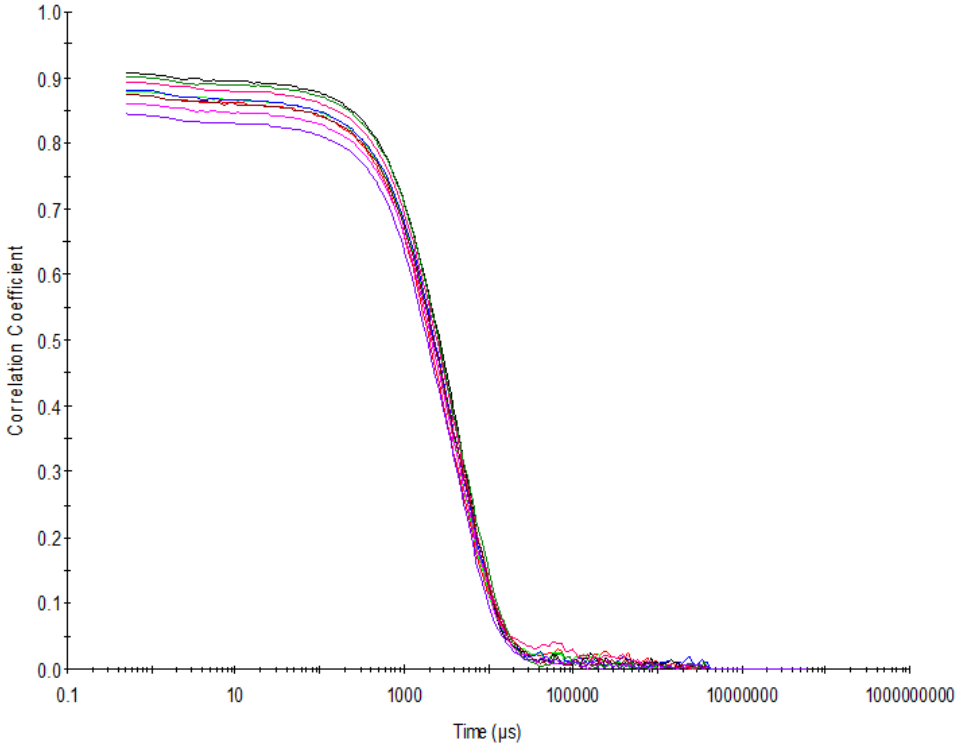

Figure S118 - Raw correlation data for 9 DLS runs at 25 °C after heating to 40 °C with compound **5** at a concentration of 0.56 mM in DMSO: H_2O 1: 1.

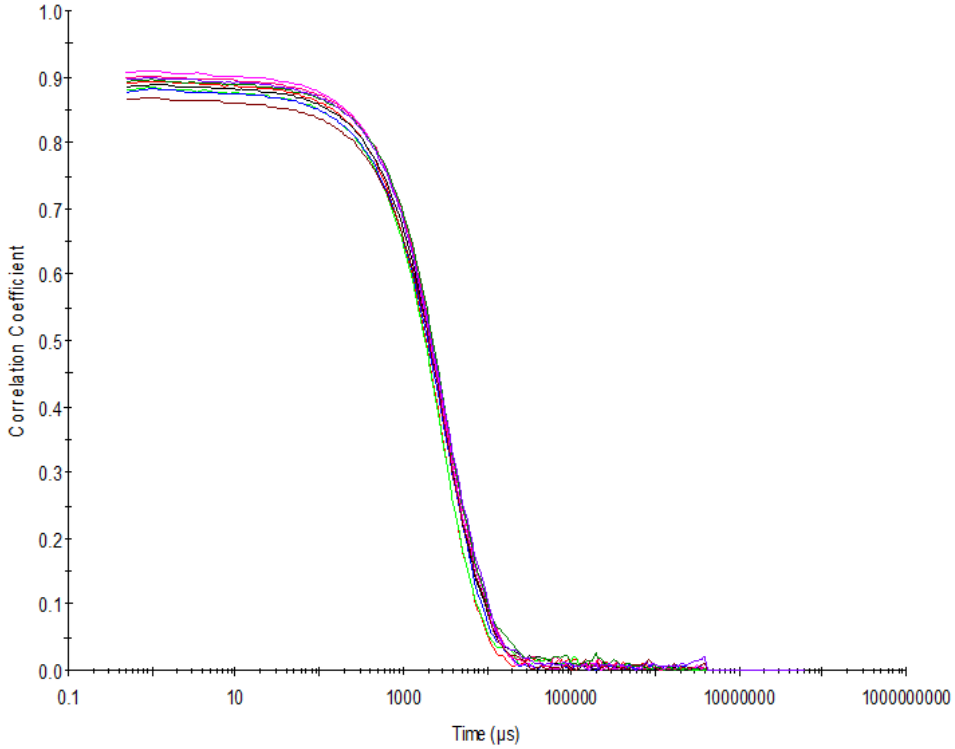

Figure S119 - Raw correlation data for 9 DLS runs at 25 °C after heating to 40 °C with compound **5** at a concentration of 5.56 mM in DMSO: H_2O 3: 7.

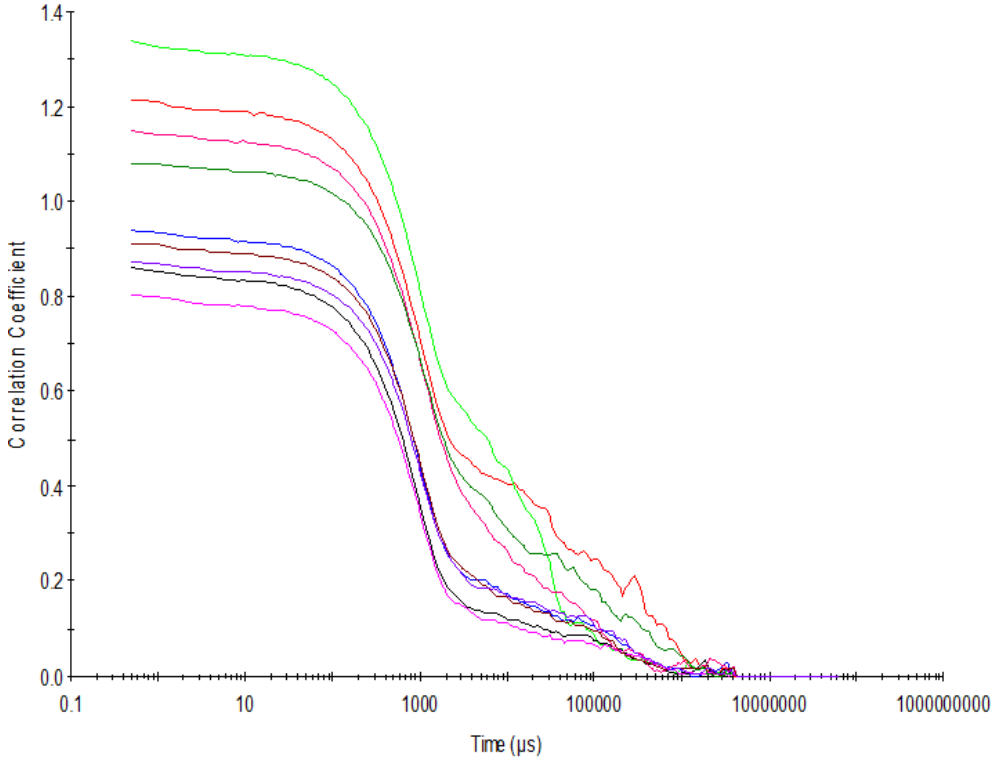

Figure S120 - Raw correlation data for 9 DLS runs at 25 °C after heating to 40 °C with compound **5** at a concentration of 0.56 mM in DMSO: H_2O 3: 7.

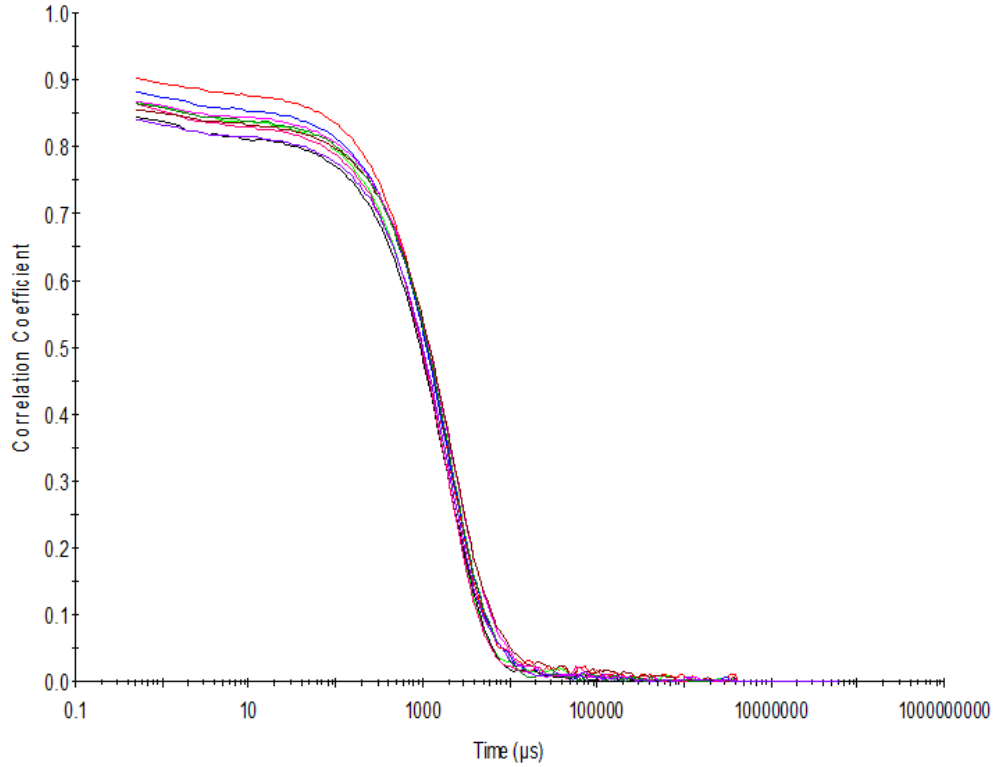

Figure S121 - Raw correlation data for 9 DLS runs at 25 °C after heating to 40 °C with compound **5** at a concentration of 0.56 mM in DMSO: H_2O 1: 4.

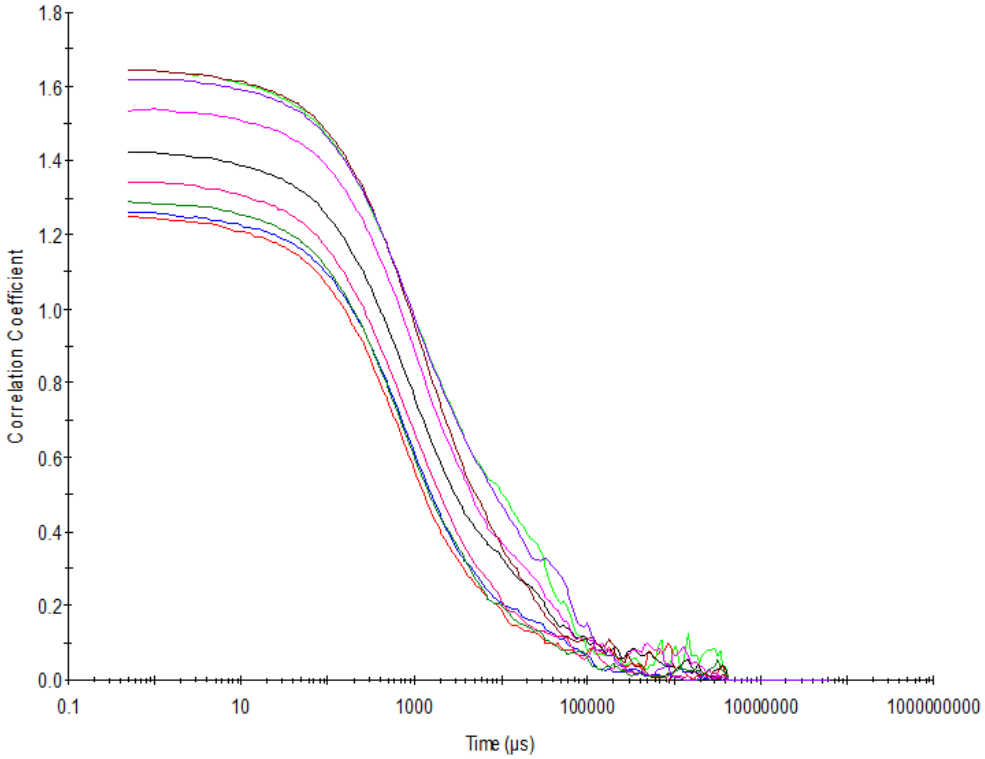

Figure S122 - Raw correlation data for 9 DLS runs at 25 °C after heating to 40 °C with compound **5** at a concentration of 5.56 mM in EtOH: H_2O 1: 19.

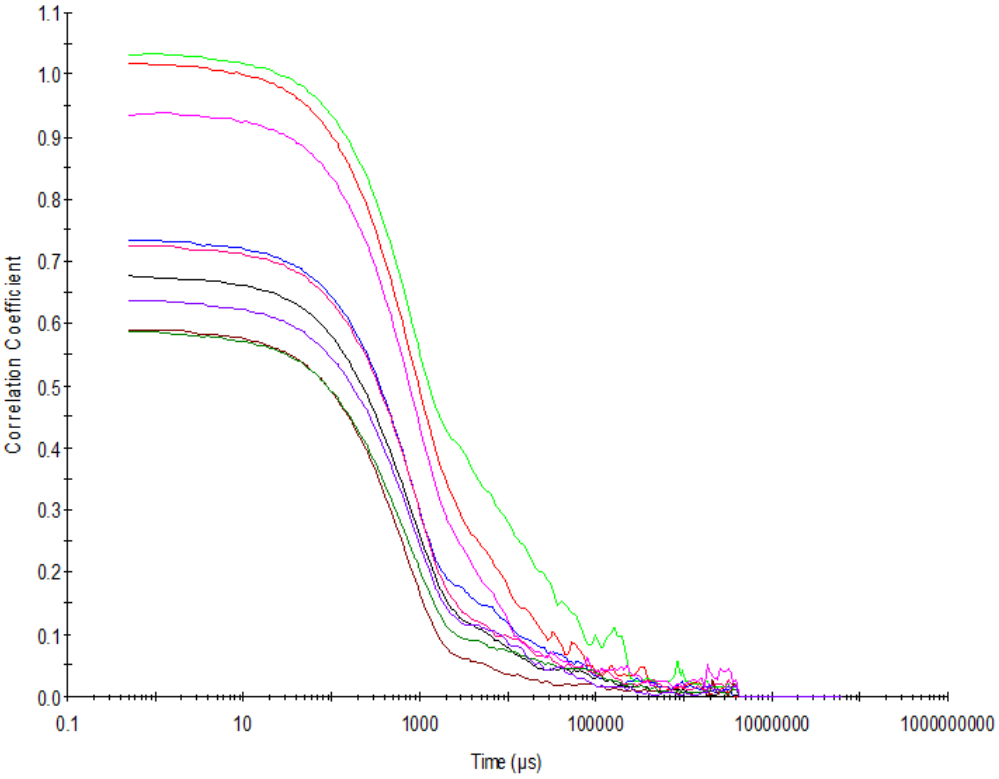

Figure S123 - Raw correlation data for 9 DLS runs at 25 °C after heating to 40 °C with compound **5** at a concentration of 0.56 mM in EtOH: H_2O 1: 19.

Size distribution calculated by DLS

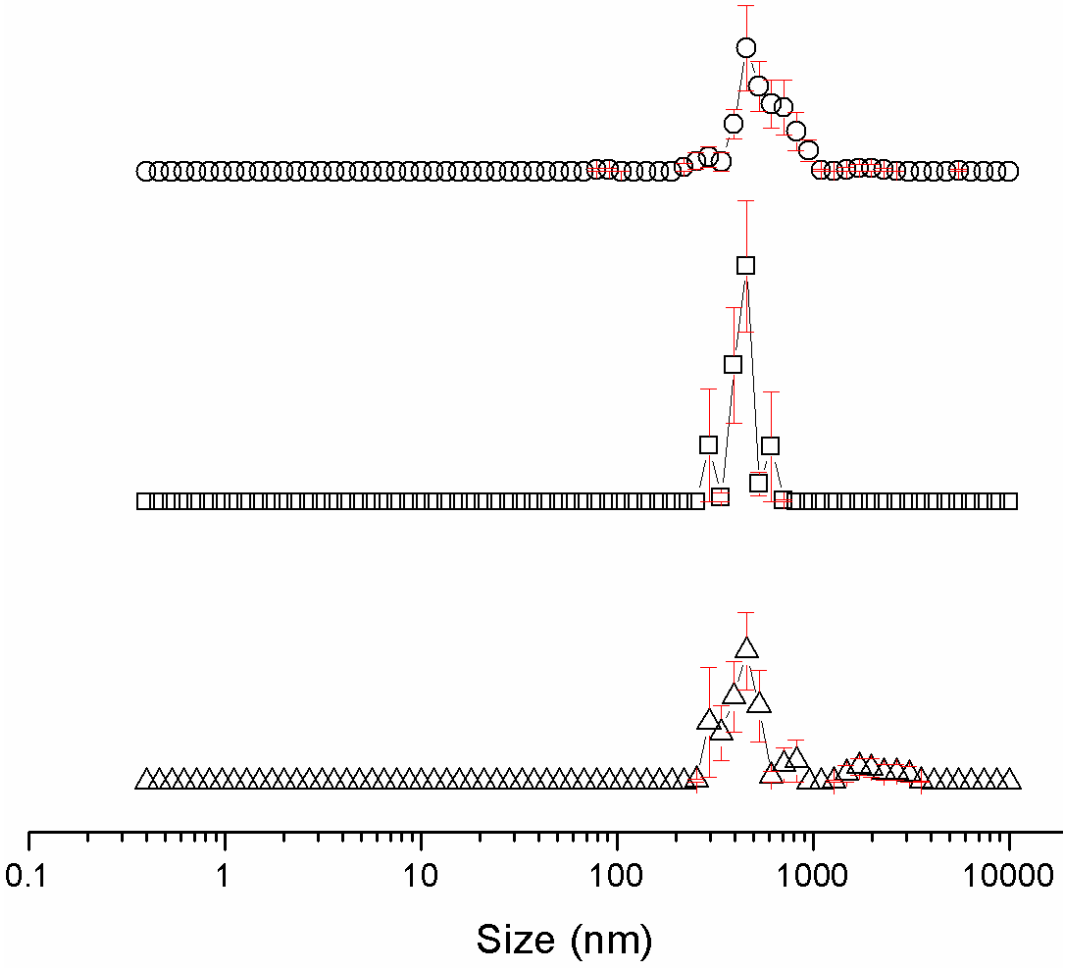

Figure S124 - Average intensity particle size distribution, calculated from 9 DLS runs, of aggregates formed by dissolving compound **1** at a concentration of 111.12 mM in DMSO at Δ) 25 °C, □) heating to 40 °C and ○) cooling to 25 °C. Only 9 of the available 10 DLS runs were used as in some cases, due to the heating and cooling processes there were some obvious temperature equilibration issues for the first run.

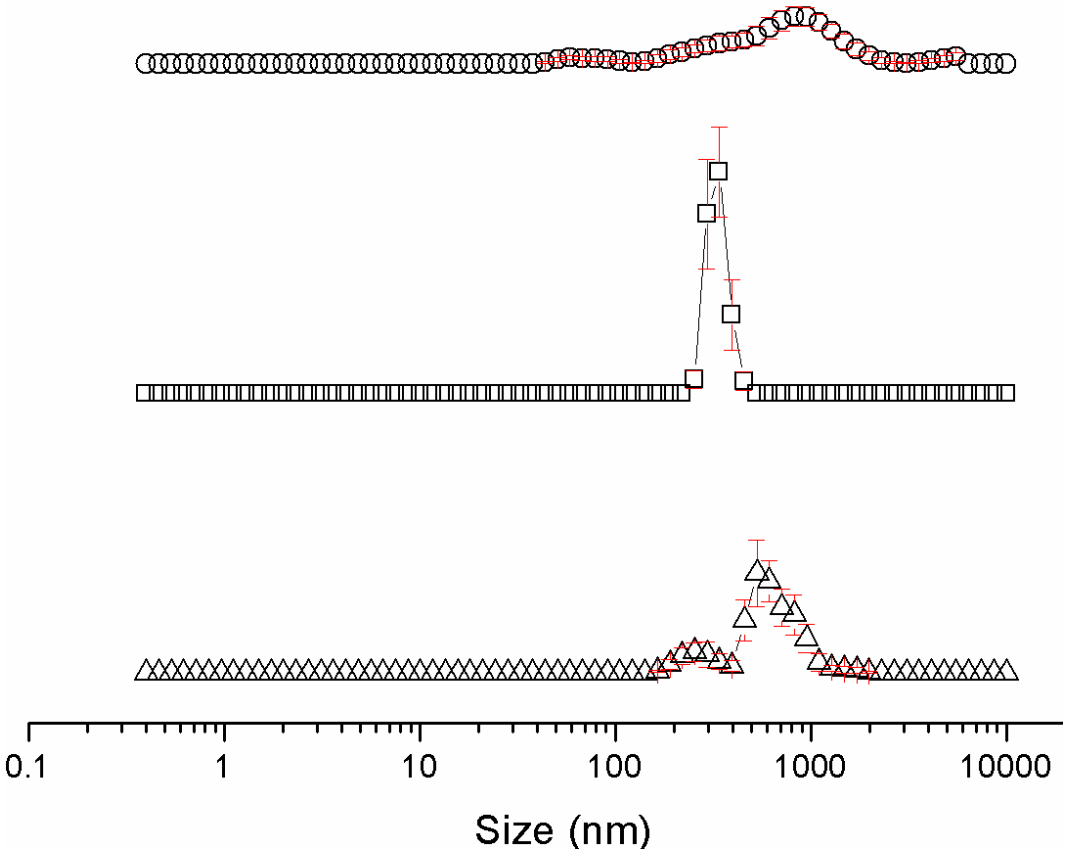

Figure S125 - Average intensity particle size distribution, calculated from 9 DLS runs, of aggregates formed by dissolving compound **1** at a concentration of 55.56 mM in DMSO at Δ) 25 ^{o}C, □) heating to 40 ^{o}C and ○) cooling to 25 ^{o}C. Only 9 of the available 10 DLS runs were used as in some cases, due to the heating and cooling processes there were some obvious temperature equilibration issues for the first run.

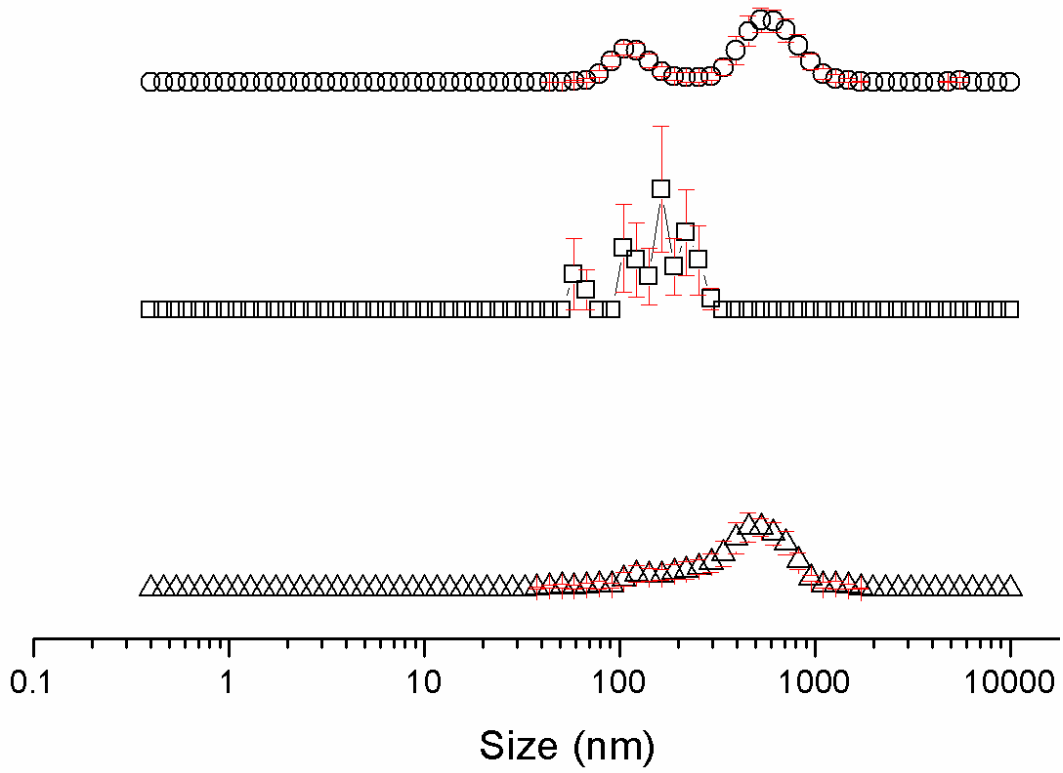

Figure S126 - Average intensity particle size distribution, calculated from 9 DLS runs, of aggregates formed by dissolving compound **1** at a concentration of 5.56 mM in DMSO at Δ) 25 ^{o}C, □) heating to 40 ^{o}C and ○) cooling to 25 ^{o}C. Only 9 of the available 10 DLS runs were used as in some cases, due to the heating and cooling processes there were some obvious temperature equilibration issues for the first run.

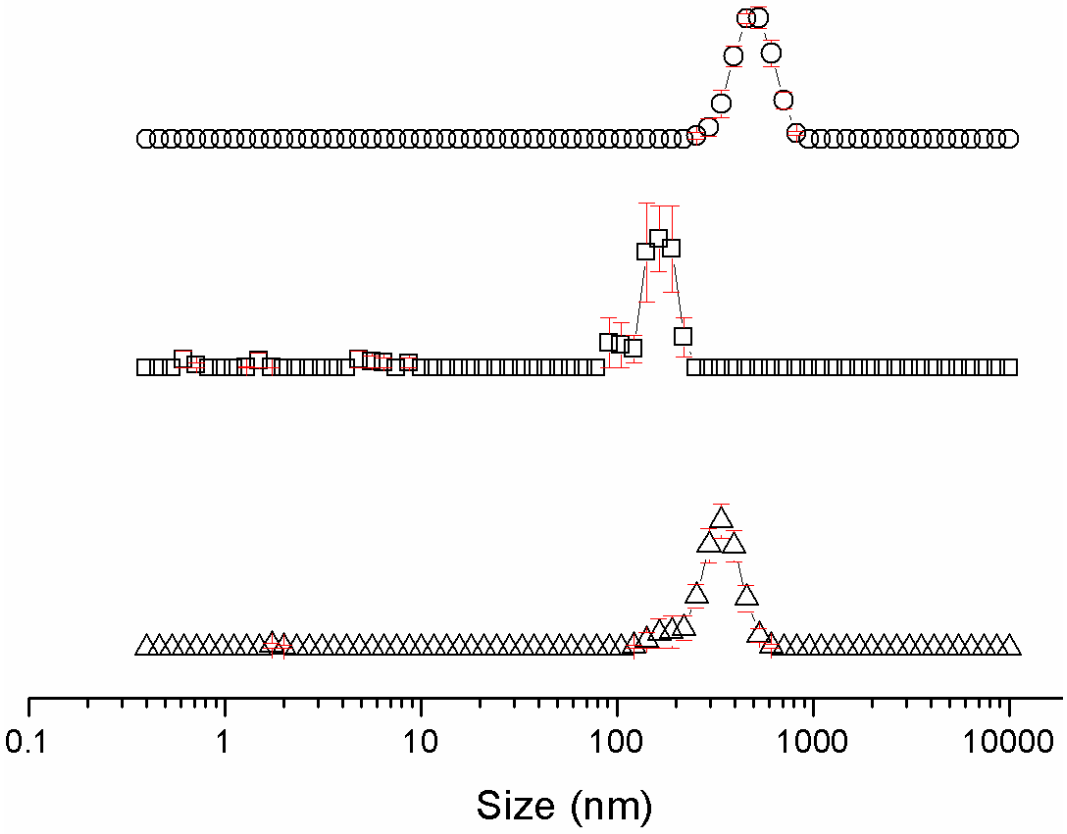

Figure S127 - Average intensity particle size distribution, calculated from 9 DLS runs, of aggregates formed by dissolving compound **1** at a concentration of 0.56 mM in DMSO at Δ) 25 ^{o}C, □) heating to 40 ^{o}C and ○) cooling to 25 ^{o}C. Only 9 of the available 10 DLS runs were used as in some cases, due to the heating and cooling processes there were some obvious temperature equilibration issues for the first run.

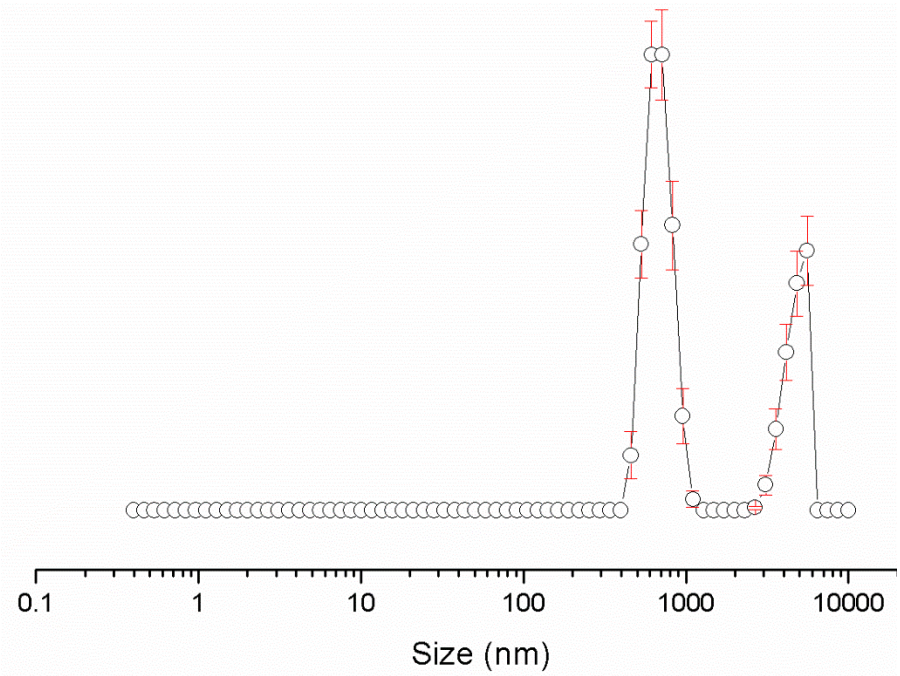

Figure S128 - Average intensity particle size distribution, calculated from 9 DLS runs, of aggregates formed by dissolving compound **1** at a concentration of 55.56 mM in a solution of DMSO: H_2O 1: 1, after heating to 40 ^oC and cooling to 25 ^oC. Only 9 of the available 10 DLS runs were used as in some cases, due to the heating and cooling processes there were some obvious temperature equilibration issues for the first run.

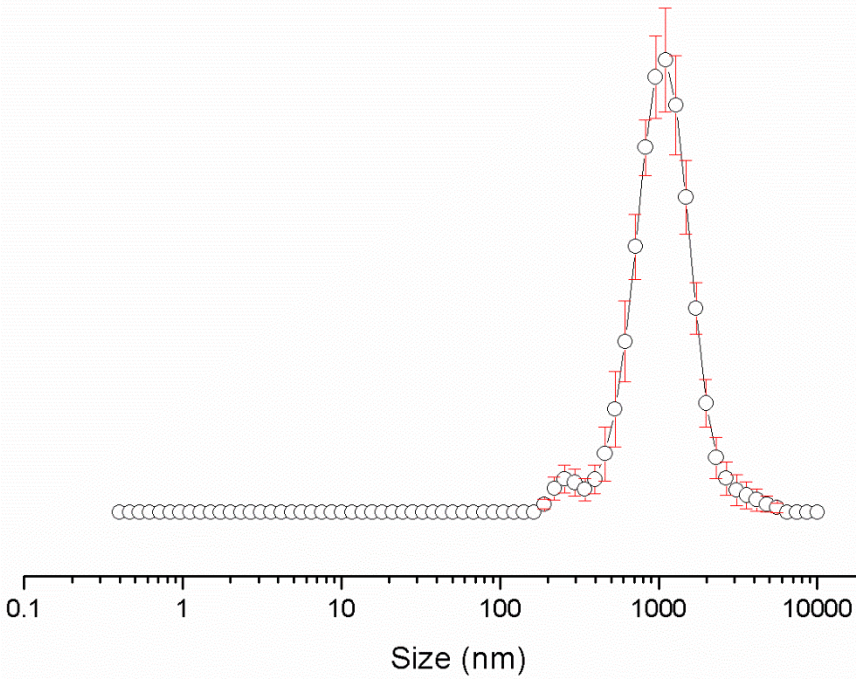

Figure S129 - Average intensity particle size distribution, calculated from 9 DLS runs, of aggregates formed by dissolving compound **1** at a concentration of 5.56 mM in a solution of DMSO: H_2O 1: 1, after heating to 40 ^oC and cooling to 25 ^oC. Only 9 of the available 10 DLS runs were used as in some cases, due to the heating and cooling processes there were some obvious temperature equilibration issues for the first run.

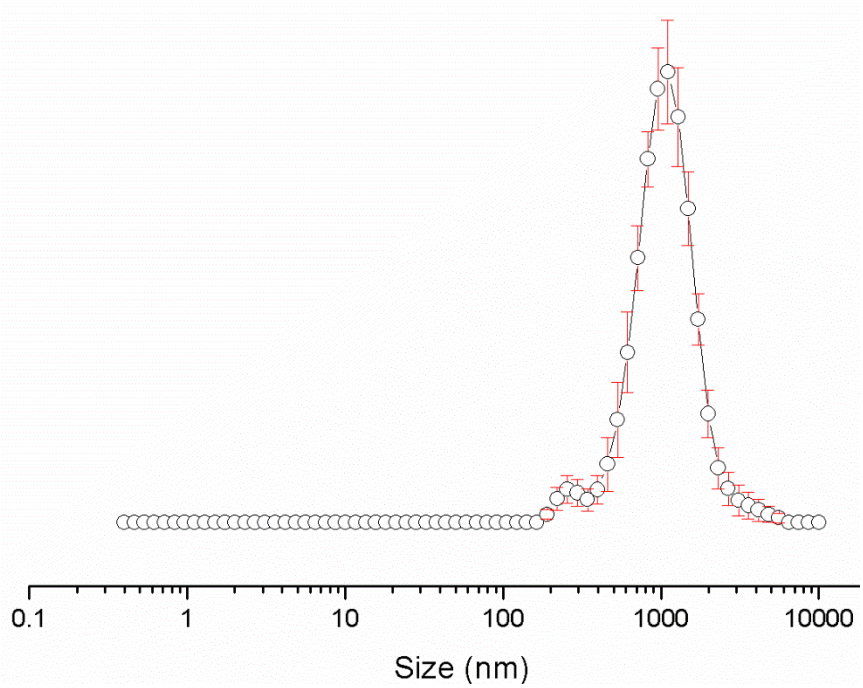

Figure S130 - Average intensity particle size distribution, calculated from 9 DLS runs, of aggregates formed by dissolving compound **1** at a concentration of 0.56 mM in a solution of DMSO: H_2O 1: 1, after heating to 40 ^oC and cooling to 25 ^oC. Only 9 of the available 10 DLS runs were used as in some cases, due to the heating and cooling processes there were some obvious temperature equilibration issues for the first run.

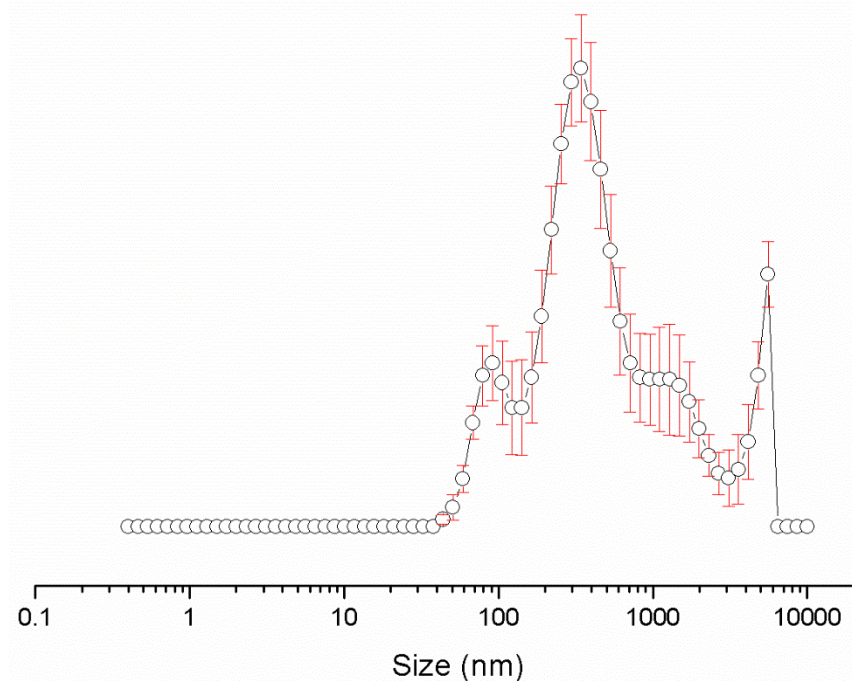

Figure S131 - Average intensity particle size distribution, calculated from 9 DLS runs, of aggregates formed by dissolving compound **1** at a concentration of 5.56 mM in a solution of DMSO: H_2O 3: 7, after heating to 40 ^oC and cooling to 25 ^oC. Only 9 of the available 10 DLS runs were used as in some cases, due to the heating and cooling processes there were some obvious temperature equilibration issues for the first run.

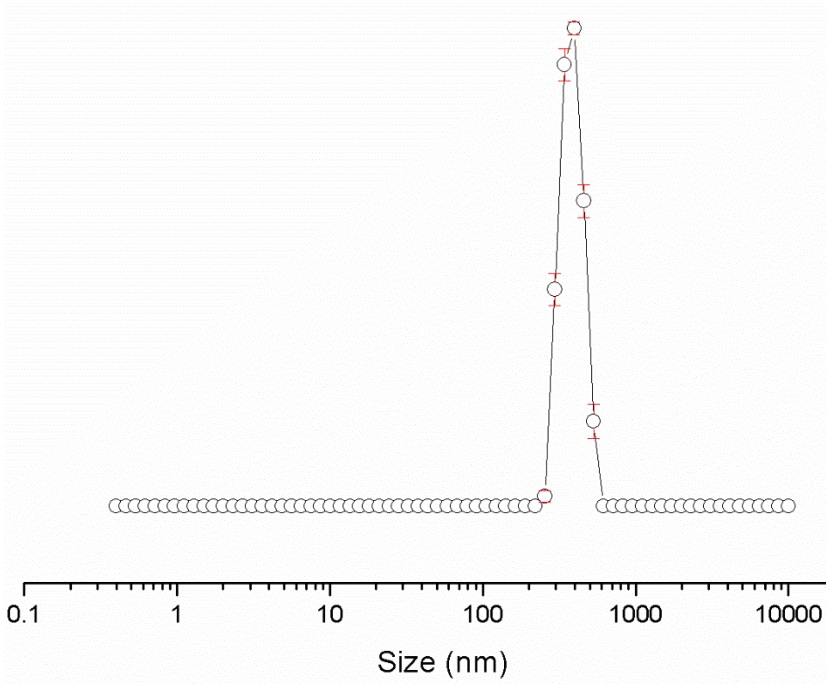

Figure S132 - Average intensity particle size distribution, calculated from 9 DLS runs, of aggregates formed by dissolving compound **1** at a concentration of 0.56 mM in a solution of DMSO: H_2O 3: 7, after heating to 40 ^oC and cooling to 25 ^oC. Only 9 of the available 10 DLS runs were used as in some cases, due to the heating and cooling processes there were some obvious temperature equilibration issues for the first run.

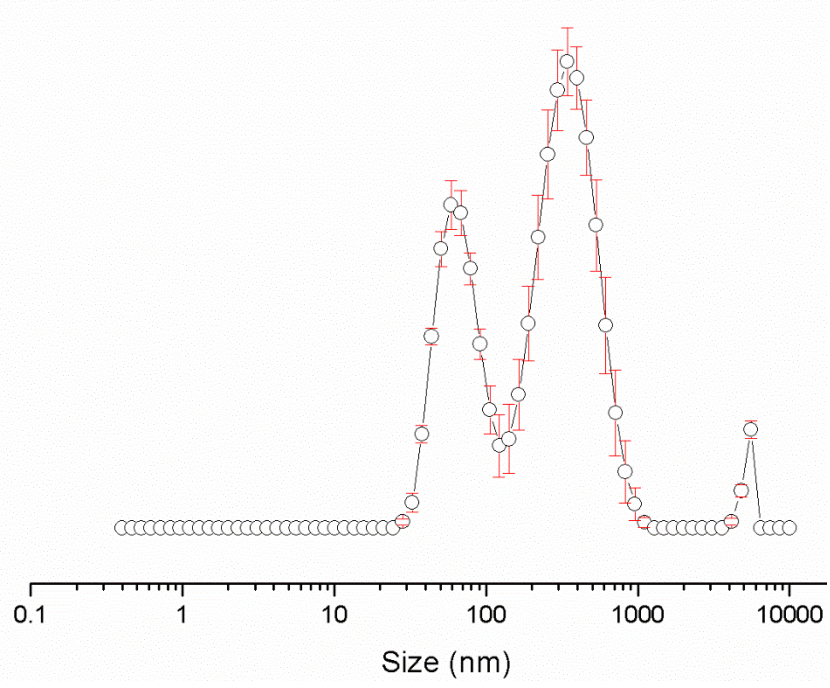

Figure S133 - Average intensity particle size distribution, calculated from 9 DLS runs, of aggregates formed by dissolving compound **1** at a concentration of 0.56 mM in a solution of DMSO: H_2O 1: 4, after heating to 40 ^oC and cooling to 25 ^oC. Only 9 of the available 10 DLS runs were used as in some cases, due to the heating and cooling processes there were some obvious temperature equilibration issues for the first run.

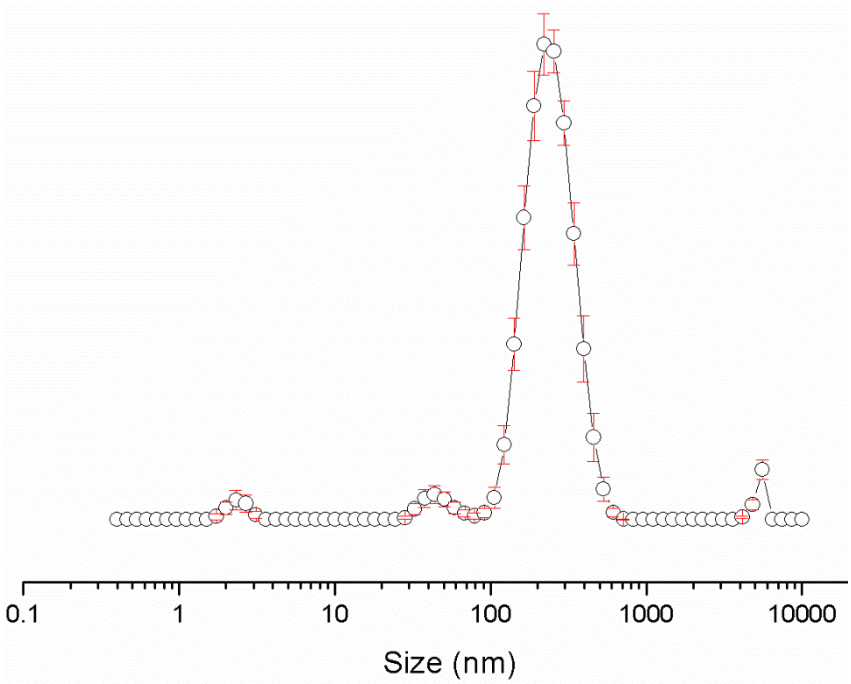

Figure S134 - Average intensity particle size distribution, calculated from 9 DLS runs, of aggregates formed by dissolving compound **1** at a concentration of 5.56 mM in a solution of EtOH: H_2O 1: 19, after heating to 40 ^oC and cooling to 25 ^oC. Only 9 of the available 10 DLS runs were used as in some cases, due to the heating and cooling processes there were some obvious temperature equilibration issues for the first run.

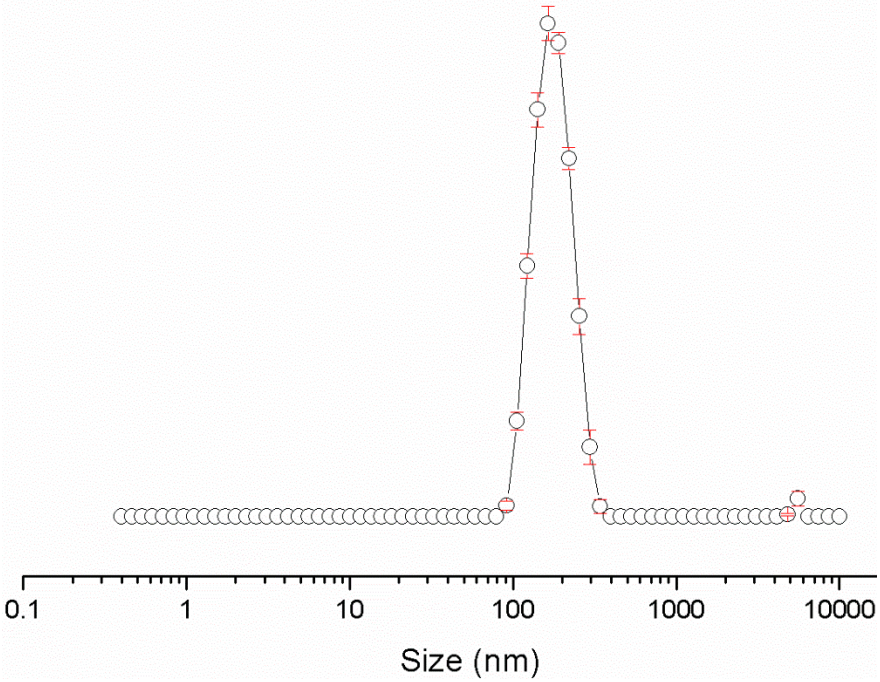

Figure S135 - Average intensity particle size distribution, calculated from 9 DLS runs, of aggregates formed by dissolving compound **1** at a concentration of 0.56 mM in a solution of EtOH: H_2O 1: 19, after heating to 40 ^oC and cooling to 25 ^oC. Only 9 of the available 10 DLS runs were used as in some cases, due to the heating and cooling processes there were some obvious temperature equilibration issues for the first run.

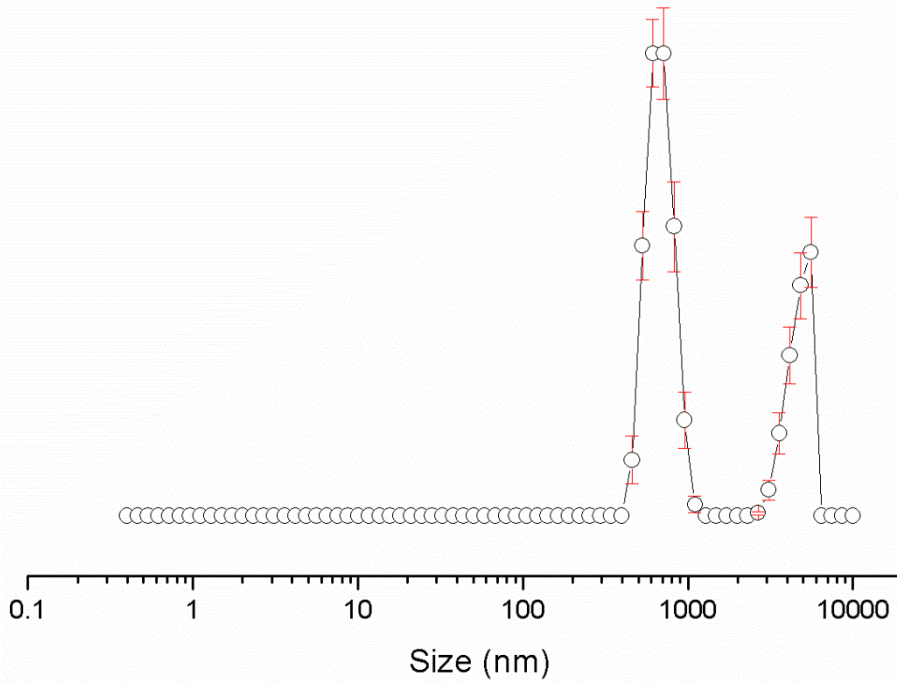

Figure S136 - Average intensity particle size distribution, calculated from 9 DLS runs, of aggregates formed by dissolving compound **2** at a concentration of 55.56 mM in a solution of DMSO: H_2O 1: 1, after heating to 40 ^oC and cooling to 25 ^oC. Only 9 of the available 10 DLS runs were used as in some cases, due to the heating and cooling processes there were some obvious temperature equilibration issues for the first run.

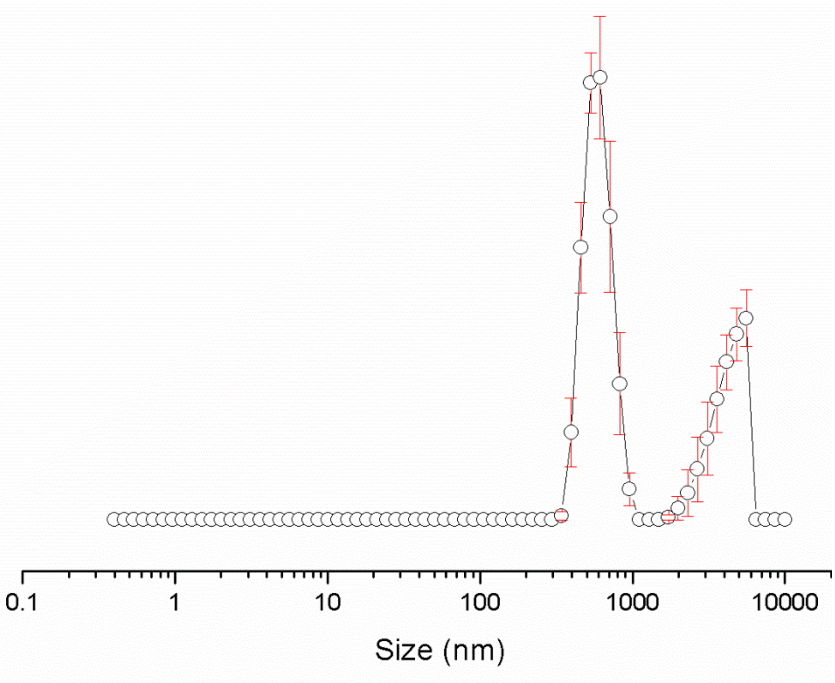

Figure S137 - Average intensity particle size distribution, calculated from 9 DLS runs, of aggregates formed by dissolving compound **2** at a concentration of 5.56 mM in a solution of DMSO: H_2O 1: 1, after heating to 40 ^oC and cooling to 25 ^oC. Only 9 of the available 10 DLS runs were used as in some cases, due to the heating and cooling processes there were some obvious temperature equilibration issues for the first run.

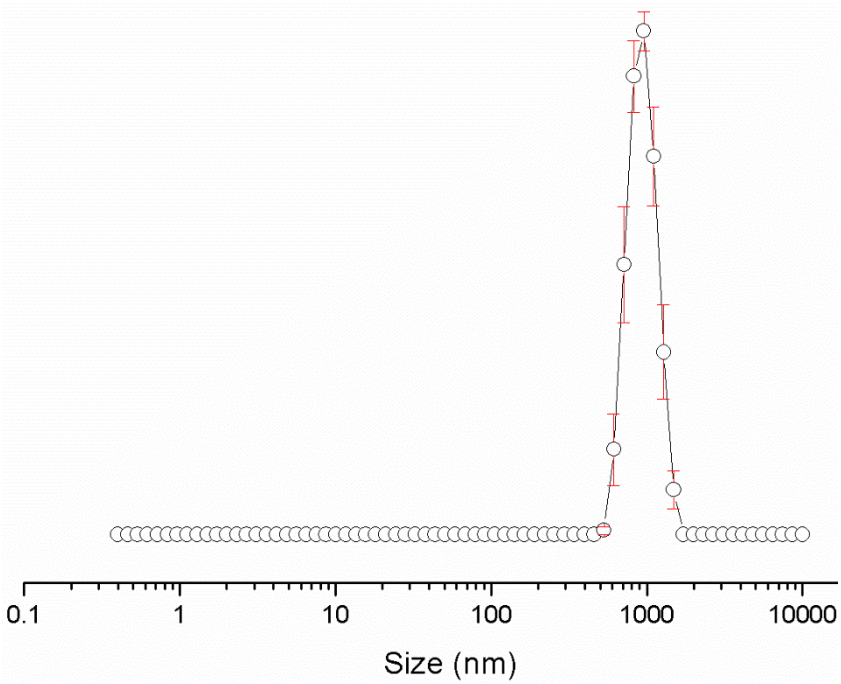

Figure S138 - Average intensity particle size distribution, calculated from 9 DLS runs, of aggregates formed by dissolving compound **2** at a concentration of 0.56 mM in a solution of DMSO: H_2O 1: 1, after heating to 40 ^oC and cooling to 25 ^oC. Only 9 of the available 10 DLS runs were used as in some cases, due to the heating and cooling processes there were some obvious temperature equilibration issues for the first run.

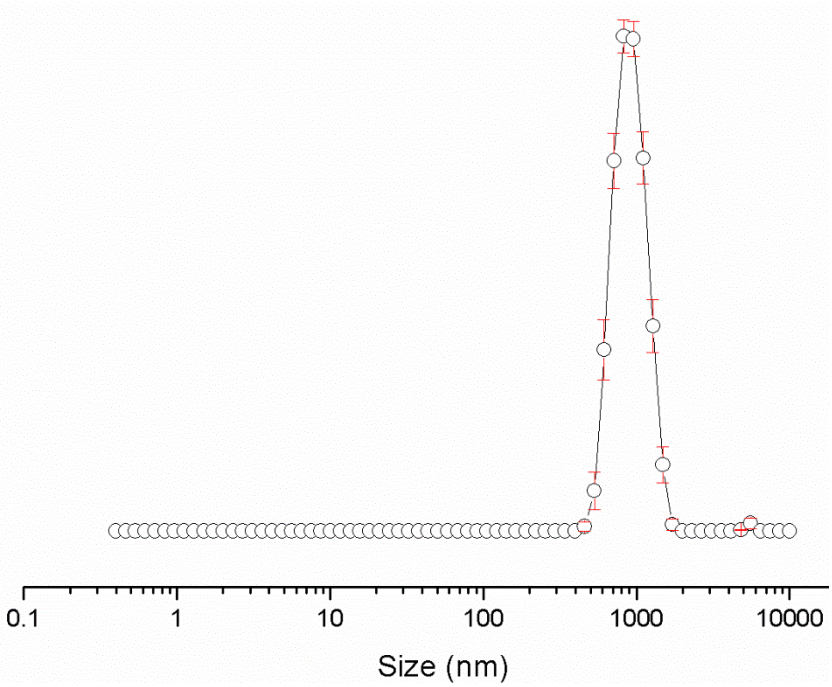

Figure S139 - Average intensity particle size distribution, calculated from 9 DLS runs, of aggregates formed by dissolving compound **2** at a concentration of 5.56 mM in a solution of DMSO: H_2O 3: 7, after heating to 40 ^oC and cooling to 25 ^oC. Only 9 of the available 10 DLS runs were used as in some cases, due to the heating and cooling processes there were some obvious temperature equilibration issues for the first run.

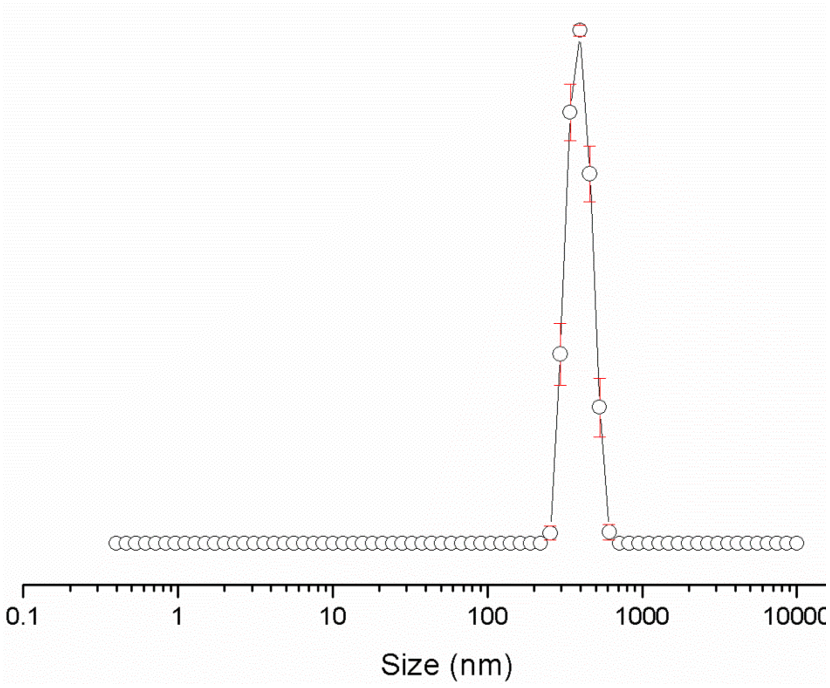

Figure S140 - Average intensity particle size distribution, calculated from 9 DLS runs, of aggregates formed by dissolving compound **2** at a concentration of 0.56 mM in a solution of DMSO: H_2O 3: 7, after heating to 40 ^oC and cooling to 25 ^oC. Only 9 of the available 10 DLS runs were used as in some cases, due to the heating and cooling processes there were some obvious temperature equilibration issues for the first run.

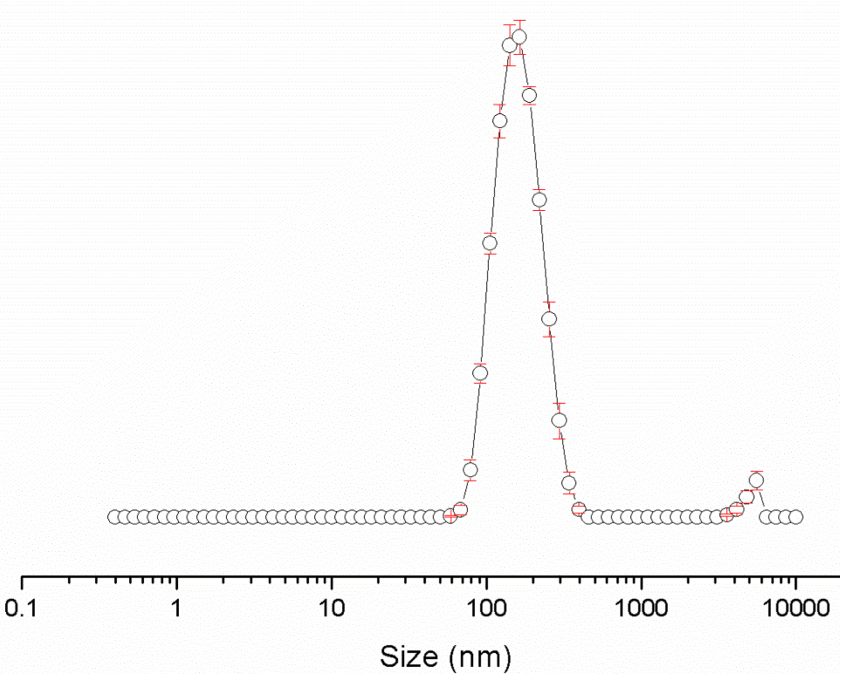

Figure S141 - Average intensity particle size distribution, calculated from 9 DLS runs, of aggregates formed by dissolving compound **2** at a concentration of 0.56 mM in a solution of DMSO: H_2O 1: 4, after heating to 40 ^oC and cooling to 25 ^oC. Only 9 of the available 10 DLS runs were used as in some cases, due to the heating and cooling processes there were some obvious temperature equilibration issues for the first run.

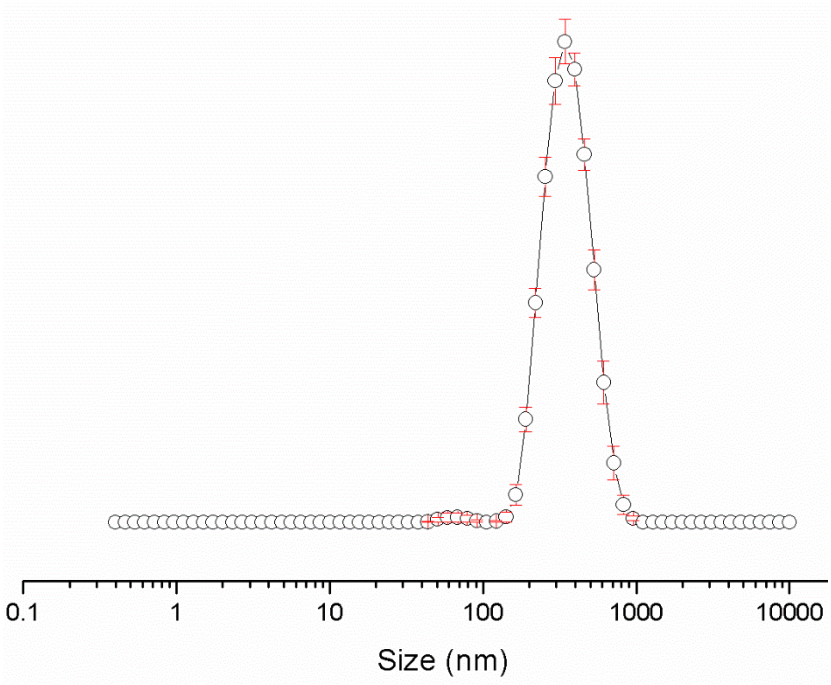

Figure S142 - Average intensity particle size distribution, calculated from 9 DLS runs, of aggregates formed by dissolving compound **2** at a concentration of 5.56 mM in a solution of EtOH: H_2O 1: 19, after heating to 40 ^oC and cooling to 25 ^oC. Only 9 of the available 10 DLS runs were used as in some cases, due to the heating and cooling processes there were some obvious temperature equilibration issues for the first run.

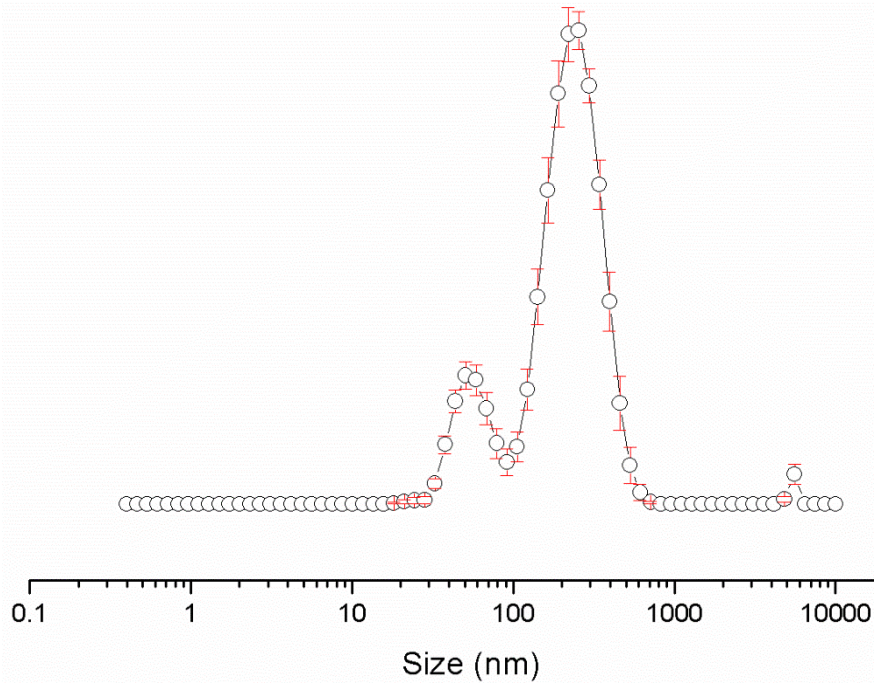

Figure S143 - Average intensity particle size distribution, calculated from 9 DLS runs, of aggregates formed by dissolving compound **2** at a concentration of 0.56 mM in a solution of EtOH: H_2O 1: 19, after heating to 40 ^oC and cooling to 25 ^oC. Only 9 of the available 10 DLS runs were used as in some cases, due to the heating and cooling processes there were some obvious temperature equilibration issues for the first run.

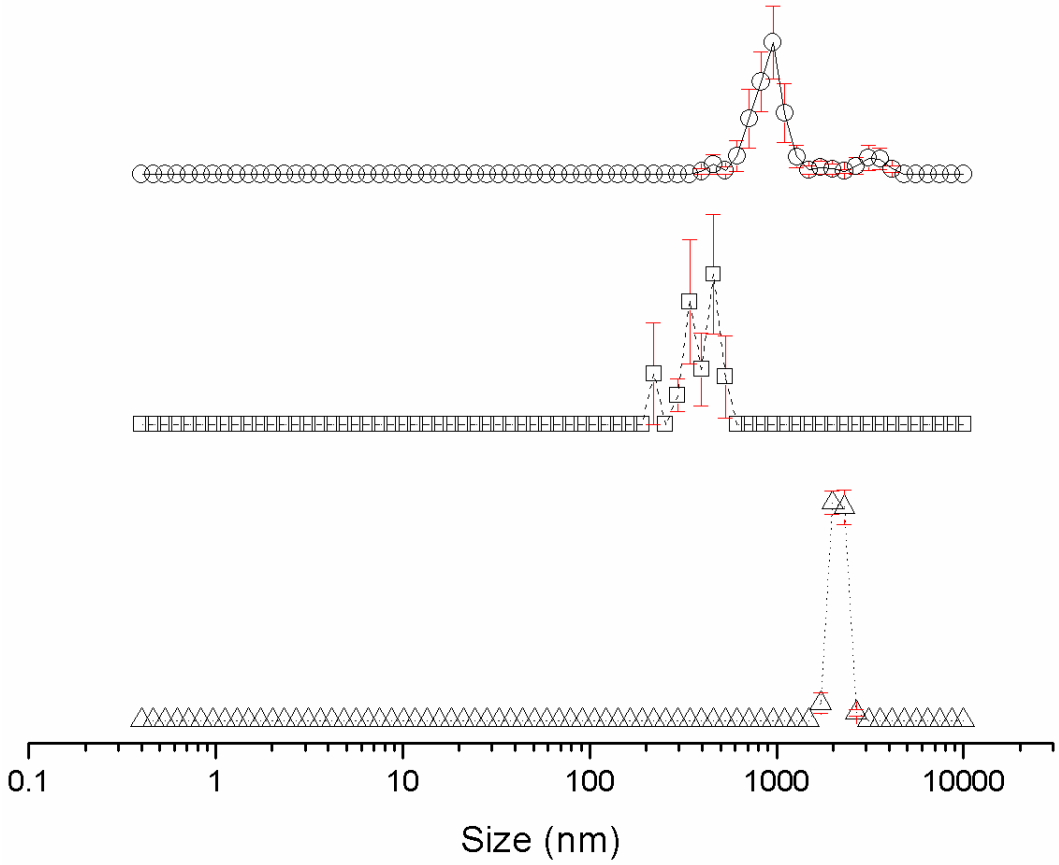

Figure S144 - Average intensity particle size distribution, calculated from 9 DLS runs, of aggregates formed by dissolving compound **3** at a concentration of 111.12 mM in DMSO at Δ) 25 ^{o}C, □) heating to 40 ^{o}C and ○) cooling to 25 ^{o}C. Only 9 of the available 10 DLS runs were used as in some cases, due to the heating and cooling processes there were some obvious temperature equilibration issues for the first run.

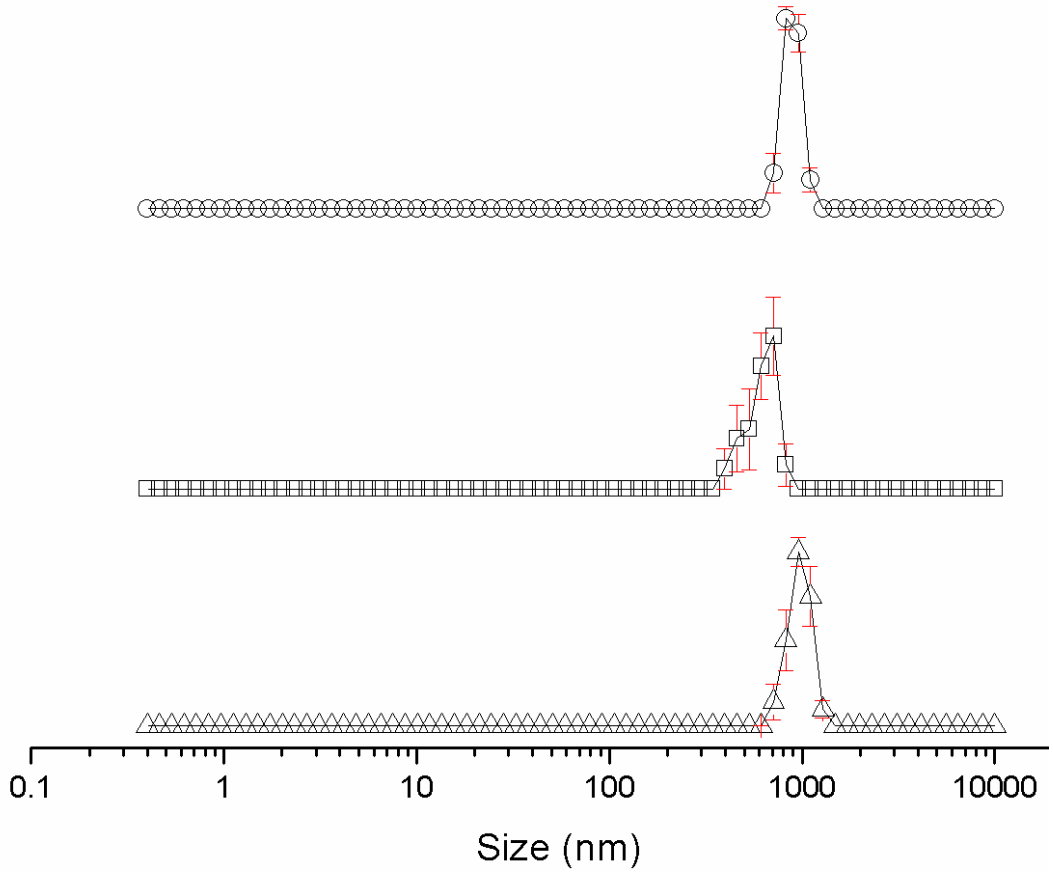

Figure S145 - Average intensity particle size distribution, calculated from 9 DLS runs, of aggregates formed by dissolving compound **3** at a concentration of 55.56 mM in DMSO at Δ) 25 ^{o}C, □) heating to 40 ^{o}C and ○) cooling to 25 ^{o}C. Only 9 of the available 10 DLS runs were used as in some cases, due to the heating and cooling processes there were some obvious temperature equilibration issues for the first run.

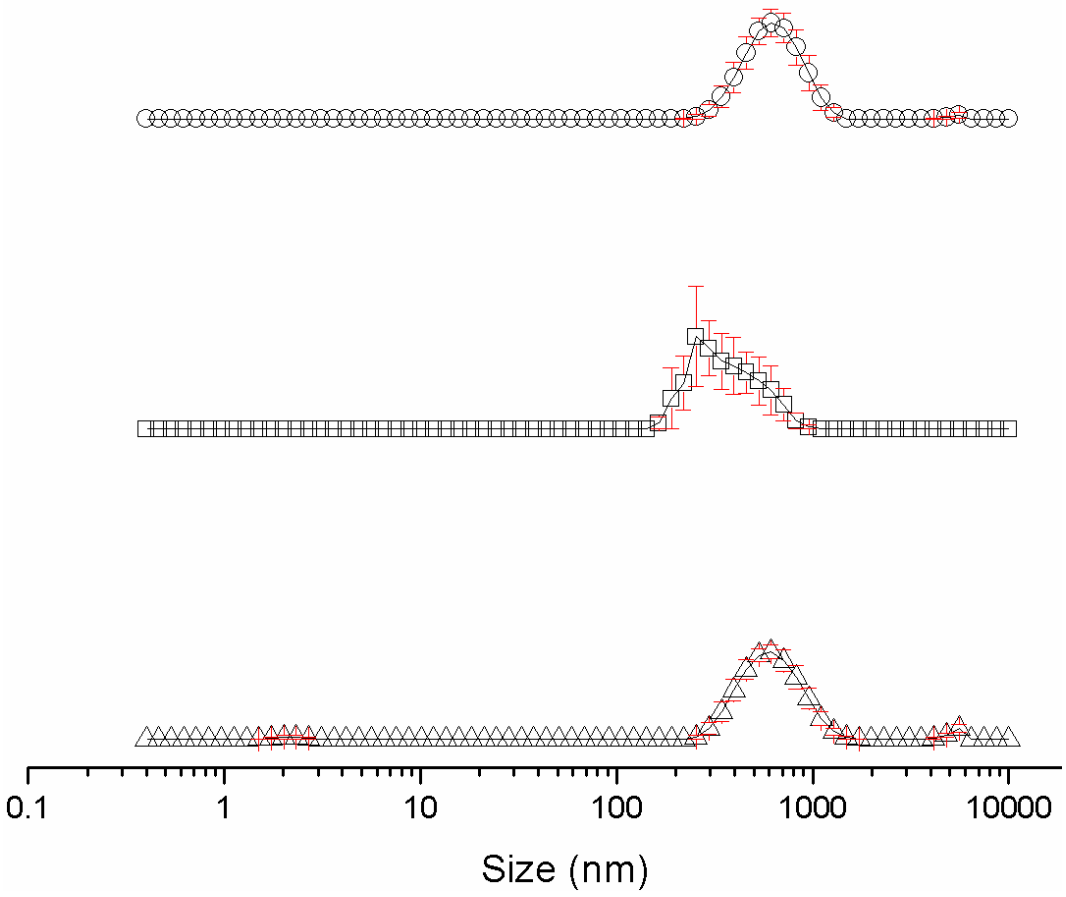

Figure S146 - Average intensity particle size distribution, calculated from 9 DLS runs, of aggregates formed by dissolving compound **3** at a concentration of 5.56 mM in DMSO at Δ) 25 ^{o}C, □) heating to 40 ^{o}C and ○) cooling to 25 ^{o}C. Only 9 of the available 10 DLS runs were used as in some cases, due to the heating and cooling processes there were some obvious temperature equilibration issues for the first run.

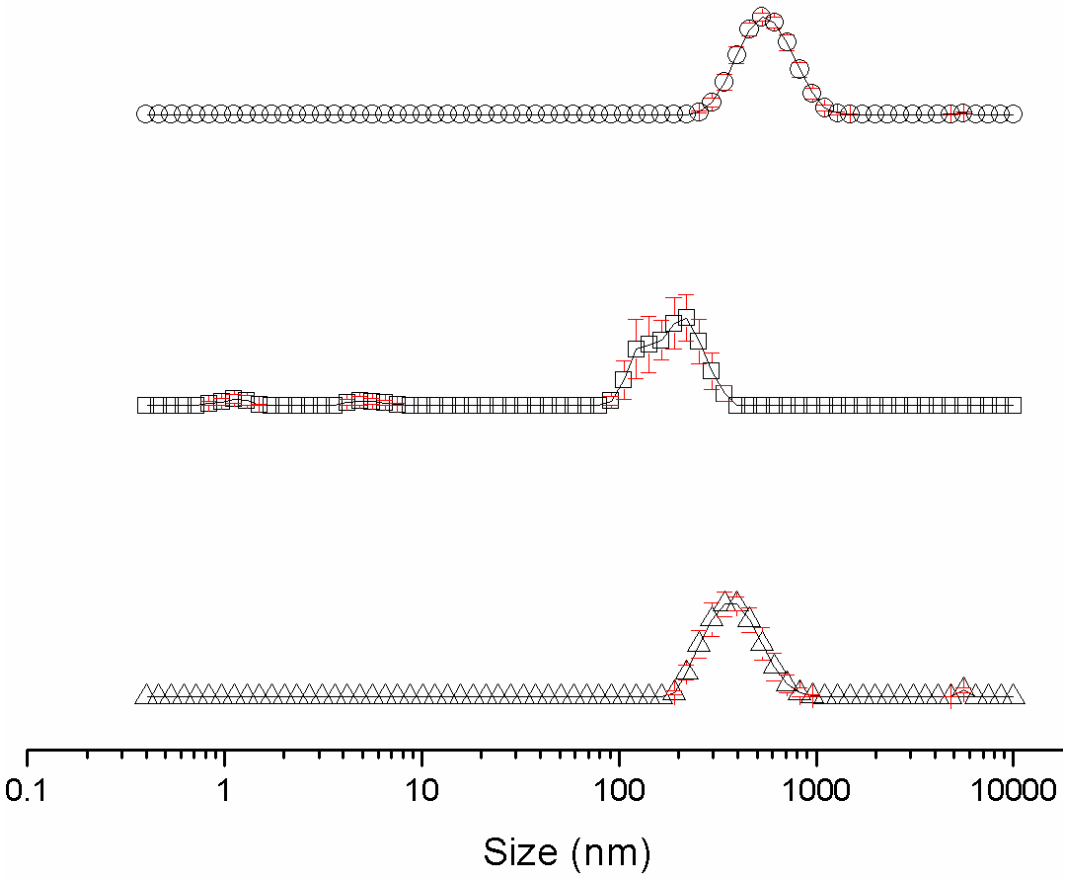

Figure S147 - Average intensity particle size distribution, calculated from 9 DLS runs, of aggregates formed by dissolving compound **3** at a concentration of 0.56 mM in DMSO at Δ) 25 ^{o}C, □) heating to 40 ^{o}C and ○) cooling to 25 ^{o}C. Only 9 of the available 10 DLS runs were used as in some cases, due to the heating and cooling processes there were some obvious temperature equilibration issues for the first run.

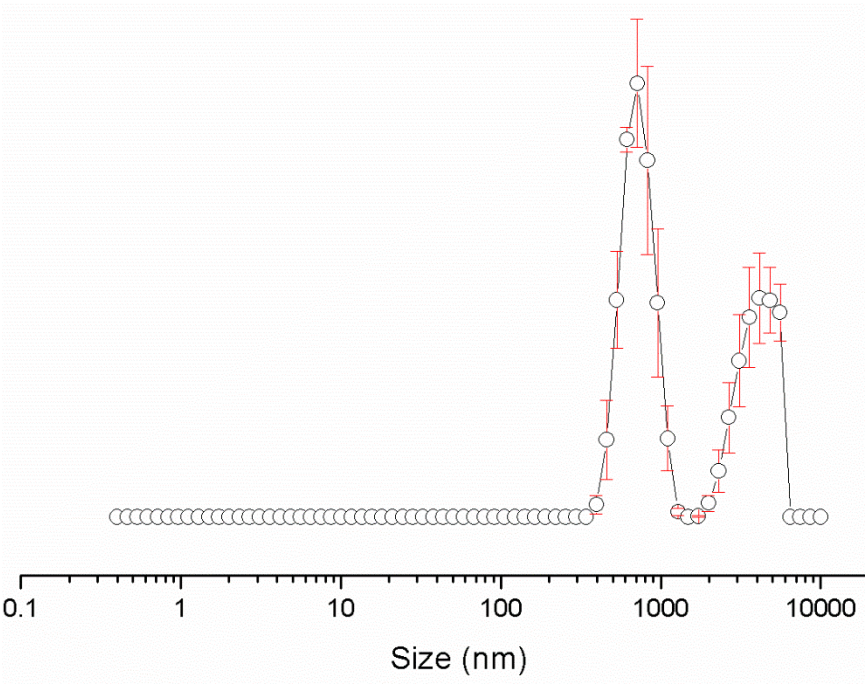

Figure S148 - Average intensity particle size distribution, calculated from 9 DLS runs, of aggregates formed by dissolving compound **3** at a concentration of 55.56 mM in a solution of DMSO: H_2O 1: 1, after heating to 40 ^oC and cooling to 25 ^oC. Only 9 of the available 10 DLS runs were used as in some cases, due to the heating and cooling processes there were some obvious temperature equilibration issues for the first run.

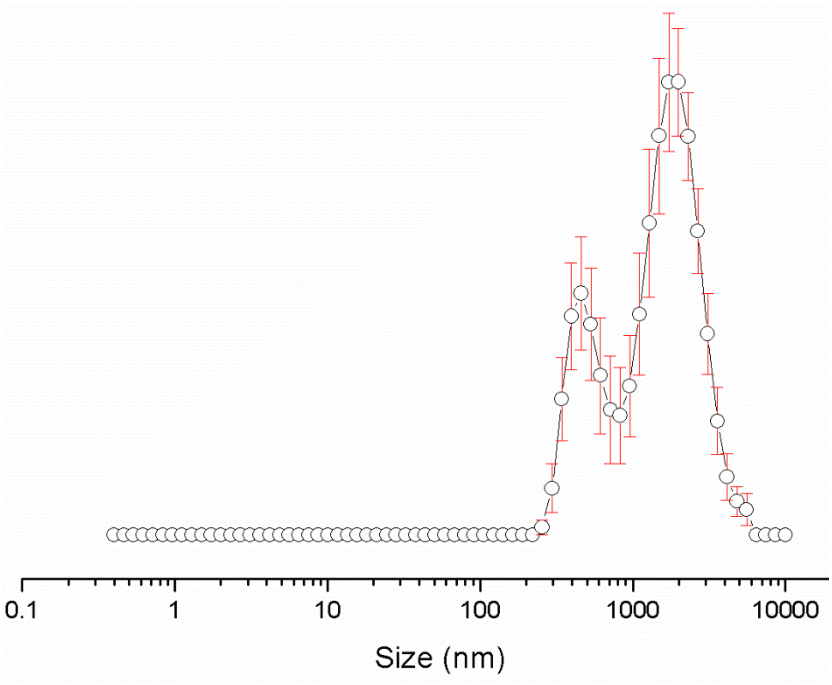

Figure S149 - Average intensity particle size distribution, calculated from 9 DLS runs, of aggregates formed by dissolving compound **3** at a concentration of 5.56 mM in a solution of DMSO: H_2O 1: 1, after heating to 40 ^oC and cooling to 25 ^oC. Only 9 of the available 10 DLS runs were used as in some cases, due to the heating and cooling processes there were some obvious temperature equilibration issues for the first run.

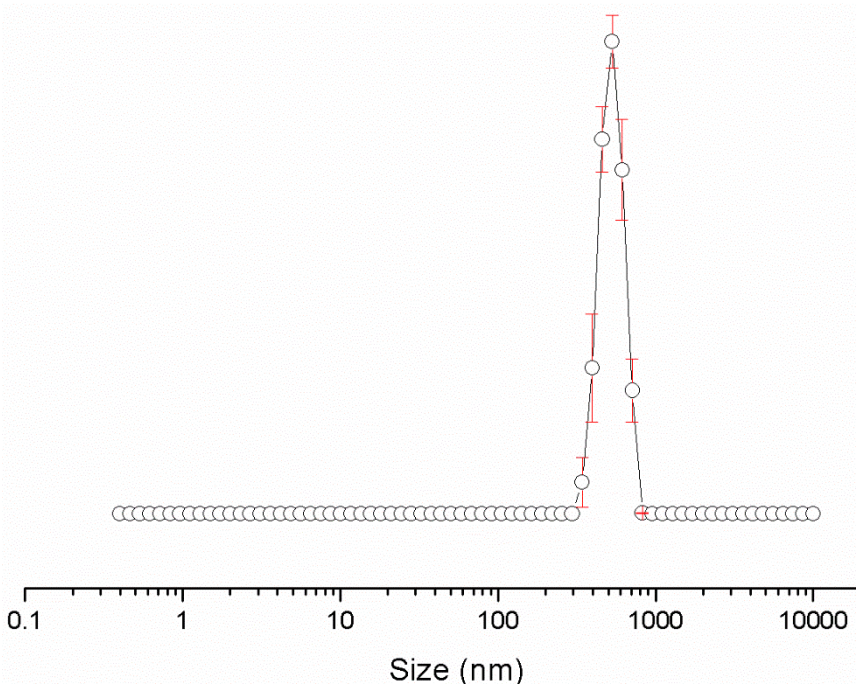

Figure S150 - Average intensity particle size distribution, calculated from 9 DLS runs, of aggregates formed by dissolving compound **3** at a concentration of 0.56 mM in a solution of DMSO: H_2O 1: 1, after heating to 40 ^oC and cooling to 25 ^oC. Only 9 of the available 10 DLS runs were used as in some cases, due to the heating and cooling processes there were some obvious temperature equilibration issues for the first run.

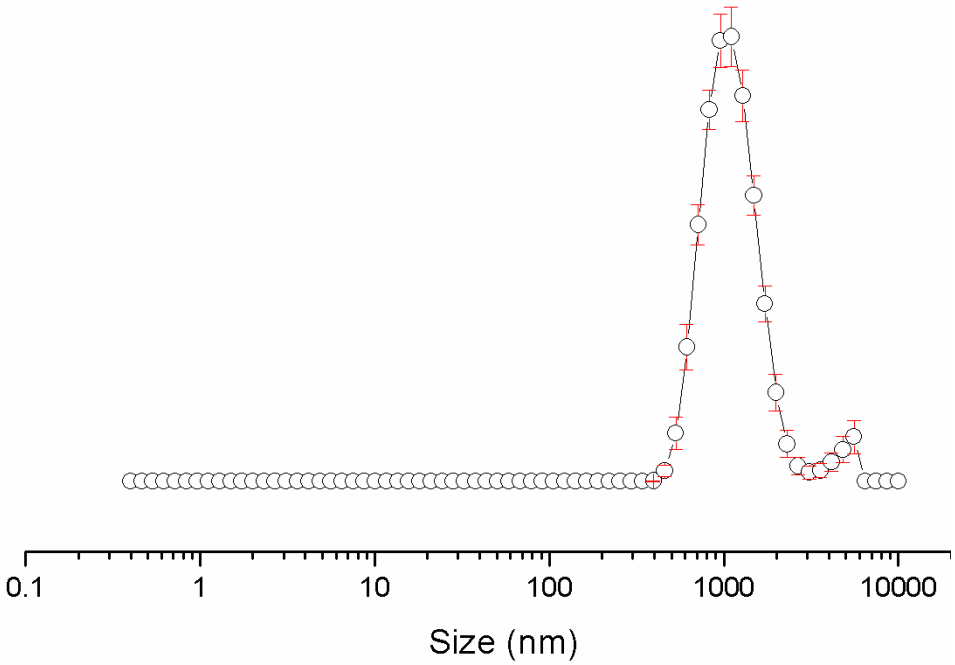

Figure S151 - Average intensity particle size distribution, calculated from 9 DLS runs, of aggregates formed by dissolving compound **3** at a concentration of 5.56 mM in a solution of DMSO: H_2O 3: 7, after heating to 40 ^oC and cooling to 25 ^oC. Only 9 of the available 10 DLS runs were used as in some cases, due to the heating and cooling processes there were some obvious temperature equilibration issues for the first run.

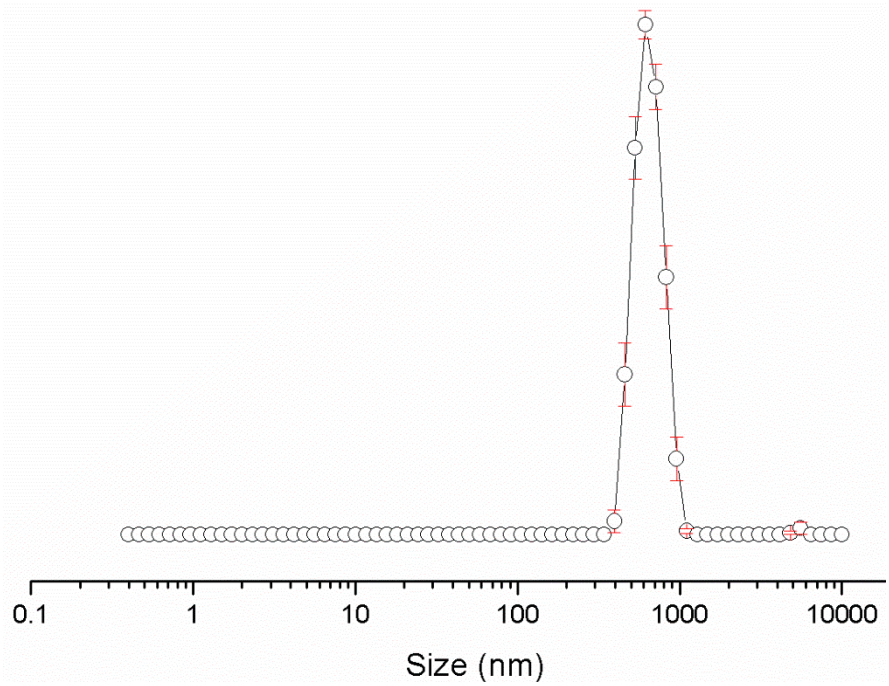

Figure S152 - Average intensity particle size distribution, calculated from 9 DLS runs, of aggregates formed by dissolving compound **3** at a concentration of 0.56 mM in a solution of DMSO: H_2O 3: 7, after heating to 40 ^oC and cooling to 25 ^oC. Only 9 of the available 10 DLS runs were used as in some cases, due to the heating and cooling processes there were some obvious temperature equilibration issues for the first run.

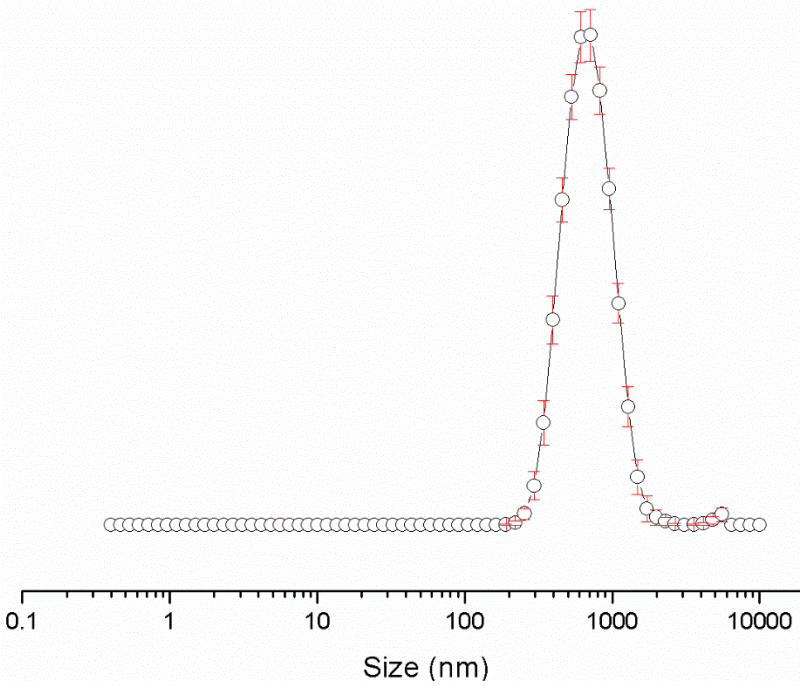

Figure S153 - Average intensity particle size distribution, calculated from 9 DLS runs, of aggregates formed by dissolving compound **3** at a concentration of 0.56 mM in a solution of DMSO: H_2O 1: 4, after heating to 40 ^oC and cooling to 25 ^oC. Only 9 of the available 10 DLS runs were used as in some cases, due to the heating and cooling processes there were some obvious temperature equilibration issues for the first run.

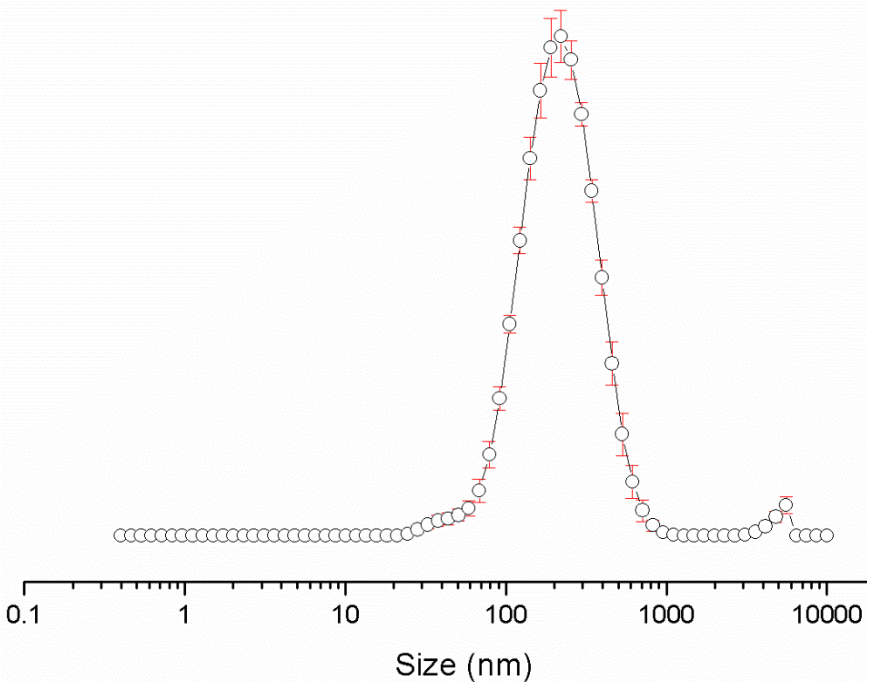

Figure S154 - Average intensity particle size distribution, calculated from 9 DLS runs, of aggregates formed by dissolving compound **3** at a concentration of 5.56 mM in a solution of EtOH: H_2O 1: 19 after heating to 40 ^oC and cooling to 25 ^oC. Only 9 of the available 10 DLS runs were used as in some cases, due to the heating and cooling processes there were some obvious temperature equilibration issues for the first run.

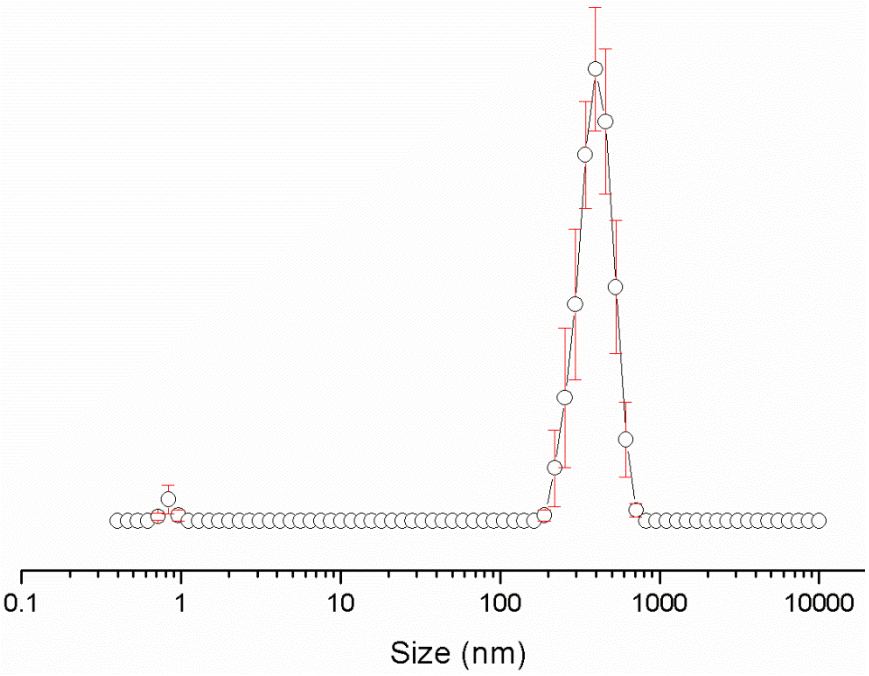

Figure S155 - Average intensity particle size distribution, calculated from 9 DLS runs, of aggregates formed by dissolving compound **3** at a concentration of 0.56 mM in a solution of EtOH: H_2O 1: 19, after heating to 40 ^oC and cooling to 25 ^oC. Only 9 of the available 10 DLS runs were used as in some cases, due to the heating and cooling processes there were some obvious temperature equilibration issues for the first run.

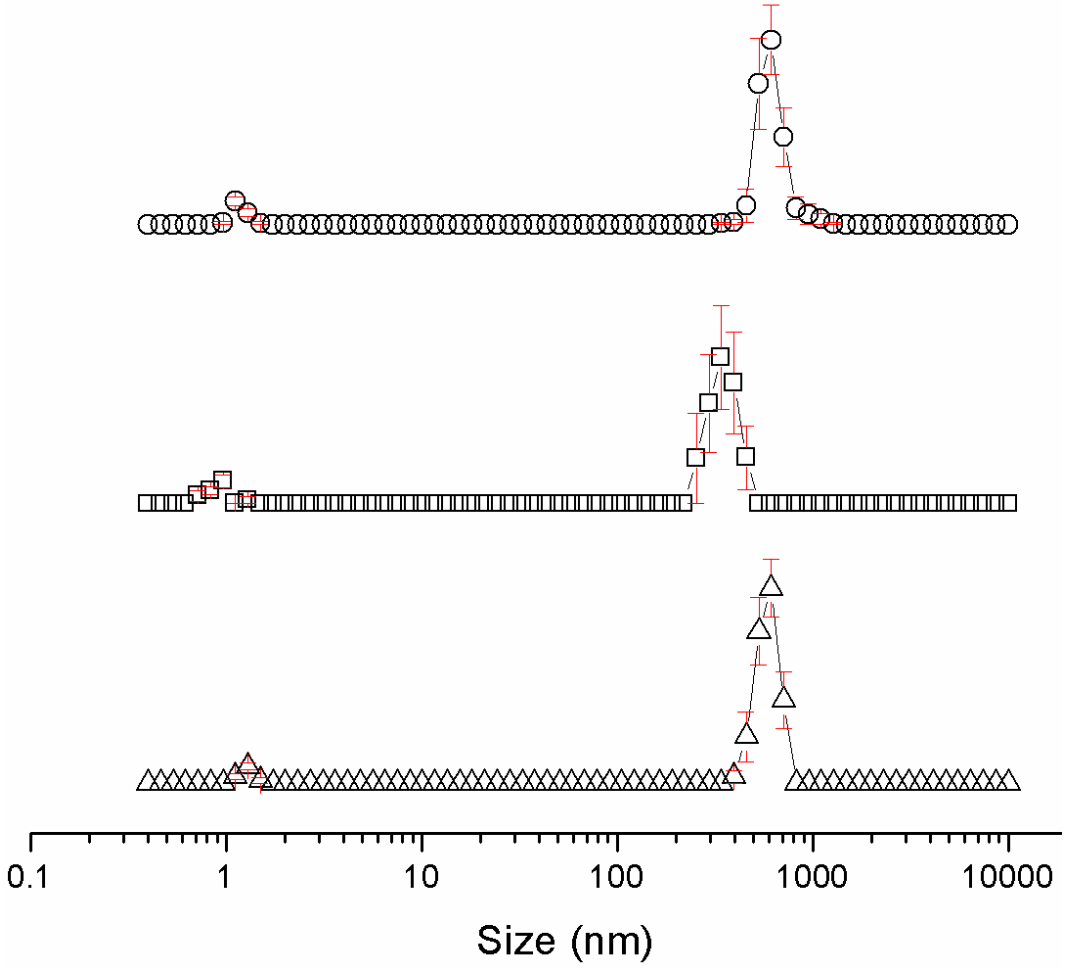

Figure S156 - Average intensity particle size distribution, calculated from 9 DLS runs, of aggregates formed by dissolving compound **4** at a concentration of 111.12 mM in DMSO (1 mL) at Δ) 25 ^{o}C, □) heating to 40 ^{o}C and ○) cooling to 25 ^{o}C. Only 9 of the available 10 DLS runs were used as in some cases, due to the heating and cooling processes there were some obvious temperature equilibration issues for the first run.

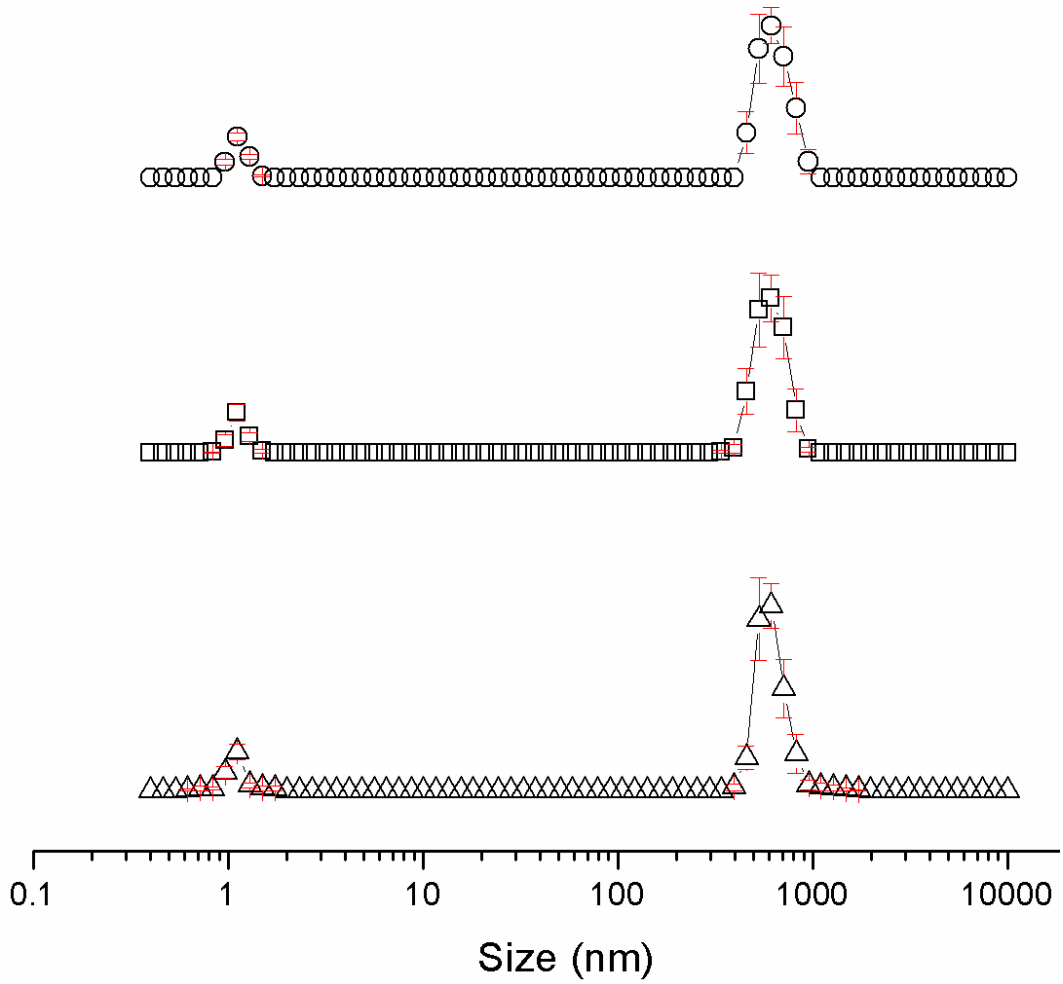

Figure S157 - Average intensity particle size distribution, calculated from 9 DLS runs, of aggregates formed by dissolving compound **4** at a concentration of 55.56 mM in DMSO at Δ) 25 ^{o}C, □) heating to 40 ^{o}C and ○) cooling to 25 ^{o}C. Only 9 of the available 10 DLS runs were used as in some cases, due to the heating and cooling processes there were some obvious temperature equilibration issues for the first run.

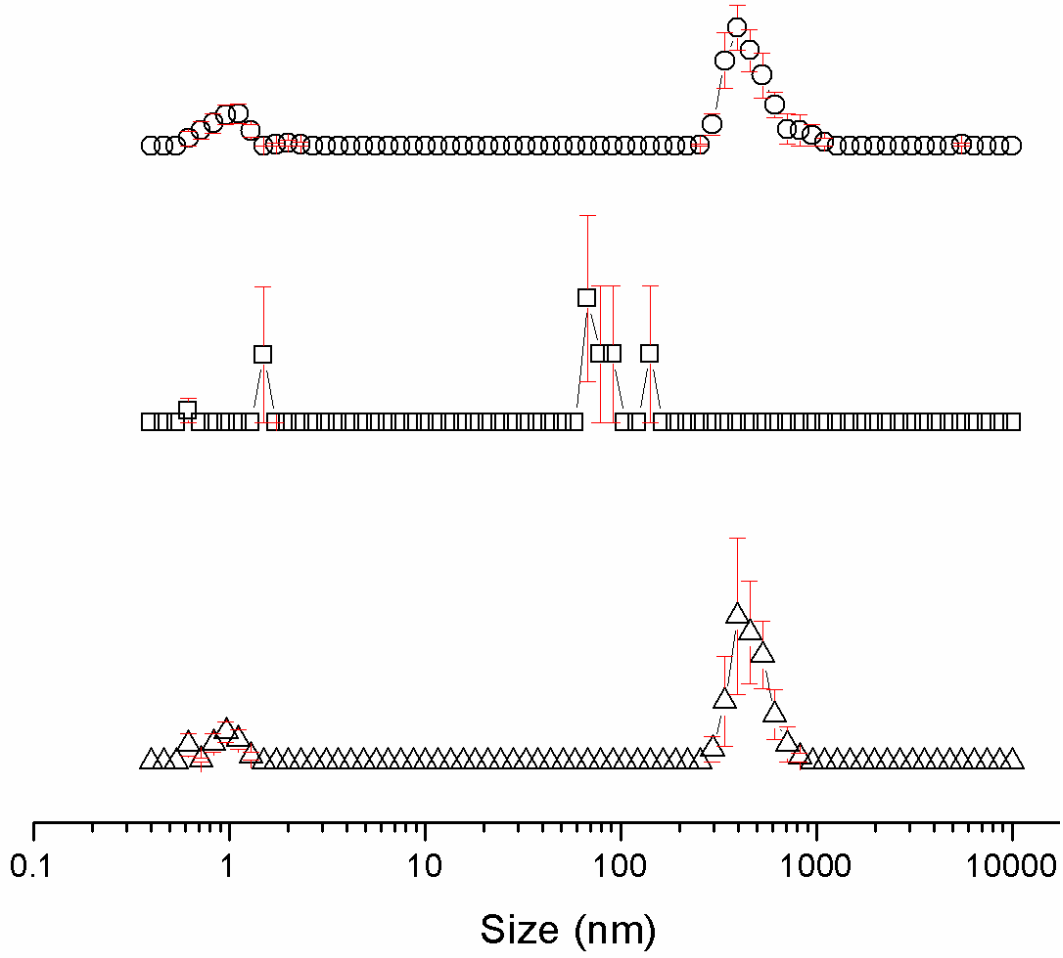

Figure S158 - Average intensity particle size distribution, calculated from 9 DLS runs, of aggregates formed by dissolving compound **4** at a concentration of 5.56 mM in DMSO at Δ) 25 ^{o}C, □) heating to 40 ^{o}C and ○) cooling to 25 ^{o}C. Only 9 of the available 10 DLS runs were used as in some cases, due to the heating and cooling processes there were some obvious temperature equilibration issues for the first run.

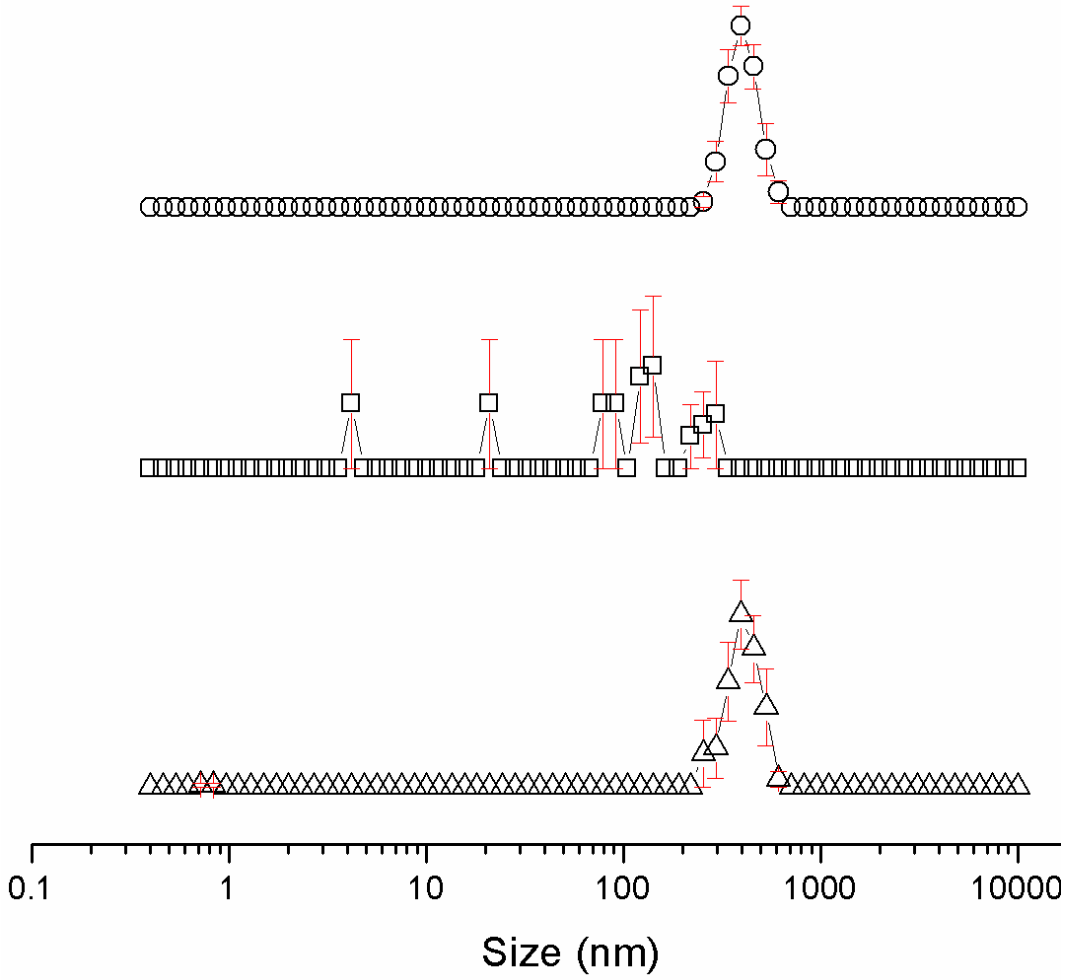

Figure S159 - Average intensity particle size distribution, calculated from 9 DLS runs, of aggregates formed by dissolving compound **4** at a concentration of O.56 mM in DMSO at Δ) 25 ^{o}C, □) heating to 40 ^{o}C and ○) cooling to 25 ^{o}C. Only 9 of the available 10 DLS runs were used as in some cases, due to the heating and cooling processes there were some obvious temperature equilibration issues for the first run.

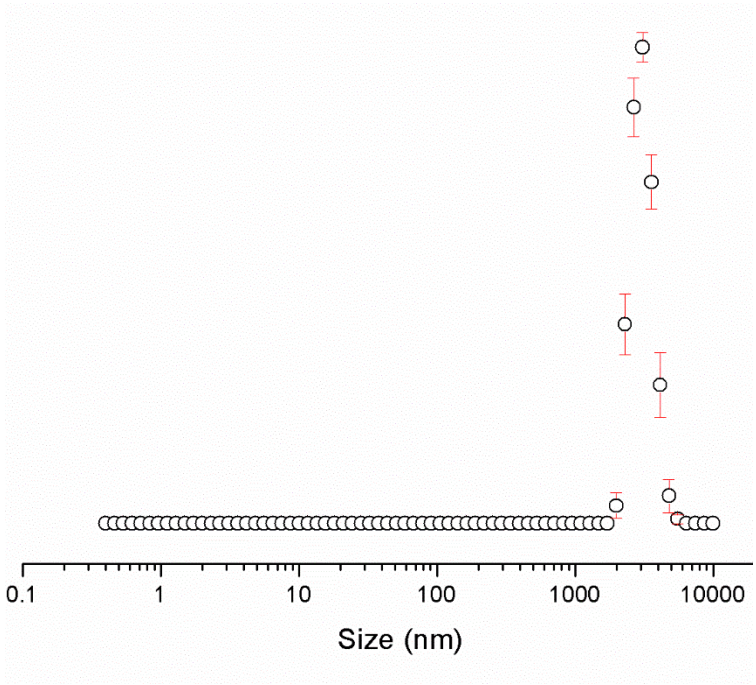

Figure S160 - Average intensity particle size distribution, calculated from 9 DLS runs, of aggregates formed by dissolving compound **4** at a concentration of 55.56 mM in a solution of DMSO 1: 1 H_2O, after heating to 40 ^oC and cooling to 25 ^oC. Only 9 of the available 10 DLS runs were used as in some cases, due to the heating and cooling processes there were some obvious temperature equilibration issues for the first run.

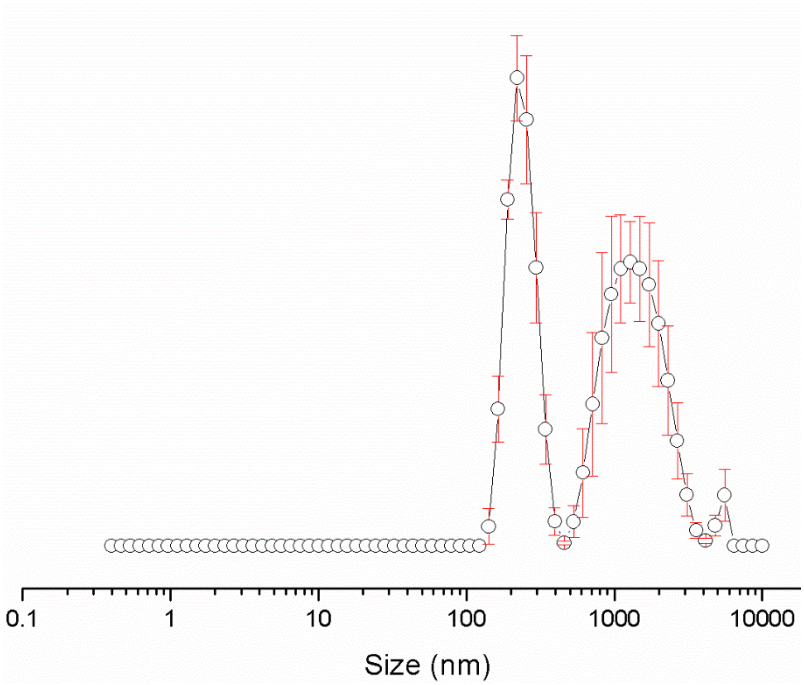

Figure S161 - Average intensity particle size distribution, calculated from 9 DLS runs, of aggregates formed by dissolving compound **4** at a concentration of 5.56 mM in a solution of DMSO: H_2O 1: 1, after heating to 40 ^oC and cooling to 25 ^oC. Only 9 of the available 10 DLS runs were used as in some cases, due to the heating and cooling processes there were some obvious temperature equilibration issues for the first run.

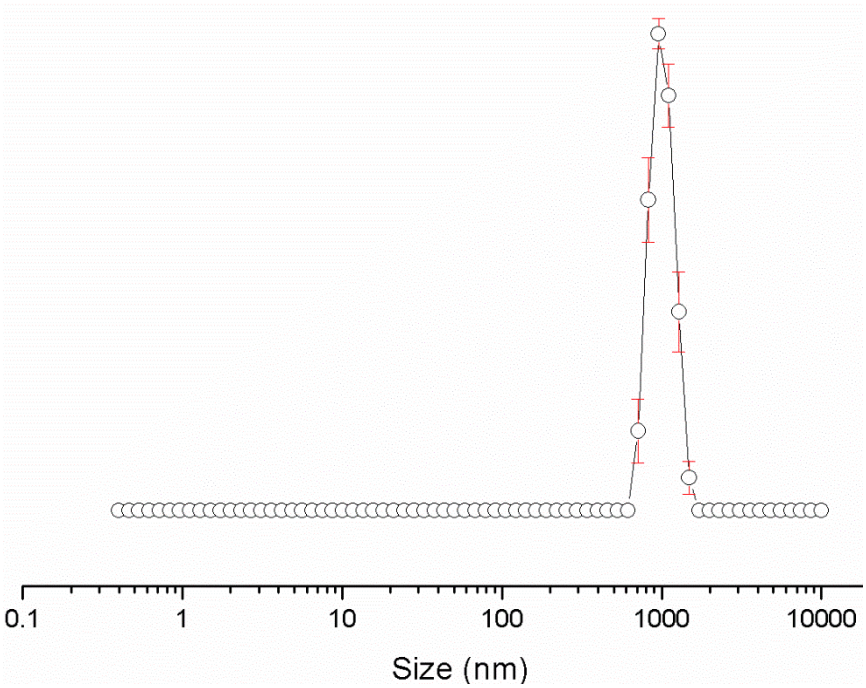

Figure S162 - Average intensity particle size distribution, calculated from 9 DLS runs, of aggregates formed by dissolving compound **4** at a concentration of 0.56 mM in a solution of DMSO: H_2O 1: 1, after heating to 40 ^oC and cooling to 25 ^oC. Only 9 of the available 10 DLS runs were used as in some cases, due to the heating and cooling processes there were some obvious temperature equilibration issues for the first run.

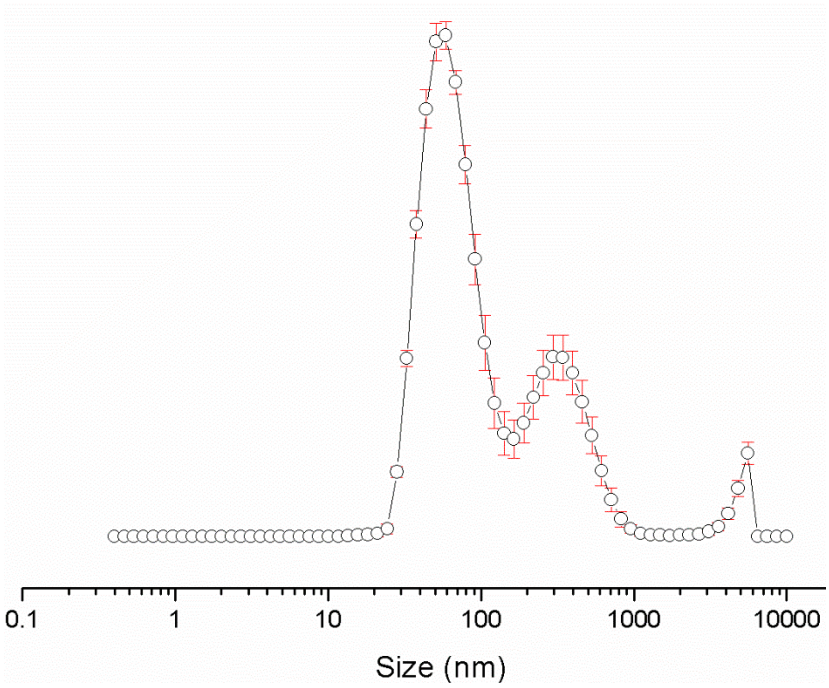

Figure S163 - Average intensity particle size distribution, calculated from 9 DLS runs, of aggregates formed by dissolving compound **4** at a concentration of 5.56 mM in a solution of DMSO: H_2O 3: 7, after heating to 40 ^oC and cooling to 25 ^oC. Only 9 of the available 10 DLS runs were used as in some cases, due to the heating and cooling processes there were some obvious temperature equilibration issues for the first run.

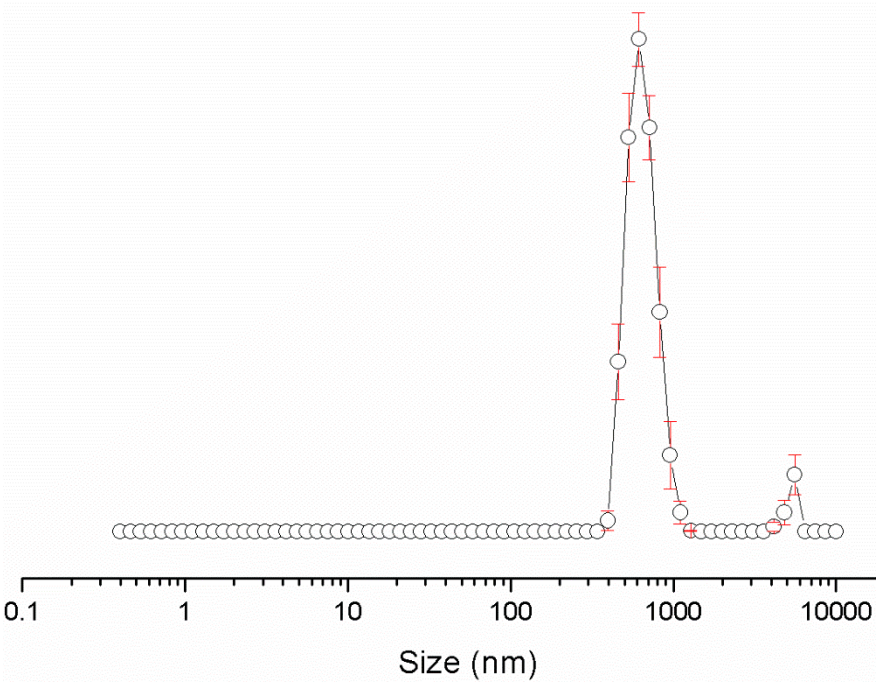

Figure S164 - Average intensity particle size distribution, calculated from 9 DLS runs, of aggregates formed by dissolving compound **4** at a concentration of 0.56 mM in a solution of DMSO: H_2O 3: 7, after heating to 40 ^oC and cooling to 25 ^oC. Only 9 of the available 10 DLS runs were used as in some cases, due to the heating and cooling processes there were some obvious temperature equilibration issues for the first run.

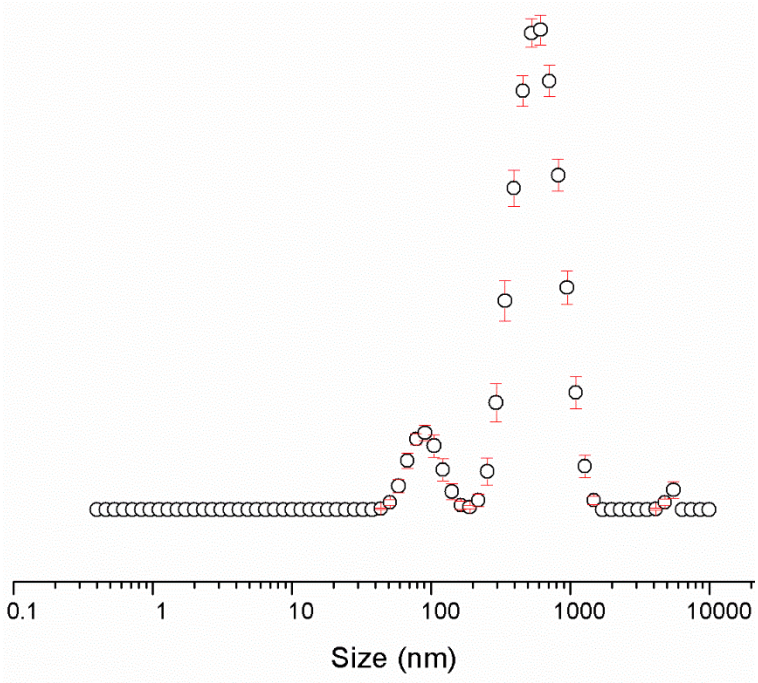

Figure S165 - Average intensity particle size distribution, calculated from 9 DLS runs, of aggregates formed by dissolving compound **4** at a concentration of 0.56 mM in a solution of DMSO: H_2O 1: 4, after heating to 40 ^oC and cooling to 25 ^oC. Only 9 of the available 10 DLS runs were used as in some cases, due to the heating and cooling processes there were some obvious temperature equilibration issues for the first run.

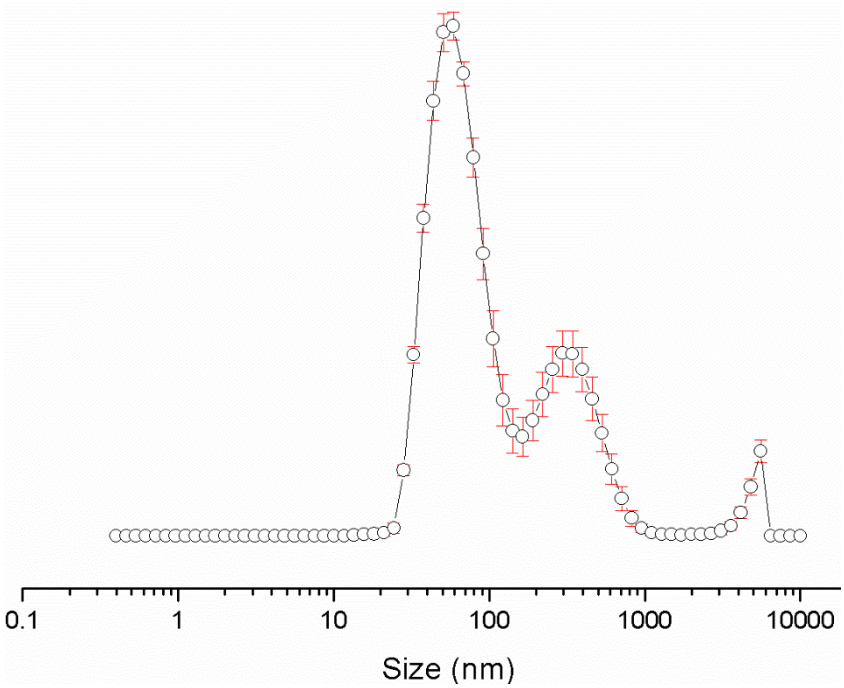

Figure S166 - Average intensity particle size distribution, calculated from 9 DLS runs, of aggregates formed by dissolving compound **4** at a concentration of 5.56 mM in a solution of EtOH: H_2O 1: 19, after heating to 40 ^oC and cooling to 25 ^oC. Only 9 of the available 10 DLS runs were used as in some cases, due to the heating and cooling processes there were some obvious temperature equilibration issues for the first run.

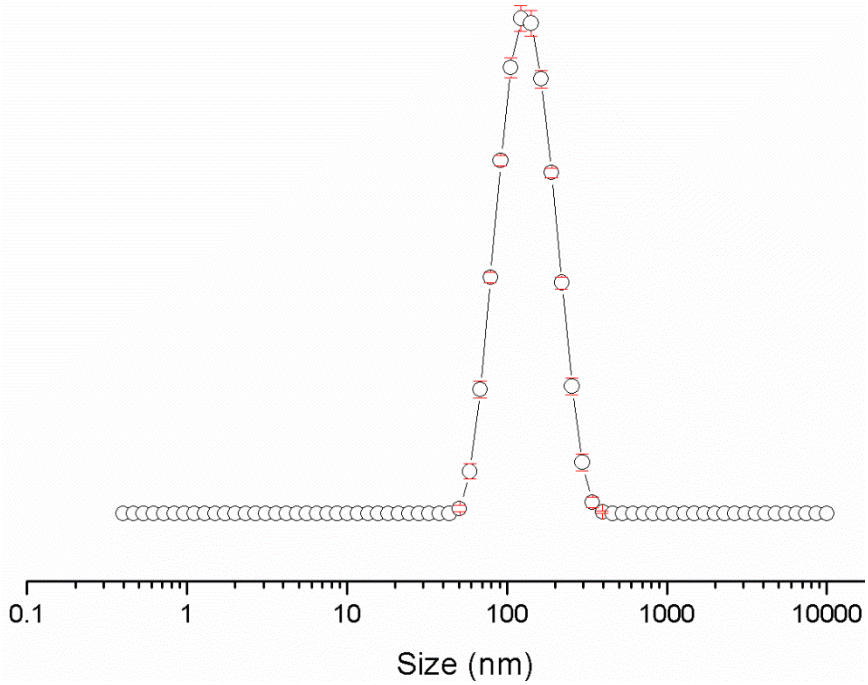

Figure S167 - Average intensity particle size distribution, calculated from 9 DLS runs, of aggregates formed by dissolving compound **4** at a concentration of 0.56 mM in a solution of EtOH: H_2O 1: 19, after heating to 40 ^oC and cooling to 25 ^oC. Only 9 of the available 10 DLS runs were used as in some cases, due to the heating and cooling processes there were some obvious temperature equilibration issues for the first run.

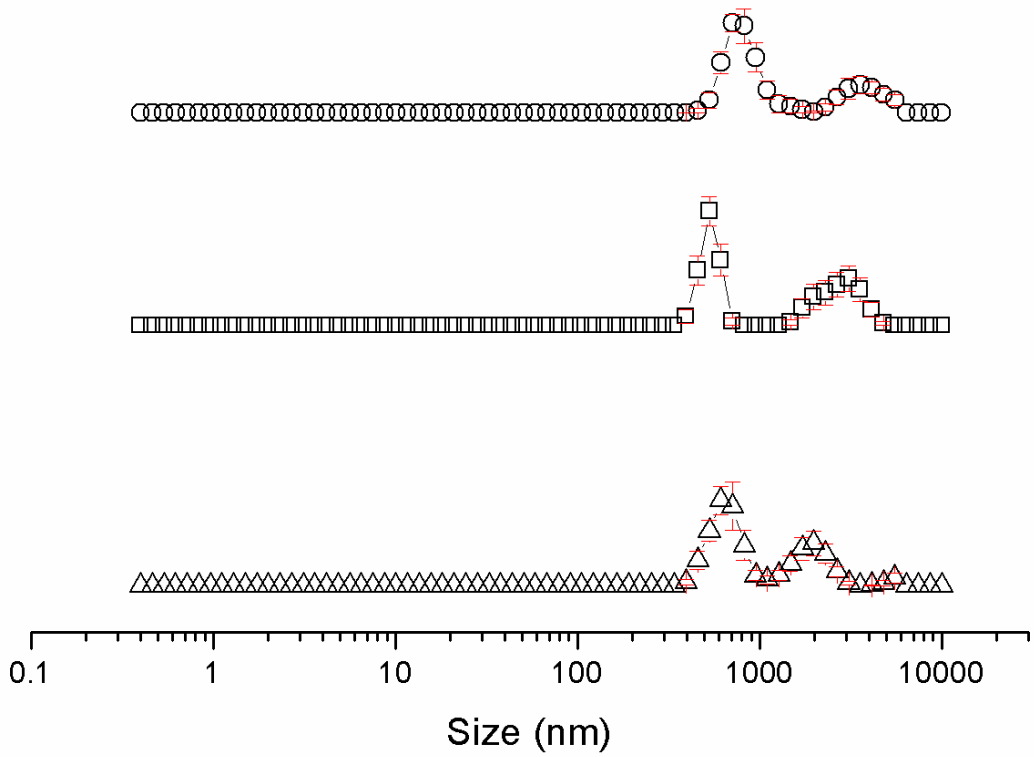

Figure S168 - Average intensity particle size distribution, calculated from 9 DLS runs, of aggregates formed by dissolving compound **5** at a concentration of 111.12 mM in DMSO at Δ) 25 °C, □) heating to 40 °C and ○) cooling to 25 °C. Only 9 of the available 10 DLS runs were used as in some cases, due to the heating and cooling processes there were some obvious temperature equilibration issues for the first run.

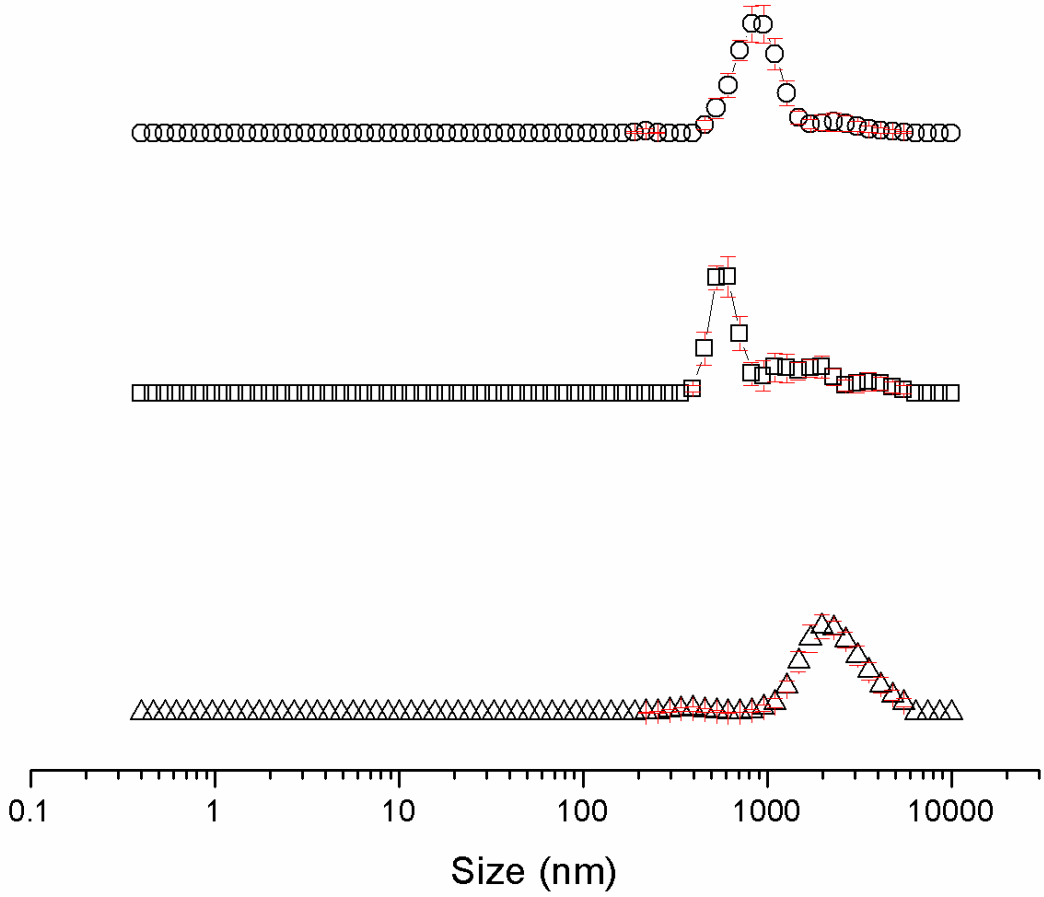

Figure S169 - Average intensity particle size distribution, calculated from 9 DLS runs, of aggregates formed by dissolving compound **5** at a concentration of 55.56 mM in DMSO at Δ) 25 ^{o}C, □) heating to 40 ^{o}C and ○) cooling to 25 ^{o}C. Only 9 of the available 10 DLS runs were used as in some cases, due to the heating and cooling processes there were some obvious temperature equilibration issues for the first run.

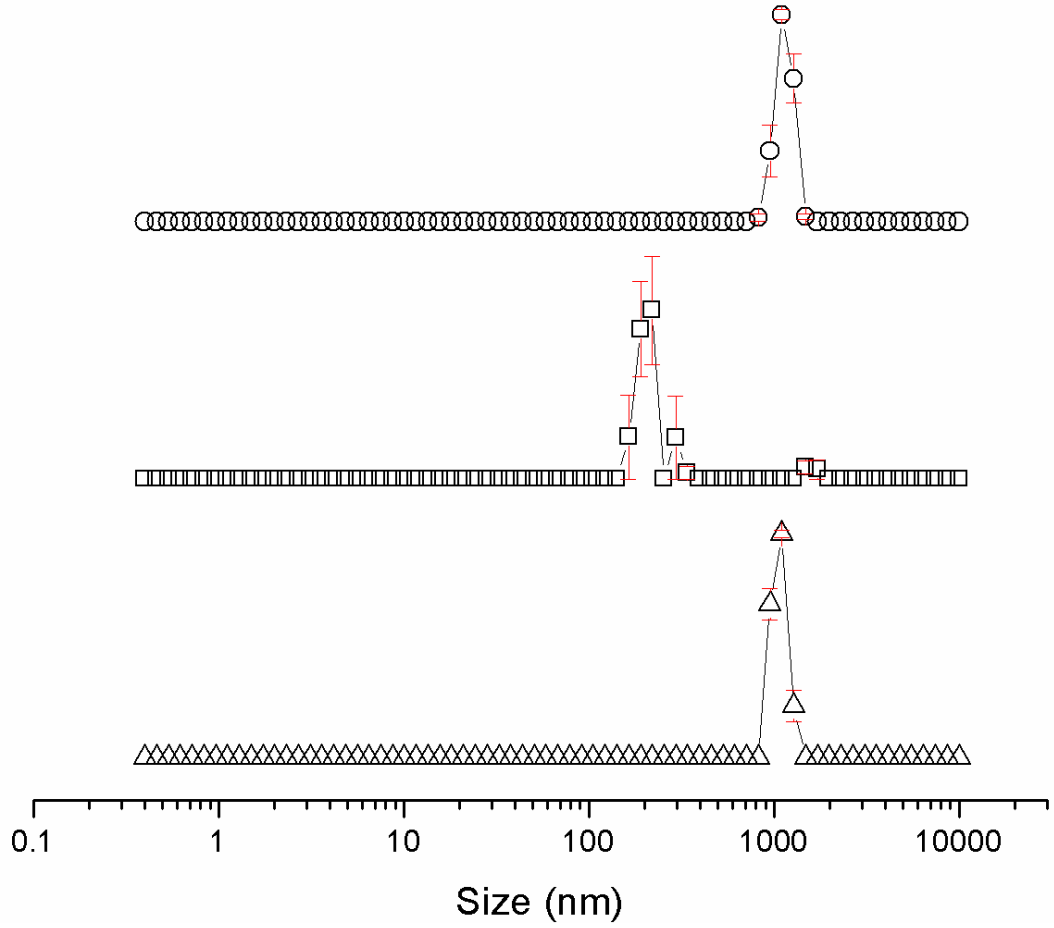

Figure S170 - Average intensity particle size distribution, calculated from 9 DLS runs, of aggregates formed by dissolving compound **5** at a concentration of 5.56 mM in DMSO at Δ) 25 ^{o}C, □) heating to 40 ^{o}C and ○) cooling to 25 ^{o}C. Only 9 of the available 10 DLS runs were used as in some cases, due to the heating and cooling processes there were some obvious temperature equilibration issues for the first run.

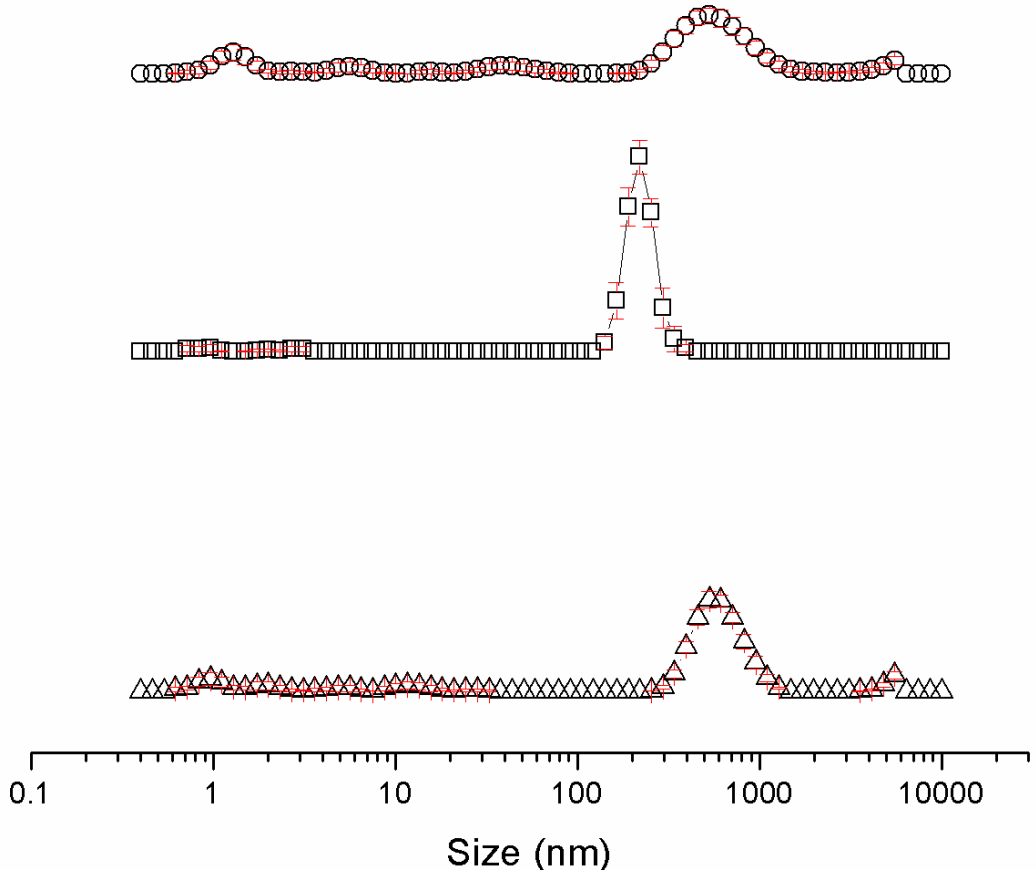

Figure S171 - Average intensity particle size distribution, calculated from 9 DLS runs, of aggregates formed by dissolving compound **5** at a concentration of 0.56 mM in DMSO at Δ) 25 ^{o}C, □) heating to 40 ^{o}C and ○) cooling to 25 ^{o}C. Only 9 of the available 10 DLS runs were used as in some cases, due to the heating and cooling processes there were some obvious temperature equilibration issues for the first run.

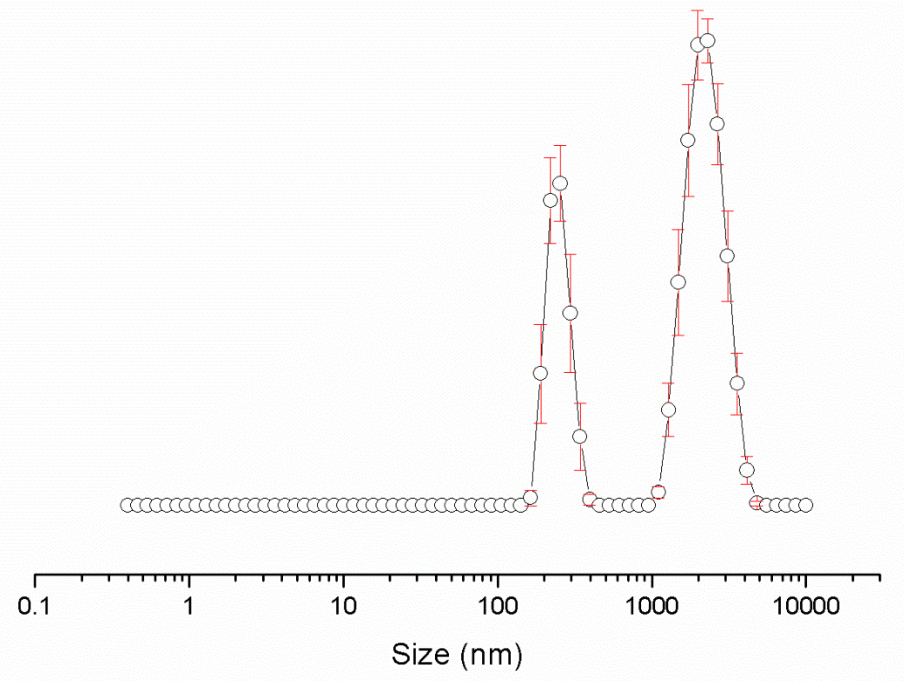

Figure S172 - Average intensity particle size distribution, calculated from 9 DLS runs, of aggregates formed by dissolving compound **5** at a concentration of 55.56 mM in a solution of DMSO: H_2O 1: 1, after heating to 40 ^oC and cooling to 25 ^oC. Only 9 of the available 10 DLS runs were used as in some cases, due to the heating and cooling processes there were some obvious temperature equilibration issues for the first run.

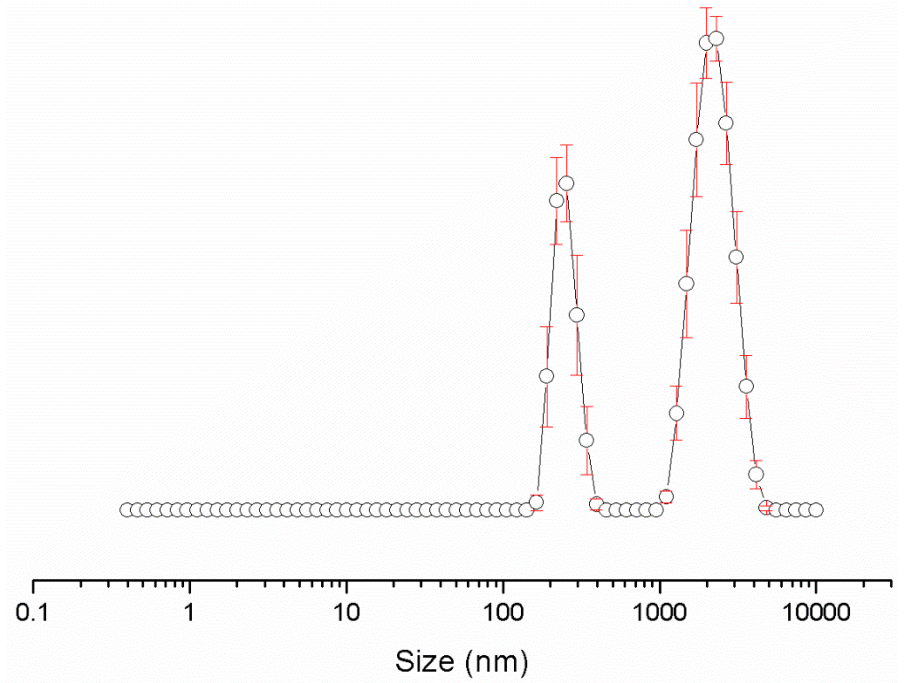

Figure S173 - Average intensity particle size distribution, calculated from 9 DLS runs, of aggregates formed by dissolving compound **5** at a concentration of 5.56 mM in a solution of DMSO: H_2O 1: 1, after heating to 40 ^oC and cooling to 25 ^oC. Only 9 of the available 10 DLS runs were used as in some cases, due to the heating and cooling processes there were some obvious temperature equilibration issues for the first run.

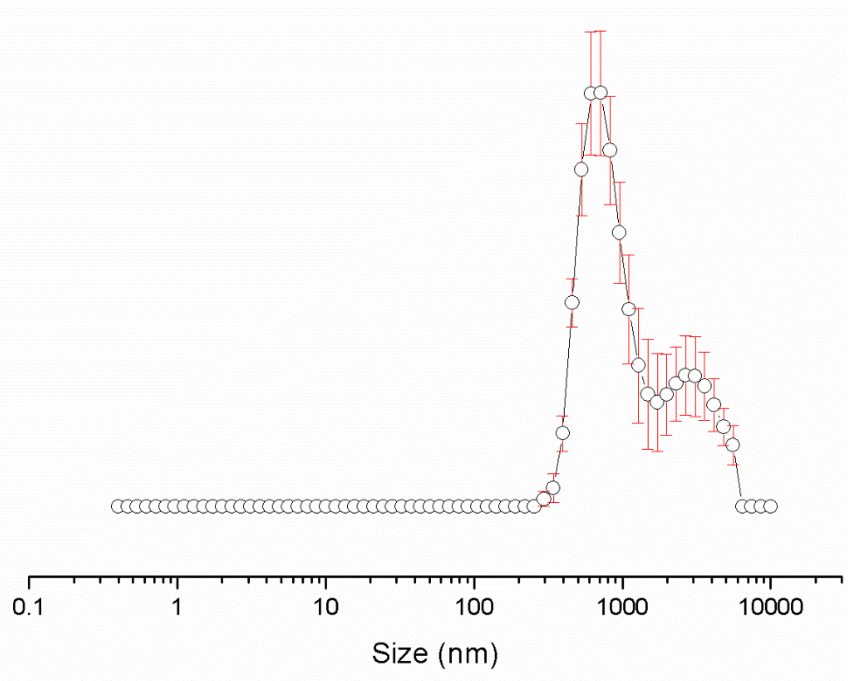

Figure S174 - Average intensity particle size distribution, calculated from 9 DLS runs, of aggregates formed by dissolving compound **5** at a concentration of 0.56 mM in a solution of DMSO: H_2O 1: 1, after heating to 40 ^oC and cooling to 25 ^oC. Only 9 of the available 10 DLS runs were used as in some cases, due to the heating and cooling processes there were some obvious temperature equilibration issues for the first run.

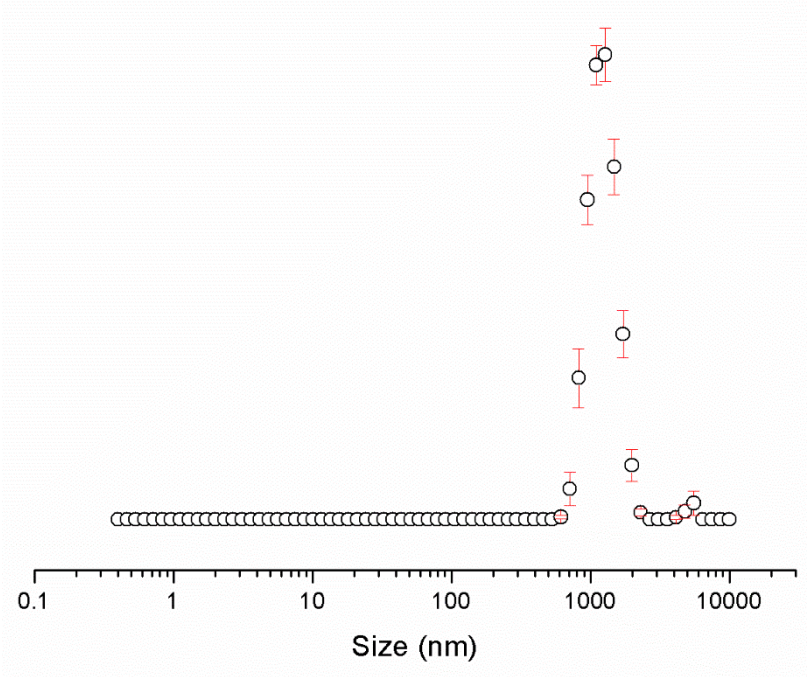

Figure S175 - Average intensity particle size distribution, calculated from 9 DLS runs, of aggregates formed by dissolving compound **5** at a concentration of 5.56 mM in a solution of DMSO: H_2O 3: 7, after heating to 40 ^oC and cooling to 25 ^oC. Only 9 of the available 10 DLS runs were used as in some cases, due to the heating and cooling processes there were some obvious temperature equilibration issues for the first run.

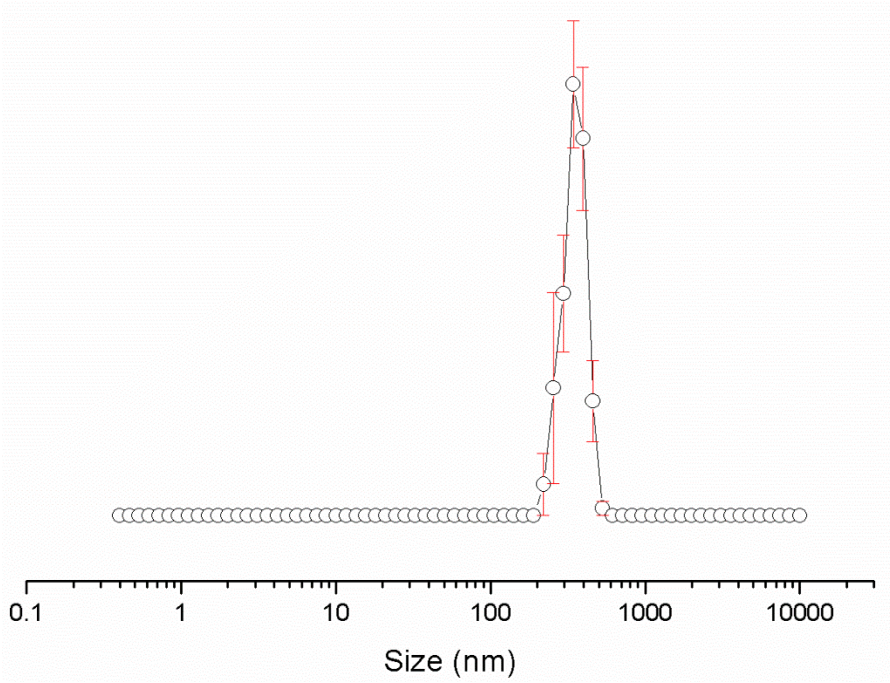

Figure S176 - Average intensity particle size distribution, calculated from 9 DLS runs, of aggregates formed by dissolving compound **5** at a concentration of 0.56 mM in a solution of DMSO: H_2O 3: 7, after heating to 40 ^oC and cooling to 25 ^oC. Only 9 of the available 10 DLS runs were used as in some cases, due to the heating and cooling processes there were some obvious temperature equilibration issues for the first run.

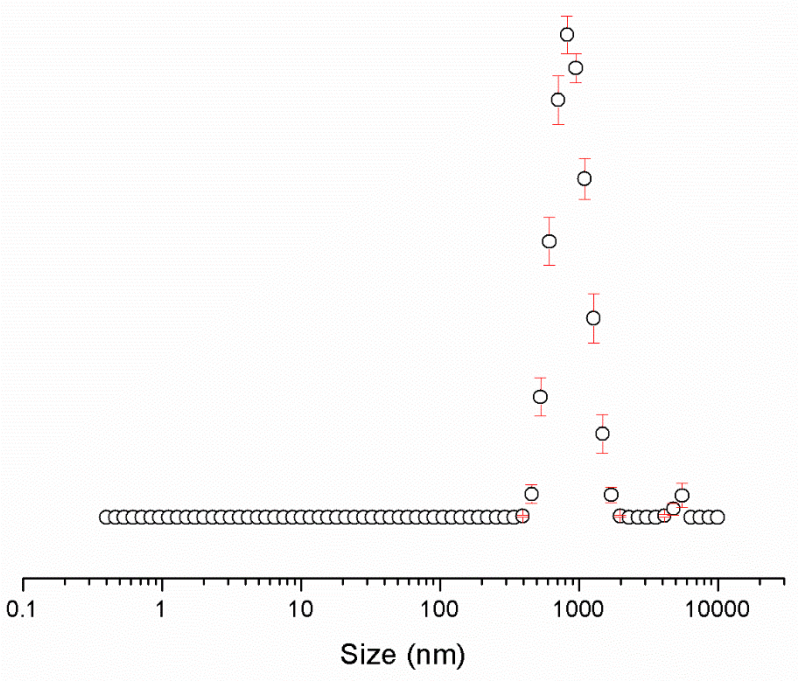

Figure S177 - Average intensity particle size distribution, calculated from 9 DLS runs, of aggregates formed by dissolving compound **5** at a concentration of 0.56 mM in a solution of DMSO: H_2O 1: 4, after heating to 40 ^oC and cooling to 25 ^oC. Only 9 of the available 10 DLS runs were used as in some cases, due to the heating and cooling processes there were some obvious temperature equilibration issues for the first run.

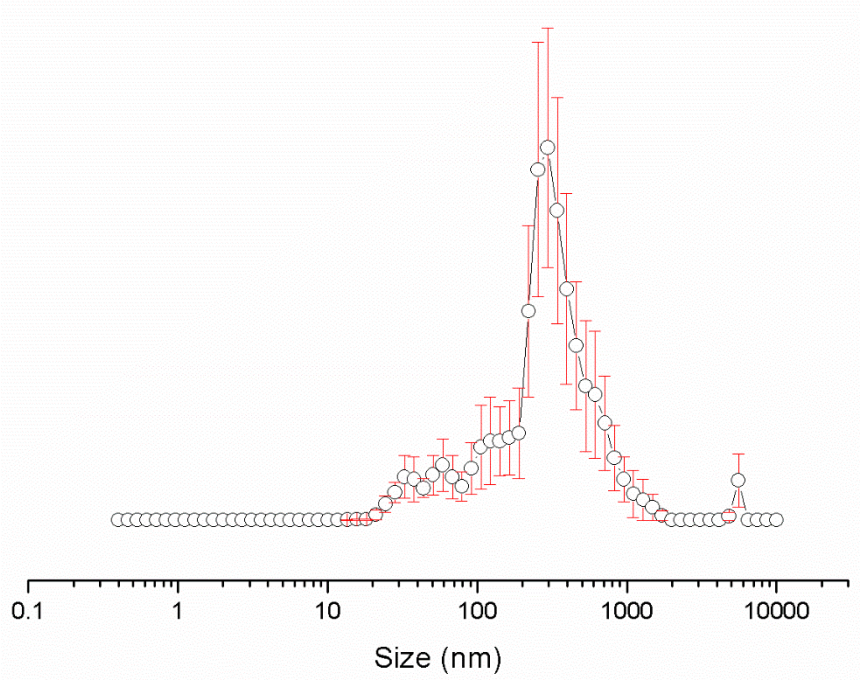

Figure S178 - Average intensity particle size distribution, calculated from 9 DLS runs, of aggregates formed by dissolving compound **5** at a concentration of 5.56 mM in a solution of EtOH: H_2O 1: 19, after heating to 40 ^oC and cooling to 25 ^oC. Only 9 of the available 10 DLS runs were used as in some cases, due to the heating and cooling processes there were some obvious temperature equilibration issues for the first run.

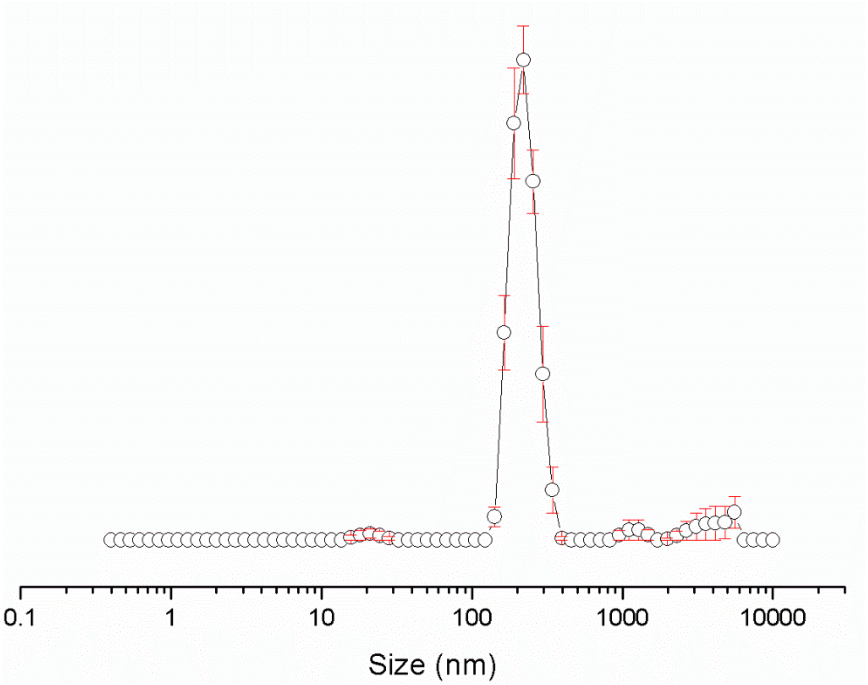

Figure S179 - Average intensity particle size distribution, calculated from 9 DLS runs, of aggregates formed by dissolving compound **5** at a concentration of 0.56 mM in a solution of EtOH: H_2O 1: 19, after heating to 40 ^oC and cooling to 25 ^oC. Only 9 of the available 10 DLS runs were used as in some cases, due to the heating and cooling processes there were some obvious temperature equilibration issues for the first run.

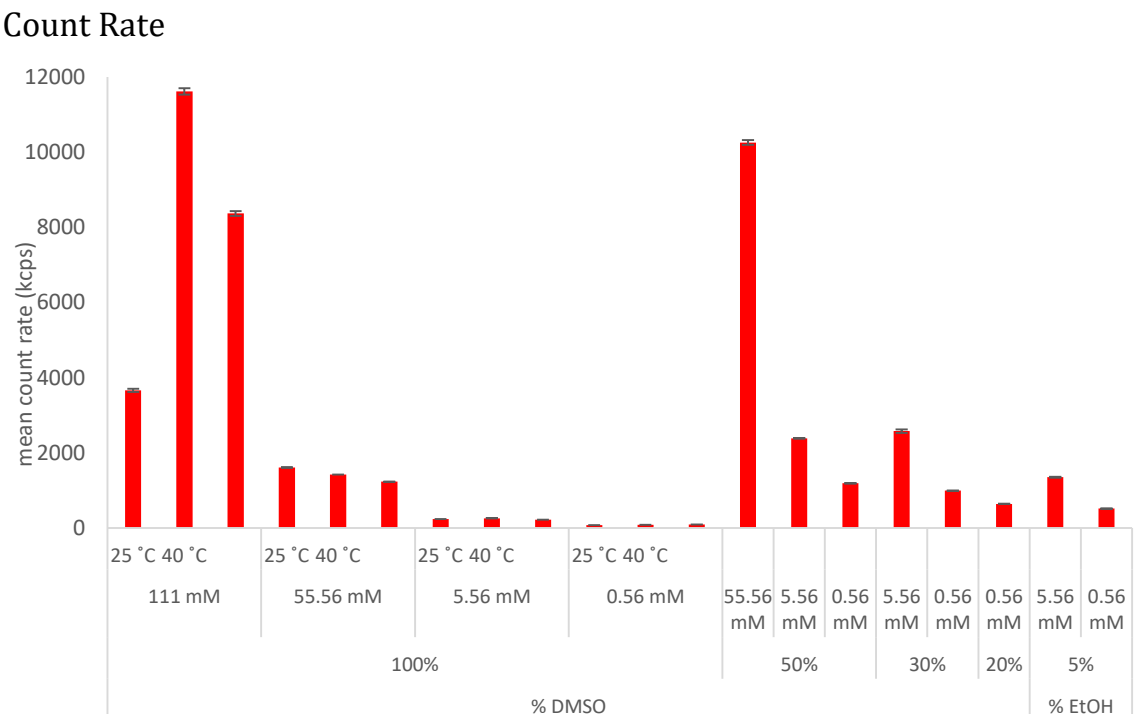

Figure S180 - Graph illustrating the average count rate from 9 DLS runs of compound **1** in aqueous DMSO/EtOH solvent mixtures at a temperature of 25°C, after heating to 40°C unless stated otherwise.

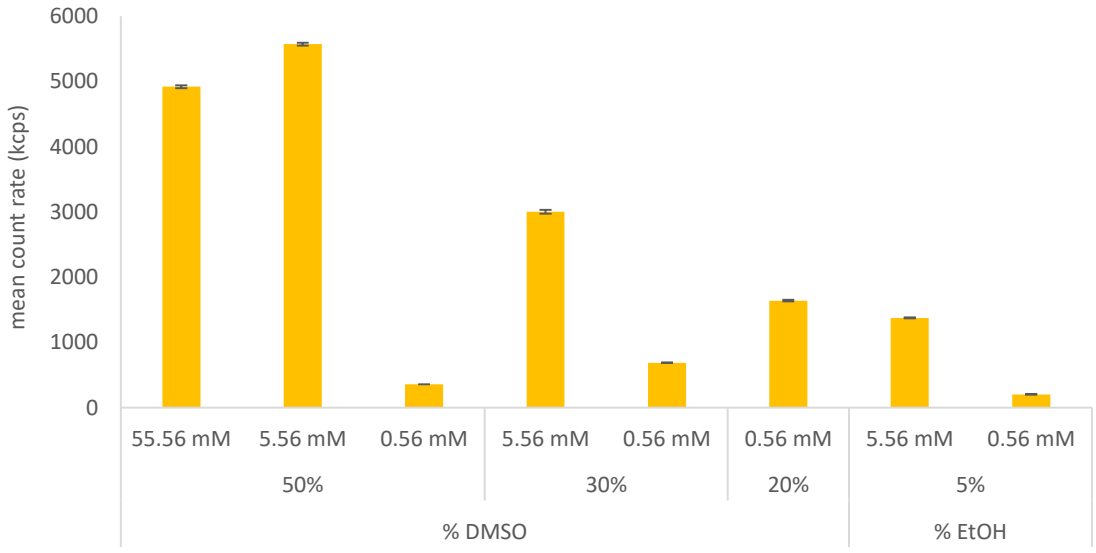

Figure S181 - Graph illustrating the average count rate for 9 DLS runs of compound **2** in aqueous DMSO/EtOH solvent mixtures at a temperature of 25°C, after heating to 40°C.

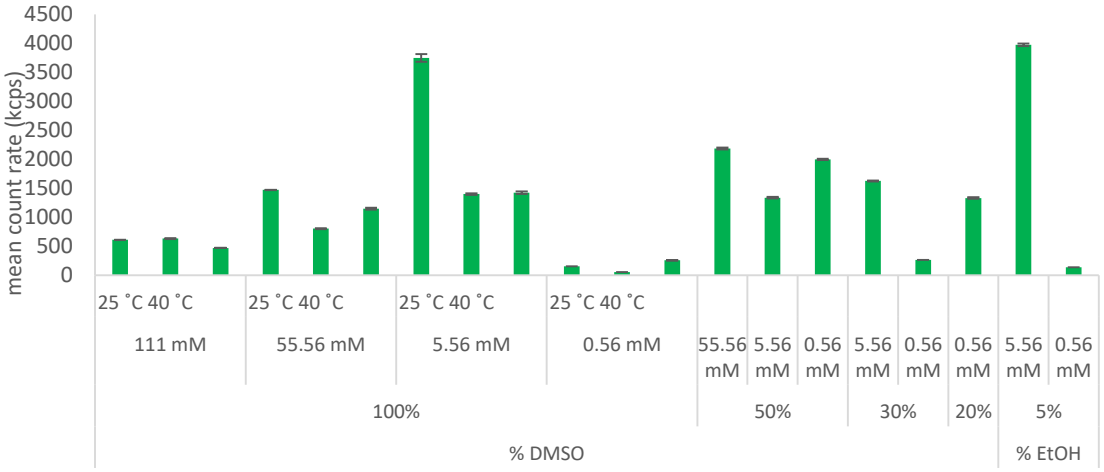

Figure S182- Graph illustrating the average count rate for 9 DLS runs of compound **3** in aqueous DMSO/EtOH solvent mixtures at a temperature of 25°C, after heating to 40°C unless stated otherwise.

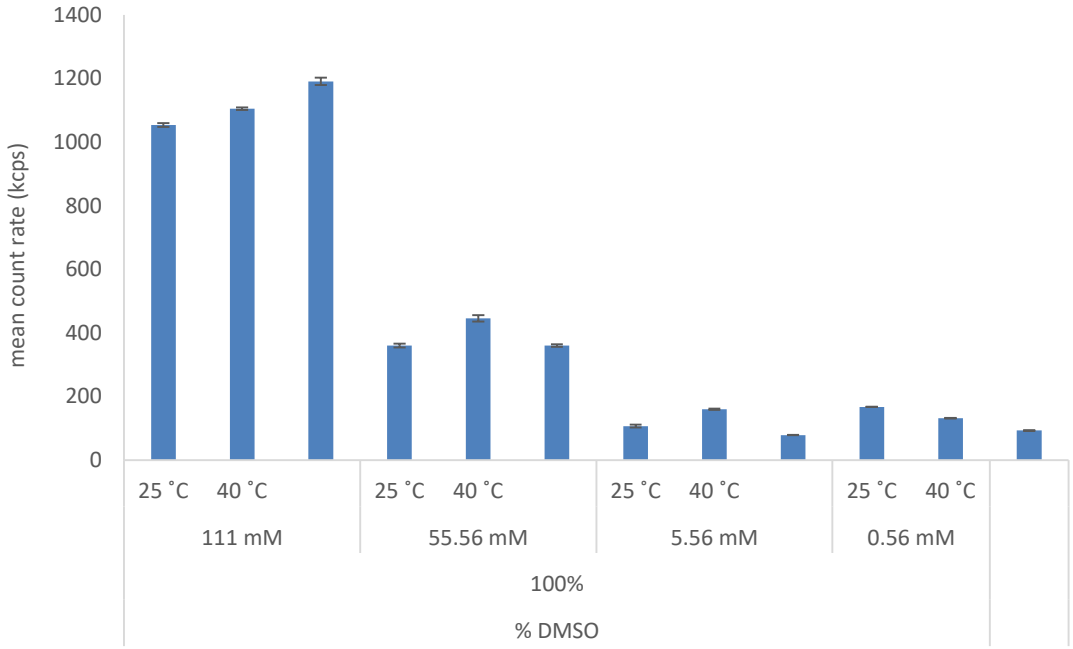

Figure S183- Graph illustrating the average count rate for 9 DLS runs of compound **4** in DMSO at a temperature of 25°C, after heating to 40°C unless stated otherwise.

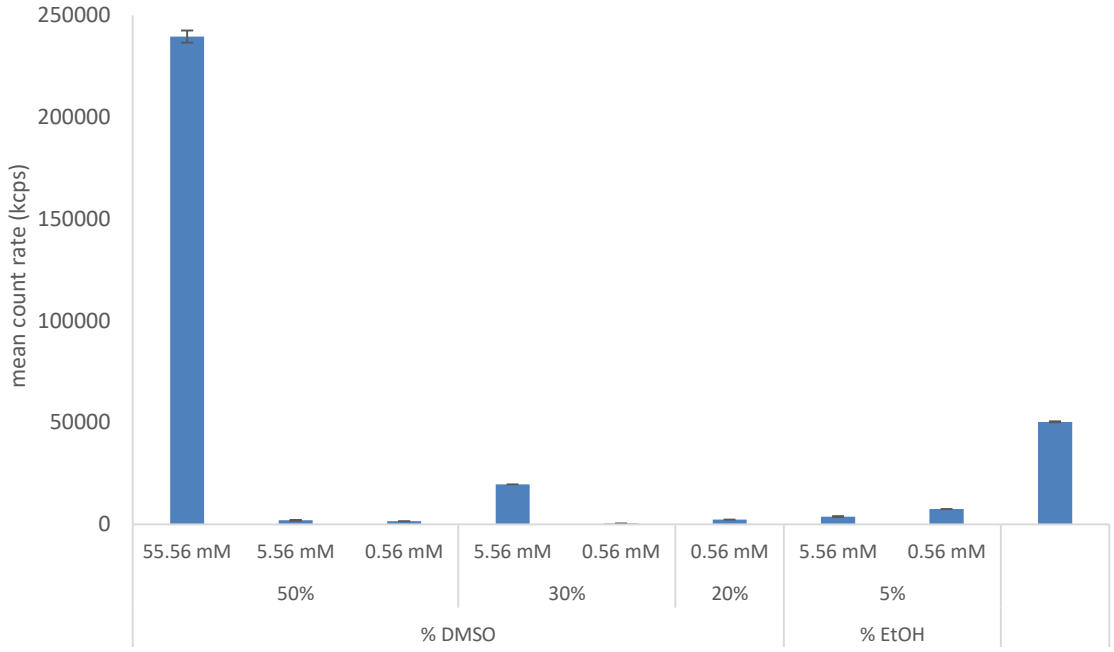

Figure S184- Graph illustrating the average count rate for 9 DLS runs of compound **4** in aqueous DMSO/EtOH solvent mixtures, at a temperature of 25°C, after heating to 40°C.

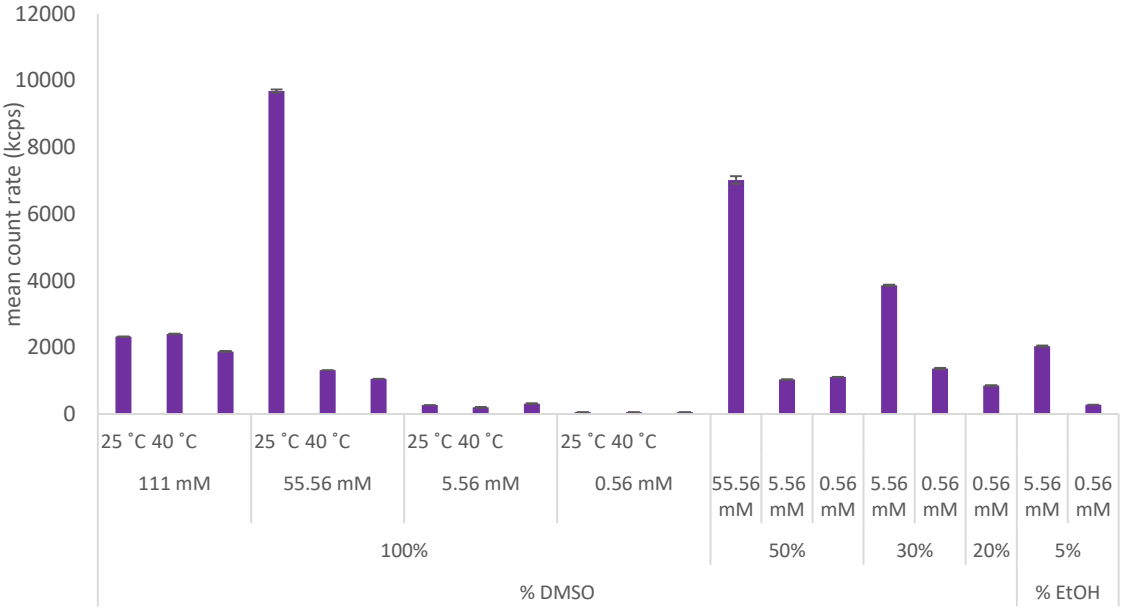

Figure S185 - Graph illustrating the average count rate for 9 DLS runs of compound **5** in aqueous DMSO/EtOH solvent mixtures, at a temperature of 25°C, after heating to 40°C unless stated otherwise.

Comparative overview of DLS results

Table S9 – Average intensity particle size distributions for compounds **1, 3, 4** and **5**, calculated from 9 DLS runs. Samples were prepared in series, with an aliquot of the most concentrated solution undergoing serial dilution and measured at 25 ^{o}C after heating to 40 ^{o}C and cooling to 25 ^{o}C.

Solvent	Conc. (mM)	**1**		**2**	**3**		**4**		**5**	
		peak maxima		peak maxima	peak maxima		peak maxima		peak maxima	
DMSO	111.12	458.7	1718	*a**	955.4	3091	615.1	1.11	712.4	3580
	55.56	825	58.77	*a**	825		615.1	1.11	825	220.2
	5. 56	531.2	105.7	*a**	615.1**		396.1	1.11	1106	
	0.56	531.2		*a**	531.2		396.1		531.2	0.72

*a** - DLS Size distribution in a solution of DMSO for compound **2** could not be gathered due to the inherent absorbance and fluorescent characteristics of this compound.

Table S10 – Average intensity particle size distribution of compounds **1**, **3**, **4** and **5**, calculated from 9 DLS runs in different solvent conditions at concentrations of 5.56 Mm and 0.56 mM. Samples were prepared in series, with an aliquot of the most concentrated solution undergoing serial dilution and measured after heating to 40 ^{o}C and cooling to 25 ^{o}C.

Solvent conditions		Conc. (mM)	**1**		**2**		**3**		**4**		**5**	
			peak maxima		peak maxima		peak maxima		peak maxima		peak maxima	
DMSO		5. 56	531.2	106	*a**		615.1		396.1	1.11	1106	
		0.56	531.2		*a**		531.2		396.1		531.2	0.72
DMSO : H_2O	1 : 1	5. 56	1990		615.1		1990	458.7	220.2	1281	2305	255
		0.56	1106		955		531.2		955		712.4	2669
	3 : 7	5. 56	342		825		1106		458.7	78.82	1281	
		0.56	396.1		396.1		615.1		615.1		342	
	1 : 4	0.56	58.77	342	342	68	712.4		91.28	615.1	825	
EtOH : H_2O	1 : 19	5. 56	220.2		164.2		220.2		58.77	295.3	295.3	
		0.56	164.2		255		396.1	0.83	122		220.2	

*a** - DLS Size distribution in a solution of DMSO for compound **2** could not be gathered due to the inherent absorbance and fluorescent characteristics of this compound.

Zeta potential

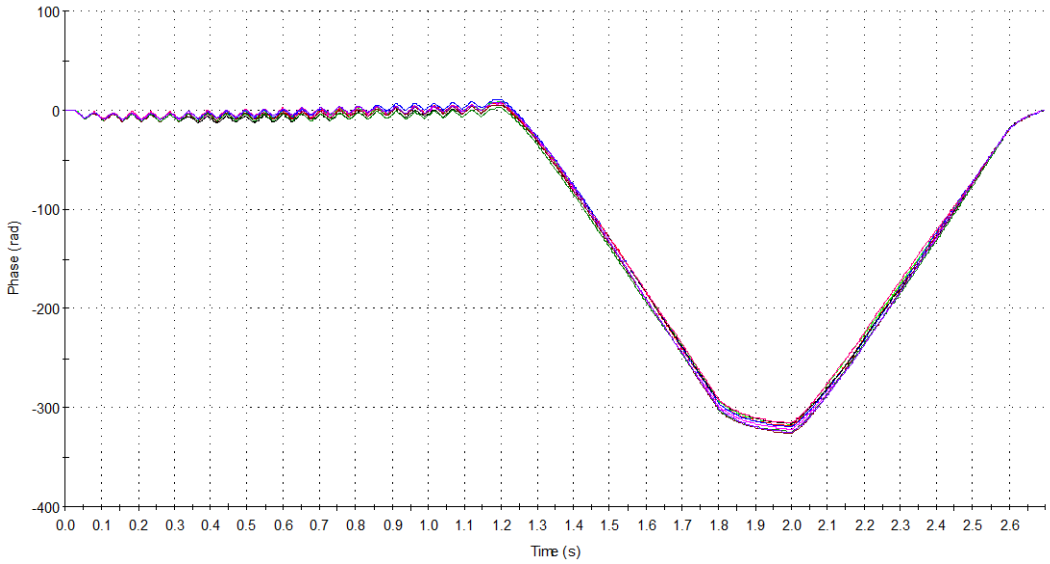

Figure S186 - Phase plot taken during the measurement of 9 Zeta Potential Transfer Standard (PTS) runs of compound **1** at a concentration of 5.56 mM in a solution of EtOH: H_2O 1: 19. Average measurement value = -81.5 mV.

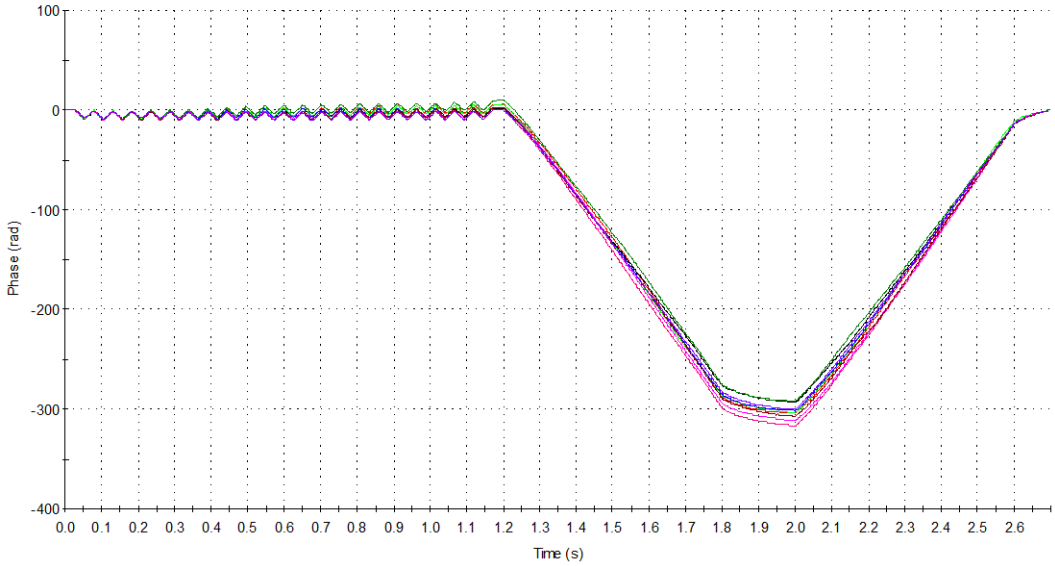

Figure S187 - Phase plot taken during the measurement of 9 Zeta Potential Transfer Standard (PTS) runs of compound **2** at a concentration of 5.56 mM in a solution EtOH: H_2O 1: 19. Average measurement value -96.2 mV.

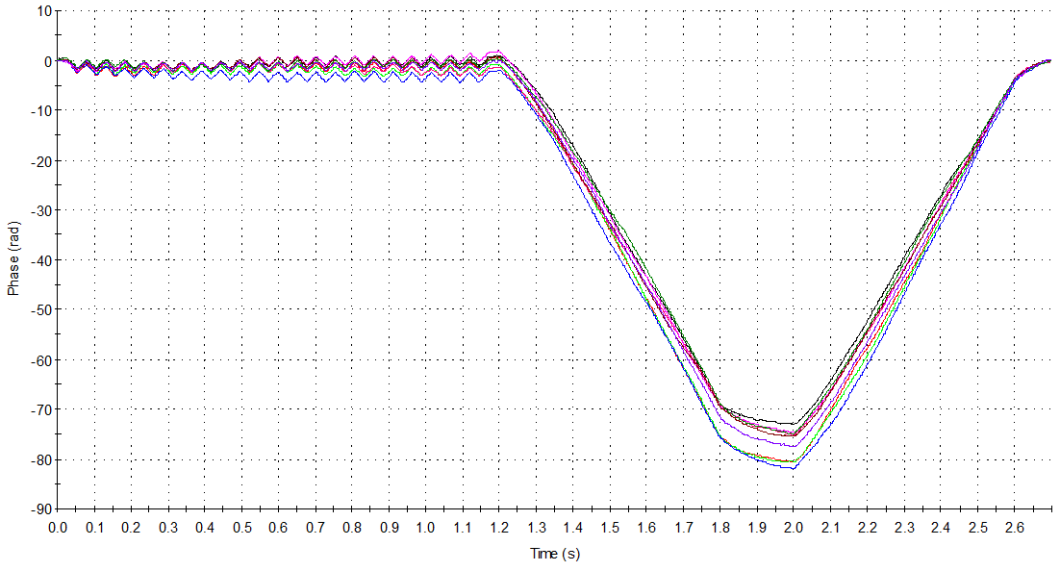

Figure S188 - Phase plot taken during the measurement of 9 Zeta Potential Transfer Standard (PTS) runs of compound **3** at a concentration of 5.56 mM in a solution EtOH: H_2O 1: 19. Average measurement value -18.5 mV.

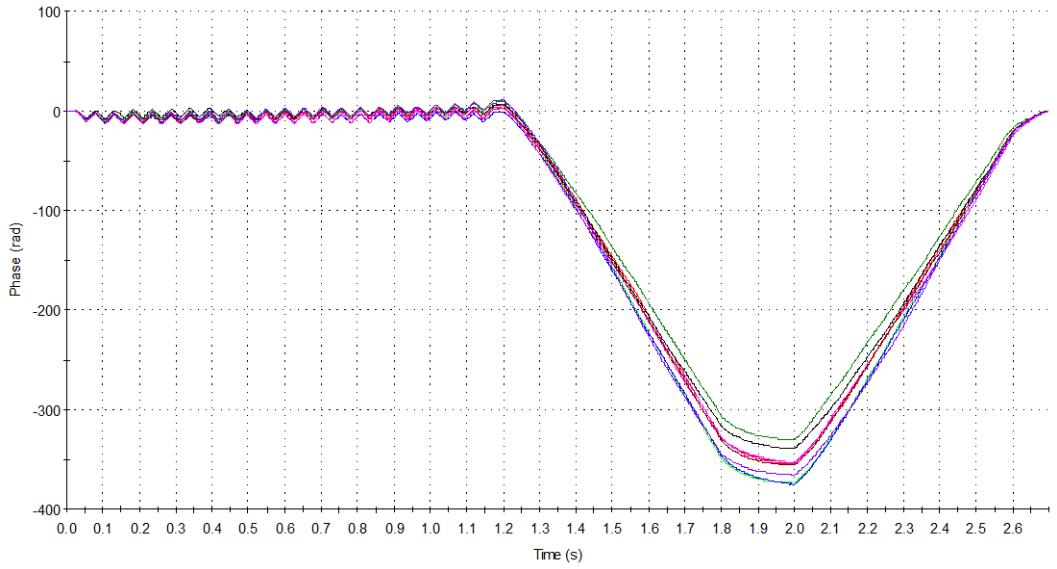

Figure S189 - Phase plot taken during the measurement of 9 Zeta Potential Transfer Standard (PTS) runs of compound **4** at a concentration of 5.56 mM in a solution EtOH: H_2O 1: 19. Average measurement value -101 mV.

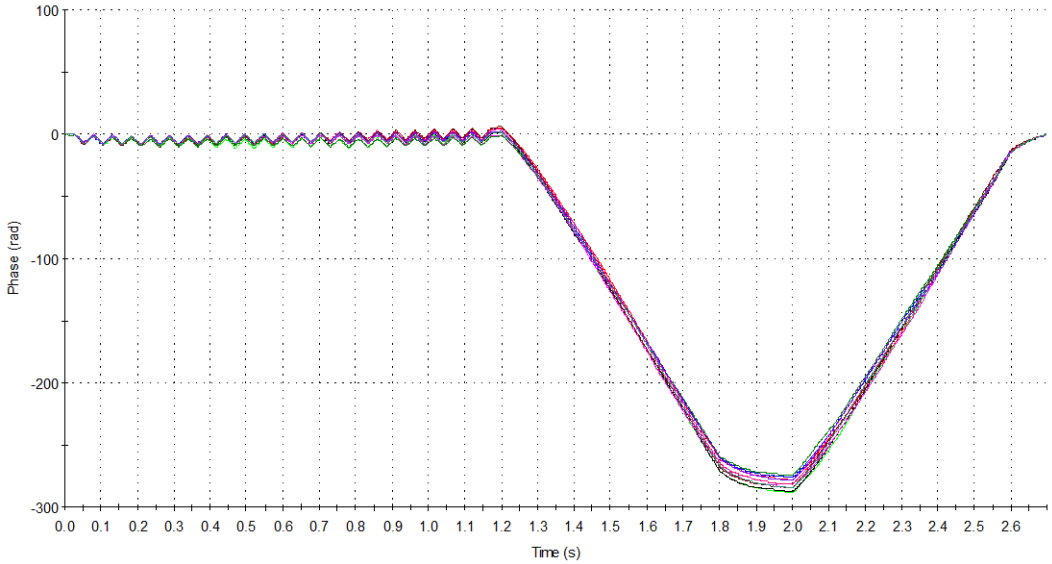

Figure S190 - Phase plot taken during the measurement of 9 Zeta Potential Transfer Standard (PTS) runs of compound **5** at a concentration of 5.56 mM in a solution EtOH: H_2O 1: 19. Average measurement value **-**79.3 mV.

UV-Vis spectra

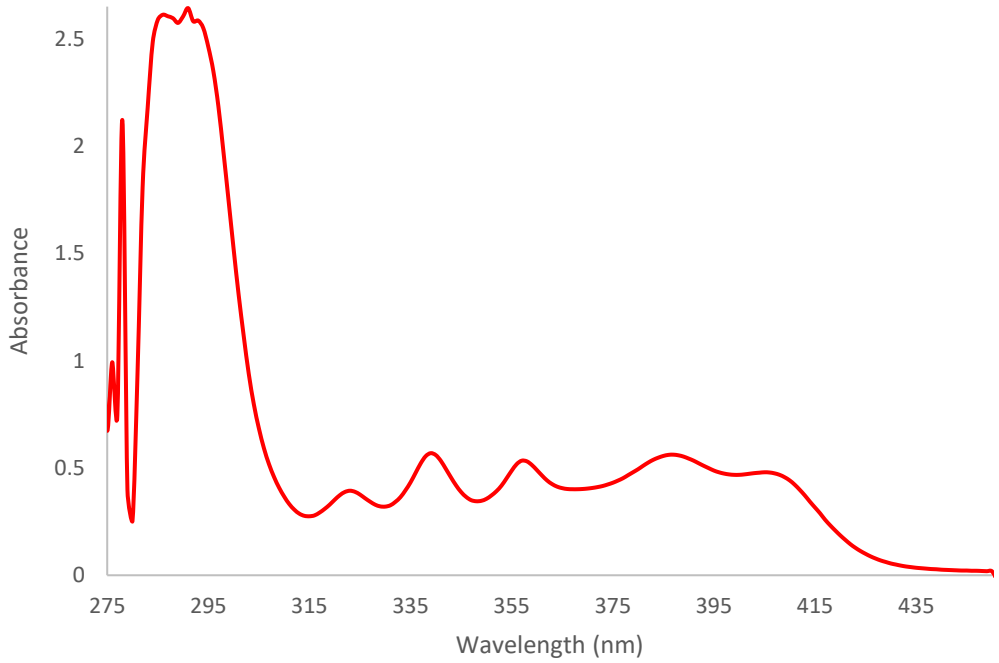

Figure S191 - UV-Vis spectra of compound **1** (0.30 mM) in DMSO.

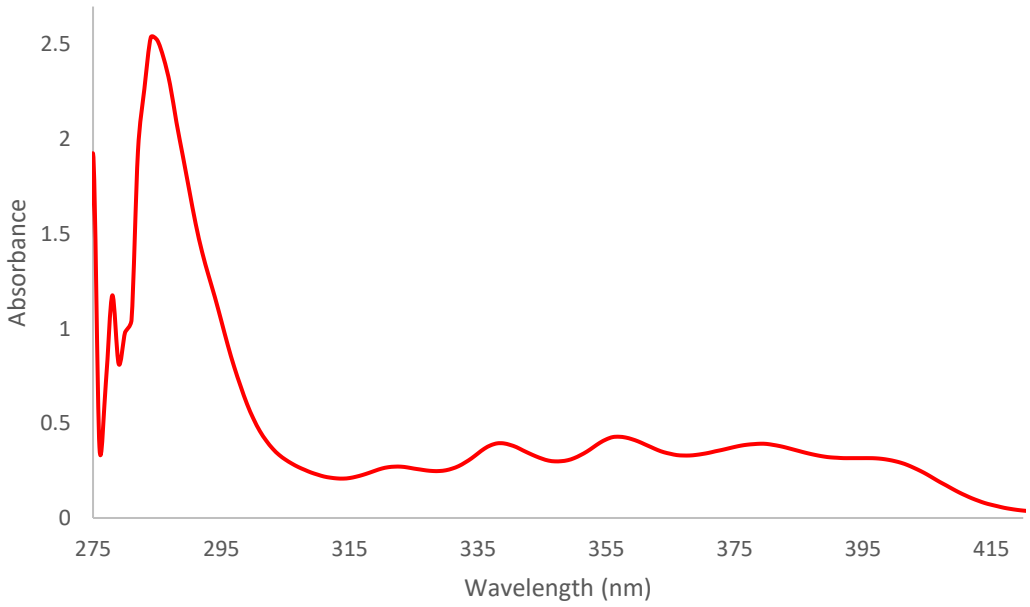

Figure S192 - UV-Vis spectra of compound **1** (0.30 mM) in a solution of DMSO: H_2O 1: 1.

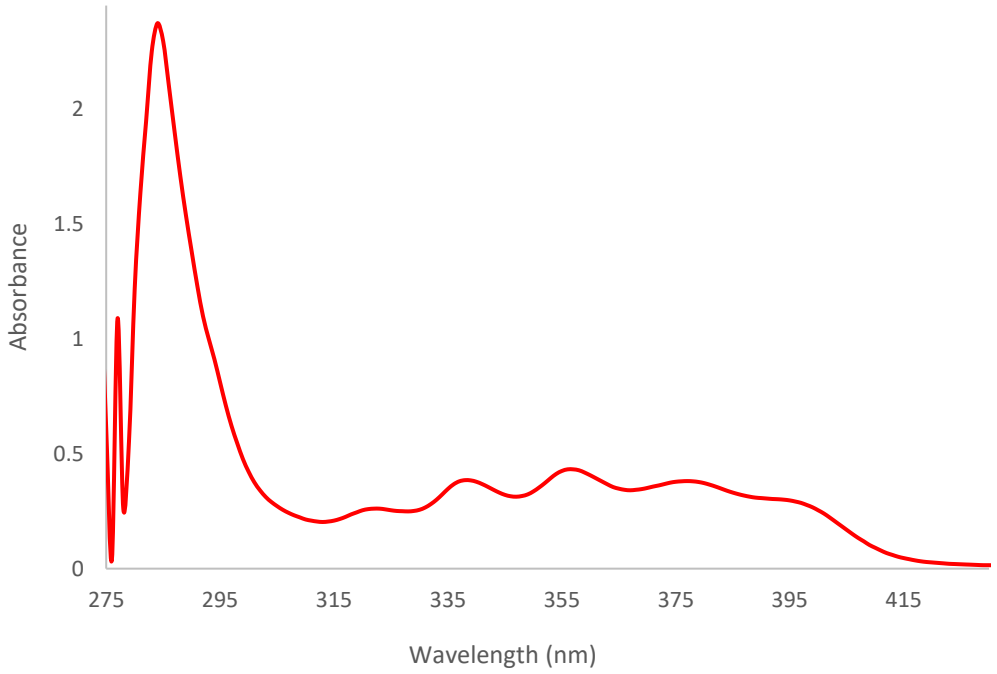

Figure S193 - UV-Vis spectra of compound **1** (0.30 mM) in a solution of DMSO: H_2O 2: 7.

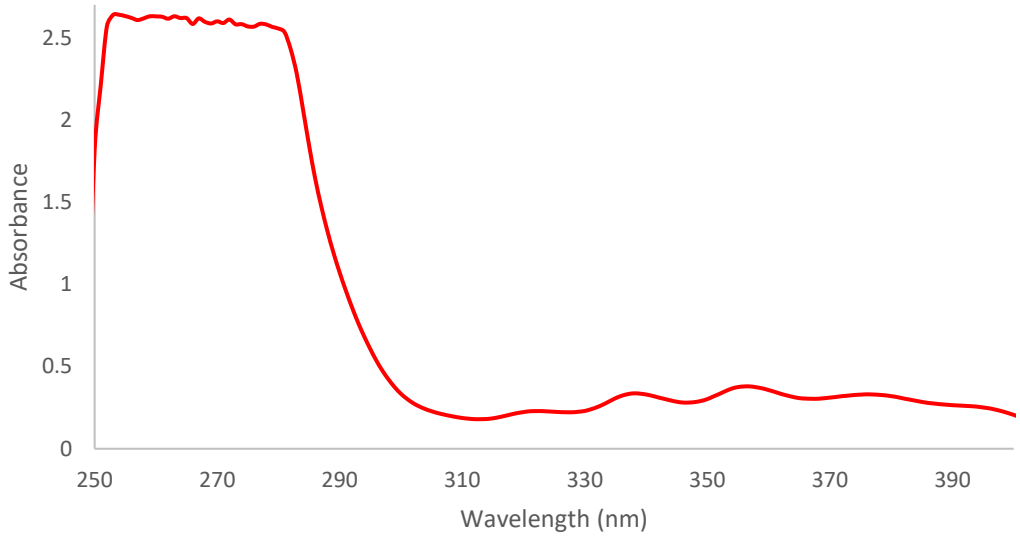

Figure S194- UV-Vis spectra of compound **1** (0.30 mM) in a solution of DMSO: H_2O 1: 4.

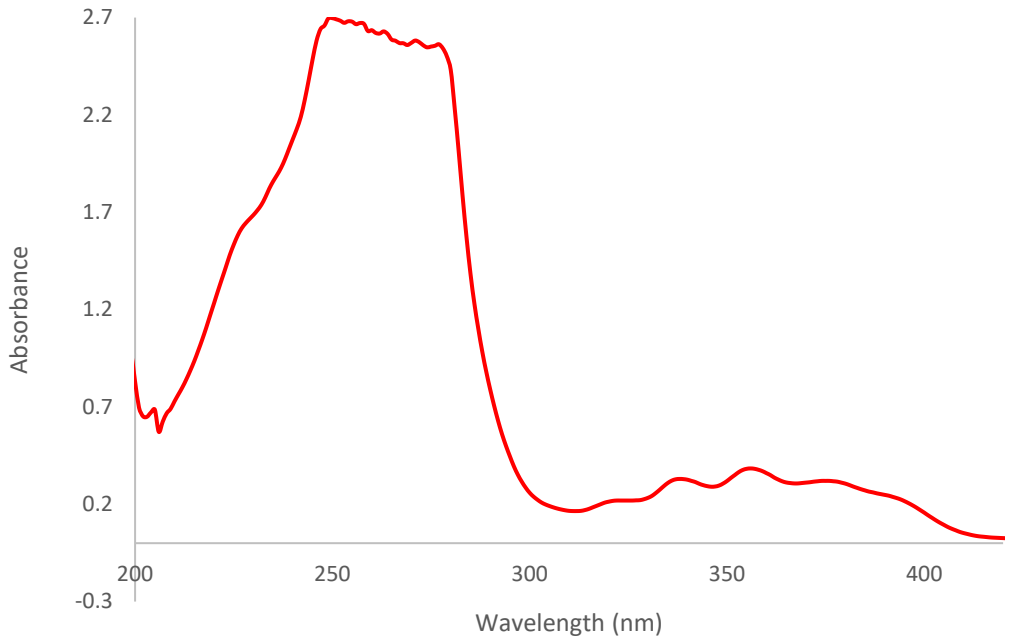

Figure S195- UV-Vis spectra of compound **1** (0.30 mM) in a solution of EtOH: H_2O 1: 19.

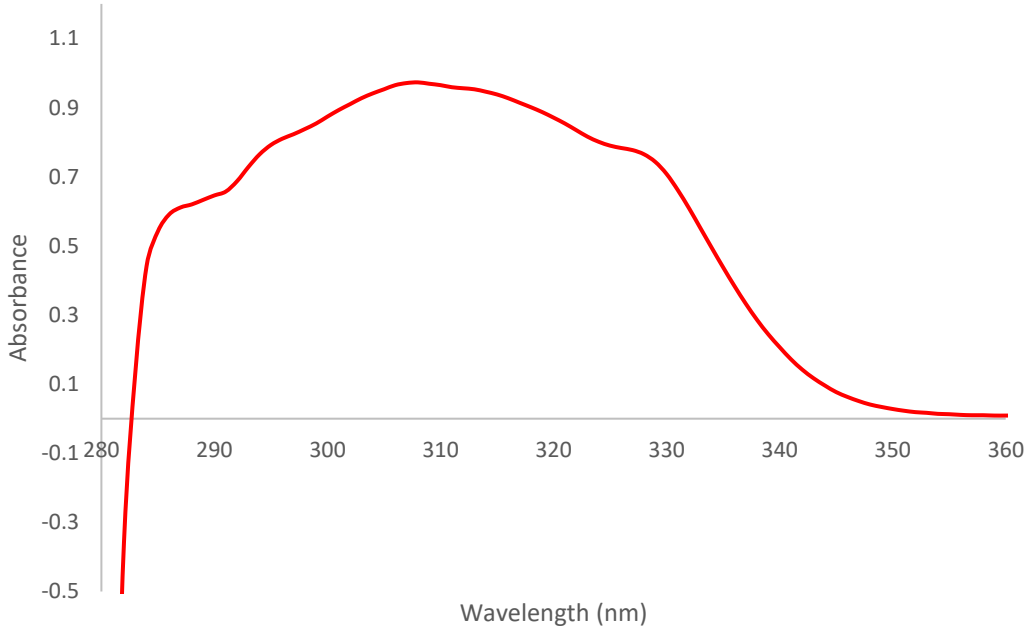

Figure S196 - UV-Vis spectra of compound **2** (0.30 mM) in a solution of DMSO.

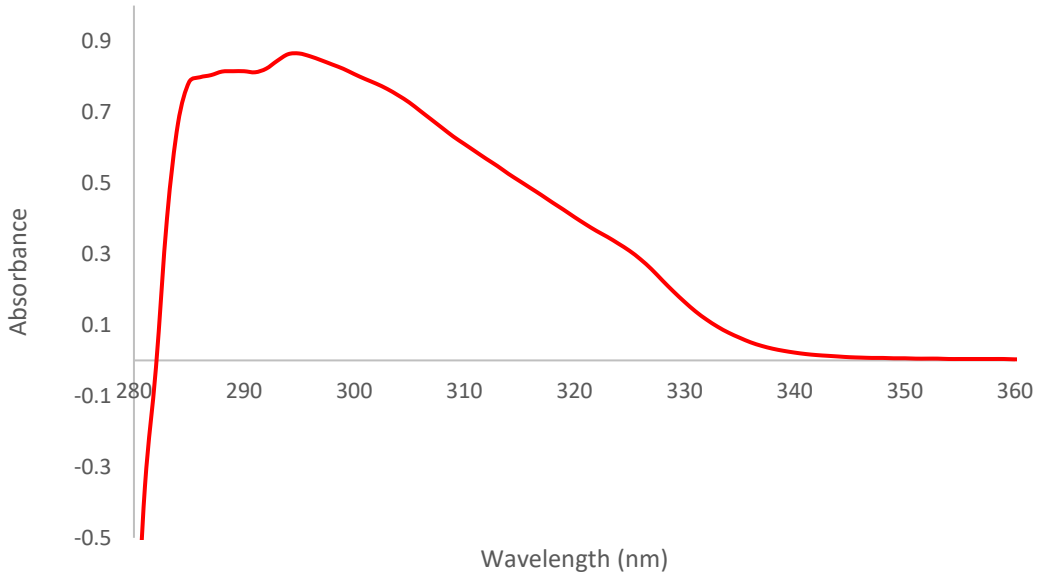

Figure S197 - UV-Vis spectra of compound **2** (0.30 mM) in a solution of DMSO: H_2O 1: 1.

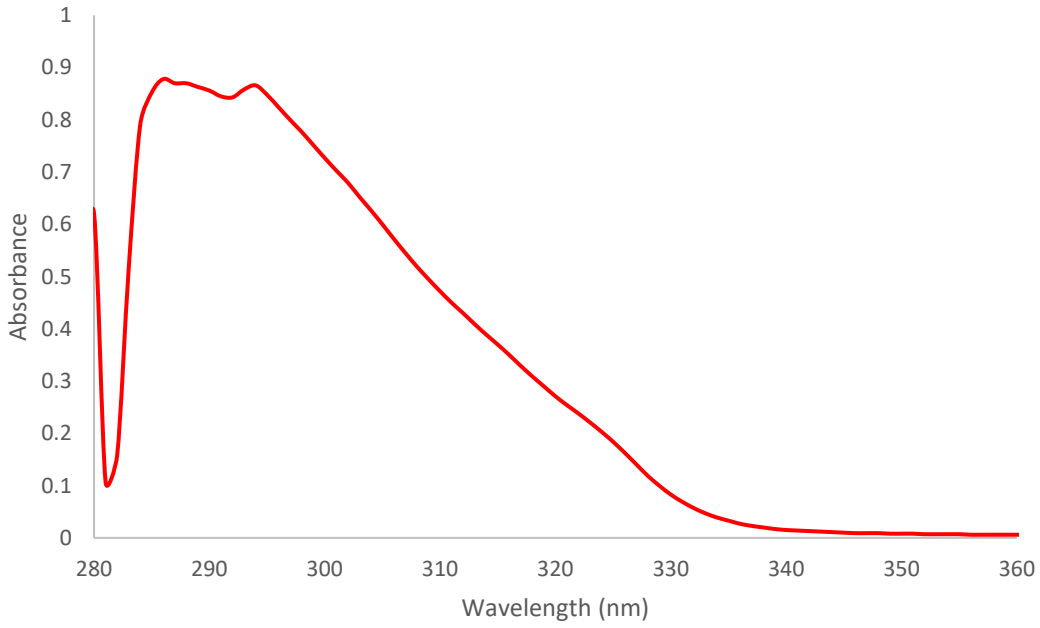

Figure S198 - UV-Vis spectra of compound **2** (0.30 mM) in a solution of DMSO: H_2O 3: 7.

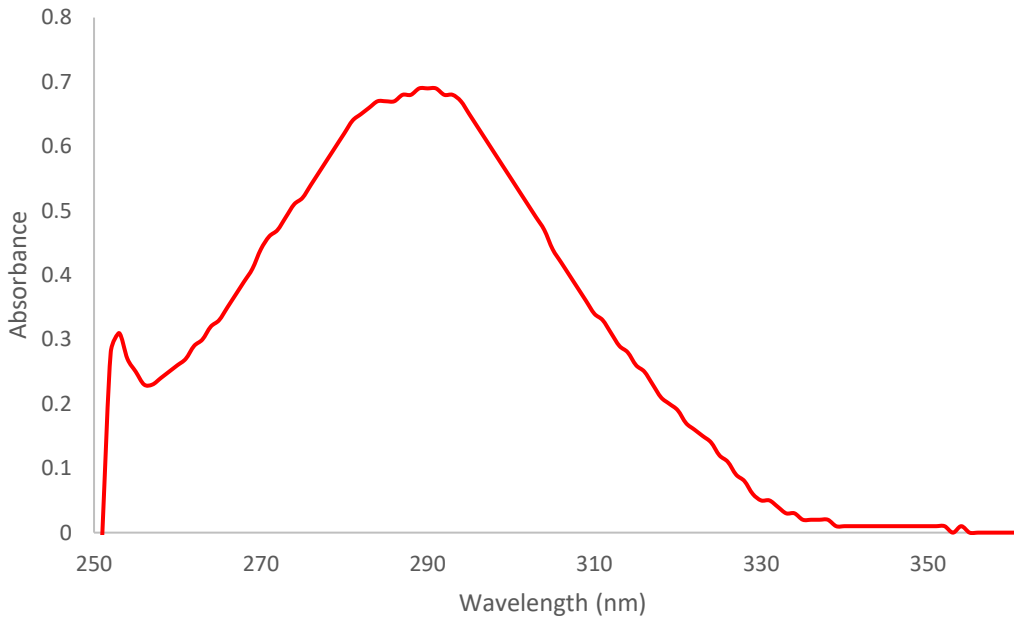

Figure S199 - UV-Vis spectra of compound **2** (0.30 mM) in a solution of DMSO: H_2O 1: 4.

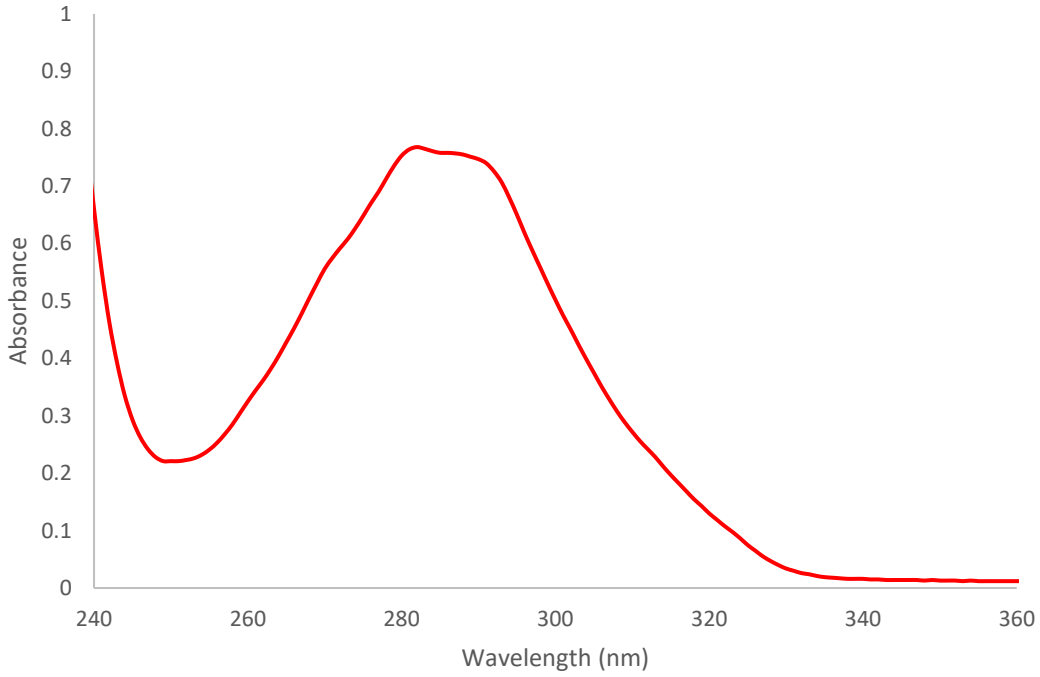

Figure S200 - UV-Vis spectra of compound **2** (0.30 mM) in a solution of EtOH: H_2O 1: 19.

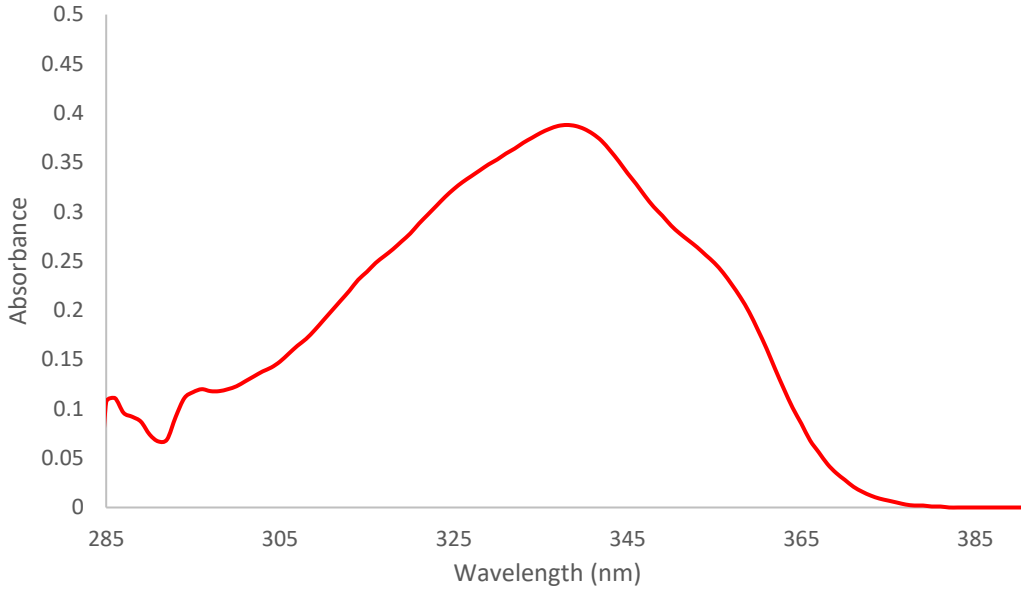

Figure S201 - UV-Vis spectra of compound **4** (0.08 mM) in a DMSO.

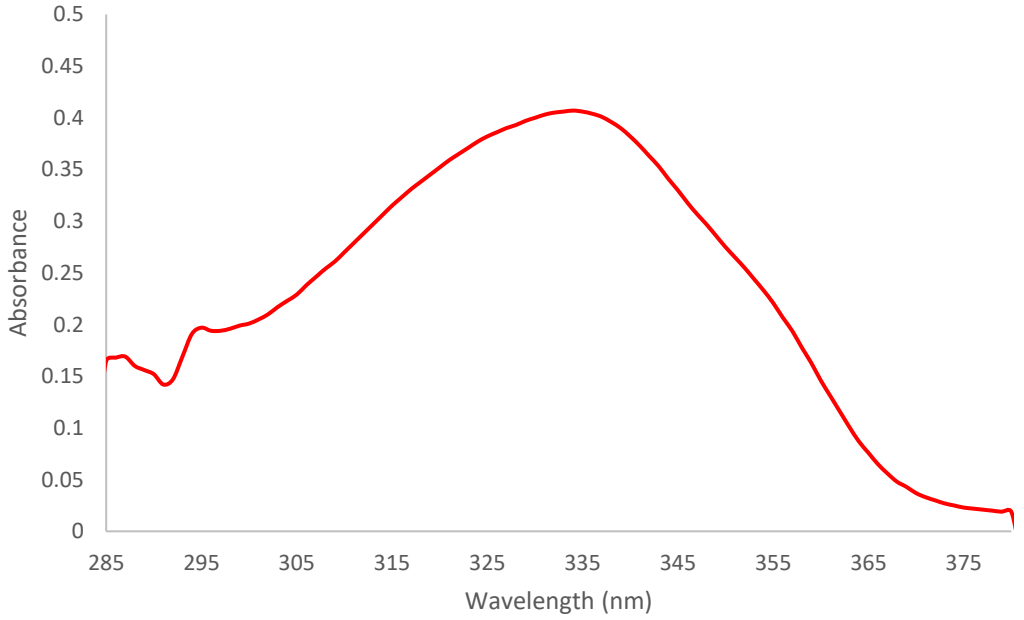

Figure S202 - UV-Vis spectra of compound **4** (0.08 mM) in a solution of DMSO: H_2O 1: 1.

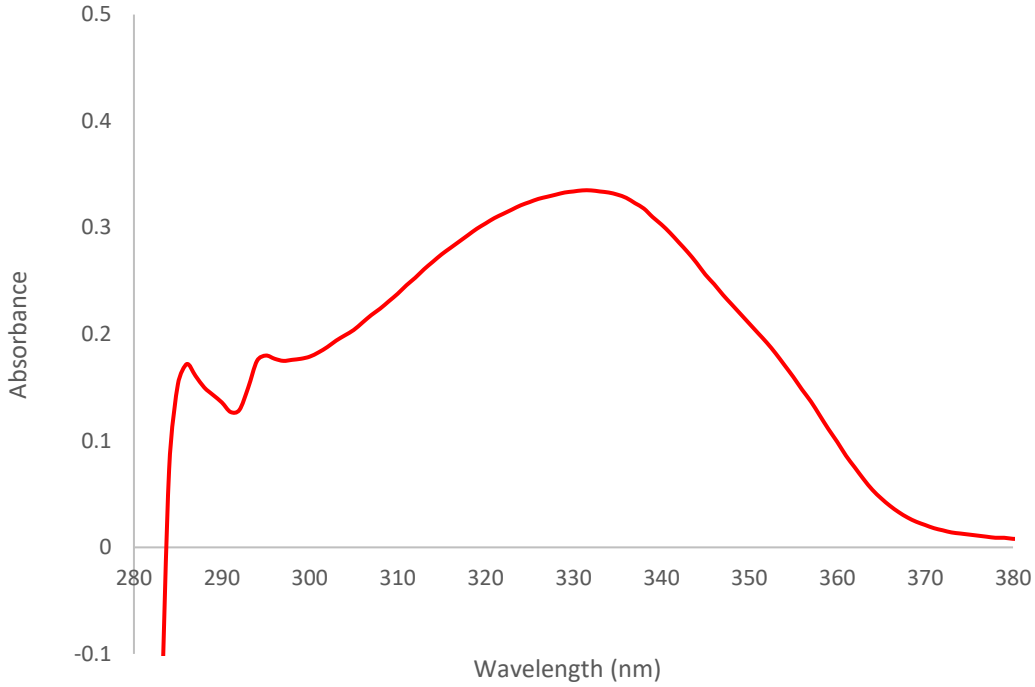

Figure S203 - UV-Vis spectra of compound **4** (0.08 mM) in a solution of DMSO: H_2O 2: 7.

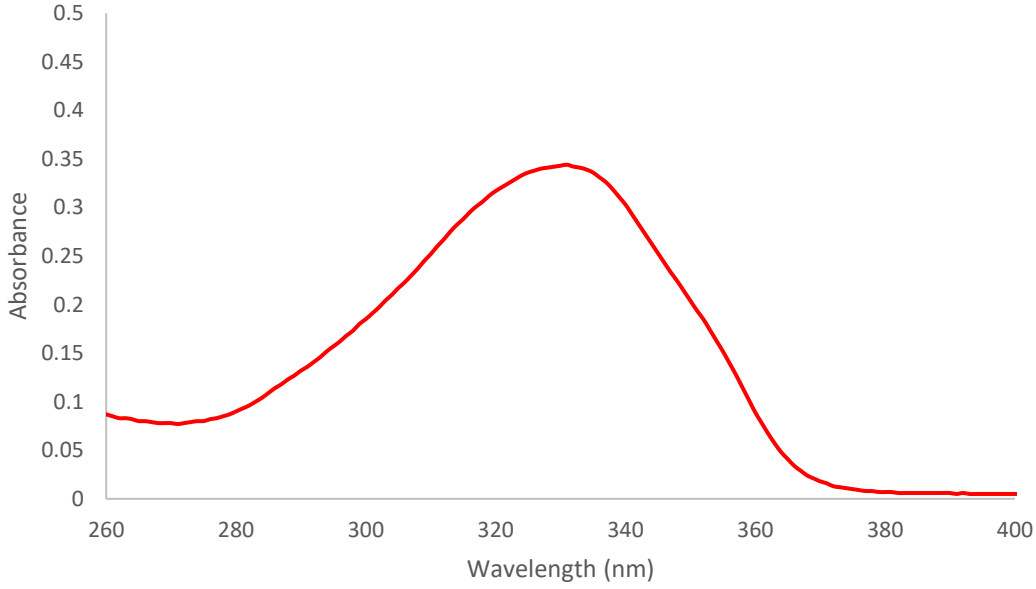

Figure S204 - UV-Vis spectra of compound **4** (0.08 mM) in a solution of DMSO: H_2O 1: 4.

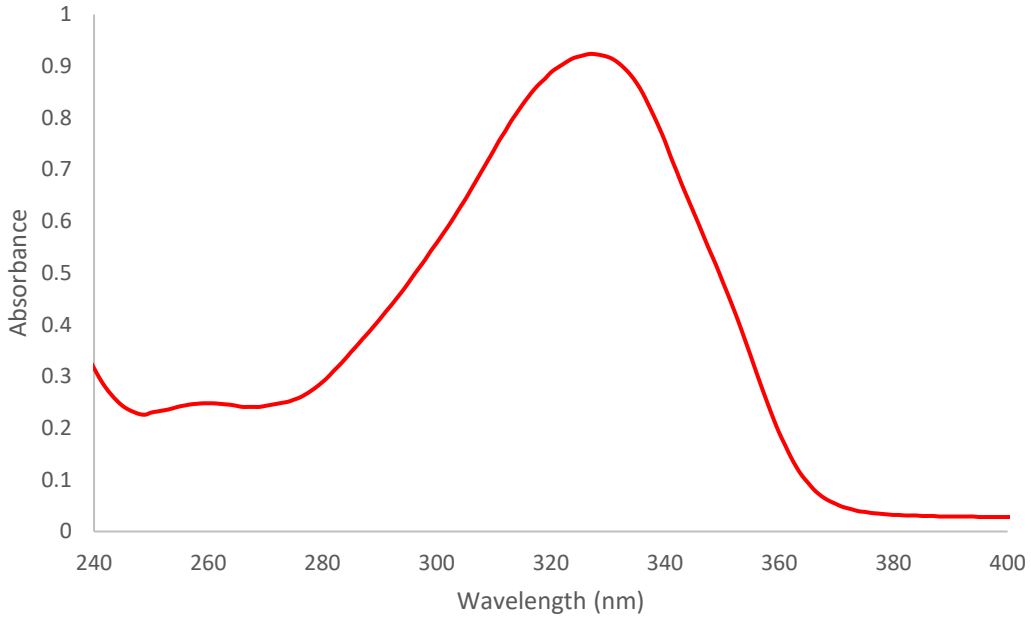

Figure S205 - UV-Vis spectra of compound **4** (0.08 mM) in a solution of EtOH: H_2O 1: 19.

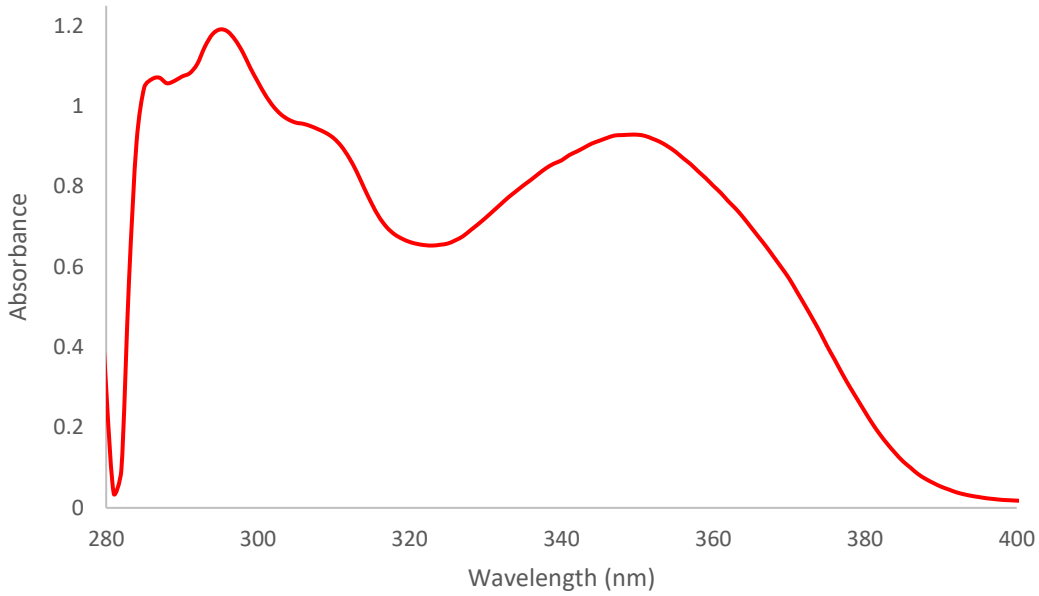

Figure S206 - UV-Vis spectra of compound **5** (0.30 mM) in DMSO.

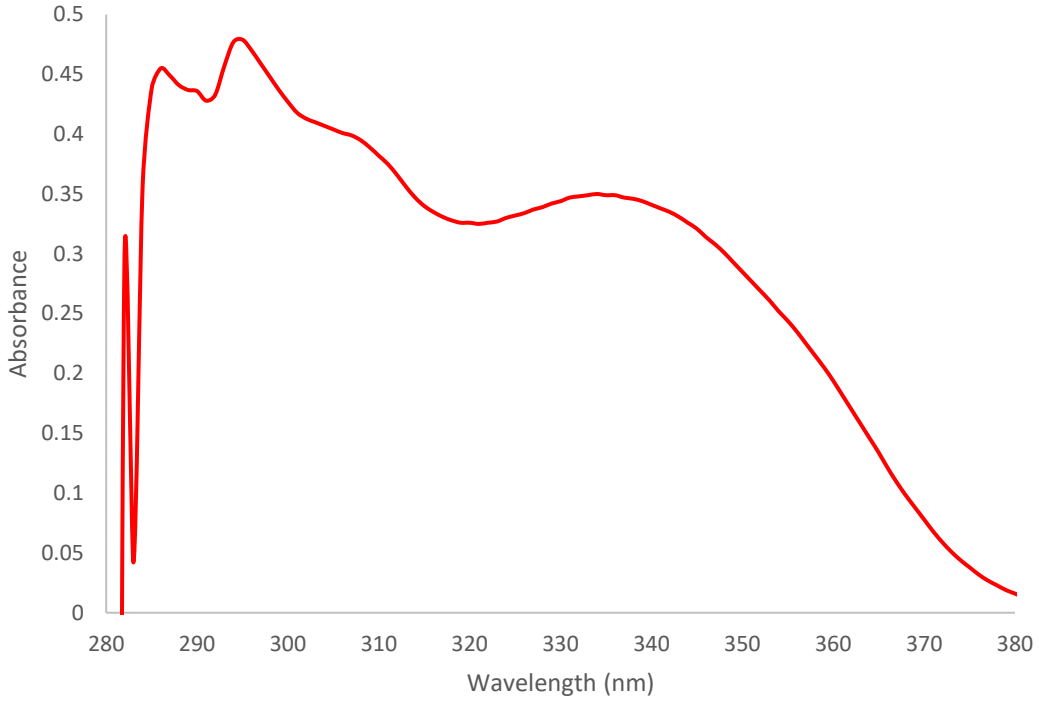

Figure S207 - UV-Vis spectra of compound **5** (0.10 mM) in a solution of DMSO: H_2O 1: 1.

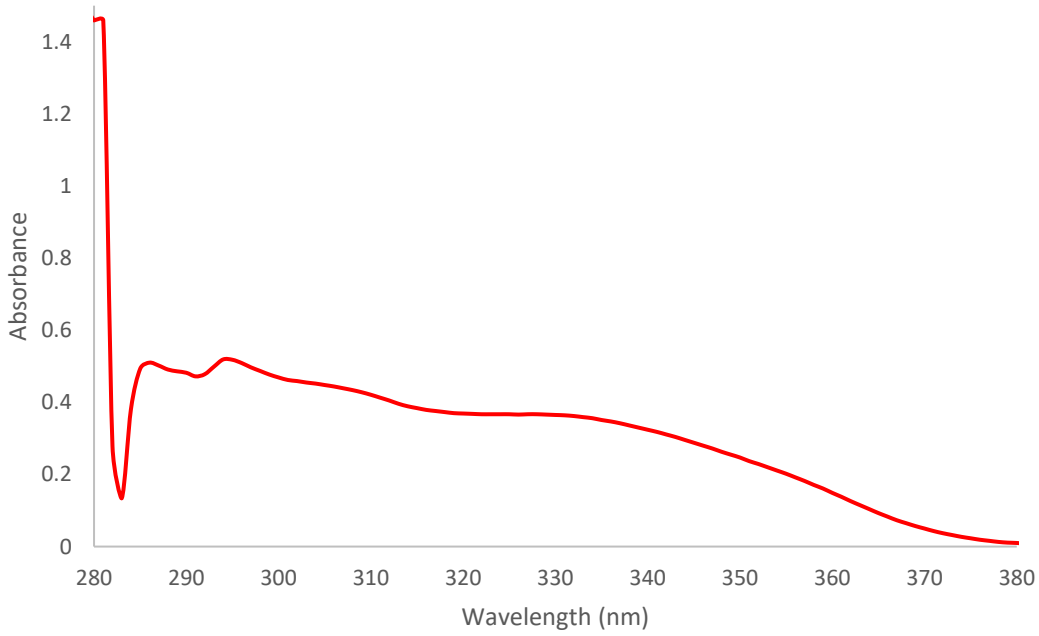

Figure S208 - UV-Vis spectra of compound **5** (0.10 mM) in a solution of DMSO: H_2O 3: 7.

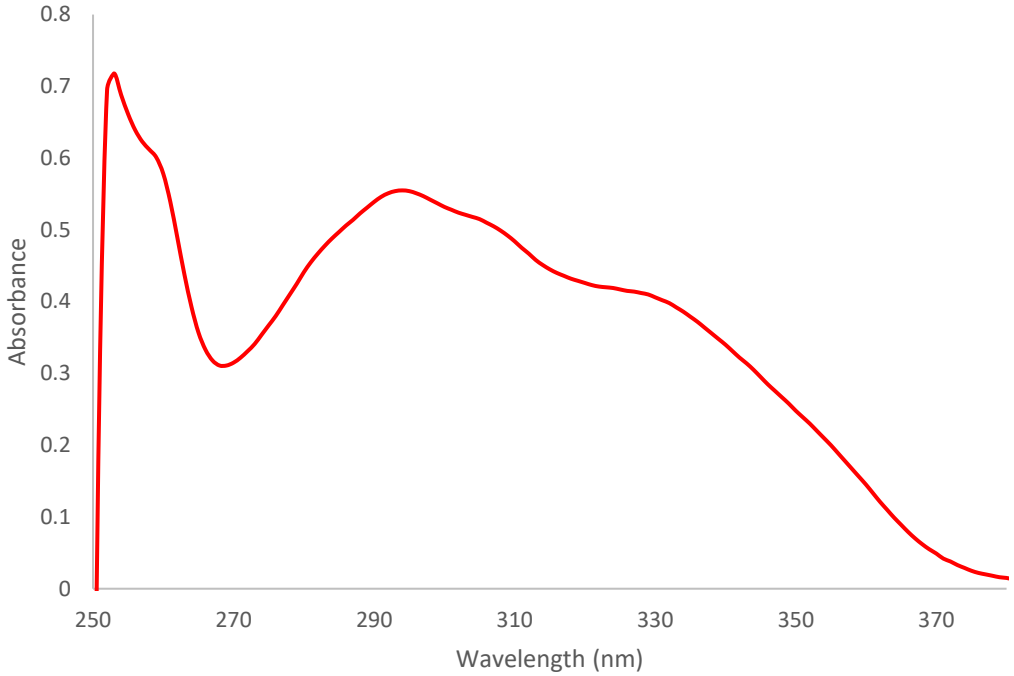

Figure S209 - UV-Vis spectra of compound **5** (0.10 mM) in a solution of DMSO: H_2O 1: 4.

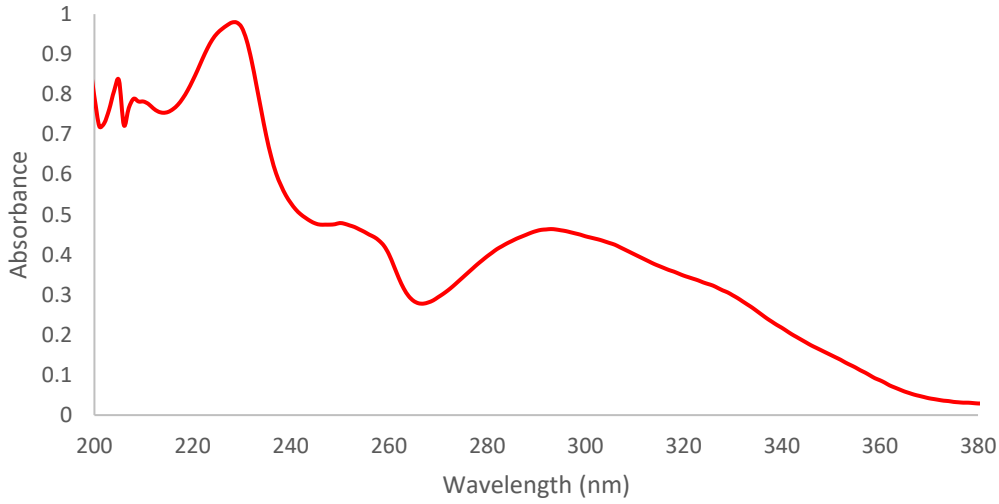

Figure S210 - UV-Vis spectra of compound **5** (0.10 mM) in a solution of EtOH: H_2O 1: 19.

Fluorescence spectra

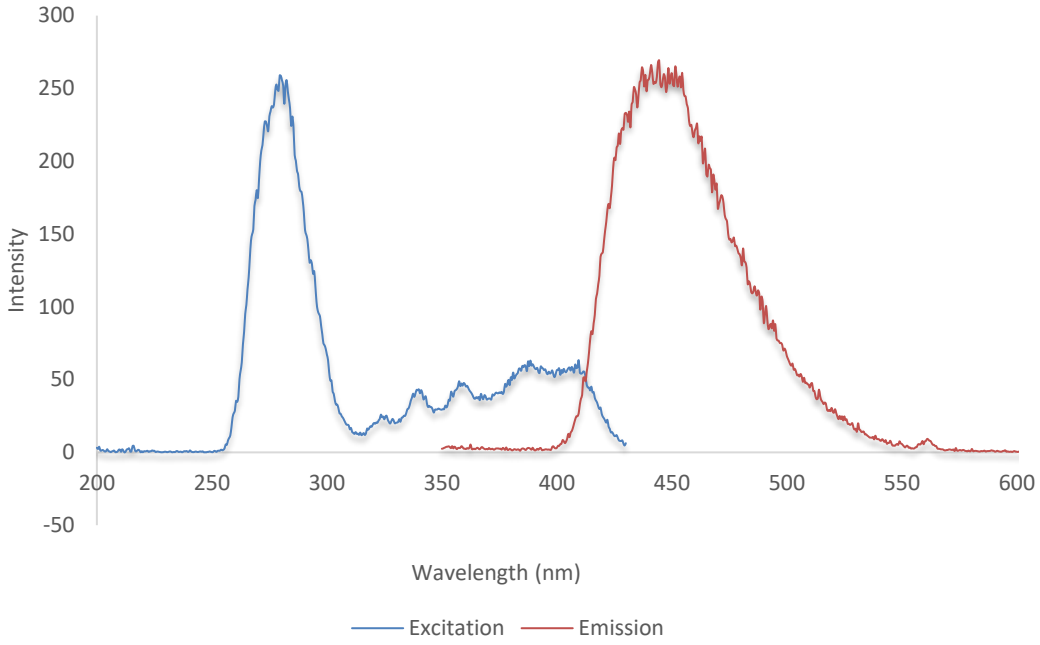

Figure S211 - Fluorescence spectra of compound **1** (0.003 mM) in a solution of DMSO.

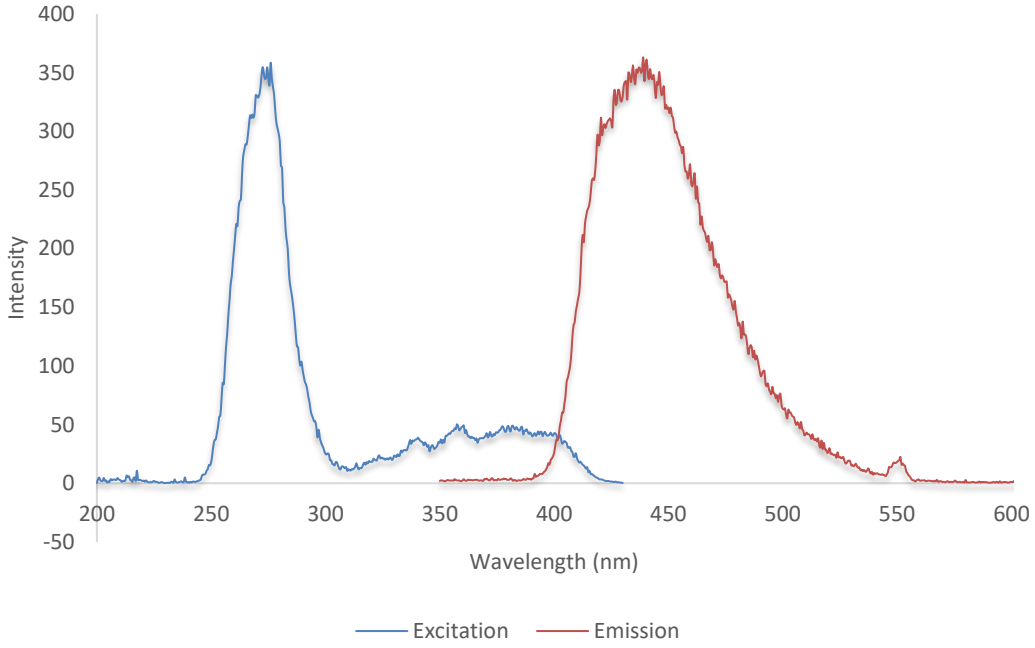

Figure S212 - Fluorescence spectra of compound **1** (0.003 mM) in a solution of DMSO: H_2O 1: 1.

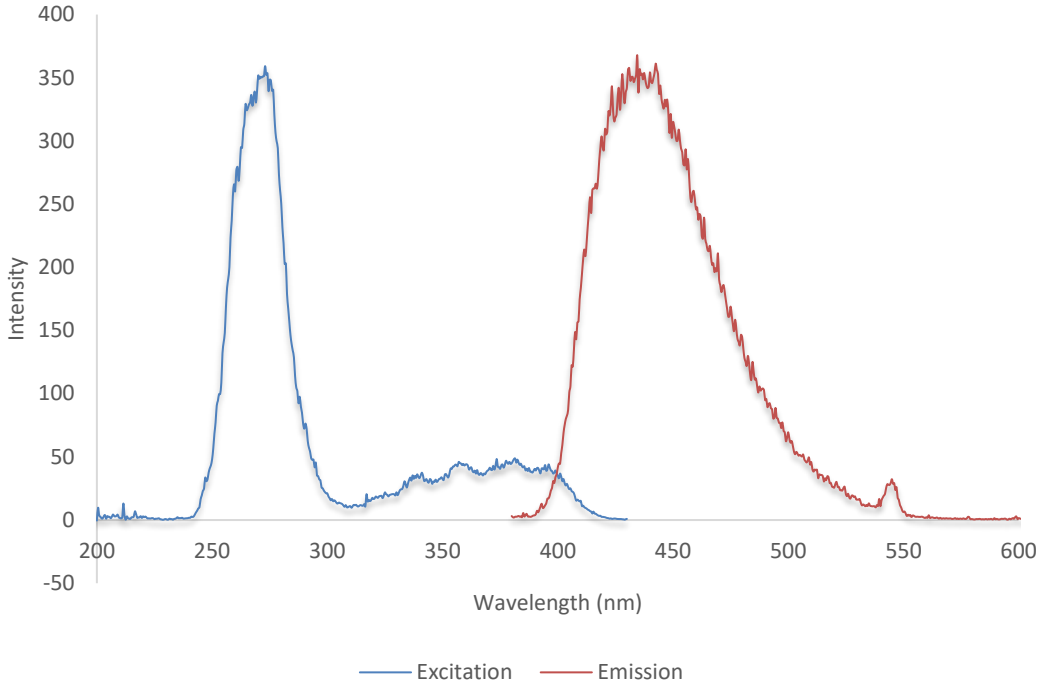

Figure S213 - Fluorescence spectra of compound **1** (0.003 mM) in a solution of DMSO: H_2O 3: 7.

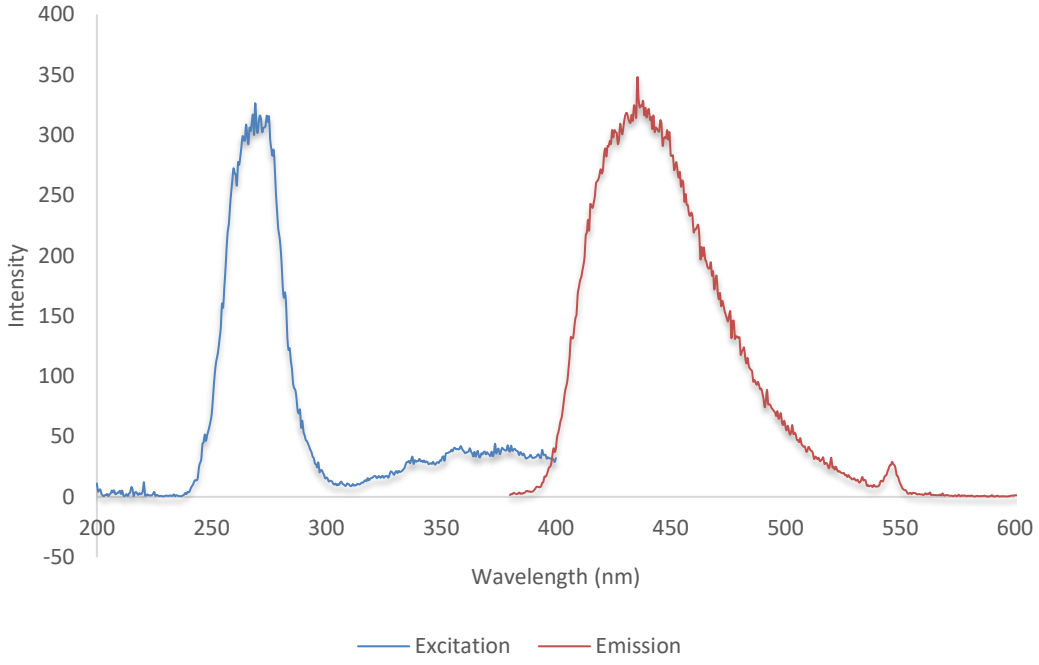

Figure S214 - Fluorescence spectra of compound **1** (0.003 mM) in a solution of DMSO: H_2O 1: 4.

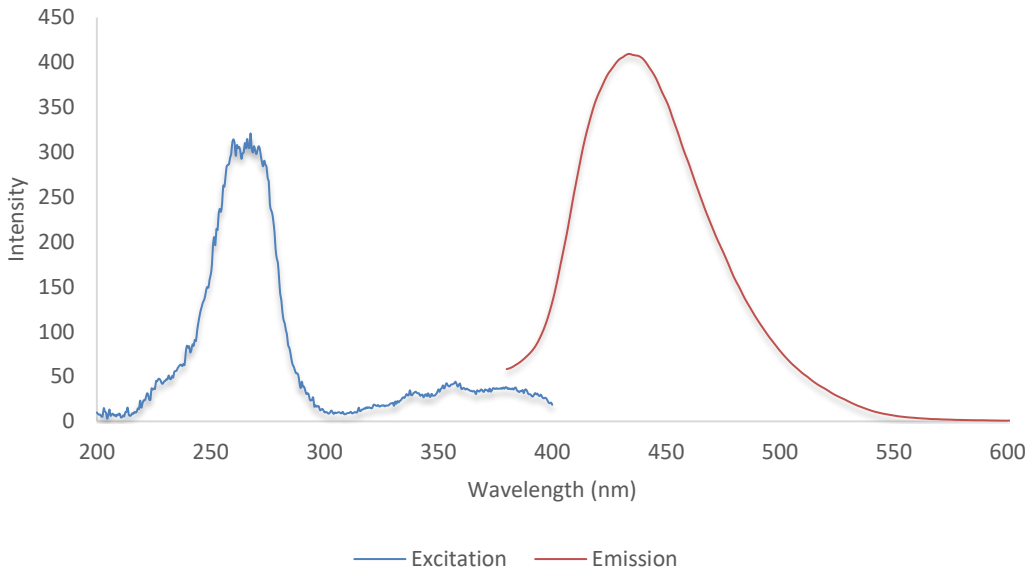

Figure S215 - Fluorescence spectra of compound **1** (0.003 mM) in a solution of EtOH: H_2O 1: 19.

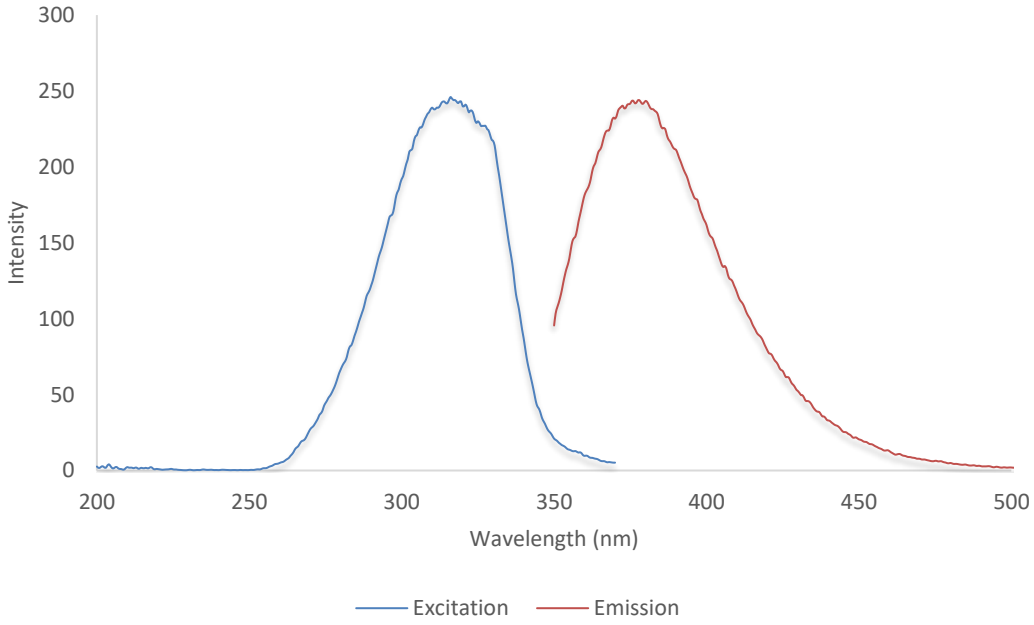

Figure S216 - Fluorescence spectra of compound **2** (0.003 mM) in DMSO.

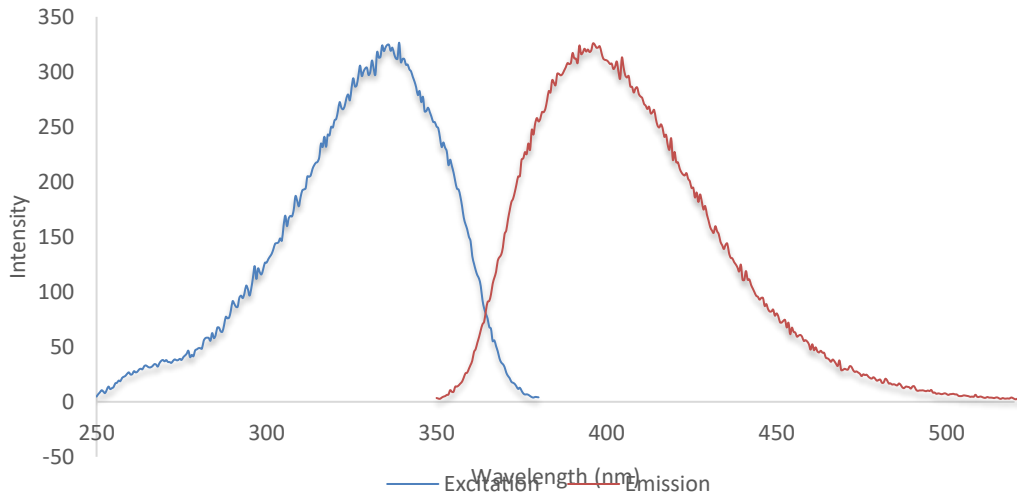

Figure S217 - Fluorescence spectra of compound **2** (0.003 mM) in a solution of DMSO: H_2O 1: 1.

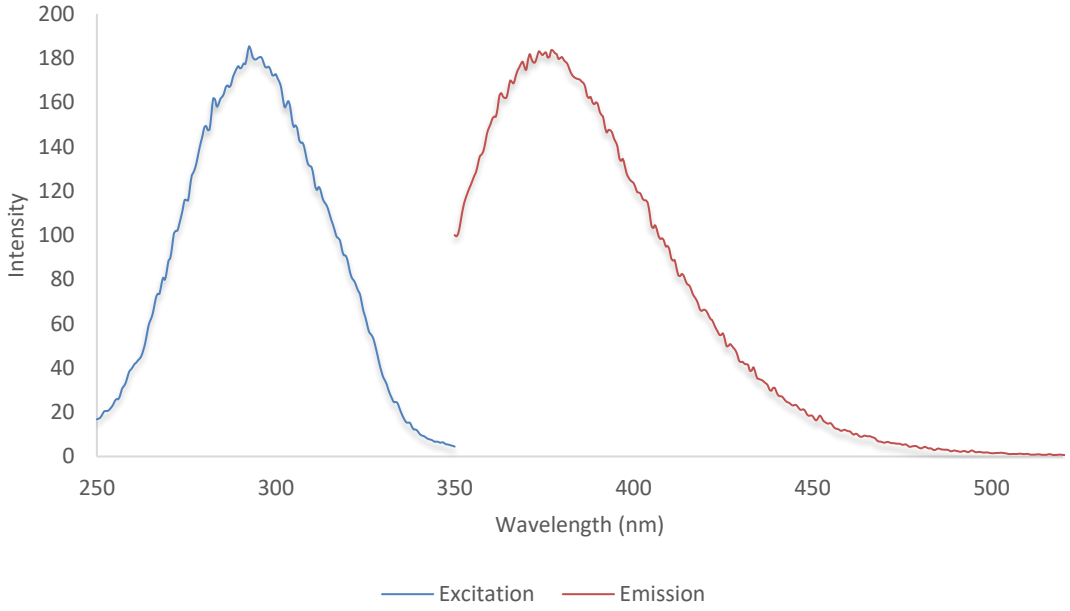

Figure S218 - Fluorescence spectra of compound **2** (0.003 mM) in a solution of DMSO: H_2O 3: 7.

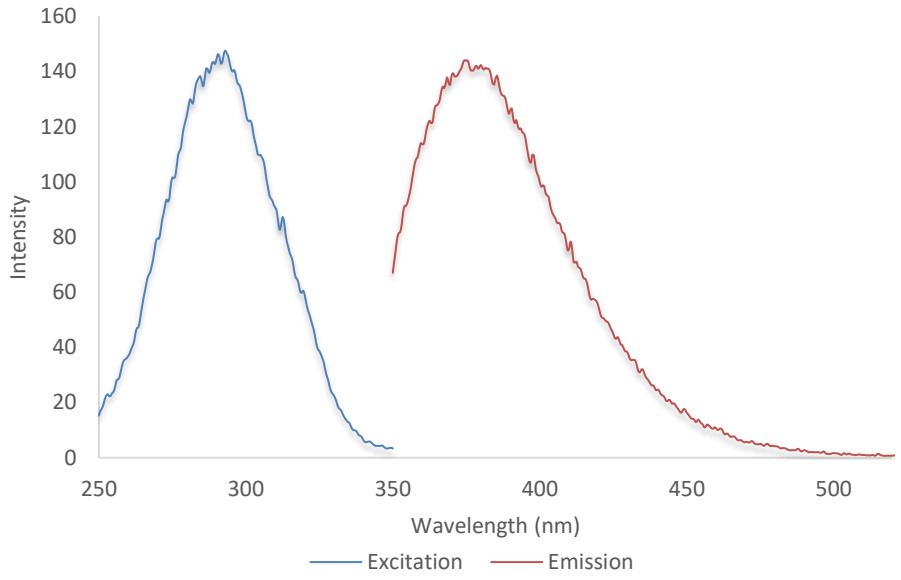

Figure S219 - Fluorescence spectra of compound **2** (0.003 mM) in a solution of DMSO: H_2O 1: 4.

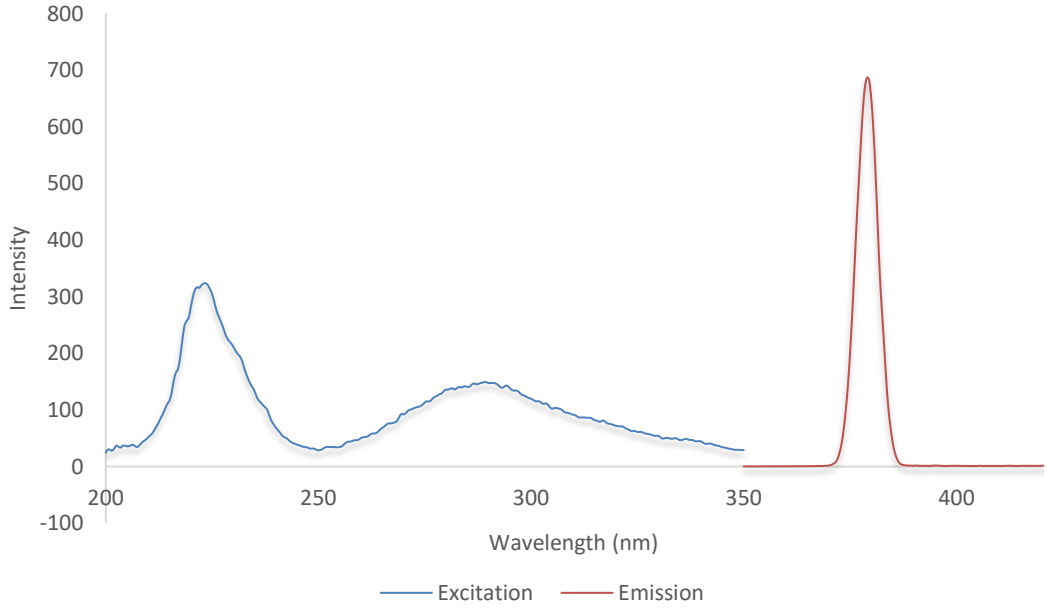

Figure S220 - Fluorescence spectra of compound **2** (0.003 mM) in a solution of EtOH: H_2O 1: 19.

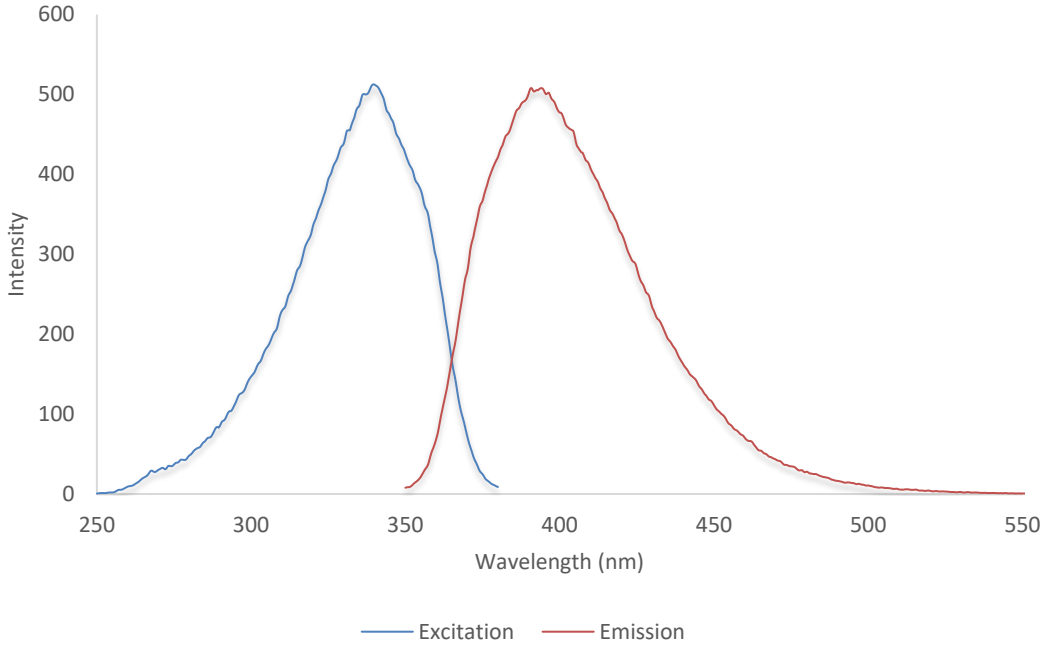

Figure S221 - Fluorescence spectra of compound **4** (0.003 mM) in DMSO.

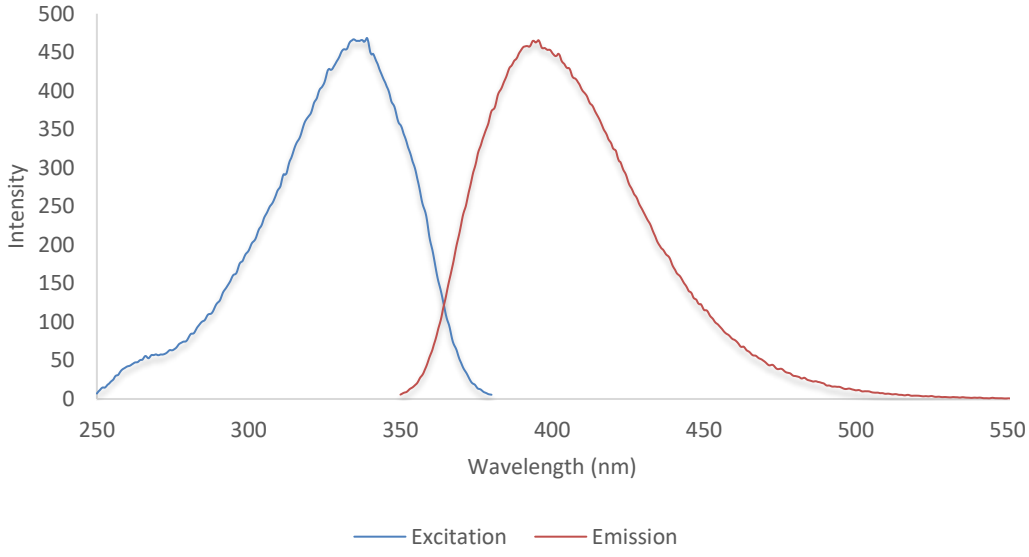

Figure S222 - Fluorescence spectra of compound **4** (0.003 mM) in a solution of DMSO: H_2O 1: 1.

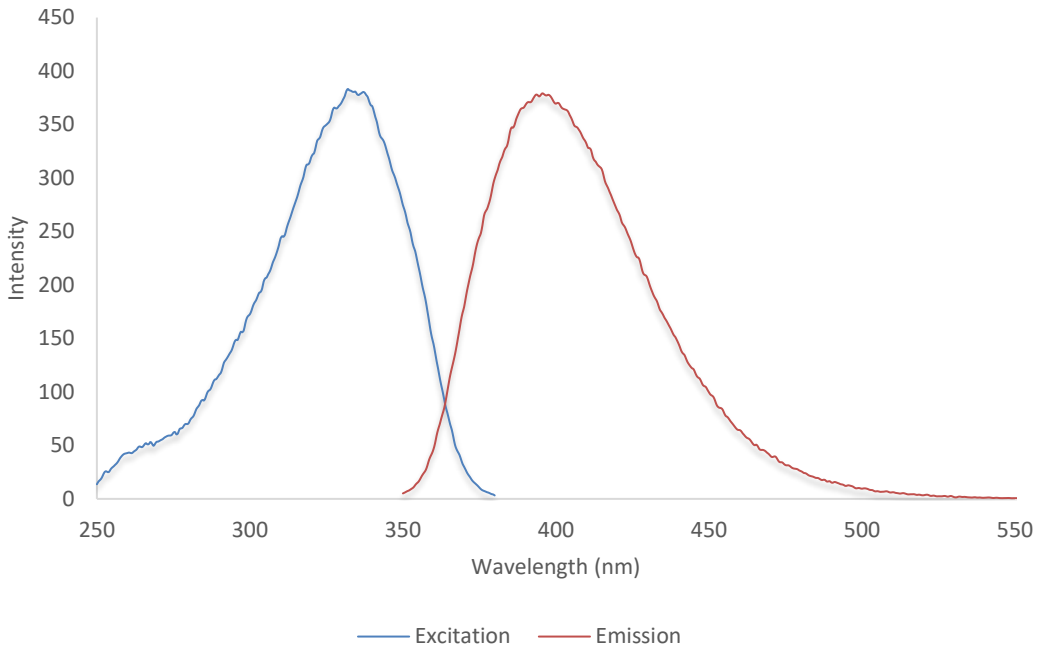

Figure S223 - Fluorescence spectra of compound **4** (0.003 mM) in a solution of DMSO: H_2O 3: 7.

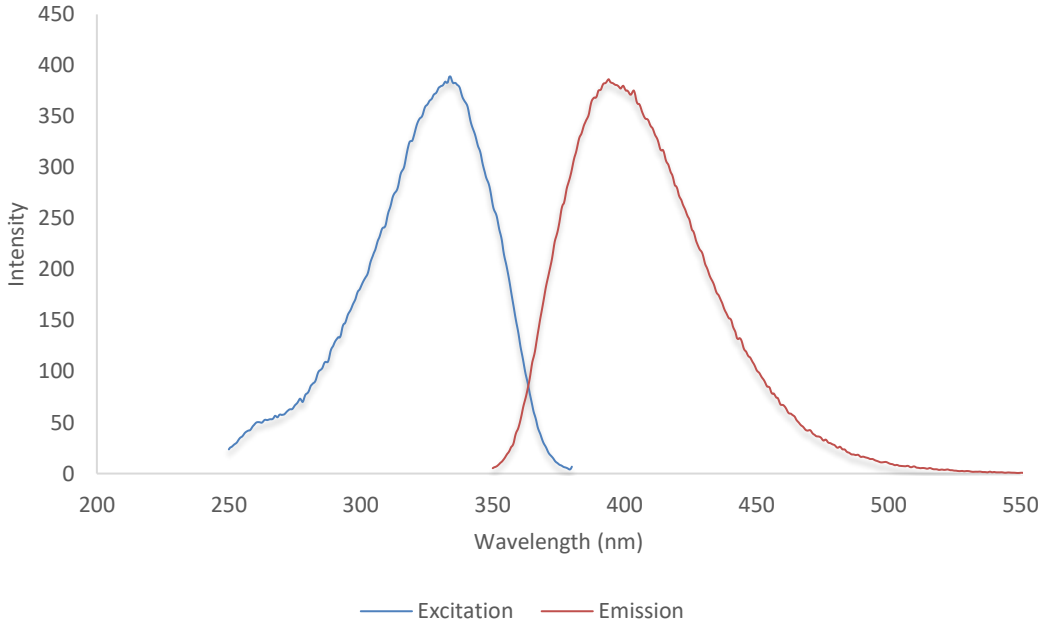

Figure S224 - Fluorescence spectra of compound **4** (0.003 mM) in a solution of DMSO: H_2O 1: 4.

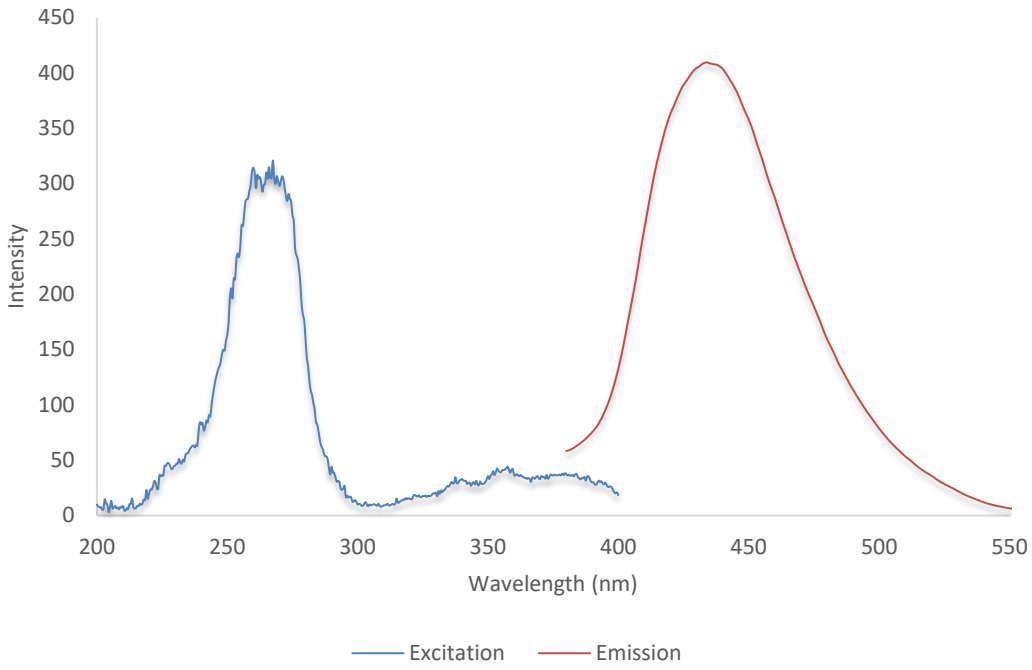

Figure S225 - Fluorescence spectra of compound **4** (0.003 mM) in a solution of EtOH: H_2O 1: 19.

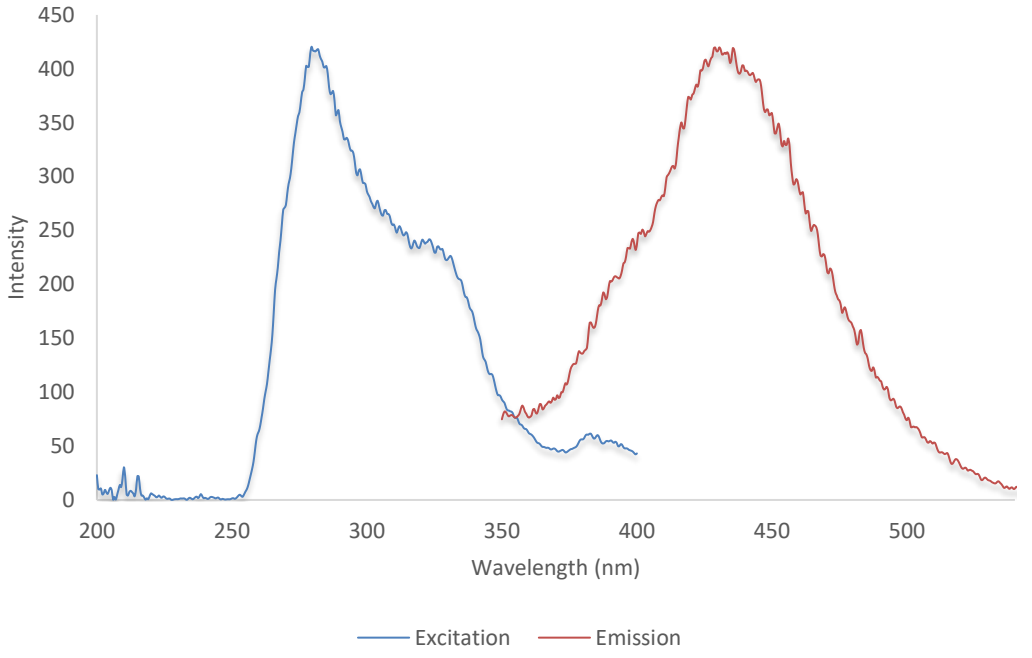

Figure S226 - Fluorescence spectra of compound **5** (0.03 mM) in DMSO.

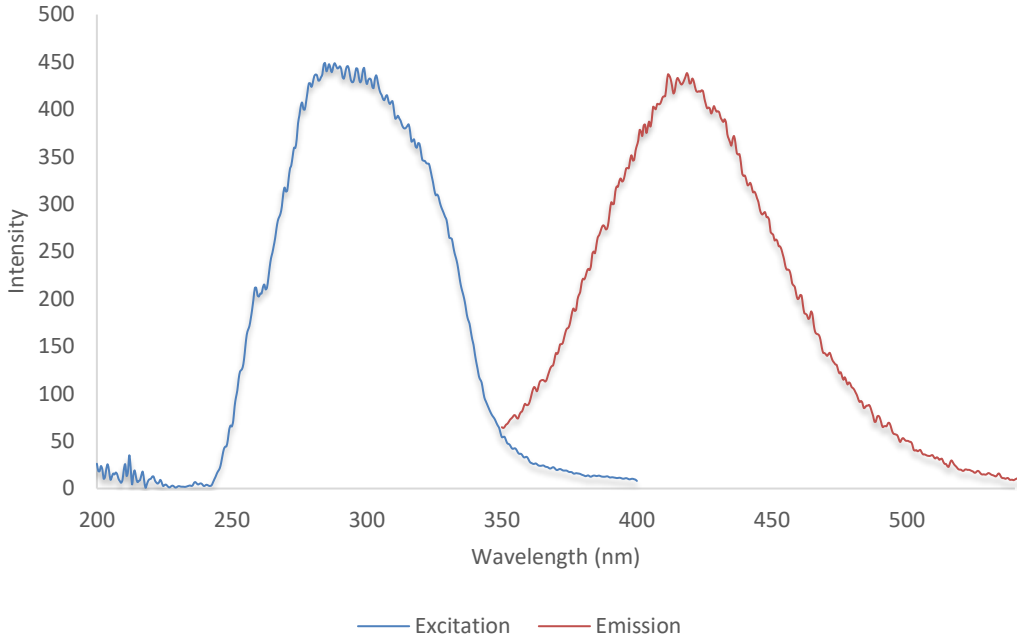

Figure S227 - Fluorescence spectra of compound **5** (0.03 mM) in a solution of DMSO: H_2O 1: 1.

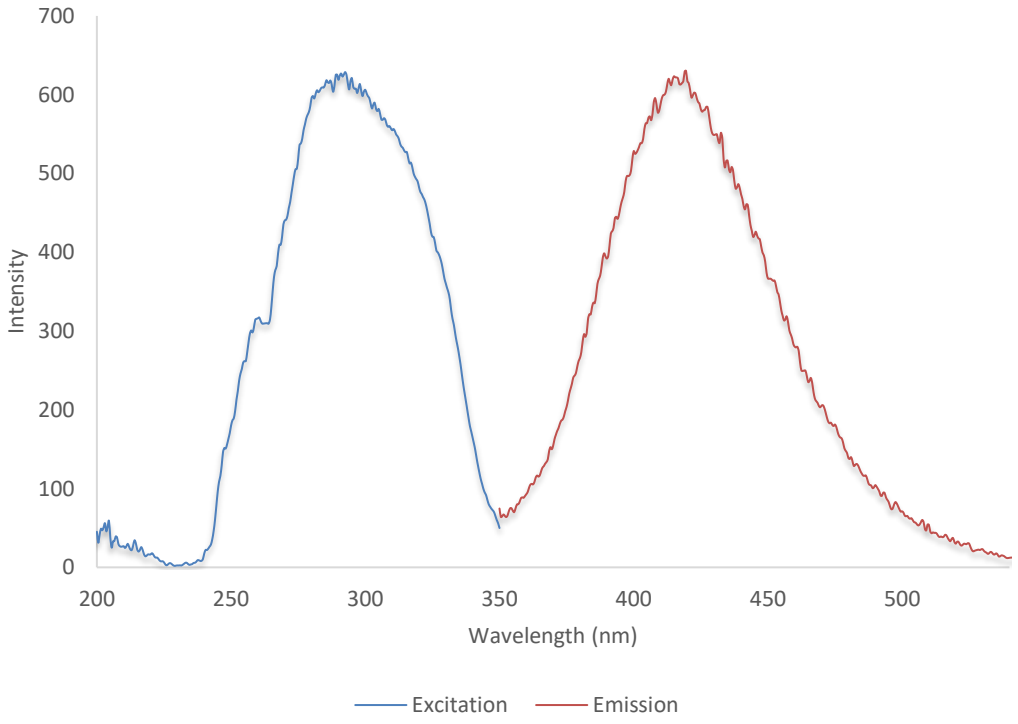

Figure S228 - Fluorescence spectra of compound **5** (0.03 mM) in a solution of DMSO: H_2O 3: 7.

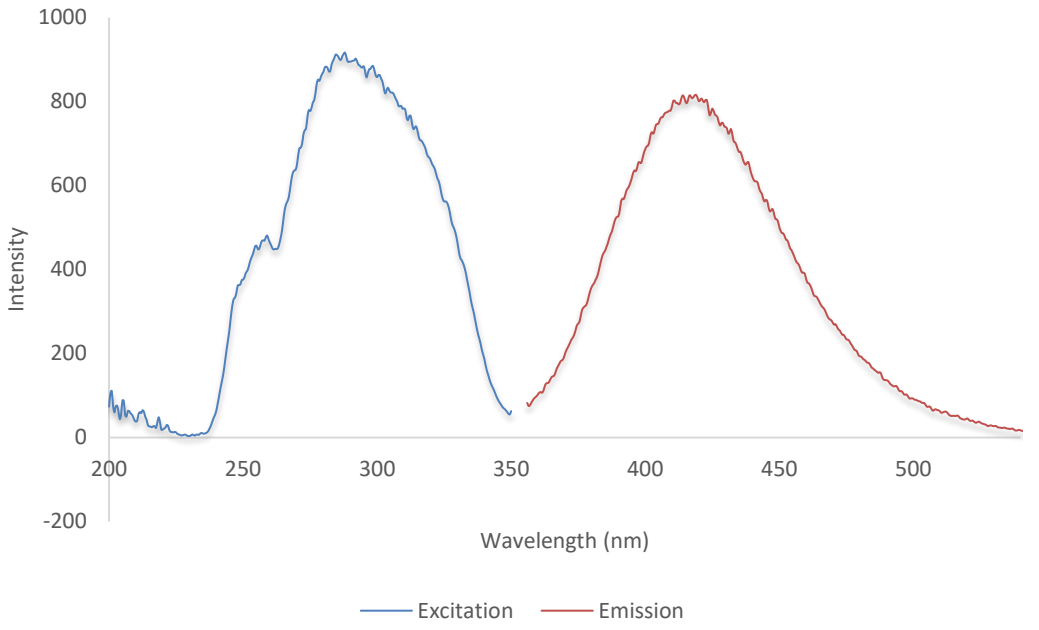

Figure S229 - Fluorescence spectra of compound **5** (0.03 mM) in a solution of DMSO: H_2O 1: 4.

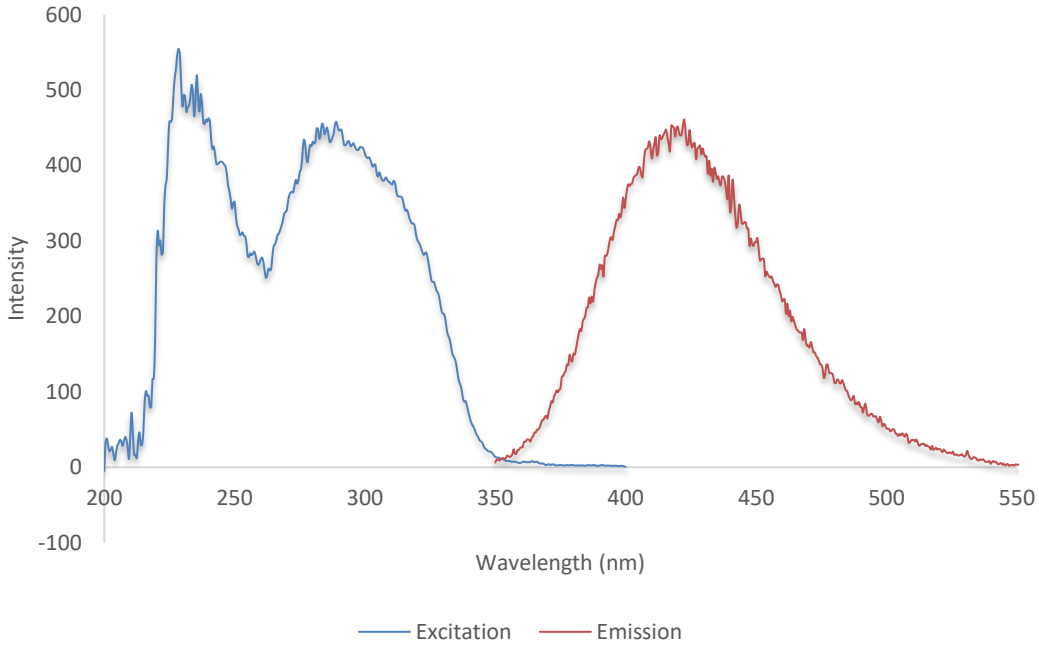

Figure S230 - Fluorescence spectra of compound **5** (0.03 mM) in a solution of EtOH: H_2O 1: 19.

Single crystal X-ray structures

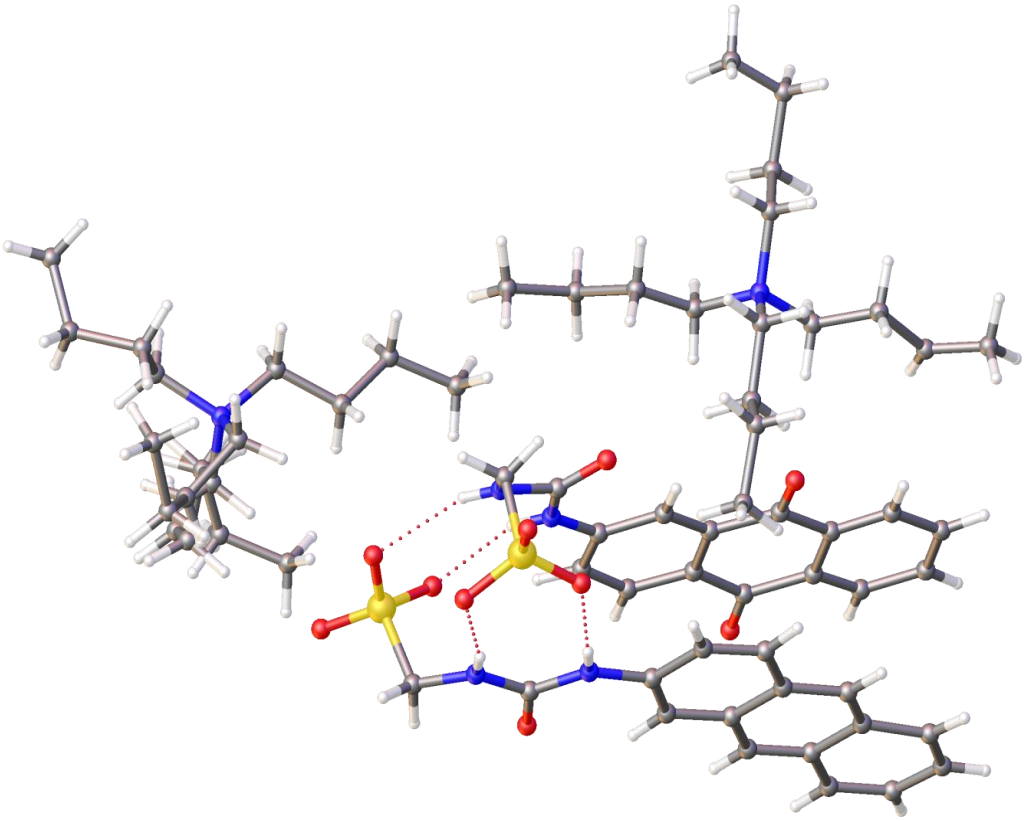

Figure S231 - Crystal data for compound **1**: red = oxygen; yellow = sulfur; blue = nitrogen; white = hydrogen; grey = carbon. CCDC 1562758, $C_{64}H_{95}N_6O_{10}S_2$ (M =1172.57): triclinic, space group P -1, a = 11.2916(13) Å, b = 12.5010(13) Å, c = 23.9203(16) Å, α = 88.359(8)°, β = 86.588(8)°, γ = 76.689(10)°, V = 3276.6(6) $Å^3$, Z = 2, T = 100(1) K, CuK\α = 1.5418 Å, Dcalc = 1.187 g/cm^3, 37394 reflections measured (7.268 ≤ 2Θ ≤ 100.870), 6862 unique (R_{int} = 0.1754, R_{sigma} = 0.1246) which were used in all calculations. The final R_1 was 0.1758 (I > 2σ(I)) and wR_2 was 0.4815 (all data).

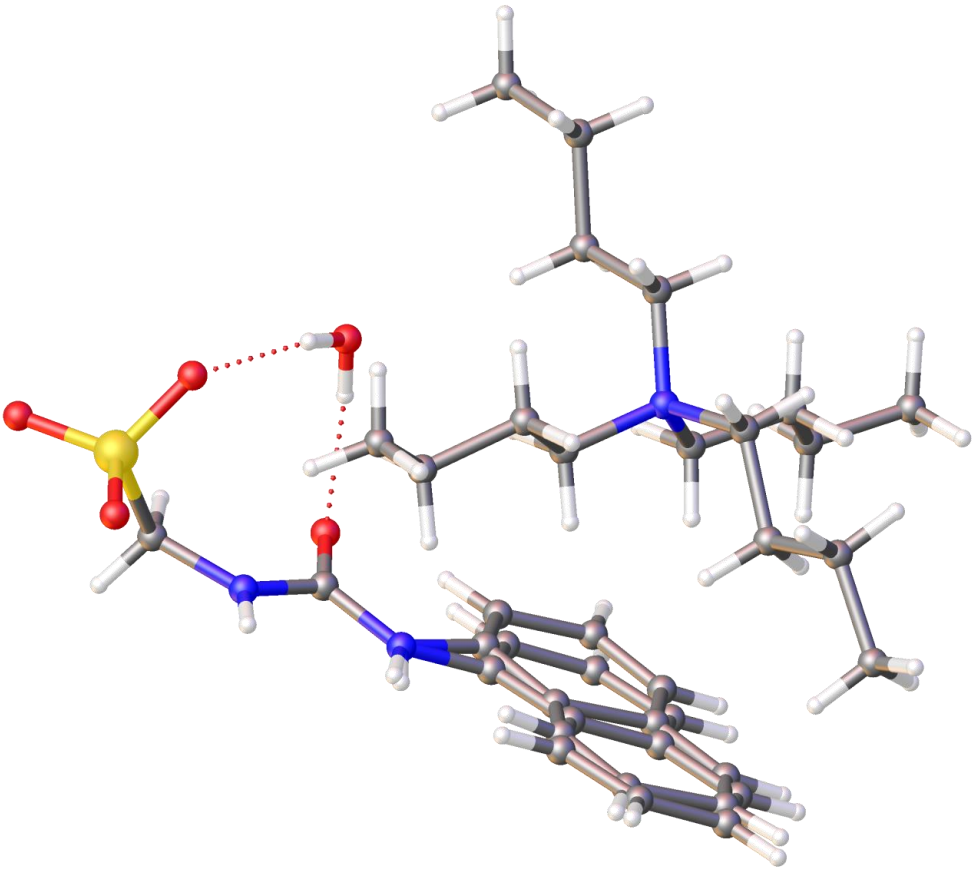

Figure S232 - Crystal data for compound **2**: red = oxygen; yellow = sulfur; blue = nitrogen; white = hydrogen; grey = carbon. CCDC 1562761, $C_{28}H_{49}N_3O_5S_2$ (M =539.76): monoclinic, space group P 1 21/n 1, a = 13.1121(18) Å, b = 16.3159(14) Å, c = 13.6871(16) Å, α = 90°, β = 900.27(11)°, γ = 90°, V = 2928.2(6) Å^3, Z = 4, T = 100(1) K, CuK\α = 1.5418 Å, Dcalc = 1.224 g/cm^3, 20834 reflections measured (8.252 ≤ 2Θ ≤ 146.390), 4527 unique (R_{int} = 0.0610 R_{sigma} = 0.0534) which were used in all calculations. The final R_1 was 0.0504 (I > 2σ(I)) and wR_2 was 0.1479 (all data).

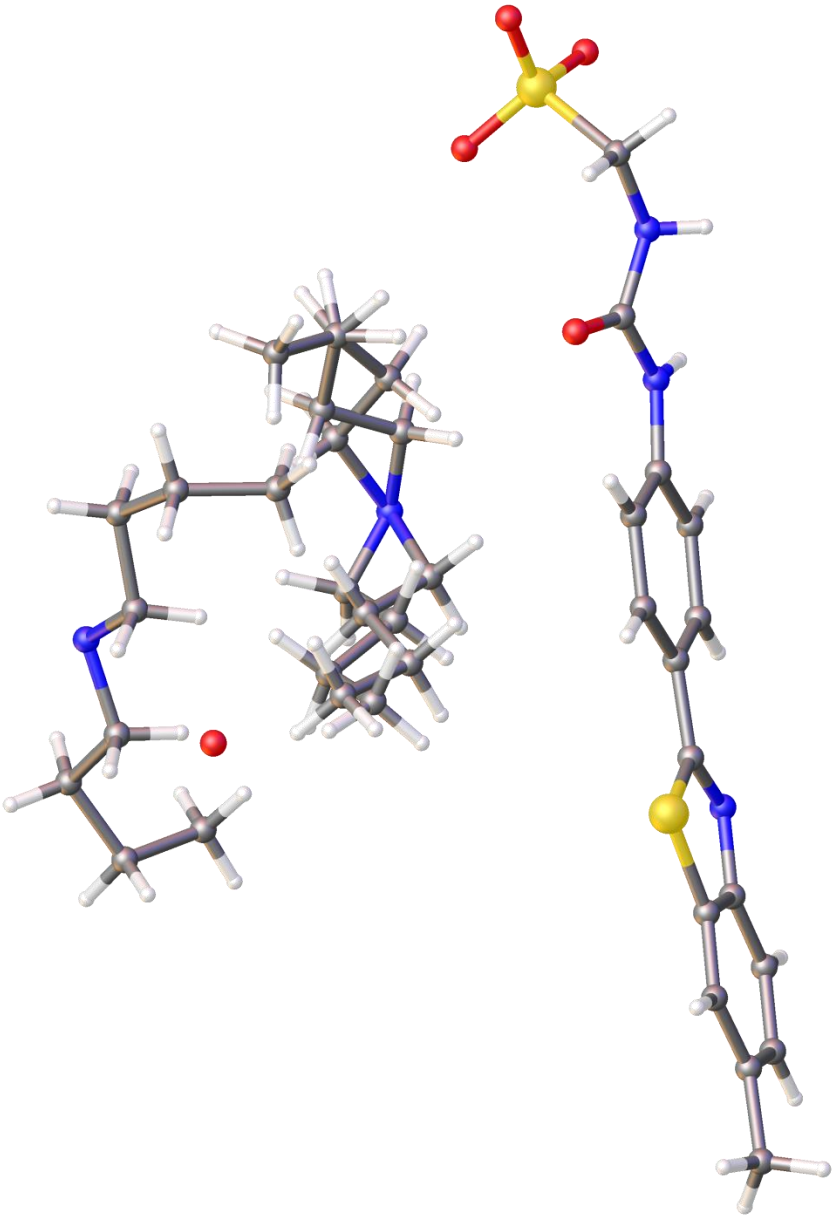

Figure S233 - Crystal data for compound **4**: red = oxygen; yellow = sulfur; blue = nitrogen; white = hydrogen; grey = carbon. CCDC 1562759, $C_{32}H_{50}N_4O_{4.5}S_2$ (M =626.88): monoclinic, space group P 1 2/n 1, a = 12.706(3) Å, b = 13.689(4) Å, c = 19.969(4) Å, α = 90°, β = 107.12(3)°, γ = 90°, V = 3319.3(16) $Å^3$, Z = 4, T = 100(1) K, CuK\α = 1.5418 Å, Dcalc = 1.254 g/cm^3, 12812 reflections measured (7.390 ≤ 2Θ ≤ 133.20), 5875 unique (R_{int} = 0.1201, R_{sigma} = 0.1653) which were used in all calculations. The final R_1 was 0.0685 (I > 2σ(I)) and wR_2 was 0.1642 (all data).

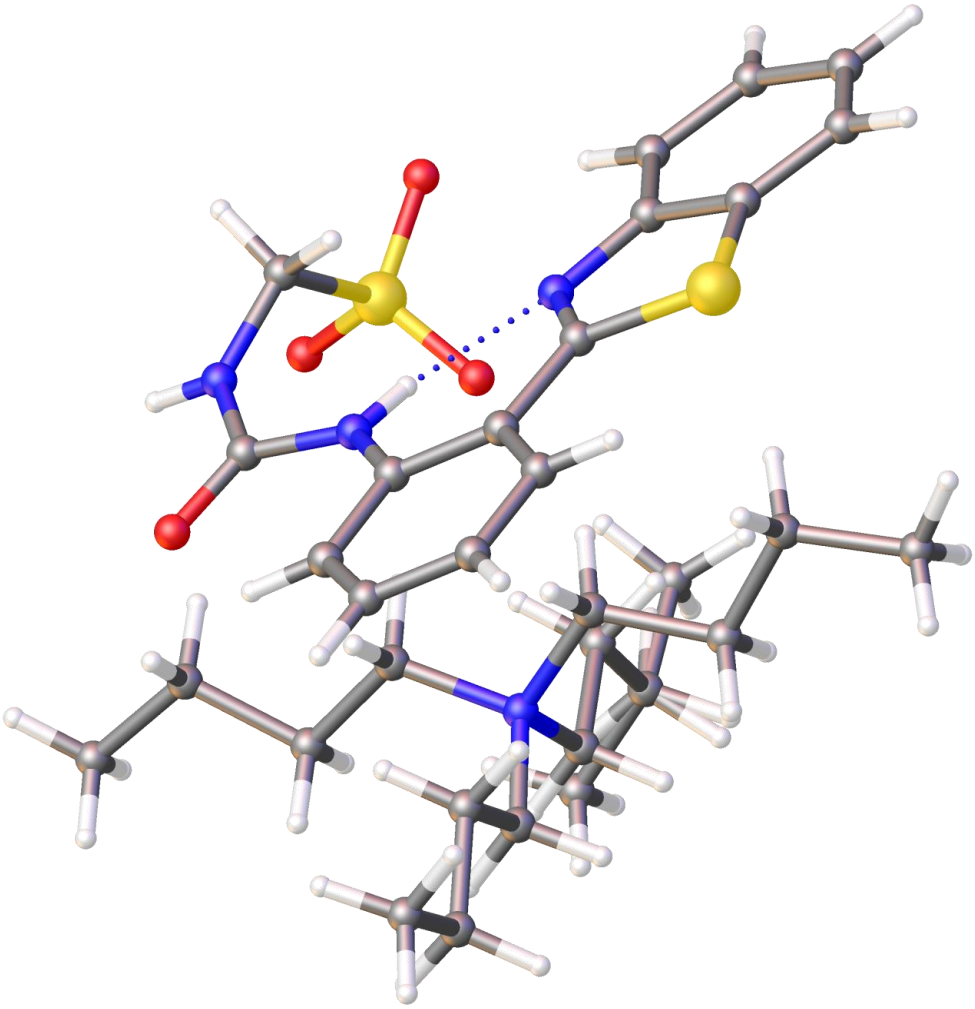

Figure S234 - Crystal data for compound **5**: red = oxygen; yellow = sulfur; blue = nitrogen; white = hydrogen; grey = carbon. CCDC 1562760, $C_{31}H_{48}N_4O_4S_2$ (M =604.85): monoclinic, space group P 1 21/c 1, a = 13.8269(16) Å, b = 14.5451(15) Å, c = 16.5512(16) Å, α = 90°, β = 103.927(11)°, γ = 90°, V = 3230.8(6) $Å^3$, Z = 4, T = 100(1) K, CuK\α = 1.5418 Å, Dcalc = 1.244 g/cm^3, 12954 reflections measured (8.200 ≤ 2Θ ≤ 133.202), 5716 unique (R_{int} = 0.0436, R_{sigma} = 0.0508) which were used in all calculations. The final R_1 was 0.0463 (I > 2σ(I)) and wR_2 was 0.1308 (all data).

Hydrogen bonding tables from single crystal X-ray structures

Table S11: Hydrogen bond distances and angles calculated from single crystal X-ray structures.

Compound	Hydrogen bond donor	Hydrogen atom	Hydrogen bond acceptor	Hydrogen bond length (D•••A) (Å)	Hydrogen bond angle (D-H•••A) (°)
1	N1	H1	O8	2.855 (14)	156.8 (8)
1	N2	H2	O10	2.976 (17)	155.3 (9)
1	N3	H3	O6	2.956 (13)	167.0 (7)
1	N4	H4	O5	2.967 (14)	163.0 (7)
2	N2	H2	O3	2.864 (3)	151.88 (13)
2	N1	H1a	O3	2.858 (3)	155.21 (13)
2	O5	H5b	O1	2.821 (3)	170.08 (17)
2	O5	H5c	O2	2.813 (3)	160.56 (16)
4	N2	H2	O2	2.865 (5)	170.9 (3)
4	N3	H3	O4	2.896 (5)	127.8 (2)
4	O5	-	O4	2.826 (7)	-
4	C6	H6	O3	3.371 (6)	159.3 (3)
4	C16b	H16b	S1	3.794 (5)	157.7 (2)
4	C14	H14	O1	3.375 (5)	162.2 (3)
5	N3	H3	O4	2.853 (2)	140.47 (13)
5	N2	H2	N1	2.697 (3)	137.56 (12)
5	N2	H2	O2	3.410 (2)	133.09 (12)
5	C12	H12	O1	2.836 (3)	123.43 (14)
5	C2	H2a	O3	3.383 (3)	178.10 (16)

Surface tension measurements

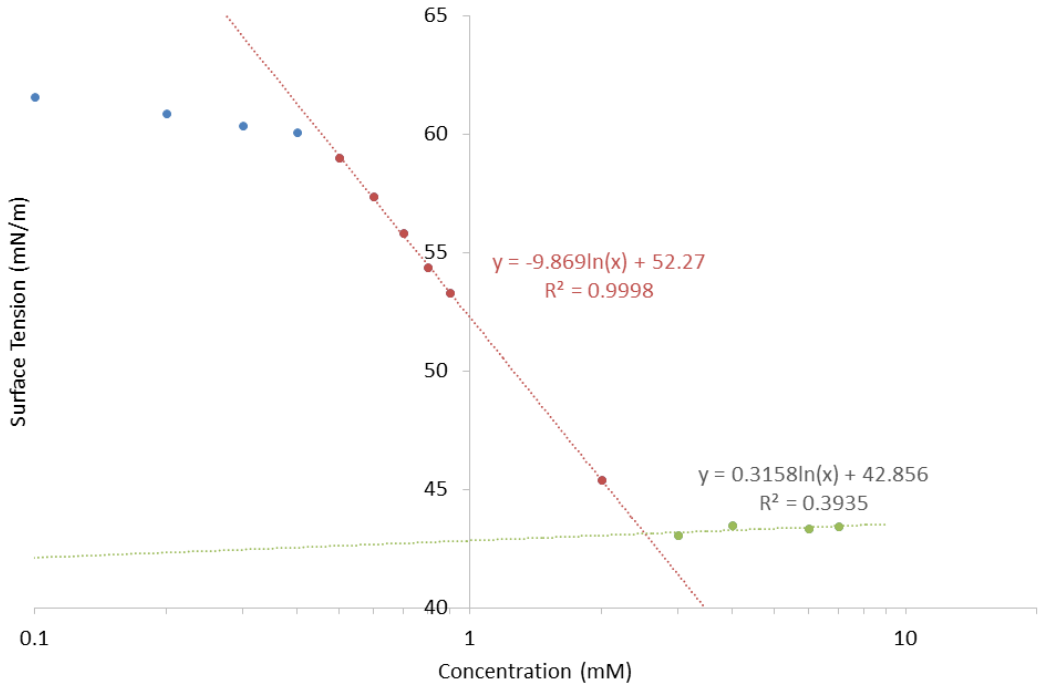

Figure S235 - Calculation of CMC for compound **1** in an EtOH: H_2O 1: 19 mixture using surface tension measurements.

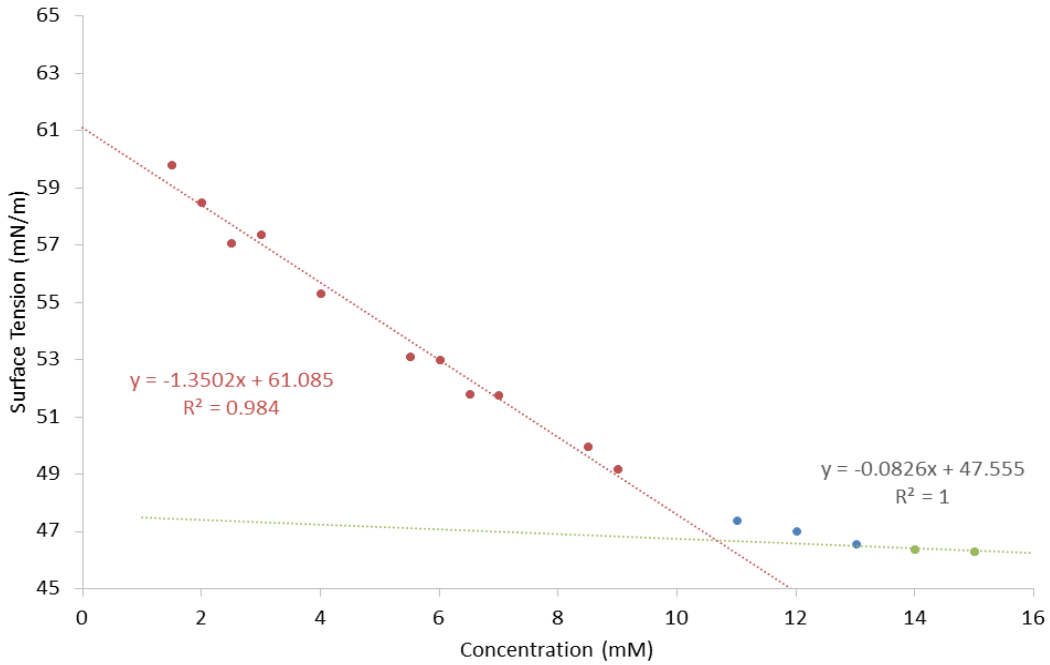

Figure S236 - Calculation of CMC for compound **2** in an EtOH: H_2O 1: 19 mixture using surface tension measurements.

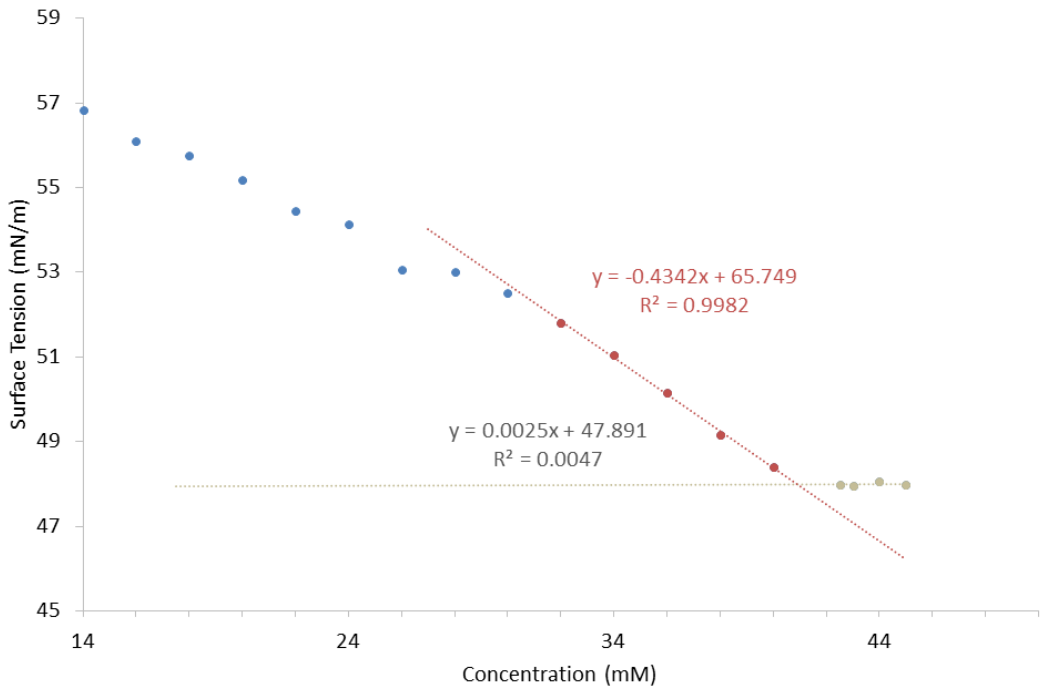

Figure S237 - Calculation of CMC for compound **3** in an EtOH: H_2O 1: 19 mixture using surface tension measurements.

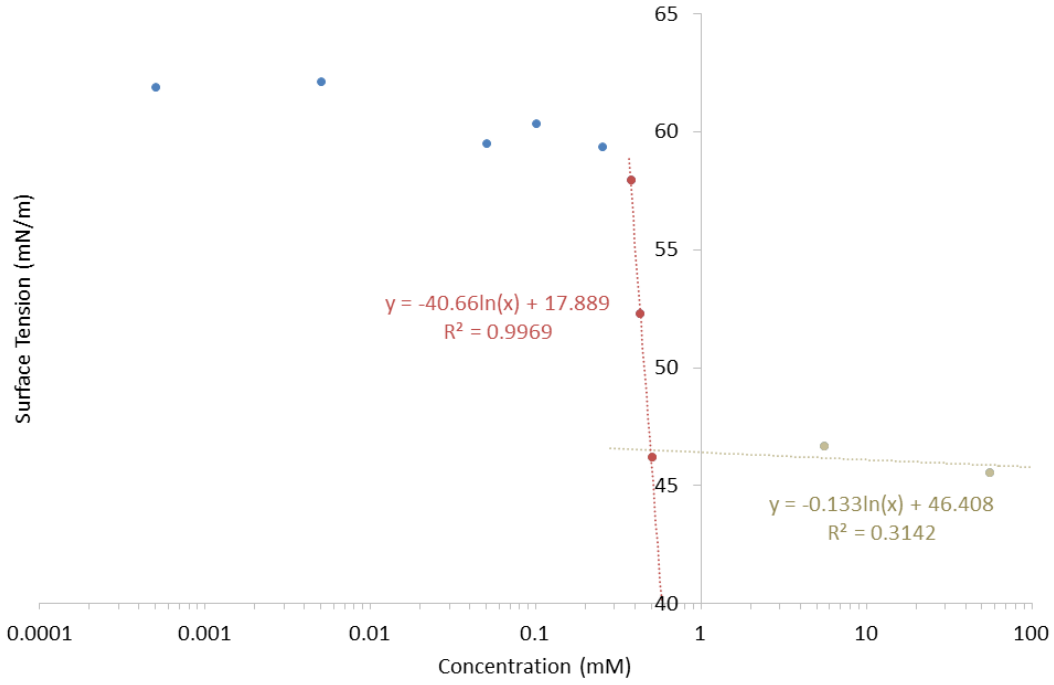

Figure S238 - Calculation of CMC for compound **4** in an EtOH: H_2O 1: 19 mixture using surface tension measurements.

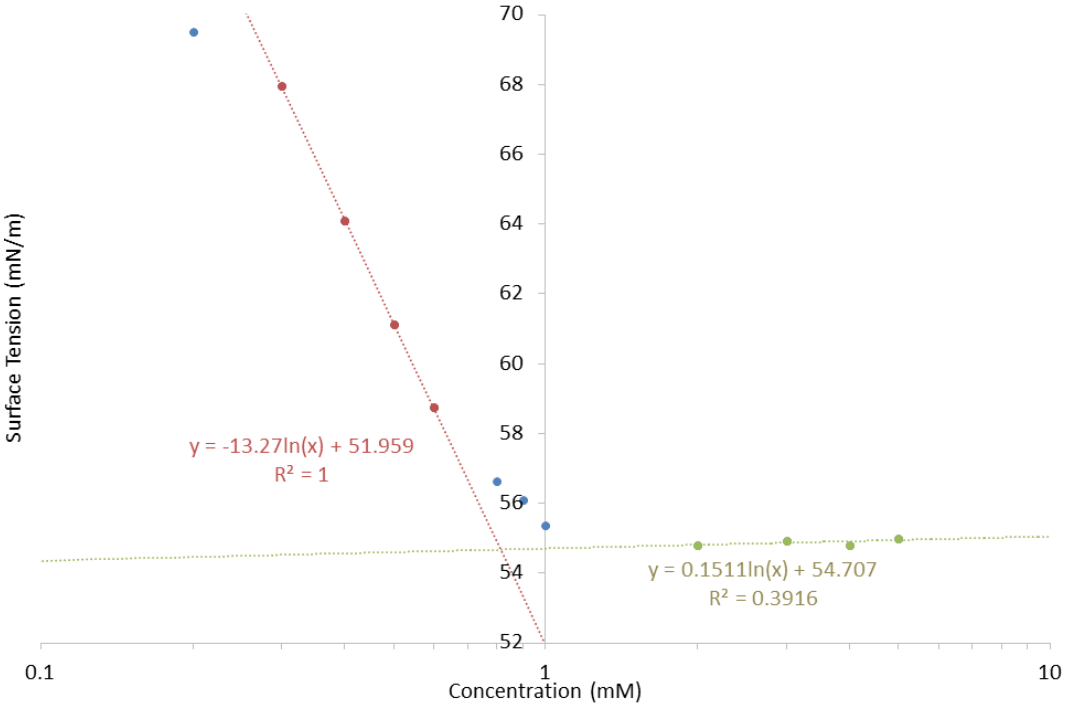

Figure S239 - Calculation of CMC for compound **4** in H_2O using surface tension measurements.

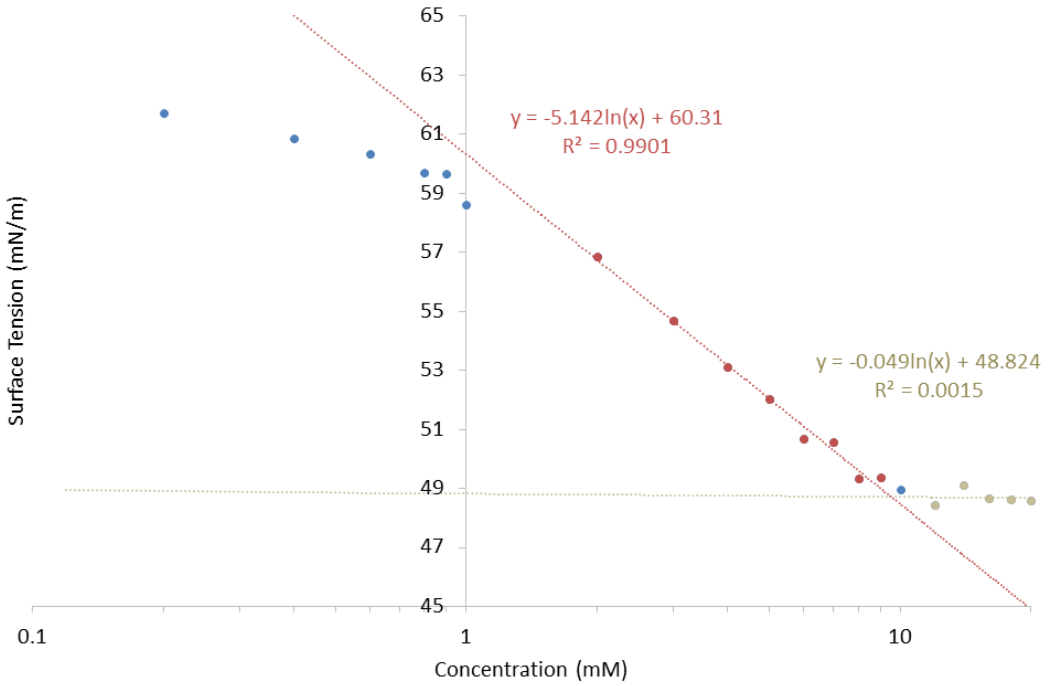

Figure S240 - Calculation of CMC for compound **5** in an EtOH: H_2O 1: 19 mixture using surface tension measurements.

Microscopy images

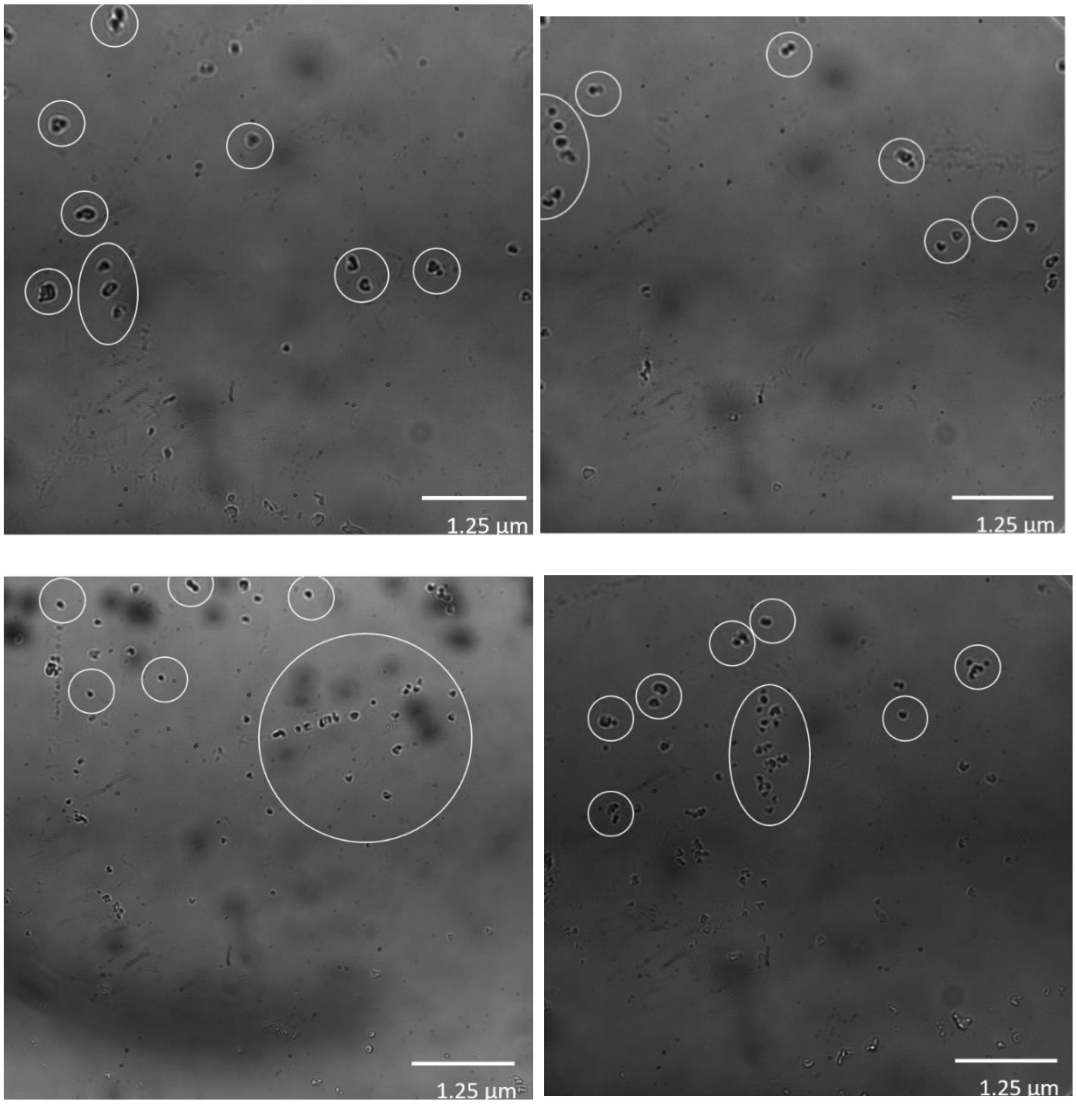

Figure S241 - A selection of transmitted light microscope images of compound **4** (0.50 mM) in an EtOH: H_2O 1: 19 solutions. Examples of the aggregate formations have been circled for clarity.

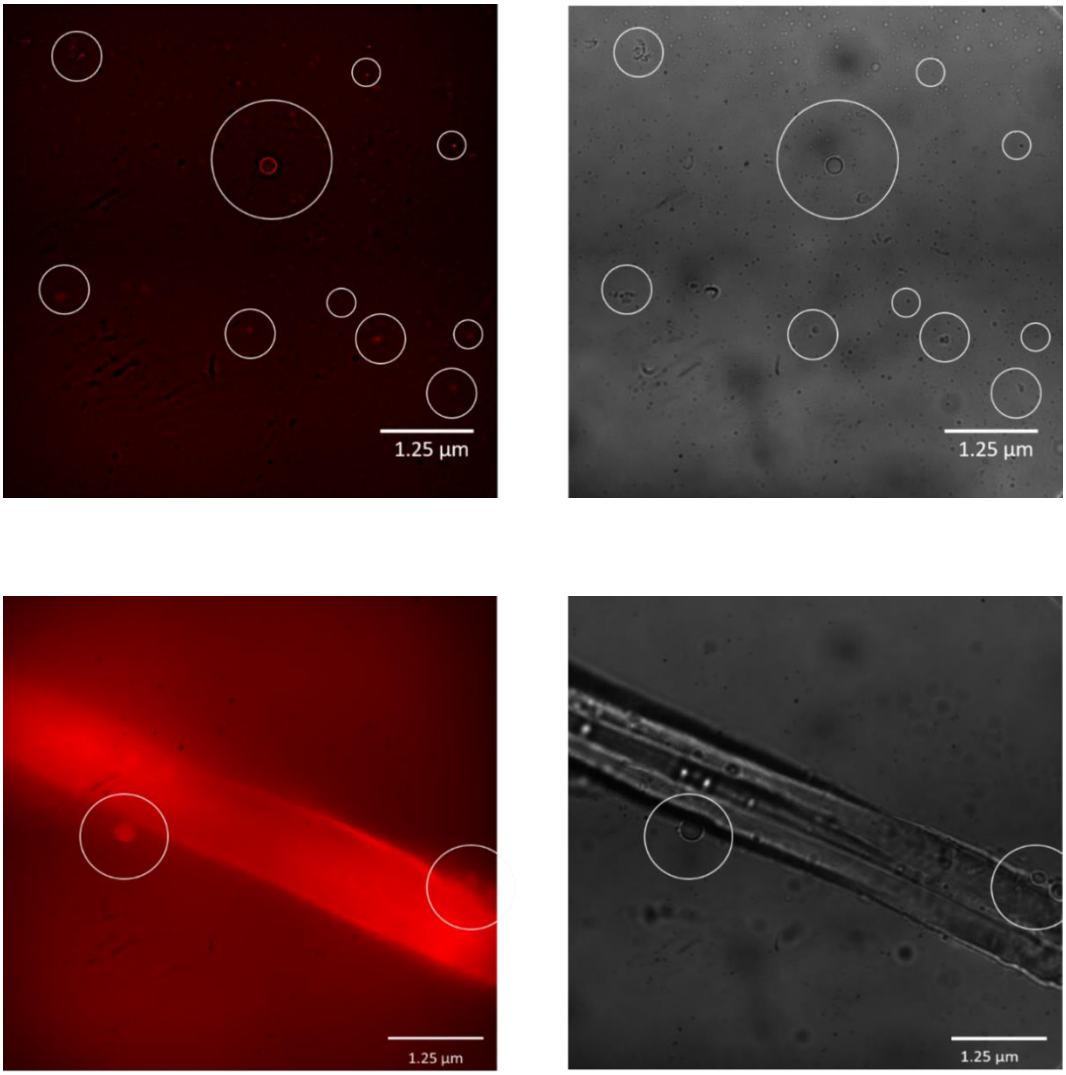

Figure S242 – A selection of DAPI filter composite images (left) and transmitted light images (right) of compound **4** at a concentration of 0.50 mM in a solution of DMSO: H_2O 1: 19. Evidence of aggregate formations are circled for clarity. Photo bleaching during the imagery lead to a loss of fluorescence emission intensity, therefore some compound aggregates could not be successfully captured in one (or both images).

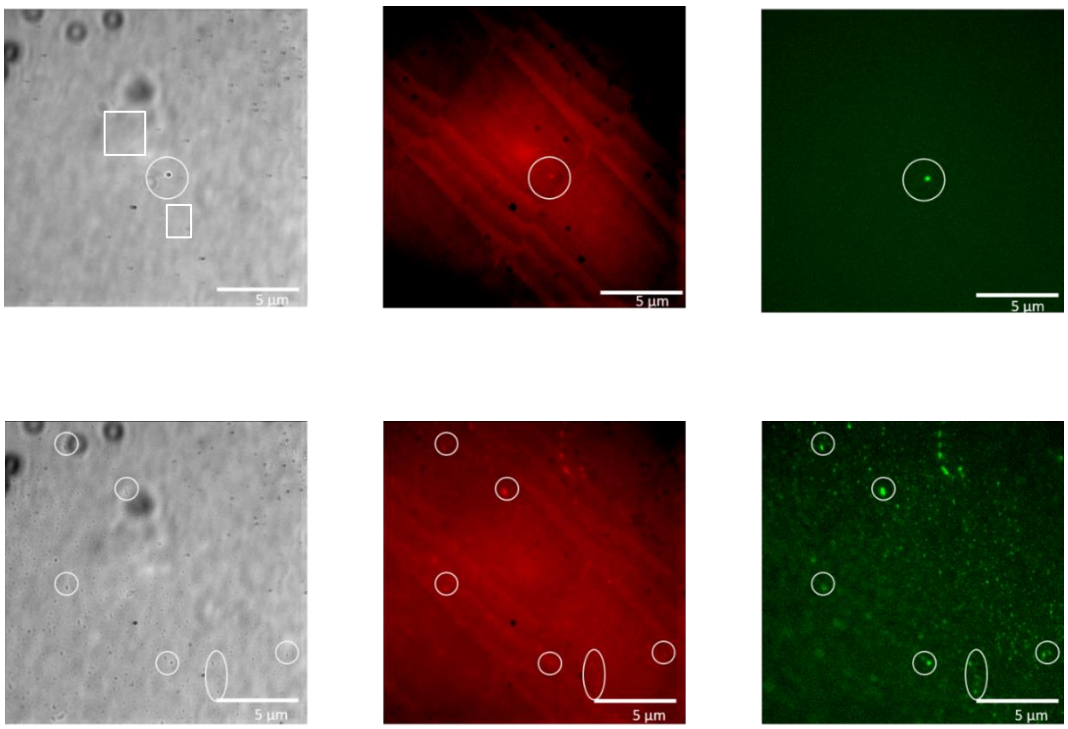

Figure S243 – A selection transmitted light images (left) DAPI filter composite images (centre) and GFP filter image (right) of compound **4** at a concentration of 0.50 mM in a solution of DMSO: H_2O 3: 7. Evidence of aggregate formations of varying sizes are circled for clarity. Photo bleaching during the imagery lead to a loss of fluorescence emission intensity, therefore some compound aggregates could not be successfully captured in one (both or all images).

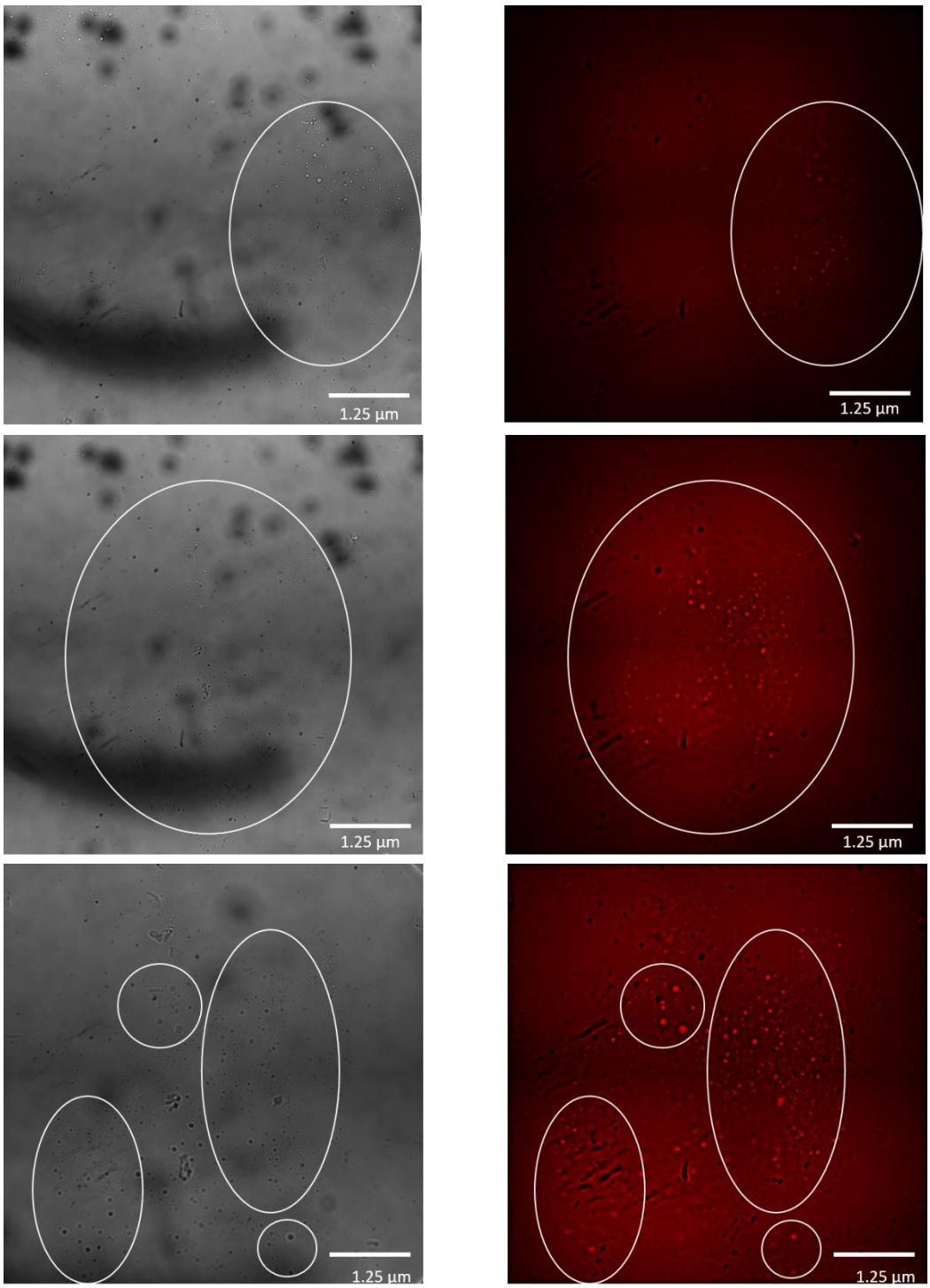

Figure S244 - A selection transmitted light images (left) and DAPI filter composite images (right) of compound **4** at a concentration of 0.50 mM in DMSO. Evidence of aggregate formations are circled for clarity. Photo bleaching during the imagery lead to a loss of fluorescence emission intensity, therefore some compound aggregates could not be successfully captured in one (or both images).

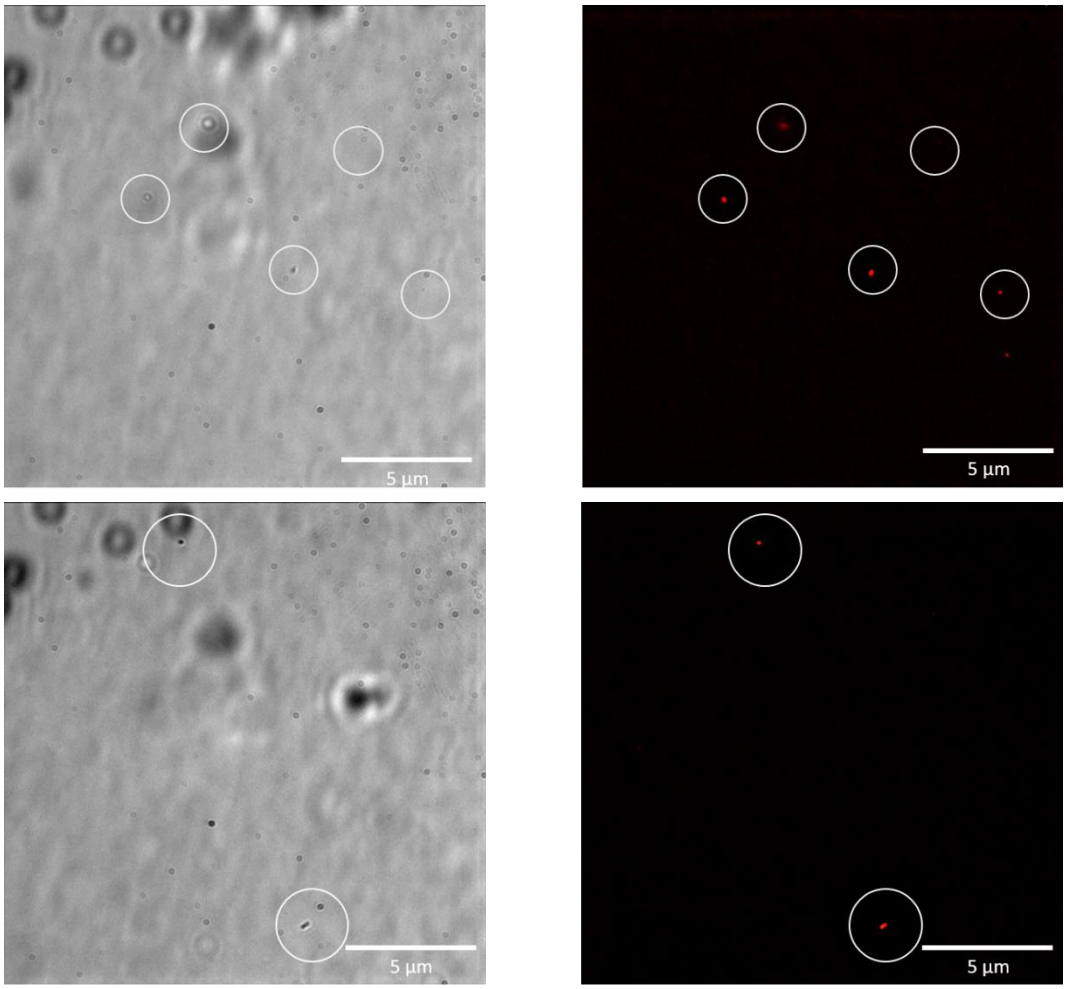

Figure S245 - A selection of transmitted light images (left) and DAPI filter composite images (right) of compound **5** at a concentration of 0.50 mM in a solution of EtOH: H_2O 1: 19. Evidence of aggregate formations are circled for clarity. Photo bleaching during the imagery lead to a loss of fluorescence emission intensity, therefore some compound aggregates could not be successfully captured in one (or both images).

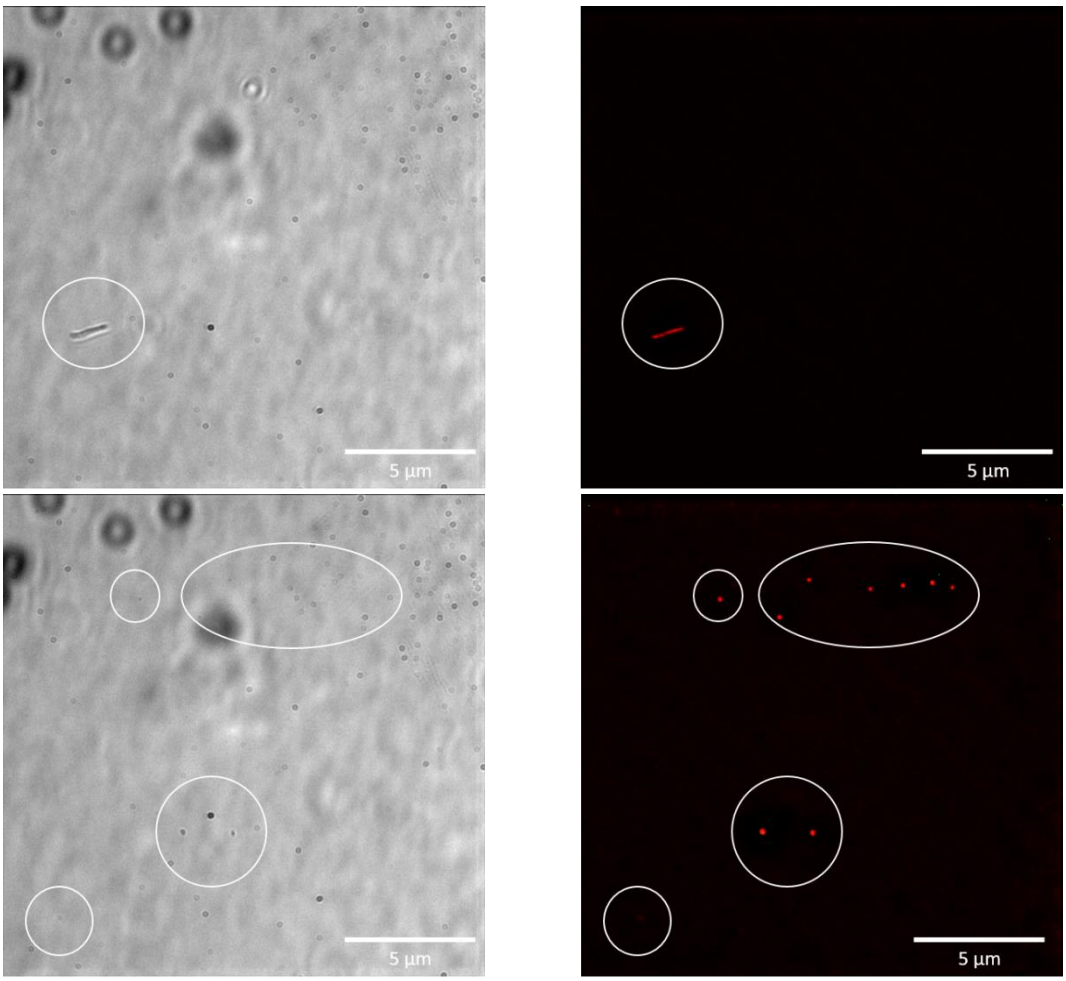

Figure S246 - A selection of transmitted light images (left) and DAPI filter composite images (right) of compound **5** at a concentration of 0.50 mM in a solution of DMSO: H_2O 1: 1. Evidence of aggregate formation are circled for clarity. Photo bleaching during the imagery lead to a loss of fluorescence emission intensity, therefore some compound aggregates could not be successfully captured in one (or both images).

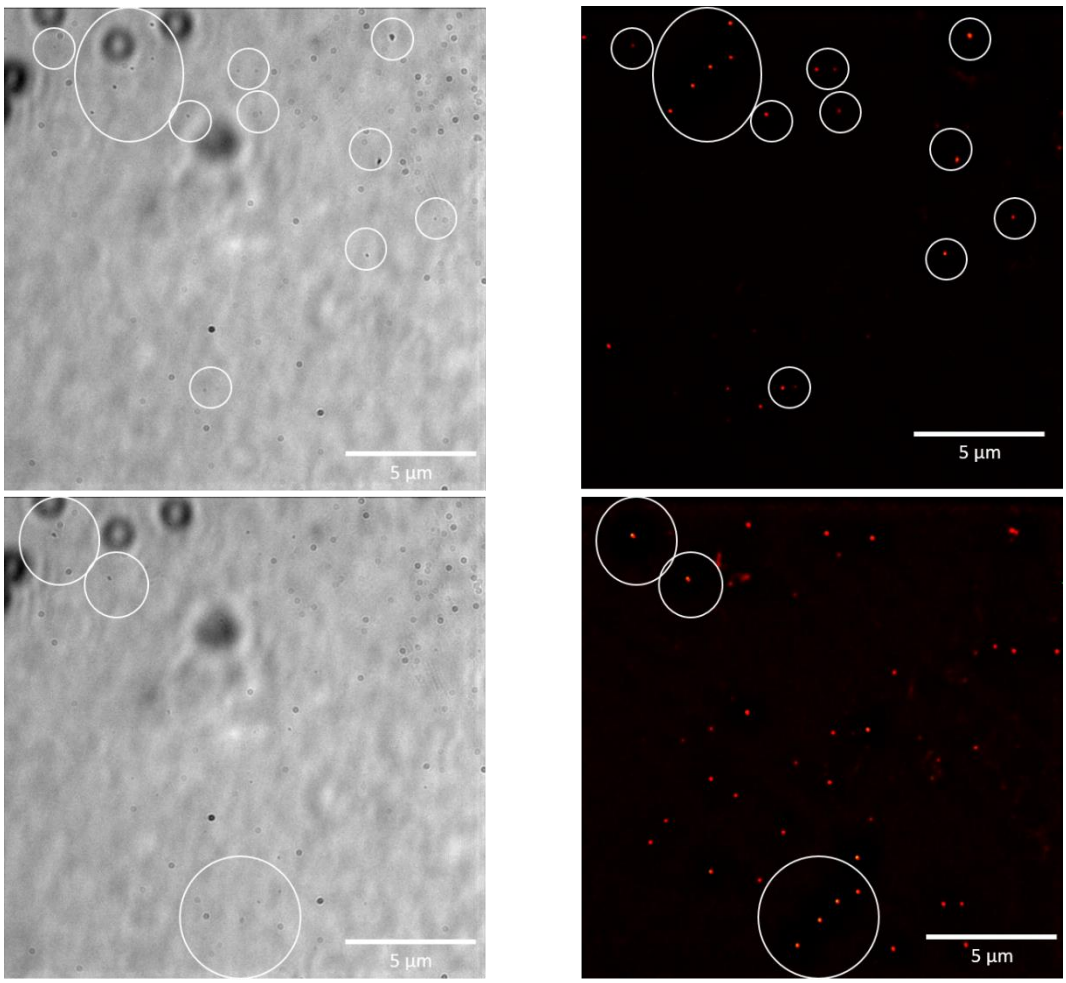

Figure S247 - A selection of transmitted light images (left) and DAPI/ GFP filter overlay images (right) of compound **5** at a concentration of 0.50 mM in a solution of DMSO: H_2O 3: 7. Evidence of aggregate formations are circled for clarity. Photo bleaching during the imagery lead to a loss of fluorescence emission intensity, therefore some compound aggregates could not be successfully captured in one (or both images).

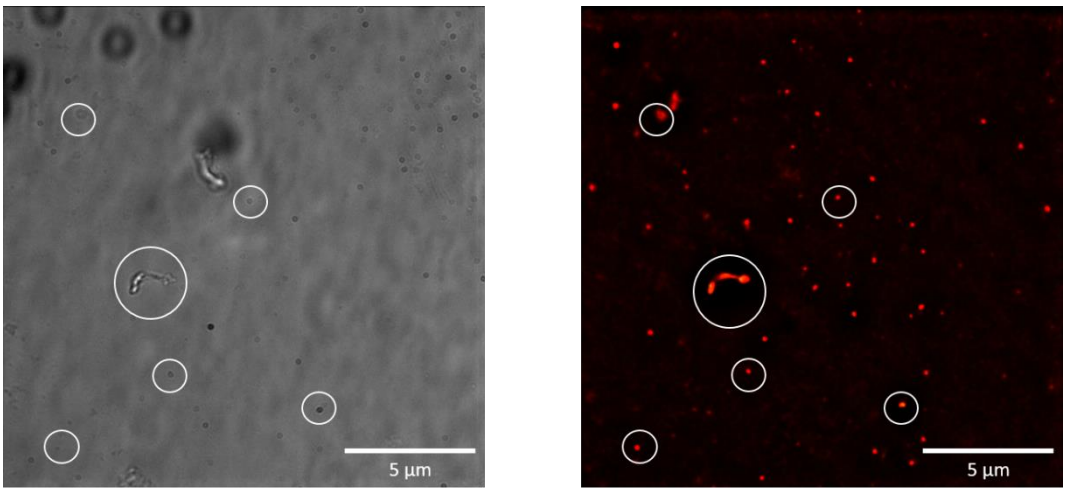

Figure S248 - A selection from transmitted light images (left) and comparison DAPI/ GFP filter overlay images (right) of compound **5** at a concentration of 0.50 mM in a solution of DMSO 1: 4 H_2O Evidence of aggregate formations are circled for clarity. Photo bleaching during the imagery lead to a loss of fluorescence emission intensity, therefore some compound aggregates could not be successfully captured in one (or both images).

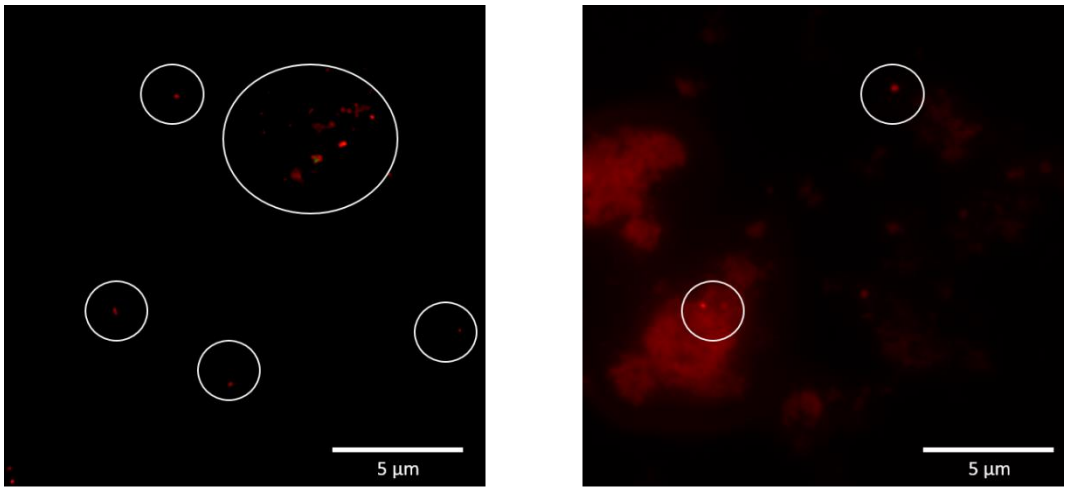

Figure S249 - A selection of DAPI filter images of compound **5** at a concentration of 0.50 mM in DMSO. Evidence of aggregate formations are circled for clarity. Photo bleaching during the imagery lead to a loss of fluorescence emission intensity, therefore some compound aggregates could not be successfully captured in one (or both images).

In-silico modelling

Computational calculations for compounds **1**-**5** were conducted in line with studies reported by Hunter using Spartan 16'' in order to identify primary hydrogen bond donating and accepting sites.[3] Calculations were performed using semi-empirical PM6 methods to model electrostatic potential maps and identify corresponding E_{max} and E_{min} values. PM6 was used over AM1 in line with research conducted by Stewart.[4]

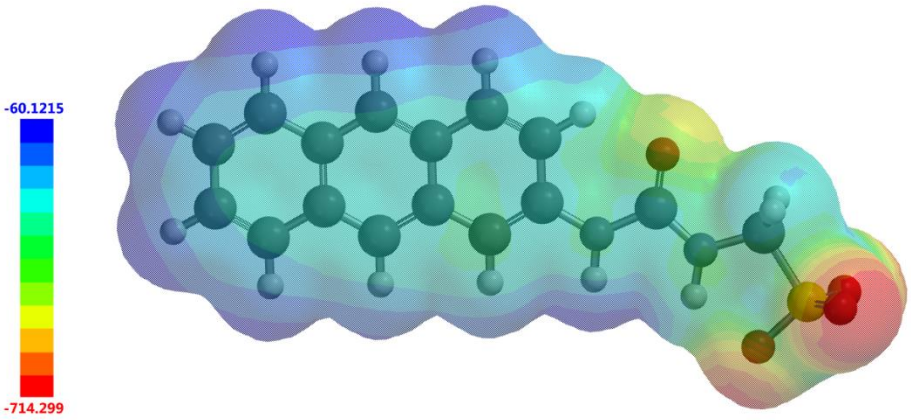

Figure S250 - Electrostatic potential map calculated for **1** using semi-empirical PM6 modelling methods. E_{max} and E_{min} values depicted in the figure legends are given in KJ/mol.

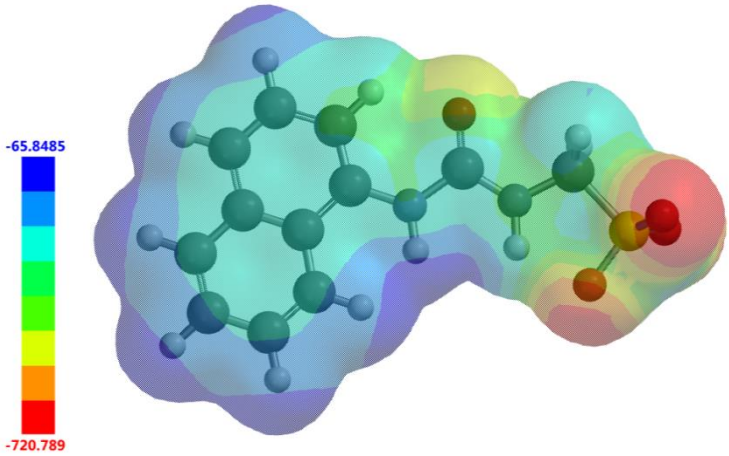

Figure S251 - Electrostatic potential map calculated for **2** using semi-empirical PM6 modelling methods. E_{max} and E_{min} values depicted in the figure legends are given in KJ/mol.

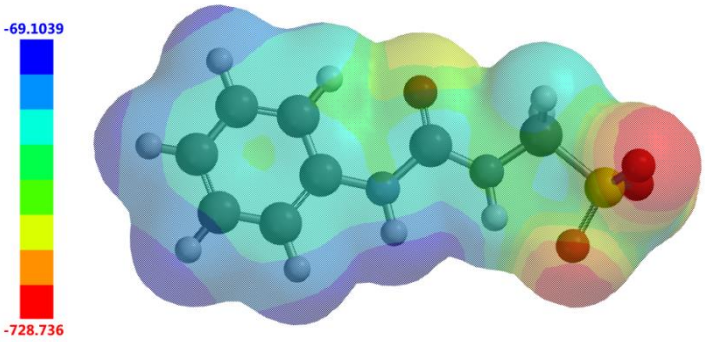

Figure S252 - Electrostatic potential map calculated for **3** using semi-empirical PM6 modelling methods. E_{max} and E_{min} values depicted in the figure legends are given in KJ/mol.

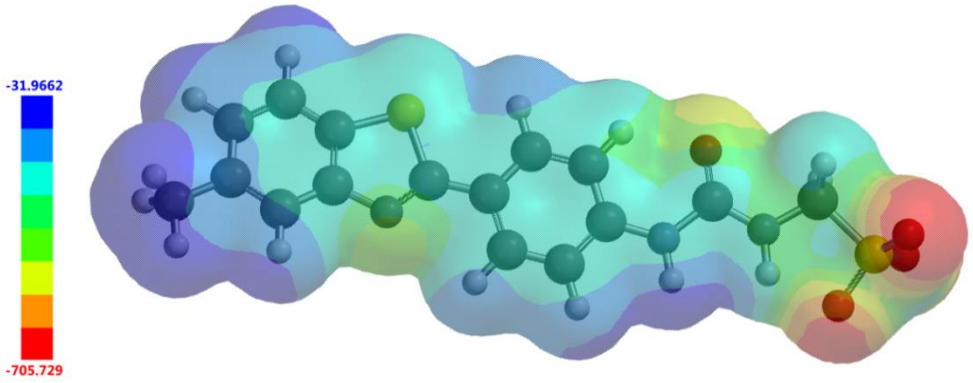

Figure S253 - Electrostatic potential map calculated for **4** using semi-empirical PM6 modelling methods. E_{max} and E_{min} values depicted in the figure legends are given in KJ/mol.

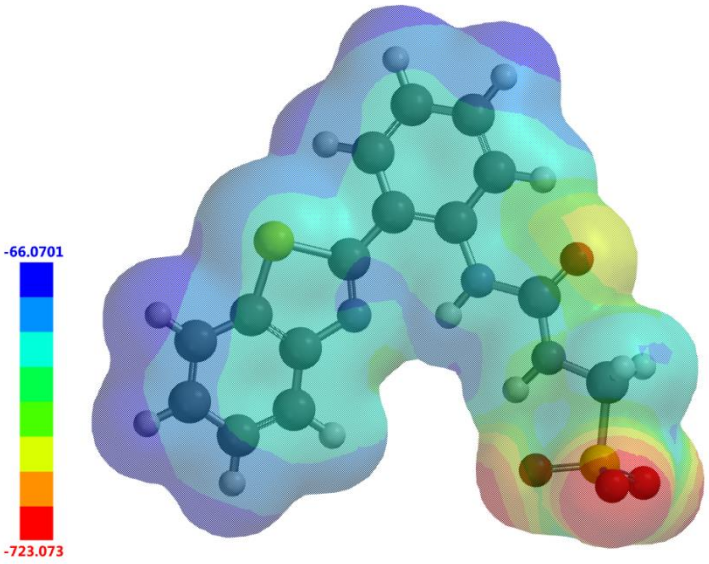

Figure S254 - Electrostatic potential map calculated for **5** using semi-empirical PM6 modelling methods. E_{max} and E_{min} values depicted in the figure legends are given in KJ/mol.

Mass Spectrum Data

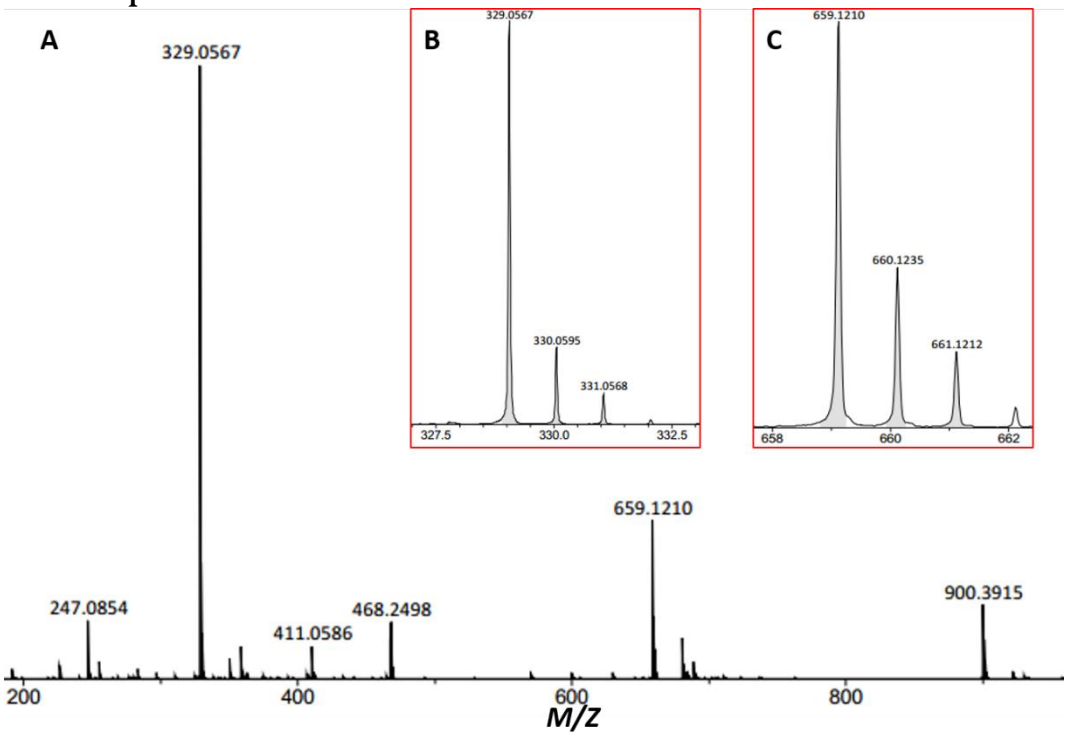

Figure S255 – Electrospray mass spectrometry spectrum of compound **1**, showing both the monomeric and protonated dimeric species (A), monomeric species (B) and protonated dimeric species (C).

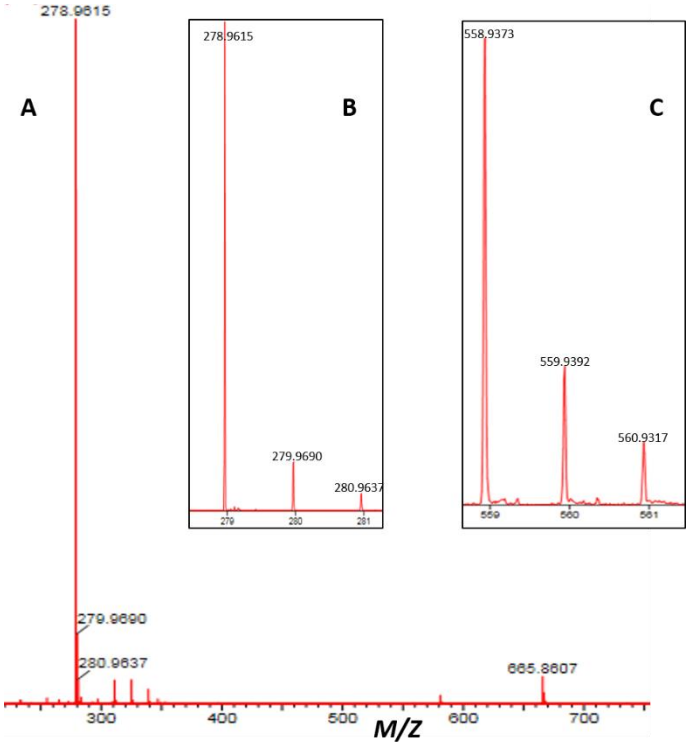

Figure S256 – Electrospray mass spectrometry spectrum of compound **2**, showing both the monomeric and protonated dimeric species (A), monomeric species (B) and protonated dimeric species (C). Analysed using Mass Lynx software.

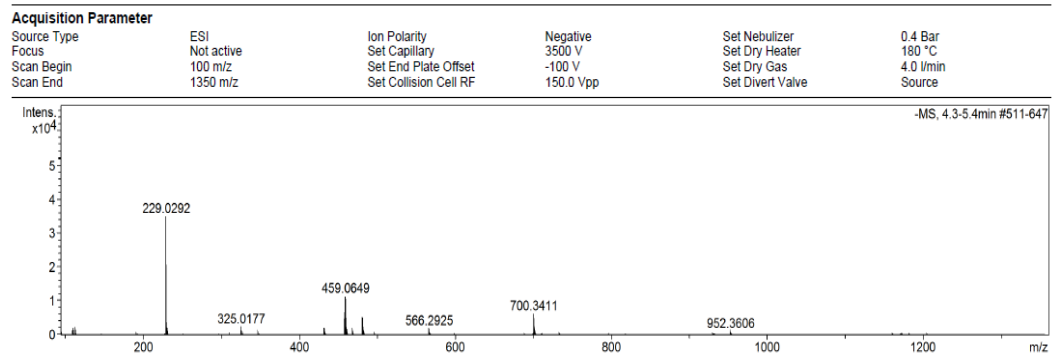

Figure S257 – Mass spectrum collected for compound **3**.

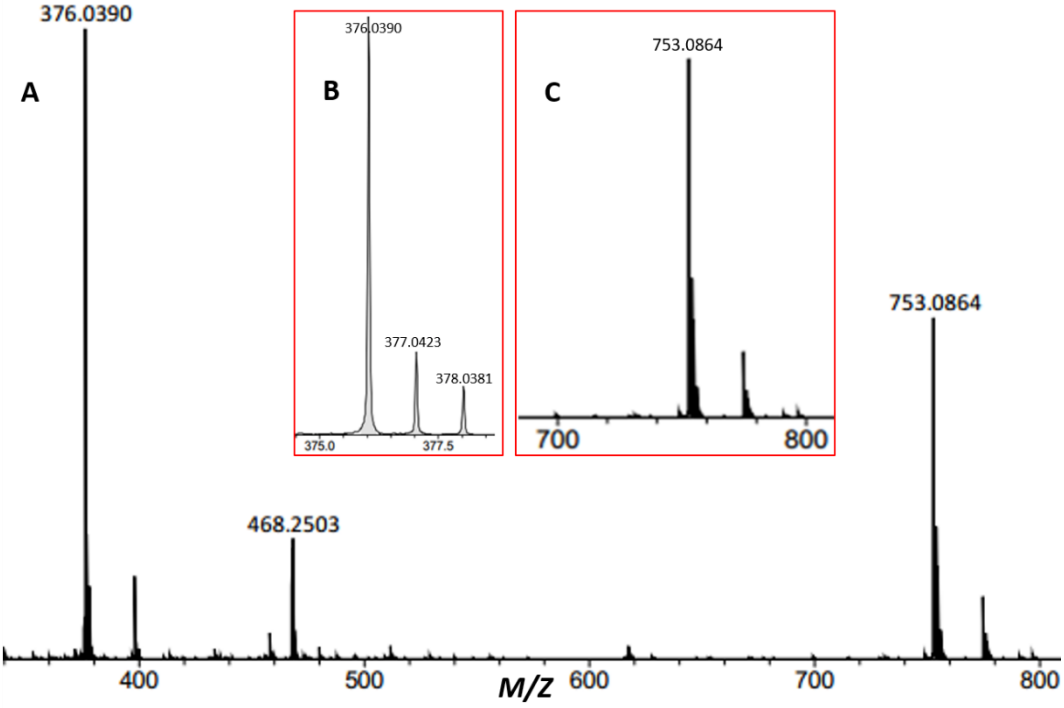

Figure S258 – Electrospray mass spectrometry spectrum of compound **4**, showing both the monomeric and protonated dimeric species (A), monomeric species (B) and protonated dimeric species (C).

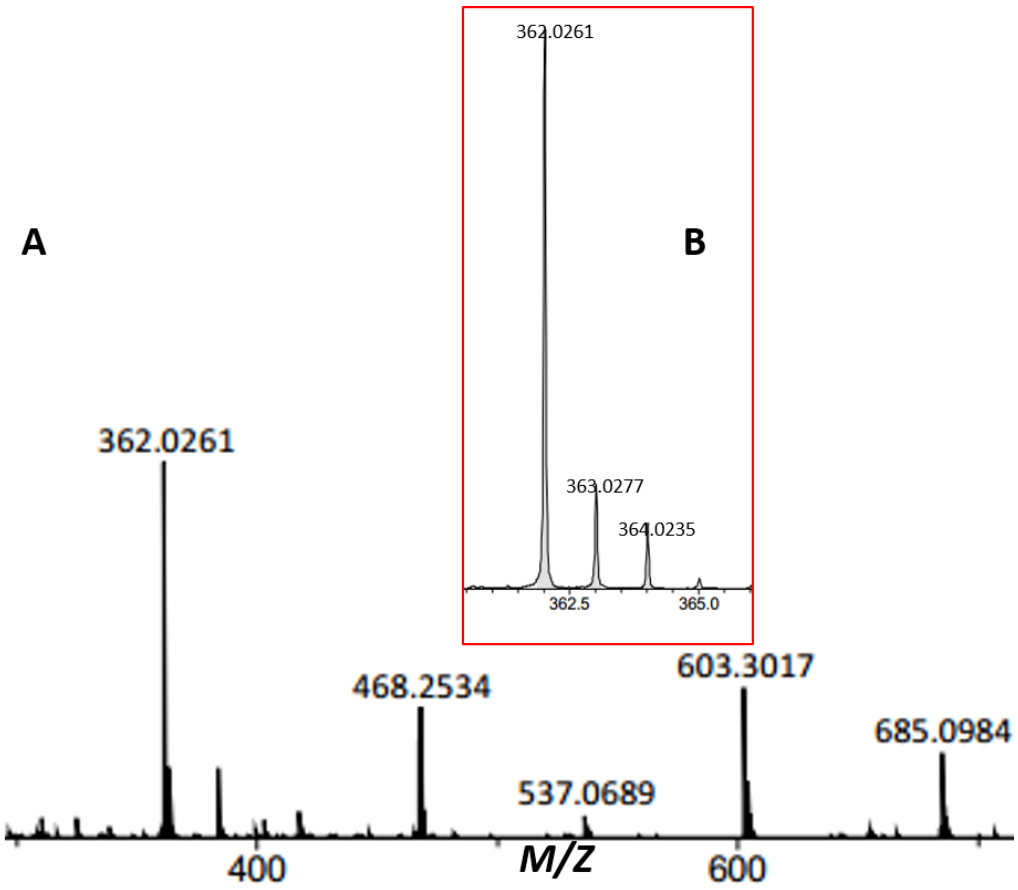

Figure S259 – Electrospray mass spectrometry spectrum of compound **5**, showing both the monomeric and protonated dimeric species (A) and monomeric species (B)

References

1. Levin, P.A. (2002) Light microscopy techniques for bacterial cell biology. In *Methods in Microbiology: Molecular Cellular Microbiology*, Vol. **31**. Sansonetti, P., and Zychlinsky, A. (eds). London: Academic Press Ltd., pp. 115–132.
2. L. R. Blackholly, H. J. Shepherd and J. R. Hiscock, *Crystengcomm*, 2016, **18**, 7021-7028.
3. C. A. Hunter, *Angewandte Chemie-International Edition*, 2004, **43**, 5310-5324.
4. J. J. P. Stewart, *Journal of Molecular Modeling*, 2007, **13**, 1173-1213.